

Green Energy and Technology

Kazunari Sasaki

Hai-Wen Li

Akari Hayashi

Junichiro Yamabe

Teppei Ogura

Stephen M. Lyth *Editors*



Hydrogen Energy Engineering

A Japanese Perspective

 Springer

Green Energy and Technology

More information about this series at <http://www.springer.com/series/8059>



Ceremony for the inauguration of the MIRAI fuel cell vehicle on March 25, 2015, in front of the hydrogen station at Kyushu University



Ceremony marking the start of operation of a 250 kW-class solid oxide fuel cell power generation system coupled with micro gas turbine at Kyushu University, on March 13, 2015

Kazunari Sasaki · Hai-Wen Li
Akari Hayashi · Junichiro Yamabe
Teppei Ogura · Stephen M. Lyth
Editors

Hydrogen Energy Engineering

A Japanese Perspective

 Springer

Editors

Kazunari Sasaki
Kyushu University
Fukuoka
Japan

Junichiro Yamabe
Kyushu University
Fukuoka
Japan

Hai-Wen Li
Kyushu University
Fukuoka
Japan

Teppei Ogura
Kyushu University
Fukuoka
Japan

Akari Hayashi
Kyushu University
Fukuoka
Japan

Stephen M. Lyth
Kyushu University
Fukuoka
Japan

ISSN 1865-3529

Green Energy and Technology

ISBN 978-4-431-56040-1

DOI 10.1007/978-4-431-56042-5

ISSN 1865-3537 (electronic)

ISBN 978-4-431-56042-5 (eBook)

Library of Congress Control Number: 2016943389

© Springer Japan 2016

This work is subject to copyright. All rights are reserved by the Publisher, whether the whole or part of the material is concerned, specifically the rights of translation, reprinting, reuse of illustrations, recitation, broadcasting, reproduction on microfilms or in any other physical way, and transmission or information storage and retrieval, electronic adaptation, computer software, or by similar or dissimilar methodology now known or hereafter developed.

The use of general descriptive names, registered names, trademarks, service marks, etc. in this publication does not imply, even in the absence of a specific statement, that such names are exempt from the relevant protective laws and regulations and therefore free for general use.

The publisher, the authors and the editors are safe to assume that the advice and information in this book are believed to be true and accurate at the date of publication. Neither the publisher nor the authors or the editors give a warranty, express or implied, with respect to the material contained herein or for any errors or omissions that may have been made.

Printed on acid-free paper

This Springer imprint is published by Springer Nature
The registered company is Springer Japan KK

Preface

The purpose of this book is to give an overview of hydrogen energy engineering, especially from a Japanese perspective. After decades of research, development, and demonstration, the era of practical fuel cells and related hydrogen technologies has just begun. Commercial products are now available for daily life in various applications such as residential stationary fuel cells for powering houses and small businesses, and in fuel cell vehicles. There is a steady acceleration in research activities directed towards the wider application of these technologies.

Besides such technological efforts, academics have a responsibility to establish scientific disciplines within this engineering field. Because hydrogen gas is a secondary-energy carrier (like electricity), a comprehensive understanding of hydrogen-related technologies is essential. This should cover the whole process including hydrogen production, storage, and utilization. Relevant scientific disciplines such as electrochemistry and materials science are regarded as important fundamental areas for research, and special emphasis should be placed on the interaction of materials with hydrogen. As we have learned from the Fukushima disaster in Japan, safety is an essential aspect of hydrogen energy technologies, as with other energy engineering fields. In particular, we have to manage high-pressure hydrogen gas. Therefore, fundamental understanding of this issue should be researched, published, and compiled to establish safe design principles.

Considerable efforts have been made globally in these fields; however, Japan can take a leadership role by sharing recent experience in hydrogen-related technologies. Such technology sharing could increase the feasibility of hydrogen use all over the world. We are especially happy to share our experience with young students and researchers, because it is exciting to work in an environment where many new challenges are fully supported by society as a whole.

Compiling the very broad aspects of hydrogen energy into a single volume is a very difficult task. A decade ago, the International Research Center for Hydrogen Energy in Kyushu University's Ito Campus was founded in order to establish hydrogen energy engineering as a core subject in Japan. Such efforts have resulted

in the establishment of a highly collaborative and interdisciplinary team in Kyushu University focusing on hydrogen energy research.

We would like to acknowledge many organizations and individuals who have kindly supported our efforts. In particular, continuous support for the International Research Center for Hydrogen Energy from the Ministry of Education, Culture, Sports, Science and Technology (MEXT) is gratefully acknowledged. The Next-Generation Fuel Cell Research Center (NEXT-FC) was established through the funding from the Ministry of Economy, Trade and Industry (METI). Special support for various technological and demonstration projects on the Ito Campus in the “Smart Fuel Cell Demonstration Project” is gratefully acknowledged, from the Cabinet Secretariat and the Cabinet Office, approved by the Ministry of Finance (MOF), for the Fukuoka International Strategic Zone. Many original findings have been made by various research projects via the New Energy and Industrial Technology Development Organization (NEDO), the Japan Science and Technology Organization (JST), and the Japan Society for the Promotion of Science (JSPS) including a Grant-in-Aid for Scientific Research, the World Premier International Research Center Initiative (WPI), and the Center of Innovation (COI) program. Close collaboration with the local government of Fukuoka Prefecture is a unique feature of the Hydrogen Projects of Kyushu University, with the significant and enthusiastic support from current Governor Hiroshi Ogawa and former Governor Wataru Aso. Continuous support and encouragement from the president of Kyushu University, Dr. Chiharu Kubo, and former presidents, Dr. Setsuo Arikawa and Dr. Chisato Kajiyama, are gratefully recognized. We also thank our industry partners for their continuous collaborations through NEXT-FC and other centers. Finally, we wish to thank many senior collaborators: Prof. Emer. Dr. Yukitaka Murakami, who initiated this hydrogen project; many professors in the Department of Mechanical Engineering; and many visiting professors including Prof. Dr. Harry L. Tuller (MIT), Prof. Dr. Ludwig J. Gauckler (ETH), Prof. Dr. John Kilner (Imperial College London), Prof. Dr. Kenichiro Ota (Yokohama National University), and Prof. Dr. Masahiro Watanabe (University of Yamanashi), whose encouragement has made this comprehensive book into a reality. We also wish to thank our colleagues who have helped so much in the finalization of this manuscript: Ms. Ayumi Zaito, Dr. Haruomi Hasuo, and Ms. Miki Fujita for editorial support and project management, as well as Dr. Nicola H. Perry, Dr. George F. Harrington, and Dr. Benjamin V. Cunnings for helping to edit the manuscript.

Fukuoka, Japan
December 2015

Kazunari Sasaki
Hai-Wen Li
Akari Hayashi
Junichiro Yamabe
Teppei Ogura
Stephen M. Lyth

Contents

Part I General Introduction

1	Why Hydrogen? Why Fuel Cells?	3
	Kazunari Sasaki	
2	Current Status: General.	15
	Kazunari Sasaki	
3	Current Status: Global.	37
	Akiteru Maruta	
4	Development Histories: Hydrogen Technologies.	53
	Kazukiyo Okano	
5	Development Histories: Fuel Cell Technologies	93
	Kazukiyo Okano	
6	Future Technological Directions	117
	Kazukiyo Okano, Akiteru Maruta and Kazunari Sasaki	

Part II Hydrogen Production

7	Introduction	123
	Stephen M. Lyth and Aleksandar Staykov	
8	Steam Reforming.	127
	Yusuke Shiratori, Quang-Tuyen Tran, Teppei Ogura, Osamu Higashi, Stephen M. Lyth and Masaki Tajima	
9	Alkaline Water Electrolysis	137
	Kohei Ito, Hua Li and Yan Ming Hao	
10	Polymer Electrolyte Membrane Water Electrolysis	143
	Kohei Ito, Takuya Sakaguchi and Yuta Tsuchiya	

11 Steam Electrolysis	151
Hiroshige Matsumoto and Kwati Leonard	
12 Photocatalytic Water Splitting	159
Aleksandar Staykov, Stephen M. Lyth and Motonori Watanabe	
Part III Hydrogen Storage	
13 Fundamentals	177
Etsuo Akiba	
14 Solid Hydrogen Storage Materials: Interstitial Hydrides	191
Etsuo Akiba	
15 Solid Hydrogen Storage Materials: Non-interstitial Hydrides	207
Hai-Wen Li, Guotao Wu, Teng He and Ping Chen	
16 Solid Hydrogen Storage Materials: High Surface Area Adsorbents	241
Huaiyu Shao and Stephen M. Lyth	
17 Liquid Hydrogen Carriers	253
Hai-Wen Li	
18 Compressed Hydrogen: Thermophysical Properties	265
Naoya Sakoda	
19 Compressed Hydrogen: High-Pressure Hydrogen Tanks	273
Hai-Wen Li and Kiyooki Onoue	
20 Hydrogen Storage: Conclusions and Future Perspectives	279
Hai-Wen Li and Etsuo Akiba	
Part IV Hydrogen Utilization	
21 Fundamentals	285
Akari Hayashi and Kazunari Sasaki	
22 Polymer Electrolyte Fuel Cells (PEFCs)	301
Akari Hayashi, Masamichi Nishihara, Junko Matsuda and Kazunari Sasaki	
23 Solid Oxide Fuel Cells (SOFCs)	313
Kazunari Sasaki, Yusuke Shiratori, Shunsuke Taniguchi and Akari Hayashi	
24 Alkaline Electrolyte Fuel Cells (AFCs)	325
Akari Hayashi, Tsuyohiko Fujigaya and Naotoshi Nakashima	
25 Hydrogen Combustion Systems	335
Koji Takasaki and Hiroshi Tajima	

Part V Hydrogen Safety

26 Hydrogen Safety Fundamentals	359
Junichiro Yamabe and Saburo Matsuoka	
27 Hydrogen Gas Safety Management	385
Masahiro Inoue	
28 Hydrogen Safety in Practice	397
Junichiro Yamabe and Nobuhiro Kuriyama	
29 Effect of Hydrogen on the Tensile Properties of Metals	403
Shigeru Hamada	
30 Effect of Hydrogen on Fatigue Properties of Metals	411
Hisao Matsunaga	
31 Effect of Hydrogen on the Fretting Fatigue Properties of Metals	427
Masanobu Kubota	
32 Structural Design and Testing	439
Junichiro Yamabe	
33 Future Perspectives	453
Junichiro Yamabe	

Part VI Applications and Perspectives

34 Development of the MIRAI Fuel Cell Vehicle	461
Yoshikazu Tanaka	
35 Residential Applications: ENE-FARM	477
Yoshio Matsuzaki	
36 Distributed Power Generation	483
Yoshinori Kobayashi	
37 Triple Combined Cycle Power Generation	497
Yoshinori Kobayashi	
38 Fuel Cells with Biofuels	507
Yusuke Shiratori and Quang-Tuyen Tran	
39 Portable Applications	523
Masaru Tsuchiya	
40 Hydrogen Infrastructure	537
Hideyuki Dohi, Masahiro Kasai and Kiyooki Onoue	
41 Business Model Analysis of Hydrogen Energy	549
Megumi Takata	

42	Public Acceptance	561
	Kenshi Itaoka, Aya Saito and Kazunari Sasaki	
43	Numerical Analysis of the Optimal Distribution of Hydrogen Filling Stations.	581
	Yuya Tachikawa, Teppei Sugiura, Motoaki Shiga, Ryusuke Chiyo and Kazunari Sasaki	
44	Hydrogen Energy Education	587
	Kazunari Sasaki and Kohei Ito	

Contributors

Etsuo Akiba Department of Mechanical Engineering, Faculty of Engineering, Kyushu University, Fukuoka, Japan

Ping Chen Dalian National Laboratory for Clean Energy, Dalian Institute of Chemical Physics, Chinese Academy of Sciences, Dalian, People's Republic of China

Ryusuke Chiyo Kozo Keikaku Engineering Inc., Nakano-Ku, Tokyo, Japan

Hideyuki Dohi International Research Center for Hydrogen Energy, Kyushu University, Fukuoka, Japan

Tsuyohiko Fujigaya Department of Applied Chemistry, Kyushu University, Fukuoka, Japan

Shigeru Hamada Department of Mechanical Engineering, Kyushu University, Fukuoka, Japan

Yan Ming Hao Department of Hydrogen Energy Systems, Faculty of Engineering, Kyushu University, Fukuoka, Japan

Akari Hayashi International Research Center for Hydrogen Energy, Kyushu University, Fukuoka, Japan

Teng He Dalian National Laboratory for Clean Energy, Dalian Institute of Chemical Physics, Chinese Academy of Sciences, Dalian, People's Republic of China

Osamu Higashi Graduate School for International Development and Cooperation, Hiroshima University, Higashi-Hiroshima, Japan

Masahiro Inoue Department of Earth Resources Engineering, Kyushu University, Fukuoka, Japan

Kenshi Itaoka International Institute for Carbon-Neutral Energy Research (I2CNER), Kyushu University, Fukuoka, Japan

Kohei Ito Department of Hydrogen Energy Systems, Faculty of Engineering, Kyushu University, Fukuoka, Japan

Masahiro Kasai International Research Center for Hydrogen Energy, Kyushu University, Fukuoka, Japan

Yoshinori Kobayashi Mitsubishi Hitachi Power Systems Ltd., Nishi-ku, Yokohama, Japan; The Institute of Industrial Science (IIS), The University of Tokyo, Meguro-ku, Tokyo, Japan

Masanobu Kubota International Institute for Carbon-Neutral Energy Research (I2CNER), Kyushu University, Fukuoka, Japan

Nobuhiro Kuriyama Research Institute of Electrochemical Energy Department of Energy and Environment, National Institute of Advanced Industrial Science and Technology, Osaka, Japan

Kwati Leonard International Institute for Carbon-Neutral Energy Research (WPI-I2CNER), Kyushu University, Fukuoka, Japan

Hai-Wen Li International Research Center for Hydrogen Energy, Kyushu University, Fukuoka, Japan

Hua Li Department of Hydrogen Energy Systems, Faculty of Engineering, Kyushu University, Fukuoka, Japan

Stephen M. Lyth International Institute for Carbon-Neutral Energy Research (WPI-I2CNER), Kyushu University, Fukuoka, Japan

Akiteru Maruta Technova Inc., Chiyoda-ku, Tokyo, Japan

Junko Matsuda International Institute for Carbon-Neutral Energy Research, Kyushu University, Fukuoka, Japan

Hiroshige Matsumoto International Institute for Carbon-Neutral Energy Research (WPI-I2CNER), Kyushu University, Fukuoka, Japan

Hisao Matsunaga Department of Mechanical Engineering, Kyushu University, Fukuoka, Japan

Saburo Matsuoka Research Center for Hydrogen Industrial Use and Storage (HYDROEGNIUS), Kyushu University, Fukuoka, Japan

Yoshio Matsuzaki Fundamental Technology Department, Tokyo Gas Co., Ltd., Minato-ku, Tokyo, Japan; Kyushu University, Fukuoka, Japan

Naotoshi Nakashima Department of Applied Chemistry, Kyushu University, Fukuoka, Japan

Masamichi Nishihara International Institute for Carbon-Neutral Energy Research, Kyushu University, Fukuoka, Japan

Tepppei Ogura School of Science and Technology, Kwansai Gakuin University, Sanda, Hyogo, Japan; Kyushu University, Fukuoka, Japan

Kazukiyo Okano Kyushu University, Ichihara-shi, Chiba, Japan

Kiyoaki Onoue Office for the Promotion of Safety and Health, Kyushu University, Fukuoka, Japan

Aya Saito Mizuho Information and Research Institute Inc., Tokyo, Japan

Takuya Sakaguchi Department of Hydrogen Energy Systems, Faculty of Engineering, Kyushu University, Fukuoka, Japan

Naoya Sakoda Department of Mechanical Engineering, Faculty of Engineering, Kyushu University, Fukuoka, Japan

Kazunari Sasaki International Research Center for Hydrogen Energy, Kyushu University, Nishi-ku, Fukuoka, Japan

Huaiyu Shao International Institute for Carbon-Neutral Energy Research, Kyushu University, Fukuoka, Japan

Motoaki Shiga Kozo Keikaku Engineering Inc., Nakano-Ku, Tokyo, Japan

Yusuke Shiratori Department of Mechanical Engineering, Faculty of Engineering, Kyushu University, Fukuoka, Japan

Aleksandar Staykov International Institute for Carbon-Neutral Energy Research (WPI-I2CNER), Kyushu University, Fukuoka, Japan

Tepppei Sugiura Kozo Keikaku Engineering Inc., Nakano-Ku, Tokyo, Japan

Yuya Tachikawa Center for Co-Evolutional Social Systems (CESS), Kyushu University, Nishi-ku, Fukuoka, Japan

Hiroshi Tajima Department of Energy and Environmental Engineering, Faculty of Engineering Sciences, Kyushu University, Fukuoka, Japan

Masaki Tajima Institute of Innovative Technology for the Earth, Minato-Ku, Tokyo, Japan

Koji Takasaki Department of Energy and Environmental Engineering, Faculty of Engineering Sciences, Kyushu University, Fukuoka, Japan

Megumi Takata Department of Business and Technology Management (Business School), Faculty of Economics, Kyushu University, Fukuoka, Japan

Yoshikazu Tanaka Toyota Motor Corporation, Toyota City, Aichi Prefecture, Japan

Shunsuke Taniguchi International Research Center for Hydrogen Energy, Kyushu University, Fukuoka, Japan

Quang-Tuyen Tran International Research Center for Hydrogen Energy, Kyushu University, Fukuoka, Japan; Institute of Innovative Technology for the Earth, Minato-Ku, Tokyo, Japan

Masaru Tsuchiya SiEnergy Systems, LLC, Cambridge, MA, USA; Kyushu University, Fukuoka, Japan

Yuta Tsuchiya Department of Hydrogen Energy Systems, Faculty of Engineering, Kyushu University, Fukuoka, Japan

Motonori Watanabe WPI International Institute for Carbon-Neutral Energy Research (WPI-I2CNER), Kyushu University, Fukuoka, Japan

Guotao Wu Dalian National Laboratory for Clean Energy, Dalian Institute of Chemical Physics, Chinese Academy of Sciences, Dalian, People's Republic of China

Junichiro Yamabe International Research Center for Hydrogen Energy, Kyushu University, Fukuoka, Japan

Part I

General Introduction

Kazunari Sasaki¹⁻³ and Stephen M. Lyth⁴⁻⁶

¹International Research Center for Hydrogen Energy, Kyushu University, Fukuoka, Japan

²Next-Generation Fuel Cell Research Center (NEXT-FC), Kyushu University, Fukuoka, Japan

³International Institute for Carbon-Neutral Energy Research, Kyushu University, Fukuoka, Japan

⁴CREST Japan Science and Technology Corporation, Kawaguchi, Japan

⁵Department of Mechanical Engineering, Sheffield University, Sheffield, UK

⁶School of Chemical and Process Engineering, Leeds University, Leeds, UK

The introductory part of this book gives an overview of the history, development, and general perspectives of fuel cells and related hydrogen energy technologies. Global activities are summarized, while details of technological developments in Japan are described, as a country where actual demonstration and commercialization of fuel cells are underway, along with a strong social interest and clear governmental commitments over the past several decades.

Chapter 1

Why Hydrogen? Why Fuel Cells?

Kazunari Sasaki

Abstract This introductory chapter describes the reasons and motivation behind realizing a fuel cell-powered hydrogen society. After describing recent development progress in fuel cells and hydrogen technologies, possible technological, industrial, and social paradigm shifts are considered, with possible roadmaps.

Keywords Fuel cells · Hydrogen technology · Electrochemical energy conversion · Hydrogen-cycle · Paradigm shift

The phrase “hydrogen society” has recently gained popularity. The year 2015 has seen the use of hydrogen as a fuel for automobiles launched at full scale, and has become known as the first year of hydrogen. In Japan, full-fledged popularization of hydrogen and fuel cell technology has begun. Commercial sales of fuel cell vehicles (FCVs) have commenced (see Fig. 1.1 on the front cover page) and the establishment of hydrogen filling stations (also known as hydrogen refueling station), where hydrogen gas can be purchased is being guided by the government’s road-map plan. ENE-FARM residential fuel cell units were introduced into the market in 2009, and the cumulative number of sales has exceeded 150,000 in December 2015. The government has established a goal to install this technology in 10 % of all households by 2030, generating electricity as well as supplying hot water. Starting in 2017, Japan plans to launch commercial sales of fuel cell power generation systems at larger scale (see Fig. 1.2 on the front cover page), and commercialization of such technologies is currently being promoted [1–4].

In the U.S., sales of zero-emission vehicles are mandated at a certain ratio in states such as California, where CO₂ emission regulations are stringent. FCVs as well as electric vehicles (EVs) will be a key to meet such CO₂ emission reduction targets. Bloom Energy has already produced positive results by providing energy supply services that utilize industrial fuel cells in the mainland U.S. In Europe,

K. Sasaki (✉)

International Research Center for Hydrogen Energy, Kyushu University,
Fukuoka 819-0395, Japan
e-mail: sasaki@mech.kyushu-u.ac.jp

© Springer Japan 2016

K. Sasaki et al. (eds.), *Hydrogen Energy Engineering*,
Green Energy and Technology, DOI 10.1007/978-4-431-56042-5_1



Fig. 1.1 Ceremony for the inauguration of the MIRAI fuel cell vehicle on March 25, 2015, in front of the hydrogen station at Kyushu University



Fig. 1.2 Ceremony marking the start of operation of a 250 kW-class solid oxide fuel cell power generation system coupled with micro gas turbine at Kyushu University, on March 13, 2015

where hydrogen pipelines have already been established, hydrogen filling stations are being constructed and demonstration fuel cell buses are being driven around various cities in Europe. New technological developments for high-pressure gas systems have also been aggressively pursued. In addition, Europe is actively conducting research and development activities on so-called “power-to-gas technology,” which can be used to convert the highly fluctuating electric power from

renewable energy sources into hydrogen gas or methane gas. This gas can then be distributed via gas pipelines and stored for later use with the utilization of electrolyzer technology as the ratio of renewable energy increases in the overall energy mix.

Why hydrogen now? Why fuel cells? What is a hydrogen-powered society like, and what are the advantages and challenges to achieving it?

For countries like Japan with limited access to energy resources, stable supplies of energy to produce electricity, heat, vehicle fuel, and so forth strongly affect the national economy, and it is necessary to produce or acquire such resources at as low prices as possible. In Japan, the trade deficit has increased in recent years according to the Trade Statistics of Japan report issued by the Ministry of Finance, and the main cause for this trend is said to be the increase in energy imports. In both 2013 and 2014, the price paid for imports for fossil fuels such as natural gas, oil, and coal reached approximately 27 trillion yen (although this has decreased recently due to cheaper crude oil prices). At present, approximately 90 % of the electric power essential for the residential and industrial sectors is produced by thermal power plants. This situation cannot be avoided in the short term. According to an Energy White Paper, thermal power plants operating for 40 years or more comprise as much as 20 % of all plants in fiscal year 2013 based on facility capacity. It is therefore inevitable that there will be a switch to the latest power generation plant technology with much higher conversion efficiency.

Fuel cell technology extracts electricity from fuels that contain hydrogen, as described in Fig. 1.3 [6–13]. It involves a reverse water electrolysis reaction, and electricity can be extracted directly *without the combustion of fuel*. Hydrogen, which is used in this reaction, is the most abundant element on earth and hydrogen gas can be formed through various different methods. For example, it is possible to supply hydrogen gas that is a byproduct of oil refining, steel milling, and soda electrolysis as a fuel for vehicles. It is also possible to extract hydrogen gas from hydrocarbon fuels, which are rich in hydrogen atoms, and this can be done by utilizing the existing energy supply networks for city gas and liquefied petroleum gas (LP gas). If hydrogen gas becomes widely available as a fuel for vehicles, the automotive industry and our daily transportation will no longer depend on crude oil, and this would contribute to our energy security. It would also make it easier to implement exhaust gas regulations in each country.

While the fuel for FCVs is generally pure hydrogen gas, other hydrogen-rich fuels such as hydrocarbons (e.g., city gas) in addition to pure hydrogen gas can be used for fuel cell power generation. Since power is generated with high energy conversion efficiency in a fuel cell, it is possible to reduce the amount of fossil fuels necessary to extract the same quantity of electricity from conventional sources; this will eventually lead to energy savings and reductions in CO₂ emissions. In other words, hydrogen society, (as shown in Fig. 1.4), can be achieved through the popularization of fuel cells that generate power via electrochemical reactions associated with hydrogen. The advantages of high-efficiency electricity extraction are not limited to residential or automotive purposes. Such technology can also be utilized in industrial applications at scales of several kilowatts to several hundreds

Energy System WITHOUT Combustion !

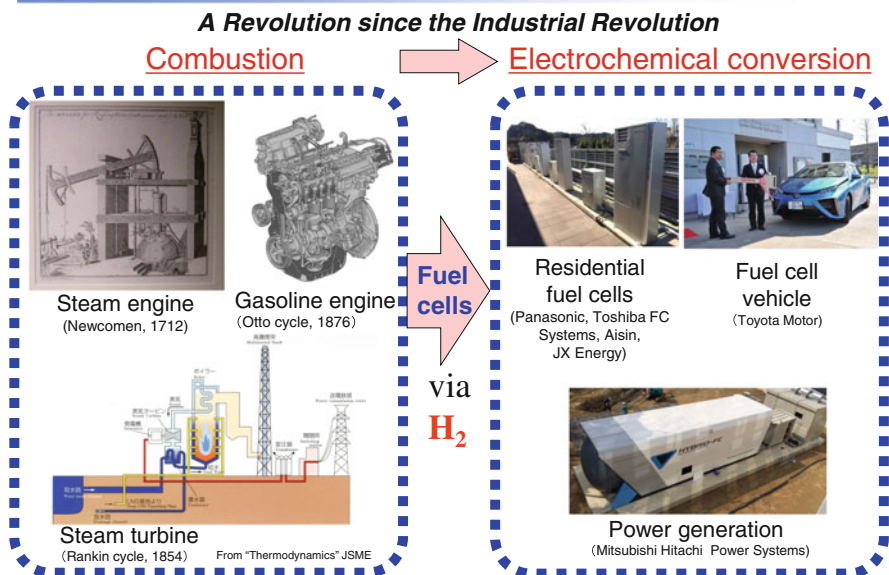


Fig. 1.3 The transition from combustion [5] to electrochemical energy conversion: “From Fire to Water”



Fig. 1.4 Wider applications with both polymer electrolyte fuel cells (PEFCs) and solid oxide fuel cells (SOFCs)

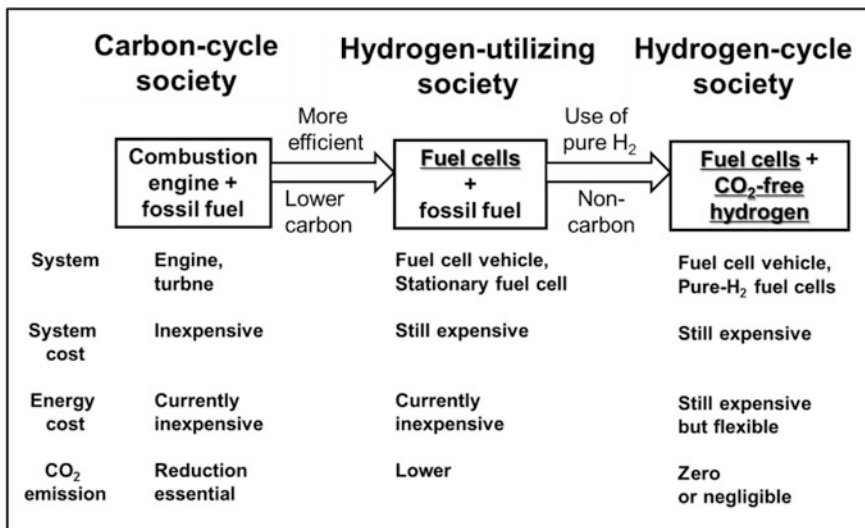


Fig. 1.5 Transition towards a hydrogen-powered society

of kilowatts and in power generation applications at even larger scales. Conversely, small portable applications are also possible. New technological development research is also targeting aerospace and marine applications (see Fig. 1.4).

In 2015, the global average CO₂ concentration exceeded 400 ppm. Pressure has been put on advanced countries, which have emitted considerable quantities of CO₂ in the past, to reduce their CO₂ emissions. In the future, when dramatic reductions of CO₂ emissions will be required internationally, we will probably gradually shift toward becoming a *hydrogen-utilizing society*, and eventually a *hydrogen-cycle society*, as demonstrated in Fig. 1.5, through full deployment of pure hydrogen gas resources that do not emit CO₂. The 2015 United Nations Climate Change Conference (COP21) held in Paris in November–December 2015 requested that the countries should aim to achieve carbon neutrality by the second half of this century [14].

By utilizing methane gas from sewage treatment plants, excess renewable electricity that is not sent through the power grid, CO₂-free hydrogen is produced from unused resources, and so forth it will no longer be just a dream to build carbon-free motorized societies.

Renewable energy output is strongly affected by the weather and other factors, and the supplies fluctuate accordingly. Therefore, systems to store such energy as hydrogen are being developed. This hydrogen can be produced via water electrolysis reactions using the excess electricity from times of renewable energy surplus. If we can master hydrogen energy storage technology, this will become a mainstay of medium-scale energy storage options along with conventional storage batteries and pumped-storage power plants. With this, the capacity to utilize more renewable energy resources will be higher. Since it will be possible to extract electricity or

hydrogen from energy sources within each region, local energy production for local consumption will become commonplace. Additionally, much of the economic gains from this decentralized energy production will likely remain in the area where they will stimulate local economic activity and foster self-reliant communities, unlike the current situation where economic gains from energy production typically flow out of communities. However, it will be necessary to carefully consider the total costs, efficiencies, and CO₂ emissions when utilizing renewable energy resources in local communities.

As is evident from the information presented above, the potential for hydrogen energy deployment using fuel cells as the core technology is extremely high, but it will naturally take some time to develop a hydrogen-powered society, as this would necessitate many societal changes. Although there are many challenges, at first, governments along with the private sector can facilitate the development of hydrogen energy infrastructure. In particular, the establishment of a hydrogen filling station network is necessary to fully popularize FCVs. Although support from the government and so forth will be inevitable for the time being, it would be worthwhile to examine possibilities for making the filling stations into “energy convenience stores” where fossil fuels, electricity, and heat can all be supplied in one location. It is also possible to manufacture, store, and sell hydrogen from excess renewable energy, and to manufacture and sell biogas-derived hydrogen generated in sewage treatment plants or food/vegetable waste systems, as shown in Fig. 1.6. Reductions in the installation and maintenance costs of hydrogen filling stations are also essential. While mass production benefits through standardization and amendments of extremely stringent safety regulations are desired, it will be



Fig. 1.6 A renewable hydrogen filling station in Fukuoka City, where hydrogen gas is produced from digestion gas consisting of CH₄ and CO₂

important to understand the phenomenon of embrittlement in materials that come in contact with high-pressure hydrogen gas to provide the scientific basis for new more reasonable regulations.

Second, hydrogen fuel cells capable of high-efficiency power generation are expected to be key components of next-generation power generation systems in the trend of electricity and gas liberalization. By increasing power generation efficiency and reducing waste throughout the energy sector in the country, it will be possible to reduce CO₂ emissions. By employing fuel cells as a core technology, coupled with a gas turbine and a steam turbine, and using natural gas as the fuel (so-called, triple combined cycle power generation), it is possible, in principle, to construct a fuel cell-based power generation system with conversion efficiencies in excess of 70 %. It may also be possible to generate power with high efficiency using fuel cells by converting coal with a few restrictions into coal gas. While further technological innovations including cost reductions are needed prior to full popularization, this technology when deployed in a given country can result in considerable reductions in fuel imports as well as CO₂ emissions. In Japan, it makes sense to consider both public subsidy introduction programs and other schemes in which the costs for updating aging thermal power plants and developing new hydrogen-related energy technology can be compared to future reductions in fuel costs and CO₂ emissions. These benefits could be on the order of a trillion yen if significant fossil fuel reductions can be achieved. In order to reach a level at which it would be viable for the government, municipalities, energy businesses, users, and investors to start making widespread investments, it will be necessary to further reduce the system costs and improve power generation efficiency.

Lastly, to realize a hydrogen-powered society as illustrated in Fig. 1.7, it will be essential to show citizens what a hydrogen-powered society will look like, and ensure the public of its safety. Efforts should be made to raise public awareness before concerns arise about using fuel cells and hydrogen technology safely. As all

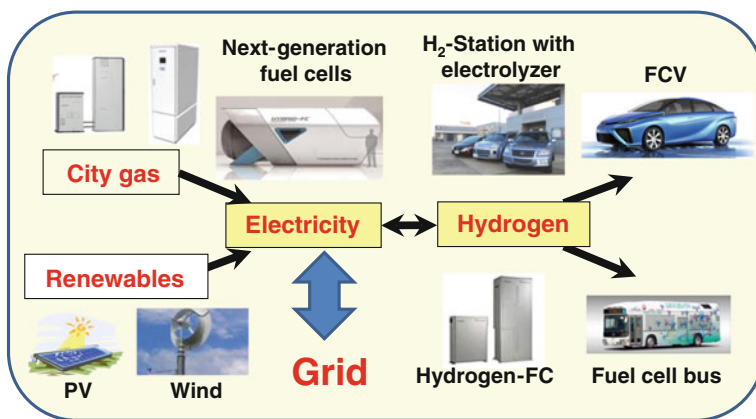


Fig. 1.7 A hydrogen-utilizing society

citizens will be using hydrogen gas, which poses explosion risks on a daily basis, it will be critical to implement hardware and software measures to reduce risks and ensure safe equipment use. This will entail the installation of leak sensors among other components. Additionally, educational programs will need to be developed to train users on the safe use of hydrogen gas. Public acceptance should also be enhanced by increasing awareness. In Japan, the Tokyo Olympics and Paralympics in 2020 will be a great opportunity to transmit information about hydrogen technology developments in Japan to the rest of the world. It is expected that the economic efficiencies and environmental advantages will have been proven by that time through demonstration studies across the country on hydrogen technology and large-scale fuel cells that utilize smart community and renewable energy infrastructure across the country. In fact, demonstration studies using hydrogen energy and fuel cells are already being implemented in many areas around the world.

Technological developments in the energy field often take several decades to be implemented fully. Meanwhile, a wide variety of related businesses such as maintenance and diagnostics will continue to develop for several decades in this field. A good strategy would be to develop such technologies in the midst of product development and start training human resources while the technology is still being developed and polished. Therefore, it will be important to provide young human resources access to training programs as part of the growth strategy. Given the prospects for future global developments, it is expected that doctoral-level training will be required for some human resources so that they can act globally to lead popularization efforts.

Full popularization of hydrogen energy has the potential to overturn conventional assumptions about energy and bring about great changes in industry and society. If such changes manifest, they should be aptly referred to as the “hydrogen revolution.” Potential paradigm shifts in technology, industry, and society that could ensue are listed below (see also Fig. 1.8).

Technological Paradigm Shifts

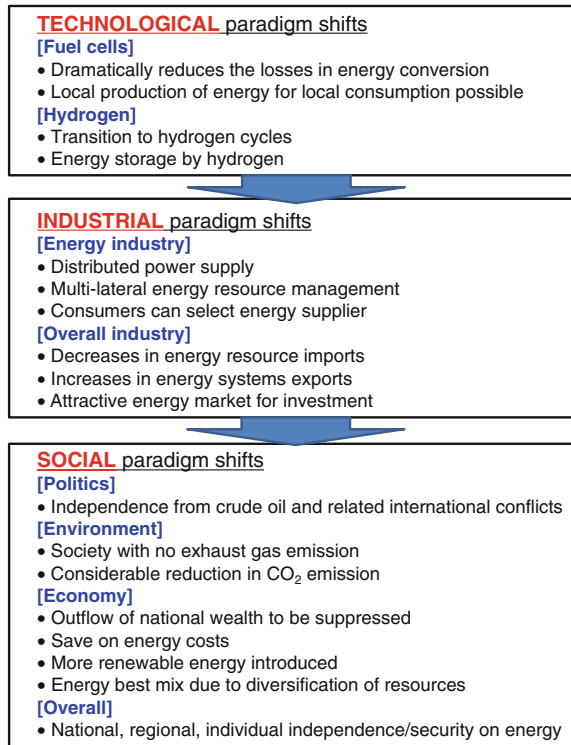
[Fuel Cells] (Conversion of chemical energy directly into electricity)

- Fuel cells exceed the efficiency limit for thermal engines and dramatically reduce losses in energy conversion.
- Fuel cells enable decentralized energy systems that are capable of *local production of energy for local consumption*.

[Hydrogen] (Can be converted into electricity within fuel cells, for CO₂-free applications)

- Transition from energy systems based on carbon cycles to those based on hydrogen cycles.
- Development of systems in which electricity that is not readily stored can be stored as hydrogen and renewable energy is utilized to its full potential.

Fig. 1.8 Technological, industrial, and social paradigm shifts made possible by fuel cells and hydrogen technologies



Industrial Paradigm Shifts

[Energy Industry] (Facing liberalization)

- Energy supply changes from centralized to distributed generation (following precedents with, e.g., computers).
- Transition from unilateral energy supply companies to service industries providing multilateral energy resource management (e.g., energy convenience stores).
- Energy production facilities customized to utilize the energy sources available in each region.
- Groups of industries that add value to the commodity called electricity.
- Consumers are given choices as to how they obtain their energy and from which industry.
- An industry is developed whereby businesses are created to suit the needs of the consumers.

[Overall Industry] (One of the pillars of the growth strategy)

- An industrial structure that profits from both the decrease in energy resource imports, and the increase in energy system and technology exports.

- Creation of a society where electricity can be stored and traded like “currency” in the form of hydrogen.
- Energy will become an even more attractive growth field/investment area.

Social Paradigm Shifts

[Politics] (Where energy security is essential for the existence of countries)

- Transition to a society that does not depend on a specific energy resource (such as crude oil).
- Transition to a society where there is no competition for energy resources, reducing the reliance on international politics, and reducing the chance of international conflict.

[Environment] (Global environmental issues are urgent)

- Transition to a mobile society that produces no exhaust gas emissions through the deployment of FCVs and battery vehicles (EVs).
- Transition to an environmentally friendly society that protects the earth through dramatic reductions in CO₂ emissions made possible by the utilization of hydrogen energy and improvement in efficiency.

[Economy] (Energy is the fundamental driving force to power economic activities)

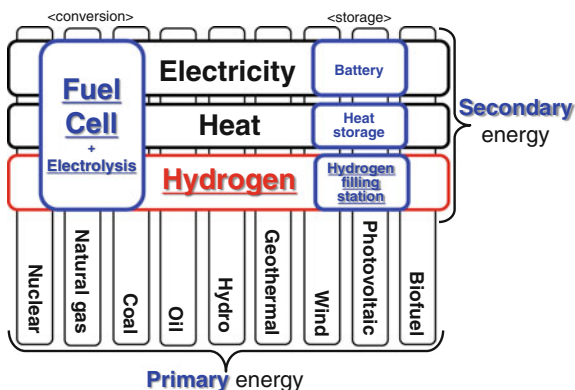
- Transition to a society in which the outflow of national wealth is suppressed, with resources instead used domestically to save on energy costs (amounting to approximately 27 trillion yen annually in Japan).
- Transition to a society in which future energy is ensured through investments in renewable energy.
- Transition to a society where the best mix of energy types can be deployed because of the diversification of energy resources.

[Overall] (Energy as a social interest)

- National independence in regards to energy supplies by means of an increase in renewable energy and the use of the best possible energy mix (energy security at the national level).
- Transition to a society in which individuals and regions are independent in terms of energy (energy security at the regional/individual level).

In order for all the potential of hydrogen and fuel cells to be realized, long-term efforts lasting from several decades to as long as a century may be required. However, it is certain that it will be feasible to solve many of the problems surrounding energy supplies for human use. A great challenge is about to start for humans, who were the first animals to use fire and have constructed and maintained civilization by burning enormous amounts of energy resources ever since the industrial revolution. The challenge will be to utilize energy with higher efficiency and produce less waste with technologies that do not require *combustion*.

Fig. 1.9 Various primary and secondary energy types coupled with hydrogen, fuel cells, and electrolyzers



The relationship between various primary and secondary energy forms is described in Fig. 1.9. Electricity can be transmitted straightforwardly, while hydrogen can be easily stored. The use of hydrogen as a secondary energy type (in addition to electricity and thermal energy) enables larger-scale and longer term energy storage compared to, e.g., secondary batteries. This makes achieving the “best” combination of various primary energies much easier, inclusive of variations in renewable electricity and the base load from nuclear power. Hydrogen can be produced from, e.g., excess renewable (photovoltaic and wind) electricity using electrolyzers. Stored hydrogen will be used for power generation utilizing stationary hydrogen fuel cells and/or for FCVs, buses, and forklift trucks. Fuel cells and electrolyzers can efficiently convert and help manage secondary energy types (i.e., electricity, heat, and hydrogen) taking advantage of co-generation and even tri-generation from various fuels. Natural gas (city gas), liquefied petroleum gas (LP gas) from oil, coal gas, and biofuel can all be used to produce hydrogen, or hydrogen-containing fuel gases for generating electricity and heat with fuel cells.

This book is organized as follows. First, an overview of the history, current state, potentials, and future directions regarding hydrogen energy and fuel cells is presented in Part I. This is followed by descriptions of the basic engineering concepts used in the manufacturing process for hydrogen and an introduction to hydrogen energy systems (Part II). Next, fundamental engineering information on hydrogen energy storage (Part III), utilization (Part IV), and safety (Part V) is presented. The final section (Part VI) summarizes the current status of technology, future developments in each application area, and social considerations for popularization. This book especially tries to present an engineering system for hydrogen energy from the unique viewpoint of Japan, where full popularization of the hydrogen energy field is about to begin.

References

1. Strategic Energy Plan (2014) Agency for Natural Resources and Energy, Ministry of Economy, Trade and Industry, Japan. http://www.enecho.meti.go.jp/en/category/others/basic_plan/pdf/4th_strategic_energy_plan.pdf. Accessed 27 Sept 2015
2. Strategic Road Map for Hydrogen and Fuel Cells (2014) Agency for Natural Resources and Energy, Ministry of Economy, Trade and Industry, Japan. http://www.meti.go.jp/english/press/2014/0624_04.html. Accessed 27 Sept 2015
3. Annual Report on Energy (Energy White Paper 2014) Agency for Natural Resources and Energy, Ministry of Economy, Trade and Industry, Japan. http://www.meti.go.jp/english/report/index_whitepaper.html. Accessed 27 Sept 2015
4. Hydrogen Energy White Paper (2015) New Energy and Industrial Technology Development Organization (NEDO), Japan. <http://www.nedo.go.jp/content/100567362>. Accessed 27 Sept 2015 (in Japanese)
5. The Japan Society of Mechanical Engineers (2002) Thermodynamics (JSME textbook series). Maruzen, Tokyo Japan (in Japanese)
6. Steele BCH, Heinzel A (2001) Materials for fuel-cell technologies. *Nature* 414:345–352
7. Larminie J, Dicks A (2003) Fuel cell systems explained, 2nd edn. John Wiley & Sons, West Sussex UK
8. Sasaki K, Nojiri Y, Shiratori Y, Taniguchi S (2012) Fuel cells (SOFC): alternative approaches (electrolytes, electrodes, fuels), In: Meyers RA (ed) Encyclopedia of sustainability science and technology. Springer Science+Business Media, New York, pp 3886–3926
9. Stolten D (2010) Hydrogen and fuel cells. Wiley-VCH, Germany
10. Singhal SC, Kendall K (2003) High-temperature solid oxide fuel cells: fundamentals, design and application. Elsevier Science & Technology, Oxford UK
11. Minh NQ, Takahashi T (1995) Science and technology of ceramic fuel cells. Elsevier Science, Amsterdam
12. Kreuer KD (2013) Fuel cells. Springer Science+Business Media, New York
13. Sasaki K, Hayashi A, Taniguchi S, Nishihara M, Fujigaya T, Nakashima N (2014) Fuel cells, Part VI Chapter 24.3 In: Kagaku Binran (Chemistry handbook), Applied Chemistry, 7th edn. Maruzen, Tokyo Japan (in Japanese)
14. United Nations Conference on Climate Change COP21/CMP11 (2015). <http://www.cop21.gouv.fr/en/>. Accessed 27 Dec 2015

Chapter 2

Current Status: General

Kazunari Sasaki

Abstract This chapter describes recent progress in fuel cells and hydrogen technologies, especially in Japan where real commercialization of these technologies is underway, including fuel cell vehicles (FCVs) and buses, hydrogen fueling stations, residential and industrial fuel cell systems, as well as electrolyzers for hydrogen production from renewable power. Possible ways to realize a future carbon-neutral and carbon-free energy society are discussed in this chapter.

Keywords Fuel cell vehicles · Hydrogen fueling stations · Residential and industrial fuel cells · Types of fuel cells · Electrolyzer · Social demonstration · Transition to carbon-free society

2.1 The First Year of Hydrogen, 2015

The year 2015 will be marked in history as the year where the use of hydrogen as an energy carrier began in a full-fledged manner in our society. Fuel cell vehicles (FCVs) were released to the general market on December 15th 2014, representing a great step forward in our efforts to achieve zero-emissions from automobiles, which have generated huge quantities of harmful exhaust gases in the past [1]. Figure 2.1 shows the MIRAI FCV produced by Toyota Motor Corporation (see also Chap. 34). Other types of fuel cells are under development as shown in Fig. 2.2.

Comparing FCVs with electric vehicles (EVs), both of which emit no exhaust gas, EVs are currently superior in terms of the cost of fuel (electricity) and the convenience of being able to charge the EV at home. However, FCVs are capable of being driven much further than EVs without recharging, and FCVs require only around 3 min to refuel with hydrogen (compared with many hours of charging for EVs). Ideally, both together will contribute greatly to our escape from the dependency on

K. Sasaki (✉)
International Research Center for Hydrogen Energy,
Kyushu University, Fukuoka 819-0395, Japan
e-mail: sasaki@mech.kyushu-u.ac.jp



Fig. 2.1 Automotive fuel cells: Toyota MIRAI FCV, handed over to Kyushu University President on March 25th 2015 as the first official commercially available university FCV in the world

petroleum-derived energy resources such as gasoline. “The-chicken-or-the-egg” discussions have been held over the establishment of the necessary hydrogen infrastructure for FCVs for many years. The volume of vehicle sales for a motor company is determined by consumers. However, it is difficult for energy suppliers to take a plunge and invest in hydrogen infrastructure (such as hydrogen filling stations) unless they know clearly how many FCVs will be sold (see Chap. 41). The impact of the launch of commercial sales of FCVs was indeed large, and businesses that had waited to see the sales numbers before acting are now beginning to enter the market. The advantages of advance entrance are also great, and future developments are expected to be led by the companies that are early adopters of this new technology. Construction of commercial hydrogen filling stations is underway in various parts of the country. Figure 2.3a shows the opening ceremony for the Kokura hydrogen filling station in Fukuoka prefecture, the second commercial hydrogen station supplying 70 MPa high-pressure hydrogen gas to open in Japan (see Chap. 40). Various attempts have been made to develop small-scale hydrogen filling stations to reduce system cost and to produce renewable hydrogen. For example, Fig. 2.3b shows a small-scale hydrogen filling stations which can produce and supply 35 MPa hydrogen gas onsite. While the hydrogen gas pressure is not sufficient to fully fill the FCV tanks, such a small system may be sufficient for small cities and local areas in an initial stage of FCV commercialization.

Research and development initiatives regarding hydrogen energy have been implemented globally for years. In Japan, improvements in the core fuel cell technology and peripheral hydrogen-related technologies were promoted actively with industry–academia–government collaborations. These collaborations led to the release of ENE-FARM, a fuel cell for residential purposes. Much of this success

Fig. 2.2 Automotive fuel cells: **a** the Honda “CLARITY Fuel Cell” vehicle to be commercialized from March 2016, **b** the Toyota Lexus FCV, and **c** the Hino fuel cell bus, all exhibited in Tokyo Motor Show 2015

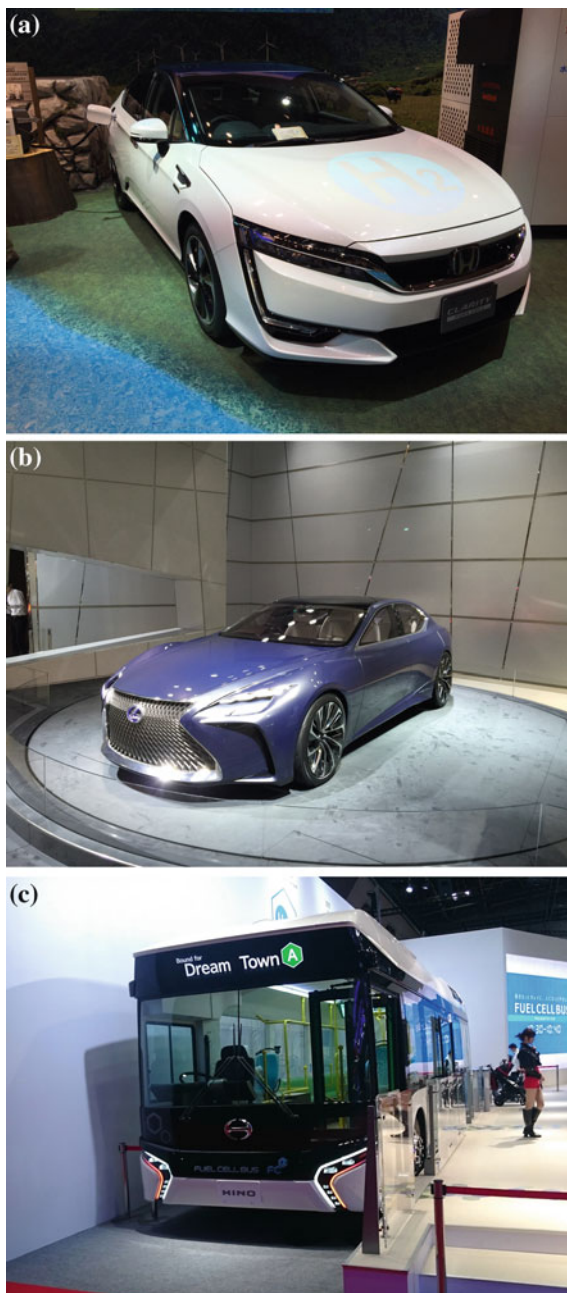


Fig. 2.3 Hydrogen filling stations: **a** the Kokura hydrogen filling station (stationary, 70 MPa), which was the second such station to open to the general public in Japan, on October 22, 2014; **b** the Fukuoka Prefecture hydrogen filling station (mobile, 70 MPa); and **c** a small-scale hydrogen filling station “Smart Hydrogen Station (SHS)” (35 MPa) developed by Honda and Iwatani exhibited in Tokyo Motor Show 2015



can be attributed to strategic measures that had continuity and prospects for commercialization, large-scale demonstrations of new technology developments followed by subsidy support. More recently, hydrogen has been given a clear position in Japan’s national energy policy as a secondary energy carrier next to electricity

and heat within the Basic Energy Plan that was revised on April 11, 2014. The “Strategic Road Map for Hydrogen and Fuel Cells” was drawn up based on this new policy [2]. The document includes a future roadmap starting with the commercial release of ENE-FARM in 2009 and that of FCVs in 2015. Acceleration in commercialization and full popularization is expected as outlined in Japan’s roadmap. Such roadmaps are still lacking in many other countries. Although the distributed quantity of hydrogen remains small, hydrogen is already being used in much larger quantities in industrial processes and so forth. If popularization of FCVs advances, it is expected that even the current hydrogen production level will be too low. Japan’s roadmap, however, clearly describes medium- to long-term strategies to obtain CO₂-free hydrogen including mass quantity imports. Hydrogen, which is used in fuel cells that can directly convert the chemical energy of fuel into electricity unlike thermal engines, has the potential to bring about innovative and fundamental changes in the ways that society is powered by energy.

2.2 Electrochemical Energy Conversion: Fuel Cells

Fuel cells are central components of hydrogen energy systems (see Part IV). They are similar to conventional batteries and rechargeable batteries such as lithium ion batteries that supply electricity. All of these electrochemical devices are centered around electrolyte layers through which only specific ions are able to pass. However, while batteries contain the chemicals that serve as the energy source inside the electrochemical devices, fuel cells do not contain this chemical energy inside the device. Therefore, the substance that functions as the energy source needs to be supplied to fuel cells in order to generate electricity. They will keep generating electricity as long as the fuel is supplied. In terms of functionality, they are actually more closely related to power generators than batteries.

There are many materials through which only specific ions can pass, and fuel cells operate at temperatures at which these ions can diffuse easily. Known mobile ions include hydrogen ions or protons (H⁺), oxygen ions (O²⁻), carbonate ions (CO₃²⁻), and hydroxyl ions (OH⁻). Different types of fuel cells are categorized in Fig. 2.4, according to the type of mobile ions that are utilized [3–5]. What is common among these different types of fuel cell is that there are electrodes on both sides of the electrolyte, fuel oxidation reactions occur at the anode, and oxygen reduction reactions occur at the cathode.

Polymer electrolyte fuel cells (PEFCs) and solid oxide fuel cells (SOFCs) are representative fuel cells for which technological development is being advanced for practical applications and full popularization. The principle of fuel cells was demonstrated in 1839 by Sir William Grove in Britain [6], whilst Baur et al. demonstrated fuel cell technology using a solid electrolyte at the Swiss Federal Institute of Technology (ETH) in 1937 [7]. Figure 2.5 shows the operational principle for both of these types of fuel cells. In PEFCs (widely used in FCVs and residential fuel cell units), hydrogen gas is supplied to the anode (fuel electrode)

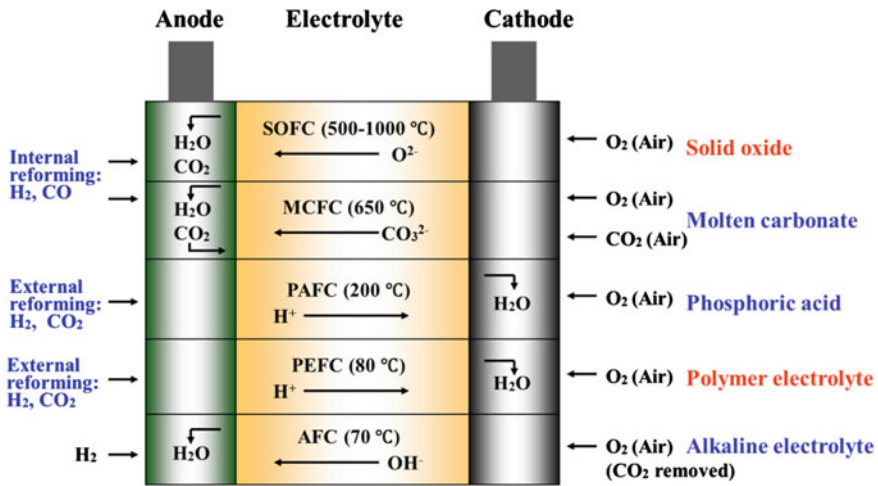


Fig. 2.4 Different types of fuel cell [3]

side as fuel (Fig. 2.5a). The hydrogen molecule is dissociated into protons and electrons at the electrode surface, which contains catalysts such as platinum. Since the electrolyte allows only the protons to pass, the protons diffuse through the electrolyte membrane. However, electrons cannot pass through the electrolyte and therefore flow through the external circuit via the electronically conductive electrode. Air is supplied to the other electrode, where the oxygen molecule, protons that have passed through the electrolyte membrane, and electrons that have arrived via the external circuit react together to form water (H₂O). Although the same reaction occurs when hydrogen gas and oxygen gas are mixed and ignited, water is formed in fuel cells only for the amount of electrons that have run through the external circuit of the fuel cell. That is, current flows from the air electrode (cathode) to the fuel electrode (anode). As a consequence, electricity can be generated by supplying hydrogen.

Using electrolyte materials in which oxygen ions act as charge carriers instead of protons is also possible. In the SOFC, as shown in Fig. 2.5b, air is supplied to the cathode in the same fashion as the PEFC. Since the SOFC uses an oxygen ion conductor, oxygen molecules in the air gain electrons from the cathode surface and dissociates into oxygen ions. The oxygen ions formed here diffuse through the electrolyte layer. At the anode, these oxygen ions and hydrogen molecules react to form water (steam), generating electrons. These electrons pass through the external circuit and are used in the reactions that take place at the air electrode. The overall SOFC reaction in which electricity is generated by supplying hydrogen is therefore identical to that of the PEFC.

Furthermore, water (steam) is formed on the cathode in PEFCs, while it is formed on the anode in SOFCs. In PEFCs, the oxygen gas, which is initially present in the air at a concentration of only 20 %, is further diluted by the steam that is

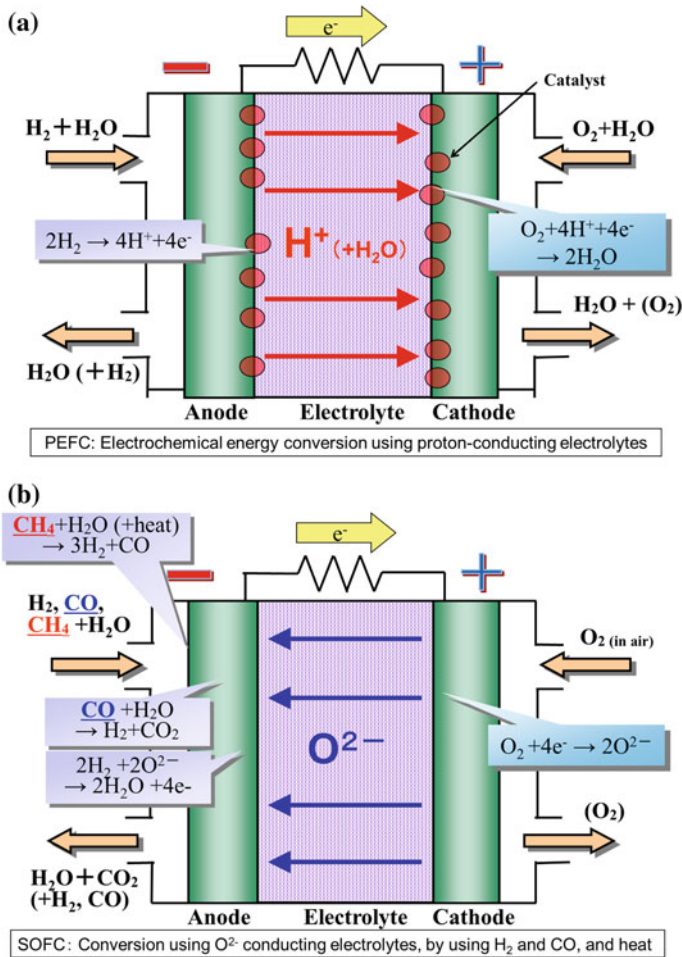


Fig. 2.5 Operational principles of **a** polymer electrolyte fuel cells (PEFCs) and **b** solid oxide fuel cells (SOFCs)

formed. In SOFCs, the steam formed on the fuel electrode is used in the steam reforming reactions ($\text{CH}_4 + \text{H}_2\text{O} \rightarrow 3\text{H}_2 + \text{CO} - 206 \text{ kJ/mol}$) with hydrocarbon fuels such as methane and in the water shift reactions ($\text{CO} + \text{H}_2\text{O} \rightarrow \text{H}_2 + \text{CO}_2 + 41 \text{ kJ/mol}$). These reactions generate more hydrogen gas. The steam reforming reaction is an endothermic reaction, and thus it is possible to form hydrogen by using the heat generated inside the fuel cell and extract more electricity. In addition, the electrochemical reactions at the electrodes occur more quickly with small voltage losses as the operating temperature is higher. These are the reasons why SOFCs have better electricity generation efficiencies than PEFCs.

As shown in the operational principles for fuel cells, there is no process that “burns” the fuel during fuel cell power generation. In thermal engines, the chemical

energy of the fuel is converted to thermal energy through combustion, and then the thermal energy is converted into electrical energy via kinetic energy in turbines as the generators rotate. In comparison, fuel cells convert chemical energy directly into electrical energy. Fuel cells therefore are capable of *direct conversion of energy from the source*, and the fuel to drive the electrochemical reactions is hydrogen. Such technology represents an innovative energy conversion method to extract electricity with high efficiency *without burning*. This is a huge accomplishment for humans, who have addressed economic development needs in the past by burning considerable quantities of fossil energy resources.

The operational temperatures for various types of fuel cell are shown in Fig. 2.4. These data reflect the temperatures at which the electrolytes show sufficient ionic conductivity. High ionic conductivity leads to higher cell voltage, which is the driving force for moving ions against the electrical resistance, and low conductivity leads to voltage losses in fuel cells. Electrochemical reactions will become slower if the temperature is too low, and this will also cause voltage losses in fuel cells. Conversely, problems such as performance decreases and cell degradation start to appear if the operational temperature is too high. The optimal operational temperature is therefore determined by the balance between both of these considerations.

Typical materials used in fuel cells are summarized in Table 2.1. In general, the issue is to activate the electrochemical reactions in fuel cells that operate at low

Table 2.1 Typical materials used in fuel cells

	Polymer electrolyte fuel cells (PEFC)	Alkaline fuel cells (AFC)	Phosphoric acid fuel cells (PAFC)	Molten carbonate fuel cells (MCFC)	Solid oxide fuel cells (SOFC)
Operational temperature (°C)	20–80	20–90	160–210	600–700	600–1000
Fuel gas	H ₂ , alcohol	H ₂	H ₂	H ₂ , CO	H ₂ , CO, C _x H _y
Oxidant	Air, O ₂	Air, O ₂ (without CO ₂)	Air, O ₂	Air (+CO ₂)	Air
Electrolyte materials	Cation exchange membrane	KOH solution	Concentrated H ₃ PO ₄ solution	(Li,K) ₂ CO ₃	ZrO ₂ (Y ₂ O ₃) ZrO ₂ (Sc ₂ O ₃) CeO ₂ (Gd ₂ O ₃) La(Sr)Ga(Mg)O ₃
Electrode materials, electrocatalyst	Pt/C Pt–Ru/C Pt–Co/C	Pt-based catalyst, Ni–Al, transition metal catalyst	Pt-based catalyst	Ni-based porous plate	La(Sr)MnO ₃ La(Sr)Co(Fe)O ₃ , Ni–ZrO ₂ (Y ₂ O ₃)
Stack component materials	Carbon paper, corrosion-resistant alloy	Ni	Carbon plate, Teflon, SiC	Ni alloy, stainless steel, LiAlO ₂	Cr-based alloy, stainless steel, La(Sr)CrO ₃

temperatures, and thus, e.g., platinum-based catalysts are inevitably used. In fuel cells that operate at higher temperatures, nonprecious catalysts such as Ni can be used. Since the electrolytes exhibit high ionic conductivity, they contain the conductive ions in large quantities. The proton conductor usually used in PEFCs is strongly acidic, whereas alkaline electrolyte fuel cells use strongly basic electrolyte materials. Thus, corrosion resistance is a challenge that needs to be solved by the deployment of peripheral materials. Ti-based materials are often used as separators in PEFCs. However, the materials that can be used for fuel cells that operate at high temperatures are limited because of limitations in regards to, e.g., oxidation and high-temperature tolerance, especially near the air electrode.

2.3 Hydrogen Utilization Technologies

As is clear from the operational principles, fuel cells comprise technology that can generate electricity with high efficiency and the reactions involve hydrogen. Hydrogen itself is the most abundant element in nature and is contained in various fuels in the form of chemically coupled hydrogen atoms. Therefore, if a society utilizing hydrogen can be cultivated, it will be possible to use various energy sources containing hydrogen. Energy diversification would be very helpful in countries like Japan, which depend on imports for most energy resources, and it would be of value to many countries at the national level in terms of energy security [8, 9].

The fundamental social values of deploying hydrogen energy technology with fuel cells at the core can be summarized as follows:

- Fuel cells can generate electricity efficiently without burning fuel (via electrochemical reactions involving hydrogen).
- When hydrogen gas is used as the fuel, only water is formed as the byproduct (however, CO₂ is generally emitted when hydrogen gas is produced).
- If vehicles can be run on hydrogen, the automotive industry and motorized communities will no longer depend on crude oil and will become sustainable (key industries and our daily transportation requirements will no longer depend on politically sensitive specific natural resources).
- Electricity obtained from fluctuating natural energy sources can be stored in the form of hydrogen (the capacity to accept electricity from renewable energy increases as it is stored as hydrogen).

As shown in Fig. 2.6, this technology has the potential to change how energy is supplied. When seen from the perspective of energy supplying businesses, this would mean that gas companies and petroleum companies will be indirectly supplying and selling electricity, as it can be supplied from city gas or LP gas when ENE-FARM technology is used, for example. If hydrogen is used as the fuel for vehicles, several businesses such as petroleum companies, which manufacture and

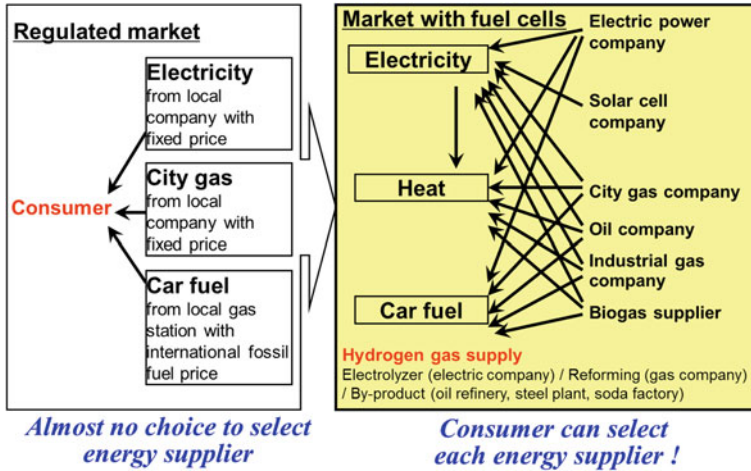


Fig. 2.6 Fuel cells and hydrogen energy as seen from the viewpoint of consumers

sell hydrogen, city gas companies, which can produce hydrogen from city gas, and industrial gas companies, which deal in hydrogen, will be selling fuel for vehicles. If hydrogen can be formed through electrolysis of water, power companies can also sell this fuel for automobiles. When seen from the perspective of consumers, there will come a time when they have more options available when purchasing energy for their residential and transportation needs. In the future, when liberalization helps to eliminate monopolies or oligopolies, new forms of energy technology will likely open “Pandora’s box” by facilitating the removal of barriers among industries and business categories. Since hydrogen can be formed by anyone, it is a technology with the potential for use in any industry.

There are various different possible applications for fuel cells. Applications that have already been commercialized in Japan include residential fuel cells (see Fig. 2.7, which shows various types of ENE-FARM units) and FCVs. The former was released in 2009, and the cumulative number of units sold exceeded 150,000 in December 2015 with the support of governmental subsidy measures (see Chap. 35). This high level of adoption was also fostered by cost reduction measures on the part of concerned businesses as well as increased concern among residents who experienced planned outages that occurred immediately after the 2011 Tohoku Earthquake Disaster. The national Japan Revitalization Strategy has specified measures to achieve popularization of 5.3 million ENE-FARM units by around 2030. This number corresponds to 10 % of all the households in Japan, and it is expected that this would result in reductions of CO₂ emissions from Japan by several percent [2]. Such technology is becoming popularized widely as “a hot-water supply system that can also generate electricity” in place of the hot water supply systems that are widely installed now. Although installation of ENE-FARM units is limited to detached residences for the time being, measures to install them in



Fig. 2.7 Various types of ENE-FARM fuel cell units for residential use. The ones shown here are installed on Ito Campus at Kyushu University

housing complexes such as apartment blocks are being launched. In this case, they need to be installed within the maintenance space or on the balcony, and thus, further miniaturization of such systems is inevitable. The PEFC ENE-FARM type represents more advanced technology, whereas miniaturization of hot water tanks for SOFC systems is likely possible given that the outlet hot water temperature is high. The SOFC ENE-FARM type whose system can be simplified also has a high potential for miniaturization, and technological developments in these areas are being conducted in parallel.

Regarding FCVs, commercially released in December 2014, three major domestic motor companies in Japan have plans for additional releases, and joint development projects have been launched with major motor manufacturers overseas. These FCVs are global products, and popularization in the state of California, U.S., and Europe, where there are strong demands for zero-emission vehicles, can be expected. Development of fuel cell buses (see Fig. 2.8) is also underway in addition to the development of smaller FCVs. A target release date of 2016 has been set for fuel cell buses. In Europe, social demonstrations, and so forth have been conducted on buses with strong public benefits, and product development is being accelerated in Japan for the Tokyo Olympics and Paralympics to be held in 2020. While fuel cell buses are thought to represent a fuel cell system equivalent to a few FCVs, they are also expected to function positively in terms of hydrogen filling station business as operational patterns can be easily determined for buses and the hydrogen charging quantities per vehicle will be large. Such buses may also play a critical role as “safe stations” to support the life lines of local residents and information bases that can offer transportation services, electricity, heat, water, and



Fig. 2.8 Fuel cell bus (FC bus)

communication access. They may even be able to provide electricity for shelters and assist in evacuations.

Importantly, future applications of fuel cells will not just be limited to ENE-FARM or FCVs. With commercial releases planned in 2017, as specified by Japan's national roadmap, industrial-scale fuel cells are expected to deliver environmentally friendly benefits in industrial fields, which account for more than half the demand for city gas. However, in this field, they will compete with existing thermal engines such as gas engines, diesel power generators, and microgas turbines. Therefore, requirements for low system costs and durability will be high. Commercialization at the level of several kilowatts to several hundreds of kilowatts, which is advantageous for high efficiency, should also be expected. For example, an 250 kW-class industrial fuel cell system shown in Fig. 2.9a with an electric efficiency approaching 55 %LHV under demonstration in Kyushu University will be commercialized from 2017 (see Chap. 36). Commercialization of industrial fuel cells has progressed relatively rapidly in the U.S., where power outages often occur. Popularization began in data centers and information and communications technology (ICT)-related facilities where even a momentary outage is unacceptable. In Japan, where liberalization of the energy industry is continuing, commercialization of SOFC-based systems is being accelerated. If they continue to grow in size, commercialized power generation units will be able to serve as replacements for existing thermal power generators.

A "triple combined cycle," which combines fuel cells with gas turbines and steam turbines, is expected to become the sole technology that can exceed the power generation efficiency of the "(double) combined cycle" that is currently utilized in the latest current thermal power generation technologies. The extreme power generation capabilities of the new technology may even be able to achieve power generation efficiencies higher than 70 % (see Chap. 37). It is also important

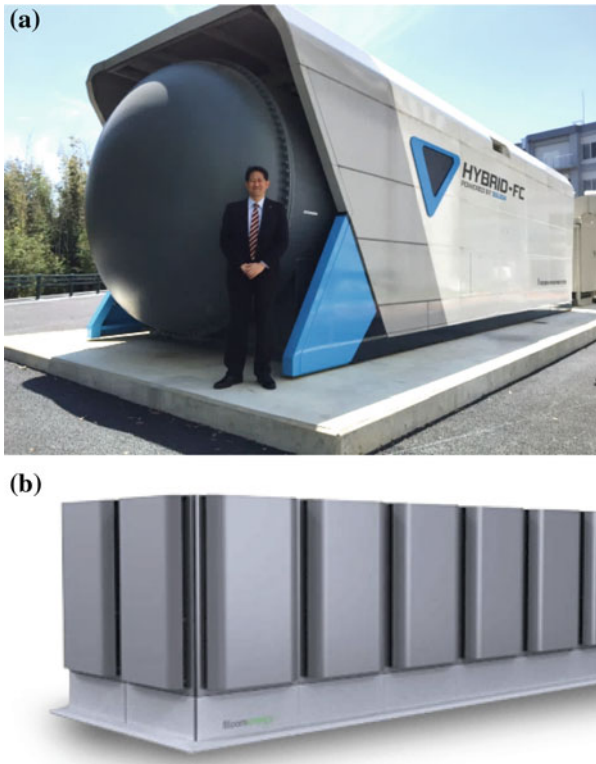


Fig. 2.9 Industrial-scale fuel cells **a** manufactured by Mitsubishi Hitachi Power Systems in Japan and **b** by Bloom Energy in the U.S

to note that coal, which exists in rich deposits, could be used as a power generation fuel in addition to natural gas. There already are some efforts in place to develop power generation systems that combine fuel cells driven by gasified coal with gas turbine and steam turbine systems. Further efforts should be made to increase the energy conversion efficiency of fuel cell systems [10].

The use of various types of fuels could be another important challenge. In particular, the application of renewable-sourced biogas and biofuels can realize carbon-neutral power generation (see Chap. 38).

Besides these applications, fuel cells are beginning to be used in forklift trucks in the U.S. Compared to the storage battery-type forklifts, which require a long time for charging, the hydrogen charging time for the fuel cell forklifts is much shorter. While expectations are high for hydrogen PEFCs, they will require hydrogen filling stations. If high output development becomes possible, there will be an opportunity to deploy direct alcohol-type fuel cells whose fuel is alcohol, which is easier to handle. Power supplies for mobile devices and portable power generators are also potential applications with high expectations. While direct alcohol-type fuel cells

may reach the commercial market faster than other technologies, development of SOFC-type devices that can use various different fuels are also being developed (see Chap. 39).

Demands for decarbonization measures are not limited to vehicles and buses. Low carbonization is also desired in ships; hence, there is a chance that such technology could soon be deployed on ocean going vessels. Research and development activities aimed at utilizing hydrogen fuel cells in aircrafts are also being conducted. In aerospace applications, where such technologies have been deployed in space shuttles and the space station, the acquisition of energy supplies during the periods when photovoltaic cells (e.g., in the shadow of the earth) cannot be used has been a challenge. Compared to storage batteries, which become heavier in proportion to the capacitance, hydrogen energy storage, which uses the electricity generated by the photovoltaic cells for electrolyzing water to store hydrogen, can lead to weight reductions, and this may be an option that can meet the high expectations for performance in aerospace applications. Even among the general public, hydrogen energy technology will become more important as an energy storage technology if measures to store the electricity generated by fluctuating renewable energy sources as hydrogen can be fully adopted (see Part II).

2.4 Hydrogen Production and Storage Technologies

In a society that utilizes hydrogen, how hydrogen is produced, stored, and transported to the place of use will be key points. Hydrogen gas is essential for FCVs, and it is already widely produced in industrial fields. Specifically, oil refineries handle large volumes of hydrogen gas, which is an essential substance used for example during the desulfurization processes. FCVs require hydrogen gas with high purity to prevent catalyst deterioration, thus the gas has to be supplied to FCVs after purification, according to international standards. Steelworks use large quantities of coal in blast furnaces, and the trace content of hydrogen contained in the coal comes out as hydrogen gas in large volumes when the coal is steamed. Therefore, it should be possible to sell this byproduct gas as fuel for FCVs if it is purified, thereby adding value to such industries. Furthermore, soda electrolysis generates large volumes of hydrogen gas as byproducts during caustic soda production, and this too is a potential source for FCV fuel. However, hydrogen gas from these processes is already used widely in other industrial processes. Another potential source for fuel is through the production of hydrogen gas by having city gas and steam react at a high temperature of about 700 °C (i.e., steam reforming, see Chap. 8). In this case, the city gas infrastructure can be utilized as it is. This could enable hydrogen gas production at a relatively low cost, but it will also require maintaining the reformers at high temperatures in order to produce the hydrogen.

Hydrogen can also be formed through water electrolysis using alkaline electrolytes or solid polymer electrolytes (see Chaps. 9 and 10). In these cases, the existing electricity supply network can be utilized as energy transportation



Fig. 2.10 Water electrolysis-type hydrogen filling station (Ito Campus, Kyushu University)

infrastructure (see Fig. 2.10, which shows a water electrolysis-type hydrogen filling station). Efficiency levels for water electrolysis are approximately 70 % with alkaline water electrolysis and 80 % with PEFC-type water electrolysis (see Fig. 2.11, which shows a PEFC-type water electrolysis system installed inside the hydrogen filling station). While the price for mass production of hydrogen will be high, there is the operational flexibility to produce only the amount of hydrogen that is necessary at the time when it is needed. This requires no shipments and this technology is suited to local small-scale hydrogen production and supply.



Fig. 2.11 Polymer electrolyte fuel cell (PEFC)-type water electrolysis system (inside the hydrogen filling station at Kyushu University)

In the medium- to long-term outlooks, establishment of more efficient, CO₂-free hydrogen production methods with lower costs are highly desirable. Reverse operation of SOFC power generation (via solid oxide electrolyzer cells; SOECs) is expected to deliver even higher conversion efficiencies than can be currently achieved with the PEFC-type (see Chap. 11). In addition, it is also expected that mass imports of hydrogen gas produced from unused resources overseas will be available when producing CO₂-free hydrogen. For example, hydrogen production by electricity using inexpensive electricity from hydroelectric power plants overseas, production of hydrogen gas from brown coal or natural gas taken from small-scale gas fields, and so forth are all expected to allow for the import of CO₂-free hydrogen (carbon offsets via underground carbon capture and storage technologies may be needed in some situations). In addition, if direct production of hydrogen via photocatalysis and other technologies becomes possible in the far future, we will be able to create a renewable hydrogen circulation society, although challenges still remain regarding conversion efficiencies, durability, and scale increases (Chap. 12).

The technologies to store and transport the hydrogen gas acquired in such ways will be the key to the successful realization of a hydrogen-fueled society (see Part III). During the development processes for FCVs, researchers tried various technologies for hydrogen production and hydrogen storage for automobiles. Trials using on-vehicle gasoline reforming, alcohol reforming, hydrogen storage as liquid hydrogen or in hydrogen storage materials, and incorporation of the hydrogen storage system inside the tank were all considered. Eventually, it was decided to store high-pressure hydrogen gas for the fuel cells of FCVs. This fuel is usually



Fig. 2.12 Hydrogen tanks for high-pressure hydrogen storage (inside the hydrogen filling station at Kyushu University)

stored in high-pressure tanks at hydrogen filling stations (see Fig. 2.12, which shows a high-pressure hydrogen storage tank at the hydrogen filling station). However, it is important to note that liquid hydrogen or liquefied hydrogen may be more advantageous to use when hydrogen is stored or transported in large quantities. There are examples of such use in rocket fuels. In regards to hydrogen transport in liquid form, existing fuel transportation vehicles and infrastructure can be used for liquid hydrogen as well as for the storage of chemical substances that are rich in hydrogen atoms such as organic hydrides. Further advancements are expected in hydrogen storage technologies that employ alloy-type or complex-type materials with a high capability for hydrogen storage. Carbon-based materials with large surface areas to adsorb hydrogen may also be applicable. At the same time as the development of hydrogen storage materials, technological developments regarding hydrogen carriers appropriate for mass hydrogen storage are being implemented. The expectations are high for substances that contain many hydrogen atoms and have high energy densities such as ammonia and methylcyclohexane. In this case, measures to ensure safety and security including social acceptance will be inevitable for societies that deploy such substances as part of the overall energy system.

2.5 Prospects of a Hydrogen Society

The fundamental values that are derived from using fuel cells and hydrogen energy are unequivocally tied to efficient energy conversion without combustion. Particularly for Japan, where fossil fuel imports amounted to 27 trillion yen in 2013 [11], the deployment of fuel cells that can efficiently use various hydrogen-atom-containing energy resources is expected to result in significant energy savings. If we can reduce the large sums of financial capital that are expended in Japan on energy, the impact will be immeasurable. At present, approximately 88 % of electricity is provided by thermal power generation, and anticipation is high for the role of fuel cells as alternatives to thermal power plants for both residential and industrial purposes including power generation.

If plans are to continue to use thermal power generation systems to provide most of the country's electricity for a while, then the use of hydrogen in the power generation field will be important. In terms of power generation efficiency, electrochemical energy conversion processes (fuel cells) that directly convert fuel into electricity are intrinsically better than the thermal energy conversion process that burns the fuel. However, it will still take some time to develop larger fuel cell systems. In the meantime, the potential of hydrogen to reduce CO₂ emissions can be fully exploited if hydrogen energy sources can contribute to the quantity aspect of power generation in addition to the quality aspect (power generation efficiency). For example, hydrogen can sometimes be mixed into fuel sources at thermal power plants, and this could have benefits of CO₂ emission reductions corresponding to the amount of added hydrogen. However, hydrogen gas also has high ignitability

and too much of an increase in combustion temperature will lead to increased emissions of NO_x , which can then result in deteriorated efficiencies if steam needs to be added to take care of these emissions (see Chap. 25). In the medium- to long-term view, a hydrogen-fueled society in which hydrogen gas is used in quantity will involve the utilization of CO_2 -free hydrogen sources for power generation.

Furthermore, as specified in the basic energy plans of not only Japan but also many other countries, there are set goals to expand the use of renewable energy. However, imbalances between the demand and supply for electricity can lead to large-scale outages in the worst-case scenario owing to frequency fluctuations or other reasons. Therefore, it is difficult to accept highly fluctuating electricity originating from natural energy unless energy storage functions are provided, even if the power grid is made more robust. In regions where more renewable energy power generation systems have been installed, power generation levels could exceed power usage levels as more, e.g., photovoltaic cells come into full operation during periods with less power demand. To ensure stable supplies of electricity, energy storage technology that can function as a buffer during energy fluctuations will be necessary in addition to a thicker power grid. Although pumping-up power plants can store energy at a large scale, it takes a long time, often more than a decade, for such plants to proceed through the planning phase to the installation and operation phases. Alternatively, lithium ion batteries and NaS batteries can be used to store energy with high efficiency, but these technologies are associated with high costs when storing energy in large quantities over long periods of time.

A promising technology, shown in Fig. 2.13, is water hydrolysis-type hydrogen filling stations for FCVs that can serve as “energy storage stations.” These stations store electricity by converting it into hydrogen through water electrolysis reactions during times when there is too much electricity being generated by renewable energy infrastructure. It is also possible to sell the hydrogen gas made from the excess electricity as fuel for FCVs thereby generating additional value for the product. By converting the stored hydrogen gas back into electricity and releasing it into the power grid, it would be possible to store the electrical energy in mass. In this case, the total efficiency of this energy storage system would be determined by the product of the efficiency of the water electrolysis system and the efficiency of the fuel cell system, and therefore, efforts to further improve the efficiency of both systems will be inevitable. However, the costs will start to change if hydrogen gas is produced from excess electricity that cannot be released into the power grid. If electricity can be converted not only to hydrogen but also to methane for mass energy storage, the entire existing city gas infrastructure can become an energy storage network. It would be desirable to have hydrogen energy contribute more to the power system as a part of a comprehensive energy storage network that works in combination with energy storage technology that employs hydrogen-rich energy carriers.

As discussed above, while technical innovation is steadily being advanced to facilitate a society in which hydrogen is widely used, one barrier that remains is social acceptance (see Chap. 42). While awareness of hydrogen and fuel cell

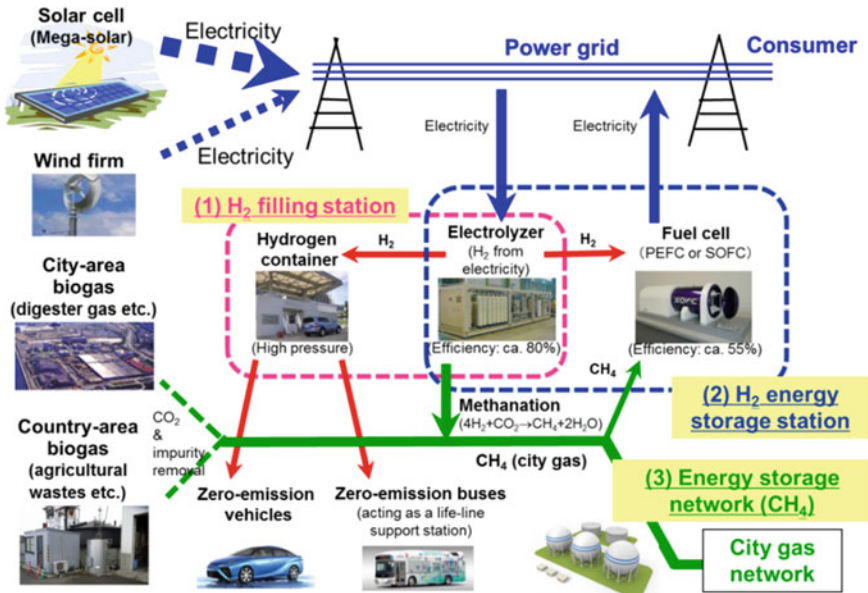


Fig. 2.13 Hydrogen energy technologies for renewable energy storage

technology has improved dramatically because of the commercialization and popularization of FCVs and ENE-FARM residential units, high-pressure hydrogen gas up to 70 MPa is still a fuel that is difficult to handle from the viewpoint of the general public. Safety measures and their technological principles in using high-pressure hydrogen gas are essential in designing and operating hydrogen energy systems such as FCVs and hydrogen filling stations (see Chap. 43).

The public’s understanding of the benefits of hydrogen technology will greatly affect how well hydrogen and fuel cells are utilized within society. Ideally, efforts to improve such awareness should address the benefits to the environment as well as to social systems. In doing so, we will be able to realize the hydrogen society sooner and accelerate measures for practical applications. The “Smart Fuel Cell Demonstration Project” is part of an international strategic zone program being implemented at Kyushu University in order to demonstrate hydrogen technologies to the public. As shown in Fig. 2.14, an attempt is being made to simulate the type of “hydrogen society” that will actually be realized around 2030 using hydrogen and fuel cells on the entire Ito Campus at Kyushu University by 2015. This “society” uses approximately 1/30,000 of the annual electricity consumption for the whole nation. During the actual introduction and operation of FCVs, hydrogen filling stations, large-scale fuel cells, residential fuel cells, and so forth, we plan to examine the technical issues that are encountered when building a hydrogen society. Furthermore, best practices will be developed for control systems and social systems, whilst visions surrounding the use of hydrogen energy will be studied. Coordination with other related technologies will be inevitable as hydrogen

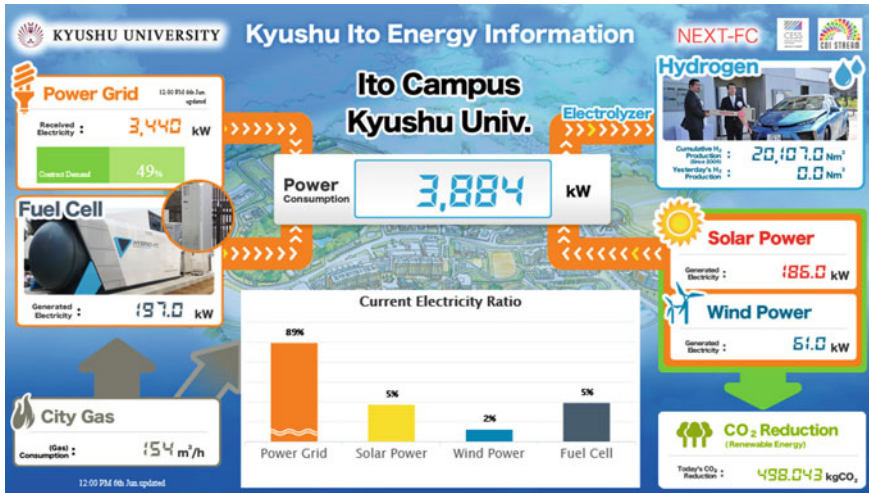


Fig. 2.14 “Hydrogen Campus” where fuel cells and hydrogen energy technologies are fully adopted

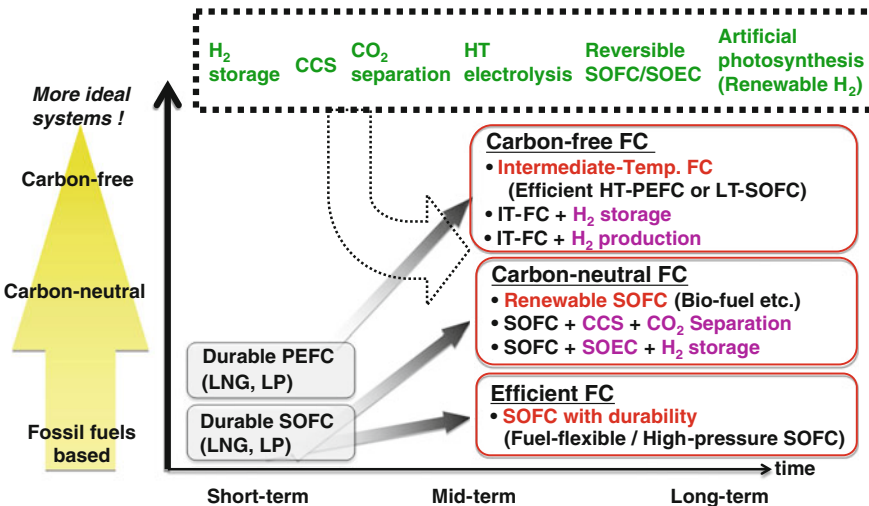


Fig. 2.15 Energy technologies related to fuel cells

energy technologies are not isolated systems (see Fig. 2.15; coordination with peripheral technologies; CCS: Carbon Capture and Storage), but we hope that the system will eventually be able to evolve to a total energy system that is centered on fuel cell technology.

Hydrogen energy technology has the potential to start a revolution that will affect the foundations of the current energy society. As the era of widespread coal and

petroleum use lasted for more than a century, it will be necessary to think of hydrogen energy in units of 100 years. As the “first year of hydrogen” has come in 2015, further technological innovations for the next generation as well as the following generation that are based on technological developments over the past several decades will most definitely be forthcoming. Because energy technology development takes place over the long term, training of the next generation human resources to support it will be strategically important. In the future, it will also be necessary to foster skilled human resources that are capable of leading the world and implementing new energy policies as international development and standardization continue (see Chap. 44).

References

1. Toyota Motor Corporation MIRAI Homepage (2015). <https://ssl.toyota.com/mirai/fcv.html>. Accessed 27 Sept 2015
2. Strategic Road Map for Hydrogen and Fuel Cells (2014) Agency for Natural Resources and Energy, Ministry of Economy, Trade and Industry, Japan. http://www.meti.go.jp/english/press/2014/0624_04.html. Accessed 27 Sept 2015
3. Steele BCH, Heinzl A (2001) Materials for fuel-cell technologies. *Nature* 414:345–352
4. Sasaki K, Nojiri Y, Shiratori Y, Taniguchi S (2012) Fuel cells (SOFC): alternative approaches (electrolytes, electrodes, fuels). In: Meyers RA (ed) *Encyclopedia of sustainability science and technology*. Springer Science+Business Media, New York, pp 3886–3926
5. Sasaki K, Hayashi A, Taniguchi S, Nishihara M, Fujigaya T, Nakashima N (2014) Fuel cells, Part VI Chapter 24.3. In: *Kagaku Binran (Chemistry handbook)*, Applied Chemistry, 7th edn. Maruzen, Tokyo Japan (in Japanese)
6. Grove WR (1838) On a new voltaic combination. *Philos Mag J Sci* 13:430. doi:10.1080/14786443808649618
7. Baur E, Preis H (1937) Über Brennstoff-Ketten mit Festleitern. *Z Elektrochem* 44(9):695–698
8. Strategic Energy Plan (2014) Agency for Natural Resources and Energy, Ministry of Economy, Trade and Industry, Japan. http://www.enecho.meti.go.jp/en/category/others/basic_plan/pdf/4th_strategic_energy_plan.pdf. Accessed 27 Sept 2015
9. World Energy Outlook (2014) International Energy Agency, Paris France
10. Matsuzaki Y, Tachikawa Y, Somekawa T, Hatae T, Matsumoto H, Taniguchi S, Sasaki K (2015) Effect of proton-conduction in electrolyte on electric efficiency of multi-stage solid oxide fuel cells. *Sci Rep* 5:12640. doi:10.1038/srep12640
11. Annual Report on Energy (Energy White Paper 2014) Agency for Natural Resources and Energy, Ministry of Economy, Trade and Industry, Japan. http://www.meti.go.jp/english/report/index_whitepaper.html. Accessed 27 Sept 2015

Chapter 3

Current Status: Global

Akiteru Maruta

Abstract This chapter describes world-wide activities in the development, demonstration, and commercialization of hydrogen technologies in various countries, including the U.S., Europe, and Asian countries. Emphasis is given on the preparation of hydrogen filling station networks supported by central and local governments as well as private companies.

Keywords Hydrogen filling stations · Hydrogen infrastructure · United States of America · Europe · Asia · Governmental support

3.1 United States of America (US)

The US Department of Energy (DOE) has played a leading role in supporting research and development projects for fuel cells and hydrogen energy. The DOE's Office of Energy Efficiency and Renewable Energy (EERE) has allocated around 100 million USD for the Hydrogen and Fuel Cells Program over the last several years. The DOE's focus is on fuel cell R&D and hydrogen fuel R&D, as shown in Table 3.1.

The DOE's federal Hydrogen and Fuel Cells Program does not include any R&D or financial support for hydrogen infrastructure development. Instead, the state of California has been in the lead in establishing hydrogen infrastructure. The flagship organizations of this state are the California Fuel Cell Partnership (CaFCP), which is a government–private partnership organization, and the California Energy Commission (CEC), which financially supports it. The Air Resources Board (ARB) is also a critical organization that is working to improve air quality in the state, and therefore is cooperating in the development of hydrogen energy infrastructure.

A. Maruta (✉)

Technova Inc., The Imperial Hotel Tower, 13F, 1-1 Uchisaiwaicho 1-chome,
Chiyoda-ku, Tokyo 100-0011, Japan
e-mail: maruta@technova.co.jp

Table 3.1 The DOE’s budget for the hydrogen and fuel cell program

Key activity	FY 15	FY 15	FY 16
	(\$ in thousands)		
	Request	Approp.	Request
Fuel cell R&D	33,000	33,000	36,000
Hydrogen fuel R&D	36,283	35,200	41,200
Manufacturing R&D	3000	3000	4000
System analysis	3000	3000	3000
Technology validation	6000	11,000	7000
Safety, codes and standards	7000	7000	7000
Market transformation	3000	3000	3000
NREL site-wide facilities support	1700	1800	1800
Total	\$92,283	\$97,000	\$103,000

Source Sunita [1]

The CaFCP announced in the “California Roadmap” of 2012 that 68 hydrogen filling stations should be installed within the state by the beginning of 2016 (45 stations in the area consisting of 5 clusters and 23 stations in the connection zones between the clusters) (Fig. 3.1). This roadmap also estimated that nearly 100 stations will be required by 2017 or 2018 depending on the popularization of fuel cell vehicles (FCVs.)

Governor Brown signed the California Assembly Bill 8, which required expansions in the use of clean automobiles in September 2013 and announced that the state will spend 20 million dollars every year to install up to 100 hydrogen filling stations over the state, in order to support this development plan. Furthermore, subsidies for hydrogen station installation cover up to 70 % of installation costs (75 % when constructed in a short period of time), although the final amounts will depend on the scale of station implementation. Combinations of multiple funds will be allowed for the installation.

As of June 2015, 9 stations have been opened within the state (Fig. 3.1) and 19 more are planned to be opened by this fall. In addition, construction of 28 stations through the use of subsidies amounting to 46.6 million dollars by the CEC has been requested (1 of these is a mobile filling station). A total of 230 FCVs are currently operating in California, and 16 fuel cell (FC) buses have been introduced along fixed bus routes.

In October 2013, seven states (Connecticut, Maryland, Massachusetts, New York, Oregon, Rhode Island, and Vermont) as well as California signed a memorandum of understanding “to introduce a total of 3.3 million zero-emission vehicles (ZEVs) by 2025.” These ZEVs include FCVs as well as battery electric vehicles (BEVs), and plug-in hybrid electric vehicles (PHEVs). The northeastern states including New York have been very positive about FCV adoption and are planning to launch infrastructure establishment mainly in large coastal cities.

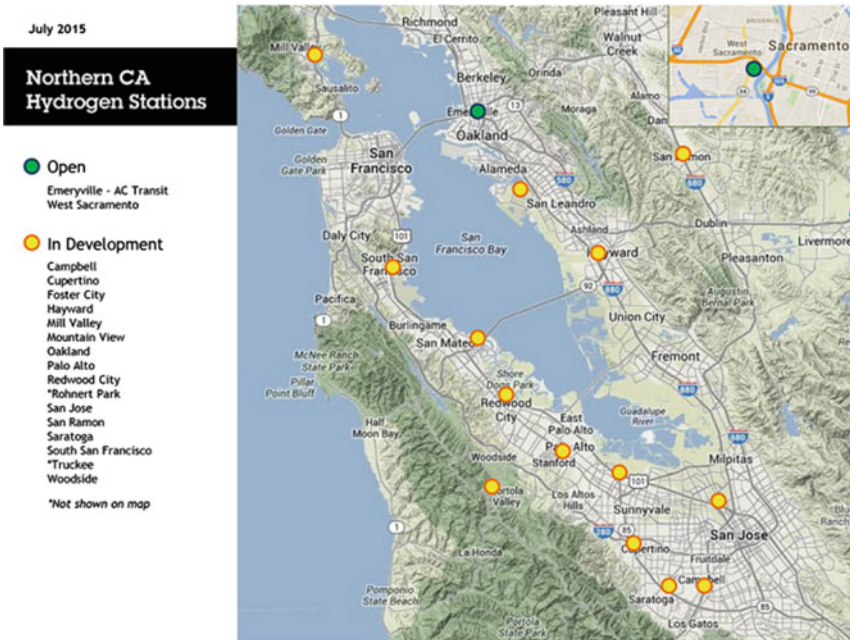
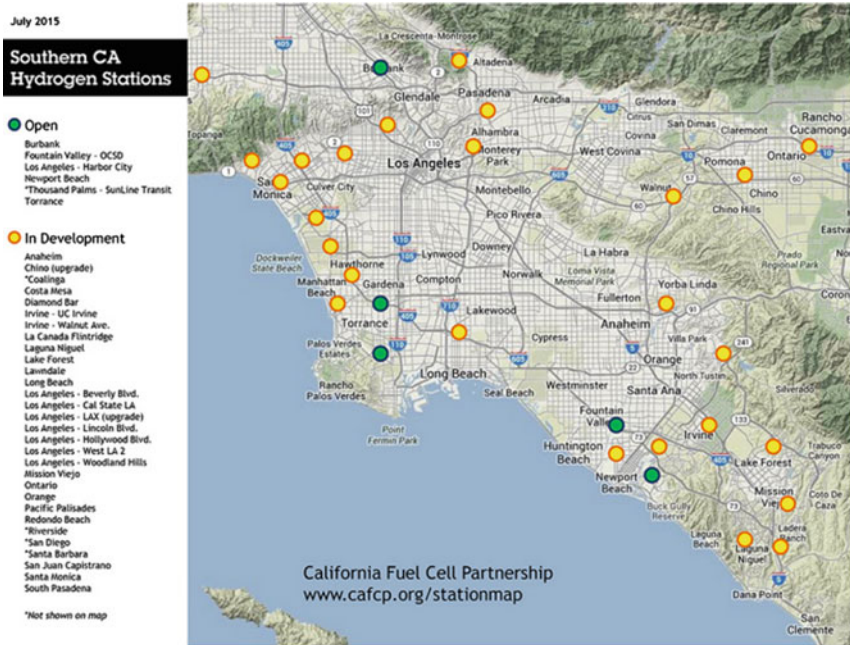


Fig. 3.1 Hydrogen station deployment plan for the California roadmap [2]

Although the purpose is slightly different, the state of Hawaii is planning to utilize FCVs for military purposes in coordination with GM, the DOE, and the Department of Defense (DOD). Additionally, the state will produce hydrogen for fuel cell buses by utilizing its rich renewable energy sources (wind power and geothermal energy).

To expand such state-level movements to the national level while supporting them, the DOE launched “H2USA,” which is a government–private partnership program, in May 2013. Japanese automobile manufacturers, GM, Daimler (Mercedes-Benz USA), and Hyundai Motor are participating in this program to establish the required infrastructure at the national scale and examine the best mechanisms for market introduction.

In regards to fuel cells, popularization of PEMFCs started in the U.S. with forklifts (material handling) and backup power applications. With the subsidy program by American Recovery and Reinvestment Act of 2009 (ARRA), 700 fuel cell forklift units were introduced. Additionally, 7500 units have been introduced even without DOE funds, due to the clear customer benefits of utilizing fuel cell forklifts (such as short refueling time and clean emissions) for large-scale consumer product companies and retail businesses. Fuel cell backup power application is also expanding due to the low reliability of US electricity grids. 900 fuel cell backup power units were introduced with ARRA subsidies, and an additional 6000 units were purchased even without the subsidy. Bloom Energy and other companies have been rapidly developing their businesses for industrial fuel cells with a focus on applications in the information technology (IT) field such as data centers; these companies are receiving some assistance from governmental or regional subsidies.

The DOE announced a new program focusing on medium temperature fuel cells called Reliable Electricity Based on Electrochemical Systems (REBELS), in 2014. This program is intended to develop an unprecedented and innovative fuel cell by combining the advantages of PEFCs and SOFCs. The budget is being provided by the Advanced Research Projects Agency-Energy (ARPA-E) program.

The DOE has clear cost objectives. These are set to 40 USD/kW for fuel cells in automobiles by 2020 (with mass production of 500,000 units), and a final goal of 30 USD/kW. However, the current cost (as of 2013) is 55 USD/kW. For stationary small fuel cells (5 kW), the set objectives are 1500 USD/kW, a power generation efficiency of 45 %, and an durability of 60,000 h or longer by 2020. For stationary medium fuel cells (100 kW–3 MW), the targets are set to 1500 USD/kW with the use of natural gas, (or 2100 USD/kW with the use of biogas), a power generation efficiency of 50 %, and a durability of 80,000 h or longer by 2020. At present, the DOE has concentrated its efforts on reducing platinum loading, the development of non-platinum catalysts, and the development of a low-cost membrane electrode assembly (MEA), including reduction of deterioration. Argonne National Laboratory and Lawrence Berkeley National Laboratory have developed nanoframe catalysts for platinum loading reduction efforts and have achieved 6.2 kW/g of platinum-group metal (PGM) by applying a 3 M nanostructure thin film (NSTF) in the MEA.

The DOE has supported the development of molten carbonate fuel cells (MCFCs) for large-scale stationary systems. However, the DOE does not have a program to popularize small residential stationary fuel cells, although it supports fuel cell popularization as small backup power supplies. While developments are underway in niche markets such as forklifts, emergency power supply applications, and military applications, the expected launch times for practical applications of fuel-cell-powered electric vehicles (FCEVs) by automobile manufacturers has been set to rather medium- to long-term prospects; mass production has been scheduled for 2020 or later (GM). Commercialization of PEFCs is occurring in a wide range of fields including backup power supplies and small mobile devices. For SOFCs, Bloom Energy has released a series of 100 kW-class power generation modules, which are currently of world-class quality in terms of commercialized SOFCs. GE has also announced the development of a 1 MW-class SOFC-based high-efficiency distributed power generation system with a power generation efficiency of 65 % when combined with gas engines. Venture companies are also actively working on portable SOFCs.

3.2 European Union

In Europe, the European Commission Directorate-General for Research and Innovation (DG-RTD) had been responsible for the fuel cell and hydrogen programs within Europe's Framework Programme (FP) for many years. The "Fuel Cells and Hydrogen Joint Undertaking (FCH JU)," which is a public-private partnership, was launched in 2008 as an organization to promote hydrogen/fuel cell projects. It has been responsible for project creation and implementation as well as understanding corporate needs. This FCH JU program was implemented until 2014, and those efforts resulted in the introduction of 74 fuel cell buses, 260 hydrogen-powered vehicles, and the installation of 20 new hydrogen filling stations. At present, FCH2 JU is being implemented as the second stage of FCH JU for the period 2014–2020.

Furthermore, starting in January 2013, Hydrogen Infrastructure for Transport (HIT) was launched as a part of the Trans-Europe Transport Network (TEN-T). Denmark, France, the Netherlands, and Sweden are participating in this program to construct hydrogen infrastructure with reference to the German CEP and H2 Mobility programs as well as the British UK H2 Mobility program. The TEN-T plans to establish two hydrogen filling stations in Denmark (Fredericia and Aalborg) and one station in the Netherlands (Rotterdam).

In January 2013, a "Clean Power for Transport Package (CPTP)" policy was developed to promote clean energy in the transportation field. That policy specifies that hydrogen infrastructure will be expanded nationwide in countries that already have hydrogen filling stations by the end of 2020. It is expected that the total number of hydrogen filling stations in Europe will reach 245 by the end of 2020 thanks to this policy.

In regards to fuel cells, the FCH JU has been implementing continuous and wide-range measures. These measures include experimental and simulation analyses of the performance/durability of catalysts/electrodes or electrolyte materials that have been newly developed. Additionally, porous structures of membrane/electrode assemblies made of new materials are being tested under simulated operating conditions and the effects of startup at below freezing temperatures or with low-humidity conditions are being evaluated. Furthermore, a study on the effects of impurities on cell characteristics and many other similar studies are being conducted. Demonstrations for 1000 fuel cells (high-temperature SOFCs, medium temperature SOFCs, high-temperature PEFCs, and low-temperature PEFCs) are being conducted in 12 European countries through the “Ene.Field” program. Following the commercial release by CFCL, which was founded in Australia, various companies including Swiss HEXIS are now working on commercial releases of SOFCs and demonstration projects with prospects for commercial release. Austrian Plansee, whose strength lies in metallic interconnect materials, has also addressed high output developments for metal-support-type SOFCs.

3.3 Germany

In Germany, the Federal Ministry of Transport, Building, and Housing (Bundesministerium für Verkehr und Wohnungswesen; BMVBS, renamed in January 2014 as the Bundesministerium für Verkehr und digitale Infrastruktur; BMVI) led the hydrogen/fuel cell technology innovation program (NIP). The NIP stipulates investments of a total amount of 1.4 billion euro (government and private parties are each responsible for half) for hydrogen/fuel cell technology developments over 10 years from 2007 to 2016. Among the government share of 700 million euro, 500 million euro comes from BMVI and the rest comes from the Federal Ministry for Economic Affairs and Energy (Bundesministerium für Wirtschaft und Energie; BMWi). 54 % of the NIP budget is for transportation applications, 36 % for stationary applications and 10 % for special market applications. The Nationale Organisation Wasserstoff-und Brennstoffzellentechnologie (NOW) was established as the implementing organization for the NIP.

The timeframe for the establishment of hydrogen filling stations in Germany can be divided into the market startup stage (up to 2015) and the full-fledged development stage (2016 and later). Hydrogen filling station establishment during the market startup stage (up to 50 stations nationwide) was implemented within the framework of the demonstration project entitled Clean Energy Partnership (CEP), and the BMVBS provided about half of station establishment subsidies. The locations of the stations were announced in 2014; multiple stations will be located in the major cities and hydrogen filling stations will also be setup between the cities (Fig. 3.2).

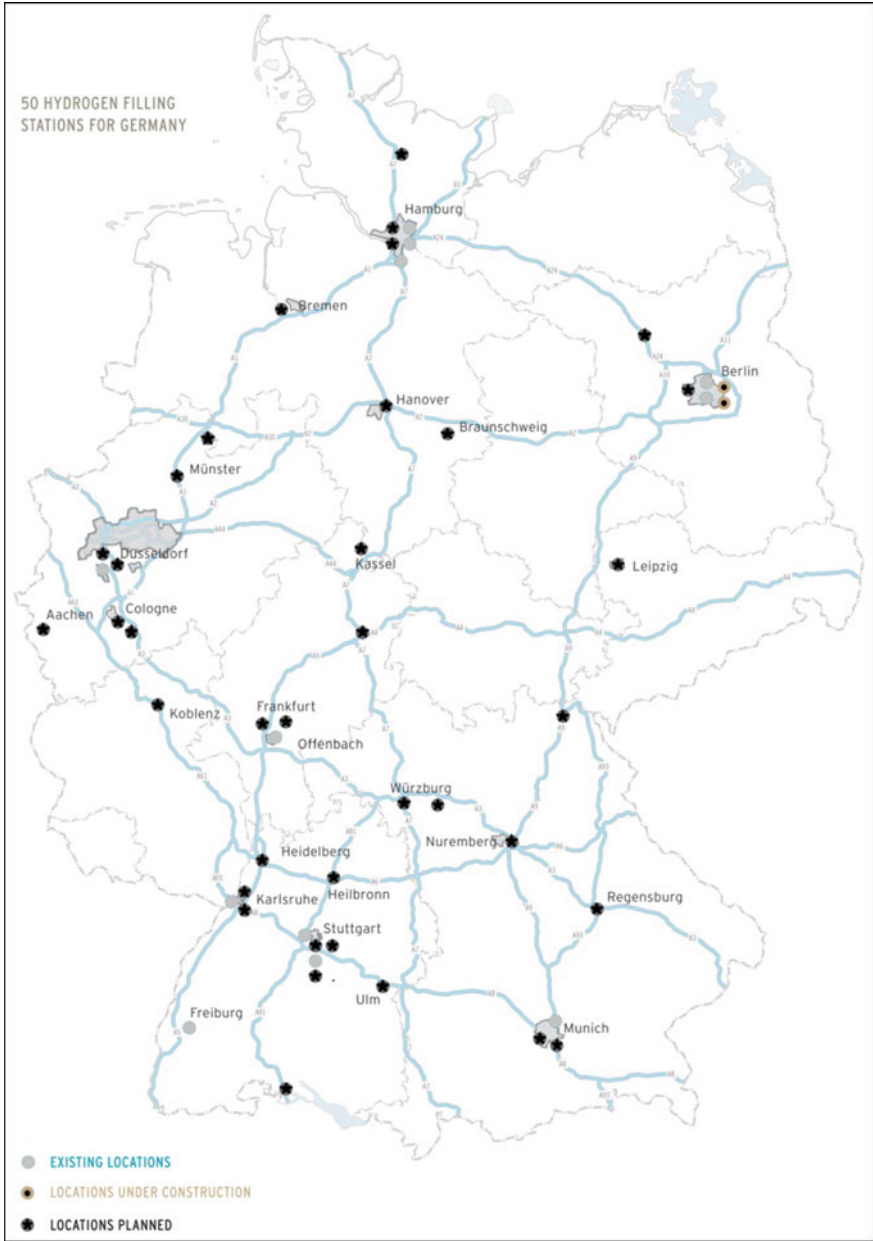


Fig. 3.2 Locations of 50 hydrogen stations in Germany as of 2015 [3]

Full-fledged development in 2016 and later is being planned within the framework of “H2 Mobility.” H2 Mobility is a public–private partnership organization in which Japanese automobile manufacturers also participate, and it works to prepare hydrogen filling station expansion plans and business plans. Six mainly German companies that participate in H2 Mobility (Daimler, Air Liquide, Linde, OMV, Shell, and Total) announced an action plan in September 2013 in which they indicated their intention to set up 100 hydrogen filling stations by 2017 and 400 stations by 2023 (at least 10 stations in each urban area, 1 every 90 km on highways). The total investment in this infrastructure establishment is estimated to reach 350 million euro, and governmental support has been requested. The current number of hydrogen filling stations in Germany is 17. Station deployment is slightly behind schedule, but it is expected that all 50 stations will be open by early 2016 (Fig. 3.3).

Regarding fuel cells, government-led support programs for environmental technologies as well as various demonstration projects are being implemented actively, thus improving the technical levels of the related industries. Commercialization is being implemented for PEMFCs over a wide range of fields including fuel cells for submarines, which have already been put into practical use, backup power supplies, battery charging power supplies, and small mobile devices.

In stationary fuel cell applications, demonstrations for a total of 500 (currently about 350) stationary fuel cells are being implemented through the Callux program (Fig. 3.4). The participating companies are Baxi Innotech (PEMFC), Hexis (SOFC), and Vaillant (SOFC). Germany intends to address the commercialization of stationary fuel cells in 2016. They will also implement the FuelCell@Home program, which specializes in commercial SOFCs. For many years, nationwide activities have tried to have the Research Center Juelich and the Fraunhofer Institute conduct basic research and transfer the outcome technologies to private companies to be implemented. This has worked well, but they have struggled in addressing full popularization issues for stationary fuel cells. In particular, the key company Ceramic Fuel Cell Limited (CFCL), which commercializes high-efficiency stationary SOFCs, has been hampered by some recent management problems. Importantly, Germany has long winters when heating is inevitable, and thus co-generation technologies would be appropriate for use. Fundamental studies have been made at universities and research institutes including Max-Planck Institutes and the German Aerospace Center (DLR).

3.4 Scandinavian Countries

Norway has promoted “HyNor,” a hydrogen highway plan, since 2006. However, the government-managed petroleum company Statoil that had been cooperating in HyNor withdrew from the hydrogen business after purchasing Hydro, which had been developing electrolysis stations, and announced that they would return to their main business focus. These developments have forced changes in the HyNor plan.

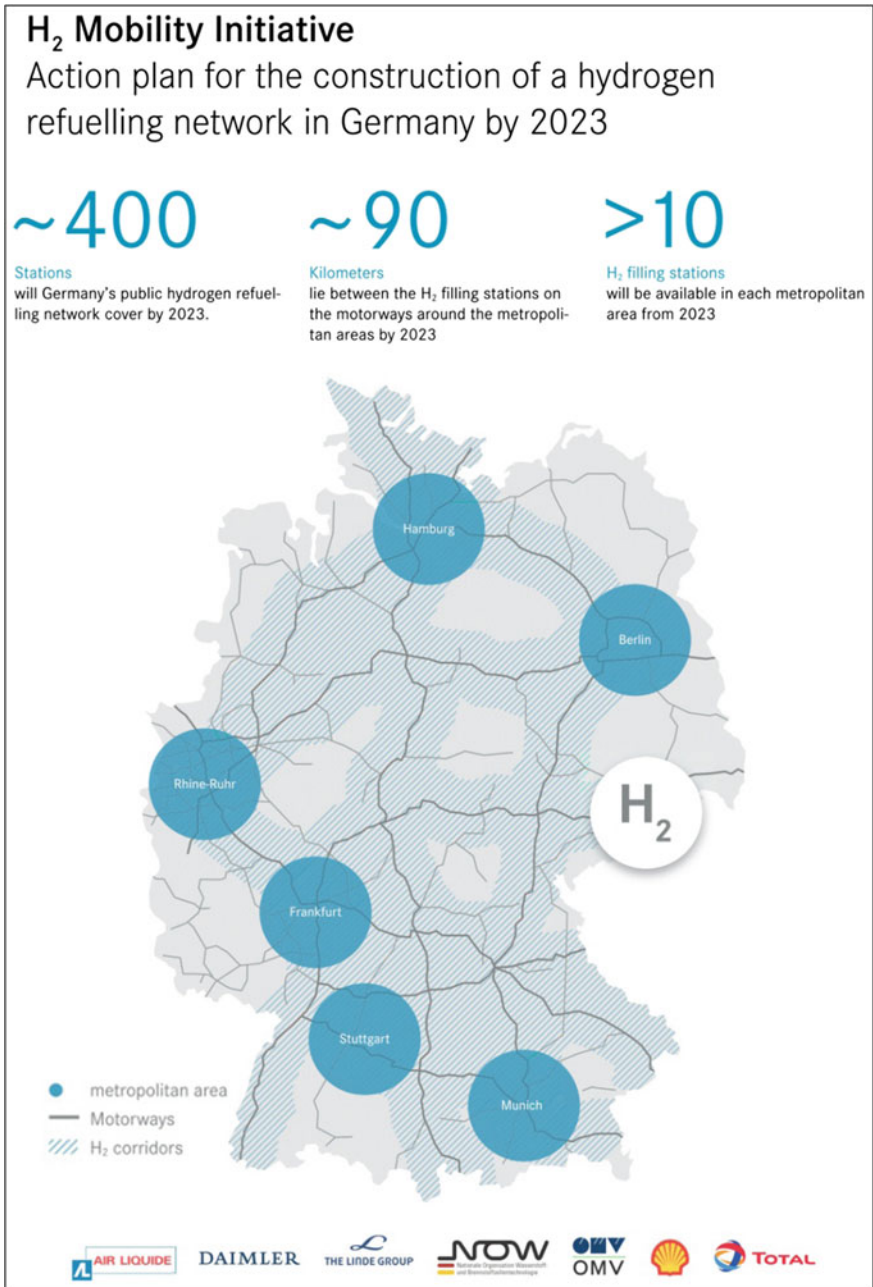


Fig. 3.3 Hydrogen station plan for Germany by 2023 [4]

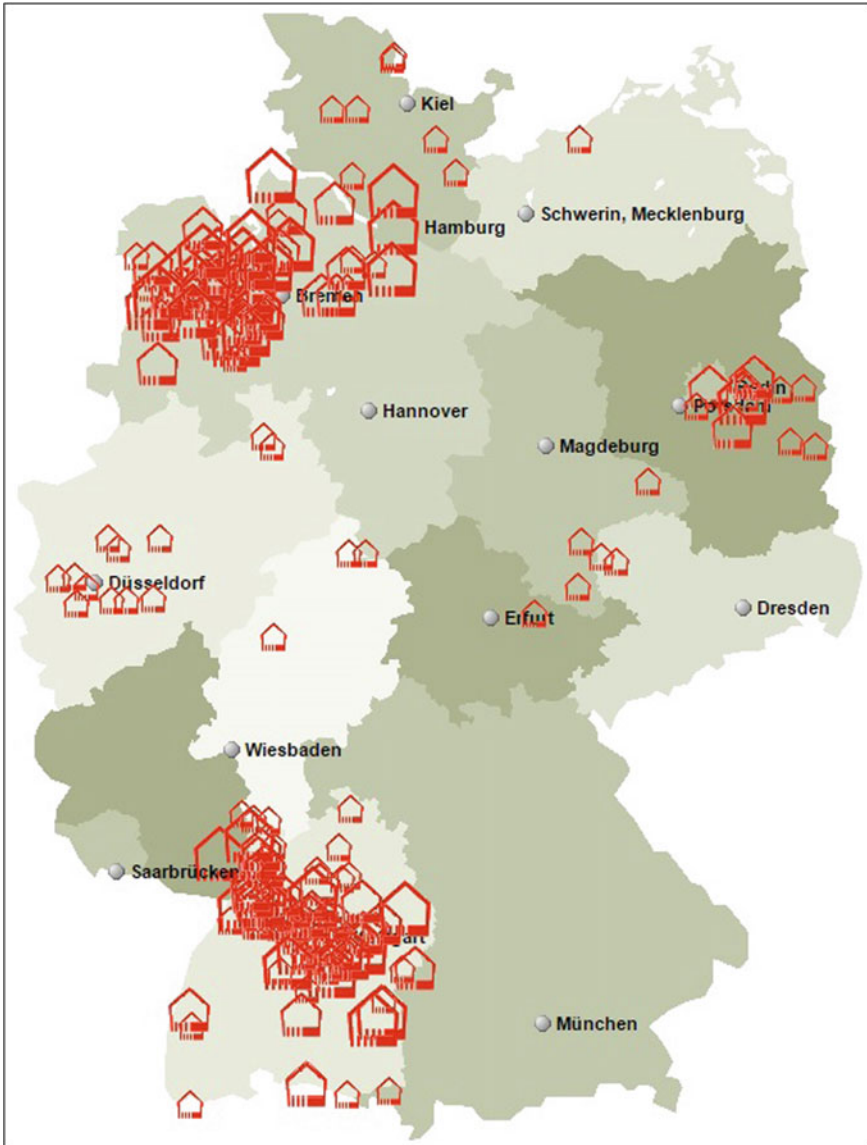


Fig. 3.4 Stationary fuel cell systems installed by the Callux program [5]

Specifically, the management company HYOP was founded in order to keep the existing hydrogen filling stations in operation, and it was decided that the hydrogen highway developments would be concentrated in Oslo for the time being.

At present, there are 6 hydrogen filling stations in Norway (of which 1 is a special station for fuel cell buses), approximately 10 FCVs, and 5 fuel cell buses in

operation. Although target years have not been specified, they plan to popularize approximately 10,000 FCVs and establish 10–20 hydrogen filling stations during the second stage, and approximately 100,000 FCVs and 70 hydrogen filling stations during the third stage. A key characteristic of the plans for Norway, where most of the electricity comes from hydroelectric generation, is that hydrogen filling stations will be mainly designed to be the onsite water electrolysis type.

Denmark is also actively establishing hydrogen filling stations, and three stations (one in Copenhagen, two in western Denmark) are presently operational. They plan to increase the number to 16 in the near future. The hydrogen highway program of Denmark is called HydrogenLink, and there are high expectations that it will contribute to a line that connects North Europe and Germany. Since Denmark is promoting wind energy to replace fossil fuel, hydrogen stations are also electrolyzer-based. H2 Logic, Danish compact hydrogen station assembler, is the leading the market.

Sweden currently has two hydrogen filling stations (Malmo and northern Sweden). The program in Sweden is called HydrogenSweden, but details about the program have not been announced. It is said that they plan to establish about 10 stations in the future.

These Scandinavian countries have formed the Scandinavian Hydrogen Highway Partnership (SHHP) to promote hydrogen infrastructure establishment in a coordinated manner (Fig. 3.5). In October 2012, these three countries along with Iceland signed a memorandum of understanding with automobile manufacturers

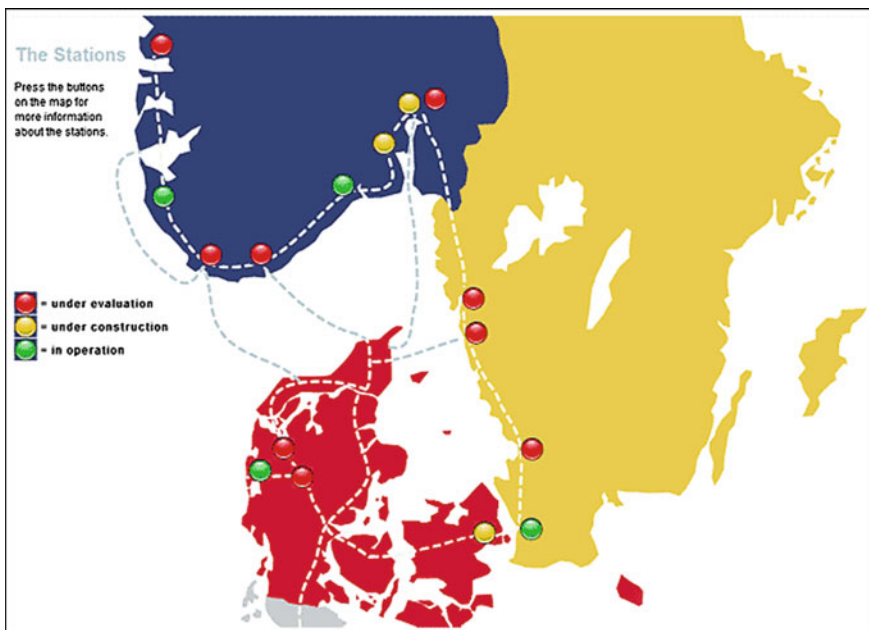


Fig. 3.5 Scandinavia hydrogen highway [6]

(Toyota, Nissan, Honda, and Hyundai) and infrastructure companies to try to address FCV introduction in 2014 to 2017.

Furthermore, in the fuel cell field, selective technologies are being advanced, as the Danish Topsoe announced that it would pull out of SOFC development and specialize in high-temperature steam electrolysis (SOEC).

3.5 The United Kingdom

Following Germany, the United Kingdom launched “UK H2 Mobility,” as a public–private partnership in 2012. Similar to Germany’s H2 Mobility program, businesses are to closely cooperate with one another to draw a roadmap for hydrogen filling station development.

When the UK H2 Mobility program was launched in January 2012, three ministries of the British government (the Department for Transport, the DOE and Climate Change, and the Department for Business, Innovation, and Skills) as well as domestic and international automobile manufacturers and energy companies agreed to participate. The UK H2 Mobility program released a Phase 1 Report (roadmap) in February 2013. This roadmap estimates the number of FCV sales that it will take to reach approximately 300,000 by 2030 and a cumulative number of 1.6 million vehicles. To accomplish this, they intend to establish 65 stations nationwide during the first stage (2015–2020), 330 stations in 2020–2025, and 1150 stations in 2025–2030 (Fig. 3.6).

In regards to fuel cells, the British company Intelligent Energy, which has been good at developing PEFCs using pure hydrogen as the fuel, has been trying to

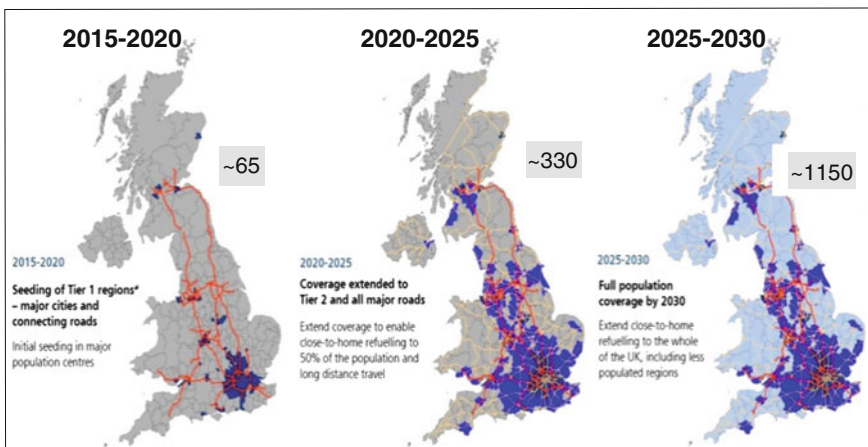


Fig. 3.6 The United Kingdom’s H2 mobility roadmap [7]

develop multipurpose products. In addition, Ceres Power is trying to develop a metal-supported SOFC based on technology from Imperial College for ceria-based thin film electrolyte materials.

3.6 France

France also launched the public–private partnership “H2 Mobility France” in 2013 to develop France’s hydrogen infrastructure deployment plan. The partnership includes government agencies, energy companies, hydrogen infrastructure producers, FCV manufactures, and research organizations. In 2014, H2 Mobility France revealed the “Study for a Fuel Cell Electric Vehicle national deployment plan,” which depicts a 35 MPa-based hydrogen station network plan as a realistic infrastructure solution for France. The initial hydrogen deployment focuses on captive fleets, mainly using “HyKangoo,” a range extender EV with a 5 kW fuel cell, for La Poste’s postal delivery operation. Since these vehicles do not require high-performance hydrogen stations, the plan expects to build 35 MPa-based hydrogen station network throughout the country (Fig. 3.7).

3.7 Switzerland

Switzerland has a long tradition with fuel cells. Christian Schoenbein was the first person to theorize the concept of fuel cells, which stimulated William Grove in UK to invent the fuel cell. The first solid electrolyte fuel cell (using a zirconia-based electrolyte) was invented by Nernst, and demonstrated by Bauer et al. in 1937 (see Chap. 2). Switzerland started to act as a country to coordinate fuel cell-related collaborative activities in the International Energy Agency (IEA) around the end of 1980s. The Swiss Federal Office of Energy has managed national R&D programs since 1990, focusing on SOFC system development and PEFC fundamental research, and later hydrogen storage and related studies. Based on such research and development activities for more than two decades, a Swiss company HEXIS is planning to start the commercialization of residential SOFC co-generation systems.

3.8 South Korea

In South Korea, the Green Growth Committee, which is an organization under the direct control of the President, announced the “Green Car Industry Development Strategy and Challenges” Report in December 2010, with goals to address the popularization of approximately 10,000 FCVs and 43 hydrogen filling stations in 2015 and approximately 100,000 FCVs and 168 hydrogen filling stations in 2020.



Fig. 3.7 H2 mobility France’s hydrogen station deployment plan [8]

However, these were goals set up by the previous regime, and the current regime has not announced any specific policies regarding the next generation automobiles including FCVs and EVs. At present, the hydrogen filling station development plan is being examined and the results are to be announced in June 2015. While there are currently 18 hydrogen filling stations in South Korea, not all of them are accessible to the public. However, South Korea practically follows the U.S. and Europe in terms of regulations and standards for hydrogen filling stations, and most of the station-related devices and dispensers have been entirely prepared by American or European manufacturers.

In regards to fuel cells, Hyundai Motor launched limited commercial sales of FCVs. Additionally, POSCO has set a goal to achieve an annual production scale of 100 MW with MCFCs. South Korean LG purchased the SOFC development division of British Rolls-Royce, which had a long history of research and development activities that reinforced fully fledged practical applications.

3.9 The People's Republic of China

China also promotes research and development activities for FCVs. Development of PEFC-mounted buses and automobiles is currently at the demonstration stage in China. The “New 863 Program” for 2011–2015 mainly focuses on the development of PEFC FCVs and related technology, large SOFC stacks, and co-generation systems combining PEFC and SOFC technology. China has several PEMFC stack manufacturers, among which Sunrise Power and Shen-Li High Tech are leading the market. Tsinghua University, Tongji University as well as Dalian Institute of Chemical Physics (DICP) are also working on PEMFC technology development.

China has a long tradition with ceramic materials so that there are several institutions that activate studying SOFC-related materials. Some companies have actually taken over the place of earlier manufacturers in the field of ceramic-type fuel cells.

References

1. Satyapal S (2015) 2015 DOE annual merit review. In: Proceedings “overview of DOE hydrogen and fuel cells program”. http://www.hydrogen.energy.gov/pdfs/review15/01_satyapal_plenary_2015_amr.pdf. Accessed 11 Dec 2015
2. California Fuel Cell Partnership. A California road map. <http://cafc.org/carsandbuses/caroadmap>. Accessed 11 Dec 2015
3. Butsch H (2014) HRS infrastructure in Germany and Europe-current activities. http://www.hydrogen.energy.gov/pdfs/review14/h2in_butsch_2014_o.pdf. Accessed 11 Dec 2015
4. http://www.now-gmbh.de/fileadmin/user_upload/RE_Inhalte_Mediathek_NEU_2013/Praesentationen_Verkehr_und_Infrastruktur/Bystry_H2Mobility.pdf. Accessed 29 Jul 2015
5. Callux Program. <http://www.callux.net/projektarte.html>. Accessed 11 Dec 2015
6. Scandinavia Hydrogen Highway. <http://www.hydrogencarsnow.com/index.php/scandinavian-hydrogen-highway/>. Accessed 11 Dec 2015
7. UK H2 Mobility (2013) https://www.gov.uk/government/uploads/system/uploads/attachment_data/file/192440/13-799-uk-h2-mobility-phase-1-results.pdf. Accessed 11 Dec 2015
8. http://www.afhypac.org/images/documents/h2_mobilit_france_en_final_updated.pdf Accessed 29 Jul 2015

Chapter 4

Development Histories: Hydrogen Technologies

Kazukiyo Okano

Abstract This chapter describes the long history of the development of hydrogen and related technologies starting in the sixteenth century. Various applications in the history of hydrogen gas are described including airships, aerospace power, electrolyzers, hydrogen combustion, and hydrogen transportation ships for global hydrogen energy networks. The consequent efforts are then described including the realization of hydrogen filling stations, fuel cell vehicles, and stationary fuel cells.

Keywords History · Hydrogen gas · Airship · Aerospace · Electrolyzer · Power plant · Hydrogen filling station

The history of hydrogen starts in the 1500s, when it was mainly used in basic research and in balloons. The use of hydrogen then expanded to, e.g., airships in the 1900s. After the Haber–Bosch process to synthesize ammonia was invented, large quantities of hydrogen were needed and large-capacity alkaline water electrolysis devices were developed to mass produce this hydrogen.

Hydrogen has also been produced in mass quantities for industrial processes such as petroleum refining, metalworking, the production of glass, food products, and semiconductors. However, the use of hydrogen in the energy field was originally limited to rocket fuels and boiler fuels, since no equipment to use hydrogen as energy had been developed at that time. However, the situation changed dramatically after the first oil shock in 1973. Hydrogen suddenly became a potential clean energy source that could replace petroleum. Since then, expectations for hydrogen energy use have fluctuated over time depending on the state of energy resources (e.g., the availability of other alternative energy resources for petroleum) and

K. Okano (✉)
Kyushu University, 6-8-5 Wakamiya, Ichihara-shi, Chiba 290-0006, Japan
e-mail: okano@icntv.ne.jp

© Springer Japan 2016
K. Sasaki et al. (eds.), *Hydrogen Energy Engineering*,
Green Energy and Technology, DOI 10.1007/978-4-431-56042-5_4

pressing environmental problems (e.g., air pollution prevention measures to protect against NO_x and SO_x, and measures to prevent global warming with reductions in CO₂ emissions). In 1996, when it was announced in the 2nd Assessment Report of the Intergovernmental Panel on Climate Change (IPCC) that increases in CO₂ concentrations were likely the cause of global warming, hydrogen became a strong contender as a countermeasure that could be used to achieve CO₂ emission reductions.

After 1996, research and development activities aimed at finding practical applications for hydrogen energy were accelerated, and researchers maintained a keen interest in the international activities of the IPCC and the Conference of the Parties (COP) regarding the global environment. Commercial release of fuel cell vehicles (FCVs) followed the commercialization of fuel cells, and the year 2015 can now be regarded as the era in which the use of hydrogen as energy fully started. This history of hydrogen is summarized in Figs. 4.1 and 4.2.

4.1 Discovery of Hydrogen and Its First Use (1700–1970)

In the beginning of the sixteenth century, Paracelsus from Switzerland discovered that a gas was formed during the reaction between sulfuric acid and iron. Myelin, also from Switzerland, reported in the seventeenth century that this gas burned. Boyle from Britain found that a flammable gas could be formed by adding acid to iron scraps in 1761. In 1766, Henry Cavendish from Britain confirmed that inflammable air was formed during the reaction between hydrochloric acid and zinc, and he was named as the discoverer of hydrogen because he reported key findings in an article to the Royal Society of London that described experiments whereby water was formed by reacting hydrogen and oxygen in the presence of electric sparks. Since none of these elements had names, one was called vital air and the other inflammable air.

In 1785, Antoine L. Lavoisier in France successfully reproduced the experiment of Cavendish and named the vital air as oxygen and the inflammable air as hydrogen. It was in a reconnaissance balloon for the military that hydrogen was used in a practical application for the first time; the first balloon injected with hydrogen was created by Jacques Alexander Cesar Charles in France during 1783.

Manufacture of hydrogen by water electrolysis was first made possible by William Nicholson and Sir Anthony Carlisle in the U.K. in 1800, when they discovered that hydrogen and oxygen could be formed by running electricity through water. This method was later named “electrolysis.”



Fig. 4.1 Development history of hydrogen energy technologies (before 1990)

1990	1995	2000
<ul style="list-style-type: none"> ▼ 1990 The US congress passed the Spark-A. Matsunaga Hydrogen R&D and D Act. The Hydrogen Technical Advisory Panel (HTAP) was mandated by the Matsunaga Act. ▼ 1992 US DOE Hydrogen Program -----2000 ▼ 1993 Japan's New Sunshine Program-----2000 ▼ 1993 Japan's WE-NET (World Energy Network) Project -----2003 R&D project for large scale hydrogen energy systems Japan's first hydrogen fueling station was constructed in 2002 in the WE-NET project 	<ul style="list-style-type: none"> ▼ 1995 Conference of the Parties; COP1 was held ▼ 1997 COP3, Kyoto Protocol ▼ 1996 IPCC 2nd Assessment Report (Greenhouse gas emissions could cause changes to the climate unprecedented in human history) ▼ 1994 The world's first commercially permitted solar-hydrogen station in Clean Air Now Project was built for H₂ ICE vehicles at Xerox in El Segundo CA ▼ 1994 Daimler Benz demonstrated its first NECAR1 (Fuel cell vehicle) in Germany ▼ 1995 The Chicago Transit Authority operated 3 fuel cell buses in regular service ▼ 1996 Europe's first hydrogen fueling station was built in Erlangen by EQHPP Munich Airport Hydrogen Project ▼ 1997---2006 	<ul style="list-style-type: none"> ▼ 2000 European H₂ and FC Technology Platform ▼ 2008 -2013 EU's FCH JU Multi-Annual Implementation Plan * FCV and FC bus demonstration lighthouse Project in EU <ul style="list-style-type: none"> ▼ 2002 -----2005 ▼ 2006 -----2009 CUTE FC bus demo HYLEET CUTE FC bus demo ▼ 2010 CHIC fuel bus demo in 5 cities -----2016 ▼ 2004 Zero Regio Project -----2010 ▼ 2002 ---German CEP FCV demo project ---2016 ▼ 2009 ---- German H2 Mobility ▼ 2000 NRW FC and Hydrogen Network ▼ 2007 German National Innovation Program, H2 and FC Technology --- 2016 ▼ 2001 ECTOS and STEP FC bus project ▼ 2006 Scandinavian Hydrogen Highway Partnership (SHHP) ----- 2015 <ul style="list-style-type: none"> ▼ 2005 Linde developed ionic compressors for hydrogen ▼ 2012 Hydrogenics unveiled the world's largest 200m³/h PEM electrolysis stack ▼ 2007 The BC hydrogen highway, Vancouver --2011 ▼ 1999 -- Demonstration of FCVs, California Fuel Cell Partnership -----2012 <ul style="list-style-type: none"> ▼ 2003 US President announced hydrogen fuel initiative. FutureGen project---- ▼ 2013 H2USA Initiative ----- ▼ 2005 DOE FCV demo project--2009 ▼ 2003 Japan's national R&D projects on hydrogen technologies ----- ▼ 2002 Japan's JHFC1 and JHFC2 FCV demo project -----2010 <ul style="list-style-type: none"> ▼ 2006 MAZDA leased RX-8 H2 RE ▼ 2013 Chiyoda Corp. verified large-scale hydrogen storage vehicles in the market ▼ 2010 Kawasaki Heavy Industries started to build the liquefied -----2025 hydrogen supply chain from Australia
2000	2010	2015

Fig. 4.2 Development history of hydrogen energy technologies (after 1990)

4.2 Use of Hydrogen in the Aerospace Fields (1900–Present)

Count Ferdinand von Zeppelin of Germany invented the first balloon that used hydrogen to maintain the buoyancy of an airframe in 1900, and airships to cross the Atlantic were put into service during the 1920s and 1930s. However, after the fire accident on the Hindenburg airship, which was about to land in the U.S. in 1937, people around the world began to believe that hydrogen was a dangerous gas that could explode. The accident was later investigated by the U.S. National Aeronautics and Space Administration (NASA), and the primary cause turned out to be the alumina-type paint that was applied to the ship's body; this paint-ignited static sparks that caused the ship's body to catch fire, and thus the hydrogen inside was also ignited. Hydrogen itself was not the cause of the accident after all (see Fig. 4.3).

In the U.S., NASA was founded in 1958 to pursue space exploration and development activities. As an agency, NASA has made great historical contributions to hydrogen use, as it employs hydrogen as a fuel and is the world's largest liquid hydrogen user. The Kennedy Space Center in Florida has the world's largest liquid hydrogen storage tank with a capacity of 3200 m³, and this is where they store the liquid hydrogen to be used for space shuttle launches. Figure 4.4 shows a space shuttle, and Fig. 4.5 shows the storage tank.

In 1961, the first rocket by Aerojet Rocketdyne that used liquid hydrogen fuel was launched. The first space shuttle was launched in 1981, and the Soviet Union successfully completed a flight with TU-155, the world's first jet engine aircraft that used liquid hydrogen fuel, in 1988.

At present, several countries including the U.S., various European countries, Russia, Japan, and China have successfully launched spacecraft or artificial satellites with large rockets that employed liquid hydrogen fuel.

Fig. 4.3 Hindenburg disaster
(Source Gus Pasquerella, 1937, Public Domain)

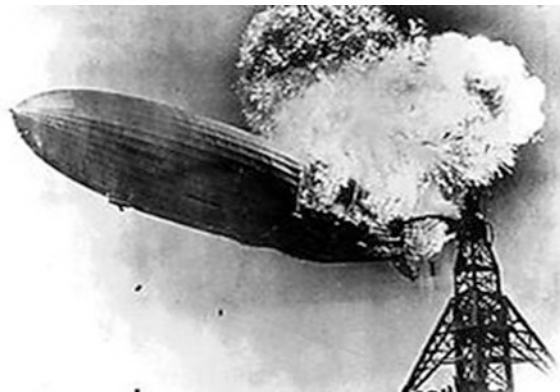


Fig. 4.4 Space shuttle
(Source NASA, public domain)



Fig. 4.5 LH₂ tank at the Kennedy Space Center
(Source Kazukiyo Okano)



4.3 Production of Hydrogen for Industrial Use (1920–Present)

4.3.1 Hydrogen Production by Alkaline Water Electrolysis

The production of hydrogen for industrial use began in Europe and North America in the 1920s. The Stuart Oxygen Company in Canada, which was later named the Electrolyzer Corporation, was the first company to manufacture and release a commercial water electrolysis system for another company in San Francisco in

Fig. 4.6 World's largest electrolyzer at Aswan (Source Kazukiyo Okano)



1920. The demand for industrial hydrogen increased considerably when German Fritz Haber developed the Haber process to synthesize ammonia, which is used as a raw material in fertilizers, from nitrogen and hydrogen in 1906. Then, in 1930–1977, many large-capacity alkaline water electrolysis systems of the 20,000–30,000 Nm^3/h -class were manufactured and installed by companies such as Lurgi, DeNora, Norsk Hydro, and Brawn Boveri/DEMAG in Europe.

The 32,000 Nm^3/h tank-type water electrolysis system manufactured by Brawn Boveri/DEMAG in 1970 was the largest system in the world and one was installed in Aswan, Egypt (see Fig. 4.6). Norwegian Norsk Hydro developed the proprietary filter-press-type water electrolysis system, which was quite popular during the 1990s. While alkaline water electrolysis systems traditionally could be divided into tank-types and filter-press-types, the current large systems have been narrowed down only to the filter-press-types, which have a smaller installation area, high efficiency, and room for pressure increases.

As the method for large-capacity hydrogen production changed from the water electrolysis method to the less expensive petroleum reforming method during the 1980s, many manufacturers were forced to stop producing water electrolysis systems and several were taken over by or merged with other companies. The technology is currently under the purview of Norwegian NEL Hydrogen, German ELT, and Swiss IHT. While there is practically no demand for such large-capacity water electrolysis systems and only small-capacity systems are being produced today, large-capacity alkaline water electrolysis systems will be necessary again if the time comes when hydrogen is produced at large scales using renewable energy in the future.

Both Canadian Stuart Energy, founded in 1948, and Belgian Vandenberghe, founded in 1987, achieved good results with relatively small-capacity alkaline water electrolysis systems of up to the 100 Nm^3/h -class; Stuart Energy eventually purchased Vandenberghe in 2003. However, Hydrogenics, a relatively new company in Canada that was founded in 1995, purchased Stuart Energy in 2003 and became the largest manufacturer of small water electrolysis systems that supply most of the 60 Nm^3/h -class water electrolysis systems for hydrogen filling stations and



Fig. 4.7 Stuart energy electrolyzer (*Source* Kazukiyo Okano, 1995)

power-to-gas plants in the U.S. and Europe. Figure 4.7 shows Vancouver's 80 Nm³/h tank-type water electrolysis system that was manufactured by Stuart Energy in 1995; it is used as a station for fuel cell buses (its internal electrolytic cells are also shown in the right figure).

4.3.2 Hydrogen Production by Solid Polymer-Type Electrolyte Water Electrolysis

The GE company in the U.S. developed a fuel cell that utilized an ion-exchange membrane as the solid polymer-type electrolyte, and it began to apply this fuel cell technology to water electrolysis. This led to the development of a high-efficiency hydrogen production method that could be used in oxygen generation systems for submarines in the early 1970s.

However, they pulled out from new energy technology development when governmental subsidies were discontinued in the early 1980s and they sold their fuel cell and water electrolysis division to United Technologies (UT). Then, a former employee from UT founded Proton Onsite in 1996 and commercialized the solid polymer-type electrolyte electrolyzer, which has been adopted in many 10 Nm³/h-class hydrogen stations. In addition, Canadian Hydrogenics released an unprecedented, large 200 Nm³/h water electrolysis system that employs solid polymer-type water electrolysis cell stacks and delivered it to a power-to-gas project in Germany (see Fig. 4.8).

In Japan, the Government Industrial Research Institute, Osaka (currently the National Institute of Advanced Industrial Science and Technology, Kansai) started basic research on solid polymer-type water electrolysis systems in 1975 through the Sunshine Program, which aimed to develop water electrolysis cell manufacturing methods using electroless deposition techniques. This technology was also utilized later in the World Energy Network (WE-NET) Project. While the WE-NET Project developed large-capacity systems, smaller systems were commercialized for

Fig. 4.8 200 Nm³/cell stack
(Source Hydrogenics)



Fig. 4.9 50 Nm³/h PEM
electrolyzer (Source
KOBELCO-Solutions)



industrial purposes by Shinko Pantec Co., Ltd. (Kobelco Eco-Solutions Co., Ltd. at present) (see Fig. 4.9). Hitachi Zosen Corporation and so forth are also working on such developments.

4.3.3 Hydrogen Production from Hydrocarbons

Steam reforming of hydrocarbons was industrialized in the 1930s in the U.S., and since about the 1960s, this technology has become fixed as the most economic large-scale hydrogen manufacturing method. The 2700 Nm³/h natural gas reformer at HydroEdge LH₂ Plant in Sakai is shown in Fig. 4.10. The partial oxidation method was developed during the 1950s.

When the petroleum industry in Japan started processing imported crude oil during the 1920s, large quantities of hydrogen were required for the purification methods that were used to remove the impurities from crude oil and hydrodesulfurization methods for heavy oil, gas oil, and so forth. Thus, the refineries installed large-scale production plants with single unit capacity-class 30,000–100,000 Nm³/h systems that were capable of manufacturing hydrogen; this was accomplished in part by hydrocarbon reforming, wherein hydrogen was also produced as a byproduct during the catalytic reforming processes. In the future, it is estimated that

Fig. 4.10 2700 Nm³/h natural gas reformer (Source HydroEdge)



hydrogen sales of about 4.7 billion Nm³/year to external parties, such as the automobile industry, would be possible using their reserve capacity for production. In addition, ammonia synthesis plants have hydrogen production systems, and it is estimated that their reserve capacity for hydrogen production would be able to supply approximately 600 million Nm³/year for automobiles and so forth in the future. Furthermore, approximately 2.8 billion Nm³/year of hydrogen could be supplied from byproduct hydrogen captured from chemical and petrochemical industries that produce caustic soda and chlorine during brine electrolysis, and the steel industries that use coke furnaces during steel manufacturing. Combining all of these potential sources, it will be possible to supply hydrogen at 8.1 billion Nm³/year for automobiles only from existing facilities.

Compact package types that were developed based on the concept of phosphoric acid fuel cells instead of chemical plants are popular as relatively small reforming-type hydrogen production systems to be used for hydrogen filling stations and industrial purposes. Figure 4.11 shows the 300 Nm³/h reforming-type hydrogen production system for hydrogen filling stations that was developed by Osaka Gas; it is used during LPG reforming. Systems for natural gas reforming are also available.

Since around 1992, Tokyo Gas and Mitsubishi Heavy Industries have been working on the development of a membrane reactor that incorporates a hydrogen separation membrane module. These devices are meant to represent the next

Fig. 4.11 Osaka gas HYSERVE-300P (Source OsakaGas)



generation of small reformers that are capable of reforming natural gas at 550 °C, which is lower than typical temperatures by 200 °C, and they have a compact system design and excellent reforming reaction efficiency. An experimental system of 40 Nm³/h is in operation at Tokyo Gas. Development of such devices is also being conducted at other businesses as well as research institutes such as universities. Ultimately, popularization can be expected if long-term durability of the hydrogen separation membrane and higher system efficiency can be addressed.

4.3.4 Production of Liquid Hydrogen

Production of liquid hydrogen at industrial scales started in the U.S. during the latter half of the 1950s, and the production capacity reached 160 t/day during the early 1960s. Today, the production capacity is 210 t/day. In Canada and Europe production began in the 1980s, and now Canada has a production capacity of 24 t/day, while Europe has a production capacity of 26 t/day. At present, there are 13 overseas plants worldwide (not counting Japan) with production capacities of 4 t/day or larger. Demand for liquid hydrogen started to grow mainly because of aerospace development programs in Europe and the U.S., and there are liquefaction plants in the U.S. equipped with two units of liquefaction systems that have a 35 t/day capacity, which is the largest in the world. In the 1970s and later, demand for liquid hydrogen shifted mostly from space applications to industrial applications.

In Japan, a liquefaction system to produce liquid hydrogen for rockets was installed by the Osaka Hydrogen Industry Co., Ltd. (presently, the Iwatani Industrial Gases Corp.) in Amagasaki in 1978. At present, there are hydrogen liquefaction plants in Sakai, Ichihara, Shunan, and Oita with a total production capacity of 21.4 t/day. The 10 t/day liquefaction facility at the HydroEdge Plant in



Fig. 4.12 LH₂ plant at HydroEdge (Source Iwatani Corp.)



Fig. 4.13 LH₂ 20 ft container (Kawasaki Heavy Industries)

Sakai is shown in Fig. 4.12. While production of liquid hydrogen started for rocket fuel, the quantity of hydrogen distributed for industrial purposes increased gradually as it can be easily transported and stored. Production of liquid hydrogen is expected to increase in line with increased demand at hydrogen filling stations. While liquid hydrogen, which has a temperature of about $-253\text{ }^{\circ}\text{C}$, is generally transported in tank trucks, it can also be shipped by small means of land or ocean transport and stored in fixed storage tanks. A 20 ft container with a built-in 14.65 m^3 tank manufactured by Kawasaki Heavy Industries is shown in Fig. 4.13. There are 40 ft containers that have also been manufactured.

4.4 Hydrogen Energy Technology Research and Development Triggered by the Oil Crisis (1970–2000)

4.4.1 *Foundation and Activities of Hydrogen Energy-Related Organizations (1973–1989)*

Triggered by the oil crisis in 1973, hydrogen energy started to attract much attention as an alternative energy source to petroleum. Consequently, hydrogen-related research programs were initiated at several universities and other research organizations in various locations around the world. In Japan, the Hydrogen Energy Society that was the predecessor to the Hydrogen Energy Systems Society of Japan (HESS), was founded in 1973. They claimed even then that hydrogen was a type of clean energy that would be necessary to use to prevent the depletion of fossil fuels and reduce the environmental pollution associated with the combustion of fossil fuels. Then, during the following year of 1974, people from universities all over the world who were interested in hydrogen gathered at Miami University in the U.S., and the attendees included Dr. T. Nejat Veziroglu, Miami



Fig. 4.14 15th world hydrogen energy conference (WHEC) in Yokohama (Source Kazukiyo Okano)

University, Dr. John O'M. Bockris, a professor at Flinders University in Australia, and Professor Tokio Ota of Yokohama National University who founded the International Association of Hydrogen Energy (IAHE) there. The first World Hydrogen Energy Conference (WHEC) was held in Miami in 1976. Since then, this conference has been held around the world every 2 years and it has become the largest international conference on hydrogen in the world. The 3rd WHEC was held in Tokyo in 1980, and the 15th WHEC was held in Yokohama in 2004, at which a total of 1500 participants from 40 different countries were present (see Fig. 4.14). In 1989, the U.S. National Hydrogen Association (NHA) was founded, and this organization has made considerable contributions to the history of hydrogen development. For example, the NHA holds an international symposium every year. However, it merged with the U.S. Fuel Cell Council in 2010 and changed its name to the Fuel Cell and Hydrogen Energy Association (FCHEA). At present, hydrogen associations have been formed all over the world and these organizations are actively working in Europe, Asia, America, and so forth. An ISO/TC/197 Committee that reviews international standards on hydrogen technologies was also founded in 1989.

4.4.2 Renewable Energy Utilization Hydrogen Projects in Europe (1986–1999)

In the 1980s, there was a drive in Europe to implement technological developments and demonstration projects involving the production of hydrogen through photovoltaic and hydroelectric power generation processes. Hydrogen utilization was mainly promoted by Germany, and the following three large projects were launched in 1986 with a goal of establishing hydrogen societies in the future:

- **The Euro–Quebec Hydro-Hydrogen Pilot Project (EQHHPP)**

The Euro–Quebec Hydro-Hydrogen Pilot Project (EQHHPP) was a large-scale international project implemented by Europe and Canada. The project was launched officially in 1986 with Germany as the central organizing force. The EQHHPP enabled research on hydrogen energy systems that could produce hydrogen through water electrolysis using the power generated by hydroelectric power plants in Canada. That hydrogen would then be transported to Europe as liquid hydrogen. The EQHHPP also conducted research on hydrogen application technologies such as transport and storage technologies for liquid hydrogen, including hydrogen fueled buses, fuel cell power generation plants, fuel cell ships, jet engine aircrafts, hythane (hydrogen blended with compressed natural gas) buses, and also, technologies related to safety measures (see Figs. 4.15 and 4.16). Although it ended in 1998 because of a lack of funding, this was a pioneering project that showed to the world that long-distance sea transport of liquid hydrogen was possible, thus illustrating the fact that a large-scale international hydrogen supply network would be possible. The project influenced the efforts of many other countries.

- **Solar-Wasserstoff-Bayern (SWB) Project**

The Solar-Wasserstoff-Bayern (SWB) Project was initiated by the German state of Bayern to produce hydrogen through water electrolysis driven by the power generated from photovoltaic cells. That hydrogen, which was stored as hydrogen gas, was to be used in applications such as fuel cells, fuel cell forklifts, and so forth. An experimental field was constructed within the large premises of Neunburg vorm Wald in southeast Germany in 1986. In addition to making comparisons of various

System Overview

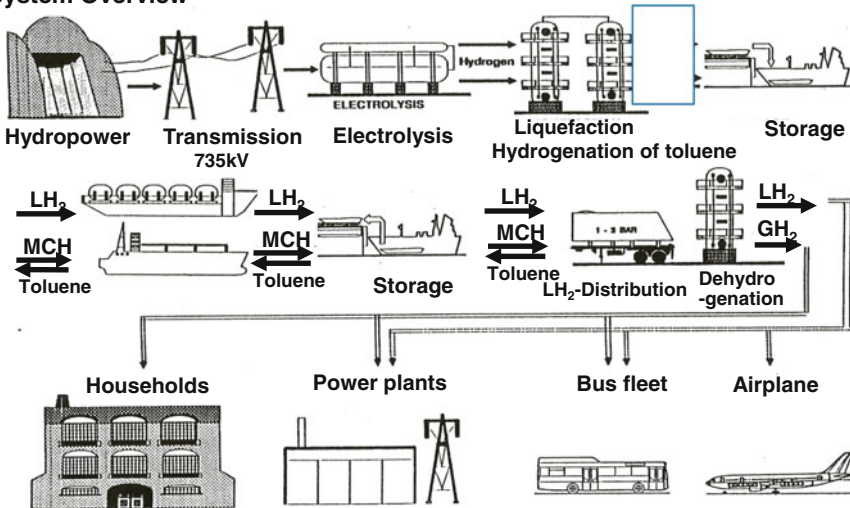


Fig. 4.15 Hydrogen energy system (Source EQHHPP)

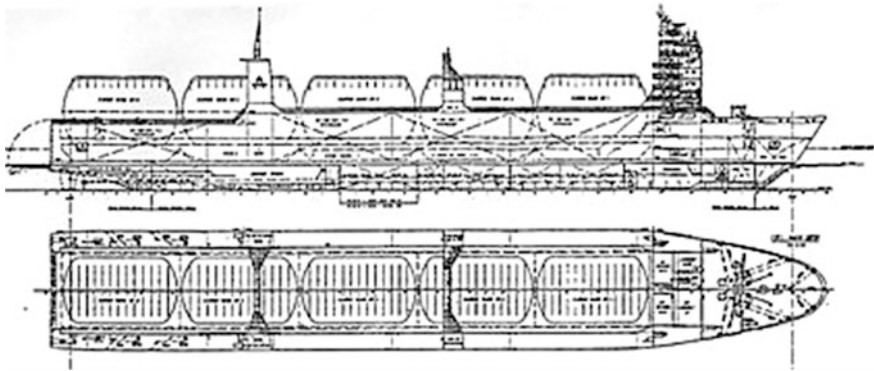


Fig. 4.16 Liquid hydrogen tanker for the EQHHP (Source EQHHP)

photovoltaic cells and researching the best practices for operational control of hydrogen production systems, the researchers at this field site constructed 30 kW phosphoric acid fuel cells using the hydrogen produced and stored using normal pressure or pressurized alkaline water electrolysis technologies. Furthermore, they demonstrated the effective operation of fuel cell forklifts and developed a system that could be used to fill hydrogen engine vehicles with liquid hydrogen. The SWB Project ended in 1999. Figure 4.17 shows the solar-hydrogen system of the SWB Project, and Fig. 4.18 shows the experimental field that was used.

• German–Saudi Arabian Joint Project (Hysolar)

Hysolar was a joint project between Germany and Saudi Arabia that was implemented from 1986 to 1995. During Hysolar, researchers experimented on a

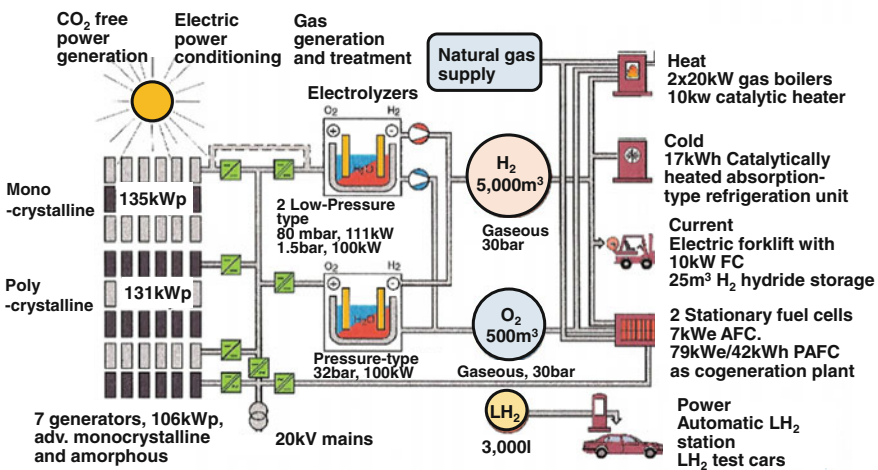


Fig. 4.17 Solar hydrogen test system (Source SWB)

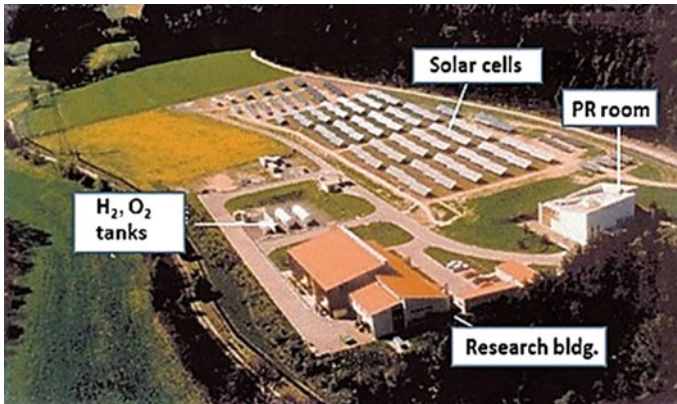


Fig. 4.18 Solar-Wasserstoff-Bayern (SWB) site at Neunburg vorm Wald (*Source* SWB)

hydrogen production system that would produce hydrogen via water electrolysis reactions with the power generated from 350 kW photovoltaic cells that were installed in the Saudi Arabia desert. Key research was also conducted on the operational best practices for photovoltaic-water electrolysis systems at German research institutes.

4.5 Hydrogen Energy Technology Developments by National Projects (1990–Present)

Influenced by the above projects that were going on in Europe, the U.S. and Japan launched two large hydrogen technology development projects as a part of their national policies in the 1990s. The European Union also announced its Hydrogen Vision in 2003 and founded an organization to promote it.

4.5.1 U.S. Department of Energy Hydrogen Program (1992–Present)

In the U.S., which had fallen behind Europe in the development of hydrogen energy technology, a legislative bill was developed that was entitled the Hydrogen Research, Development, and Demonstration Act. This bill was prepared by Japanese-American Representative Spark Matsunaga from Hawaii with the cooperation of Japanese-American Patrick Takahashi, a professor at the University of Hawaii who was an expert in hydrogen technology. The bill was submitted to Congress in 1990 and passed. This bill led to the foundation of a Hydrogen

Technical Advisory Panel (HTAP) that would provide policy proposals to the DOE, which was the main governmental organization promoting the Hydrogen Program. The DOE Hydrogen Program was launched in 1992 and systematic research and development efforts intended to produce world-class hydrogen technologies were conducted over a period of many years. Through this program, broad research themes with development potentials were timely selected throughout the hydrogen energy field, and this was made possible by the proposals of HTAP. Importantly, HTAP was comprised of diverse members familiar with both hydrogen technologies and the international trends regarding hydrogen energy development. The members not only included researchers from universities and national institutes, but also engineers from major companies, corporate managers of venture companies, and so forth.

In 2003, President George Bush announced a hydrogen fuel initiative that would invest \$1.2 billion for 10 years into the development of technologies to commercialize fuel cells that can operate on hydrogen. In addition, the Secretary of the DOE founded the International Partnership for Hydrogen and Fuel Cells in the Economy (IPHE) to promote the development of hydrogen technologies through international cooperation. While the U.S. government has continued to promote research and development activities for hydrogen technologies, funding sources for such activities have changed over the years. These activities began to be supported through tax credits after enactment of the American Recovery and Reinvestment ACT in 2009. Some of the current efforts have been to promote the market introduction of fuel cells and hydrogen-related facilities. In 2006, HTAP was changed to the Hydrogen and Fuel Cell Technical Advisory Committee (HTAC) to reflect its handling of both hydrogen and fuel cells. They continue to lead the world in research and development, and more than 1500 people have attended the Annual Merit Review Meetings as observers. These meetings present the outcomes of overall DOE projects on an annual basis.

4.5.2 Japan's WE-NET (World Energy Network) Project (Fiscal Years 1993–2003)

At the end of fiscal year 1993, Japan's Ministry of International Trade and Industry (MITI) launched a long-term, large-scale project to conduct research on hydrogen energy systems as well as the required technological development. This project was based on an idea similar to that of Europe's EQHHPP. The concept of WE-NET is shown in Fig. 4.19, and its targets are shown in Fig. 4.20. In this project, a large sum of the budget was invested in a wide range of research and technological development activities including (i) conceptual designs for large-capacity PEM water electrolysis systems, liquid hydrogen transport tankers, and liquid hydrogen storage tanks, (ii) research on heat insulation structures, low-temperature materials, and hydrogen storage materials, and (iii) development of pure hydrogen fuel cells,

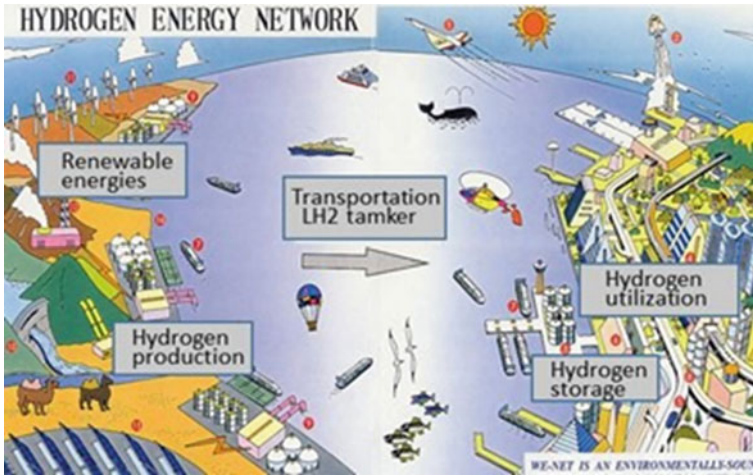


Fig. 4.19 Concept of the world energy network (WE-NET) hydrogen system (Source New Energy and Industrial Technology Development Organization: NEDO)

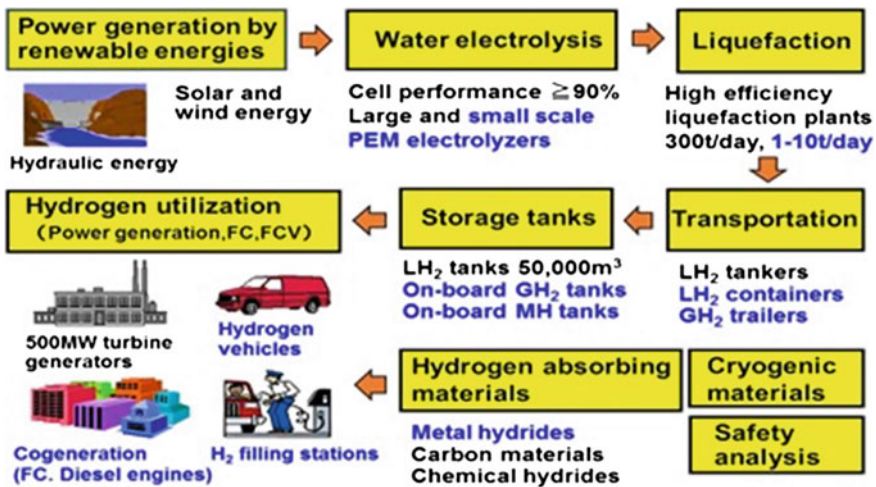


Fig. 4.20 Research and development targets for the world energy network (Source WE-NET)

500 MW hydrogen turbine technology, hydrogen engines, and hydrogen filling stations. In addition to the conceptual design for the overall system, examinations of economic feasibility and safety were made until fiscal year 2003. Cell efficiency improvement activities were focused on the research and development of PEM electrolyzer technology, and researchers attempted to develop technology capable of reaching 90 % efficiency. However, it was found that practical applications with the targeted development of 1 m × 1 m large-area electrodes would not be easy

because of problems with the membrane strength among other issues. The findings from performance experiments on heat insulation structural materials for tanks and the conceptual design on the hull did show that the construction of liquid hydrogen transport tankers would be possible (see Figs. 4.21, 4.22, and 4.23).

With high-efficiency hydrogen turbines to combust hydrogen and oxygen, the system was designed to be capable of combined cycle power generation with a high efficiency of 61 %. Experiments were also conducted on the hydrogen/oxygen combustor, which is one of the main components of the system. However, problems with the heat-resistant materials and cooling system were encountered when the gas inlet temperature reached extremely high levels of around 1700 °C. While such

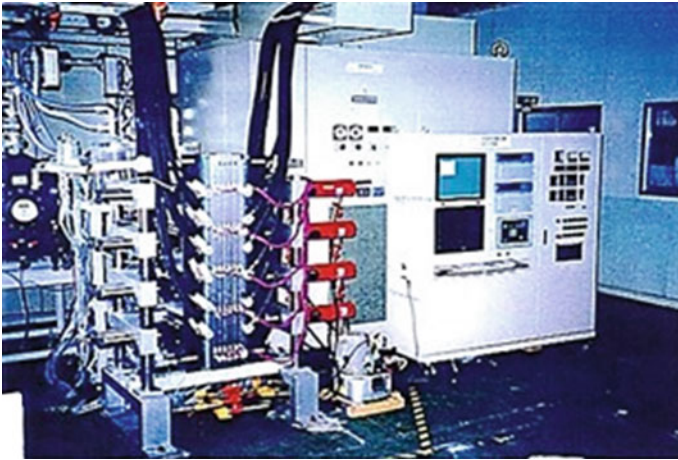


Fig. 4.21 Electrolysis cell test (Source Fuji Electric Co.)



Fig. 4.22 200,000 m³ liquid hydrogen tanker (Source Kawasaki Heavy Industries)



Fig. 4.23 50,000 m³ LH₂ tank (Source ENAA)

problems might be possible to solve with additional long-term development efforts, development activities were eventually discontinued because of the lack of funding. Notably, development would have been relatively easier for hydrogen and air combustion methods, but the efficiency would have been lower. Figure 4.24 shows the hydrogen/oxygen turbine cycle, and Fig. 4.25 shows the test system for the hydrogen/oxygen combustor.

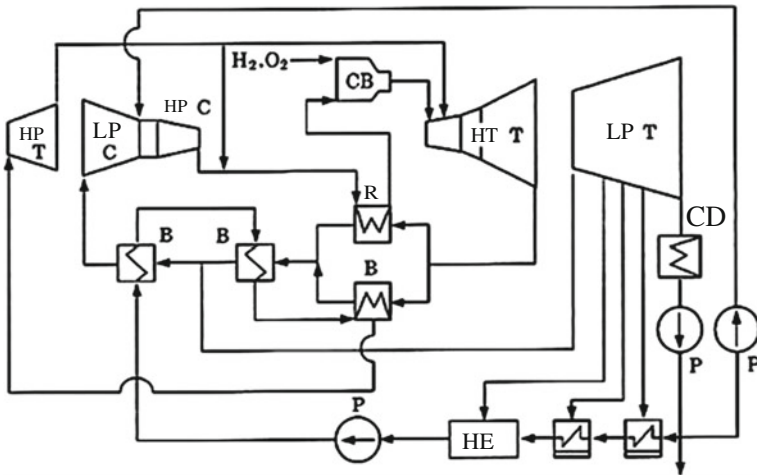


Fig. 4.24 H₂-O₂ turbine cycle (T Turbine, C Compressor, B Steam generator, R Regenerator, HE Heater, CD Condenser, CB Combustor, P Pump, HP High-pressure, LP Low-pressure, HT High-temperature) (Source NEDO/WE-NET)

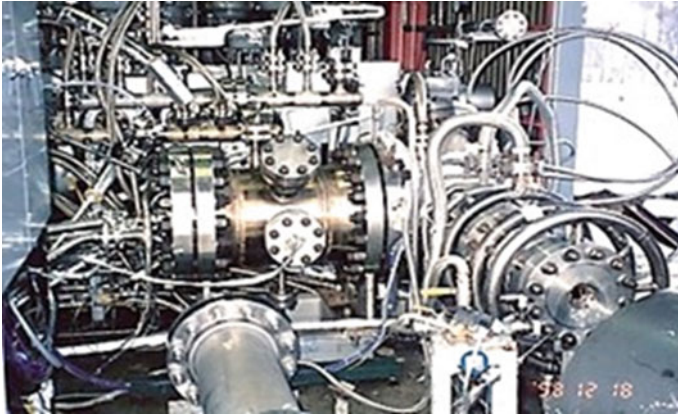


Fig. 4.25 H₂-O₂ combustor tests (Source NEDO/WE-NET)

During the latter half of the project, examinations of the economic feasibility of installing and operating hydrogen filling stations for fuel cells were conducted and technological development activities continued to be implemented with short-term themes. Accordingly, the first natural gas reforming-type hydrogen filling station was established in Osaka, the first PEM water electrolysis-type hydrogen filling station was established in Takamatsu, and the first compressed hydrogen transport-type hydrogen filling station was established in Tsurumi, Yokohama in early 2002. When the WE-NET Project ended during the fiscal year of 2003, the results indicated that it would be possible to build a large-scale hydrogen supply system to transport large quantities of liquid hydrogen from overseas. Moreover, the project's research and development outcomes for overall hydrogen technologies have had a large influence on current research and development attempts in Japan.

4.5.3 European Union Research and Development Through European Hydrogen Vision (2002–Present)

In the European Union, the European Hydrogen Vision was launched in 2003 to support the development of hydrogen societies. This initiative was a part of the 6th Framework Program for Research and Technological Development (FP6), which ran from 2002 to 2006. In 2004, the European Hydrogen and Fuel Cell Technology Platform (HFP) was established as the promoting organization for demonstration projects involving fuel cell buses and small fuel cell moving systems. In FP6, 80 hydrogen/fuel cell development projects were implemented. In addition, a Joint Technology Initiative (JTI) was started in 2007 to promote research and development activities for the 7th Framework Program (FP7); the JTI was responsible for the implementation of many demonstration projects involving fuel cell buses and so

forth, which were known as Lighthouse projects. The FP7 ended in 2013. In 2014, the New Research Program Horizon 2020 was founded to continue research and development activities.

4.5.4 Hydrogen Storage Technology Research and Development (1960–Present)

- **Metal Hydrides (MHs)**

The history of metal hydrides (MH) began during the mid-1800s when Scottish chemist Thomas Graham reported that palladium absorbed hydrogen. Research to utilize this phenomenon of hydrogen absorption began in earnest during the 1960s, and this in turn led to experimental evidence that magnesium-based alloys and vanadium-based alloys could absorb and release hydrogen and that the reaction dynamics would vary based on the alloy composition. These findings were reported by J.J. Reilly from the U.S. Brookhaven National Institute. In 1968, Zijlstra and Westendorp from the Philips Institute in the Netherlands accidentally discovered a rare earth MH. This discovery led to the birth of LaNi_5 , which delivers excellent characteristics and can be used in practical applications such as nickel-hydrogen batteries that employ AB_5 -type MHs as the negative electrode; these became widely popular during the 1990s. At present, large nickel-hydrogen batteries using high-performance superlattice alloys as the negative electrode have been developed and are being used widely in hybrid and fuel cell vehicles.

In Japan, research on MHs was started in 1974 at the National Chemical Laboratory for Industry and the Government Industrial Research Institute in Osaka (today, both have been incorporated into the National Institute of Advanced Industrial Science and Technology), and such research has been implemented with continuance since that time. Similar development activities were also later implemented as a part of the WE-NET Project with the goal of achieving a hydrogen absorption capacity of 3 wt% (this was later changed to 5 wt%).

Development of MHs has been extensively performed worldwide as they are expected to enable safe and ideal mounting methods. FCVs mounted with MHs were manufactured by Toyota in 1996, Mazda in 1997, and Honda in 1999. In 2001, Toyota prototyped the FCHV-2, which is a FCV that contains newly developed MHs, and it achieved a cruising distance of 300 km. Figures 4.26, 4.27, and 4.28 show the MH-mounted vehicles from these three companies. The WE-NET Project promoted hydrogen filling stations with a design that could store the hydrogen as low-pressure MHs so that hydrogen could be filled into MH-mounted vehicles at a low pressure. However, these MH-mounted vehicles were heavy and only had a hydrogen absorption capacity for MH of 3 wt%, which did not reach the 6 wt% threshold that was considered feasible. The automotive industry therefore gave up on MH-mounted vehicles and decided to mount 35 MPa, and later 70 MPa, high-pressure hydrogen instead.

Fig. 4.26 Toyota FCHV-2
(Source Toyota Motor)



Fig. 4.27 Mazda Demio FCEV
(Source Mazda Motor)



Fig. 4.28 Honda FCX-1
(Source Honda Motor)



Consequently, plans for new hydrogen filling stations in Osaka and Takamatsu were changed in a hurry so that they were equipped with 40 MPa compressors, high-pressure accumulators, dispensers, and so forth. However, a MH hydrogen storage facility at a station that had been under construction was completed as planned and experiments involving hydrogen charging tests were conducted to check the performance of the test vehicles. The findings confirmed that the filling method would be sufficient if MH-mounted vehicles were to be put into use in practical applications in the future. However, other problems were encountered. Notably, vehicles with MHs require heat to release hydrogen and exhaust heat from the fuel cells can potentially be used as the heat source. Heat from FCVs was at 80 °C or lower, and it is extremely difficult to develop MHs that can release hydrogen at temperatures lower than 100 °C with a hydrogen absorption capacity

of 6 wt%. Again, only a 3 wt% hydrogen absorption capacity has been achieved globally.

- **High-Pressure Carbon Fiber-Reinforced Plastic Hydrogen Vessels**

More practical applications for FCVs became possible when light-weight carbon fiber-reinforced plastic (CFRP) vessels were developed that could handle the mounting of 5 kg of hydrogen at 35 MPa or 70 MPa. Since around 1995, Canadian Dynetek has sold several 35 MPa vessels, and U.S. Quantum Technologies, SCI, Lincoln, and so forth have also released similar products. The development of 70 MPa vessels has been relatively slow, but Lincoln manufactured the first products, in 2001.

In the U.S., Lincoln has also developed high-pressure accumulators for hydrogen filling stations and large CFRP hydrogen vessels for hydrogen transport trailers in addition to small vessels for vehicles. This was made possible by their extensive experience in manufacturing high-pressure composite gas vessels for military and aerospace applications, natural gas vessels for automotive applications, and so forth, which dates back to 1963. Lincoln developed a CFRP composite vessel trailer, with a weight of 8 t, which can transport up to 600 kg of hydrogen at 25 MPa. A 20 MPa steel vessel weighing 14 t is mounted in a conventional trailer capable of transporting 200 kg of hydrogen. In Japan, the use of large CFRP vessels is expected to increase in the future, as regulations are eased. Kawasaki Heavy Industries have developed a 45 MPa CFRP composite vessel trailer within a NEDO project (see Fig. 4.29).

In regards to the domestic production of hydrogen vessels for automobiles, Toyoda Gosei Co., Ltd. developed a 35 MPa tank in 2004 and is currently supplying 70 MPa vessels for Toyota's FCVs. In addition, Samtech Co., Ltd. is developing vessels for automobiles as well as large vessels for pressure accumulators.



Fig. 4.29 45 MPa carbon fiber-reinforced plastic (CFRP) composite vessel trailer (Source Kawasaki Heavy Industries)

4.6 Development of Hydrogen Vehicles and Demonstration Projects for the Commercial Use of Hydrogen (1970–2009)

4.6.1 Development of Hydrogen Vehicles

Development of hydrogen engines for automobiles was first initiated by BMW in the 1970s. In Japan, Professor Furuhashi at the Musashi Institute of Technology (currently Tokyo City University) began his research at around the same time. In 1974, he conducted a demonstrative drive of “Musashi No. 1,” the first 2000 cc hydrogen engine vehicle in Japan, which was made by modifying a Nissan Junior 2-ton truck (see Fig. 4.30). Improvements were later made to the design and vehicle No. 10, namely, “Musashi No. 10,” was exhibited at the COP3 meeting held in Kyoto in 1997.

BMW began public roadway tests on 15 vehicles in 1999, and they embarked on a global clean world tour with their new vehicles in 2001. BMW then made further improvements to the design and developed a mass-produced, high-end Hydrogen 7, which was leased on a commercial basis in 2006. However, they announced that they would pull out of the hydrogen engine vehicle business in 2009 (see Fig. 4.31).

Fig. 4.30 Musashi No. 1 demonstration in Tokyo (Source Tokyo City University)



Fig. 4.31 BMW Hydrogen 7



Fig. 4.32 RX-8
Hydrogen RE (Source Mazda
Motor)



The U.S. Ford Motor Company developed and released shuttle buses mounted with V10 hydrogen engines in 2006, and they are currently in use in the U.S. and Canada.

Mazda developed a hydrogen rotary engine vehicle and put it on exhibit in the 1991 Tokyo Motor Show as rotary engines were suited to hydrogen combustion. In 1995, they conducted public roadway driving tests with the MH-mounted Mazda Capera Cargo. In 2006, they launched lease sales of the RX-8 Hydrogen RE, and they have participated in the HyNor Project of Norway since October 2008 (see Fig. 4.32). In addition, lease sales of Premacy hydrogen RE Hybrids started in 2009.

Overall, many companies have conducted research and development activities on hydrogen engine vehicles as they have advantages such as low cost, quick practical applications, and automatic switching capabilities with gasoline, but popularization has been stagnating because of reasons such as low efficiency compared to FCVs and short driving distances of about 100 km. While BMW achieved a long-distance driving range of 650 km for a vehicle by mounting it with liquid hydrogen, the company eventually pulled out of the business due to the high cost of liquid hydrogen vessels and difficulties associated with the suppression of the generation of boil-off gas.

4.6.2 Demonstration of the Commercial Use of Hydrogen in the Munich Airport Hydrogen Project

German TÜV SÜD and 12 hydrogen-related companies launched the Munich Airport Hydrogen Project in 1997 with subsidies from the state of Bayern. During this project, they established a Munich Airport consortium called ARGEMUC and conducted demonstrations on a commercial utilization system that covered all aspects of hydrogen energy from its production to use. In 1999, liquid hydrogen storage tanks and an automatic liquid hydrogen filling facility, using robots, were installed. Figure 4.33 shows the hydrogen filling station, and Fig. 4.34 shows the robotic dispenser. The automatic liquid hydrogen filling station was capable of refueling both hydrogen engine cars made by BMW and hydrogen engine buses made by MAN, which were used at the airport. In addition to the hydrogen production facilities such as a natural gas reforming system, and an alkaline water

Fig. 4.33 Hydrogen station at Munich airport



Fig. 4.34 LH₂ fueling robot dispenser



electrolysis system, other technologies were also installed at the airport and these technologies included MH storage facilities, pressure accumulators, and compressed hydrogen filling facilities. Since there were few such comprehensive hydrogen facilities in operation, as many as 10,000 people from around the world visited the airport to view the system until the project ended in 2005.

4.7 Development of Fuel Cell Vehicles and Hydrogen Filling Stations (1990–2013)

4.7.1 Development of the First Fuel Cell Vehicles and Fuel Cell Buses

Development of FCVs, promoted as no-pollution vehicles that generated only water, has continued around the world since GM presented the first prototype in 1966. Forty-eight years later, Toyota designed the world's first commercial vehicle called the MIRAI and released it on December 15, 2015. During this period, the most important developmental

issues encountered were the selection of the fuel cell and the fuel. Fuel cells for automobiles shifted from alkaline fuel cells (AFCs) to phosphoric acid fuel cells (PAFCs), and eventually the developers settled on PEFCs. Regarding the fuel, it was difficult to supply pure hydrogen without the infrastructure, so on-vehicle reforming that used methanol or desulfurized gasoline were developed; however, these were not put into practical application. Then, it became possible to mount enough hydrogen to drive 500 km when light-weight CFRP high-pressure vessels were developed after trial-and-error tests for many years. Considerable efforts to improve performance, durability, low-temperature startup properties, and power output densities of PEFCs have been made and reliability has been established through long-term demonstration projects in the U.S., Germany, Japan, and so forth. The costs for such vehicles were also reduced dramatically. The history of FCV development until now is outlined below.

The first FCV in the world was an AFC FCV called “Electravan,” which operated on liquid hydrogen–oxygen, and it was prototyped and presented by GM in 1966 (see Fig. 4.35). In Japan, Sanyo Electric developed an open cart-type FCV with a mounted hydrazine-air fuel cell in 1972. Then in 1993, U.S. Energy Partners developed a fuel cell sport car with a mounted PEFC, which was followed by Daimler’s presentation of NECAR1, a FCV that uses pure hydrogen fuel and a mounted PEFC by Ballard in 1994 (see Fig. 4.36).

Fig. 4.35 GM FCV
Electravan (Source General
Motors)



Fig. 4.36 Daimler
FCV NECAR 1 (Source
Daimler)



Around 1996, most global FCV manufacturers had developed on-board reforming FCVs that used methanol or gasoline because of concern over the difficulties with hydrogen infrastructure development. Demonstrative operations were conducted at various places in 1999–2001. FCVs with on-board reforming of methanol were capable of operating at relatively low temperatures of around 300 °C, and demonstrative operations were implemented in the Kanto region by Daimler, Mazda, Honda, and Nissan (see Figs. 4.37, 4.38, 4.39 and 4.40). Toyota also developed a FCV that was mounted with an auto-thermal reformer for gasoline. Mazda, Toyota, and Honda developed MH-mounted vehicles during this same

Fig. 4.37 Nissan R'nessa



Fig. 4.38 Honda FCX-2



Fig. 4.39 Mazda Premacy FCEV





Fig. 4.40 Daimler NECAR-5

period. However, product development for on-board reforming FCVs was given up for several reasons such as the vehicles could not be started up instantaneously, it was difficult to prevent the reforming water tank from freezing during winter, and extra space was needed for the reformer. Overall, these vehicles were just not suited to frequent startups and shutdowns. As an alternative, developers devised a method to mount 35 MPa high-pressure hydrogen on the vehicles; this hydrogen was stored in CFRP vessels. At present, hydrogen storage pressures have reached 70 MPa.

Development of fuel cell buses first started in 1985 with the Fuel Cell Bus Project at Georgetown University, and this project was funded by the U.S. DOE. Since the development of PAFCs was more advanced at the time, a 30 ft bus was manufactured by BMI and Fuji Electric provided the hybrid system that relied on methanol reforming with a 50 kW PAFC and battery (see Fig. 4.41). The bus shuttled people between Washington D.C. and Georgetown and it was operated as a university school bus for several years starting in 1994. The DOE bus project then advanced to 100 kW PAFC-mounted buses and PEFC-mounted buses. Around the



Fig. 4.41 Phosphoric acid fuel cell (PAFC)-mounted fuel cell bus

same time (i.e., in 1994), buses mounted with 80 kW AFCs were manufactured by Belgian Elenco, and Canadian Ballard released a commercial model with a mounted 205 kW PEFC.

4.7.2 Demonstration of Fuel Cell Vehicles and Fuel Cell Buses Around the World (1999– 2013)

In 1999 and later, several demonstration projects that involved driving FCVs and fuel cell buses in cities were conducted around the world. The first project launched was the CAFCP Project in California during 1999, and Daimler, GM, Ford, Hyundai, Volkswagen, Toyota, Nissan, and Honda all participated by conducting long-term driving tests on FCVs. Figure 4.42 shows the vehicle base and hydrogen station. Then in 2001, the ECTOS Project was launched in Iceland to demonstrate the use of fuel cell buses. Moreover, large-scale fuel cell bus projects called CUTE and HyFLEET CUTE that were supported by the EU began in Europe during 2002, and this was followed by several demonstration projects such as the CEP for FCVs in Berlin, the Japan Hydrogen and Fuel Cell (JHFC) vehicle demonstration project in Japan, a FCV demonstration project by the U.S. DOE in 2005, and the SHHP Project that was implemented by three Scandinavian countries including Norway in 2006. Later, many other demonstration projects were conducted in various countries. In the JHFC Project, a total number of 135 vehicles were driven over 1.07 million km during the 9 years of the project, while a total of 92 vehicles were driven 1.76 million km during the 5 years of the DOE Project. These projects resulted in dramatic improvements of FCVs and fuel cell buses and helped to nurture the development of relevant application technologies. Particularly for fuel cells in automobiles, technical problems such as durability, output density, low-temperature startup properties, and external dimensions were



Fig. 4.42 California fuel cell (FC) partnership

nearly solved and costs were reduced. Furthermore, hydrogen filling stations were constructed in various parts of the world as FCVs started to be driven more frequently, and associated technologies were nurtured in these countries as well. Hence, these demonstration projects played a considerable role in putting FCVs and hydrogen filling stations into practical use as well as making their popularization in the market smooth.

4.7.3 History of Hydrogen Station Development and the Current Situation (1999–Present)

In 1994, the first hydrogen filling station in the U.S. was constructed on the premises of Xerox in El Segundo, which is just south of the city of Los Angeles. It was a solar-water electrolysis station that provided hydrogen to three hydrogen engine pickup trucks operated by Xerox under the Clean Air Now Project. The 12 Nm³/h alkaline water electrolysis system from Stuart Energy is shown in Fig. 4.43, while the pressure accumulator and a simple dispenser are shown in Fig. 4.44. The stations that were established following the Xerox station were of the liquid hydrogen storage type. One station was used to supply hydrogen to three fuel cell buses manufactured by Ballard, which were put into operation in Chicago in 1995. Another liquid hydrogen station for hydrogen engine buses was installed for the EQHHPP Project in Erlangen, Germany in 1996, and a station to supply liquid hydrogen to hydrogen engine vehicles by BMW was installed at Munich Airport in 1999.

In Japan, the first filling stations were developed for the WE-NET Project. A natural gas reforming-type station was constructed in Osaka and a PEM water electrolysis-type station was constructed in Takamatsu; this was followed by the installation of a compressed hydrogen transport-type station in Tsurumi, Yokohama. Figure 4.45 shows the Osaka station, and Fig. 4.46 shows the Takamatsu station. Later in the 2000s, hydrogen filling stations that employed



Fig. 4.43 Electrolyzer at the Xerox station



Fig. 4.44 Simple hydrogen dispenser



Fig. 4.45 Japan's first H₂ station in Osaka



Fig. 4.46 Takamatsu H₂ station

various technologies were established in countries around the world for demonstrative operation projects on FCVs and fuel cell buses.

Verification of the reliability and establishment of practical application technologies occurred thanks to the long-term operation of such stations. In Japan, 19 hydrogen filling stations were established during the JHFC Demonstration Project, and these were operated for many years. This enabled researchers to develop practical application technologies such as 70 MPa high-pressure filling technology. In 2014, 300 Nm³/h-class commercial stations were established in Amagasaki and Ebina, as shown in Figs. 4.47 and 4.48. The Amagasaki station adopted liquid hydrogen storage technology, whereas the Ebina Chuo station adopted compressed



Fig. 4.47 Iwatani Amagasaki H₂ station (Source Iwatani Corp.)



Fig. 4.48 JX Ebina Chuo H₂ station (Source JX Nippon Oil & Energy Corp.)

hydrogen storage technology in combination with a gasoline station. Both are off-site type stations.

Hydrogen filling stations can be classified as either the off-site type or the onsite type depending on the type of hydrogen source that is used. The optimal type is ultimately selected by reviewing the circumstances of each station. However, it can be expected that off-site-type stations will be constructed more frequently during the initial stages of FCV introduction because of the relatively low costs.

Off-site type. With off-site stations, various methods are used to transport compressed hydrogen or liquid hydrogen to the station where it is stored. Compressed hydrogen transport-type stations typically have lower facility costs, while liquid hydrogen transport-type stations are more suitable for large stations that service buses and so forth.

Onsite type. With onsite stations, various methods are used to produce hydrogen at the station, for example, by using city gas and LPG reforming technologies or by employing water electrolysis. This type is most suitable for large stations. Water electrolysis-type onsite stations will be inevitable for the utilization of renewable energy such as photovoltaic energy and wind power.

To promote full-fledged construction of hydrogen filling stations, various countries have established promotion systems and are implementing a variety of activities. The SHHP Project by three Scandinavian countries started station construction quite early, and H2-Mobility in Germany, which has been promoted since around 2009, has also been involved in station construction. Station infrastructure establishment has also been carried out through various government and industry collaborations. Notable promoting organizations include a 13-company union in Japan, the U.S.A.'s H2USA program, Britain's UKH2-Mobility program, and France's program based on the H2-Mobility initiative in Germany.

In Japan, the motor companies Toyota, Nissan, and Honda will be jointly paying for a part of the operation expenses to promote the establishment of hydrogen filling stations in conjunction with public support from the government and municipalities in the forms of subsidies and so forth. In addition, Toyota Tsusho, Iwatani, and Taiyo Nippon Sanso jointly founded Nippon Mobile Hydrogen Station Service, which is a company that can install and operate low cost mobile hydrogen stations. This company is examining the possibility of installing hydrogen filling stations in convenience stores. There are also other movements to promote the establishment of hydrogen filling stations. While establishment of hydrogen stations is inevitable for the popularization of FCVs, it will be necessary to dramatically reduce construction costs, which are estimated to be 400–500 million yen. Furthermore, laws and regulations will need to be revised to facilitate the establishment of hydrogen stations. In addition to employing the low cost package types and mobile types, measures to reduce the cost through improvements in system design, regulation relaxation and so forth are being undertaken.

4.8 Measures Taken to Promote the Hydrogen Society (2003–Present)

4.8.1 *Mitigation of Laws and Regulations, and Verification of Hydrogen Safety*

Since conventional laws and regulations in Japan do not address the utilization of hydrogen in cities as energy, they have turned out to be obstacles for the formation of a hydrogen society. It was suggested that the traditional laws and regulations would hinder popularization of fuel cells and hydrogen when Koizumi's Cabinet first announced its policy to promote the commercialization of fuel cells in 2002. Hence, the laws and regulations were reviewed and new initiatives were implemented by politicians from 2003.

A follow-up "liaison meeting of the ministries concerned with practical application of fuel cells" was convened by the Cabinet Secretariat, and officials reviewed 28 relevant items in 6 laws. In fiscal years 2003 and 2004, large-scale experiments on safety, analysis of phenomena in case of accidents, and so forth were implemented to obtain the safety verification data necessary for further regulatory review. This led to the construction of HySEF, which is a facility to enable continual safety experiments on fire and explosion hazards associated with the use of FCVs and hydrogen vessels. This facility was constructed within the Japan Automobile Research Institute in Ibaraki in 2004. HySEF is made of concrete and it has an inner diameter of 18 m, a height of 16 m, and a wall thickness of 1.2 m (see Fig. 4.49).

Laws that were reviewed during this process included the High Pressure Gas Safety Act, Building Standards Act, Road Traffic Act, and Electricity Business Act, and the primary deregulations were enacted in 2005. Technical standards for hydrogen filling stations were established and this enabled the construction of hydrogen filling stations in urban areas as well as the joint establishment of

Fig. 4.49 HySEF test dome



hydrogen and gasoline stations. Next, it became necessary to establish laws to start the popularization of fuel cells in 2015, and cabinet-level decisions were made in 2013 regarding an implementation plan to review 36 regulations to facilitate popularization in 2015 and later. This review will be completed within fiscal year 2015. Examples of these regulations include an expansion of the range of steel materials that can be used, standards for small-scale hydrogen stations and the establishment of joint hydrogen-oil service stations, simplification of security inspection procedures, simplified guidelines for the use of pressure accumulators in CFRP vessels, and targets for increased hydrogen retention quantities in urban areas.

4.8.2 Release of Fuel Cell Vehicles and Support for Popularization

FCVs, for which demonstration projects have been implemented for many years, were released for commercial sales for the first time in the world by Toyota on December 15, 2014. The commercially available MIRAI FCV is shown in Fig. 4.50. The fact that the MIRAI is not just a demonstration vehicle, but a practical commercially available vehicle running on hydrogen is a huge milestone for the establishment of the hydrogen society. Toyota also made a historic announcement that they would disclose 5680 patents related to FCVs free of charge in 2015 in order to facilitate global popularization of FCVs and establish a large global market for them by inviting other manufacturers into the market. Honda plans to release their model in March 2016, and Nissan plans to release one in 2017, and continues a joint development effort with Daimler and Ford. The Japanese government and municipalities such as Tokyo Metropolis have expressed their intention to support such popularization efforts through purchasing subsidies.

4.8.3 Attempt to Establish a Hydrogen Society Through Japan's Basic Energy Plan

In Japan's National Basic Energy Plan, the government has stated that the aim of the policy includes the establishment of a hydrogen society ahead of other

Fig. 4.50 Toyota MIRAI FCV (Source Toyota)



countries, starting in 2014. They developed a roadmap that specifies expansions in popularization efforts for household and industrial fuel cells, cost reductions for hydrogen fuel and FCVs, and the establishment of a large-scale hydrogen supply chain that includes transport of hydrogen by sea. The introduction of hydrogen power generation for industrial purposes is a priority goal and policies are being developed to position hydrogen energy as a central secondary energy source for other applications as well.

4.8.4 Establishment of a Large-Scale Hydrogen Supply Chain (Mass Sea Transport of Hydrogen)

Large-scale production of CO₂-free hydrogen has become possible through water electrolysis technology that uses large quantities of renewable energy such as photovoltaic and wind power. Hydrogen production from coal or natural gas is also possible with carbon capture and storage (CCS) technology. However, it has been difficult to implement these technologies domestically in Japan, and thus, a hydrogen supply system whereby hydrogen can be produced at more appropriate locations overseas and then transported by sea will need to be established. Such a hydrogen supply system was studied by the WE-NET Project in the past, and issues regarding the economic efficiencies, feasibility, and so forth have already been examined.

Kawasaki Heavy Industries in Japan is promoting a project that will liquefy the hydrogen produced by gasification/CCS of brown coal in Australia and transport it to Japan in liquid hydrogen tankers. Thus, this will help to establish the hydrogen supply chain that is required for the development of a hydrogen society in Japan. They plan to launch pilot system operations in 2017 using a 2500 m³ prototype tanker (see Fig. 4.51) and to start commercial service provisioning in 2025 using 160,000 m³ large tankers (see Fig. 4.52).

In addition, Chiyoda Corporation has launched a project to transport hydrogen produced overseas to Japan by sea as methylcyclohexane obtained through the hydrogenation of toluene. Hydrogen can then be extracted from methylcyclohexane

Fig. 4.51 Prototype LH₂ tanker (Source Kawasaki Heavy Industries)



Fig. 4.52 Large-scale LH₂ tanker (Source Kawasaki Heavy Industries)



with dehydrogenation reactions and this will be accomplished by using hydrogen turbine power generation at the hydrogen power station in Kawasaki. While methylcyclohexane has advantages in that it can be transported and stored under normal temperatures and pressures, dehydrogenation reactions are needed to extract the hydrogen. At first, problems were encountered with the catalyst used in the dehydrogenation reactions, i.e., the catalyst had too short a lifetime, but Chiyoda Corporation developed a new catalyst fit for practical applications and this made hydrogen transport in the form of methylcyclohexane possible. They plan to construct a hydrogen power station by 2020.

In the 1990s, activities to address large-scale hydrogen supply chain plans in the EQHHPP and the WE-NET Project were halted, but such activities are being viewed favorably again now that global warming has rapidly advanced in concurrence with the increased consumption of fossil fuels. Thus, the time has come when we need to tackle the challenges associated with the mass introduction, distribution, and utilization of hydrogen once again. In the future, the entire country must work on the establishment of hydrogen supply chains to use hydrogen as a replacement for fossil fuels, unlike the past research and development projects.

References

1. History of Hydrogen-Great Lakes Fuel Cell Education Foundation Homepage (2005) p 1
2. History of Hydrogen-Great Lakes Fuel Cell Education Foundation Homepage (2005) p 2
3. History of Hydrogen-Great Lakes Fuel Cell Education Foundation Homepage (2005) p 3
4. ELB Electrolysetechnik GmbH Homepage. Dec 15 2013
5. NEL Hydrogen. Homepage. <http://nel-hydrogen.com>. Accessed 4 Oct 2015
6. Guy Verkoeyen, Company History, Presentation at Het Waterst of Net Congress, P1 Helmond, 29 Nov 2013
7. Fuel Cell Today Homepage, News 2012 June. Hydrogenics wins order from E.ON for power-to-gas energy storage project in Germany
8. Takano K (2010) Hydrogen distribution from domestic refineries and factories: potential capacity and issues. *J Hydrog Energy Syst Soc Jpn (HESS)* 35(3):29–33 (in Japanese)
9. Iseki T, Ikeda Y, Kume T, Yasuda H, Ito M, Takagi Y, Hirosaka H, Tanaka H (2012) Durability improvement of membrane-on-catalyst module for hydrogen production from natural gas. *Fuel Cell Seminar 2012, Connecticut, Nov 5–8 2012*

10. Iwatani Corp. Homepage, Liquid Hydrogen for FCV Commercialization South Africa Embassy Economic Office Workshop, 25 Nov 2014
11. IAHE Homepage, History of IAHE. <http://www.iahe.org/history.asp>. Accessed 4 Oct 2015
12. WE-NET Homepage. Hydrogen Technology Development Projects in Oversea's countries, P1. Hydrogen and WE-NET related data (in Japanese)
13. Lloyd AC (1999) USA hydrogen projects. In: Proceedings of WE-NET symposium, Tokyo, pp 271–278, 25 Feb 1999
14. Fukuda K (1999) WE-NET first stage: summary of research and development results. In: Proceedings of WE-NET hydrogen energy symposium, Tokyo, pp 1–26, Feb 24 1999 (in Japanese)
15. Koda E (1999) Optimisation of hydrogen combustion turbine systems. In: Proceedings of WE-NET hydrogen symposium, Tokyo, pp 223–228, 25 Feb 1999 (in Japanese)
16. FCH2-JU-Multi Annual Work Plan-MAWP2014–2020, Fuel Cell and Hydrogen Joint Undertaking (FCH JU), Multi-Annual Work Plan 2014–2020. <http://www.nerghy.eu/>. Accessed 5 Oct 2015
17. Chart of Patent licensing Support (2004) High efficiency hydrogen storage alloy, National Center for Industrial Property Information and Training, Mar 2005 (in Japanese)
18. Japan Automobile Research Institute (JARI), Section 3–5 Developmental situation in Japanese automobile manufacturers, Investigated report on the fuel cell vehicle 2003, pp 99–121, Mar 2004 (in Japanese)
19. Knudsen J, DOE Hydrogen and Fuel Cells Program (2012) Annual progress report. Hydrogen delivery, 6. Development of high pressure hydrogen storage tank for storage and gaseous truck delivery
20. Tokyo City University, History of the hydrogen energy vehicle research, Apr 2009 (in Japanese)
21. Wurster R (2001) Overview of existing experience in hydrogen and fuel cells in Germany and Europe, Paris. Hydrogen demonstration activities, Munich airport hydrogen project, 13 Dec 2001
22. Japan Automobile Research Institute (JARI), Section 3-3 Developmental situation of stationary type and/or the other fuel cell, investigation report on the fuel cell vehicle 2003, Mar 2004 (in Japanese). 3-3 Development situation in overseas automobile manufacturer, pp 64–73, 3-5 3-5 Development situation in Japan automobile manufacturer, pp 98–120
23. ENAA (2002) Development of hydrogen refueling station for fuel cell vehicles, FCDIC, Fuel Cell RD &D in Japan, pp 206–207
24. Ikeda T (2014) Part 1-Chapter 3-Section 2, Demonstration of hydrogen station and FCV hydrogen infrastructure. In: Hydrogen utilization technology assembly. vol 4 (NTS), pp 91–101, 25 Apr 2014 (in Japanese)
25. Butsch H (2014) NOW HRS infrastructure in Germany and Europe-current activities, Washington D.C., 19 June 2014. http://www.hydrogen.energy.gov/pdfs/review14/h2in_butsch_2014_o.pdf#search=NOW+H2+mobility+action+plan+through+2023. Accessed 5 Oct 2015
26. Japan Automobile Research Institute (JARI). Homepage, Hydrogen and Fuel Cell Vehicle Safety Evaluation Facility (2005) (in Japanese), <http://www.jari.or.jp/tabid/140/Default.ASPX>. Accessed 8 Nov 2015
27. TOYOTA Homepage, MIRAI. <http://toyota.jp/mirai/>. Accessed 2 Oct 2015 (in Japanese)
28. Tobe C (2015) New era of a hydrogen energy society. In: Proceedings of FC EXPO 2015, keynote session pp 1–3, 25 Feb 2015
29. Kawasaki Heavy Industries, Hydrogen energy supply chain utilizing brown coal, Plenary Session 9, 52th Japan–Australia joint business conference, Australia, 14 Oct 2014
30. Okada Y, Saito M, Onda N, Sakaguchi J (2008) Vision of global hydrogen supply chain and development of hydrogen storage and transportation system by the organic chemical hydride method. *J Fuel Cell Technol (HESS)* 33(4):8–12 (in Japanese)

Chapter 5

Development Histories: Fuel Cell Technologies

Kazukiyo Okano

Abstract This chapter describes the history of fuel cells. Various efforts to develop fuel cell systems are described for aerospace, transportation, and stationary applications, leading to the recent progress in commercialization of residential fuel cell systems and fuel cell vehicles, especially in Japan.

Keywords History of fuel cells · Polymer electrolyte fuel cells · Solid oxide fuel cells · Aerospace applications · Automobile applications · Power generation · Residential applications

5.1 Discovery of the Principle of Fuel Cells and Implementation of Fuel Cell Experiments (1801–1962)

The development history of fuel cell technologies is summarized in Fig. 5.1. In 1801, Humphry Davy in the UK published a report on the possibility of using fuel cells with solid carbon as the fuel, in a scientific journal. In 1838, the German/Swiss Christian Friedrich Schoenbein discovered the principle on which fuel cells work. Then, in 1839, Sir William Grove in the UK successfully conducted an experiment on a fuel cell for the first time. In this work, he supplied hydrogen and oxygen to two platinum electrodes immersed in dilute sulfuric acid and generated a current (see Fig. 5.2). In 1889, Charles Langer and Ludwig Mond in the U.K. expanded on the concept, using hydrogen from coal gas in place of pure hydrogen, and air in place of pure oxygen. They developed a fuel cell that could be considered the prototype for PAFCs. This was accomplished by preparing a quasi-solid electrolyte of dilute sulfuric acid absorbed in porous gypsum, and porous platinum plate electrodes. They were the first to name their invention the “fuel cell”.

Later, German Walter Nernst discovered in 1899 that stabilized zirconia could exhibit conductivity for oxide ions and this hinted at the possibility of SOFCs. In 1921, German E.

K. Okano (✉)

Kyushu University, 6-8-5 Wakamiya, Ichihara-Shi Chiba 290-0006, Japan
e-mail: okano@icntv.ne.jp

© Springer Japan 2016

K. Sasaki et al. (eds.), *Hydrogen Energy Engineering*,

Green Energy and Technology, DOI 10.1007/978-4-431-56042-5_5

Fig. 5.2 William Grove fuel cell. *Source* Public Domain

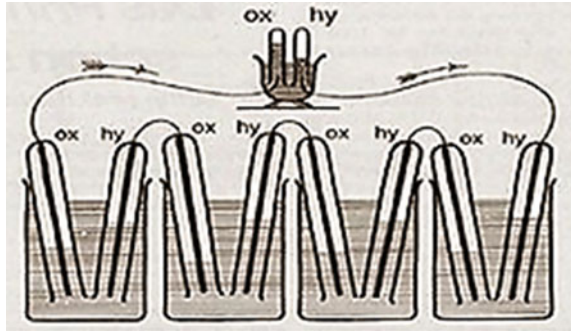
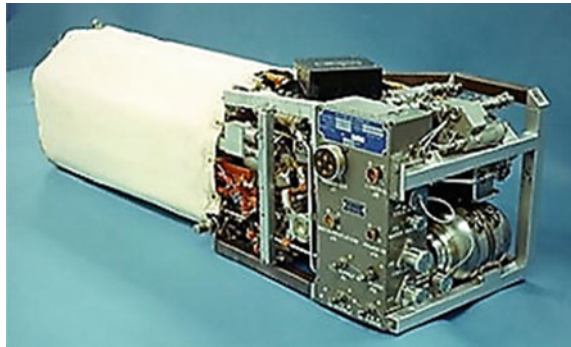


Fig. 5.3 AFC for the space shuttle. *Source* FCDIC



Baur conducted an experiment on an MCFC. The first solid electrolyte fuel cell was demonstrated by Baur et al. in Switzerland in 1937, using a zirconia-based electrolyte. In 1952, British Francis Thomas Bacon developed an AFC (the Bacon Cell), and he later successfully conducted an experiment on a 5 kW fuel cell in 1959. In 1961, the first PAFC was designed by Americans G.V. Elmore and H. A. Tanner. DuPont developed proton-conducting Nafion in 1962 using perfluorosulfonic acid polymer membranes, and they tested the first PEFC in 1966.

5.2 Utilization of Fuel Cells in Space (1965–Present)

The first fuel cell that was put into practical use was a PEFC developed by GE in the U. S., starting in the late 1950s. The PEFC design was developed by L. Niedrach, who made improvements to the cell developed by W. T. Grubb from GM, by modifying the catalyst. The resulting 32-cell 1 kW PEFCs were manufactured through a joint development project with NASA. Two of these units were eventually mounted on the spacecraft Gemini 5 in 1965. The polymeric membrane at the time was of the polystyrene type, with low proton conductivity and low durability. A PEFC with improved

durability, and incorporating a fluorine-type membrane, was later developed by DuPont, and mounted on a satellite in 1969. However, AFCs were considered to be more suitable for space applications than PEFCs due to their higher efficiencies, so three units of a 31-cell 1.4 kW AFC manufactured by UTC were mounted on the spacecraft Apollo 7 in 1968. Later, 32-cell 12 kW AFCs with higher efficiencies were adopted by the Apollo Program (1968–1972), and the subsequent space shuttle program (see Fig. 5.3).

5.3 Commercial Prototype Development of Various Fuel Cells (1958–2015)

5.3.1 Development of Alkaline Fuel Cells (1958–Present)

The alkaline fuel cells developed by Francis Thomas Bacon in 1952 were improved on for space applications by Pratt and Whitney (the aircraft engine division of UTC). NASA procured one of these and mounted it on Apollo 7 in 1968. This fuel cell was also adopted in their subsequent space shuttle program. From the late 1950s to the 1960s, researchers began to use suspended solutions of fine polytetrafluoroethylene (PTFE) resin powder with high water-repellent effects during the manufacture of gas diffusion electrodes for AFCs, and the performance of electrodes was improved dramatically. After Union Carbide developed a high-performance gas diffusion electrode in the late 1960s, American company Cyanamid developed a fuel cell with a precious metal catalyst. In addition, Allis Chalmers successfully manufactured a 2 kW AFC and conducted long-period operation with a dehydration mechanism utilizing an asbestos capillary membrane. This has been called the prototype of AFCs for space shuttles.

German Siemens prototyped a 100 kW-class AFC in 1988 and mounted it in a submarine. In the late 1960s until the 1980s, FCVs with mounted AFCs were developed in the U.S. and Europe and these were put to use in demonstration projects. In 1966, Union Carbide and GM conducted a driving test by mounting a 23 kW AFC on a van, and Kordesh et al. manufactured a 6 kW AFC to conduct a demonstration project in 1969 that employed a FCV with a mounted hybrid power supply combined with a battery. In Belgium, Elenco, which was founded in 1976, developed a fuel cell bus mounted with a 78 kW AFC.

In the U.K., ZEVCO, founded in 1997, developed AFCs and put them into service in fuel cell taxis mounted with 5 kW AFCs in the city of London. ZEVCO also manufactured three fuel cell trucks for park maintenance, which were put into operation in December 1999. To support these efforts, a simple hydrogen filling station was established in London, located by a park. A photograph of an AFC taxi in London is shown in Fig. 5.4.

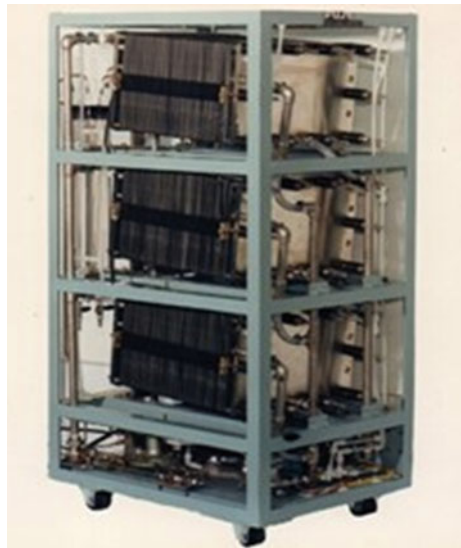
In Japan, several companies started research in the 1960s that resulted in the development of a 10 kW AFC for ships (Fuji Electric, 1972), and a 9 kW AFC (Japan Storage Battery). Yuasa Battery also developed a 4.5 kW AFC in 1970. Fuji Electric went on to manufacture a 7.5 kW backup power supply in 1985, which is

Fig. 5.4 Alkaline fuel cell (AFC) taxi in London



shown in Fig. 5.5, and a 3.5 kW portable welding power supply in 1988. In addition to the above developments, Sanyo Electric, Matsushita Electric, Toshiba, and so forth were also conducting research and development activities during this time. Furthermore, research on cell technologies was actively being conducted at various companies and universities to address cell performance improvements. However, this stopped when the development of AFCs was discontinued at the end of 1980, because developers concluded that commercialization of AFCs using hydrogen and oxygen would be difficult for most applications other than special purposes.

Fig. 5.5 7.5 kW alkaline fuel cells (AFC). Source Fuji Electric Co.



5.3.2 *Development of Phosphoric Acid Fuel Cells (1967–Present)*

The time for development of fuel cells for consumer-use began in the latter half of the 1960s. UTC made a strategic decision to work on the development of PAFCs given that their use could be economically feasible, even though GE pulled out at this time. Jointly, with American gas companies and power companies, UTC implemented the TARGET Program starting in 1967 (a plan to commercialize 12.5 kW PAFCs for industrial use), and then they promoted the GRI Program in 1977 (a plan to commercialize 40 kW PAFCs for industrial use) in association with a gas company.

Tokyo Gas and Osaka Gas in Japan participated in the TARGET and GRI Programs, and they used the fuel cells developed by UTC to conduct field tests on four 12.5 kW units in 1972 and on four 40 kW units in 1984 (see Figs. 5.6 and 5.7).

Fig. 5.6 Target program for 12.5 kW. *Source* Osaka Gas Co.



Fig. 5.7 GRI program for 40 kW PAFCs. *Source* Osaka Gas Co.



Besides these fuel cells for industrial use, the power companies in the U.S. launched the FCG-1 Program in 1971, a plan to commercialize PAFCs with megawatt-class electric power.

UTC developed a 4.5 MW plant for Consolidated Edison Electric Power in New York City, but it could not be put into operation because of technical problems. Tokyo Electric Power introduced an improved second unit and put it into operation at its Goi Thermal Power Plant, but since the technology had not yet matured for fuel cells back then, many problems were encountered with the fuel cell itself as well as with the reformer and other equipment. Use of this unit was eventually discontinued in 1983 after it had been in operation for 2400 h. Next, Tokyo Electric Power embarked on a research project with an 11 MW PAFC to be used at the district level in a joint power supply system in association with a thermal plant to deal with rapid increases in urban redevelopment points and so forth. Consequently, the world's largest 11 MW PAFC plant manufactured by UTC was constructed at the Goi Thermal Power Plant with cooperation from Toshiba, and it is shown in Fig. 5.8. This system was in operation for 23,000 h, over a 7 year period from 1991 to 1997. PAFCs were considered to have a high potential for future use, in part because they could be operated at temperatures of only 200 °C and did not require special materials for use. Therefore, development of PAFCs was promoted in Japan at a large scale under the Moonlight Program. This program began in 1981 with the goal of catching up with the PAFC development trends in the U.S.

During the early 1980s, Japan had only fundamental technologies: Fuji Electric and Kansai Electric Power were developing 30 kW PAFCs for use as the first fuel cell power generation systems in Japan, and Toshiba soon began operating a 50 kW PAFC experimental system within their premises. Additionally, with the help of the Moonlight Program, two 1 MW plants with different operating conditions were constructed in 1987; one was of the low-temperature, low-pressure type, and the other was of the high-temperature, high-pressure type.

Toshiba and the Hitachi Group were particularly interested in the high-temperature, high-pressure types and they eventually developed one at Chubu Electric Power. Moreover, Mitsubishi Electric and the Fuji Electric Group developed a 3600 m²-class cell and manufactured a PAFC stack, as shown in Fig. 5.9. They also constructed a 1 MW plant at Kansai Electric Power (see Fig. 5.10).

Fig. 5.8 World's largest 11 MW PAFC. *Source* Toshiba FC Power Systems



Although this plant successfully achieved a 1 MW output, it could only be operated for short periods, as PAFC cell technology was still not mature.

However, the fuel cell technologies (especially the cell stack production techniques) of these companies advanced rapidly and were then utilized in subsequent projects for power supplies on remote islands and in industrial 200 kW PAFCs. Fuji Electric constructed a methanol reforming 200 kW PAFC on Tokashiki Island in Okinawa and it began operating in 1989; this facility, shown in Fig. 5.11, was in operation for a total of 8449 h. Additionally, Mitsubishi Electric constructed a city gas reforming 200 kW PAFC at the Osaka Plaza Hotel and it too began operating in 1989. This facility, shown in Fig. 5.12, was in operation for a total of 13,038 h. Although these fuel cells were capable of being in operation for even longer periods, operations were terminated when the government's program ended.

Around this time in 1989, a New Energy and Industrial Technology Development Organization (NEDO) Project was launched to conduct research on technological issues when a new distributed power generation system is connected to the existing power supply system. Then, as the technology for PAFC advanced, Fuji Electric began working on the development of an industrial 50 kW power generation system.

They installed fourteen 50 kW PAFC units, one 550 kW photovoltaic power generation system, and one 33 kW wind power generation facility at the Rokko Experiment Center of Kansai Electric Power. Operation tests were conducted at this facility until 1993 (see Fig. 5.13).

Fig. 5.9 Phosphoric acid fuel cell (PAFC) stack, 250 kW \times 4 units. *Source* Fuji Electric Co.



Fig. 5.10 1 MW phosphoric acid fuel cell (PAFC) plant at Kansai Electric Power. *Source* AIST



Fig. 5.11 200 kW PAFC at Okinawa. *Source* Fuji Electric Co.

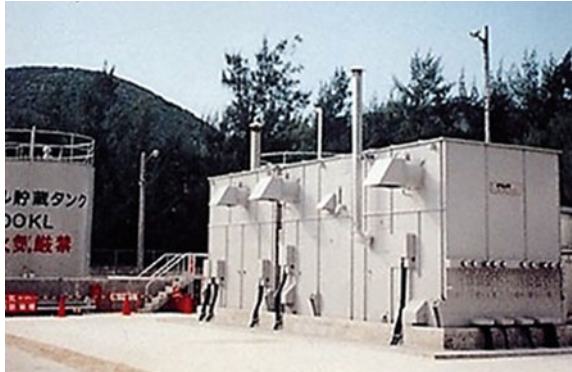


Fig. 5.12 200 kW PAFC at Osaka. *Source* New Energy and Industrial Technology Development Organization: NEDO

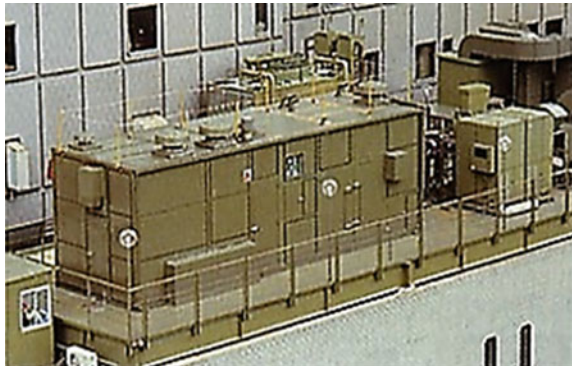


Fig. 5.13 14 units of 50 kW phosphoric acid fuel cells (PAFCs) at Rokko. *Source* NEDO



By manufacturing many PAFCs, as described above, design and manufacturing technology was improved dramatically for 50 kW PAFCs. Previously, PAFC units had been in the process of development and had frequent failures in auxiliary machines.

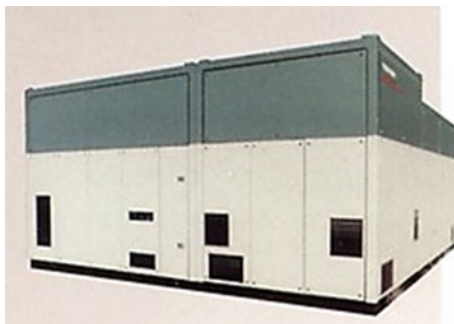
Electric power companies were eager to conduct research on fuel cells at this point in time, and many experimental plants utilizing PAFCs were put into operation under national projects as well as their own projects. In 1991, a PAFC power generation technology research association was formed to promote the New Sunshine Program, and large-capacity plants were developed. In conjunction with this program, Fuji Electric manufactured a 5 MW compression-type station for power generation using a 1 m-square large cell, and it was installed at Kansai Electric Power in 1995 where it stayed in operation for 6400 h. Additionally, an industrial 1 MW normal pressure type station was manufactured by Toshiba and installed at Tokyo Gas in 1995; this station stayed in operation for 16,000 h. Figure 5.14 shows the 5 MW stack, and Fig. 5.15 shows the 1 MW system. Since even larger investments would be required to develop these types of large commercial plant systems, the development of PAFC plants was terminated after tests at these facilities were completed.

Meanwhile, the city gas industry was actively working on related technological developments with the expectation that PAFCs would be promising cogeneration systems for the future. Starting in the late 1980s, they supported the development of 200 kW units by ONSI, Toshiba, and Mitsubishi Electric, the development of 50, 100, and 500 kW units by Fuji Electric, and the development of a 1 MW unit by Toshiba, among other projects. Then in 1991, three city gas companies and Fuji Electric embarked on commercial PAFC system development and addressed improvements in fuel cell system reliability. However, they had difficulty achieving

Fig. 5.14 5 MW phosphoric acid fuel cell (PAFC) stacks by Fuji Electric Co. *Source* Fuji Electric Co.



Fig. 5.15 1 MW onsite phosphoric acid fuel cell (PAFC) by Toshiba. *Source* Toshiba Corp.



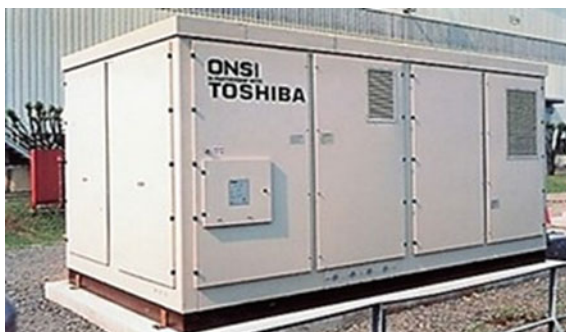
operation times of 40,000 h, which was the goal for commercial systems at the time, even though the cell durability had improved. Such durability, which was the largest issue in fuel cell technology development, had only been about 10,000 h. Dispersion and loss of phosphoric acid electrolyte during operation were found to be the main causes for deterioration in durability. Hence, phosphoric acid management proved to be the key to solving durability problems. Specifically, by flooding the cell with phosphoric acid, gas diffusion could be prevented when large volumes of phosphoric acid were retained around the cell. After several years of trial and error, a successful phosphoric acid management method to supply an appropriate amount of phosphoric acid was established, and this led to durability of 60,000 h or longer. After this issue was largely solved, commercialization of 100 kW PAFCs began in 1998. A total of 49 units were delivered to domestic and international customers by the end of 2014, and one of them has now been in operation for longer than 100,000 h at a sewage treatment plant. The latest 100 kW PAFC is shown in Fig. 5.16. During this time, domestic manufacturers other than Fuji Electric pulled out from the PAFC business. However, compact and highly reliable fuel reformers and system technology nurtured during the PAFC development phase was later utilized in hydrogen production systems at hydrogen filling stations as well as in household fuel cells. Additionally, the new catalyst technology for PAFC electrodes, in which platinum was used, was put to use in PEFCs with a similar electrode structure, primarily, in household fuel cells.

In the U.S., an accumulation of PAFC technologies was employed by International Fuel Cells (IFC, the fuel cell division of UTC), who started the production of a 200 kW PAFC in 1991 at its subsidiary, ONSI Corporation. Eventually, this technology was commercialized, and ONSI has sold more than 400 units of the 200 kW PAFC (shown in Fig. 5.17), since 1991. Toshiba also worked on PAFC development for a short time around 2001 in cooperation with IFC, and investments in IFC resulted in the founding of Toshiba IFC. Later in 2009, UTC Power developed and commercialized a 400 kW PAFC. However, ClearEdge Power, a venture business that produces small PEFC systems, acquired the old fuel cell manufacturer UTC Power in 2013.

Fig. 5.16 Fuji commercial 100 kW phosphoric acid fuel cell (PAFC). *Source* Fuji Electric Co.



Fig. 5.17 ONSI commercial 200 kW phosphoric acid fuel cell (PAFC). *Source* Toshiba Corp.



5.3.3 Development of Molten Carbonate Fuel Cells (1976–Present)

In Japan, the national Moonlight Program and Sunshine Program, which have been in place since fiscal year 1981, targeted the development of 10 kW-class cell stacks during the first stage of the programs until fiscal year 1986. The development of the system from a 100 kW-class stack up to a 1 MW power generation plant for a demonstration project was completed during the second stage, which ended in fiscal year 1999, and the development of a commercial 300 kW-class small power generation system was completed during the third stage, which lasted until fiscal year 2004. These accomplishments were made possible by utilizing the experience that had accumulated during the previous years. Notably, development was conducted for a long time with the participation of many companies. Ishikawajima-Harima Heavy Industries and Hitachi took charge in 1993 and developed the 100 and 250 kW-class stacks shown in Figs. 5.18 and 5.19, respectively, and these became

Fig. 5.18 100 kW stack. *Source* FCDIC

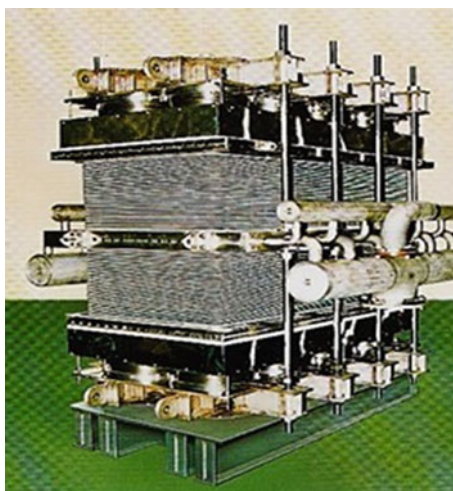




Fig. 5.19 250 kW stack. *Source* FCDIC



Fig. 5.20 Molten carbonate fuel cell (MCFC) 1 MW test plant. *Source* FCDIC

components of the 1 MW plant. The 1 MW plant at Chubu Electric Power, which was used to conduct operational tests, stayed in operation for 4916 h until 1999. Figure 5.20 shows a photograph of the plant.

In 2003, a pressurized 300 kW MCFC system was constructed by Ishikawajima-Harima Heavy Industries in the NEDO project and operated with a waste gasification system at Chubu Electric Power Co. (see Fig. 5.21).

Even though the MCFC power generation system technology had been developed through the domestic development projects, the technology largely failed to reach commercialization because of problems associated with cell durability and high costs. However, in 2002, a 250 kW MCFC that was manufactured by U.S.



Fig. 5.21 300 kW molten carbonate fuel cell (MCFC) plant. *Source* FCDIC

Fig. 5.22 FCE 250 kW commercial molten carbonate fuel cell (MCFC) at the Toride Factory of Kirin Brewery Co.



Fuel Cell Energy (FCE) was introduced at the Toride Plant of Kirin Brewery, and an additional 14 units of the 250 kW systems were introduced at various plants around Japan by the end of 2006 (see Fig. 5.22).

In the U.S., a national project by the Energy Research and Development Administration (ERDA) was launched in 1976 to implement new hydrogen energy developments including the operation of a 2 MW plant; this project was succeeded by DOE projects in 1978. In 2003, the U.S. FCE commercialized a 250 kW system. Later, FCE expanded their commercialized models to include 300 and 440 kW systems for vessels and 1.4 and 2.8 MW MCFCs.

In South Korea, POSCO Power established a production system that incorporated the technology of FCE, and they manufactured an MCFC plant with strong backup support from the government. The world's largest 58.8 MW (2.8 MW \times 21 units) MCFC fuel cell plant, which operates on digester gas from



Fig. 5.23 WH 25 kW solid oxide fuel cell (SOFC) at Osaka Gas. *Source* Osaka Gas Co.



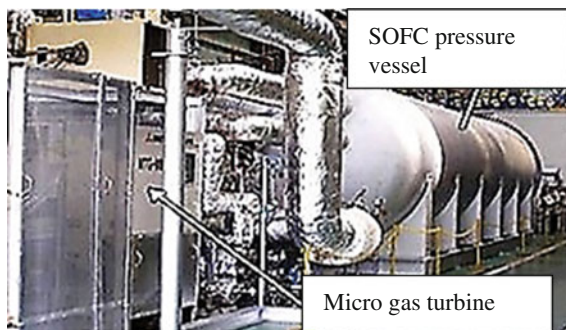
Fig. 5.24 MHI-Chubu EPC 10 kW solid oxide fuel cell (SOFC). *Source* FCDIC

sewage sludge, was constructed in Hwasung City, South Korea, in 2011. At present, MCFCs are mainly popularized in the U.S. and South Korea.

5.3.4 Development of Solid Oxide Fuel Cells (1960–Present)

Since the 1960s, research and development activities for SOFCs have been mainly conducted by U.S. Westinghouse (WH), German Brawn Boveri, and Siemens. Around 1980, WH developed their tubular-type, vertically striped cells. Tokyo Gas and Osaka Gas introduced a 3 kW tubular-type SOFC from WH in 1987 and operation evaluations were conducted for a period of 3000 h. This triggered a startup of many projects involving SOFC research and development in Japan. In

Fig. 5.25 200 kW solid oxide fuel cell (SOFC)-MGT demo system. *Source* FCDIC



addition, Tokyo Gas and Osaka Gas have operated a 25 kW normal pressure type SOFC by WH since 1992. They recorded the world's longest operation time of 13,194 h with this unit starting in 1995, which is when they modified the cells (see Fig. 5.23).

In 1998, WH merged with Siemens to found Siemens-Westinghouse Power Corporation (SWPC), and they continued to develop tubular-type SOFCs. Then in 2000, they installed and operated a 220 kW SOFC/GT system at the University of California, Irvine, for the first time in the world.

In Japan, basic research started in the 1960s at Nagoya University and the University of Tokyo. In 1974, the Electrotechnical Laboratory developed a 100 W SOFC. Because of the research on SOFCs that was launched as part of the national Moonlight Program in fiscal year 1981, planar-type and tubular-type cells as well as power generation systems were able to be developed by various companies during the first stage (1989–1991), second stage (1992–2000), and third stage (2001–2004) of the SOFC NEDO Project. Mitsubishi Heavy Industries and Chubu Electric Power developed an integrated laminated planar fuel cell called the MOLB type and launched operations on a 15 kW stack in 2000. Later, Mitsubishi Heavy Industries (MHI) developed tubular segmented-in-series cells and manufactured a pressurized, internal reforming type 10 kW SOFC in 2001; this system was operated at Chubu Electric Power (see Fig. 5.24). Mitsubishi Heavy Industries also developed a hybrid system composed of a 200 kW SOFC and micro gas turbine (MGT) in 2013, and this system was operated for a total of 4000 h (see Fig. 5.25).

In the U.S., efforts to address efficiency improvements and cost reductions were initiated under the Solid State Energy Conversion Alliance (SECA) Project, for SOFCs that could utilize hydrogen generated from coal gasification. This project lasted from 2005 to 2010. In regards to SOFC use for industries in general, Bloom Energy, an American venture business, released a 100 kW SOFC in 2008, which became popular in the market after a short period of time. Later, they also released a 200 kW SOFC. Meanwhile, research on scandia-stabilized zirconia, LaGaO₃-type electrolytes, ceria-based electrolytes, and so forth, helped to enable lower temperature operation. Particularly during the 2000s, the technology advanced, and decreases in operating temperatures from 1000 °C to 650–750 °C became possible

by around 2005. The operating temperature decreases helped to improve the durability of the units and reduce operation costs. This, in turn, resulted in the expansion of SOFC applications into the field of household fuel cells and facilitated their commercialization.

In regards to household SOFCs, Australian Ceramic Fuel Cells became involved in the European market, including in Germany and the U.K., and they began introducing systems in Europe.

In 2011 Swiss Sulzer Hexis also developed a 1 kW SOFC during this time. Moreover, various other companies have also made significant contributions to developments domestically. For example, Kyocera/Osaka Gas developed a household 1 kW SOFC in 2005, JX Nippon Oil and Energy Corporation released a household 700 kW SOFC in 2011, and Aisin Seiki released a similar product in 2012, both by using Kyocera-made flat-tubular SOFC cell stacks.

5.3.5 Development of Polymer Electrolyte Fuel Cells (1987–Present)

GE developed a 5 kW PEFC for space shuttles in 1970–1976 and a 3 kW PEFC for submarines, used by the U.S. Navy in 1974–1976. This technology used the fluorine-based ion exchange membrane that was developed by Dupont for the Gemini 5 mission. However, they transferred the technology to Siemens in 1983 and the SPE (solid polymer electrolyte) registered trademark and technology to UTC in 1984. Siemens later developed a PEFC for submarines, and a fuel cell submarine mounted with nine of these 30 kW PEFC units was launched by the German Navy in 2002.

Furthermore, Mitsubishi Heavy Industries started the construction of the deep-sea research vessel “Urashima” in 1998, and this vessel was driven by a combination of PEFCs operating on hydrogen that was stored in hydrogen absorbing alloys and batteries. Its performance test was completed in 2000. By utilizing the advantages of fuel cells, the deep-sea research vessel was able to achieve the world’s longest continuous operation record of 317 km in 2005.

The Canadian company, Ballard, was founded in 1979 and began development on fuel cells in 1983. In 1987, they developed a high-performance PEFC with dramatic improvements in output density by using a Dow membrane developed by Dow Chemical. Although the use of the Dow membranes delivered an output that was 2.5 times that of units that employed Nafion 117 membranes, Dow membranes were not adopted in later products because of problems associated with their mechanical strength.

Ballard made improvements on the PEFC stack that had achieved an output density of 85 W/L in 1988, and dramatic improvements in performance of 1200 W/L were demonstrated in 1996. In 1993, Ballard not only developed a fuel cell bus, but they also worked on the development of fuel cells for automobiles in

cooperation with Daimler-Chrysler. Furthermore, Ballard developed and released a compact and versatile standardized cell stack for general purposes including small power generation systems and automobiles.

Fuel cell application products adopting this cell stack were developed and popularized by a venture business, and the achievements of Ballard in regards to the establishment of the PEFC market were considerable.

Forklift manufacturers such as Crown, Yale, and Raymond commercialized fuel cell forklifts by adopting GenDrive, which is a fuel cell system for forklifts that was commercialized by PlugPower. The system utilizes fuel cell stacks by Ballard, and popularization began at a large scale around 2008.

Furthermore, methanol reforming fuel cell backup power supplies were developed by IdaTech using the fuel cell stacks by Ballard and these also became very popular at around the same time. Ballard itself also manufactured and released backup power supplies for pure hydrogen and methanol reforming backup power supplies by acquiring IdaTech, which possessed the reforming technology. Additionally, Ballard commercialized a large-capacity 1000 kW power generation system for pure hydrogen, and the market for PEFCs, for which the durability had improved and the costs had decreased, grew rapidly thanks in part to the U.S. government's policy of supporting such efforts. At this time, Daimler was conducting development projects for fuel cells for use in automobiles in Canada by utilizing the PEFC technology of Ballard. Furthermore, Canadian Hydrogenics was distributing fuel cells for forklifts, and these were adopted in fuel cell forklifts designed by CAT, Hyster, and so forth. They also manufactured pure hydrogen fuel cell backup power supplies and fuel cells for buses.

In Japan, a national PEFC development project was launched during fiscal year 1992. During phase I (starting in fiscal year 1992), cell stacks were developed, during phase II (starting in fiscal year 1996), industrial, portable, and household power generation systems were developed, and in fiscal year 2000, the final year of the project, several companies tackled the technical issues. Notably, Toshiba developed a city gas reforming 30 kW system, Mitsubishi Electric developed a methanol reforming, portable 10 kW system, and Sanyo Electric developed a city gas reforming 2 kW power generation system. In addition, Asahi Kasei and Asahi Glass revealed that the domestically produced ion exchange membranes could be used in PEFCs and that their

Fig. 5.26 Field tests of residential fuel cells. *Source* NEDO



performance was world class. Starting in the late 1990s, various companies started developing 1 kW-class household fuel cell systems.

In Japan, the government launched so-called “the Millennium Project” in fiscal year 2000 to standardize the PEFC technologies, a project for fundamental technology development for high-efficiency fuel cell systems, and a project aimed at technological development of practical applications for high-efficiency fuel cells.

In fiscal year 2002, a demonstration project on stationary fuel cells was launched, and NEDO implemented field tests of stationary residential fuel cells that were developed by six companies at the Japan Gas Appliances Inspection Association (JIA); the reliability of such residential fuel cell technology had not yet been established (see Fig. 5.26).

While failures occurred frequently in both the main devices and auxiliary parts of the fuel cells of various manufactures in field tests lasting from 2001 until 2004, the testing facilitated improvements in the technology and gave the manufacturers precious experience in the manufacturing and operation of the various products. Much experience was also obtained during large-scale national demonstration projects that were implemented starting in 2005.

Fig. 5.27 Panasonic polymer electrolyte fuel cell (PEFC).
Source FCDIC



Fig. 5.28 Toshiba polymer electrolyte fuel cell (PEFC).
Source Toshiba FC P.S.



Fig. 5.29 Aisin solid oxide fuel cell (SOFC). *Source* FCDIC



As a consequence, the manufacturers were able to not only improve the reliability of the parts and the entire systems, but they were also able to achieve dramatic cost reductions. Although they did not reach the final target of 500,000 yen/unit, the cost was reduced to 2 million yen or lower by 2014. Products have been commercialized since fiscal year 2009 with the help of government subsidies, and market introduction of over 100,000 units in total has been achieved by September 2014.

Examples of these fuel cells are shown below. Specifically, the EneFarm PEFC manufactured by Panasonic is shown in Fig. 5.27, a PEFC by Toshiba Fuel Cell Power Systems is shown in Fig. 5.28, and a SOFC by Aisin Seiki is shown in Fig. 5.29. In general, the smaller units consist of fuel cell stacks and fuel processing units, while the larger units consist of a hot-water tank and a backup boiler. In the Panasonic system (Fig. 5.27), the fuel cell stack and the hot-water tank are integrated into one unit and backup boiler is a separated optional unit.

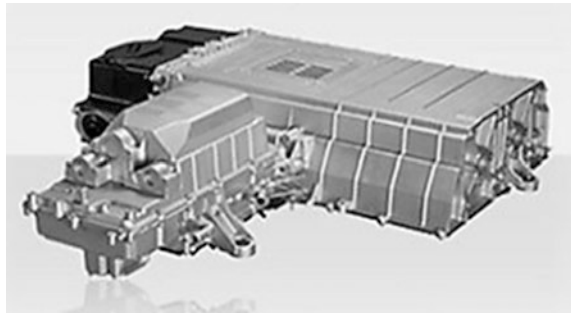
During the development of FCVs, for which expectations were high for PEFC technology, automobile manufacturers conducted their own development research. They solved several technical issues related to durability problems and low-temperature startup problems, and they further developed compact and reliable cell stacks. Additionally, they were able to achieve dramatic cost reductions. Robotization of fuel cell manufacturing, which may reduce the production costs even further, is also being advanced by domestic and international manufacturers for mass production efforts in the future.

Since the construction of pure hydrogen infrastructure was considered to be a difficult undertaking at the time when manufacturers began to develop fuel cells, domestic and international manufacturers focused their efforts on the development of on-vehicle reforming of methanol or desulfurized gasoline technologies for which the fuel infrastructure would be easier to establish and performed field tests. Although ultra-small auto-thermal reformers for fuel reforming were also developed at this time, development of these systems was eventually discontinued because of the many problems that were encountered. For example, instantaneous startup of fuel cells with on-vehicle reforming was practically impossible, it was difficult to prevent the water tanks from freezing during winter, extra space was needed for the

Fig. 5.30 Toyota's first 20 kW fuel cell. *Source* Toyota



Fig. 5.31 Toyota's 114 kW fuel cell for Mirai. *Source* Toyota



technology, and additional costs were revealed after operation. It was then collectively decided that mounting compressed hydrogen would be a better option. Metal hydride (MH)-mounted vehicles were considered ideal because the hydrogen could be mounted safely. However, the MH-mounted vehicles that could release hydrogen using exhaust heat from the fuel cell at 80 °C only had a hydrogen storage capacity of 3 wt% or lower, as discussed earlier, and they were heavy. A hydrogen storage capacity of 6 wt% would be required for practical applications. Thus, their development was largely discontinued at the stage of prototype development.

Toyota however continued development while considering various fuel mounting methods for FCVs and developed a MH-mounted FCEV with a fuel cell output of 20 kW in 1996; this was a modified model of the RAV-4. They also developed a methanol reforming FCEV-2 with a fuel cell output of 40 kW in 1999. In 2001, they developed a MH-mounted FCHV-3, a hydrogen-gas (GH_2) mounted FCHV-4 with a fuel cell output of 90 kW, and a gasoline reforming FCHV-5 with a fuel cell output of 90 kW. Later on, they developed a GH_2 -mounted FCHV with a fuel cell output of 90 kW in 2002 and a 70 MPa GH_2 -mounted FCHV-adv with a fuel cell output of 90 kW in 2008. Ultimately, they released the “Mirai,” which is a FCV mounted with a 70 MPa GH_2 and a self-manufactured 114 kW PEFC, at the end of 2014. The first 20 kW PEFC for FCEVs manufactured in 1996 is shown in Fig. 5.30, and the fuel cell for the “Mirai” is shown in Fig. 5.31. The fuel cell for the “Mirai” has a volume output density of 3.1 kW/L, which is 2.2 times that of the previous model FCHV-adv, and it employs an inner water circulation system without a humidifier.



Fig. 5.32 Honda's history of polymer electrolyte fuel cell (PEFC) development. *Source* Honda

Nissan developed a methanol reforming vehicle mounted with a 10 kW PEFC in 1999, a methanol reforming FCV mounted with a 30 kW PEFC by Ballard in 2000, and an X-TRAIL mounted with their own PEFC and 70 MPa GH_2 in 2005. They also developed a 130 kW stack in 2008 by adopting metal separator technology and improving the MEA. In 2011, they developed a 85 kW fuel cell, whose output density was 2.5 times that of conventional fuel cell stacks; the amount of platinum usage in this fuel cell was reduced to 1/4 and the cost was reduced to 1/6 of that of conventional fuel cells. In addition, they released the concept car TeRRA in 2012. Later in 2013, they announced plans to release a vehicle in 2017 that will be jointly developed with Renault, Daimler, and Ford.

Honda developed the MH-mounted FCX-1 using a fuel cell with 60 kW of output by Ballard and also a methanol reforming FCX-2 using their own fuel cell in 1999. In 2001, they conducted a 10,000 km driving test with the FCX-V3, which was mounted with their own GH_2 and had 70 kW of output. In 2004, they improved on the FCX GH_2 -mounted vehicle by achieving 86 kW of fuel cell output and by increasing the volume output density by 2.2 times. Then, the so-called V-flowFC was developed with 100 kW output, thus enabling startup at minus 30 °C. This technology was coupled with the special body Clarity and released for lease sales in Japan and the U.S. in 2008. During this period, fuel cell stacks were reduced in size considerably. Honda then announced that they would release a FCV with further improvements in March 2016. While the fuel cell technology that was developed by Honda from 1999 to 2008 is shown in Fig. 5.32, a PEFC that has been further improved upon will be mounted in the vehicles that are to be released in 2016.

Thanks to the outcomes of research and development activities over many years by automobile manufacturers, 80 to 100 kW -class practical PEFCs have been developed. Such technology now has improved durability and low-temperature startup, as demonstrated by operational tests over 13 years. With these performance improvements along with size reductions, better manufacturing methods, and cost reductions, commercialization has become possible. The biggest weakness in PEFC technology was its low durability, but the mechanisms of electrode performance degradation were eventually identified and corrected through governmental projects as well as cooperative efforts among industry, government, and academia. Modified design, materials, and manufacturing methods increased durability and made commercialization possible. The challenges that remain for the future will be to further reduce the costs of the fuel cells and the vehicles through promotion and mass production activities.

References

1. Fuel Cell Today, History, p 1 Origins. <http://www.fuelcelltoday.com/history>. Accessed 30 Sept 2015
2. Fuel Cell Today, History, p 2 The Space Program. <http://www.fuelcelltoday.com/history>. Accessed 30 Sept 2015
3. Osaka Science & Technology Center, III. Alkaline Fuel Cell (AFC) (2003) History of fuel cell development, Mar 2003, pp 25–29 (in Japanese)
4. Osaka Science & Technology Center, II. 3. History of fuel cell developments, pp 14–16. 4,500 kW Large capacity fuel cell by Tokyo Electric Power Company, pp 74–77, 11 MW Large capacity fuel cell by Tokyo Electric Power Company, pp 77–80, Investigation of issues on the history of fuel cell development and commercialization (Agency for Natural Resources and Energy commissioned projects investigation report in 2002) Mar 2003 (in Japanese)
5. Osaka Science & Technology Center, IV (Mar 2003) Phosphoric Acid Fuel Cell (PAFC), History of Fuel cell Development, pp 52–87 (in Japanese)
6. Osaka Science & Technology Center, V (2003) Molten Carbonate Fuel Cell (MCFC), Investigation of issues on the history of fuel cell development and commercialization (Agency for Natural Resources and Energy commissioned projects investigation report in 2002) Mar 2003, pp 99–104 (in Japanese)
7. Mcphail JS, Leto L, Della Pietra M, Cigolotti V, Moreno A 2 (2015) Introducing the MCFC Players in the World, International Status of Molten Carbonate Fuel cell Technology 2015. Advanced Fuel Cells Implementing Agreement IEA Annex23-MCFC, pp 7–11
8. Osaka Science & Technology Center, II. 3 (2003) History of Fuel cell Development, Investigation of issues on the history of fuel cell development and commercialization (Agency for Natural Resources and Energy commissioned projects investigation report in 2002) Mar 2003, p 16 (in Japanese)
9. Osaka Science & Technology Center, II. 3 (2003) History of Fuel cell Development, p 16. VI. Solid Oxide Fuel Cell (SOFC), pp 105–109, Investigation of issues on the history of fuel cell development and commercialization (Agency for Natural Resources and Energy commissioned projects investigation report in 2002), Mar 2003 (in Japanese)
10. Endo M (2012) The future perspective and Current status of SOFC, FC-DIC. J Fuel Cell Technol 12(1):60–66 (in Japanese)
11. Okano K (2009) Diffusion of hydrogen and fuel cell application in the market, FCDIC. J Fuel Cell Technol 9(1):132–138
12. Japan Automobile Research Institute (JARI), Section 3–6 Developmental situation of other fuel cells (such as for stationary type), Investigated report on the fuel cell vehicle 2003 (Mar 2004), pp 122–125 (in Japanese)
13. Japan Gas Association (2002) Fuel Cell Development by the Gas Industry, FCDIC Fuel Cell RD & D in Japan, 2002, pp 26–29
14. Kamiyama Y (2015) Japanese Government's Efforts towards a Hydrogen Energy Society, 2. Stationary Fuel Cells, (1) Residential Fuel cells. In: Proceedings of FC EXPO 2013, Keynote Session p 4, 27 Feb 2015
15. Ogiso S (2015) Toyota's Next Generation Vehicles Strategy & FCV Development. Toyota Fuel cell Stack. In: Proceedings of FC EXPO 2015, Keynote Session, p 35, 27 Feb 2015
16. Iiyama A (2011) Development of fuel cell vehicle aiming the commercialization by NISSAN motor co. ltd. In: Proceedings of 5th Iwatani Hydrogen Forum in Tokyo, pp 1–28, 24 Feb 2011 (in Japanese)
17. Japan Automobile Research Institute (JARI), Section 3–5 Developmental situation in Japanese automobile manufacturers, Investigated report on the fuel cell vehicle 2003 (Mar 2004), pp 99–121
18. Moriya T (2015) Toward the fuel cell vehicle development and the hydrogen society of Honda—the evolution of the fuel cell stack—. In: Proceedings of 9th Iwatani Hydrogen Forum in Tokyo, p 28, 5 Mar 2015 (in Japanese)

Chapter 6

Future Technological Directions

Kazukiyo Okano, Akiteru Maruta and Kazunari Sasaki

Abstract This short chapter describes future technological directions of hydrogen energy technologies with respect to the prevention of global warming problem and the reduction of fossil fuel usage. The importance and perspective of technological development related to hydrogen production, storage, transportation, and utilization are described.

Keywords Global warming · CO₂ reduction · Alternative energy sources · Renewables · Hydrogen transportation · Global hydrogen network

There are two main reasons why the world has high expectations for hydrogen. One is that hydrogen energy can slow the rate of global warming and protect the global environment, and the other is that it has the potential to play an important role in helping us to escape from dependency on fossil fuels.

At present, the world is facing serious problems as a result of climate change, which is largely being driven by increases in average temperature on Earth owing to increases in the atmospheric concentrations of CO₂, as a result of growing fossil fuel consumption. On November 2, 2014, the United Nations Intergovernmental Panel on Climate Change (IPCC) released a synthesis report titled “Climate Change 2014: Synthesis Report. Contribution of Working Groups I, II, and III to the Fifth Assessment Report of the Intergovernmental Panel on Climate Change.” This report

K. Okano

Kyushu University, 6-8-5 Wakamiya, Ichihara-Shi, Chiba 290-0006, Japan
e-mail: okano@icntv.ne.jp

A. Maruta

Technova Inc., The Imperial Hotel Tower, 13F, 1-1 Uchisaiwaicho 1-Chome,
Chiyoda-Ku, Tokyo 100-0011, Japan
e-mail: aki.maruta@gmail.com

K. Sasaki (✉)

International Research Center for Hydrogen Energy, Kyushu University,
Fukuoka 819-0395, Japan
e-mail: sasaki@mech.kyushu-u.ac.jp

included updated scientific evaluations of global warming and descriptions of measures that could help to mitigate it. Future predictions indicate that it is highly likely that the average global temperature will rise by 2.6–4.8 °C by 2100 if no severe measures are taken, and importantly, the increase in the average temperature will be nearly proportional to the cumulative emissions of CO₂. The scenarios outlined to reduce temperature increases to less than 2 °C compared to the level before the industrial revolution with a high probability and prevent excessive warming, abnormal weather, and so forth state that the improvements in energy efficiency and increases in low-carbon energy use by 3–4 times the 2010 level will be necessary.

Furthermore, in a scenario for suppressing global warming, the International Energy Agency (IEA) has identified several measures that, if taken, could reduce the expected levels of CO₂ emissions in 2050 by half. These measures include more widespread utilization of renewable energy, improvements in power generation and energy utilization efficiencies, new fuel conversion technologies, and the use of nuclear energy.

Several conditions exist for suitable alternative energy sources to fossil fuels. Namely, the ideal alternative would be one that is CO₂-free, does not emit hazardous substances, can be used with high efficiency, can be used as a fuel for transportation, industrial processes, and power generation, can be supplied in mass quantities, and can be used safely. It also needs to be manufactured from diverse resources. Thus, hydrogen offers great potential for the creation of sustainable societies as it can be manufactured using renewable energy and water.

Global warming prevention measures will require the utilization of types of energy that can satisfy many of the above conditions. Such energy will likely include renewable energy as well as biomass energy and hydrogen energy. While renewable energy is the most desired energy to be used, it has inherent problems such as large output fluctuations and uneven distributions in remote areas. Thus, control of power generation levels can be difficult. Furthermore, renewable energy can be difficult to store in mass quantities, which often results in waste when the power generation level exceeds the demands. However, many of these problems can be solved by using hydrogen as the energy storage medium.

Water electrolysis reactions can be used to convert the electric energy generated from renewable energy sources into hydrogen, thus it becomes possible to transport the energy from remote places and store it in mass quantities. Excess power from renewable energy can also be used effectively with such storage technology, that is, by utilizing hydrogen as the energy storage medium. Hence, with new hydrogen technology, renewable energy will be able to be converted into a form of energy that can be controlled and is convenient. The stored hydrogen can be converted back to electricity when needed through power generation in fuel cells, engines, turbines, and so forth or it can be used as fuel in transportation vehicles.

As described above, hydrogen appears to be the most effective energy technology for global warming prevention, and moreover, expectations are high that hydrogen will help countries achieve energy security as it can be manufactured from various different resources in many parts of the world. If hydrogen is to be

used as an alternative to fossil fuels in the future, it must become practical to supply an enormous amount of hydrogen continuously. If 10 % of Japan's predicted 2030 level of fossil fuel consumption (the Agency of Natural Resources and Energy has estimated this amount to be 3.27 million kL of crude oil) is converted to hydrogen, this would yield approximately 100 billion Nm^3/year by simple heat quantity conversion calculations.

This value of 100 billion Nm^3/year is an enormous amount of hydrogen. For illustrative purposes, this value is equivalent to 20 % of approximately 500 billion Nm^3/year of hydrogen that is produced by industry for the entire world. In Japan, which is poor in renewable energy resources, the locations appropriate for CCS are limited and thus it will be difficult to manufacture that much CO_2 -free hydrogen domestically. However, it may be possible to procure large quantities of CO_2 -free hydrogen at amounts of 100 billion Nm^3/year or larger if we can construct regional or even global hydrogen supply chains. With adequate supply chains in place, it would be possible to produce the hydrogen through utilization of unused resources overseas and at locations that are appropriate for coal gasification/CCS, natural gas reforming/CCS, and water electrolysis plants driven by renewable energy such as wind and hydroelectric power. The hydrogen could then be converted into liquid hydrogen or methylcyclohexane as the transport medium and transported overseas.

The feasibility and economic issues associated with creating a hydrogen energy system with such long-distance sea transport of hydrogen from overseas were studied in the national WE-NET Project in the 1990s, and continuous efforts are going on in Japan to realize such systems on a commercial basis.

As described in this introductory part, hydrogen is the ultimate energy that can help to slow global warming and provide countries with a high amount of energy security. Thus, expectations are high that the introduction of hydrogen technology will be accelerated in the future through global cooperation efforts.

Part II

Hydrogen Production

Tepei Ogura^{1,2} and Stephen M. Lyth³⁻⁶

¹School of Science and Technology, Kwansei Gakuin University, Nishinomiya, Japan

²Kyushu University, Fukuoka, Japan

³International Institute for Carbon-Neutral Energy Research, Kyushu University, Fukuoka, Japan

⁴CREST, Japan Science and Technology Corporation, Kawaguchi, Japan

⁵Department of Mechanical Engineering, Sheffield University, Sheffield, UK

⁶School of Chemical and Process Engineering, Leeds University, Leeds, UK

Part II of this book summarizes the main methods of hydrogen production. This starts with an explanation of the current industrial-scale steam reforming of fossil-fuel hydrocarbons, followed by a discussion on the feasibility of utilizing biogas as an alternative and more environmentally friendly fuel and hydrogen feedstock. The relative merits of the three main types of hydrogen production by water electrolysis are discussed, namely alkaline water electrolysis (AWE), polymer electrolyte membrane water electrolysis (PEMWE), and steam electrolysis. Finally, photocatalytic water splitting is discussed as a possible next-generation method of hydrogen generation.

Chapter 7

Introduction

Stephen M. Lyth and Aleksandar Staykov

Abstract This chapter introduces the basics of hydrogen production and sets up the topics for discussion in the following chapters, including steam reforming, alkaline water electrolysis, polymer electrolyte membrane water electrolysis, steam electrolysis, and photocatalytic water splitting.

Keywords Hydrogen production · Steam reforming · Water electrolysis · Steam electrolysis · Photocatalysis · Water splitting

Hydrogen gas production is a key industrial process and an important milestone for renewable energy and “green” economics. Hydrogen is a colorless and odorless gas, lighter than air, found mainly in the upper layers of the atmosphere. Under standard conditions it is not very reactive, which allows for its relatively safe storage and usage. Nevertheless, H_2 participates in chain reactions with O_2 leading to the formation of water. That reaction is strongly exothermic and the precise electrochemical pathway control of that process in fuel cells leads to the transformation of significant amount of chemical energy to electricity. Thus, hydrogen gas can be used as green fuel because the byproduct of its combustion or electrochemical reaction with oxygen is water. Unfortunately, only a small amount of hydrogen on earth is in the form of H_2 while the vast majority of hydrogen is in the form of various organic and inorganic chemical compounds. Therefore, the industrial synthesis of hydrogen gas is required for energy production. The largest reservoir of elemental hydrogen on Earth is in the form of water. This is an extremely stable molecule and its dissociation requires a significant amount of energy. The second largest reservoir of hydrogen is in the form of hydrocarbons—a major component of organic matter. The nature of both of these naturally abundant pools of hydrogen

S.M. Lyth (✉) · A. Staykov
International Institute for Carbon-Neutral Energy Research (WPI-I2CNER),
Kyushu University, Fukuoka 819-0395, Japan
e-mail: lyth@i2cner.kyushu-u.ac.jp

A. Staykov
e-mail: alex@i2cner.kyushu-u.ac.jp

determines the possible methods for hydrogen production, i.e., hydrogen originating from water, or hydrogen originating from organic compounds.

In this Part II, the fundamental principles and recent progress on some of the main hydrogen production technologies are reviewed. First, hydrogen production from hydrocarbon feedstocks is discussed (reforming), including methane from natural gas or biogas. Second, electrochemical production of hydrogen (electrolysis) will be discussed. This covers alkaline electrolysis, polymer electrolyte membrane electrolysis, and steam electrolysis. Finally, the production of hydrogen using energy from sunlight is discussed (photocatalysis). A detailed description of the history of hydrogen production for industrial use is given in Chapter 4.

The vast majority of hydrogen produced today is the result of methane and natural gas industrial reforming and dehydrogenation at high temperature. The result is syngas, which is a mixture of H_2 and CO and/or CO_2 . This method of hydrogen production is widely applied for the automobile industry, the chemical industry, and for small- and large-scale fuel cell appliances. The hydrogen gas quality depends on level of impurities. The high concentration of CO in hydrogen is potentially harmful for its further utilization, because CO is considered as a catalytic poison for various metal surfaces. The actual price of the H_2 originating from hydrocarbon feedstock depends on the impurity level and CO concentration, and is related to further H_2 purification. In some cases, hydrogen gas impurities might have a mitigating effect on hydrogen embrittlement (see Part V). Recently, hydrogen production facilities have been combined with CO_2 capture and storage technologies in order to comply with the green energy government requirements and achieve low greenhouse gas emissions.

Water electrolysis is a different method for the synthesis of hydrogen gas, using electrical power. This method is based on an electrochemical reaction in which water oxidation on the anode leads to the formation of oxygen gas; and proton reduction on the cathode leads to hydrogen gas formation. The principle is essentially a reversed fuel cell. The efficiency of the process depends on the electrode structure, and properties such as ionic and electronic conductivity. The carbon-neutrality of water electrolysis is related to the source of electrical power for the process. Ideally, renewable energy such as solar, wind, or hydroelectric power should be used. A special class of water electrolysis is high temperature steam electrolysis, which is characterized by lower overpotential for the electrochemical reaction. Steam electrolysis is extremely suitable for nuclear power plants, thermal power plants, or solar cell plants where water is heated to high temperature, and where there is often an excess of electricity. State-of-the-art, highly efficient steam electrolyzers are currently based on perovskite materials. Steam electrolysis is fairly well understood and ready for practical application. However, significant research efforts are directed toward decreasing the applied electrical overpotential, and improvement of the overall yield. Eventually, hydrogen produced by electrolysis will be a method to store electrical power from renewable sources and further used to deploy steady electrical output through its utilization in fuel cells.

The transformation of hydrogen in water to hydrogen in organic molecules is a key process in nature, known as photosynthesis. Under irradiation with visible light, CO_2 and H_2O are transformed to O_2 and glucose. Thus, the ultimate goal is to use water molecules and sunlight under controlled laboratory or industrial conditions for the synthesis of hydrogen gas. Such hydrogen gas would be carbon neutral and would not have any environmentally harmful byproducts, or waste heat. This process is known as artificial photosynthesis and was discovered by Fujishima in 1967, when the photocatalytic activity of TiO_2 was discovered. Since then, great strides have been made in efficiency and fundamental understanding of this system. Artificial photosynthesis still suffers from low yield as well as incomplete utilization of the solar spectrum. Despite significant research achievements, at present it remains a laboratory method for production of small quantities of H_2 .

Chapter 8

Steam Reforming

**Yusuke Shiratori, Quang-Tuyen Tran, Teppei Ogura,
Osamu Higashi, Stephen M. Lyth and Masaki Tajima**

Abstract This chapter introduces steam reforming, still the major method of large-scale hydrogen gas production. First, steam reforming of natural gas and its implementation as an industrial process is introduced. The combination of steam reforming with carbon capture is briefly discussed in order to make the process carbon-neutral. Finally, steam reforming of biofuels is considered.

Keywords Hydrogen production · Steam reforming · Hydrocarbons · Natural gas · Biofuels

Y. Shiratori

Department of Mechanical Engineering, Kyushu University, Fukuoka 819-0395, Japan
e-mail: y-shira@mech.kyushu-u.ac.jp

Q.-T. Tran · M. Tajima

International Research Center for Hydrogen Energy, Kyushu University,
Fukuoka 819-0395, Japan
e-mail: tran.tuyen.quang.314@m.kyushu-u.ac.jp

T. Ogura

School of Science and Technology, Kwansai Gakuin University, 2-1 Gakuencho,
Sanda, Hyogo 669-1337, Japan
e-mail: t-ogura@kwansai.ac.jp

T. Ogura

Kyushu University, Fukuoka 819-0395, Japan

O. Higashi

Graduate School for International Development and Cooperation, Hiroshima University,
1-5-1 Kagamiyama, Higashi-Hiroshima 739-8529, Japan
e-mail: hi036@hiroshima-u.ac.jp

S.M. Lyth (✉)

International Institute for Carbon-Neutral Energy Research (WPI-I2CNER),
Kyushu University, Fukuoka 819-0395, Japan
e-mail: lyth@i2cner.kyushu-u.ac.jp

M. Tajima

Research Institute of Innovative Technology for the Earth, KDX Toranomon Bldg.,
1-4-3 Toranomon, Minato-Ku, Tokyo 105-0001, Japan
e-mail: tajima@rite.or.jp

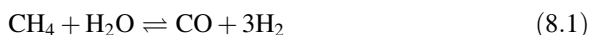
8.1 Introduction

Steam reforming of natural gas is currently the most common method for industrial-scale hydrogen production. While this technique produces significant carbon dioxide emissions, it can be combined with CO₂ capture, concentration, and storage (CCS) to become a carbon-neutral process. In addition, methane can be obtained by fermentation of biomass rather than from natural gas. This results in carbon-neutral production of hydrogen, and with the addition of CCS could even be a carbon-negative process.

8.2 Catalytic Steam Reforming

Steam reforming is a method for producing hydrogen, carbon monoxide, or other useful products from hydrocarbon fuels, such as natural gas. This is achieved in a processing device called a reformer, which reacts a hydrocarbon with steam at high temperature. Industrial steam reforming of hydrocarbons began in the 1930s and became the most economic method for hydrogen production in the 1960s, as discussed in detail in Sect. 4.3. Currently, the steam methane reformer is widely used in industry to make hydrogen. Small-scale steam reforming for fuel cells is the subject of intense research, typically involving a methane reformer (as discussed in Chap. 38). However, other fuels are also being considered such as propane, gasoline, liquefied petroleum gas (LPG), diesel, and ethanol. Steam reforming of natural gas is the most common method of producing commercial bulk hydrogen.

At high temperatures (typically 700–900 °C) and in the presence of nickel, steam reacts with methane to yield carbon monoxide (CO) and hydrogen (H₂). This steam-methane reforming process is approximately 70 % efficient. Two key reactions take part in the overall reforming process. The first (Eq. 8.1) converts methane and water steam to a mixture of CO and H₂. This reaction is strongly endothermic (i.e. it consumes heat) and the change in enthalpy is $\Delta H_r = 206$ kJ/mol.



Additional hydrogen can be recovered by a lower temperature gas-shift reaction with the CO produced. The reaction is summarized in Eq. 8.2:



This second reaction is mildly exothermic and the change in enthalpy is $\Delta H_r = -41$ kJ/mol.

The hydrogen produced by catalytic steam reforming is not carbon-neutral. On a global scale it is responsible for significant production of CO₂. Although this method is the main source of industrial hydrogen today, it should be replaced in the near future with novel methods for hydrogen production, or combined with CCS techniques.

8.3 Biomass Fermentation for Methane Production

One promising method to avoid the use of fossil fuels in hydrogen production through steam reforming is to produce hydrocarbons by the fermentation of biomass. Methane fermentation can be performed by anaerobic digestion. In this process, biomass (i.e. waste organic matter) is converted into biogas (i.e. methane and carbon dioxide) through the action of various microorganisms. Various conditions for this reaction should be met. These include anaerobic environment (i.e. the absence of oxygen); reasonable temperature and pressure (to avoid deactivating the microorganisms); suitable C/N range; and near-neutral pH [1].

Figure 8.1 shows a breakdown of the processes involved in methane fermentation. This is divided into four phases. In Phase I, complex organic matter is converted into dissolved organic matter (i.e. monomers or oligomers), via *hydrolysis*. In Phase II, organic acids and alcohols are produced via *acidogenesis*. In Phase III, acetate and hydrogen are produced via *acetogenesis*. Finally, in Phase IV, methane and carbon dioxide are produced via *methanation*. In this final process, approximately 70 % of the methane originates from the acetate [2–5].

In general, 80–90 % of the *chemical oxygen demand* (COD) of complex organic matter is converted to biogas, and the remaining 10–20 % becomes part of the

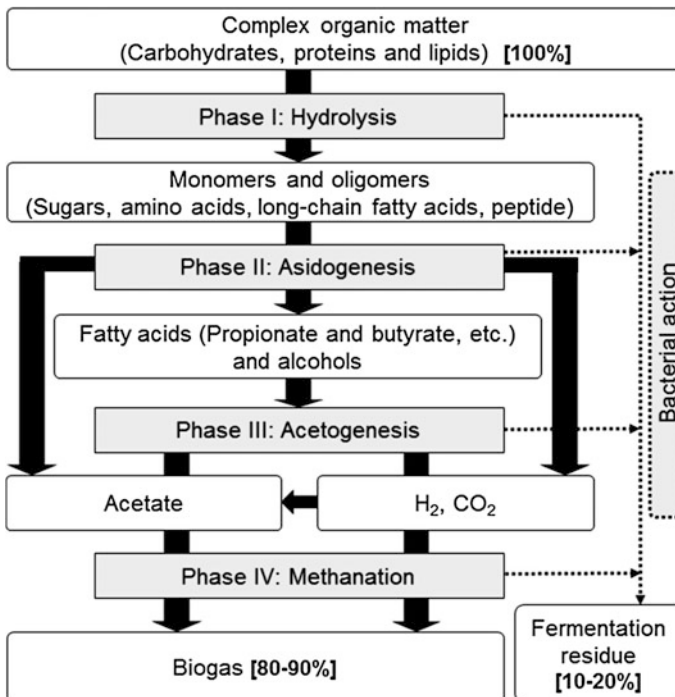


Fig. 8.1 Methane fermentation processes. Source Surendra et al. [2], Li [3]

fermentation residue as bacteria [3]. Biogas has better environmental quality compared with natural gas due to its lower impurity levels. The CH_4 content is 50–80 %; the CO_2 content is 20–45 %; the H_2S content is 0–1.5 %; and the NH_3 content is 0–0.45 % [6]. The calorific value of biogas is approximately 21–25 MJ/m^3 (i.e. 6–7 kWh/m^3 electricity equivalent) [2, 3].

Biomass fermentation is already being used experimentally in South East Asia for methane production to be used as a conventional fuel. This has the advantage of providing low cost carbon-neutral fuel that can be produced locally from organic waste [4]. In the Greater Mekong Subregion (GMS), around 113 million people lived in rural areas [7]. Of these, 80 % depend on wood or charcoal as their primary fuel, mainly for cooking [8]. This has led to severe deforestation and indoor air pollution [9, 10], impacting health and the environment [11]. Figure 8.2 shows photos of typical wood stoves used for cooking, and the resulting deforestation in the Magway region of central Myanmar [12].

Small- and medium-scale biogas plants are currently being rolled out in South East Asia for rural households, with the aid of international cooperation and funding [13, 14]. This is resulting in a reduction of health risks due to indoor air pollution; reduction of the workload of children in terms of collecting wood; and more sustainable forest management [15, 16]. Such biogas plants generally have similar design with common components (e.g. Fig. 8.3). Biomass resources (such as animal manure) are fed into the digester through an inlet pipe. The digester itself is constructed from bricks and concrete, or polyethylene. Fermentation occurs in the digester, where biogas and liquid fertilizer are generated. The typical size of a small-scale digester is 6–16 m^3 . Biogas is supplied for cooking or lighting via the gas outlet pipe. Liquid fertilizer is obtained from the outlet pipe [13, 14, 17].

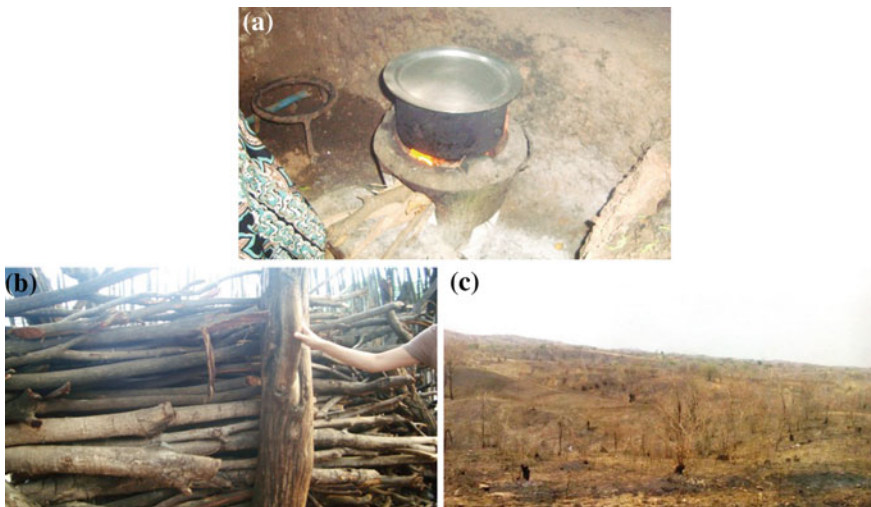


Fig. 8.2 a Traditional wood stove used in rural households. b Typical wood stock for fuel in rural households. c Deforestation in the Magway region, Myanmar (2014)

Figure 8.4 shows a real biogas utilization system in use in Vietnam. We estimate the potential amount of annual biogas production from animal manure in South East Asia to be approximately 1.3 billion m^3 , with a calorific value of 75–90 TJ/day [2, 3, 18–20]. Rice straw can also be treated in such digesters, with a potential generation of biofuel of approximately 1.1 million tons. Recent research has shown that mixing animal manure with rice straw has benefits compared with monodigestion of manure [21, 22]. Traditionally, rice straw is burned in the field after harvest [23]. The *National Biogas Program* in Vietnam and Cambodia has been promoting small-scale biogas plants. In case of Vietnam, a total of 105,000 biogas plants were installed from 2006–2012. Marketing strategies such as financial support and after-sales service resulted in a large number of sales [24, 25]. The “Farm Household Biogas Project Contributing to Rural Development in Can Tho City,” promoted by the Japan International Research Center for Agricultural Science (JIRCAS) helped to distribute small-scale biogas plants in the Mekong Delta area, from 2012 [26].

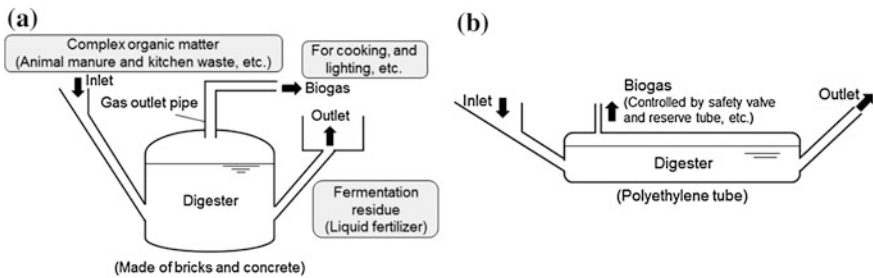


Fig. 8.3 **a** Dome-type digester for biofuel production. **b** Tube-type digester. Bond et al. [14], JIRCAS [26]



Fig. 8.4 Dome-type biogas digester installation in Vietnam (July 2013)

8.4 Application of Biogas in Fuel Cells

Biogas can be utilized in efficient energy conversion devices such as solid oxide fuel cells (SOFCs). For example, researchers at Kyushu University demonstrated a biogas-fueled SOFC, and succeeded in continuous electricity generation using a lab-scale button cell [27]. Kyushu University started a project on *sustainable development of rural areas by effective utilization of bio-waste with highly efficient fuel cell technology* as part of Science and the Technology Research Partnership for Sustainable Development (SATREPS) program, supported by the Japan Science and Technology Agency (JST), and the Japan International Cooperation Agency (JICA). Figure 8.5 shows the concept of an energy circulation system suitable for Mekong Delta region, where aquaculture is one of the biggest industries. This will be demonstrated by the Kyushu University project in the period FY2015-FY2019. In theory, it is possible to realize a sustainable agriculture system based on biogas digesters coupled with SOFC technology. In Fig. 8.5, sludge from aquaculture ponds, agricultural residue, and animal manure is collected; biogas and fermentation residue are generated by fermentation in the digester; the biogas is used for electricity generation utilizing SOFC technology; fermentation residue is used as fertilizer in neighboring farms; and shrimp-pond water is purified via a phytoremediation process. This is a multilevel system providing a highly efficient power generation and water management system for example reduction of greenhouse gas emissions; stable electricity supply; enhancement of living standards; reduction of the amount of organic waste; creation of new industries; prevention of shrimp disease; stable food supply; and improvement of the local environment. The exhaust heat of the SOFC power generation system is used to warm the biogas

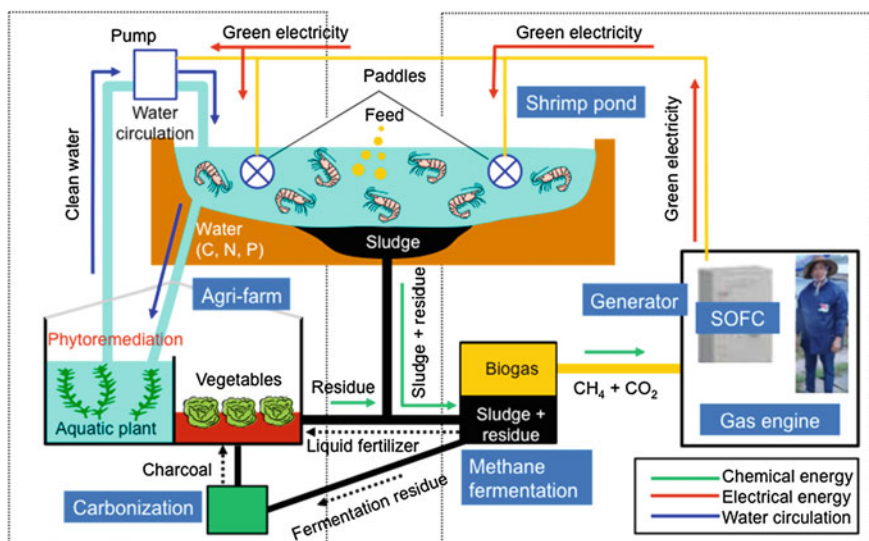


Fig. 8.5 Fuel cell incorporated energy circulation system [28]

digester, so that stable and efficient biogas production can be achieved [28]. In order to realize such a novel technology in South East Asia, the operational performance, environmental performance, economic efficiency, and social-acceptance should be sufficiently reliable.

8.5 Steam Reforming with Carbon Capture and Sequestration

If carbon-capture and sequestration (CCS) were utilized in combination with steam reforming of methane from natural gas, then the hydrogen production process would be carbon-neutral. If CCS were utilized with steam reforming of biogas, then the whole process of hydrogen production would actually be carbon-negative. One version of this process is outlined in Fig. 8.6, as developed at Kyushu University [29]. Here, CH_4 (either in the form of natural gas, or biofuel) is reformed. This produces hydrogen and carbon dioxide, as outlined above. The CO_2 is then separated from the hydrogen at first using a technique called *pressure swing adsorption* (PSA). This takes advantage of the different affinity of various mixed gases for an adsorbent material such as zeolites, activated carbon, or molecular sieves. The PSA off gas still consists of a mixture of H_2 and CO_2 . These can be further separated by using for example a poly(amidoamine) (PAMAM) dendrimer membrane. The CO_2 selectivity of this material is 230, and the permeability is $3.7 \times 10^{-15} \text{ m}^3/(\text{m}^2\text{sPa})$ (i.e. 0.99 GPU) at 42 kPa of CO_2 partial pressure and 298 K. The resulting H_2 then is fed back to efficiently fuel the steam reformer. The resulting CO_2 can be sequestered, for example by storage in underground reservoirs, subsurface saline aquifers, ocean water, aging oil fields, or porous sandstone [30]. Under the appropriate conditions (e.g. the high pressures present deep underground), it can eventually be converted to stable, solid carbonate rock forms, via mineralization [30].

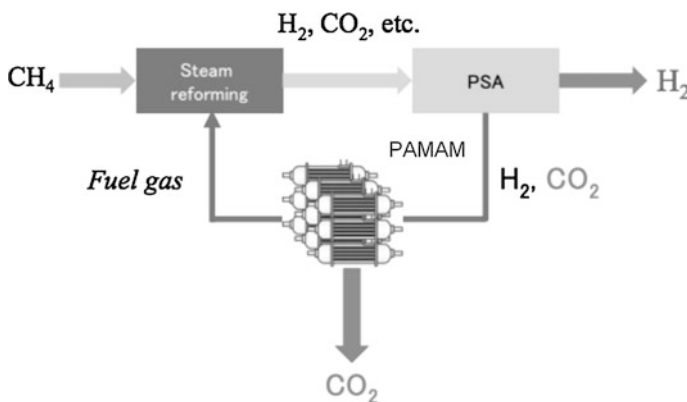


Fig. 8.6 Schematic diagram of CO_2 capture via pressure swing adsorption (PSA), in combination with a poly(amidoamine) (PAMAM) membrane separation for H_2 production

References

1. Asia biomass handbook (2008) The Japan Institute of Energy, Japan (in Japanese)
2. Surendra KC, Takara D, Hashimoto AG, Khanal SK (2014) Biogas as a sustainable energy source for developing countries: opportunities and challenges. *Renew Sustain Energy Rev* 31:846–859
3. Li YY (2005) Methane fermentation technology and its application and prospects. *JEFMA* No. 53, pp 4–18 (in Japanese)
4. Weiland P (2010) Biogas production: current state and perspectives. *Appl Microbiol Biotechnol* 85:849–860
5. Nakamura K, Kamagata Y (2006) Recent topics on methanogenic syntrophs. *J Environ Biotechnol* 5:81–89 (in Japanese)
6. Adekan BA (2012) Chapter 1. Potentials of selected tropical crops and manure as sources of biofuels. In: Kumar S (ed) *Biogas*. INTECH, pp 1–34
7. data.worldbank.org, rural population, 2013. <http://data.worldbank.org/indicator/SP.RUR.TOTL>
8. Benjamin KS (2013) Confronting energy poverty behind the bamboo curtain: A review of challenges and solutions for Myanmar (Burma). *Energy Sustain Dev* 17:305–314
9. Fernandes SD, Trautmann NM, Streets DG, Roden CA, Bond TC (2007) Global biofuel use, 1850–2000. *Glob Biogeochem Cycles* 21(2)
10. Dasgupta S, Deichmann U, Meisner C, Wheeler D (2005) Where is the poverty-environment nexus? Evidence from Cambodia, Lao PDR, and Vietnam. *World Dev* 33(4):617–638
11. Wertz-Kanounnikoff S, Kongphan-apisak M (2008) Reducing forest emissions in Southeast Asia, A review of drivers of land-use change and how payments for environmental services (PES) schemes can affect them. CIFOR Working paper No.41
12. Ministry of Forestry Myanmar (2005) National Action Program of Myanmar to Combat Desertification in the Context of UNCCD
13. Prakash CG (2013) SNV supported domestic biogas programmes in Asia and Africa. *Renew Energy* 49:90–94
14. Bond T, Templeton MR (2011) History and future of domestic biogas plants in the developing world. *Energy Sustain Dev* 15:347–354
15. Gosens J, Lu Y, He G, Bluemling B, Beckers TAM (2013) Sustainability effects of household-scale biogas in rural China. *Energy Policy* 54:273–287
16. Keovilay P (2012) Household biogas technology to improve rural livelihoods in Laos. *J Dev Sustain Agric* 7:158–163
17. Thu CTT, Cuong PH, Hang LH, Chao NV, Anh LX, Trach NX, Sommer SG (2012) Manure management practices on biogas and non-biogas pig farms in developing countries—using livestock farms in Vietnam as an example. *J Cleaner Prod* 27:64–71
18. FAOSTAT. <http://faostat3.fao.org/home/E>
19. San V, Ly D, Check NI, Check NI (2013) Assessment of sustainable energy potential of non-plantation biomass resources in Sameakki Meanchey District in Kampong Chhnang Province, Cambodia. *Int J Environ Rural Dev* 4–2:173–178
20. Sajjakulnukit B, Yingyuad R, Maneekhao V, Pongnarintasut V, Bhattacharya SC, Salam PA (2005) Assessment of sustainable energy potential of non-plantation biomass resources in Thailand. *Biomass Bioenergy* 29(3):214–224
21. Hosomi M (2014) Development of low environmental impact-systems to attain co-benefits piggery wastewater treatment and forage rice production. Final report of “Environmental research and technology development fund (1B-1103)”
22. Silvestre G, Gómez MP, Pascual A, Ruiz B (2013) Anaerobic co-digestion of cattle manure with rice straw: economic and energy feasibility. *Water Sci Technol* 67(4):745–755
23. Diep NQ, Fujimoto S, Minowa T, Sakanishi K, Nakagoshi N (2012) Estimation of the potential of rice straw for ethanol production and the optimum facility size for different regions in Vietnam. *Appl Energy* 93:205–211

24. ACE Europe (2013) Mid-term Evaluation SNV programme 2007–2015, In-depth study of the Vietnamese Biogas Programme
25. Buysman E, Mol APJ (2013) Market-based biogas sector development in least developed countries—The case of Cambodia. *Energy Policy* 63:44–51
26. JIRCAS, Registration of a biogas CDM project in Viet Nam with the UNFCCC CDM Executive Board (CDM-EB), Research Highlights 2012 . http://www.jircas.affrc.go.jp/english/publication/highlights/2012/2012_05.html
27. Shiratori Y, Ijichi T, Oshima T, Sasaki K (2010) Internal reforming SOFC running on biogas. *Int J Hydrogen Energy* 35:7905–7912
28. Shiratori Y, Tuyen TQ, Kitaoka T, Higashi O, Chien DM, Huong DTT, Cong HT (2014) Sustainable development of rural area by effective utilization of bio-wastes with highly efficient fuel cell technology. In: The 23rd symposium on solid oxide fuel cells in Japan, Tokyo, 17 Dec 2014 (in Japanese)
29. Kimura S, Honda K, Kitamura K, Taniguchi I, Shitashima K, Tsujia T, Fujikawa S (2014) Preliminary feasibility study for on-site hydrogen station with distributed CO₂ capture and storage system. *Energy Procedia* 63:4575–4584
30. Kitamura K, Jiang F, Valocchi AJ, Chiyonobu S, Tsuji T, Christensen KT (2014) The study of heterogeneous two-phase flow around small-scale heterogeneity in porous sandstone by measured elastic wave velocities and lattice Boltzmann method simulation. *J Geophys Res Solid Earth* 119(10):7564–7577

Chapter 9

Alkaline Water Electrolysis

Kohei Ito, Hua Li and Yan Ming Hao

Abstract This chapter introduces alkaline water electrolysis for hydrogen production from water splitting, beginning with the basic principles of operation. This is followed by discussion of the types of cell components in general use in commercially available devices. The use of alkaline water electrolysis in industry is discussed, and finally recent trends in research are explored.

Keywords Alkaline water electrolysis · Electrochemistry · Hydrogen production · Water splitting · Electrochemical energy conversion · AWE

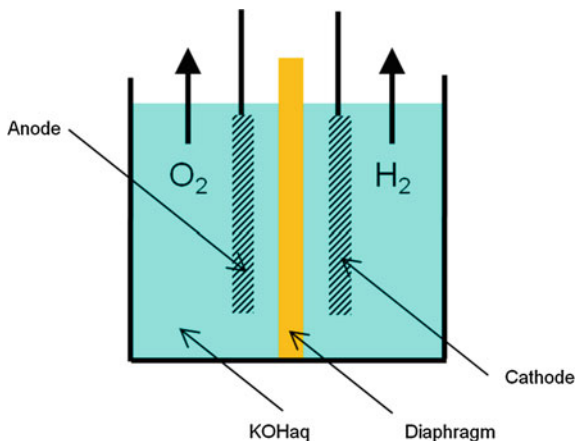
9.1 Introduction

One of the most popular ways to split water electrochemically is to use an alkaline water electrolyzer (AWE). This technique has been used in the chemical industry for many years and the state of development of AWEs for hydrogen production is highly advanced, largely due to the simplicity of this technique. Highlights in the development of highly efficient AWEs are the move toward high temperature and high pressure operation. However, the long-term success of AWEs will depend on the development of newer technologies such as polymer electrolyte membrane water electrolyzers (PEMWEs), or steam electrolysis, as discussed in the next few chapters. Particular reference is made to Refs. [1–3].

K. Ito (✉) · H. Li · Y.M. Hao
Department of Hydrogen Energy Systems, Faculty of Engineering,
Kyushu University, Fukuoka 819-0395, Japan
e-mail: kohei@mech.kyushu-u.ac.jp

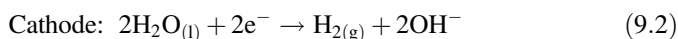
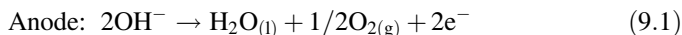
© Springer Japan 2016
K. Sasaki et al. (eds.), *Hydrogen Energy Engineering*,
Green Energy and Technology, DOI 10.1007/978-4-431-56042-5_9

Fig. 9.1 Schematic of a simple alkaline water electrolyzer (AWE)

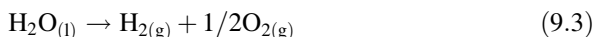


9.2 Principles of Operation

Figure 9.1 shows a schematic of a typical AWE. The electrolyte is typically an alkaline solution of $\text{KOH}_{(\text{aq})}$ or $\text{NaOH}_{(\text{aq})}$. The oxygen evolution reaction (OER) and hydrogen evolution reaction (HER) occur at the anode and cathode, respectively:



The overall reaction is as follows:



Oxygen gas is produced at the anode, because OH^- is more easily oxidized compared with H_2O . At the cathode, H^+ is reduced to form hydrogen gas, since H_2O is more easily reduced than K^+ or Na^+ .

9.3 Efficiency

The *Faradaic efficiency* (otherwise known as the *coulomb efficiency*, or the *current efficiency*) defines the efficiency of charge transfer in an electrochemical system. In an AWE, this is effectively the efficiency of oxygen gas production at the anode, and the efficiency of hydrogen gas formation at the cathode. The *overpotential* is the potential difference between the thermodynamically determined electrochemical

potential and the experimentally observed value. The *voltage efficiency* describes the fraction of energy lost due to overpotential.

From Faraday's first law of electrolysis, we know that the mass of water electrolyzed at the AWE cathode is directly proportional to the amount of charge transferred, in Coulombs. The Faraday constant (F) is the electrical charge associated with one mol of electrons, and it has a magnitude of 96,485 C/mol. Therefore, the total magnitude of charge hypothetically required to produce one mole of hydrogen by water electrolysis (L_o) is:

$$L_o = zF/\nu \quad (9.4)$$

where ν is the stoichiometric coefficient of the reaction, and z is the number of electrons transferred.

In practice, this value is often converted from the charge required to convert one mole of material, to that required to produce the *molar volume* of gas at nominal temperature and pressure. This is more useful, since hydrogen is produced as a gas at the electrode and the volume can easily be monitored. Substituting the ideal gas law into Eq. (9.4) yields the hypothetical total charge needed to produce the molar volume (Q_o):

$$Q_o = L_o/(RT/P) = (zF/\nu)/(RT/P) \quad (9.5)$$

where R is the ideal gas constant, T is the temperature, and P is the pressure. This value is generally quoted in units of C/Nm^3 rather than simply C/m^3 where the N refers to the *normal volume*, measured at 0 °C (T_o) and 1 atm (P_o). In the case of the HER (Eq. 9.2), the stoichiometric coefficient is 1, and the number of electrons is 2. Therefore, Q_o for hydrogen is calculated from Eq. (9.5) to be $8.6 \times 10^6 C/Nm^3$ (i.e. 2.39 kWh/ Nm^3). The value for the OER is double this, since the number of electrons is 4 in this case.

The *Faradaic efficiency* (ϵ_F) is the ratio of the hypothetical charge, Q_o , to the observed charge, Q .

$$\epsilon_F = Q_o/Q \quad (9.6)$$

The Faradaic efficiency will decrease if there is a short circuit in the AWE cell. Since Eq. (9.3) will proceed in both directions, the Faradaic efficiency will also decrease if hydrogen and oxygen gas can permeate through the diaphragm and react with each other (known as *crossover*).

Using the change in Gibbs free energy (ΔG) for Eq. (9.3), we can calculate the *theoretical decomposition potential* (U_G):

$$U_G = \Delta G/zF \quad (9.7)$$

In the case of liquid water electrolysis, ΔG is 237.2 kJ/mol (at 25 °C and 1 atm), and therefore U_G is calculated to be 1.229 V. The voltage efficiency (ϵ_V) is given by

the ratio of the measured decomposition potential (U) to the theoretical decomposition potential:

$$\varepsilon_V = U_G/U \quad (9.8)$$

In a real AWE, the overpotential must also be taken into account. This includes both nonlinear, and ohmic (linear) contributions. Thus, the voltage efficiency must be lower than 1, and operation at higher current density tends to decrease the voltage efficiency.

The efficiency in terms of the change in enthalpy (ΔH) can also be considered. The potential based on the enthalpy change is called the *thermoneutral potential*, U_H :

$$U_H = \Delta H/zF \quad (9.9)$$

In water electrolysis, ΔH is 285.8 kJ/mol (at 25 °C and 1 atm), and therefore $U_H = 1.481$ V. When an AWE is operated at low current density, an additional heat is supplied to compensate for the endothermic processes, the thermoneutral voltage efficiency can be greater than 1, and this value is frequently applied in regenerative fuel cell systems, which consist of a fuel cell and a water electrolyzer. Using the thermoneutral voltage efficiency for the water electrolyzer consistent with the voltage efficiency is calculated for the fuel cell in this case, giving a combined efficiency of less than 1 for the regenerative fuel cell system.

Electrolysis potentials depend on operating conditions. Representative electrolysis potentials under atmospheric pressure at 70–80 °C range from 1.84–2.25 V (0.13–0.23 A/cm²) [1]. Both anode and cathode nonlinear overpotential losses are large, and they are competitive. This is the main factor of energy loss and therefore decreases in the voltage efficiency in AWEs. When the current density increases, the ohmic overpotential is dominant, attributed to ionic conduction through the electrolyte solution and diaphragm. Although the electrolysis potential in AWEs is similar to that in polymer electrolyte membrane (PEM) water electrolyzer (as discussed in the next chapter), the AWE is operated at a low current density to suppress overpotential losses. To compensate for this, the physical size of AWEs is generally relatively large, due to the greater number of cells and/or active electrochemical area required.

The *work done* is also utilized as a performance index for AWEs. This is the electric energy required to produce hydrogen or oxygen gas. The work done is derived by multiplying the charge Q with the electrolysis potential, U .

$$W = Q \times U = (Q_0/\varepsilon_F) \times (U_G/\varepsilon_V) \quad (9.10)$$

The hypothetical limit for the work done is obtained using a value of 1 for both ε_F and ε_V . Obtaining a value for U_G based on the change in Gibbs energy (at 25 °C and 1 atm) yields $W = 2.94$ kWh/Nm³. Calculating based on the enthalpy change

results in a value of $W = 3.54 \text{ kWh/Nm}^3$. Commercialized AWEs can reach values of $4.3 \sim 4.9 \text{ kWh/Nm}^3$ (at 70–90 °C and atmospheric pressure) [1].

Another parameter used to evaluate the overall performance of AWEs is the *energy conversion efficiency*. This is defined as the ratio between the measured work done and the hypothetical value.

$$\varepsilon_W = W_0/W = (Q_o \times U_G)/(Q \times U) = \varepsilon_F \times \varepsilon_V \quad (9.11)$$

Substituting the known values into this equation yields an efficiency of 60–66 % based on the change in Gibbs energy, and 72–82 % based on the change in enthalpy.

9.4 Cell Components

Due to the alkaline environment of an AWE, expensive acid resistant materials are not required to be utilized. Both the anode and cathode generally comprise nickel-coated iron, or nickel-based materials. These electrodes have a mesh-like, or porous structure in order to maximize their surface area. Asbestos was once widely used in the diaphragm, but due to the toxic nature of this material there is a high motivation to replace this with a porous polymer composite material. Either $\text{NaOH}_{(\text{aq})}$ or $\text{KOH}_{(\text{aq})}$ are generally used in the electrolyte. $\text{KOH}_{(\text{aq})}$ is more preferable due to its higher ionic conductivity and the lower solubility of carbon dioxide in this solution. Carbon dioxide from the air is easily dissolved into $\text{NaOH}_{(\text{aq})}$ solution, resulting in carbonate formation, and a corresponding drop in the ionic conductivity. A concentration of 25–30 % $\text{KOH}_{(\text{aq})}$ is generally utilized.

9.5 Uses in Industry

The AWE is probably the most successful type of commercialized electrolysis system to date. This is largely due to the simple materials required (without the need for acid resistance), and the cheap electrode materials. AWEs have played an important role in the supply of hydrogen gas to industrial chemical plants. For example, a large AWE was constructed at Aswan in Egypt, utilizing power from a neighboring hydroelectric plant, and producing more than 30,000 m^3/h of hydrogen gas for the ammonia production industry. However, recently thermochemical methods of large-scale hydrogen production have become more popular, due to the rising price of electricity [2]. The focus for AWEs has shifted to small-scale plants, in the 10–100 m^3/h range, concentrating on higher energy conversion efficiency. In general, AWEs are expected to become a key technology in the coming hydrogen society, to produce hydrogen gas for fuel cell vehicles (FVCs).

9.6 Recent Trends

The further development of AWEs has largely been focused on the development of new cell structures and electrode materials. In terms of the cell structure, reducing the distance between the electrodes has been a major focus. The large gap between the electrodes and the diaphragm (as observed in Fig. 9.1) results in high solution resistance and resistance caused by produced gas. This is the cause of the main overpotential losses in the system. Devices that narrow this gap, or even removing the gap altogether have been designed, and this contributes to a reduction in the overpotential. Increasing the operation temperature can also result in higher efficiency. This increases the ionic conductivity and decreases overpotential. However, the alkaline solution can become more corrosive at higher temperature. Therefore, materials that are more resistant to these conditions are required for higher AWE operation temperature. Using such measures, the performance can be improved and values of 3.8–4.3 kWh/Nm³ can be achieved [3]. Increasing the operation pressure is another recent trend in improving the performance of AWEs. For hydrogen gas to be useful in an hydrogen energy society, it must generally be compressed to example 35 or 70 MPa for use in FCVs. Developments in the cell structure have resulted in hydrogen being directly produced with a pressure up to 17 MPa [4].

References

1. Denkkagakukai (2013) Denkkikagaku Binran (Handbook of electrochemistry) 6th edn. Maruzen (in Japanese)
2. Mitsushima S, Matsuzawa K (2011) Present technologies and subjects of water electrolysis. J Hydrogen Energy Syst Soc Jpn 36(1) (in Japanese)
3. Zeng K, Zhang D (2010) Recent progress in alkaline water electrolysis for hydrogen production and applications. Prog Energy Combust Sci 36:307–326
4. Dunn PM (2011) I.E.3 high-capacity, high pressure electrolysis system with renewable power sources. Hydrogen and fuel cells program, 2011 annual progress report. http://www.hydrogen.energy.gov/pdfs/progress11/ii_e_3_dunn_2011.pdf

Chapter 10

Polymer Electrolyte Membrane Water Electrolysis

Kohei Ito, Takuya Sakaguchi and Yuta Tsuchiya

Abstract This chapter introduces polymer electrolyte membrane water electrolyzers (PEMWEs) for hydrogen production from water splitting, beginning with the basic principles of operation. This is followed by a discussion of the types of cell components in general use and in commercially available devices. The use of PEMWEs in industry is discussed, and finally recent trends in research are explored.

Keywords Electrochemistry · Hydrogen production · Water splitting · Electrochemical energy conversion

10.1 Introduction

This chapter summarizes the cell design, operating principles, and recent research in *polymer electrolyte membrane water electrolyzers* (PEMWEs). This is otherwise known as *proton exchange membrane water electrolysis*, or *solid polymer electrolyte water electrolysis*. Particular reference is made to Refs. [1, 2] at the end of this chapter.

10.2 Principles of Operation

The simplified structure of a PEMWE is shown in Fig. 10.1. Protons are conducted through the PEM, which acts much like an acid solution. The following electrochemical reactions proceed when external voltage is applied:

K. Ito (✉)

Department of Mechanical Engineering, Faculty of Engineering, Kyushu University,
Fukuoka 819-0395, Japan
e-mail: kohei@mech.kyushu-u.ac.jp

T. Sakaguchi · Y. Tsuchiya

Department of Hydrogen Energy Systems, Faculty of Engineering, Kyushu University,
Fukuoka 819-0395, Japan

© Springer Japan 2016

K. Sasaki et al. (eds.), *Hydrogen Energy Engineering*,
Green Energy and Technology, DOI 10.1007/978-4-431-56042-5_10

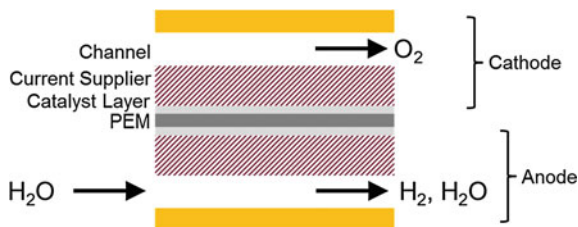
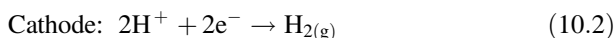
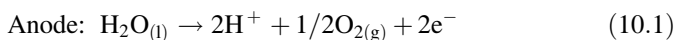
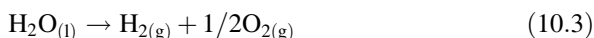


Fig. 10.1 Schematic diagram of a polymer electrolyte membrane water electrolyzer (PEMWE). This comprises a polymer electrolyte membrane (PEM), catalyst layers, and current suppliers. Separators provide electrical contact and channels for water and gas flow. The structure is almost identical to the polymer electrolyte membrane fuel cell (PEMFC)



The overall reaction is



Water is oxidized at the anode to form oxygen gas, protons, and electrons. The resulting protons are conducted through the PEM, and are then reduced at the cathode, reacting with electrons to produce hydrogen gas. This is in contrast to the case of AWEs (Chap. 9), in which OH^- ions are the ionic charge carrier.

10.3 Efficiency

The *Faradaic efficiency* and the *voltage efficiency* (as defined in Chap. 9 for alkaline water electrolyzers, AWEs) are commonly used to evaluate the performance of PEMWEs. However, the main energy losses in PEMWEs are quite different compared with AWEs. The Faradaic efficiency of PEMWEs is generally higher, partially due to the dense PEM used to separate the electrodes, as compared with the porous diaphragm used in AWEs. This significantly reduces gas crossover. Moreover, higher current density operation can be achieved with the lower ohmic overpotential. However, gas crossover can become an issue in PEMWEs if they are operated under high pressure (e.g. several tens of megapascals). The advantages and drawbacks of high pressure operation will be explained later in this chapter.

Regarding the *theoretical decomposition potential* and the voltage efficiency, Eqs. 9.7 and 9.8 describing AWEs also hold for PEMWEs. However, the factors contributing to overpotential are quite different between the two different classes of electrolyzer. For example, the gap between electrodes in a PEMWE (e.g. several

hundred microns) is much smaller than in an AWE, resulting in a significant decrease in ohmic losses. This results in a lower electrolysis voltage in PEMWEs compared with AWEs running at the same current density, and correspondingly high voltage efficiency. A representative electrolysis voltage for PEMWEs is 1.65–1.80 V (1–2 A/cm²) [1]. The *anode overpotential* is the main contributor to the increase in electrolysis voltage. Although the impacts of anode and cathode overpotential are same as in the case of AWEs, the anode overpotential is dominant in the case of PEMWEs. Therefore, reducing the anode overpotential is the most pertinent issue for achieving higher performance in practical PEMWEs.

The *work done* (as described in Eq. 9.10) and the *energy conversion efficiency* (Eq. 9.11) are also both utilized to quantify the performance of PEMWEs. As mentioned above, the overvoltage in PEMWEs is inherently small compared with AWEs. Thus, the work done in a PEMFC is also comparatively small, resulting in a higher energy conversion efficiency of 80–90 %, based on the enthalpy change of water electrolysis [1].

10.4 Cell Components

The PEMWE consists of a PEM, catalyst layers, *current suppliers* (equivalent to gas diffusion layers in PEMFCs), and *separators* (equivalent to bipolar plates) (see Fig. 10.1). Fluorine-based cation exchange polymers are generally used in the membrane. Nafion is a well-known ionomer material commonly used in PEMFCs and also typically utilized in PEMWEs. However, the thickness and equivalent weight (EW) of the membrane have different requirements. Under operation, the PEMWE membrane is fully hydrated, and experiences swelling. When the PEMWE is stopped, the membrane is dehydrated and contracts. This cycling behavior results in significant mechanical stresses being imposed, and therefore the membrane should have sufficient thickness to stand up to this load. The EW relates to the degree of expansion and contraction, and an appropriate EW must be chosen in addition to appropriate thickness.

Iridium, or iridium-based electrocatalysts are generally used at the anode, and platinum is used at the cathode. Factors influencing the choice of these materials are resistance to corrosion in acid, and the catalytic activity. The electrocatalyst layer is generally fabricated via electroless deposition, or spray printing with hot pressing. Development of the electrocatalyst layer is probably the largest issue in PEMWE research [3]. Electrocatalysts with higher activity, longer durability, and lower cost are required. In particular, novel catalyst supports at the anode are needed. Carbon is conventionally used as platinum support, for example in PEMFCs. However, in the case of PEMWEs the anode potential is high, leading to significant carbon corrosion.

The current supplier has several important roles in the PEMWE. It must be electrically conductive, allow mass transport (i.e. the produced oxygen and hydrogen must be able to pass through it), and it should improve thermal transport

between the electrocatalyst layer and the separator. It is equivalent to the gas diffusion layer (GDL) in the case of PEMFCs. However, unlike the GDL (which is usually made of carbon fiber) the current supplier is generally platinum-plated sintered titanium at the anode, in order to survive in the highly corrosive environment. The platinum plating reduces contact resistance. Porous carbon is used as the current supplier at the cathode.

10.5 Uses in Industry

The advantages of PEMWEs compared with AWEs [2] are the lower ohmic overpotential (due to the smaller electrode gap); simple material constraints (since corrosive alkaline liquid solutions are not utilized); negligible mass diffusion; simplified pressure management (due to the high mechanical strength of the PEM); high purity product gases; a simplified and more compact system; high current density operation (due to the low overpotential); and lower running costs (also due to the small overpotential). The main disadvantage is the requirement for resistance to acid corrosion in the catalyst layer and the current supplier, and the high costs associated with this issue.

The above advantages mean that PEMWEs are the primary choice for hydrogen production in hydrogen stations, where relatively small system size is required. Recently, PEMWEs have been combined with PEMFCs to function as regenerative fuel cells (RFCs) [4]. RFCs are expected to utilize renewable energy more effectively, compensating for the lag between supply and demand. When electricity supplied by renewable energy is surplus to demand, it is used by the PEMWE to produce hydrogen gas, which is stored. When renewable electricity is in short supply, the PEMFC utilizes the stored hydrogen to generate electricity. Similar systems can also be designed using secondary batteries. However, such battery-based systems are limited to small scale due to their relatively low capacity. This becomes a problem in the case of for, e.g., wind power utilization, which has a comparatively long fluctuation cycle, and may provide surplus electricity over several days.

10.6 Recent Trends

A major challenge in PEMWEs is higher temperature operation (e.g. from 60–120 °C) in order to improve voltage efficiency. The glass transition temperature of Nafion places a limit on the highest temperature that can be used. Higher temperature reduces the change in Gibbs free energy for water electrolysis, resulting in a smaller theoretical decomposition potential. Additionally, the anode overpotential (the main loss contributing to the decrease in voltage efficiency) decreases with increasing temperature. Therefore, PEMWEs operating at higher temperature should have improved

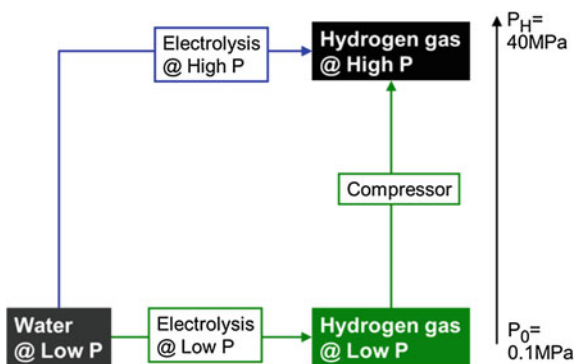
efficiency. However, higher temperature also leads to dehydration of the PEM, and sufficient water content needs to be maintained [5]. One solution to this issue has been to make Nafion composites with titanium oxide, which improves the hydrophilicity [6]. Improved energy conversion efficiency has been achieved, decreasing the work done from 4.5 kWh/m³ at 80 °C to 4.2 kWh/m³ at 100 °C [7].

Increasing the operation pressure in PEMWEs is also an active area of research. For hydrogen to be utilized in society at a large scale, higher pressure is preferred, especially in the case of hydrogen stations. This is because the volumetric energy density of hydrogen gas in ambient conditions is very low. Mechanical compressors are currently used to pressurize hydrogen gas, but the efficiency of these does not meet acceptable level, and they have loud noise. Therefore, there are distinct advantages in the *direct* production of high pressure hydrogen gas, as shown in Fig. 10.2 [8]. Although a higher electrolysis potential is predicted thermodynamically for the production of high pressure hydrogen, the fact that no mechanical compressor is required is a huge advantage.

The optimum pressure conditions in high pressure PEMWEs should be clarified. High pressure operation results in increased gas crossover, resulting in a lower current efficiency [9]. Sealing the gas in the cell is also a challenging issue. Moreover, high pressure operation increases the risks to safety. The high pressure hydrogen is only separated from oxygen gas by a thin (e.g. 100 μm) PEM. These technical issues should be addressed, and the technical level determines the upper limit of pressure that is currently possible to achieve.

Figure 10.3 shows a schematic diagram of an electrochemical hydrogen pump (EHP), which has a similar structure to a PEMFC. The EHP is an attractive technology for the production of high pressure hydrogen. Low pressure hydrogen gas is supplied to the anode and is catalytically split into protons and electrons. These recombine at the cathode, generating high pressure hydrogen gas [10]. In principle, EHP can be assumed to be an *isothermal* process, while mechanical compression is an *adiabatic* process. This suggests that EHP has intrinsically higher compression efficiency. In addition, high pressure hydrogen is not in close proximity to oxygen gas as compared with the PEMWE. These advantages of efficiency and safety mean

Fig. 10.2 Schematic diagram showing the advantage of directly producing high pressure (*P*) hydrogen using a PEMWE, compared with low pressure production followed by compressor



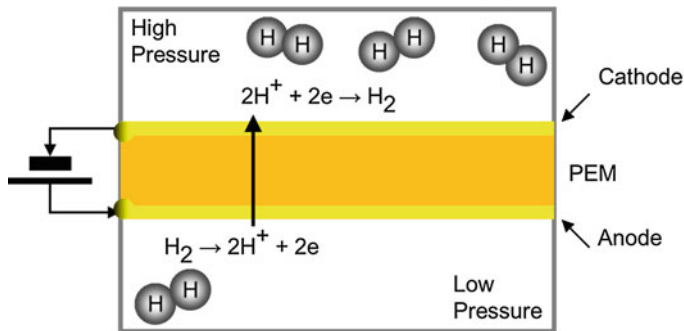


Fig. 10.3 Schematic of an electrochemical hydrogen pump (EHP) cell. The structure is similar to a PEMFC. Hydrogen gas supplied to anode is compressed via an electrochemical process

that the EHP is a promising alternative to mechanical compression. A disadvantage in EHP is difficult water management. Water is not supplied to the EHP because it is not a water electrolyzer. Water is not produced because it is not a fuel cell. Therefore, the EHP does not have a self-hydrating mechanism. Once the PEM is dehydrated, the ohmic overpotential increases. Water management for PEM hydration in the EHP is a critical issue [11]. Pressure generation of up to 100 MPa using an EHP has been demonstrated [12]. It is expected that this technology will eventually be widely adopted.

References

1. Denkkagakukai (2013) Denkkagaku Binran (Handbook of electrochemistry) 6th edn. Maruzen (in Japanese)
2. Mitsushima S, Matsuzawa K (2011) Present technologies and subjects of water electrolysis. *J Hydrogen Energy Sys Soc Jpn* 36(1) (in Japanese)
3. Carmo M, Fritz DL, Mergel J, Stolten D (2013) A comprehensive review on PEM water electrolysis. *Int J Hydrogen Energy* 38(12):4901–4934
4. Barbir F (2005) PEM electrolysis for production of hydrogen from renewable energy sources. *Solar Energy* 78:661–669
5. Bose S, Kuila T, Nguyen TXH, Kim NH, Lau K, Lee JH (2011) Polymer membranes for high temperature proton exchange membrane fuel cell: recent advances and challenges. *Prog Polym Sci* 36:813–843
6. Baglio V, Ornelas R, Matteucci F, Martina F, Ciccarella G, Zama I, Arriaga LG, Antonucci V, Aricò AS (2009) Solid polymer electrolyte water electrolyser based on Nafion-TiO2 composite membrane for high temperature operation. *Fuel Cells* 9:247–252
7. Antonucci V, Di Blasi A, Baglio V, Ornelas R, Matteucci F, Ledesma-Garcia J, Arriaga LG, Aricò AS (2008) High temperature operation of a composite membrane-based solid polymer electrolyte water electrolyser. *Electrochim Acta* 53:7350–7356
8. Eiji H, Nakazawa K, Taruya K, Ishikawa H, Okabe M (2011) Mechanical structure and performance evaluation of high differential pressure water electrolysis cell. *Honda R&D Tech Rev* 23:90–97

9. Ito K, Maeda Y, Sakaguchi T, Tsukamoto S, In-ada A, Tsuchiya Y, Nakajima H (2015) Analysis and visualization of water flow impact on hydrogen production efficiency in solid polymer water electrolyzer under high-pressure condition. *Int J Hydrogen Energy* 40:5995–6003
10. Rohland B, Eberle K, Strobel R, Scholta J, Garche J (1998) Electrochemical hydrogen compressor. *Electrochim Acta* 43(24):3841–3846
11. Ito K, Hao YM, Nakajima H, Yoshizumi H, Sasaki K (2013) Electrochemical characterization of hydrogen pump with internal humidifier and dead-end anode channel. *ECS Trans* 58 (1):681–691
12. Bouwman PJ, Konink J, Semerel D, Raymakers L, Koeman M, Dalhuijsen W, Milacic E, Mulder M (2014) Electrochemical hydrogen compression. *ECS Trans* 64(3):1009–1018

Chapter 11

Steam Electrolysis

Hiroshige Matsumoto and Kwati Leonard

Abstract This chapter introduces steam electrolyzers for hydrogen production, beginning with the basic principles of operation. This is followed by a discussion of the types of cell components generally used and in commercially available devices, particularly the electrolyte and electrode materials. The efficiency is also explored. The use of alkaline water electrolysis in industry is discussed, and finally recent trends in research are explored.

Keywords Steam electrolysis · Electrochemistry · Hydrogen production · Water splitting · Electrochemical energy conversion

11.1 Principles of Operation

Steam electrolysis is a well-known method to split water to produce hydrogen and oxygen gas using electrical energy. Using this technique, hydrogen can be manufactured without CO₂ emissions, provided that the required electricity is derived from a renewable energy source such as solar and wind power. The classification of water electrolysis depends on the type of electrolyte used and the operating temperature. Analogous to water electrolysis (Chaps. 9 and 10) steam electrolysis uses ion conducting solid oxide electrolytes and operates mostly at elevated temperature, between 700 and 1000 °C [1]. It is essentially similar to the solid oxide fuel cell (SOFC) in terms of cell structure, electrode, and electrolyte materials except that it runs in “reverse.” If an *oxide ion conductor* is used as the electrolyte, steam is introduced at the cathode. With the application of the required potential for water splitting, water molecules dissociate to form hydrogen gas and oxygen ions. The

H. Matsumoto (✉) · K. Leonard
International Institute for Carbon-Neutral Energy Research (WPI-I2CNER),
Kyushu University, Fukuoka 819-0395, Japan
e-mail: matsumoto@i2cner.kyushu-u.ac.jp

K. Leonard
e-mail: kwati@i2cner.kyushu-u.ac.jp

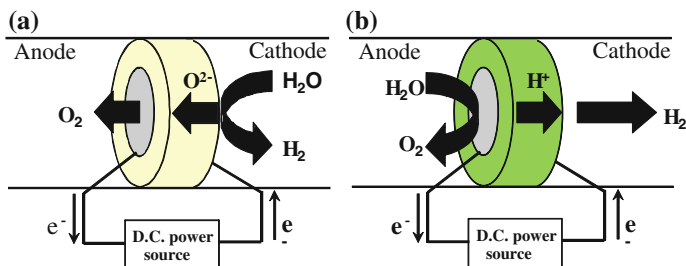
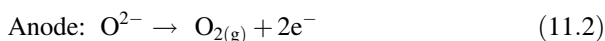
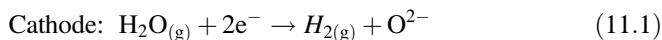


Fig. 11.1 Schematic illustration of electrolysis: **a** using an oxide ion conductor electrolyte; and **b** using a proton conductor electrolyte

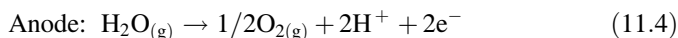
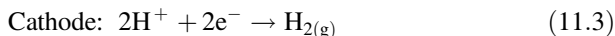
hydrogen gas diffuses to the surface and is collected while the oxygen ions are transported through the electrolyte to the anode (the air electrode). Here, they are oxidized to oxygen gas, releasing electrons. Figure 11.1a shows a schematic diagram of the working principle of a steam electrolyzer. The electrode equations are as follows:



Both electrode reactions take place where gas (i.e. water vapor, hydrogen, or oxygen), electrolyte, and electrode come together at the same place, and this is called the *triple phase boundary*. The electrode structure must be porous, so as to facilitate gas diffusion to the interface. In the case that a mixed electron and oxide ion conductor is used as the anode, the reaction occurs at the interface between the two phases (the electrode and gas phases).

Steam electrolysis is carried out at elevated temperature (e.g. 1000 °C), whereas alkaline water electrolysis (AWE, Chap. 9) and polymer electrolyte membrane water electrolysis (PEMWE, Chap. 10) are operated at relatively low temperatures (generally less than 100 °C). As a result, the electrodes overvoltages are much smaller, and therefore platinum-group metals are not required as catalysts. On the other hand, in order to operate at a high temperature, the durability and stability become significant technical challenges [2–5].

Rather than using an oxide ion conductor as the electrolyte, a *proton conductor* can also be utilized. Figure 11.1b shows a schematic diagram of the process of steam electrolysis using a proton conductor. The anode and cathode reactions occur as follows:



The major difference between steam electrolysis using oxide ion and proton conducting electrolytes is that steam is introduced at the anode side in the case of proton conduction. This is beneficial because the obtained hydrogen requires no separation. In the case of oxide ion conducting electrolytes, further separation from water is required.

11.2 Electrolyte and Electrode Materials

The most commonly used oxide ion conducting electrolyte is yttria-stabilized zirconia, with a typical composition $(\text{ZrO}_2)_{0.92}(\text{Y}_2\text{O}_3)_{0.08}$. An alternative class of electrolytes includes LaGaO_3 -based systems which are characterized by high electrical conductivity at intermediate temperature. Typical chemical compositions of proton conducting oxides include $\text{BaZr}_{0.9}\text{Y}_{0.1}\text{O}_{3-\delta}$ and $\text{SrCe}_{0.95}\text{Yb}_{0.05}\text{O}_{3-\delta}$ [6, 7]. Many of these oxides have an ABO_3 perovskite crystal structure [8–11]. Both oxide ion conductors and proton conductors are designed to have oxide ion (oxygen) vacancies in the lattice via acceptor doping. When oxide ion vacancies are the main conductive species in the material, oxide ion conductivity is developed. On the other hand, proton conductivity occurs when ambient water molecules are incorporated into the oxide vacancies, forming protons that are bonded to oxygen in the lattice via hydrogen bonds. These protons can then move from one oxygen atom to another by breaking and forming hydrogen bonds with other oxygen atoms, a mechanism referred to as hopping.

Nickel composites (cermet) are generally used at the cathode for hydrogen generation. Nickel is commonly utilized with stabilized zirconia (Ni–yttria stabilized zirconia), an oxide ion conductor, or doped ceria, $\text{Ce}_{1-x}\text{M}_x\text{O}_{2-\delta}$ ($M = \text{Gd}, \text{Sm}$), to maximize the triple-phase boundary. On the anode side where oxygen is generated, a perovskite-type oxide with high electron conductivity is used in combination with a transition metal. Some examples include $\text{La}_{1-x}\text{Sr}_x\text{MnO}_{3-\delta}$, $\text{La}_{1-x}\text{Sr}_x\text{Co}_{1-y}\text{Fe}_y\text{O}_{3-\delta}$, and $\text{Sm}_{0.5}\text{Sr}_{0.5}\text{CoO}_{3-\delta}$. When the cell has more than two stacks in series, an interconnector is used to connect the cathode with the anode in between the cells. The interconnectors are required to be stable at the operating temperature in both oxidizing and reducing atmosphere. Typically $\text{La}_{1-x}\text{Sr}_x\text{CrO}_{3\pm\delta}$ is used.

11.3 Efficiency

Hydrogen and oxygen can readily react at high temperature, or under the influence of a catalyst, to produce water. However, the reverse reaction does not occur spontaneously. Therefore, the change in Gibbs free energy for Eq. (11.5) is positive.

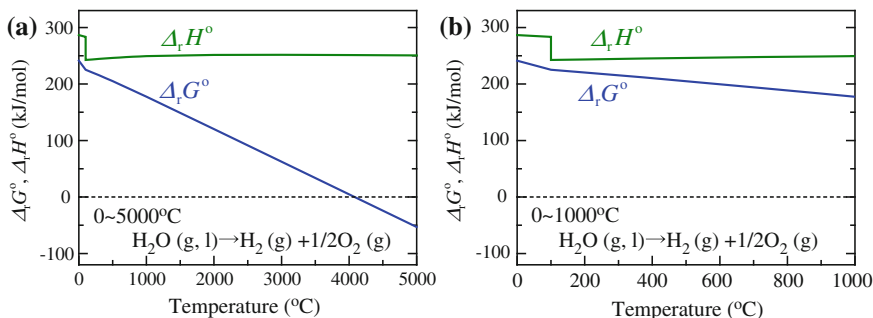
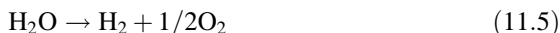


Fig. 11.2 Standard change in Gibbs free energy and standard change in enthalpy for water electrolysis: **a** from 0–5000 °C, and **b** from 0–1000 °C



A closer observation of the thermodynamic data in Fig. 11.2a reveals that the Gibbs free energy change for the decomposition reaction of water is negative at a temperature greater than approximately 4100 °C. Hence, the decomposed state of water (as hydrogen and oxygen) is more stable than water. However, it is not a suitable hydrogen production approach because there is no method to separate hydrogen and oxygen at 4100 °C.

The electrolysis reaction for water splitting, as illustrated by the electrode reactions are Eqs. (11.1)–(11.4), which can only occur if the required electrical potential for water splitting is applied. This implies that the reaction is not spontaneous at room temperature, or even at several 100 °C. It is also possible to initiate the anodic reaction by lowering the electrochemical potential of the reaction. Similarly, on the cathode side, the reaction can also be initiated by increasing the electrochemical potential. Since electrons take part in both electrode reactions, a potential difference can be created by increasing the electrochemical potential of the anode relative to the cathode. The addition of this electrical work initiates the splitting of water into hydrogen and oxygen. The minimum required electrical work is equal to the change in Gibbs free energy for water formation, whereas the minimum electrolysis voltage is given by $\Delta_r G$ divided by $2F$ (F being Faraday's constant, 96,485 C/mol). For electrolysis of liquid water to obtain hydrogen and oxygen at 1 bar and 25 °C, $\Delta_r G$ is equal to the standard free energy of water formation, $\Delta_r G^\circ = 237.1$ kJ/mol, and the minimum electrolysis potential is 1.23 V ($=237.1$ kJ/mol/2/96,485 C/mol).

A comparison between steam electrolysis and water electrolysis in terms of the electrolysis voltage and the input, as well as the output of heat, is illustrated in Fig. 11.3. When hydrogen and oxygen at 1 bar are generated from water at 25 °C, 1.23 V is the minimum required voltage, as mentioned above. An electrolysis voltage of 1.48 V is obtained by dividing the enthalpy change for the reaction by

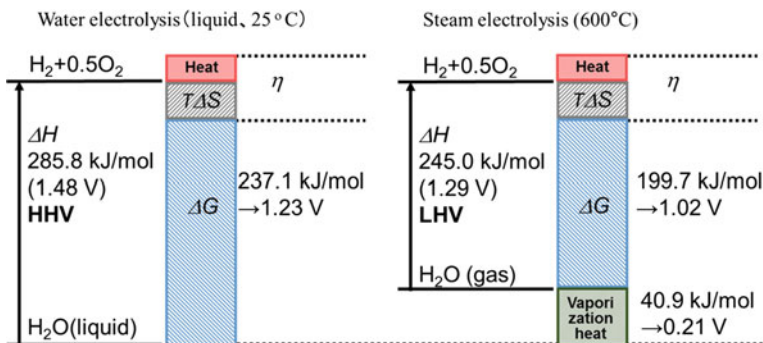


Fig. 11.3 Thermodynamic comparison of water electrolysis (25 °C) and steam electrolysis (600 °C)

$2F$, and this represents the situation where the input electrical energy meets the output chemical energy of generated hydrogen (i.e. the enthalpy change of water formation), and thus leads to thermally neutral conditions. If the voltage for water electrolysis is lower than 1.48 V, the reaction becomes endothermic. On the other hand, the standard Gibbs free energy for steam electrolysis at 600 °C is 199.7 kJ/mol. Thus, a minimum electrolysis voltage of 1.02 V is required at 1 bar. The enthalpy change is 245.0 kJ/mol, and accordingly the thermally neutral voltage is 1.29 V.

11.4 Examples of Steam Electrolysis

An example of steam electrolysis at 600 °C using SrZr_{0.5}Ce_{0.4}Y_{0.1}O_{3- α} (SZCY541) as electrolyte is reported in ref. [10]. The cathode for hydrogen generation was made from a composite of Ni and SrZr_{0.5}Ce_{0.4}Y_{0.1}O_{3- α} (SZCY541). The anode for oxygen generation was made from Sm_{0.5}Sr_{0.5}Co_{3- δ} . Steam electrolysis was conducted in order to evaluate the effect of two different kinds of electrolyte thickness. In one case, a thick electrolyte (~0.5 mm) was utilized in an electrolyte supported cell, and in the other case, an electrode-supported thin-film-type electrolyte was used (~22 μm). Figure 11.4 shows SEM images of the as-fabricated thin-film electrolyte. The top-down view in (a) shows a very dense electrolyte, while the layer thickness is around 22 μm in (b). Current-voltage characteristics of the two cells are shown in (c). The thin-film electrolyte cell has much smaller overvoltage compared to the electrolyte-supported cell. Additionally, the terminal voltage of the thin-film electrolyte cell was about 1.2 V at a current density of 0.1 A/cm². The experiments were carried out using 1 % H₂ and 1 % O₂, diluted by Ar gas. For 100 % H₂ and 100 % O₂, the obtained voltages would translate to a terminal voltage of 1.4 V. This implies a higher heating value (HHV) efficiency of 106 %,

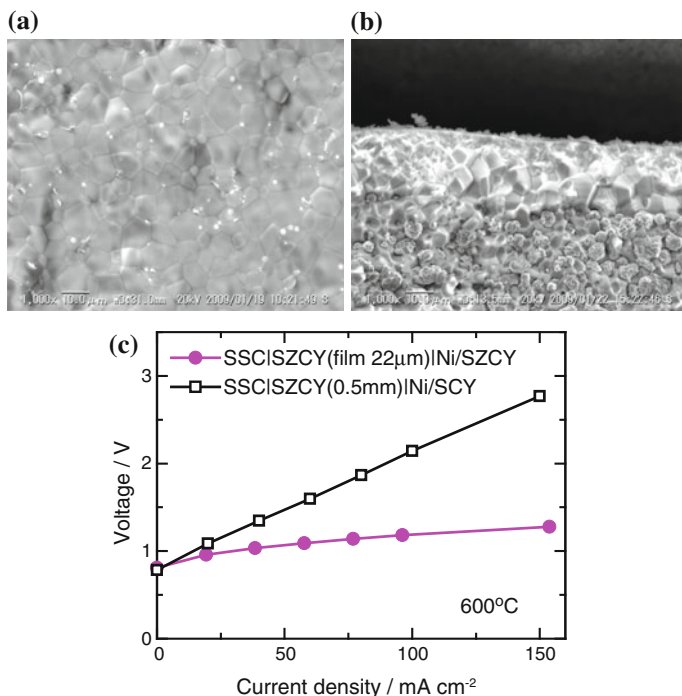


Fig. 11.4 Scanning electron microscopy (SEM) images of: **a** the surface; and **b** the cross section of an SZCY541 electrode-supported thin-film electrolyte ($\sim 22 \mu\text{m}$ thick). **c** I–V characteristics of steam electrolysis using the $22 \mu\text{m}$ thick SZCY541 electrolyte (*filled circles*) and a 0.5 mm thick electrolyte (*empty squares*), both operated at $600 \text{ }^\circ\text{C}$. (Obtained with permission from Ref. 10)

and a lower heating value (LHV) efficiency of 92 %, respectively. This experiment, therefore, reveals that steam electrolysis for hydrogen production has extremely high efficiency.

11.5 Summary and Future Prospects

Steam electrolysis is a technique which generally results in a lower water decomposition voltage relative to other electrolysis methods such as AWE or PEMWE, in part due to the much higher operating temperature. It is possible to envisage operation at temperatures of about $600 \text{ }^\circ\text{C}$ or lower using proton conducting oxides, leading to improved durability and simpler materials restrictions. At present, a HHV efficiency of 106 % and an LHV efficiency of 92 % (0.1 A/cm^2 at $600 \text{ }^\circ\text{C}$) have been achieved. Electrolytes with high electrical conductivity have also been discovered. Going forward, we envisage that high hydrogen production efficiencies will be achieved at a current density of 0.5 A/cm^2 and an electrolytic voltage of 1.4 V.

References

1. Doenitz W et al (1980) Hydrogen production by high temperature electrolysis of water vapour. *Int J Hydrogen Energy* 5(1):55–63
2. Badwal SPS (1992) Zirconia-based solid electrolytes: microstructure, stability and ionic conductivity. *Solid State Ionics* 52(1–3):23–32
3. Ishihara T, Matsuda H, Takita Y (1994) Doped LaGaO₃ perovskite type oxide as a new oxide ionic conductor. *J Am Chem Soc* 116(9):3801–3803
4. Takahshi T, Iwahara H (1980) Protonic conduction in perovskites type oxides solid solutions. *Rev Chim Miner* 17(4):243–253
5. Iwahara H, Esaka T, Uchida H, Maeda N (1981) Proton conduction in sintered oxides and its application to steam electrolysis for hydrogen production. *Solid State Ionics* 3–4:359–363
6. Iwahara H, Yajima T, Hibino T, Ozaki K, Suzuki H (1993) Protonic conduction in calcium, strontium and barium zirconates. *Solid State Ionics* 61(1–3):65–69
7. Nomura K, Tanase S (1997) Electrical conduction behavior in (La_{0.9}Sr_{0.1}) M^{III}O_{3-δ} (M^{III} = Al, Ga, Sc, In, and Lu) perovskites. *Solid State Ionics* 98(3–4):229–236
8. Okuyama Y, Ikeda S, Sakai T, Matsumoto H (2014) Incorporation of a proton into La_{0.9}Sr_{0.1}(Yb_{1-x}M_x)O_{3-δ} (M = Y, In). *Solid State Ionics* 262:865–869
9. Matsumoto H, Shimura T, Iwahara H, Higuchi T, Yashiro K, Kaimai A, Kawada T, Mizusaki J (2006) Hydrogen separation using proton-conducting perovskites. *J Alloy Compd* 408–412:456–462
10. Matsumoto H, Sakai T, Okuyama Y (2013) Proton-conducting oxide and applications to hydrogen energy devices. *Pure Appl Chem* 85(2):427–435
11. Leonard K, Lee Y, Okuyama Y, Miyazaki K, Matsumoto H (2015) Influence of dopant levels on the hydration properties SZCY and BZCY proton conducting ceramics for hydrogen production. *Int J Hydrogen Energy*

Chapter 12

Photocatalytic Water Splitting

Aleksandar Staykov, Stephen M. Lyth and Motonori Watanabe

Abstract This chapter deals with the topic of photocatalytic water splitting. Photosynthesis in nature is discussed leading into artificial photosynthesis in the lab. The basic principles of photocatalytic water splitting are introduced, followed by materials used for artificial photosynthesis, visible-light-driven photocatalysis, and dye-sensitized visible-light-driven photocatalysis, inorganic visible light-driven photocatalysis, and organic–inorganic hybrid systems.

Keywords Photocatalytic water splitting · Artificial photosynthesis · Photocatalysis · Hydrogen production · Renewable hydrogen production

12.1 Introduction

Currently, the vast majority of hydrogen is derived from reforming of fossil fuels [1]. Fossil fuels are a finite resource, and this process emits significant CO₂. Renewable production of hydrogen is paramount for widespread use in fuel cells, and the establishment of a hydrogen economy [2, 3]. Production of hydrogen from water directly using sunlight is a highly desirable, carbon-neutral method. Photocatalysis could make this a reality. However, this area of research is still at a very fundamental level, limited to laboratory demonstrations, and further research is needed before large-scale application. The biggest reserve of elemental hydrogen on Earth is chemically bound in water. If this can be accessed then it could offer an abundant, carbon-free source of hydrogen gas. Water can be split into hydrogen and

A. Staykov (✉) · S.M. Lyth · M. Watanabe
International Institute for Carbon-Neutral Energy Research (WPI-I2CNER),
Kyushu University, Fukuoka 819-0395, Japan
e-mail: alex@i2cner.kyushu-u.ac.jp

S.M. Lyth
e-mail: lyth@i2cner.kyushu-u.ac.jp

M. Watanabe
e-mail: mwata@i2cner.kyushu-u.ac.jp

oxygen by chemical reaction. One method to do this is via electrolysis, as previously discussed. However, the source of energy for electrolysis should be 100 % renewable, otherwise the problem of CO₂ production is still an issue.

Hydrogen production using light from the sun is one of the holy grails of hydrogen energy engineering. This would have several advantages. The system is simple, since only photocatalyst, sunlight, and water are required. The conditions required are mild, since the reaction occurs even at room temperature. Finally, no carbon dioxide is formed. The direct conversion of solar energy to hydrogen is highly advantageous. However, there are many other challenges that must be overcome before photocatalytic water splitting can be practically implemented at a large scale. These will be discussed below, with a focus on semiconductor-based photocatalysts for water splitting. The fundamental principles and recent progress on hydrogen production by photocatalytic water splitting are reviewed.

12.2 Photosynthesis

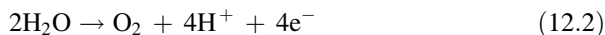
Photocatalytic water splitting is essentially artificial photosynthesis. Photosynthesis is a process in plants in which light energy is used to convert water and carbon dioxide into oxygen and carbohydrates (such as sugars) [4]. It takes part inside chloroplasts within the plant's cells, where chlorophyll-containing proteins absorb light energy. The chlorophyll light absorbing pigments are metal-organic porphyrin-based molecules with a magnesium ion center. Photosynthesis is generally separated in two subprocesses: light dependent and light independent. In the light-dependent process, water is stripped of its electrons to produce oxygen gas and protons. The electrons then take part in a light-independent process in which adenosine triphosphate (ATP, an energy storing and transporting molecule) is produced, and carbon dioxide is converted to sugars. Photosynthesis is important for life on Earth as a source of energy, and for the building of basic organic molecules. It is also important in maintaining atmospheric oxygen levels as well as controlling CO₂ levels. Indeed, around 1×10^{11} metric tons of CO₂ are converted to biomass every year by photosynthesis [5].

Is it possible to harness this process in an artificial photosynthesis reaction? The water splitting reaction within the photosynthesis process is light dependent. If achieved artificially, this would allow us to use sunlight for the synthesis of hydrogen. In this way, we would be able to achieve the production of carbon-neutral hydrogen gas using energy from the sun, without any environmentally harmful byproducts.

12.3 Artificial Photosynthesis

Photocatalysts generally have semiconductor-like properties. The band gap is the energy gap between the conduction band (CB) and the valence band (VB), and corresponds to the wavelength of absorbed light that triggers the photocatalytic reaction [6]. The basic mechanism of photocatalytic water splitting system is summarized in Fig. 12.1. When a photon with energy greater than the band gap is absorbed by the photocatalyst (ultraviolet (UV) light in this case), an electron from the VB of TiO₂ is excited (i) to the CB [7, 8]. This results in the generation of a positively charged *hole* in the VB. The resulting electron-hole pair is a key concept in water splitting. Most of the electron-hole pairs immediately *recombine* and no further reactions take place (ii). For example, Yamada et al. [9] have reported that almost electron-hole pairs recombine in the SrTiO₃ system, without further reaction. An important condition for high yield water splitting is therefore electron-hole *separation*, and the *lifetime* of the resulting electron-hole pair. When recombination does *not* occur, the electron-hole pair can migrate to the surface. There, the holes in the VB can oxidize water (iii) to produce oxygen and protons (H⁺ ions). The electrons (often with the help of a cocatalyst, described below) generate hydrogen gas via reaction with the H⁺ ions in solution.

The photocatalytic water-splitting reactions are shown in the following equations:



For the hydrogen evolution reaction (H⁺/H₂), a potential higher than 0 V versus the normal hydrogen electrode (NHE) is required at pH = 0. For oxygen evolution (O₂/H₂O), the potential must be lower than 1.23 V versus NHE at pH = 0 [7]. The timescale of electron and hole generation is of femtosecond order, while the hydrogen evolution reaction occurs with a nanosecond timescale. The oxygen

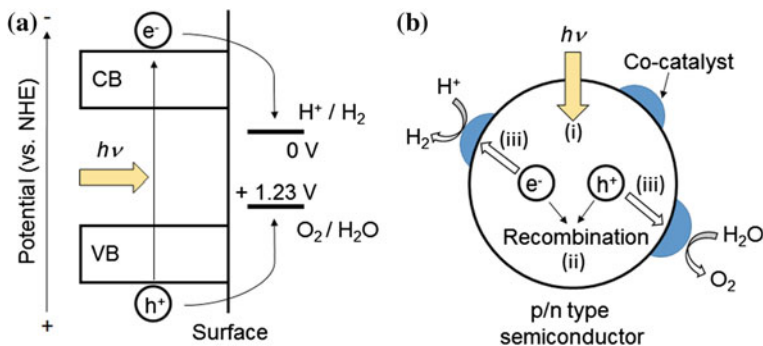


Fig. 12.1 Schematic representation of an idealized water splitting photocatalyst

evolution reaction is much slower than the hydrogen evolution reaction because it requires a four-electron reaction.

One commonly used method to suppress recombination and enhance separation is to utilize a *cocatalyst*. This is often a metal nanoparticle on the surface of the photocatalyst. The Pt nanoparticle in the above example acts as a cocatalyst. Good alignment of the Fermi level of Pt with the CB of TiO_2 leads to more facile electron transfer to the surface of the Pt nanoparticle. The actual hydrogen production then occurs on the surface of the Pt in this case. Thus, the probability of electron/hole recombination is significantly reduced. The cocatalyst also serves as a reaction site to catalyze the reactions. Typical cocatalysts for the hydrogen evolution reaction include noble metal nanoparticles such as Pt [10, 11], Rh [11, 12], or Au [13, 14]; as well as metal oxides such as NiO [15], or RuO_2 [16, 17]. For the oxygen evolution reaction, metal oxide nanoparticles such as IrO_2 [18–20] are typically used as cocatalysts.

12.4 Materials for Artificial Photosynthesis

Honda and Fujishima first reported photocatalytic water splitting in 1972, using a single crystal rutile TiO_2 anode and a Pt cathode in an electrochemical cell system [21]. The photo-driven charge separation phenomenon was subsequently named the Honda-Fujishima effect. The year 1980 was extremely important for the science of photocatalysts. In this year, Bard et al reported a simplified Pt-loaded TiO_2 powder photocatalysis system [22]; Sato et al. reported water splitting on a platinumized, powdered TiO_2 photocatalyst [10]; and Kawai et al. reported water splitting on TiO_2 powders mixed with RuO_2 [16]. After this, hydrogen gas production by photocatalytic water splitting became a highly active research topic.

The band gap corresponds to the energy of light absorbed that drives the photochemical reaction. The edge of the VB should line up with the energy level of water, and the CB edge should align with the energy level of hydrogen for water splitting to take place efficiently. Therefore band gap engineering is a key research area in the design of photocatalyst materials that can cover a broad range of the spectrum.

Group 4 (Ti^{4+} , Zr^{4+}), group 5 (Nb^{5+} , Ta^{5+}), and group 6 (W^{6+}) oxides display suitable band structure to be used as photocatalysts, and have good water splitting properties. Among these, tantalate oxides have particularly good photocatalytic activity [23, 24]. $\text{NiO}/\text{NaTaO}_3$ is highly active when doped with La [25, 26] or Sr [27]. Ge_3N_4 also shows good activity for water splitting under UV light, and was the first oxide-free type photocatalyst reported to be active for water splitting [20].

12.4.1 Visible-Light-Driven Photocatalysis

Most photocatalysts available today do not exhibit good water splitting activity when exposed to visible light. They require UV light, since many stable photocatalysts have relatively large band gaps. This has the disadvantage that UV light accounts for just 7 % of the solar spectrum at the Earth’s surface. A photocatalyst that can utilize visible light would be more effective, utilizing 47 % of the spectrum, and therefore much research is focused in this direction. The remaining solar energy is in the near-infrared region of the electromagnetic spectrum. Figure 12.2 shows the spectrum of sunlight at the Earth’s surface, with an air mass coefficient of 1.5 (AM 1.5) [28]. Note that the UV region (280–380 nm) is very narrow compared with the other regions. The UV component of sunlight on Earth is only 7 %, while the visible-light region (380–830 nm) takes up 47 % (as highlighted in Fig. 12.2). Therefore, if visible light could be used for water splitting, the efficiency would dramatically improve.

However, a key issue for water splitting is the difficulty of utilizing visible light. The relationship between absorption energy and band gap is given by the Planck relation:

$$E = h/\lambda \quad (12.3)$$

where, E is band gap, h is Planck’s constant, and λ is wavelength of the absorption edge. From this relation, the maximum band gap needed for visible-light absorption is 3.0 eV (i.e. <380 nm). Figure 12.3 shows the band-structure of various semiconductors. Many metal oxide materials (e.g. NaTaO₃, SrTiO₃, and TiO₂) have a CB higher than the H⁺/H₂ couple, and a VB below the H₂O/O₂ couple, suggesting that they can split water. However, the band gap is too large for visible-light absorption [29]. WO₃ has a suitable band gap of 2.8 eV (440 nm), and can catalyze the oxygen evolution reaction, but the CB is too low for the hydrogen evolution reaction [30]. Some chalcogenides (e.g. CdS and CdSe) at first appear to have small

Fig. 12.2 The solar spectrum at the Earth’s surface (AM1.5, global tilted). The visible-light region is highlighted (380–830 nm)

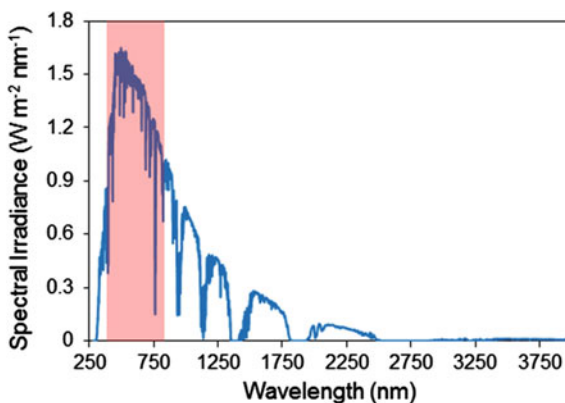
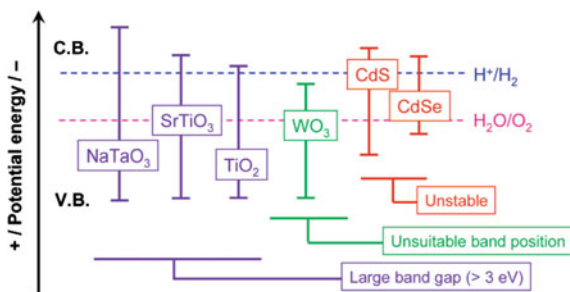


Fig. 12.3 The band structure of various semiconductor materials in relation to hydrogen and oxygen production energy levels [35]. Reprinted with permission from Ref. [35]. Copyright (2009). American Chemical Society



enough band gap for water splitting (2.4 eV, 517 nm), as well as suitably located CB and VB [31–34]. However, they lack chemical stability and are easily oxidized.

Recently, Domen et al., developed visible-light responsive oxynitride photocatalysts. If the oxygen atom in a metal oxide is replaced with a nitrogen atom, the VB of the oxynitride is shifted to a higher position, while the CB is largely unaffected [35]. Oxynitrides containing Ti⁴⁺ [36], Nb⁵⁺ [37], and Ta⁵⁺ [37–40] displayed small band gaps (1.9–2.5 eV), visible-light responsiveness, and remarkably stable photocatalytic activity.

Although some inorganic semiconductors have shown good visible-light-driven photocatalytic activity, there is still the remaining challenge of improving efficiency and stability. For example, GaN and ZnO have wide band gaps (>3.0 eV), but a solid solution of GaN and ZnO is a visible-light photocatalyst [41–44]. An optimized GaN:ZnO material (2.6 eV band gap) with a cocatalyst has good water splitting activity at 420–440 nm [45].

12.4.2 Dye-Sensitized Visible-Light-Driven Photocatalysis

Organic molecules capable of utilizing sunlight are called *photosensitizers* [46]. Nature uses pigments (mainly chlorophylls) to absorb a broad part of the visible spectrum. Artificial systems can also use such pigments; either a single pigment with a broad absorption range, or a combination of narrow-absorption pigments with different ranges, resulting in a broad spectrum absorbing composite system. Ruthenium polypyridine complexes, and in particular tris(bipyridine)ruthenium(II) (Fig. 12.4), have been extensively studied for hydrogen production. This is due to their efficient visible-light absorption, and long-lived metal-to-ligand charge transfer excited state, making the complexes strong reducing agents.

Figure 12.5 shows a conceptual schematic of dye-sensitized hydrogen production from water using TiO₂ in combination with a sensitizer dye. This dye absorbs light in the visible spectrum and reaches an excited state (Step 1). If the energy level of the excited electron in the dye is higher than the CB of the photocatalyst, electron transfer can occur (Step 2). The injected electron migrates to the reaction site at the surface (Step 3), and hydrogen production is achieved via the cocatalyst (Pt in this case)

Fig. 12.4 Structure of the photosensitizer tris (bipyridine)ruthenium(II)

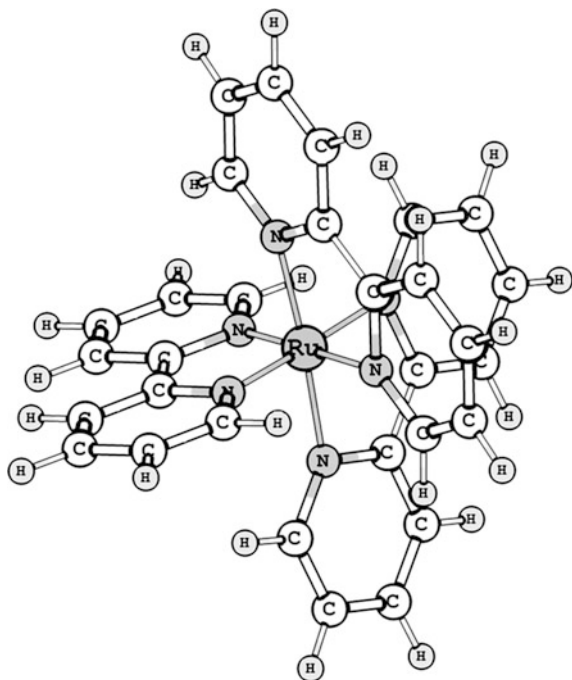
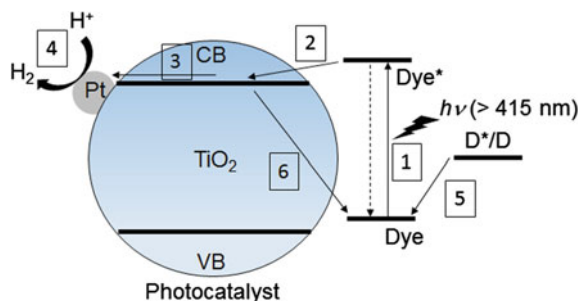


Fig. 12.5 Dye-sensitized photocatalytic water splitting



(Step 4). The oxidized dye is regenerated via injection of an electron from a sacrificial reagent or a mediator (Step 5). Additionally, some electrons are transferred back into the dye before being able to react (Step 6). Note that wide band gap semiconductors (e.g. >3.0 eV) can be used in this system.

This concept is similar to the dye-sensitized solar cell. In 1976, Tsubomura et al. [47] reported a conversion-efficiency (η) for a dye-sensitized solar cell of 1.5 % at a wavelength of 563 nm, using Rose Bengal dye in a porous ZnO electrode. In 1991, O'Regan and Grätzel et al., reported a 7 % solar energy conversion efficiency using a porous TiO₂ electrode with a Ru metal-complex dye [48].

Dye-sensitized photocatalysts were first utilized for hydrogen production in 1981, by Borgarello and Grätzel. They combined TiO_2 with a Pt/RuO_2 cocatalyst and a $\text{Ru}(\text{bpy})_3^{2+}$ dye to achieve hydrogen generation under visible light [49]. The ruthenium complex dye showed efficient charge injection because of the long electron injection lifetime and metal-to-ligand electron transfer. In addition, Houlding and Grätzel [50] reported hydrogen generation under visible light using a 8-hydroxy-orthoquinoline metal-free dye.

The efficiency and stability of hydrogen production in such a system can be improved by utilizing of, e.g., a silane coupling reagent. Direct coupling of the dye and the semiconductor using a coupling reagent can facilitate charge transfer between the two active systems. For example, Abe et al. [51] reported steady state hydrogen evolution from water using TiO_2 with an Eosin Y dye, and a silane coupling reagent, under visible-light irradiation. Very recently, chemical spacers have been considered to reduce the electron recombination rate between the dye and the semiconductor and, leading to enhancement of the water splitting reaction rate [52].

Other factors affecting the rate of hydrogen production include temperature, the solvent medium, and the stability of the photocatalyst. Han et al. [53] reported that a hydrophilic substituent on the dye led to a decrease of the recombination rate because of interactions between the hydrophilic group and the water, which in turn led to relaxation of the excited state. This effect may therefore improve the rate of hydrogen production. Lee et al. reported that the introduction of an alkyl chain in phenothiazine improved water-splitting performance. Although the effect of the alkyl chain on the rate of hydrogen production was unclear, the researchers proposed that the orientation of the dye molecules on the TiO_2 was changed, resulting in acceleration of electron injection, reduction of the decomposition reaction rate during dye excitation, and electron injection into the semiconductor and/or regeneration of the dye using sacrificial reagents [54]. The surface between semiconductor and dye can also be modified to improve the hydrogen production activity. One method of improving electron injection efficiency is to suppress back electron transfer from semiconductor. Choi et al. reported that Al_2O_3 -coated TiO_2 improved hydrogen production activity in visible light [55]. Al_2O_3 acts as a barrier layer to suppress back-injection of electrons from the dye. Peng et al. examined binuclear Ru-Bipyridyl complex dye-sensitized TiO_2 photocatalyst, which showed good apparent quantum efficiency as 16.8 % under 420 nm monochromic light irradiation [56].

If it were possible to carry out the oxygen generation (water oxidation) at the electrode or near the dye without using a sacrificial agent, light hydrolysis of the dye could be achieved. Mallouk et al. showed that colloidal IrO_2 with $\text{Ru}(\text{bpy})_3^{2+}$ displays visible-light-driven oxygen generation activity [57], indicating that electrons migrate to $\text{Ru}(\text{bpy})_3^{2+}$ after the water oxidation reaction. Recently, this system was combined in a dye-sensitized photochemical cell (using a TiO_2 anode and a Pt cathode). When this cell was irradiated with visible light, under a small bias

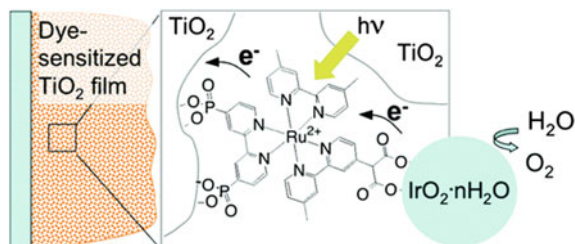


Fig. 12.6 Visible-light-driven dye-sensitized photochemical cell. The anode is TiO_2 , the cathode is Pt, $\lambda = 410 \text{ nm}$, $\text{pH} = 5.75$, aqueous buffer, -325 mV versus Ag/AgCl [58]. Reprinted with permission from Ref. [58]. Copyright (2009). American Chemical Society

(-325 mV vs. Ag/AgCl), complete decomposition of water was reported (Fig. 12.6). The overall efficiency was 0.9 % [58].

12.4.3 Inorganic Z-Scheme Visible-Light-Driven Photocatalysis

In 1979, two-step water splitting via excitation of a combination of “dual n-type semiconductors” was proposed by Bard [59]. This Z-scheme system mimics the processes in plant photosynthesis. The advantage of this system is that it can separate the electron-hole pair in each different n-type semiconductor. The proportion of electrons extracted is increased by suppressing recombination. Therefore, the activity of hydrogen production can be increased. The system contains O_2 evolution and H_2 evolution photocatalysts, and an electron mediator. When light shines on the O_2 photocatalyst, the electron-hole pair is separated and the electron migrates to the electron mediator (Fig. 12.7). The mediator passes the electron on to the H_2 generation photocatalyst, and then a second charge-separation occurs due to light absorption. The electron is used to reduce a proton to produce hydrogen. The holes at the O_2 photocatalyst are spent in oxidizing water to evolve oxygen, and those at the H_2 photocatalyst oxidize the mediator.

Ti^{4+} and Ta^{5+} oxides and nitrides are generally used as H_2 -photocatalysts, while Ta^{5+} , V^{5+} , W^{6+} , and Mo^{6+} oxides are used as the O_2 -photocatalyst. For example, Ta-Cr-doped Pt/SrTiO₃, Pt/WO₃ with an Γ^-/IO^{3-} mediator system has displayed complete photolysis of water in visible light. The quantum yield was at first approximately 0.1 % (420.7 nm) [60], and near 1 % after optimization at 420 nm [61]. In a Pt/TaON system, or Pt/ATaO₂N (A = Ca, Sr, Br), Pt/WO₃ with Γ^-/IO^{3-} also worked for Z-scheme type water splitting. The quantum yield was 0.4 % at 420 nm [62, 63]. Pt/ZrO:TaON, Pt/WO₃, and Γ^-/IO^{3-} resulted in a 6.3 % quantum yield (420.5 nm) [64]. Other redox couples have also been used for Z-scheme type photosynthesis such as $\text{Fe}^{2+}/\text{Fe}^{3+}$ [65]. A mixture of Ru/SrTiO₃:Rh and BiVO₄ particles demonstrated water decomposition of the Z-scheme type in visible light,

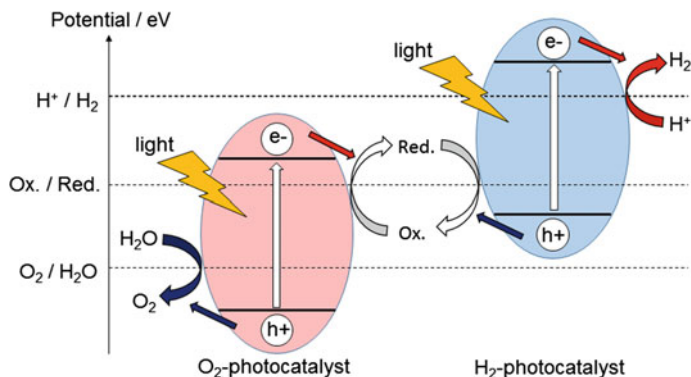


Fig. 12.7 Z-scheme photocatalytic water splitting. Reprinted with permission from Ref. [66]. Copyright (2009). American Chemical Society

without the use of mediators (1.7 % quantum yield at 420 nm). The surface of the Ru/SrTiO₃:Rh species facilitates electron transfer between particles in this case [66].

12.4.4 Organic–Inorganic Hybrid Z-Scheme Visible-Light-Driven Photocatalysis

Grätzel et al. reported Z-scheme electron transfer in a complete hydrolysis system, using a dye-sensitized photocatalyst (Fig. 12.8a) [67, 68]. This system used a mesoporous WO₃ film as a catalyst for oxygen production, and a dye-sensitized semiconductor (a mesoporous TiO₂ film) as a catalyst for hydrogen generation. In recent years, Abe et al. reported a coumarin-based dye-sensitized z-scheme water splitting reaction under visible light ($\lambda = 500$ nm, = 0.1 %) using a powder type photocatalyst, namely IrO₂/Pt/WO₃ with Pt/H₄Nb₆O₁₇, using I⁻/I³⁻ as the mediator (Fig. 12.8b) [69].

Organic materials can also be used as mediator. Hagiwara et al. [70, 71] reported Zr-doped KTaO₃ modified with a porphyrin dye (Cr-TPP), completely decomposing water via Z-scheme electron transfer (Fig. 12.9). Due to the wide band gap of KTa(Zr)O₃ (3.0 eV), it was coated with visible-light responsive porphyrin. In this system, water decomposition was achieved via electron transfer from the semiconductor to the dye. The first charge separation occurs at the KTa(Zr)O₃, and the electron in the CB migrates to the organic dye. Hydrogen production is achieved on the surface of organic dye with a cocatalyst, via a second excitation of the organic dye. Recently, this was further developed with an RhO_x, NiO/porphyrin/IrO₂- GaN:ZnO system [72].

Graphitic carbon nitride (g-C₃N₄) can be used in such photocatalyst systems. A g-C₃N₄/Au/P3HT/Pt system shows visible-light Z-scheme hydrogen production from water, although complete water splitting is not achieved (Fig. 12.10a) [73].

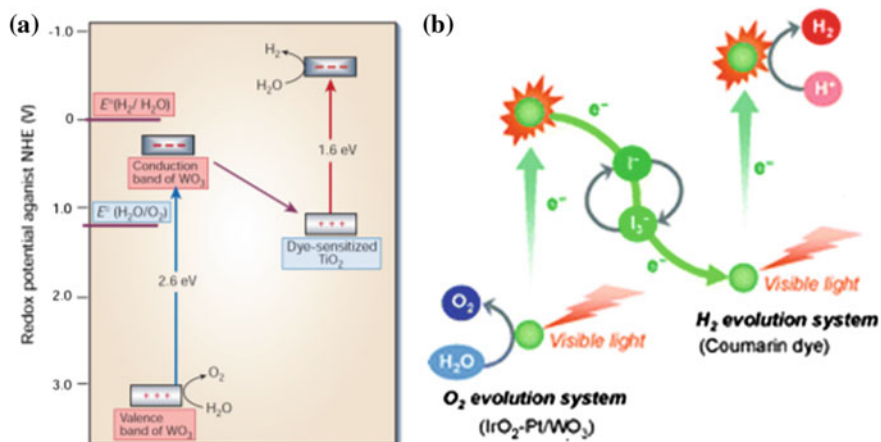
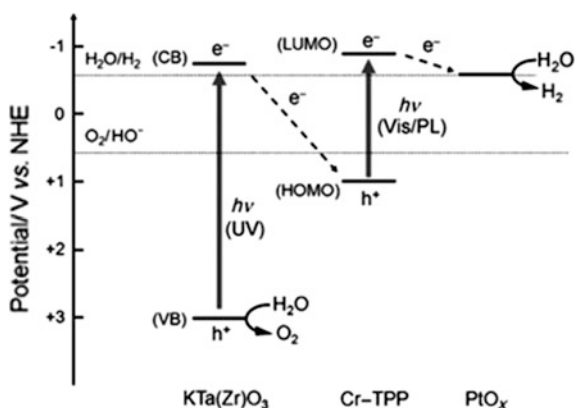


Fig. 12.8 Z-scheme, visible-light-driven dye-sensitized photocatalysis: **a** thin film photocatalyst [68] and **b** powder photocatalyst [69]. Reprinted by permission from Macmillan Publishers Ltd: [Nature] Ref [68], copyright (2001): Reproduced from Ref. [69] with permission of The Royal Society of Chemistry

Fig. 12.9 $\text{KTa}(\text{Zr})\text{O}_3$ Z-scheme water splitting [71]. Reprinted with permission from Ref. [71]. Copyright (2009) J WILEY-VCH Verlag GmbH & Co. KGaA, Weinheim



A mixture of $\text{Ru}/\text{SrTiO}_3:\text{Rh}$ and BiVO_4 particles displays water splitting properties, which have already been discussed. When the both particles are co-loaded on graphene oxide (GO), rapid electron transfer from BiVO_4 to $\text{SrTiO}_3:\text{Rh}$ is facilitated [74, 75]. This result indicates that GO can be used as a mediator for photocatalysts (Fig. 12.10b).

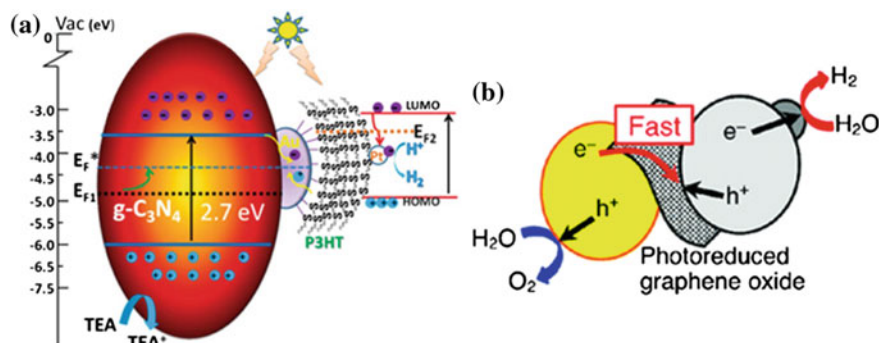


Fig. 12.10 Visible-light-driven Z-scheme dye-sensitized water splitting by **a** $g\text{-C}_3\text{N}_4/\text{Au}/\text{P3HT}/\text{Pt}$ [73], and **b** $\text{BiVO}_4/\text{GO}/\text{SrTiO}_3:\text{Rh}$ [74]. Reproduced from Ref. [73] with permission of The Royal Society of Chemistry. Reprinted with permission from Ref. [74]. Copyright (2011) American Chemical Society

References

- Ogden JM (1999) Prospects for building a hydrogen energy infrastructure. *Ann Rev Energy Environ* 24:227–279
- Bard AJ, Fox AM (1995) Artificial photosynthesis: solar splitting of water to hydrogen and oxygen. *Acc Chem Res* 28:141–145
- Arakawa H, Aresta M, Armor JN, Barteau MA, Beckman EJ, Bell AT, Bercaw JE, Creutz C, Dinjus E, Dixon DA, Domen K, DuBois DL, Eckert J, Fujita E, Gibson DH, Goddard WA, Goodman DW, Keller J, Kubas GJ, Kung HH, Lyons JE, Manzer LE, Marks TJ, Morokuma K, Nicholas KM, Periana R, Que L, Nielson JR, Sachtler WMH, Schmidt LD, Sen A, Somorjai GA, Stair PC, Stults Tumas W (2001) Catalysis research of relevance to carbon management: progress, challenges, and opportunities. *Chem Rev* 101:953–996
- Nelson N, Ben-Shem A (2004) The complex architecture of oxygenic photosynthesis. *Nat Rev Mol Cell Biol* 5:971–982
- Field CB, Behrenfeld MJ, Randerson JT, Falkowski P (1998) Primary production of the biosphere: integrating terrestrial and oceanic components. *Science* 281:237–240
- Yan H, Wang X, Yao M, Yao X (2013) Band structure design of semiconductors for enhanced photocatalytic activity: the case of TiO_2 . *Prog Nat Sci Mater Intern* 23:402–407
- Inoue Y (2009) Photocatalytic water splitting by RuO_2 -loaded metal oxides and nitrides with d^0 - and d^{10} -related electronic configurations. *Energy Environ Sci* 2:364–386
- Linsebigler AL, Lu G, Yates JT (1995) Photocatalysis on TiO_n surfaces: principles, mechanisms, and selected results. *Chem Rev* 95:735–758
- Yamada Y, Yasuda H, Tayagaki T, Kanemitsu Y (2009) Photocarrier recombination dynamics in highly excited SrTiO_3 studied by transient absorption and photoluminescence spectroscopy. *Appl Phys Lett* 95:121112
- Sato S, White JM (1980) Photodecomposition of water over Pt/TiO_2 catalysts. *Chem Phys Lett* 72:83–86
- Lehn JM, Sauvage JP, Ziessel R (1980) Photochemical water splitting continuous generation of hydrogen and oxygen on irradiation of aqueous suspensions of metal loaded strontium titanate. *Nouv J Chim* 4:623–627
- Yamaguti K, Sato S (1985) Photolysis of water over metallized powdered titanium dioxide. *J Chem Soc, Faraday Trans 1*(81):1237–1246

13. Bamwenda GR, Tshbota S, Nakamura T, Haruta M (1995) Photoassisted hydrogen production from a water-ethanol solution: a comparison of activities of Au-TiO₂ and Pt-TiO₂. *J Photochem Photobiol A* 89:177–189
14. Iwase A, Kato H, Kudo A (2006) Nanosized Au particles as an efficient cocatalyst for photocatalytic overall water splitting. *A Catal Lett* 108:7–10
15. Domen K, Naito S, Soma M, Onishi T, Tamaru K (1980) Photocatalytic decomposition of water vapour on an NiO–SrTiO₃ catalyst. *J Chem Soc Chem Commun* 543–544
16. Kawai T, Sakata T (1980) Photocatalytic decomposition of gaseous water over TiO₂ and TiO₂–RuO₂ surfaces. *Chem Phys Lett* 72:87–89
17. Inoue Y, Hayashi O, Sato K (1990) Photocatalytic activities of potassium-doped lead niobates and the effect of poling. *J Chem Soc, Faraday Trans* 86:2277–2282
18. Iwase A, Kato H, Kudo A (2005) A novel photodeposition method in the presence of nitrate ions for loading of an iridium oxide cocatalyst for water splitting. *Chem Lett* 34:946–947
19. Hara M, Waraksa C, Lean JT, Lewis BA, Mallouk TE (2000) Photocatalytic water oxidation in a buffered Tris(2,2'-bipyridyl)ruthenium complex-colloidal IrO₂ system. *J Phys Chem* 104:5275–5280
20. Sato J, Saito N, Yamada Y, Maeda K, Takata T, Kondo JN, Hara M, Kobayashi H, Domen K, Inoue Y (2005) RuO₂-loaded β-Ge₃N₄ as a non-oxide photocatalyst for overall water splitting. *J Am Chem Soc* 127:4150–4151
21. Honda K, Fujishima A (1972) Electrochemical photolysis of water at a semiconductor electrode. *Nature* 238:37–38
22. Bard AJ (1980) Photoelectrochemistry. *Science* 207:139–144
23. Kato H, Kudo A (2003) New tantalate photocatalysts for water decomposition into H₂ and O₂. *Chem Phys Lett* 295:487–492
24. Kato H, Kudo A (2003) Photocatalytic water splitting into H₂ and O₂ over various tantalate photocatalysts. *Catal Today* 78:561–569
25. Kudo A, Kato H (2000) Effect of lanthanide-doping into NaTaO₃ photocatalysts for efficient water splitting. *Chem Phys Lett* 331:373–377
26. Kato H, Asakura K, Kudo A (2003) Highly efficient water splitting into H₂ and O₂ over lanthanum-doped NaTaO₃ photocatalysts with high crystallinity and surface nanostructure. *J Am Chem Soc* 125:3082–3089
27. Iwase A, Kato H, Okutomi H, Kudo A (2004) Formation of surface nano-step structures and improvement of photocatalytic activities of NaTaO₃ by doping of alkaline earth metal ions. *Chem Lett* 33:1260–1261
28. Bird RE, Hulstrom RK, Lewis LJ (1983) Terrestrial solar spectral data sets. *Sol Energy* 30:563–573
29. Scaife DE (1980) Oxide semiconductors in photoelectrochemical conversion of solar energy. *Sol Energy* 25:41–54
30. Xin G, Guo W, Ma T (2009) Effect of annealing temperature on the photocatalytic activity of WO₃ for O₂ evolution. *Appl Surf Sci* 256:165–169
31. Enea O, Bard AJ (1986) Photoredox Reactions at semiconductor particles incorporated into clays. CdS and ZnS + CdS mixtures in colloidal montmorillonite suspensions. *J Phys Chem* 90:301–306
32. Hirai T, Okubo H, Komasa I (1999) Size-selective incorporation of CdS nanoparticles into mesoporous silica. *J Phys Chem B* 103:4228–4230
33. Li Q, Guo B, Yu J, Ran J, Zhang B, Yan H, Gong JR (2011) Highly efficient visible-light-driven photocatalytic hydrogen production of CdS-cluster-decorated graphene nanosheets. *J Am Chem Soc* 133:10878–10884
34. Hoffman AJ, Mills G, Yee H, Hoffmann MR (1992) Q-sized cadmium sulfide: synthesis, characterization, and efficiency of photoinitiation of polymerization of several vinylic monomers. *J Phys Chem* 96:5546–5552
35. Maeda K, Domen K (2007) New non-oxide photocatalysts designed for overall water splitting under visible light. *J Phys Chem C* 111:7851–7861

36. Kasahara A, Nukumizu K, Hitoki G, Takata T, Kondo JN, Hara M, Kobayashi H, Domen K (2002) Photoreactions on LaTiO_2N under visible light irradiation. *J Phys Chem A* 106:6750–6753
37. Hitoki G, Takata T, Kondo JN, Hara M, Kobayashi H, Domen K (2002) *Electrochemistry* (Tokyo, Jpn.) 70:463–465
38. Hitoki G, Takata T, Kondo JN, Hara M, Kobayashi H, Domen K (2002) An oxynitride, TaON , as an efficient water oxidation photocatalyst under visible light irradiation ($\lambda \leq 500$ nm). *Chem Commun* 16:1698–1699
39. Hitoki G, Ishikawa A, Takata T, Kondo JN, Hara M, Domen K (2002) Ta_3N_5 as a novel visible light-driven photocatalyst (<600 nm). *Chem Lett* 7:736–737
40. Yamasita D, Takata T, Hara M, Kondo JN, Domen K (2004) Recent progress of visible-light-driven heterogeneous photocatalysts for overall water splitting. *Solid State Ion* 172:591–595
41. Maeda K, Takata T, Hara M, Saito N, Inoue Y, Kobayashi H, Domen K (2005) GaN:ZnO solid solution as a photocatalyst for visible-light-driven overall water splitting. *J Am Chem Soc* 127:8286–8287
42. Maeda K, Teramura K, Takata T, Hara M, Saito N, Toda K, Inoue Y, Kobayashi H, Domen K (2005) Overall water splitting on $(\text{Ga}_{1-x}\text{Zn}_x)(\text{N}_{1-x}\text{O}_x)$ solid solution photocatalyst: relationship between physical properties and photocatalytic activity. *J Phys Chem B* 109:20504–20510
43. Maeda K, Teramura K, Lu D, Takata T, Saito N, Inoue Y, Domen K (2006) Photocatalyst releasing hydrogen from water. *Nature* 440:295
44. Sun X, Maeda K, Faucheur ML, Teramura K, Domen K (2007) Preparation of $(\text{Ga}_{1-x}\text{Zn}_x)(\text{N}_{1-x}\text{O}_x)$ solid-solution from ZnGa_2O_4 and ZnO as a photo-catalyst for overall water splitting under visible light. *Appl Catal A* 327:114–121
45. Maeda K, Teramura K, Domen K (2008) Effect of post-calcination on photocatalytic activity of $(\text{Ga}_{1-x}\text{Zn}_x)(\text{N}_{1-x}\text{O}_x)$ solid solution for overall water splitting under visible light. *J Catal* 254:198–204
46. Zhao J, Wu W, Sun J, Guo S (2013) Triplet photosensitizers: from molecular design to applications. *Chem Soc Rev* 42:5323–5351
47. Tsubomura H, Matsumura M, Nomura Y, Amamiya T (1976) Dye sensitised zinc oxide: aqueous electrolyte: platinum photocell. *Nature* 261:402–403
48. O'Regan B, Grätzel M (1991) A low-cost, high-efficiency solar cell based on dye-sensitized colloidal TiO_2 films. *Nature* 353:737–740
49. Borgarello E, Kiwi J, Pelizzetti E, Visca M, Gratzel M (1981) Sustained water cleavage by visible light. *J Am Chem Soc* 103:6324–6329
50. Houlding VH, Gratzel M (1983) Photochemical hydrogen generation by visible light. Sensitization of titanium dioxide particles by surface complexation with 8-hydroxyquinoline. *J Am Chem Soc* 105:5695–5696
51. Abe R, Hara K, Sayama K, Domen K, Arakawa H (2000) Steady hydrogen evolution from water on Eosin Y-fixed TiO_2 photocatalyst using a silane-coupling reagent under visible light irradiation. *J Photochem Photobiol A* 137:63–69
52. Watanabe M, Hagiwara H, Iribe A, Ogata Y, Shiomi K, Staykov A, Ida S, Tanaka K, Ishihara T (2014) Spacer effects in metal-free organic dyes for visible-light-driven dye-sensitized photocatalytic hydrogen production. *J Mater Chem A* 2:12952–12961
53. Han WS, Wee KR, Kim HY, Pac C, Nabetani Y, Yamamoto D, Shimada T, Inoue H, Choi H, Cho K, Kang SO (2012) Hydrophilicity control of visible-light hydrogen evolution and dynamics of the charge-separated state in $\text{Dye/TiO}_2/\text{Pt}$ hybrid systems. *Chem Eur J* 18:15368–15381
54. Lee J, Kwak J, Ko KC, Park JH, Ko JH, Park N, Kim E, Ryu DH, Ahn TK, Lee JY, Son SU (2012) Phenothiazine-based organic dyes with two anchoring groups on TiO_2 for highly efficient visible light-induced water splitting. *Chem Commun* 48:11431–11433

55. Kim W, Tachikawa T, Majima T, Choi W (2009) Photocatalysis of dye-sensitized TiO₂ nanoparticles with thin overcoat of Al₂O₃: enhanced activity for H₂ production and dechlorination of CCl₄. *J Phys Chem C* 113:10603–10609
56. Zhang LX, Veikko U, Mao J, Cai P, Peng T (2012) Visible-light-induced photocatalytic hydrogen production over binuclear Ru II–bipyridyl dye-sensitized TiO₂ without noble metal. *Chem Eur J* 18:12103–12111
57. Hara M, Waraksa CC, Lean JT, Lewis BA, Mallouk TE (2000) Photocatalytic water oxidation in a buffered tris(2,2'-bipyridyl)ruthenium complex-colloidal IrO₂ system. *J Phys Chem A* 104:5275–5280
58. Youngblood WJ, Lee SHA, Kobayashi Y, Hernandez-Pagan EA, Hoertz PG, Moore TA, Moore NL, Gust D, Mallouk TE (2009) Photoassisted overall water splitting in a visible light-absorbing dye-sensitized photoelectrochemical cell. *J Am Chem Soc* 131:926–927
59. Bard AJ (1979) Photoelectrochemistry and heterogeneous photo-catalysis at semiconductors. *J Photochem* 10:59–75
60. Sayama K, Mukasa K, Abe R, Abe Y, Arakawa H (2001) Stoichiometric water splitting into H₂ and O₂ using a mixture of two different photocatalysts and an IO₃⁻/I⁻ shuttle redox mediator under visible light irradiation. *Chem Commun* 23:2416–2417
61. Abe R, Sayama K, Sugihara H (2005) Development of new photocatalytic water splitting into H₂ and O₂ using two different semiconductor photocatalysts and a shuttle redox mediator IO₃⁻/I⁻. *J Phys Chem B* 109:16052–16061
62. Higashi M, Abe R, Teramura K, Takata T, Ohtani B, Domen K (2008) Two step water splitting into H₂ and O₂ under visible light by ATaO₂N (A = Ca, Sr, Ba) and WO₃ with IO₃⁻/I⁻ shuttle redox mediator. *Chem Phys Lett* 452:120–123
63. Abe R, Takata T, Sugihara H, Domenb K (2005) Photocatalytic overall water splitting under visible light by TaON and WO₃ with an IO₃⁻/I⁻ shuttle redox mediator. *Chem Commun* 3829–3831
64. Maeda K, Higashi M, Lu D, Abe R, Domen K (2010) Efficient nonsacrificial water splitting through two-step photoexcitation by visible light using a modified oxynitride as a hydrogen evolution photocatalyst. *J Am Chem Soc* 132:5858–5868
65. Kato H, Hori M, Kanta R, Shimodaira Y, Kudo A (2004) Construction of Z-scheme type heterogeneous photocatalysis systems for water splitting into H₂ and O₂ under visible light irradiation. *Chem Lett* 33:1348–1349
66. Sasaki Y, Nemoto H, Saito K, Kudo A (2009) Solar water splitting using powdered photocatalysts driven by Z-schematic interparticle electron transfer without an electron mediator. *J Phys Chem C* 113:17536–17542
67. Gratzel M (1999) The artificial leaf, bio-mimetic photocatalysis. *Cattech* 3:4–17
68. Grätzel M (2001) Photoelectrochemical cells. *Nature* 414:338–344
69. Abe R, Shinmei K, Hara K, Ohtania B (2009) Robust dye-sensitized overall water splitting system with two-step photoexcitation of coumarin dyes and metal oxide semiconductors. *Chem Commun* 24:3577–3579
70. Hagiwara H, Ono N, Inoue T, Matsumoto H, Ishihara T (2006) Dye-sensitizer effects on a Pt/KTa(Zr)O₃ catalyst for the photocatalytic splitting of water. *Angew Chem Int Ed* 45:1420–1422
71. Hagiwara H, Inoue T, Kaneko K, Ishihara T (2009) Charge-transfer mechanism in Pt/KTa(Zr)O₃ photocatalysts modified with porphyrinoids for water splitting. *Chem Eur J* 15:12862–12870
72. Hagiwara H, Watanabe M, Daio T, Ida S, Ishihara T (2014) Modification effects of meso-hexakis(pentafluorophenyl)[26] hexaphyrin aggregates on the photocatalytic water splitting. *Chem Commun* 50:12515–12518
73. Zhang Y, Mao F, Yan H, Liu K, Cao H, Wua J, Xiao D (2015) A polymer–metal–polymer–metal heterostructure for enhanced photocatalytic hydrogen production. *J Mater Chem A* 3:109–115

74. Iwase A, Ng YH, Ishiguro Y, Kudo A, Amal R (2011) Reduced graphene oxide as a solid-state electron mediator in Z-scheme photocatalytic water splitting under visible light. *J Am Chem Soc* 133:11054–11057
75. Lightcap IV, Kosel TH, Kamat PV (2010) Anchoring semiconductor and metal nanoparticles on a two-dimensional catalyst mat. Storing and shuttling electrons with reduced graphene oxide. *Nano Lett* 10:577–583

Part III

Hydrogen Storage

Hai-Wen Li

International Research Center for Hydrogen Energy, Kyushu University, Fukuoka, Japan

Part III gives an overview of the fundamental principles and recent progress of hydrogen storage technologies, which are one of the key issues for realizing a sustainable hydrogen society. Included in this part is a review of solid-state hydrogen storage materials, liquid-state hydrogen carries, and high-pressure compressed gas.

Chapter 13

Fundamentals

Etsuo Akiba

Abstract This chapter describes fundamental knowledge indispensable for hydride-based hydrogen storage, including the physical and chemical properties of hydrogen, phase diagrams of metal-hydrogen systems, hydrogen-material interaction, as well as thermodynamic stability and the reaction kinetics of hydrides.

Keywords Hydrogen · Phase diagram · Hydrogen-material interaction · Thermodynamics · Miedema's rule · Kinetics · Hydrogen storage

13.1 Physical and Chemical Properties of Hydrogen

Hydrogen is an element with the chemical symbol H and atomic number 1 and is the lightest element in the periodic table. Hydrogen was first produced from metals and acids in the early sixteenth century. In eighteenth century, Henry Cavendish recognized that hydrogen gas was a discrete substance.

Hydrogen is the most abundant chemical element in the universe, making up 75 % of normal matter by mass and over 90 % by number of atoms (excluding dark matter and dark energy). On the earth, hydrogen gas usually exists in diatomic molecule form as H₂. Some physical properties of hydrogen are shown in Table 13.1.

There exist two different spin isomers of hydrogen diatomic molecules, ortho-hydrogen and parahydrogen. They differ by the relative spin of their nuclei. In the orthohydrogen form, the spins of the two protons are parallel, while in the parahydrogen form the spins are antiparallel. At standard temperature and pressure, hydrogen gas contains about 25 % of the para form and 75 % of the ortho form, also known as the “normal form.” The equilibrium ratio of orthohydrogen to parahydrogen depends on temperature. At very low temperatures, the equilibrium

E. Akiba (✉)

Department of Mechanical Engineering, Faculty of Engineering, Kyushu University, Fukuoka, Japan

e-mail: e.akiba@mech.kyushu-u.ac.jp

© Springer Japan 2016

K. Sasaki et al. (eds.), *Hydrogen Energy Engineering*,

Green Energy and Technology, DOI 10.1007/978-4-431-56042-5_13

Table 13.1 Some physical properties of hydrogen, especially useful for applications

Molecular weight	2.016
Boiling point	-252.0 °C
Melting point	-259.1 °C
Density (air = 1)	0.0695
Critical pressure	13.0 bar
Critical temperature	-240.0 °C
Density of liquid (boiling point)	70.8 kg/m ³
Density of gas (20 °C, 1 bar)	0.083764 kg/m ³
Thermal conductivity (20 °C, 1 bar)	1.897 mW/cm-K

state is composed almost 100 % of the para form. The conversion from ortho to para is exothermic and produces enough heat to evaporate some of the hydrogen in the liquid phase, leading to loss of liquefied material. For liquefaction of hydrogen, conversion from ortho to para form is accelerated using catalyst to prevent evaporation of produced liquid hydrogen.

Hydrogen has three isotopes, denoted as ¹H, ²H, and ³H. ¹H is the most common hydrogen isotope with an abundance of more than 99.98 %. Because the nucleus of this isotope consists of a single proton and no neutron, it is given the formal name protium but this is rarely used. ²H is known as deuterium and contains one proton and one neutron in its nucleus. ³H is known as tritium and contains one proton and two neutrons in its nucleus. It is radioactive, decaying into ³He through beta decay, with a half-life of 12.32 years. The symbols D and T for isotopes of hydrogen instead of ²H and ³H are sometimes used for deuterium and tritium, respectively.

Hydrogen gas forms explosive mixtures with air in 4–75 % concentration by volume. Detecting low concentration hydrogen is a significantly important technique with high accuracy. The flame of hydrogen burning is nearly invisible. The enthalpy of combustion for hydrogen is -286 kJ/mol H₂.

Hydrogen forms hydrides with various elements but takes negative, neutral, and positive characters depending on elements to form hydrides. Details of hydride will be discussed later in this book.

13.2 Phase Diagram of Metal-Hydrogen Systems

Thermodynamic factors determine the major features of the metal-hydrogen systems. An understanding of the thermodynamic properties of these systems is very important, especially for certain kinds of application such as hydrogen transportation and storage, heat pumps and thermal storage, because their performance in such applications is largely determined by thermodynamic parameters. This section will focus on the practical aspects of the thermodynamic properties of the metal-hydrogen systems. The corresponding theoretical aspects of these properties

have been described in detail by Flanagan and Oates [1] and by Griessen and Riesterer [2].

The equilibrium relationship between metal and hydrogen is illustrated by means of pressure-composition-temperature (p - c - t) isotherms, as shown in the example given in Fig. 13.1. When hydrogen gas is introduced into the system, it dissolves in the lattice of the metal and forms a solid solution. This takes place over the region shown by AB in Fig. 13.1. Hydrides formed from metals and hydrogen are chemical compounds and, therefore, by using the Gibbs' phase rule

$$f = c - p + 2 \quad (13.1)$$

the degree of freedom of the system, f , is unity in the region where the metal (in practice the hydrogen solid-solution phase) is in equilibrium with its hydride and gaseous hydrogen (in this case the number of components c is 2, and the number of phases p is 3). This means that, for a given temperature, the hydrogen equilibrium pressure is constant in the two-phase region, shown as the plateau section, BC, in the isotherm given in Fig. 13.1. These characteristics can be used advantageously in "thermodynamic machines" and hydrogen-storage systems, because during the hydrogenation and dehydrogenation processes the hydrogen pressure remains constant. However, in reality the plateau region is not flat but shows a more or less sloping curve and the hydrogen absorption and desorption pressures differ.

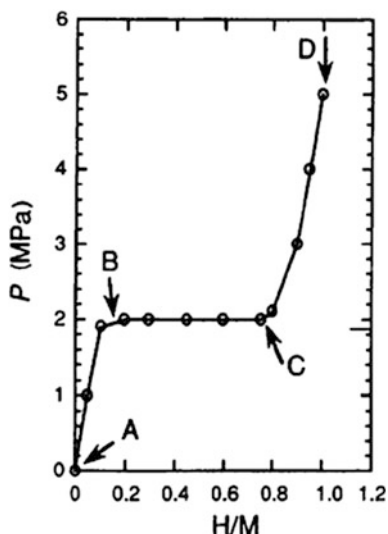


Fig. 13.1 Pressure-composition (p - c) isotherm

13.3 Hydrogen-Material Interaction

The principle of formation of transition metal hydrides is essentially the formation of a metallic bond. Transition metals belonging to groups 3 through 5 and Pd form stable binary hydrides. The radius of these metals is in the range 123–200 pm but that of hydrogen ranges 35–40 pm. Therefore, hydrogen can occupy the interstitial site of the metallic sublattice. However, even though the hydrogen atom is small, 20–30 % of volume expansion usually can be observed after metal hydride is formed. The interaction of hydrogen materials of most intermetallic compounds that form stable hydrides is similar to binary hydrides.

In the case of alkali and alkaline earth elements with low electropositivity, the hydride consists of the cation of these metals and the anion of hydrogen (H^-). For example, NaH has the same structure as NaCl. Mg and Al are most promising hydride forming elements because they are rich in the earth's crust and form hydrides with more than 7 wt% of gravimetric capacity. The bonding state of Mg and Al hydrides has been intensively studied and it has been reported that both hydrides have an intermediate nature of ionic and covalent bonding, but not bonding of a metallic (interstitial) nature.

In the electronic structure of transition metal hydrides, hydrogen gives an electron to the d-band to make a bonding state. In case of alloys with Mg and rare earth elements, the energy band of these elements is far too low to form a bonding state with hydrogen. Hydrogen will bond with the d-band of transition metals to form an alloy, just below the Fermi level. Figure 13.2 shows a schematic drawing of the electronic structure of hydrides of intermetallic compounds.

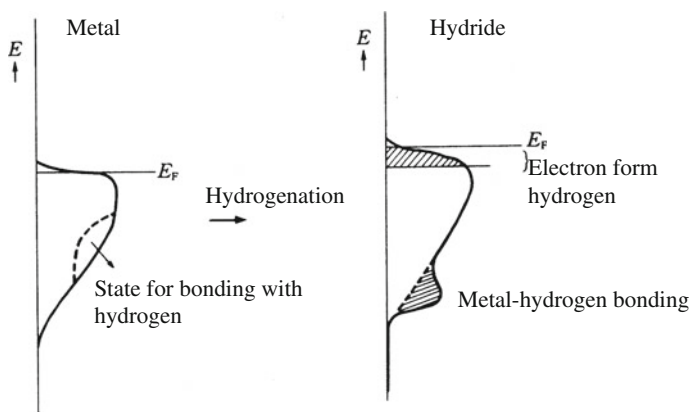


Fig. 13.2 Schematic drawing of electronic structure of hydrides of intermetallic compounds

13.4 Enthalpy of Hydride Formation and Equilibrium Pressure

The enthalpy (heat) of hydride formation is a very important parameter of metal-hydrogen systems, particularly with applications of “thermodynamic machines,” where the enthalpy of hydride determines the power and efficiency. The enthalpy of hydride formation, ΔH , is usually calculated from the variation in equilibrium pressure, P_{H_2} with the temperature T by using

$$\ln P_{H_2} = \Delta H/RT - \Delta S/R \quad (13.2)$$

The plot of the hydrogen equilibrium pressure versus the reciprocal of the absolute temperature, $1/T$, is called a van't Hoff plot, where the slope and intercept with the y axis give the enthalpy change in hydride formation, ΔH , and the entropy change of hydride forming, ΔS , respectively. Figure 13.3 shows the van't Hoff plots for a selected number of intermetallic compound-hydrogen systems, while in Fig. 13.4, the van't Hoff plots for the two plateau regions in Fig. 13.5 are presented. The equilibrium desorption pressures at hydrogen-to-metal ratios H/M of 0.25 and 0.7 were plotted and the slopes of these plots give the different enthalpies of decomposition of the LaNi_5H_6 and LaNi_5H_3 phases (-32.7 and -26.8 kJ/mol H_2 , respectively).

The change in Gibbs free energy of hydride formation can be described by

$$\Delta G = \Delta H - T\Delta S \quad (13.3)$$

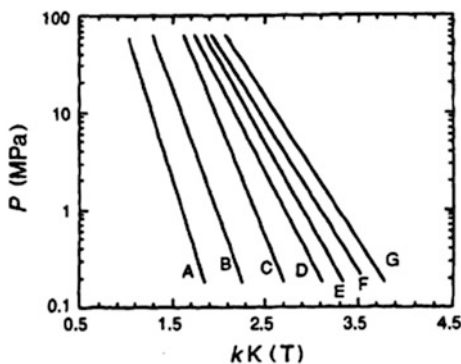
or

$$\Delta G = -RT \ln K = RT \ln P_{H_2} \quad (13.4)$$

and Eq. 13.2 can be derived directly from these two equations.

Equilibrium pressures of metal-hydrogen systems can be determined from p - c isotherms like that shown in Fig. 13.1. However, the observed isotherms may have a sloping plateau, and exhibit “sorption hysteresis” (see Fig. 13.5). In

Fig. 13.3 van't Hoff plots for selected alloy-hydrogen systems: A Mg_2Ni ; B LaNi_4Al ; C ZrMn_2 ; D $\text{LaNi}_{4.8}\text{Al}_{0.2}$; E LaNi_5 ; F TiFe ; G $\text{Ti}_{1.2}\text{Mn}_{1.8}$



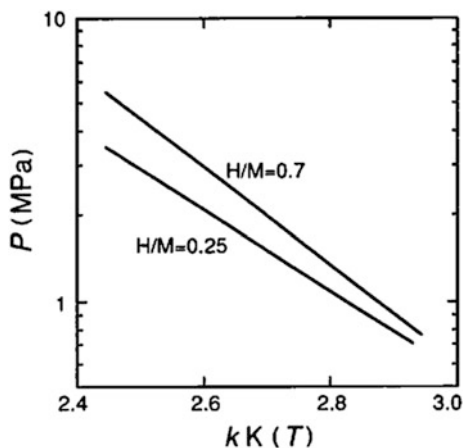


Fig. 13.4 van't Hoff plots for the $\text{LaNi}_5\text{-H}_2$ system for the two-plateau region

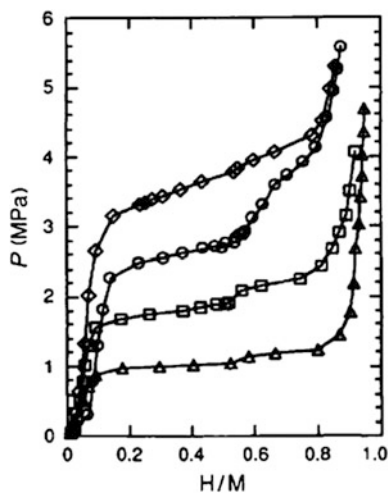


Fig. 13.5 Pressure-composition isotherm of the $\text{LaNi}_5\text{-H}_2$ system: at 353 K (*open triangle*), 373 K (*open square*), and 393 K (desorption, *open circle*; absorption, *open diamond*)

addition, it has been found that factors such as the preparative method used to make the intermetallic compounds, the variation in the ratio of the component metals, the annealing conditions, the procedures used for the activation process, and the number of hydrogenation–dehydrogenation cycles that are carried out influence the equilibrium hydrogen pressure [3].

In general, the difference in standard entropy between an alloy and its hydride is very small and is on the order of 10 J/(mol K). The change in entropy with hydride formation is mainly provided by the loss of the standard entropy of hydrogen gas

(130.858 J/(mol K) at 298 K), which means that ΔS can be assumed to be a constant and does not depend on the nature of the intermetallic compound [4]. Equation 13.5 can be used instead of Eq. 13.2, where C ($-\Delta S/R$) is a constant and does not depend upon the intermetallic compound. A sufficient number of sets of temperatures and equilibrium pressures are needed for calculation of the enthalpy of hydride formation when using Eq. 13.2. However, by using Eq. 13.5, only a pair of the temperature and equilibrium hydrogen pressure values is required to approximately calculate the enthalpy of formation. This method is very convenient to obtain a first impression of the thermodynamic properties of the ternary hydrides. However, when using Eq. 13.2 the experimental conditions used during the measurements have to be carefully monitored, because various factors may influence these values.

$$\ln P_{\text{H}_2} = \Delta H/RT + C \quad (13.5)$$

Accurate data for the enthalpy of hydride formation can be obtained using calorimetry. However, this method requires very sensitive measurements to be made and only relatively few studies have been reported [5–9]. A typical apparatus that is used for measurements of the enthalpy of formation by this technique is a Calvet-type calorimeter with twin sample cells [5]. This apparatus uses a high-pressure hydrogen supply and is able to measure the amount of reacted hydrogen. Table 13.2 shows the enthalpy of hydride formation of some typical intermetallic compounds. Although this data has been mainly derived from the van't Hoff plots of the hydrogen equilibrium pressure, of the type shown in Fig. 13.3, some results obtained from calorimetric measurements are also listed for a few of the systems.

Table 13.2 Thermodynamic properties of some typical intermetallic-hydrogen systems

IMC (M)	Amount of hydrogen. x in MH_x	Hydrogen equilibrium pressure, P (T) (MPa (K))	Enthalpy of hydride formation, H (kJ/mol H_2)	Reference
LaNi_5^{a}	6.3	0.097 (285)	-31.83 ± 0.09	Murray et al. [10]
LaNi_5	6	0.37 (313)	-31.2	Buschow and van Mal [11]
$\text{LaNi}_{4.8}\text{Al}_{0.2}$	6	0.2 (323)	-35	Mendelsohn [12]
LaNi_4Al	4	0.2 (453)	-53	Mendelsohn [12]
MmNi_5^{b}	6.3	1.3 (293)	-30	Osumi et al. [13]
TiFe	2	0.73 (313)	-28.1 ($x < 1.04$)	Reilly and Wiswall [14]
TiCo	1.4	0.101 (403)	-57.7 ($x < 0.6$)	Osumi et al. [15]
$\text{Ti}_{1.2}\text{Mn}_{1.8}$	2.47	0.7 (293)	-28	Gamo et al. [16]

(continued)

Table 13.2 (continued)

IMC (M)	Amount of hydrogen. x in MH_x	Hydrogen equilibrium pressure, P (T) (MPa (K))	Enthalpy of hydride formation, H (kJ/mol H_2)	Reference
ZrMn ₂	3.46	0.23 (374)	-44.4	Ishido et al. [17]
ZrV ₂	5.5	10^{-7} (323)	-202	Shaltiel et al. [18]
Mg ^c	2	0.92 (638)	-76.15 ± 9.2	Chase et al. [19]
Mg ₂ Ni	4	1.15 (633)	-62.7	Nomura et al. [20]
CaNi ₅ ^a	6	0.077 (313)	-33.1 ± 0.5 ($1.1 < x < 2.0$)	Murray et al. [6]
CaNi ₅	6.2	0.08 (313)	-33.5 ($1.1 < x < 4.5$)	Sandrock et al. [21]

^aData obtained using calorimetry; ^bMischmetal (Mm); ^can average of the data obtained using both calorimetry and van't Hoff plots

13.5 The Stability of Intermetallic Compound Hydrides

Because the stability of hydrides is such an important property, empirical rules have been proposed to predict the stability of a given intermetallic compound-hydrogen system. Miedema's rule of reversed stability is the most popular one [22], which proposes the following relationship between the hydride and alloy stabilities:

$$\Delta H(AB_nH_{2m}) = \Delta H(AH_m) + \Delta H(B_nH_m) - \Delta H(AB_n) \quad (13.6)$$

In this model, the enthalpy effects are considered to arise from the effective areas of contact between the component elements.

In the simplest case, the enthalpy of formation of a hydride of intermetallic compound is the difference between the sum of the hydride formation enthalpies of the two component metals and the intermetallic compound formation enthalpy. Generally, the first term on the right-hand side of Eq. 13.6 is negative and has the largest absolute value, whereas the second term on this side is small and may be positive. Therefore, the sum of the first and second terms has an almost constant value for a given class of intermetallic compound system. This means that if the third term on the right-hand side of this equation becomes more negative (equivalent to a *more stable intermetallic compound*), the left-hand side becomes more positive (equivalent to a *more unstable intermetallic compound hydride*). In the case of LaNi₅, the relationship becomes

$$\Delta H(\text{LaNi}_5\text{H}_6) = \Delta H(\text{LaH}_3) + \Delta H(\text{Ni}_5\text{H}_3) - \Delta H(\text{LaNi}_5) \quad (13.7)$$

The values for each term on the right-hand side of this equation are -252 , $+4$, and -168 kJ/(mol alloy), respectively, which then gives a value for the formation enthalpy of the intermetallic compound hydride as -80 kJ/(mol alloy) [viz. -27 kJ/(mol H₂)]. This agrees well with the observed value of -32 kJ/(mol H₂) [22]. LaCo₅ belongs to the same series of alloys as LaNi₅, but is less stable than the latter. Calculations show that $\Delta H(\text{LaCo}_5)$ is -50 kJ/(mol H₂) [22], and the hydride of LaCo₅ is found to be more stable than that formed with LaNi₅, clearly showing that these AB₅-type hydrides obey the rule of reversed stability. A similar relationship is also found in the Mg₂XH_y (where X = Fe, Co or Ni) systems. Mg₂Fe and Mg₂Co alloys do not actually exist but their hydrides were prepared using mechanical alloying or sintering techniques [23, 24]. Therefore, it can be assumed that Mg₂Fe and Mg₂Co alloys are less stable than the Mg₂Ni alloy. The observed hydrogen equilibrium pressures of Mg₂FeH_x and Mg₂CoH_x are both lower than that of Mg₂NiH_x when measured at the same temperature [23, 24]. Therefore, the hydrides of Mg₂Fe and Mg₂Co are more stable than that of Mg₂Ni. This means that in these systems *less stable alloys form more stable hydrides*.

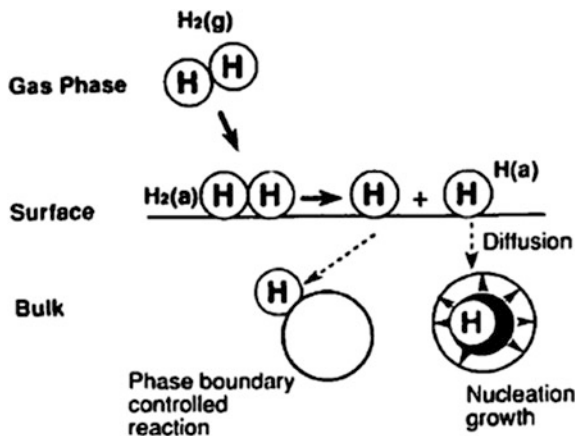
13.6 Reaction Kinetics

The direct reactions between intermetallic compounds and gaseous hydrogen are solid-phase gas-phase reactions, which differ in some aspects from homogeneous reactions. First, the presence of “boundaries” influences the reaction kinetics and mechanisms.

Hydrogen gas exists only at the surface of the intermetallic compound [25]; a hydrogen molecule (H₂) is first adsorbed on the surface, where it is dissociated into individual hydrogen atoms (H). Then the hydrogen atoms diffuse into the bulk of the intermetallic compound and form the hydride (see Fig. 13.6). Therefore, the surface (one of the “boundaries”) plays an important role in the whole reaction. As previously mentioned, intermetallic compounds consist of small particles, and the reaction proceeds independently inside each of the particles. The hydrogen atoms on the surface diffuse into the particles to react with the metal atoms, and in some cases, the reaction is controlled by diffusion through the boundary that exists between the hydride layers and the metallic atoms [17, 26].

Theoretically, a homogeneous reaction is initiated in the same manner at any atom because the molecules are moving vigorously in both the liquid and the gas phases. In contrast, a solid-phase-gas-phase reaction generally starts in a particular part of the solid where reaction nuclei can readily form such as grain boundaries, crystal defects, and impurities. All of the atoms of the solid do not contribute equally to the reaction because atoms are fixed in given positions. This is a second important feature of the solid-phase-gas-phase reaction. Therefore, in many cases, a simple kinetic equation cannot be used to describe the reaction. The method of

Fig. 13.6 Schematic representation of the reaction that occurs between an alloy and gaseous hydrogen



preparation, activation procedures, and the past history of the intermetallic compound sample significantly influence the reaction kinetics, because they determine the particle size, the number of defects, and the size and nature of any precipitate species in the grain boundaries [27, 28]. To date, there have been only a few studies of the relationship between the microstructure of intermetallic compounds and the reaction kinetics, even though the microstructures are known to determine the reaction kinetics and mechanisms of these materials.

As previously described, activated intermetallic compounds exist in the form of very fine powders and have low thermal-conductivity values. Efficient removal of the reaction heat is therefore essential, otherwise the reaction rate would be largely determined by heat-transfer processes. However, in practice the thermal conductivities of the reactors used for hydrogenation are not high enough to achieve this, and therefore, the reaction rates are largely controlled by heat transfer in almost all cases [29]. Currently, the observed reaction kinetics are overall reaction rates, which include contributions from both the intrinsic reaction rate and the heat-transfer rate, and are greatly influenced by the microstructures of the intermetallic compounds. In this section, the methods of measurement, analysis of the reaction rates, and some of the experimental results that have been obtained, will be discussed.

In solid-state reactions, the fraction of a material that has reacted is used as a parameter for representing the change in the concentration of that substance in the original solid. If the parameter “ α ” represents the ratio of the amount of reacted material to the total, i.e., original amount of material, the solid-state rate equations can be generally expressed by

$$F(\alpha) = kt \quad (13.8)$$

where k and t are the rate constant and the reaction time, respectively. Historically, the rates of gas-phase-solid-phase reactions have been extensively studied using the gravimetric method, for decomposition reactions of inorganic salts, such as carbonates and oxalates. The parameter α is very convenient for the analysis of such data, because it can be easily calculated from the weight changes that are observed.

Table 13.3 gives various rate equations, both observed and theoretically derived, that have been used to study solid-phase-gas-phase reactions. Usually, the reaction mechanism is analyzed by comparing the observed rate with those given by the equations in this table [30].

Hancock and Sharp [31] have proposed a very convenient method for the analysis of a reaction mechanism. Equation 13.9, shown in Table 13.3, is known as the Avrami–Erofeev equation and is given as

$$\alpha = 1 - \exp(-Bt^m) \quad (13.9)$$

where m is used instead of l . From Eq. 13.9, the following can be derived:

$$-\ln[\ln(1 - \alpha)] = \ln B + m \ln t \quad (13.10)$$

where B and m are constants. It has been found that all of the equations listed in Table 13.3 can also be expressed by Eq. 13.10 for $0.15 < \alpha < 0.50$. By using Table 13.4, in conjunction with Eq. 13.10, the rate equation which best fits the observed data can be found for the appropriate value of m . This procedure is a very effective one for the analysis of systems that show an induction period, and for those in which the exact starting time of the reaction cannot be determined.

The method of Hancock and Sharp [31] is suitable for the study of the decomposition of intermetallic compound hydrides, in particular when carried out

Table 13.3 Selection of various rate equations that have been used to analyze gas-solid phase reactions

Type of reaction	Equation
Branching reaction	$dx/dt = A + B\alpha^n$
Nucleation and growth processes	$\alpha = kt^n$ $\alpha = 1 - \exp(-Bt^l)$
Autocatalytic reaction	$\ln[\alpha/(1 - \alpha)] = k(t - t_c)$
Order of reaction	$\alpha = kt$ $dx/dt = k(1 - \alpha)$
Phase-boundary-controlled reaction	$1 - (1 - \alpha)^{1/n} = kt/r_0$ $1 - (1 - \alpha)^{1/3} = kt/r_0$ $1 - (1 - \alpha)^{1/2} = kt/r_0$
Diffusion-controlled contracting reaction	$[1 - (1 - \alpha)^{1/3}]^2 = kt/r_0$ $(1 - \alpha) \ln(1 - \alpha) + \alpha = kt$

Table 13.4 Values of m that have been used in Eq. 13.10, and the corresponding rate equations

Rate equation	m
$\alpha^2 = kt$	0.62
$(1 - \alpha)\ln(1 - \alpha) + \alpha = kt$	0.57
$[1 - (1 - \alpha)^{1/3}]^2 = kt$	0.54
$1 - 2\alpha/3 - (1 - \alpha)^{2/3} = kt$	0.57
$-\ln(1 - \alpha) = kt$	1.00
$1 - (1 - \alpha)^{1/2} = kt$	1.11
$1 - (1 - \alpha)^{1/3} = kt$	1.07
$\alpha = kt$	1.24
$[-\ln(1 - \alpha)]^{1/2} = kt$	2.00
$[-\ln(1 - \alpha)]^{1/3} = kt$	3.00

under vacuum, or in the absence of hydrogen. However, hydrogen gas must be present during hydride formation, and in such cases, the hydrogen pressure is an important factor in the determination of the reaction kinetics [25]. In general, three types of pressure dependence are expected. The effective hydrogen pressure, i.e., the “driving force of the reaction,” is not the partial hydrogen pressure but is the difference between the ambient hydrogen pressure and the hydrogen equilibrium pressure, as follows:

$$\Delta P = P_{\text{H}_2} - P_e \quad (13.11)$$

where P_{H_2} and P_e are the hydrogen pressure in the system, and the hydrogen equilibrium pressure at the reaction temperature, respectively. Three typical rate equations can be derived:

$$dn/dt = A\Delta P \quad (13.12)$$

$$dn/dt = A\Delta P^{1/2} \quad (13.13)$$

$$dn/dt = A\Delta P^0 \quad (13.14)$$

where n represents the fraction of the alloy that has reacted, and A is a constant. The reaction scheme for hydride formation is shown schematically in Fig. 13.6. The relationship between the hydrogen pressure and the concentration of the hydrogen atoms is given by Sievert’s law

$$[H(a)] = K_a K_p \Delta P^{1/2} \quad (13.15)$$

where $[H(a)]$, K_a , and K_p represent the amount of adsorbed hydrogen, the square root of the dissociation constant of the adsorbed hydrogen, and the square root of

the adsorption constant of gaseous hydrogen, respectively. Equation 13.12 is the first-order rate equation for this system.

First-order kinetics for the reaction would indicate that the rate-determining step is either the decomposition of hydrogen molecules, or a process whose rate is proportional to $[H(a)]^2$. In the case of Eq. 13.13, the reaction rate is proportional to the concentration of hydrogen atoms that are present at the surface. Equation 13.14 shows the zero-order rate equation, which is a characteristic form of the gas-phase-solid-phase reactions. This relationship indicates that the number of surface atoms of hydrogen which is not influenced by the hydrogen pressure ΔP . The preferred sorption process is therefore one which involves hydrogen adsorption, and even at very low hydrogen pressures the surface is fully covered by hydrogen atoms.

References

1. Flanagan TB, Oates WA (1988) Thermodynamics of intermetallic compound-hydrogen systems. In: Schlapbach L (ed) Hydrogen in intermetallic compounds I. Springer, Berlin, pp 49–85
2. Griessen R, Riesterer T (1988) Heat of formation models. In: Schlapbach L (ed) Hydrogen in intermetallic compounds I. Springer, Berlin, pp 219–284
3. Lynch JF, Reilly JJ (1982) Behavior of H-LaNi₅ solid solutions. *J Less-Common Met* 87: 225–236
4. Osumi Y, Suzuki H, Kato A, Oguro K, Nakane M (1981) Effect of metal-substitution on hydrogen storage properties for mischmetal-nickel alloys. *Nippon Kagaku Kaishi* 124: 1493–1502
5. Murray JJ, Post ML, Taylor JB (1980) Differential heat flow calorimetry of the hydrides of intermetallic compounds. *J Less-Common Met* 73:33–40
6. Murray JJ, Post ML, Taylor JB (1983) The thermodynamics of the system CaNi₅-H₂ using differential heat conduction calorimetry. *J Less-Common Met* 90:65–73
7. Post ML, Murray JJ, Taylor JB (1984) Metal hydride studies at the National Research Council of Canada. *Int J Hydrogen Energy* 9:137–145
8. Post ML, Murray JJ, Grant DM (1989) The LaNi₅-H₂ System at T = 358 K: an investigation by heat-conduction calorimetry. *Z Phys Chem N F* 163:135–140
9. Wenzl H, Lebsanft E (1980) Phase diagram and thermodynamic parameters of the quasibinary interstitial alloy Fe_{0.5}Ti_{0.5}H_x in equilibrium with hydrogen gas. *J Phys F* 10:2147–2156
10. Murray JJ, Post ML, Taylor JB (1981) The thermodynamics of the LaNi₅-H₂ system by differential heat flow calorimetry I: Techniques; the $\alpha + \beta$ two-phase region. *J Less-Common Met* 80:201–209
11. Buschow KHJ, van Mal HH (1972) Phase relations and hydrogen absorption in the lanthanum-nickel system. *J Less-Common Met* 29:203–210
12. Mendelsohn (1977) LaNi_{5-x}Al_x is a versatile alloy system for metal hydride applications. *Nature* 269:45–47
13. Osumi Y, Suzuki H, Kato A, Nakane M, Miyake Y (1978) Absorption-desorption characteristics of hydrogen for mischmetal based alloys. *Nihon Kagaku Kaishi* 1472–1477 (in Japanese)
14. Reilly JJ, Wiswall (1974) Formation and properties of iron titanium hydride. *Inorg Chem* 13:218–222

15. Osumi Y, Suzuki H, Kato A, Nakane M, Miyake Y (1979) Absorption-desorption characteristics of hydrogen for titanium-cobalt alloys. *Nihon Kagaku Kaishi* 855–860 (in Japanese)
16. Gamo T, Moriwaki Y, Yanagihara N, Yamashita T, Iwaki T (1985) Formation and properties of titanium-manganese alloy hydrides. *Int J Hydrogen Energy* 10:39–47
17. Ishido Y, Nishimiya N, Suzuki Y (1977) Preparation and equilibrium study on $ZrMn_2H_x$. *Denki Kagaku* 45:52–54
18. Shaltiel D, Jacob I, Davidov D (1977) Hydrogen absorption properties of AB_2 Laves-phase pseudobinary compounds. *J Less-Common Met* 53:117–131
19. Chase MW Jr, Davis CA, Downey JR Jr, Frurip DJ, McDonald RA, Syverud AN (1985) *J Phys Chem Ref Data* 14, Suppl No 1:1266
20. Nomura K, Akiba E, Ono S, Suda S (1979) Kinetics of the reaction between Mg_2Ni and H_2 . In: *JIMIS-2 Hydrogen in Metals*, Minakami, Japan. The Japan Institute of Metals, Sendai, pp 353–356
21. Sandrock GD, Murray JJ, Post ML, Taylor JB (1982) Hydrides and deuteride of $CaNi_5$. *Mat Res Bul* 17:887–894
22. van Mal HH, Buschow KJJ, Miedema AR (1974) Hydrogen absorption in $LaNi_5$ and related compounds: experimental observations and their explanation. *J Less-Common Met* 35:65–76
23. Didisheim JJ, Zolliker P, Yvon K, Fischer P, Schefer J, Gubelmann M, Williams AF (1984) Dimagnesium iron(II) hydride, Mg_2FeH_6 , containing octahedral FeH_6^{4-} anions. *Inorg Chem* 23:1953–1957
24. Zolliker P, Yvon K, Fischer P, Schefer J (1985) Dimagnesium cobalt(I) pentahydride, Mg_2CoH_5 , containing square-pyramidal pentahydrocobaltate(4-) (CoH_5^{4-}) anions. *Inorg Chem* 24:4177–4180
25. Flanagan TB (1978) Thermodynamics of metal, alloy and intermetallic/hydrogen systems. In: Andresen AF, Maeland AJ (eds) *Hydrides for energy storage: proceedings of an international symposium, Geilo, August 1977*. Oxford, Pergamon, pp 43–59
26. Rudman PS (1979) Hydrogen-diffusion-rate-limited hydriding and dehydriding kinetics. *J Appl Phys* 50:7195–7199
27. Boulet JM, Gerard N (1983) The mechanism and kinetics of hydride formation in Mg-10 wt% Ni and $CeMg_{12}$. *J Less-Common Met* 89:151–161
28. Mintz MH, Bloch J (1985) Evaluation of the kinetics and mechanisms of hydriding reactions. *Prog Solid State Chem* 16:163–194
29. Rudman PS (1983) Hydriding and dehydriding kinetics. *J Less-Common Met* 89:93–110
30. Sharp JH, Brindley GW, Achar BNA (1966) Numerical data for some commonly used solid state reaction equations. *J Am Ceram Soc* 49:379–382
31. Hancock JD, Sharp JH (1972) Method of comparing solid-state kinetic data and its application to the decomposition of Kaolinite, Brucite and $BaCO_3$. *J Am Ceram Soc* 55:74–77

Chapter 14

Solid Hydrogen Storage Materials: Interstitial Hydrides

Etsuo Akiba

Abstract This chapter describes the formation mechanisms, specific characteristics and classification of interstitial hydrides. Several typical hydrogen storage alloys and their hydrides are selected to discuss crystal structures and hydrogenation/dehydrogenation properties.

Keywords Interstitial hydride · Self-trapping · Classification · Alloy · Laves phase · Superlattice · Solid solution · Hydrogen storage

14.1 Hydrogen Absorbing Alloys and Formation of Interstitial Hydrides

Numerous binary or pseudo binary intermetallic compounds have been found to be excellent hydrogen-absorbing materials. After absorbing hydrogen, they form ternary hydrides or intermetallic compound hydrides. Thus far, extensive application-oriented studies have been made in order to use the hydrides in hydrogen-storage containers, heat pumps, high-performance secondary batteries, etc.

This chapter, however, is less concerned with the applications of the devices themselves, but deals mainly with the fundamental chemical and physical properties of ternary hydrides, which are also important from the applications point of view. The purpose of this chapter is to describe the most important characteristics of the ternary hydrides, such as the rapid absorption and desorption of large amounts of hydrogen, and the associated changes in physical properties.

In the 1990s, it was reported that Ti based-solid solutions are also promising candidates for hydrogen absorption and desorption under moderate conditions. This chapter includes solid solution hydrides in addition to hydrides of intermetallic compounds.

E. Akiba (✉)

Department of Mechanical Engineering, Faculty of Engineering, Kyushu University,
Fukuoka 819-0395, Japan
e-mail: e.akiba@mech.kyushu-u.ac.jp

The mechanism of hydrogen absorption and desorption of metal/alloy is the so-called formation of interstitial hydride as shown in Fig. 14.1. Hydrogen molecules in the gas phase are adsorbed on the surface of the hydrogen adsorbing alloy and dissociate into two hydrogen atoms. Subsequently, the hydrogen atoms on the surface diffuse into the bulk and find an interstitial site of the metal sublattice to occupy. The metal sublattice expands by 20–30 % in volume with formation of interstitial hydrides but basically the metallic sublattice does not change.

Fukai [1] proposed a self-trap mechanism for hydrogen occupation in an interstitial site. There are two potentials to explain an interstitial hydride formation: the ground-state energy of hydrogen (hydride formation energy); and elastic energy of lattice. As shown in Fig. 14.2, the hydride formation energy stabilizes the system with an increase of displacement of M–H bonding, but the elastic energy of lattice destabilizes. There is an optimum displacement that gives a local minimum of the total energy of the system. This phenomenon has the appearance of a hydrogen atom self-diffusing into the lattice to its occupation site concomitant with a certain expansion of the lattice. Therefore, it is called a self-trapping mechanism.

Fig. 14.1 Formation of interstitial hydride

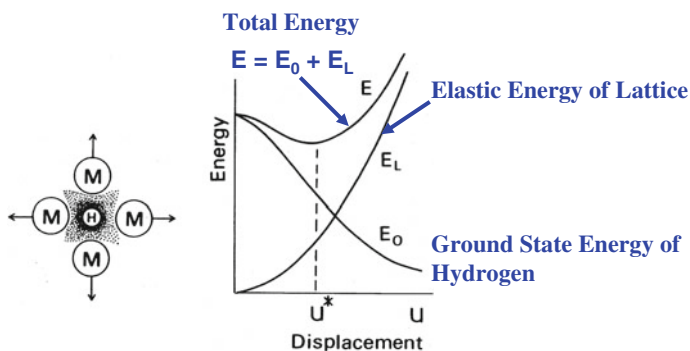
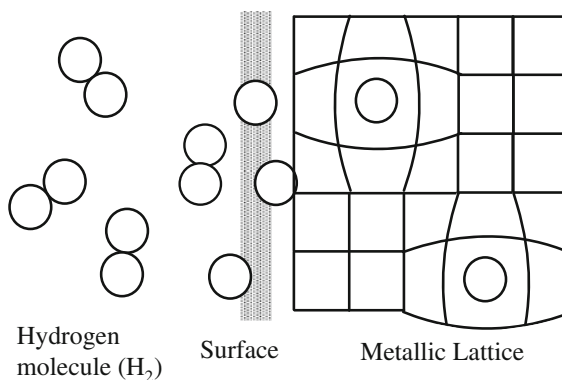


Fig. 14.2 Self-trapping mechanism [1] (used with permission from Springer, Copyright 1993)

In this chapter, the words “hydrogen absorbing alloy” and “interstitial hydrides” are used to express these metal-based hydrogen storage materials.

14.2 Properties of Interstitial Hydrides

An interstitial hydride is normally formed by the reaction between intermetallic compounds or solid solution of metals and gaseous hydrogen. The specific characteristics of the alloy-hydrogen system, when compared to a pure metal-hydrogen system (i.e., the binary) are as follows:

- wider range of hydride stability,
- better sorption kinetics,
- a larger variety of hydrides can be produced.

For many kinds of applications these features of the interstitial hydrides are more favorable than those of the corresponding binary systems and so-called complex hydrides because only Pd and V form hydrides under ambient pressure and temperature.

Table 14.1 lists the hydrogen content and hydrogen density of interstitial hydrides with other hydrogen-containing materials or hydrogen-storage systems. Interstitial hydrides can contain a larger quantity of hydrogen than the same volume of liquid hydrogen, and they also have an advantage in the amount of hydrogen on a weight basis. Therefore, certain interstitial hydrides are very suitable for applications such as hydrogen storage and transportation.

Table 14.1 Hydrogen densities and hydrogen contents shown for several hydride systems

System	Hydrogen density (mol. H ₂ dm ⁻³)	Hydrogen content (wt %)
Hydrogen gas (273 K, 1 atm)	0.045	100
Liquid hydrogen (20 K)	35	100
Water (293 K)	56	11.2
MgH ₂	55	7.6
Mg ₂ NiH ₄	47	3.6
LaNi ₅ H ₆	52	1.4
TiFeH ₂	47	1.9
(Ti–V–Cr)H ₂	102	4.0
High pressure cylinder (1.5 MPa)	6.6	1.2 ^a
High pressure cylinder (70 MPa)	20	5.7 ^{a,b}

^aIncludes weight of the cylinder

^bHydrogen cylinders for Toyota MIRAI (2014)

The discovery of interstitial hydrides was made some 50 years ago when Reilly and Wiswall, Jr. first reported the hydride formation of Mg_2Ni [2] and then later, the formation of TiFe [3]. In 1970, van Vucht et al. [4] reported the hydride formation of LaNi_5 that absorbs and desorbs hydrogen at room temperature under moderate pressures.

At the same time in the early 1970s, an “energy crisis” was taking place, and hydrogen as a medium for transportation and storage of energy attracted considerable attention. These two facts stimulated research and led to the rapid development of the intermetallic compounds-hydride systems. Major hydride-forming intermetallic compounds based on Laves phases were developed in Israel [5] and Japan [6].

14.3 Classification by Elements

In general, hydrogen-absorbing alloys consist of a metal component which forms stable hydrides and a component which is not metallic elements of group 3–5 in the periodic table and Pd those form stable hydrides. There are some exceptions to this (for example, ZrV_2), but these compounds always consist of two metals, both of which form stable hydrides. Intermetallic hydrogen absorbing alloys are often categorized by the metals which form stable hydrides, and according to this grouping, the most popular alloys are those based on the rare earth metals, such as LaNi_5 and MmNi_5 , and so on (Mm refers to mischmetal, a mixture of rare earth metals with Ce and La as the main components). Mg based alloys may contain larger amounts of hydrogen but their working temperature is relatively high. Most of the Ti based alloys (such as $\text{Ti}_{1.2}\text{Mn}_{1.8}$) and the Zr based alloys (such as ZrMn_2 , ZrV_2) are Laves phase alloys. In these systems, Ti and Zr normally substitute for one another in all ratios. Therefore, for practical applications, Zr and Ti based alloys are often used (for example, $\text{Ti}_{0.98}\text{Zr}_{0.02}\text{V}_{0.43}\text{Fe}_{0.09}\text{Cr}_{0.05}\text{Mn}_{1.5}$ alloys) [7]. Other metals, such as Ca, V, Hf, Pd and U, also form alloys with the ability to absorb hydrogen.

14.4 Classification by Atomic Ratio and Crystal Structure

Another and more popular way of classification of intermetallic hydrogen absorbing alloys is by atomic ratio and crystal structure. Atomic ratio, in other words the ratio of stable hydride forming elements to non-forming elements is related to hydrogen capacity and crystal structure is related to hydrogen equilibrium pressure. Usually stable hydride forming elements are named the A elements and non-forming elements are the B elements. The ratio of A element and B element is used for classification such as AB_5 , AB_2 , AB , A_2B , AB_3 . In addition to intermetallic alloys, solid solution alloys with the BCC structure also forms interstitial hydrides. In this section, these alloys are described in viewpoints of crystal structure and hydrogenation properties. Table 14.2 lists crystal structure of typical interstitial hydrides.

Table 14.2 Crystal-structure parameters of selected examples of intermetallic compounds and their hydrides

Material	Space group	Lattice parameters (Å)	Atomic-position parameters	Reference
LaNi ₅	<i>P6/mmm</i>	$a = 5.017$ $c = 3.986$	La <i>1a</i>	Furrer et al. [23]
			Ni <i>2e</i>	
			Ni <i>3g</i>	
LaNi ₅ D ₇	<i>P6₃mc</i>	$a = 5.388$ $c = 8.559$	La <i>2a</i>	Thompson et al. [24]
			Ni(1) <i>2b</i> $z = -0.012$	
			Ni(2) <i>2b</i> $z = -0.012$	
			Ni(3) <i>6c</i> $x = 0.5,$ $z = 0.203$	
			D(1) <i>2b</i> $z = 0.348$	
			D(2) <i>2b</i> $z = 0.348$	
			D(3) <i>6c</i> $x = -0.153,$ $z = 0.250$	
			D(4) <i>6c</i> $x = 0.153,$ $z = 0.250$	
LaNi ₄ Al	<i>P6/mmm</i>	$a = 5.064$ $c = 4.070$	La <i>1a</i>	Percheron-Guegan et al. [25]
			Ni(1) <i>2c</i>	
			Ni(2) <i>3g</i>	
			Al <i>3g</i>	
LaNi ₄ AlD _{4.8}	<i>P6/mmm</i>	$a = 5.313$ $c = 4.242$	La <i>1a</i>	Percheron-Guegan et al. [25]
			Ni (1) <i>2c</i>	
			Ni (2) <i>3g</i>	
			Al <i>3g</i>	
			D(1) <i>12n</i> $x = 0.471,$ $z = 0.103$	
			D(2) <i>6m</i> $x = 0.137$	
Ti _{1.2} Mn _{1.8}	<i>P6₃/mmc</i>	$a = 4.862$ $c = 7.969$	Ti + Mn <i>2a</i>	Fruchart et al. [26]
			Ti <i>4f</i> $z = 0.439$	
			Mn <i>6h</i> $x = 0.833$	
Ti _{1.2} Mn _{1.8} D _{3.1}	<i>P6₃/mmc</i>	$a = 5.271$ $c = 8.579$	Ti + Mn <i>2a</i>	Fruchart et al. [26]
			Ti <i>4f</i> $z = 0.442$	
			Mn <i>6h</i> $x = 0.826$	
			D(1) <i>24l</i> $x = 0.040,$ $y = 0.343, z = 0.552$	
			D(2) <i>12k</i> $x = 0.462,$ $z = 0.625$	
			D(3) <i>6h</i> $x = 0.451$	
			D(4) <i>6h</i> $x = 0.202$	

(continued)

Table 14.2 (continued)

Material	Space group	Lattice parameters (Å)	Atomic-position parameters	Reference
ZrMn ₂	<i>P6₃/mmc</i>	<i>a</i> = 5.035 <i>c</i> = 8.276		Didisheim et al. [27]
		<i>a</i> = 5.036 <i>c</i> = 8.271		
ZrMn ₂ D _{3.0}	<i>P6₃/mmc</i>	<i>a</i> = 5.391 <i>c</i> = 8.748	Zr 4 <i>f</i> <i>z</i> = 0.066	Didisheim et al. [27]
			Mn(1) 2 <i>a</i>	
			Mn(2) 6 <i>h</i> <i>x</i> = 0.836	
			D(1) 24 <i>l</i> <i>x</i> = 0.0042, <i>y</i> = 0.325, <i>z</i> = 0.562	
			D(2) 12 <i>k</i> <i>x</i> = 0.456, <i>z</i> = 0.632	
			D(3) 6 <i>h</i> <i>x</i> = 0.463	
			D(4) 6 <i>h</i> <i>x</i> = 0.202	
TiFe	<i>Pm-3m</i>	<i>a</i> = 2.9789	Fe 1 <i>a</i>	Thompson et al. [14]
			Ti 1 <i>b</i>	
TiFeD _{1.9}	<i>Cmmm</i>	<i>a</i> = 7.029 <i>b</i> = 6.233 <i>c</i> = 2.835	Fe 4 <i>i</i> <i>y</i> = 0.2887	Fischer et al. [29]
			Ti 4 <i>h</i> <i>x</i> = 0.223	
			D(1) 4 <i>e</i>	
			D(2) 2 <i>c</i>	
			D(3) 2 <i>a</i>	
Mg ₂ Ni	<i>P6222</i>	<i>a</i> = 5.216 <i>c</i> = 13.20	Ni(1) 3 <i>b</i>	Schefer et al. [30]
			Ni(2) 3 <i>d</i>	
			Mg(1) 6 <i>f</i> <i>z</i> = 0.1149	
			Mg(2) 6 <i>i</i> <i>x</i> = 0.1635	
Mg ₂ NiD ₄	<i>C2/c</i>	<i>a</i> = 14.342 <i>b</i> = 6.403 <i>c</i> = 6.483 <i>β</i> = 113.52°	Ni 8 <i>f</i> <i>x</i> = 0.1194, <i>y</i> = 0.231, <i>z</i> = 0.083	Zolliker et al. [16]
			Mg(1) 8 <i>f</i> <i>x</i> = 0.265, <i>y</i> = 0.483, <i>z</i> = 0.075	
			Mg(2) 4 <i>e</i> <i>y</i> = 0.014	
			Mg(3) 4 <i>e</i> <i>y</i> = 0.513	
			D(1) 8 <i>f</i> <i>x</i> = 0.211, <i>y</i> = 0.300, <i>z</i> = 0.304	
			D(2) 8 <i>f</i> <i>x</i> = 0.136, <i>y</i> = 0.316, <i>z</i> = 0.881	
			D(3) 8 <i>f</i> <i>x</i> = 0.011, <i>y</i> = 0.287, <i>z</i> = 0.054	
			D(4) 8 <i>f</i> <i>x</i> = 0.13 <i>l</i> , <i>y</i> = 0.995, <i>z</i> = 0.082	

14.4.1 AB₅-Type Alloys

AB₅ alloys usually have a CaCu₅ type structure, as shown Fig. 14.3. This type of hydrogen absorbing alloy was firstly found via degradation of the permanent magnet SmCo₅ with hydrogenation. SmCo₅ absorbs hydrogen with a H/metal ratio of about 0.5 [8]. The Philips Company continued the survey to find materials with improved hydrogen absorption. LaNi₅ has the same crystal structure as SmCo₅ but hydrogen capacity is more than double that of SmCo₅ [9].

The crystal structure of LaNi₅ hydrides has been explored extensively. The X-ray diffraction pattern of LaNi₅ is shown in Fig. 14.4. Anisotropic line broadening can be clearly observed. To analyze the crystal structure of powder samples, the Rietveld method is used. However, in the 1980s there was no Rietveld analysis software that could be applied to diffraction patterns with anisotropic line

Fig. 14.3 Crystal structure of LaNi₅ (blue La, purple Ni)

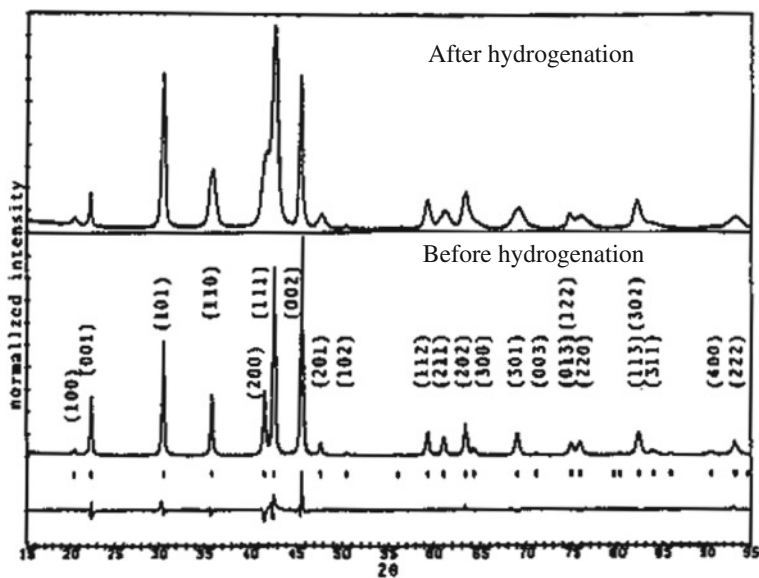
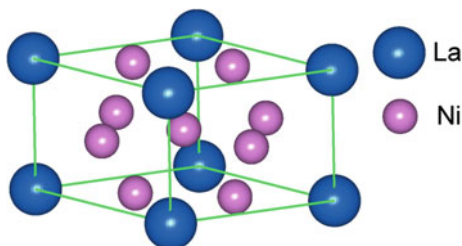
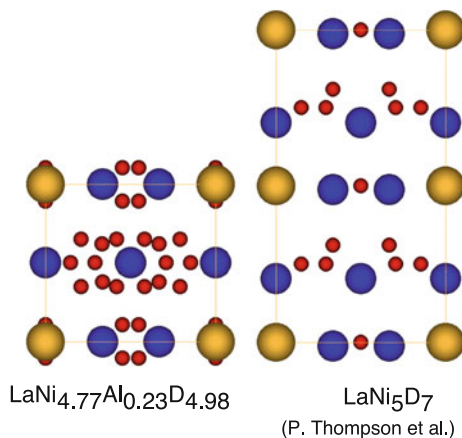


Fig. 14.4 X-ray diffraction patterns of LaNi₅ before and after hydrogenation/dehydrogenation [10] (used with permission from Elsevier, Copyright 1985)

Fig. 14.5 The difference in crystal structure between hydrides of LaNi_5 and $\text{LaNi}_{4.77}\text{Al}_{0.23}$ looking from $[100]$ direction. P. Thompson et al. [24]

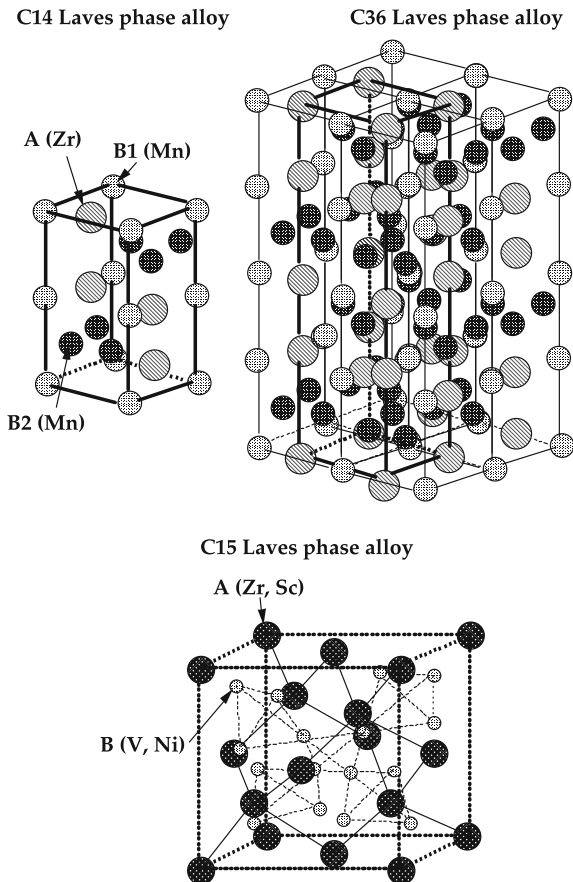


broadening. American and French groups independently analyzed the crystal structure of $\text{LaNi}_5\text{H}_{6-7}$ using modified Rietveld software for neutron powder diffraction patterns. The results are shown in Table 14.2. The structure of $\text{LaNi}_5\text{H}_{6-7}$ is not a simple expansion of the LaNi_5 alloy. The difference is shown in Fig. 14.5. The $z = 0.5$ plane consisting of Ni atoms is shifted along the z direction with increasing hydrogenation. Therefore, the unit cell of the LaNi_5 hydride is double in size in the z direction compared with the LaNi_5 alloy, and the space group changes from $P6/mmm$ to $P6_3mc$. Because the metal sublattice changes its position slightly with every hydrogenation/dehydrogenation cycle, the cycling lifetime of LaNi_5 is not sufficient for practical applications. To solve this issue, usually the Ni site of LaNi_5 is substituted by a third element. Al and Sn are the most popular elements for this purpose. After substitution, $\text{La}(\text{Ni}, \text{Al})_5$ and $\text{La}(\text{Ni}, \text{Sn})_5$ showed different structural changes compared with LaNi_5 upon hydrogenation. These pseudo-binary alloys showed simple expansion and contraction of the metal sublattice, and consequently the cycle life of these alloys is excellent for practical applications.

Akiba et al. [11] found an intermediate hydride phase of LaNi_5H_3 at above 353 K. However, this phase had not been observed in $\text{La}(\text{Ni}, \text{Al})_5$ and $\text{La}(\text{Ni}, \text{Sn})_5$. Recently, using in situ synchrotron radiation a similar intermediate phase reported as LaNi_5H_3 was observed during hydrogenation of $\text{LaNi}_{5-x}\text{Sn}_x$ [12].

14.4.2 AB₂-Type Alloys

Hydrogen absorbing alloys with AB₂ composition usually have the Laves phase structure. The Laves phase is the most common phase in intermetallic alloys with AB₂ molar ratio. The Laves phase that is the closest packing consists of two elements with ideal A atom to B atom radius ratio of 1.225. Because the Laves phase is a layered structure, there are various possible crystal structures. Among

Fig. 14.6 Crystal structures of typical Laves phase alloys

them C14, C15 and C36 Laves phases usually absorb hydrogen. Figure 14.6 shows the crystal structure of these structures.

Compared to AB₅ alloys, the temperature range of hydrogenation/dehydrogenation of Laves phase alloys is much wider. Therefore, the Laves phase is much more favorable for thermal applications such as heat pumps and refrigeration than AB₅ alloys. In addition, the hydrogen capacity of Laves phases is usually larger than that of AB₅. For example, TiMn₂ (the Laves phase) has 1.9 wt% hydrogen capacity, compared with 1.4 wt% for LaNi₅.

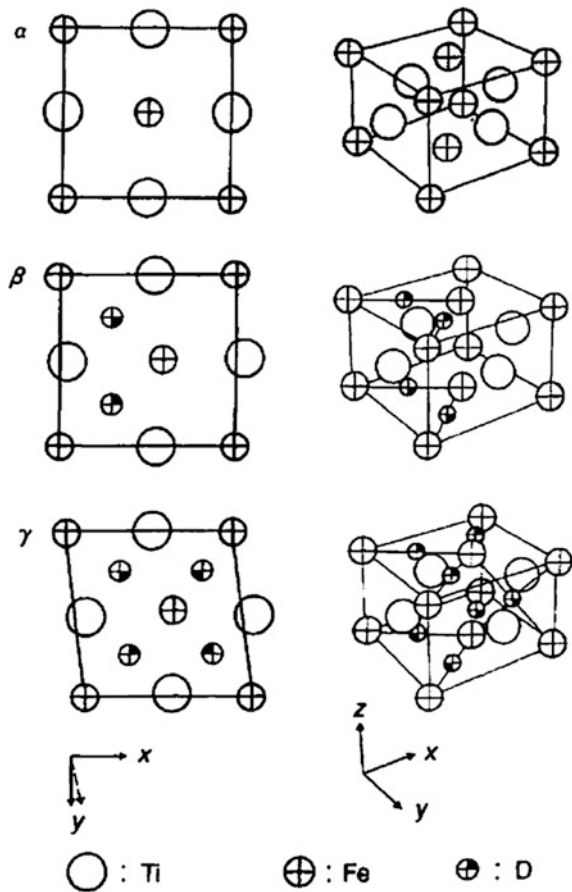
14.4.3 AB-Type Alloys

The most well known AB alloy for hydrogen storage is TiFe. This alloy was discovered in the early 1970s [13]. The hydrogen capacity reaches 1.9 wt% and

absorbs and desorbs hydrogen at ambient temperature, with almost the characteristics as LaNi_5 . Ti and Fe are rich in the earth's crust, and the cost of the alloy is reasonable. However, TiFe needs severe conditions for initial activation, of over 3 MPa hydrogen pressure and 400 °C. Consequently, in the 1980s TiFe was intensively investigated to solve this technical barrier for application.

Hydrogenation of TiFe is two-step reaction. In the first step, the structure of TiFe possessing a CsCl-type lattice deforms to the orthorhombic configuration with occupation of hydrogen in $[\text{Ti}_4\text{Fe}_2]$ octahedral sites with $\text{H}/\text{M} \approx 0.5$. In the second step, the metal sublattice further deforms but the crystal system is still orthorhombic. Figure 14.7 shows the change of crystal structure with hydrogenation. Hydrogen atoms occupy both $[\text{Ti}_4\text{Fe}_2]$ and $[\text{Ti}_2\text{Fe}_4]$ sites after the second step of hydrogenation at $\text{H}/\text{M} \approx 1$ [14].

Fig. 14.7 Structure change of TiFe with hydrogenation



14.4.4 A2B-Type Alloys

The most commonly studied A2B hydrogen-absorbing alloy is probably Mg_2Ni . Mg_2Ni forms Mg_2NiH_4 and the hydrogen capacity is 3.6 wt%. However, the hydrogen absorbing/desorbing temperature is around 300 °C, which is not suitable for most of applications. Considering that Mg alone has 7.6 wt% capacity but a reaction temperature of over 350 °C and sluggish reaction kinetics, Mg_2Ni is a significant improvement in reaction temperature and reaction kinetics for Mg-based alloys. Up to now, even though the working temperature is far above room temperature, Mg_2Ni is the only one successful example of an improvement over Mg as a Mg-based hydrogen absorbing alloy.

Mg_2Ni has a complicated hexagonal structure (C_a , $hP18$, $P6_222$). Mg_2NiH_4 displays a phase transformation at 235 °C. Gavra et al. [15] found the high temperature phase of Mg_2NiH_4 has a simple CaF_2 -type metal sublattice, but that of the low temperature phase has complicated structures that differ by different reports. Zolliker et al. [16] finally discovered that the difference in crystal structure analyses comes from the density of microtwinning (a type of defect) that easily changes with mechanochemical treatment and other factors. The results analyzed by Zolliker et al. are also listed in Table 14.2.

Zolliker et al. synthesized Mg_2FeH_6 and Mg_2CoH_5 but stable alloys of Mg_2Fe and Mg_2Co do not exist [17]. Sometime this type of hydride is called the “hydrogen stabilized phase”. Mg_2FeH_6 and Mg_2CoH_5 are more stable than Mg_2NiH_4 , which means that the hydrogen desorption temperatures of Mg_2FeH_6 and Mg_2CoH_5 are higher than that of Mg_2NiH_4 . It should be noted that these three hydrides obey the 18-electron rule and therefore the hydrogen content reduces with increase in atomic number or 3d electrons.

14.4.5 AB₃-Type Alloys

Kadir et al. [18] first reported hydrogen absorption by AB₃-type alloys but these have a relatively wide range of chemical compositions. As Yamamoto et al. [19] reported, alloys between the compositions of LaNi_2 to LaNi_5 have layered structures consisting of AB₂ and AB₅ units. The alloys reported by Kadir (as well as other AB₃ type alloys) have the structures shown in Fig. 14.8. In 2000, Kohno et al. [20] reported that this type of alloy can be favorably used for Ni-Metal hydride batteries and were later named “superlattice” alloys by SANYO Company.

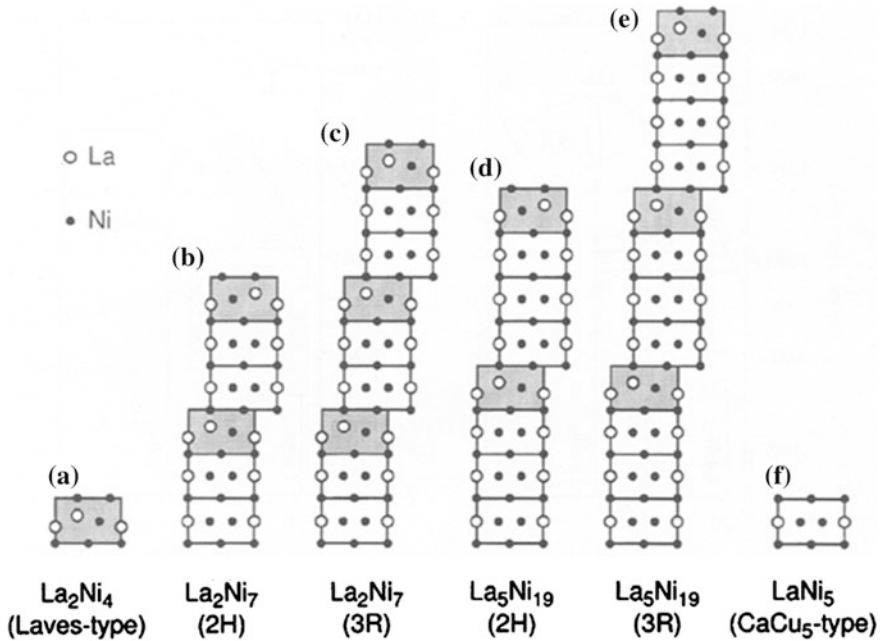


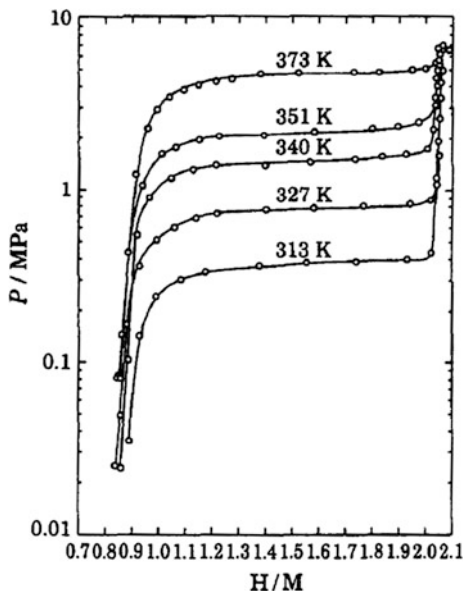
Fig. 14.8 Crystal structures of AB₃-type alloys for hydrogen storage [19] (used with permission from Elsevier, Copyright 1997)

14.4.6 BCC Solid Solutions

Body centered cubic (BCC) metals and alloys intrinsically have large hydrogen capacity because they have more interstitial sites in the lattice than FCC and HCP structures. Akiba and Iba [21] developed new BCC alloys by a new concept, namely Laves-phase-related BCC solid solutions. The hydrogen capacity of this new generation of BCC alloys reached around 3 wt%.

Figure 14.9 shows the pct diagram of vanadium, a typical hydrogen absorbing BCC metal. Vanadium has two plateaus with different equilibrium pressures. Figure 14.9 shows only one plateau between $VH \sim 1$ and $VH \sim 2$. Papathanassopoulos and Wenzl measured both equilibrium pressures [22]. The lower desorption equilibrium pressure was 0.1 Pa at 353 K, while the higher one was at about 10^5 Pa at 263 K. BCC metals and alloys generally show two plateaus in their pct diagrams. Furthermore, their plateau region commonly exhibits a slight gradient. The slope in the plateau region and the pressure difference between the two plateaus is undesirable for practical applications of metal hydrides. Reported disadvantages of BCC metals and alloys as hydrogen absorbers include slow kinetics, difficulties in activation, and the slope of the plateau. Therefore, even though BCC alloys have an intrinsic large hydrogen capacity,

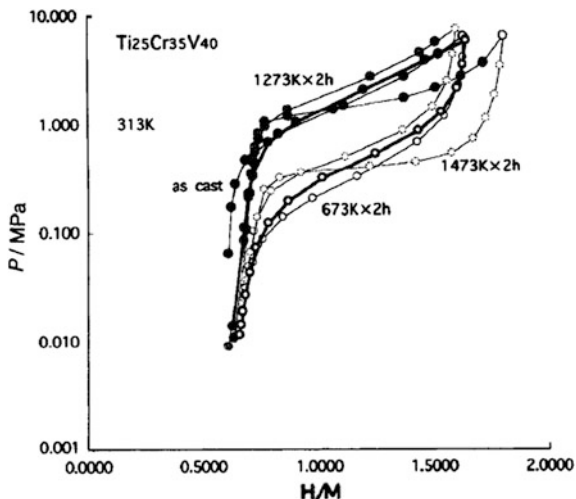
Fig. 14.9 PC-isotherms of the V-H₂ system [22]



studies on their hydrogen absorption properties had been limited before Akiba and Iba reported [21].

In the Ti–Cr–V system, the phase diagram indicates the coexistence of BCC solid solution and Laves phases. In addition, Ti–Cr–V alloys experienced smaller hysteresis than Ti–Mn–V BCC alloys found by Akiba and Iba [21], making them more suitable for application. It was found that the lattice parameter of the BCC phase in the Ti–Cr–V system was in the 0.3020–0.3040 nm range. Alloys with these lattice parameters absorbed hydrogen at ambient pressure and temperature after only one activation cycle. Figure 14.10 shows the effect of heat treatment on

Fig. 14.10 Effect of heat treatment on hydrogen absorption in Ti₂₅Cr₃₅V₄₀ [21]

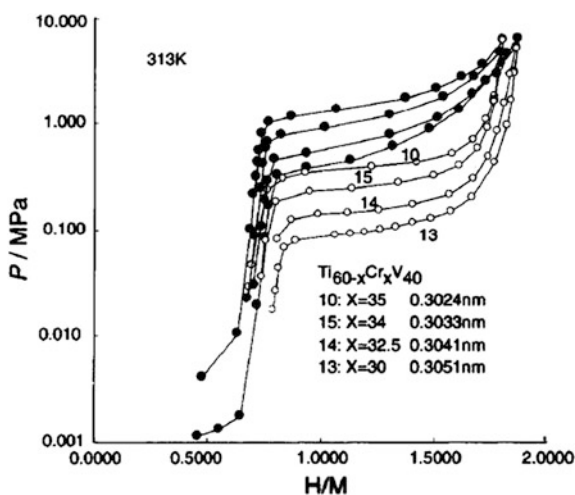


hydrogen absorption in $\text{Ti}_{25}\text{Cr}_{30}\text{V}_{40}$ which does not form the Laves phase after low temperature heat treatment. The as-cast alloy had a sloping plateau but the alloy treated at 1473 K showed much a flatter plateau. It is interesting to note that the hydrogen capacity of the heat-treated alloy reached about 2.2 wt%. From the results of electron probe micro-analysis (EPMA), the heat-treated alloys are well homogenized, but the Ti concentration in the as-cast alloy was observed to vary from place to place (Table 14.3). Figure 14.11 shows the composition dependence of the hydrogen equilibrium pressure of Ti–Cr–V alloys. When the atomic ratio of Ti/Cr varied, the equilibrium pressure was changed dramatically. A difference of 5 at.% in composition of the alloy changed the lattice parameter by 0.025 nm and the equilibrium pressure by one order of magnitude. By comparison with conventional AB5 and AB2 intermetallic hydrogen absorbers, the equilibrium pressure

Table 14.3 Surface analysis for $\text{Ti}_{25}\text{Cr}_{35}\text{V}_{40}$ [21]

Heat treatment	Ti ₂₅	Cr ₃₅	V ₄₀	Position
1437 K, 2 h	21.68	36.24	42.08	Close to α -Ti
	21.87	36.72	41.42	Close to α -Ti
	22.35	37.08	40.57	
	22.35	36.33	41.32	
	22.39	36.54	41.07	
	17.91	36.83	45.26	
	20.50	36.67	45.82	
	21.14	35.81	43.27	
As-cast	21.30	35.66	43.03	
	23.92	37.86	38.22	Close to α -Ti
	25.15	34.93	39.93	Close to α -Ti

Fig. 14.11 PC-isotherms of Ti–Cr–V alloys [21]



of this system is more sensitive to a change in lattice parameter. The slope in plateau comes from the inhomogeneity of the alloy. It means that BCC alloys such as those of the Ti–Cr–V system tend to have a sloping plateau because their equilibrium pressure depends very much on their composition. Therefore, heat treatments to make homogeneous alloys are more important for these BCC alloys than for other intermetallics.

References

1. Fukai Y (1993) The metal-hydrogen system. Springer, Berlin
2. Reilly JJ, Wiswall RH Jr (1968) The reaction of hydrogen with alloys of magnesium and nickel and the formation of Mg_2NiH_4 . *Inorg Chem* 7:2254–2256
3. Reilly JJ, Wiswall RH Jr (1974) Formation and properties of iron titanium hydride. *Inorg Chem* 13:218–222
4. van Vucht JHN, Kuijpers FA, Bruning HCAM (1970) Reversible room-temperature absorption of large quantities of hydrogen by intermetallic compounds. *Philips Res Rep* 25:133–140
5. Shaltiel D, Jacpb I, Davidov D (1977) Hydrogen absorption and desorption properties of AB2 Laves-phase pseudobinary compounds. *J Less-Common Met* 53:117–131
6. Ishido Y, Nishimiya N, Suzuki Y (1977) Preparation and equilibrium study on $ZrMn_2H_x$. *Denki Kagaku* 45:52–54
7. Bernauer O, Töpler J, Noréus D, Hempelmann R, Richter D (1989) Fundamentals and properties of some Ti/Mn based Laves phase hydrides. *Int J Hydrogen Energy* 14:187–200
8. Zijlstra H, Westendorp FF (1969) Influence of hydrogen on the magnetic properties of $SmCo_5$. *Solid State Comm* 7:857–859
9. Kuijpers FA, van Mal HH (1971) Sorption hysteresis in the $LaNi_5$ -H and $SmCo_5$ -H systems. *J Less-Common Met* 23:395–398
10. Nomura K, Uruno H, Ono S, Shinozuka H, Suda S (1985) Effects of lattice strain on the hysteresis of pressure-composition isotherms for the $LaNi_5$ -H₂ system. *J Less-Common Met* 107:221–230
11. Akiba E, Nomura K, Ono S (1987) A new hydride phase of $LaNi_5H_3$. *J Less-Common Met* 129:159–164
12. Machida A, Higuchi K, Katayama Y, Sakaki K, Kim H, Nakamura Y (2015) Observation of transient structural changes on hydrogen absorption process of $LaNi_{4.75}Sn_{0.25}$ by time resolved X-ray diffraction. *J Japan Inst Met Mater* 79:124–130
13. Reilly JJ, Wiswall RH Jr (1974) Formation and properties of iron titanium hydride. *Inorg Chem* 13:218–222
14. Thompson P, Reilly JJ, Hastings JM (1989) The application of the Rietveld method to a highly strained material with microtwins: $TiFeD_{1.9}$. *J Appl Cryst* 22:256–260
15. Gavra Z, Mintz MH, Kimmel G, Hadari Z (1979) Allotropic transitions of magnesium nickel hydride (Mg_2NiH_4). *Inorg Chem* 18:3595–3597
16. Zolliker P, Yvon K, Jorgensen JD, Rotella F (1986) Structural studies of the hydrogen storage material magnesium nickel hydride (Mg_2NiH_4). 2. Monoclinic low-temperature structure. *Inorg Chem* 25:3590–3593
17. Zolliker P, Yvon K, Fischer P, Schefer J (1985) Dimagnesium cobalt(I) pentahydride, Mg_2CoH_5 , containing square-pyramidal pentahydrocobaltate(4–) (CoH_5^{4-}) anions. *Inorg Chem* 24:4177–4180

18. Kadir K, Sakai T, Uehara I (1997) Synthesis and structure determination of a new series of hydrogen storage alloys; RMg_2Ni_9 ($R = \text{La, Ce, Pr, Nd, Sm and Gd}$) built from MgNi_2 Laves-type layers alternating with AB_5 layers. *J Alloys Compd* 257:115–121
19. Yamamoto T, Inui H, Yamaguchi M, Sato K, Fujitani S, Yonezu I, Nishio K (1997) Microstructures and hydrogen absorption/desorption properties of La-Ni alloys in the composition range of La-77.8 ~ 83.2 at.%Ni. *Acta Mater* 45:5213–5221
20. Kohno T, Yoshida H, Kawashima F, Inaba T, Sakai I, Yamamoto M, Kanda M (2000) Hydrogen storage properties of new ternary system alloys: La_2MgNi_9 , $\text{La}_5\text{Mg}_2\text{Ni}_{23}$, $\text{La}_3\text{MgNi}_{14}$. *J Alloys Compd* 311:L5–L7
21. Akiba E, Iba H (1998) Hydrogen absorption by Laves phase related BCC solid solution. *Intermetallics* 6:461–470
22. Papatthanassopoulos K, Wenzl H (1982) Pressure-composition isotherms of hydrogen and deuterium in vanadium films measured with a vibrating quartz microbalance. *J Phys F: Met Phys* 12:1369–1381
23. Furrer A, Fischer P, Halg W, Schlapbach L (1978) In: Andresen A, Maeland AJ (eds) *Hydrides for energy storage*, Pergamon, Oxford, pp.73–82
24. Thompson P, Reilly JJ, Corliss IM, Hastings JM, Hempelmann R (1986) The crystal structure of LaNi_5D_7 . *J Phys F* 16:675–686
25. Percheron-Guegan A, Lartigue C, Achard JC, Germe P, Tasst F (1980) Neutron and X-ray diffraction profile analyses and structure of LaNi_5 , $\text{LaNi}_{5-x}\text{Al}_x$ and $\text{LaNi}_{5-x}\text{Mn}_x$ intermetallics and their hydrides (deuterides). *J Less-Common Met* 74:1–12
26. Fruchart D, Soubeyroux JL, Hempelmann R (1984) Neutron diffraction in $\text{Ti}_{1.2}\text{Mn}_{1.8}$ deuteride: structural and magnetic aspects. *J Less-Common Met* 99:307–319
27. Didisheim JJ, Yvon K, Shaltiel D, Fischer P (1979) The distribution of the deuterium atoms in the deuterated hexagonal laves-phase ZrMn_2D_3 . *Solid State Commun* 31:47–50
28. van Essen RM, Buschow KHJ (1980) Composition and hydrogen absorption of C14 type Zr-Mn compounds. *Mater Res Bull* 15:1149–1155
29. Fischer P, Schefer J, Yvon K, Schlapbach L, Riesterer T (1987) Orthorhombic structure of $\gamma\text{-TiFeD}_{\approx 2}$. *J Less-Common Met* 129:39–45
30. Schefer J, Fischer P, Halg W, Stucki I, Schlapbach L, Didisheim JJ, Yvon K, Andresen AF (1980) New structure results for hydrides and deuterides of the hydrogen storage material Mg_2Ni . *J Less-Common Met* 74:65–73

Chapter 15

Solid Hydrogen Storage Materials: Non-interstitial Hydrides

Hai-Wen Li, Guotao Wu, Teng He and Ping Chen

Abstract This chapter describes syntheses methods, crystal structures, de-/re-hydrogenation properties as well as their improvement from both thermodynamic and kinetic aspects of typical non-interstitial hydrides, such as complex hydrides including alanates, amides and borohydrides, magnesium hydride, aluminum hydride and ammonia borane.

Keywords Non-interstitial hydride · Complex hydride · Synthesis · Thermodynamics · Kinetics · Chemical combination · Electronegativity · Hydrogen storage

Distinct from the interstitial hydrides in which hydrogen occupies the interstitial sites of metal lattices, hydrogen tends to form a covalent or ionic bond with the neighbor atom in the non-interstitial hydrides, such as complex hydrides including alanates, amides and borohydrides, ammonia borane, aluminum hydride and magnesium hydride. In this chapter, we describe the syntheses methods, crystal structures, de-/re-hydrogenation properties as well as material designing strategies of typical non-interstitial hydrides.

H.-W. Li (✉)

International Research Center for Hydrogen Energy, Kyushu University, Fukuoka 819-0395, Japan

e-mail: li.haiwen.305@m.kyushu-u.ac.jp

G. Wu · T. He · P. Chen

Dalian National Laboratory for Clean Energy, Dalian Institute of Chemical Physics, Chinese Academy of Sciences, 457 Zhongshan Road, Dalian 116023, People's Republic of China

e-mail: wgt@dicp.ac.cn

T. He

e-mail: heteng@dicp.ac.cn

P. Chen

e-mail: pchen@dicp.ac.cn

© Springer Japan 2016

K. Sasaki et al. (eds.), *Hydrogen Energy Engineering*,

Green Energy and Technology, DOI 10.1007/978-4-431-56042-5_15

15.1 Alanates

Alanates are generally expressed as $M(\text{AlH}_4)_n$, where n refers to the valence of a metal, M . The significant improvement in the reversible hydrogen storage properties of sodium alanate, NaAlH_4 , by addition of a Ti-based catalyst was reported by Bogdanović et al. in 1997 [1]. This triggered extensive investigations of the non-interstitial hydrides, especially for complex hydrides of alanates, amides and borohydrides.

15.1.1 Synthesis Methods

Lithium and sodium alanates are used widely in organic chemistry as strong reducing agents and are commercially available. $M(\text{AlH}_4)_n$ can be synthesized through the following methods: (1) metathesis reaction between NaAlH_4 and metal chloride MCl_n , followed by the removal of byproduct NaCl [2]; (2) direct reaction between metal hydride MH_n and Al under high temperature and pressure [3]; and (3) ball milling of MH_n and AlH_3 [4].

15.1.2 Crystal Structure

The crystal structure of the most-investigated NaAlH_4 was first determined by Lauher et al. in 1979 using single crystal diffraction [5]. The structure was refined to be tetragonal with space group $I4_1/a$, in which Na atoms are surrounded by eight isolated $[\text{AlH}_4]^-$ in tetrahedral configuration. The location of deuterium atoms in NaAlD_4 (Fig. 15.1) was determined by Hauback et al. [6] through powder neutron diffraction data at 8 and 295 K. The Al-D bond lengths were found to be 1.627 (2) Å and 1.626(2) Å at 8 and 295 K, respectively, which does not change on cooling from 295 to 8 K.

15.1.3 Dehydrogenation and Rehydrogenation Properties

The dehydrogenation of NaAlH_4 occurs via the following three steps accompanied with the formation of an intermediate Na_3AlH_6 [1].

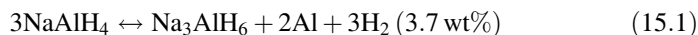
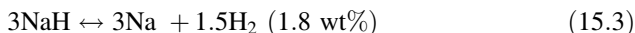
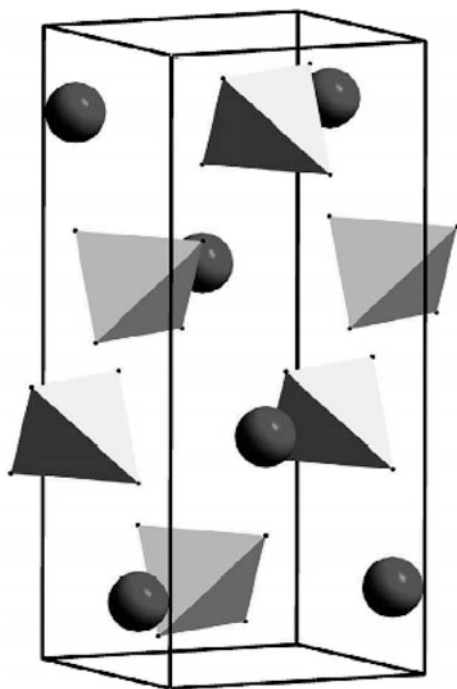


Fig. 15.1 Crystal structure of NaAlH_4 . The $[\text{AlH}_4]^-$ anions are shown as tetrahedral and the Na cations as *black spheres* [6] (used with permission from Elsevier, Copyright 2003)



The first and second step dehydrogenation reactions proceed at 210 and 250 °C, respectively, which release 5.5 wt% of hydrogen in total. Since the dehydrogenation temperature of NaH is above 400 °C, the maximum effective dehydrogenation capacity of NaAlH_4 for onboard storage is considered to be 5.5 wt%. Such multistep dehydrogenation of NaAlH_4 is clearly observed in the PCT curve at 150–199 °C, as shown in Fig. 15.2 [7]. The plateaus on the right hand side are responsible for the first-step dehydrogenation, while those on the left hand side are responsible for the second-step dehydrogenation.

The first and second step dehydrogenation enthalpies, ΔH , estimated from the van't Hoff equation, based on the PCT curves, are 37 and 47 kJ/mol H_2 , respectively. Supposing the entropy change, ΔS , corresponding to the entropy change from molecular hydrogen to dissociated solid hydrogen, we can deduce that the dehydrogenation temperature at 0.1 MPa H_2 for the first and second step would be 33, and 110 °C, respectively [7]. However, due to the sluggish kinetics for both steps, the experimentally observed dehydrogenation temperatures are 210–220 °C for the first step and 250 °C for the second step [8]. Furthermore, the sluggish kinetics becomes more obvious during rehydrogenation completed at 270 °C under 17.5 MPa of hydrogen for 3 h [9]. In fact, NaAlH_4 was not regarded as a reversible hydrogen storage material under practical conditions until Bogdanović et al.

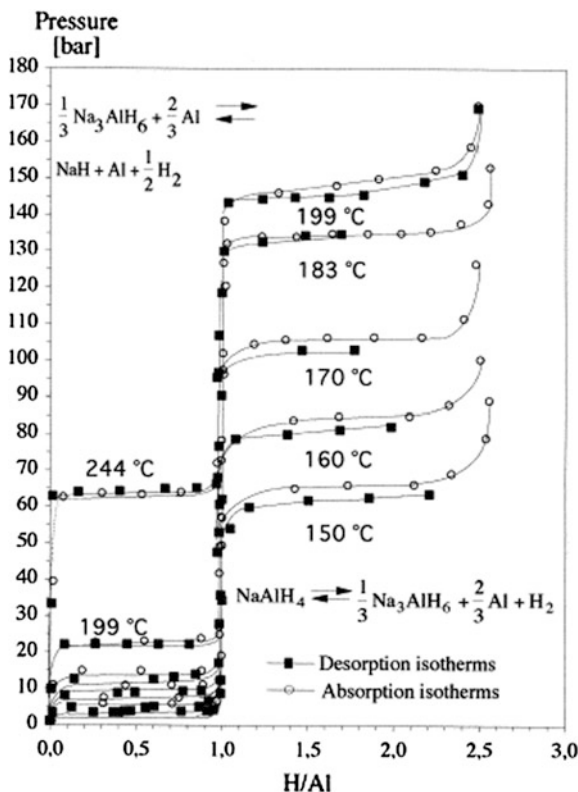
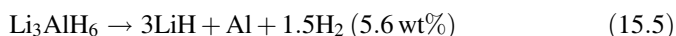


Fig. 15.2 Pressure-concentration-temperature (PCT) curves for NaAlH_4 [7] (used with permission from Elsevier, Copyright 2000)

reported significantly improved de/rehydrogenation of NaAlH_4 with the addition of Ti-based dopants. In this case the dehydrogenation proceeds at 150°C and the rehydrogenation can be achieved at 170°C under 15.2 MPa of hydrogen [1].

Similar to that of NaAlH_4 , decomposition of LiAlH_4 proceeds via multi-step reactions [10]. It decomposes into Li_3AlH_6 accompanied by the release of 5.3 wt% hydrogen, as shown in Eq. 15.4. The exothermic nature results in the first-step dehydrogenation being irreversible. The formed Li_3AlH_6 then decomposes into LiH and Al at $228\text{--}282^\circ\text{C}$, as in Eq. 15.5. This step is an endothermic reaction, the enthalpy change of which was estimated as 25 kJ/mol H_2 .



The rehydrogenation of Li_3AlH_6 to LiAlH_4 was theoretically predicted to require a high hydrogen pressure of 100 MPa at ambient temperature [11]. The

dehydrogenated products of LiH and Al, however, can be rehydrogenated to LiAlH₄ by ball milling under 9.75 MPa H₂ in tetrahydrofuran (THF) solvent, by which the reversible capacity is 4 wt% at 80–110 °C [12].

Unlike for NaAlH₄ and LiAlH₄, the dehydrogenation of Mg(AlH₄)₂ does not experience the intermediate [AlH₆]³⁻ phase, but directly forms MgH₂ and Al via an endothermic reaction with the release of 5.5 wt% of hydrogen. On the other hand, CaAlH₅ forms as the dehydrogenation intermediate of CaAlH₄ [4].

15.1.4 Dopant-Improved De/Rehydrogenation Properties

Stimulated by the significant improvement effect of Ti-based dopants on the de/rehydrogenation properties of NaAlH₄, extensive investigations have been carried out in order to search for effective dopants. ScCl₃, CeCl₃ and PrCl₃ were found to show superior cycling properties and outstanding kinetics than those of TiCl₃, whereas the catalytic effect of transition metal chlorides comprised of V, Zr, Fe, Ni, etc. are not comparable to those of TiCl₃ [13]. Different Ti-based dopants such as TiCl₂, TiF₃, TiBr₄ and TiH₂ indicate similar catalytic effect on the de/rehydrogenation of NaAlH₄ [14].

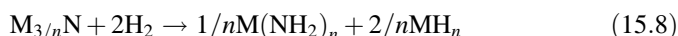
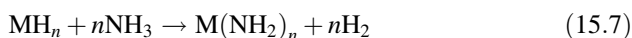
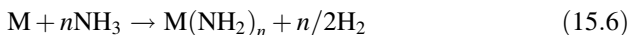
Several catalytic mechanisms, so far, have been proposed for Ti-based dopants in NaAlH₄, including: (a) Ti presents on the surface in the form of amorphous TiAl₃ [15], (b) Vacancy-mediated dehydrogenation [16, 17], (c) Increase in the surface area of Ti species [18], and (d) Hydrogen bonding is the primary bottleneck for hydrogen kinetics [19]. Despite the fact that the catalytic mechanism of Ti is still not established, its catalytic effects (such as decreasing the initial dehydrogenation temperature, improving the dehydrogenation rate, and improving the cyclic abilities) have also been confirmed in Na₂LiAlH₄, LiAlH₄ and Mg(AlH₄)₂, etc. [20]. It is worth emphasizing that catalyzed NaAlH₄ have been applied to bench scale storage tanks designed by General Motors and Sandia National Laboratories [21], as well as Helmholtz Zentrum Geesthacht [22].

15.2 Amides

Amide-hydride composite systems have the general form of M(NH₂)_n-M'H_m, where M or M' refers to a metal, and *n* or *m* is the valence of M or M', respectively. Alkali-metal amides have been successfully synthesized in early 1900s and used as reagents in organic synthesis [23]. The thermal decomposition of amides alone usually gives off ammonia rather than hydrogen. Amides have not been considered as candidates for hydrogen storage until LiNH₂-LiH composite was reported to reversibly store a large amount of hydrogen by Chen et al. in 2002 [24].

15.2.1 Synthesis

Metal amide $M(\text{NH}_2)_n$ can be synthesized via the following three methods: (1) chemical reaction between metal, M, (such as Li, Na, K, Mg or Ca) and NH_3 , which proceeds at 200–300 °C under 0.5–0.8 MPa NH_3 (see Eq. 15.6) [25–30]; (2) chemical reaction between metal hydride MH_n and NH_3 , which can be realized by ball milling under NH_3 at room temperature (see Eq. 15.7) [31–33]; (3) chemical reaction between nitrides such as Li_3N and H_2 at 200–300 °C, as shown in Eq. 15.8 [24, 34–37].



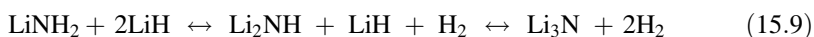
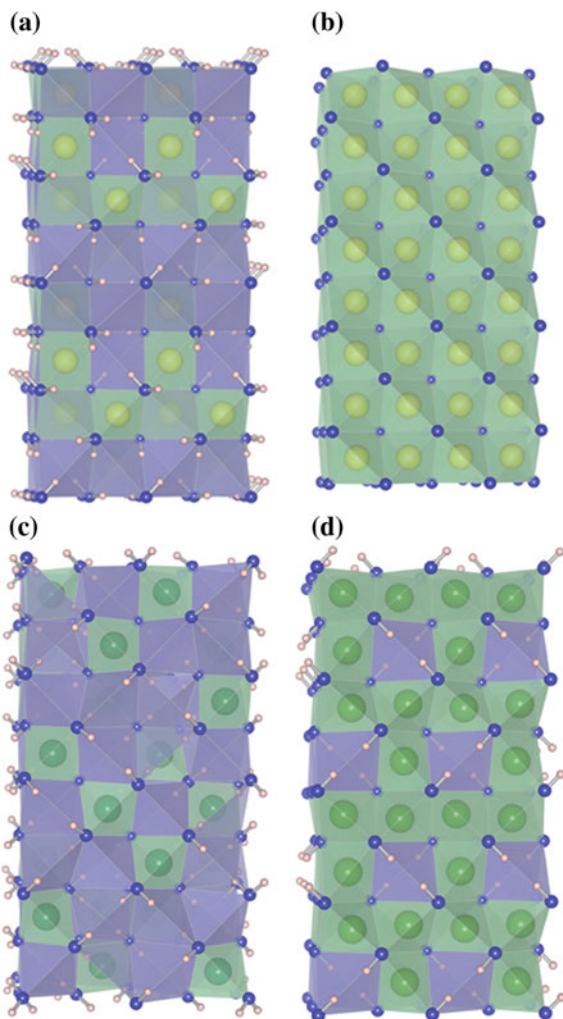
15.2.2 Crystal Structure

Figure 15.3 shows the structures of LiNH_2 , Li_2NH , $\text{Mg}(\text{NH}_2)_2$ and $\text{Li}_2\text{Mg}(\text{NH})_2$. NH_2^- and NH^{2-} anions in the structures of LiNH_2 , Li_2NH , $\text{Mg}(\text{NH}_2)_2$ and $\text{Li}_2\text{Mg}(\text{NH})_2$ are all arranged in a close-packed configuration. The metal cations (Li^+ and/or Mg^{2+}) are tetrahedrally coordinated by the anions. The difference between the amides and imides, from a structural point of view, can be regarded as the different extents of cation occupation in the tetrahedral interstices in the nitrogen framework, i.e., more interstices are occupied by cations in imide (Li_2NH , $\text{Li}_2\text{Mg}(\text{NH})_2$) than that in amide (LiNH_2 , $\text{Mg}(\text{NH}_2)_2$) [38]. The apparent structural similarity implies that the transport and exchange of small cations of Li^+ and H^+ in the N framework of amide/imide phases may play an important role in the reversible de/rehydrogenation of LiNH_2 - LiH and $\text{Mg}(\text{NH}_2)_2$ - 2LiH systems [38].

15.2.3 Chemical Combinations for Tuning Thermodynamics

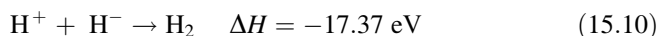
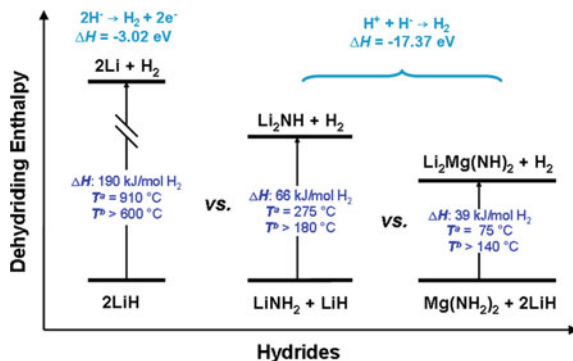
The chemical interactions between LiNH_2 and LiH can be expressed in Eq. 15.9, where LiNH_2 reacts with LiH to release one equiv. H_2 and form Li_2NH . The latter can further react with LiH to release the second equiv. H_2 and form Li_3N . Totally, up to 10.5 wt% H_2 can be de/absorbed in the composite of LiNH_2 - 2LiH [24].

Fig. 15.3 Crystal structures of **a** LiNH_2 ($I-4$, 8 cells), **b** Li_2NH (disorder $Fm-3m$, 16 cells, H not shown), **c** $\text{Mg}(\text{NH}_2)_2$ ($I4_1/abc$), and **d** $\text{Li}_2\text{Mg}(\text{NH}_2)_2$ ($Iba2$, 8 cells). The origin is set at an N atom [38] (used with permission from Cambridge University Press, Copyright 2013)



The dehydrogenation enthalpy of LiNH_2 - LiH is shown in Fig. 15.4. LiH with a formation enthalpy of -91 kJ/mol, dehydrogenates above 600 °C. The decomposition of LiNH_2 requires temperatures higher than 300 °C. However, the LiNH_2 - 2LiH composite starts to release H_2 at 180 °C, which is at a much lower temperature than that of the single counterpart [24]. The electrostatic interaction between protic $\text{H}^{\delta+}$ in LiNH_2 and hydridic $\text{H}^{\delta-}$ in LiH provides high chemical potential for the formation of molecular hydrogen (Eq. 15.10), which is regarded to be responsible for the improved thermodynamics of dehydrogenation [38].

Fig. 15.4 Dehydrogenation enthalpy of LiH, LiNH₂-LiH and Mg(NH₂)₂-2LiH composites. T^a is the calculated temperature corresponding to 0.1 MPa equilibrium H₂. T^b is the dehydrogenation onset temperature observed experimentally in the flow of pure Ar gas [38] (used with permission from Cambridge University Press, Copyright 2013)



Stimulated by this strategy, a series of composites and complexes containing both $\text{H}^{\delta+}$ and $\text{H}^{\delta-}$ components have been investigated in the past decade, as shown in Fig. 15.5. The thermodynamics of dehydrogenation can be tuned by

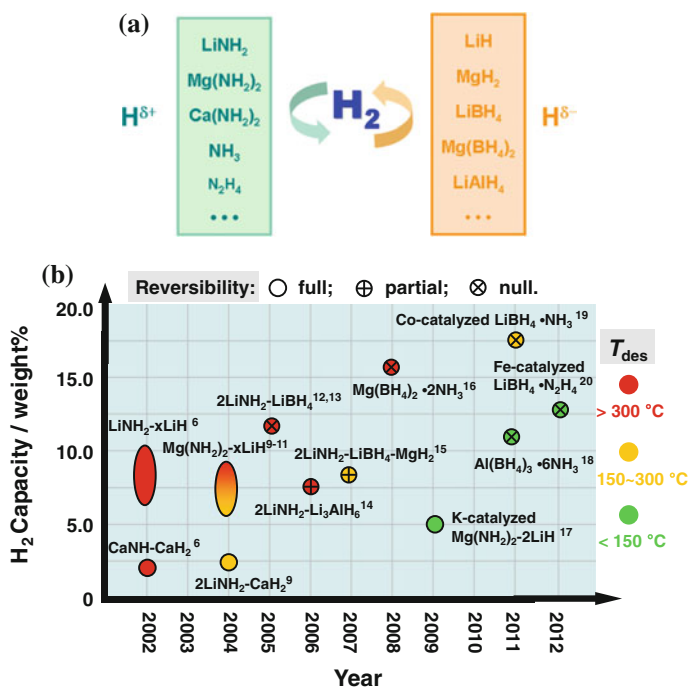


Fig. 15.5 **a** Representative chemicals containing protic/hydridic hydrogen for constructing composites or complexes; **b** the chronosequence of the development of amide-hydride materials [38] (used with permission from Cambridge University Press, Copyright 2013)

compositional change. For example, the dehydrogenation enthalpy of $\text{Li}_2\text{NH-LiH}$ is highly endothermic, whereas that of $2\text{LiNH}_2\text{-LiBH}_4$ becomes exothermic [39]. Among them, the $\text{Mg}(\text{NH}_2)_2\text{-2LiH}$ composite possesses both relatively high reversible hydrogen capacity of 5.6 wt% and suitable thermodynamic properties ($\Delta H_{\text{des}} = 39 \text{ kJ/mol H}_2$, $\Delta S_{\text{des}} = 112 \text{ J/(K mol H}_2)$), see Fig. 15.4). This means that dehydrogenation may occur below $90 \text{ }^\circ\text{C}$ under 0.1 MPa H_2 , which shows considerable promises for onboard hydrogen storage [27]. It is worth noting that the strategy of constructing composites or complexes are not limited to hydrides having protic $\text{H}^{\delta+}$ and hydridic $\text{H}^{\delta-}$, but have been used as a general guide for the designing of other non-amide systems [40, 41].

15.2.4 Strategies for Kinetic Improvement

Generally, the dehydrogenation of amide-hydride composites suffers from the kinetic barriers because of the complexity of the heterogeneous solid state reaction, in which hydrogen dissociation, interface reactions, nucleation/nuclei growth, and/or diffusion processes are regarded to be responsible for the sluggish kinetics. For example, the dehydrogenation temperature of $\text{Mg}(\text{NH}_2)_2\text{-2LiH}$ under 0.1 MPa H_2 was thermodynamically calculated to be below $90 \text{ }^\circ\text{C}$, but a temperature above $180 \text{ }^\circ\text{C}$ is required to achieve an appropriate dehydrogenation rate. Despite of controversial interpretations of the reaction mechanism of the amide-hydride system, strategies of adequate mixing and introducing catalytic additives were proven to be effective to improve the dehydrogenation and rehydrogenation kinetics [38]. Mechanical ball milling can efficiently reduce particle size of reactants and increase the homogeneity of distribution as well as the contact of amide and hydride particles in the resulting mixture, and thus, lead to significantly decreased kinetic barrier of dehydrogenation [42–44]. A notable kinetic enhancement was achieved by adding ca. 3 mol% KH to $\text{Mg}(\text{NH}_2)_2\text{-2LiH}$ system, by which the dehydrogenation onset and peak temperatures were significantly reduced by more than 70 and $50 \text{ }^\circ\text{C}$, respectively [45].

15.3 Borohydrides

Borohydrides ($\text{M}(\text{BH}_4)_n$, where n is the valence of M) contain a metal cation M^{n+} and a $[\text{BH}_4]^-$ polyatomic anion in which one B atom covalently bonds with four hydrogen atoms. Numerous variation of $\text{M}(\text{BH}_4)_n$, such as LiBH_4 , $\text{Mg}(\text{BH}_4)_2$ and $\text{Ca}(\text{BH}_4)_2$, with hydrogen gravimetric density higher than 10 wt%, have been widely regarded as potential candidates for onboard hydrogen storage [38, 46, 47].

15.3.1 Synthesis

Schlesinger and Brown first reported pure alkali-metal borohydride in 1940. They synthesized LiBH_4 by reaction between ethyl lithium and B_2H_6 [48]. Alternatively, MBH_4 can be produced with high yields by the direct reaction of the corresponding metal hydrides with B_2H_6 in ethereal solvents or by ball milling [49, 50]. A significant number of metal borohydrides have been produced through the following metathesis reaction. The byproduct $\text{M}'\text{Cl}$ can be removed using organic solvents like diethyl ether or THF [51–56].

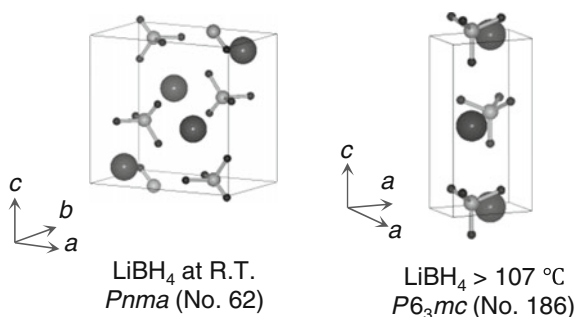


The direct synthesis of borohydride can also be accomplished by the reaction of an alkali or alkaline earth hydride with an amine borane complex under argon atmosphere [57].

15.3.2 Crystal Structure

The first-investigated borohydride for hydrogen storage, LiBH_4 , is taken as an example. The crystal structure of LiBH_4 was originally determined to be $Pcmm$ at room temperature [58]. However, recent synchrotron X-ray powder diffraction measurements indicate that LiBH_4 crystallize in the orthorhombic $Pnma$ at room temperature [59] (see Fig. 15.6). The tetrahedral $[\text{BH}_4]^-$ anions are aligned along two orthogonal directions and are strongly distorted with respect to bond lengths and bond angles. The room temperature LiBH_4 transforms into a high temperature phase with hexagonal $P6_3mc$ at approximately 108 °C (see Fig. 15.6). The tetrahedral $[\text{BH}_4]^-$ anions align along c , become more symmetric [59, 60]. However, the $P6_3mc$ was suggested to be unstable at a temperature higher than 0 K according to the calculations of the free energy at finite temperatures [61]. The detail of the high temperature structure of LiBH_4 is still under discussion.

Fig. 15.6 Low- and high-temperature crystal structures of LiBH_4 [59]. Large, medium, and small spheres denote boron, lithium, and hydrogen, respectively



15.3.3 Dehydrogenation and Rehydrogenation Properties

The extensively studied $\text{Mg}(\text{BH}_4)_2$ is taken as an example. $\text{Mg}(\text{BH}_4)_2$ releases approximately 14.9 wt% of hydrogen through several endothermic events accompanied with the formation of intermediate compounds in a temperature range of 230–530 °C (see Fig. 15.7). One of the intermediate compounds has been theoretically predicted and experimentally confirmed as being $\text{MgB}_{12}\text{H}_{12}$, comprised of $[\text{B}_{12}\text{H}_{12}]^{2-}$ with an icosahedral boron cage [62–64]. Formation of $[\text{B}_{12}\text{H}_{12}]^{2-}$ was suggested as a sequential BH condensation pathway involving a build-up of the increasing higher B_nH_{n+x} species [65, 66].

The complicated dehydrogenation pathway results in several common and important issues for most variations of $\text{M}(\text{BH}_4)_n$: (1) de-/rehydrogenation temperature higher than 230 °C and sluggish reaction rates; (2) accumulation of intermediate compounds containing $[\text{B}_{12}\text{H}_{12}]^{2-}$ that degrades the reversibility; (3) difficulties in obtaining exact enthalpy for each reaction step and identifying the rate-determining step; and (4) formation of different B_nH_{n+x} species that may affect overall entropy [38].

Reversibility is of great importance for onboard storage. Therefore, significant efforts have been made in this area during the past decade. Reversibility of LiBH_4 cycling could be achieved at very high temperatures of approximately 600 °C, which makes it impractical for use with polymer electrolyte fuel cell applications [67]. Under 40 MPa H_2 , $\text{Mg}(\text{BH}_4)_2$ is produced even at a relatively low temperature of 200 °C, and the amount increases with temperature up to 400 °C, leading to the increased rehydrogenation content and a maximum (7.6 wt%, equivalent to 51 % of $\text{Mg}(\text{BH}_4)_2$) at 400 °C. Under the same conditions, more than 90 % rehydrogenation is confirmed through the formation of $\alpha\text{-Ca}(\text{BH}_4)_2$. Comparison of the rehydrogenation properties of LiBH_4 , $\text{Mg}(\text{BH}_4)_2$ and $\text{Ca}(\text{BH}_4)_2$, suggests that control of

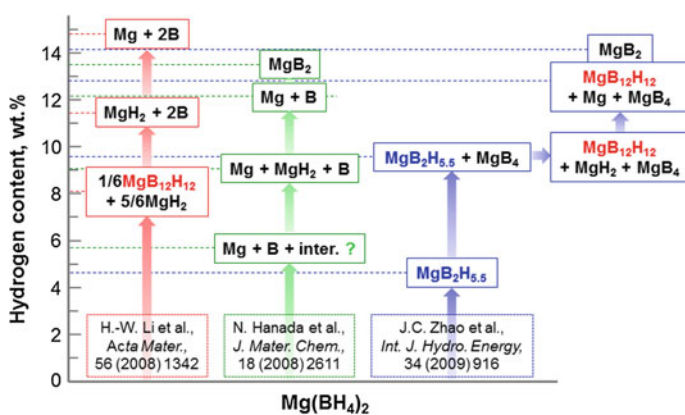
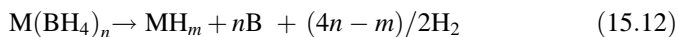


Fig. 15.7 Summary of the multi-step dehydrogenation processes of $\text{Mg}(\text{BH}_4)_2$. The *question mark* indicates the possible formation of an intermediate compound during dehydrogenation [46]

dehydrogenation products would be an important approach to improve the reversibility of metal borohydrides [68].

15.3.4 The Role of Electronegativity in Tuning Enthalpy

The Pauling electronegativity, χ_P , of M may be adopted as an indicator to roughly estimate and tailor the formation enthalpy, ΔH_{boro} , of $M(\text{BH}_4)_n$. Theoretical prediction suggests a good linear relationship between the ΔH_{boro} of $M(\text{BH}_4)_n$ and the χ_P of M (i.e., the larger χ_P of M suggests a smaller ΔH_{boro} of $M(\text{BH}_4)_n$, see Fig. 15.8). Experimental results indicate that the dehydrogenation temperature, T_d , of $M(\text{BH}_4)_n$ decreases with increasing χ_P of M (see Fig. 15.8). Assuming that borohydrides (apart from $\text{Zn}(\text{BH}_4)_2$) decompose into elemental hydrides MH_m in the first step of dehydrogenation as follows,



The dehydrogenation enthalpy, ΔH_{des} , can be estimated from the predicted ΔH_{boro} and the experimental data ΔH_{hyd} of MH_m . The good correlation between ΔH_{des} and T_d (see Fig. 15.8) supports the theoretical prediction [69]. It should be noted that T_d obtained from temperature programmed desorption spectra, including both thermodynamic and kinetic parameters, and the chemical state of dehydrogenated products will largely affect the ΔH_{des} [38].

Inspired by this interesting finding, mixing two kinds of metals having different electronegativities to produce bimetallic borohydrides $\text{MM}'(\text{BH}_4)_n$, has been proposed as an approach to tune thermodynamic stability [70]. Guided by this approach, several novel $\text{MM}'(\text{BH}_4)_n$ have been synthesized, including $\text{LiK}(\text{BH}_4)_2$,

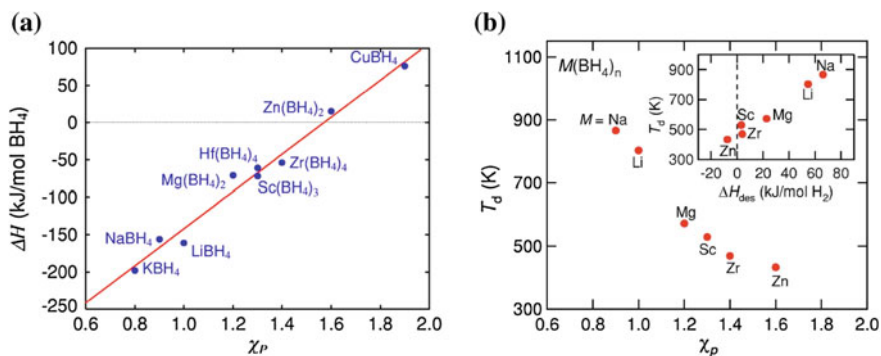
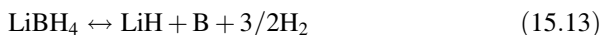


Fig. 15.8 **a** Relation between the formation enthalpy, ΔH_{boro} , of $M(\text{BH}_4)_n$ and the Pauling electronegativity, χ_P , of M. The zero-point energy contributions to ΔH_{boro} are approximately taken into consideration. **b** Dehydrogenation temperature T_d of $M(\text{BH}_4)_n$ as a function of χ_P of M. The inset shows the relation between T_d and estimated ΔH_{des} of dehydrogenation of Eq. 15.12 [69] (used with permission from the American Physical Society, Copyright 2006)

$\text{LiSc}(\text{BH}_4)_4$, $\text{Mg}_{1-x}\text{Mn}_x(\text{BH}_4)_2$, and $\text{NaY}(\text{BH}_4)\text{Cl}_2$. Most $\text{MM}'(\text{BH}_4)_n$ exhibit moderate T_d between those of $\text{M}(\text{BH}_4)_n$ and $\text{M}'(\text{BH}_4)_n$, except some of which form a large $[\text{M}'(\text{BH}_4)_n]^{m-}$ anion unit such as $[\text{Sc}(\text{BH}_4)_4]^-$ [38, 47].

15.3.5 Reactive Hydride Composites to Tune Enthalpy

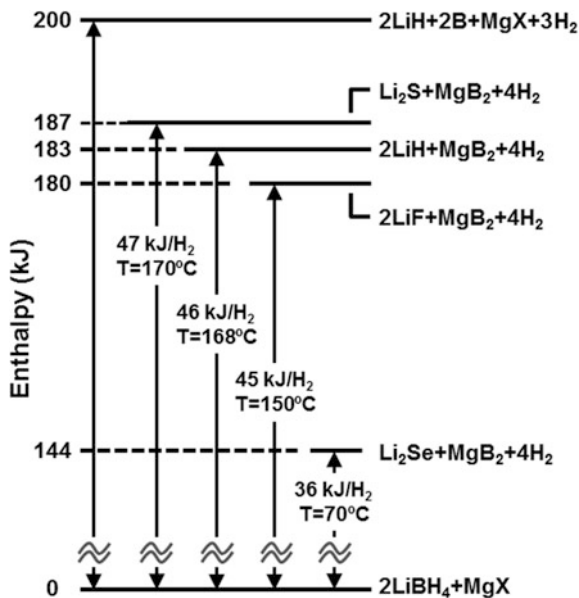
Combining $\text{M}(\text{BH}_4)_n$ with elements, metal hydrides or complex hydrides (also called reactive hydride composites), like in the LiNH_2/LiH system, is another approach to reduce ΔH_{des} through the formation of more stable dehydrogenated products. Figure 15.9 shows a typical example of the $2\text{LiBH}_4\text{-MgX}$ system for this approach (X indicates halogen) [71]. Let us take the extensively studied $2\text{LiBH}_4\text{-MgH}_2$ system as an example. Pure LiBH_4 releases approximately 13.8 wt% of hydrogen according to the following reaction,



ΔH_{des} for pure LiBH_4 , predicted to be 67 kJ/mol H_2 , can be considerably reduced to 46 kJ/mol H_2 by the formation of MgB_2 according to the following reaction [72],



Fig. 15.9 Enthalpy diagram for destabilization of LiBH_4 by the MgX (X indicates halogen) system [71] (used with permission from Elsevier, Copyright 2007)



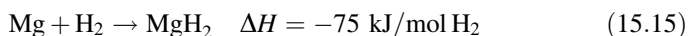
The combination with MgH_2 not only decreases T_d of LiBH_4 , but also kinetically improves rehydrogenation, thus significantly improving the reversibility. Formation of MgB_2 during dehydrogenation is crucial to maintain good reversibility. However, this largely depends on the hydrogen pressure. Hydrogen pressure at least higher than 0.3 MPa is required to suppress the formation of $\text{Li}_2\text{B}_{12}\text{H}_{12}$ from the individual decomposition of LiBH_4 [73–75]. In situ powder neutron and X-ray diffraction studies of the dehydrogenation pathway at low partial pressures of hydrogen suggest that Li-rich samples form a passivating hydride layer, hindering further hydrogenation [76]. Similar hydrogen pressure dependence phenomena of the formation of borides such as YB_4 and CaB_6 are also observed in other systems such as $\text{LiBH}_4\text{-YH}_3$ [77] and $\text{LiBH}_4\text{-CaH}_2$ [78].

15.4 Magnesium Hydride

Magnesium, the ninth most abundant element in the universe and the eighth most abundant element in the earth's crust, can absorb 7.6 wt% of hydrogen to form magnesium hydride, MgH_2 . This has been extensively investigated as a potential hydrogen storage material.

15.4.1 Synthesis

MgH_2 can be synthesized by hydrogenation of magnesium according to Eq. 15.15, which is thermodynamically favorable.



In reality, an oxide layer that covers the surface of magnesium, and the poor diffusion of hydrogen in MgH_2 kinetically inhibits this reaction. For example, the hydrogen diffusion coefficient in MgH_2 decreases from 10^{-18} to 10^{-24} m^2/s when the temperature is reduced from 300 to 100 °C [79]. Therefore, the production of MgH_2 from Mg requires high temperature (ca. 400 °C) and high pressure (above 3 MPa).

MgH_2 can be prepared by a homogenous catalysis process proposed by Bogdanović in 1984 [80]. First, metallic magnesium is dissolved in anthracene to form Mg-anthracene solution. Then, the hydrogenation of the Mg-anthracene solution produces MgH_2 with CrCl_3 or TiCl_4 catalyst.

Recently, an industrial production process of MgH_2 (purity > 93 %) was proposed by direct hydrogenation of Mg powders and tablets compressed with mechanically ground Mg ribbons. The pressure applied to fabricate Mg tablets certainly induces plastic deformation inside Mg ribbons and resultant lattice defects, which may be responsible for the improved activity of hydrogenation [81].

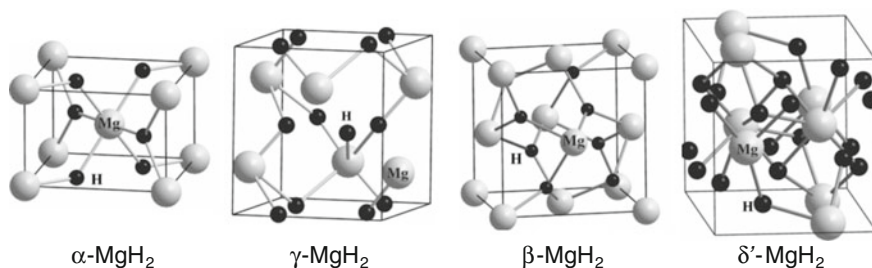


Fig. 15.10 Crystal structures of α , β , γ and δ' -MgH₂ [82] (used with permission from the American Physical Society, Copyright 2006)

15.4.2 Crystal Structure

MgH₂ has four crystal structures depending on the pressure (see Fig. 15.10). At ambient pressure α -MgH₂ takes a TiO₂-rutile-type structure. Under high pressure α -MgH₂ undergoes polymorphic transformations to form γ -MgH₂ with α -PbO₂ type orthorhombic structure, β -MgH₂ with a PdF₂-type cubic structure, and δ' -MgH₂ with AuSn₂-type orthorhombic structure, respectively [82].

15.4.3 Tuning Thermodynamics

The bonding nature of MgH₂ was found to be a mixture of covalent and ionic bonds, in which hydrogen deforms widespread charge density. As a result, MgH₂ can be expressed as Mg^{1.91+}H^{0.26-} [83]. The dehydrogenation enthalpy of MgH₂ to form Mg is 75 kJ/mol H₂, the occurrence of which requires a temperature above 300–400 °C that is much higher than the operation temperature of polymer electrolyte fuel cell (PEFC).

To date, several approaches have been proposed to destabilize the dehydrogenation of MgH₂, such as: (a) forming an alloy with a hydride non-forming transition metal like Ni [84]; (b) nano-engineering to reduce the crystal grain size <2 nm as predicted by theoretical calculation [85]; and (c) changing the reaction pathway by making composite like the typical MgH₂/Si system [40].

15.4.4 Improved Kinetics

A number of approaches including nanostructuring, and using metal additives have been used to accelerate the dehydrogenation/rehydrogenation kinetics. A typical methodology to produce nanostructured materials is ball milling, which in the case of the MgH₂ system can break the oxide layers on the surface of Mg, introduces a

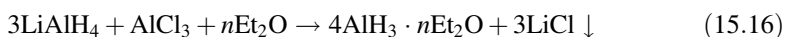
large number of defects, and decreases the diffusion length of hydrogen, thereby improving the reaction kinetics [86]. The improvement effect on kinetics is also confirmed in the nanoconfined MgH_2 inside porous scaffold materials. The smaller pores mediate faster dehydrogenation rate, possibly due to a size reduction of the confined hydride [87]. Furthermore, a large amount of additives including transition metals, metal oxides, and carbon materials, have been proven to be effective catalysts for dehydrogenation/rehydrogenation of MgH_2 . To date, Nb_2O_5 , is well known to show the best catalytic performance compared to other additives [88]. The fastest kinetics are obtained using 0.5 mol% Nb_2O_5 . At 300 °C, hydrogenation and dehydrogenation of 7 wt% of hydrogen are facilitated in 60 and 90 s, respectively. At 250 °C, more than 6 wt% is hydrogenated in 60 s and dehydrogenated again in 500 s. Hydrogenation kinetics are nearly independent of the catalyst content, even 0.05 mol% Nb_2O_5 yield the full hydrogen absorption of 7 wt% within 60 s [89].

15.5 Aluminum Hydride

Aluminum hydride (or alane) is an inorganic compound with the molecular formula AlH_3 . It is a colorless, metastable, crystalline solid having a density of 1.477 g/cm^3 at room temperature. Aluminum hydride has a gravimetric hydrogen capacity of 10.0 wt% H_2 and volumetric capacity of $148 \text{ kg H}_2/\text{m}^3$. It has been used as a solid rocket propellant, an explosive, a reducing agent, and a hydrogen source for automotive applications.

15.5.1 Synthesis

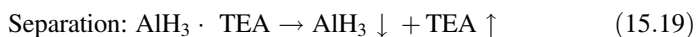
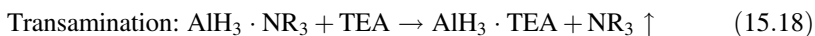
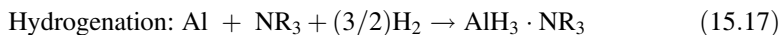
A convenient synthesis of AlH_3 diethyletherate was developed by Finholt et al. in 1947 [90], by means of the reaction between LiAlH_4 (or LiH) and AlCl_3 in diethyl ether (Et_2O) (Eq. 15.16).



The non-solvated form of AlH_3 was obtained in 1955 [91] by filtering the etherated AlH_3 solution into an inert liquid (e.g., pentane), followed by drying under high vacuum for at least 12 h. A summary about the synthesis of non-solvated AlH_3 developed by Brower et al. of Dow Chemical Company was published in 1976 [92]. Their method was similar to that above. They used excess LiAlH_4 and LiBH_4 in the etherated alane solution and desolvated in a mixture of ether and benzene, which reduced the time and temperature of desolvation. Finally, excess LiAlH_4 and LiBH_4 were removed by a wash with diethyl ether. It should be noted that AlH_3 (pure or etherated) could be synthesized through the reaction

between binary hydrides or alanates of 1st and 2nd groups with a Brønsted–Lewis acid (e.g., AlCl_3) [92–95]. Brower et al. [92] successfully prepared seven non-solvated AlH_3 polymorphs, which were named α - AlH_3 (PDF: 23-761), α' - AlH_3 (PDF: 34-1436), β - AlH_3 (PDF: 38-756), γ - AlH_3 (PDF: 38-757), δ - AlH_3 (PDF: 38-758), ε - AlH_3 (PDF: 38-759), and θ - AlH_3 (PDF: 38-760) and denoted in the database of the International Center for Diffraction Data (ICDD).

The high-pressure synthesis of α - AlH_3 from Al powder (or Al foil) and H_2 succeeded at H_2 pressures up to 9 GPa and temperatures up to 600 °C. The cyclic formation and decomposition of the hydride resulted in lowering of the hydrogenation conditions down to 4.9 GPa and 330 °C [96]. Electrochemical hydrogenation or low-pressure hydrogenation of aluminum to form AlH_3 amine complex provide promising low energy alternatives to the high-pressure route. Classen et al. [97] have patented an electrochemical hydrogenation approach using aluminum in the electrochemical cell containing THF as the solvent, sodium aluminum hydride as the electrolyte, an aluminum anode, and an iron (Fe) wire submerged in mercury (Hg) as the cathode. Two separate reaction mechanisms could produce AlH_3 at the aluminum electrode: (1) For insoluble anodes, $\text{AlH}_4^- - e^- \rightarrow \text{AlH}_3 \cdot n\text{THF} + 1/2\text{H}_2$; (2) For soluble anodes, $3\text{AlH}_4^- + \text{Al} - 3e^- \rightarrow 4\text{AlH}_3 \cdot n\text{THF}$. Zidan et al. [98] have proved the feasibility of electrochemical hydrogenation of aluminum using a cell similar to that of Classen et al. with an Al anode, platinum cathode and an electrolyte of NaAlH_4 in THF. The crystallization and separation of aluminum hydride from THF was achieved by exchanging the THF ligand with an amine group (triethylamine, TEA) and heating the liquid ($\text{AlH}_3 \cdot \text{TEA}$) under vacuum [99]. The alane amine complex was reported as AlH_3 solid by mistake in 1942 [100]. Normally AlH_3 solid can be obtained by three step reactions [101, 102], which were shown below:



15.5.2 Crystal Structure

As the most stable phase, α - AlH_3 crystallizes in the trigonal space group, $R3c$, with a hexagonal unit cell and lattice parameters $a = 4.449 \text{ \AA}$ and $c = 11.804 \text{ \AA}$ [103]. The structure consists of corner connected $[\text{AlH}_6]$ octahedra in a more dense ReO_3 -type arrangement (see Fig. 15.11). The geometry of the Al atoms in α - AlH_3 is equivalent to Al metal, and the Al atom distances increase from 2.86 Å in Al metal to 3.24 Å in α - AlH_3 [103, 104]. The crystal structure of α' - AlH_3 was determined using X-ray and neutron diffraction techniques in 2006 [104]. It takes the form of a β - AlF_3 orthorhombic structure (space group, $Cmcm$) with cell dimensions $a = 6.470 \text{ \AA}$, $b = 11.117 \text{ \AA}$ and

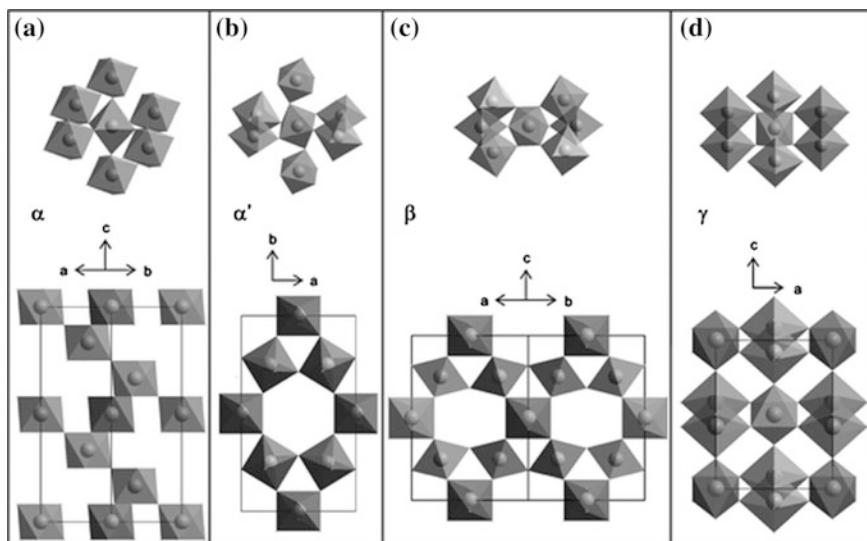


Fig. 15.11 The first coordination sphere for the octahedral units (*upper part*) and the unit cell (*lower part*) of the **a** α -, **b** α' -, **c** β - and **d** γ -phases of AlH_3 [108] (used with permission from the Royal Society of Chemistry, Copyright 2008)

$c = 6.562(2)$ Å. The structure has two Al and four H crystallographic sites in the unit cell, which also consists of corner connected $[\text{AlH}_6]$ octahedra, but forms an open 3D network with hexagonal 3.9 Å channels [104]. Furthermore, the crystal structure of β - AlH_3 was determined in 2007 [105]. It has a pyrochlore-type crystal structure (space group $Fd\bar{3}m$) with cell dimension $a = 9.004$ Å. The structure has one Al and one H crystallographic site in the unit cell, and has the corner connected $[\text{AlH}_6]$ octahedral arrangement and 3.9 Å channels similar to α' - AlH_3 . The crystal structure of γ - AlH_3 was also determined in 2007 [106, 107], which crystallizes in an orthorhombic unit cell (space group, $Pnmm$) with cell dimensions $a = 5.3806(1)$ Å, $b = 7.3555(2)$ Å, $c = 5.77509(5)$ Å [106]. It contains two types of $[\text{AlH}_6]$ octahedra. One is the normal corner-sharing octahedra with each H atom bridging two octahedra, the other is the edge-sharing octahedra. The edge sharing of the $[\text{AlH}_6]$ octahedra results in the formation of the double-bridge bonds, $\text{Al}-2\text{H}-\text{Al}$ [106, 107]. Among these four polymorphs, α - AlH_3 has the highest density while β - AlH_3 has the lowest one.

15.5.3 Thermodynamics and Kinetics

α - AlH_3 decomposes to Al and H_2 in a single endothermic reaction, $\alpha\text{-AlH}_3 \rightarrow \text{Al} + (3/2)\text{H}_2$. At 25 °C, the standard enthalpy of formation is -11.4 ± 0.8 kJ/mol, absolute entropy is 30.0 ± 0.4 kJ/(mol K) and Gibb's free energy of formation is 46.4 ± 1.0 kJ/mol, which are based on experimentally

determined (calorimetry) heat of decomposition of α -AlH₃ [108, 109]. The specific heat capacity of α -AlH₃ is 40.2 J/(mol K), and its non-Debye behavior suggests that the heat capacity and standard thermodynamic properties to higher temperatures will be unreliable [110]. α' -AlH₃, β -AlH₃, and γ -AlH₃ are less stable than α -AlH₃ and undergo an exothermic transition to α -AlH₃ at temperatures higher than 100 °C. The energies of phase transitions are -1.65 kJ/mol, -1.5 kJ/mol and -2.8 kJ/mol, respectively [108, 109].

Since AlH₃ is thermodynamically metastable at ambient conditions, the pressure-temperature diagram of hydrogen-aluminum system was investigated for a pressure range of 0–10 GPa and a temperature range of 27–800 °C where stabilized α -AlH₃ was used as starting materials [111–113]. α -AlH₃ typically decomposed near the equilibrium line [95].

Thermal and photolytic decomposition of α -AlH₃ with particle sizes in the range of 50–100 μ m (Dow Chemical Company) were originally performed by Herley et al. [114]. Volumetric measurements under isothermal conditions showed thermal decomposition curves exhibited three successive decomposition stages, consisting of an induction period, an acceleratory period and a decay period. The induction period data could be described by a cubic expression representing rapid nucleation. The data for the subsequent acceleratory and decay stages could be accurately described by Avrami-Erofeyev (A-E) kinetics representing growth of Al metal in two and three dimensions. The activation energy for the induction period was 103.8 kJ/mol. The activation energy for the acceleratory and decay period was approximately 157 kJ/mol. Thermal stability of aluminum hydride and its decomposition activation energy were both highly dependent upon the synthesis conditions and sample purity.

More recently Graetz et al. [115, 116] investigated thermal decomposition of α -AlH₃, β -AlH₃, and γ -AlH₃, which consisted of small particles (100–200 nm) and had a relatively oxide-free surface. Temperature-dependent rate constants were determined by isothermal volumetric measurements between 60 and 140 °C. They applied the same A-E equation to decomposition curves, and got good least-squares fits in the fractional decomposition range of 0.04–0.95, except for the γ phase. They also suggested that the decomposition kinetics of aluminum hydride were controlled by nucleation and growth in two and three dimensions. The activation energies for the three polymorphs were 102, 92 and 79 kJ/mol, respectively [116]. β -AlH₃ and γ -AlH₃ transformed to α -AlH₃ rapidly prior to decomposition at 100 °C and above. Phase transitions were exothermic, which supplied an energetic boost to the decomposition of β -AlH₃ and γ -AlH₃. γ -AlH₃ may decomposed directly and/or transformed to α -AlH₃ at temperatures below 100 °C [115, 116]. In situ synchrotron XRD investigation of the thermal decomposition of γ -AlH₃ heated at 2 °C/min in vacuum showed that around 60 % of γ -AlH₃ released hydrogen in the direct decomposition, while 40 % of γ -AlH₃ transformed into α -AlH₃ and then decomposed [117]. For low temperature fuel cell applications, destabilizing aluminum hydride was also investigated, and some solutions were proposed by either particle size reduction using ball milling, or utilizing additives such as alkali metal hydride and transition metals. Sandrock et al. [118, 119] showed the particle size of

α -AlH₃ reduced effectively from 100 μm (as-received) to 1 or 0.3 μm after ball milling for 1 or 3 h, which lowered the desorption temperatures and increased the desorption rates of α -AlH₃. The addition of alkali-metal hydrides such as LiH also gave very positive effects. The decomposition temperature of 20 mol% LiH doped sample reduced 40–50 °C compared with the pristine 1 h ball milling sample. The decomposition activation energies for 20 % LiH doped sample was 91.3 kJ/mol. 20 mol% LiH and 5 mol% TiCl₃ doped sample released 1 wt% hydrogen during ball milling. So Ti powder or TiO₂ were used to catalyze the decomposition of α -AlH₃. The decomposition activation energy of 2 wt% Ti powder or TiO₂ doped samples changed to 147 or 68 kJ/mol [95]. Orimo et al. [120] also demonstrated the intrinsic and mechanically modified thermal stabilities of α -AlH₃, β -AlH₃ and γ -AlH₃. Dehydrogenation of α -AlH₃, β -AlH₃ and γ -AlH₃ was observed during mechanical milling. Dehydrogenation of mechanically modified α -AlH₃ and γ -AlH₃ started at around 100–120 °C, even though ball milling was performed for just 5 min. However, in the case of β -AlH₃, there was no drastic change due to ball milling. The primary reason for the enhanced desorption may due to the breaking of the oxide layers covered on the surface of AlH₃ [121].

15.6 Ammonium Borane

Ammonia borane (NH₃BH₃, AB for short) is a solid compound, which is stable at room temperature in air. It has been paid much attention as a hydrogen storage material due to the high weight density (19.6 wt%) and volume density (145 g/L) of hydrogen [122, 123]. As previously mentioned in the amide-hydride section, the combination of protic hydrogen and hydridic hydrogen is one of the driving forces for the dehydrogenation of amide-hydride systems. Therefore, the mass transfer limitation needs to be overcome for the two phases in these systems. However, dehydrogenation of AB is facilitated by the coexistence of proton (N-H) and hydride (B-H) in one molecule. Nevertheless, the drawbacks of AB as hydrogen storage material still include high kinetic barriers in the stepwise dehydrogenation, emission of poisoning side products, and irreversibility of the dehydrogenation. Many efforts have been made to AB, resulting in a series of important progresses in the last 10 years. Therefore, in this section, the elemental knowledge and progresses on AB will be briefly introduced.

15.6.1 Crystal Structure and Dehydrogenation of AB

Normally, there are two methods to synthesize AB: (1) through the interaction of NH₃ and borane adducts (BH₃·THF et al.); and (2) through the metathesis of ammonium salts and borohydrides. AB, with a molecular crystal structure at room temperature, was firstly reported in 1955 by Shore et al. [124]. It crystallizes into

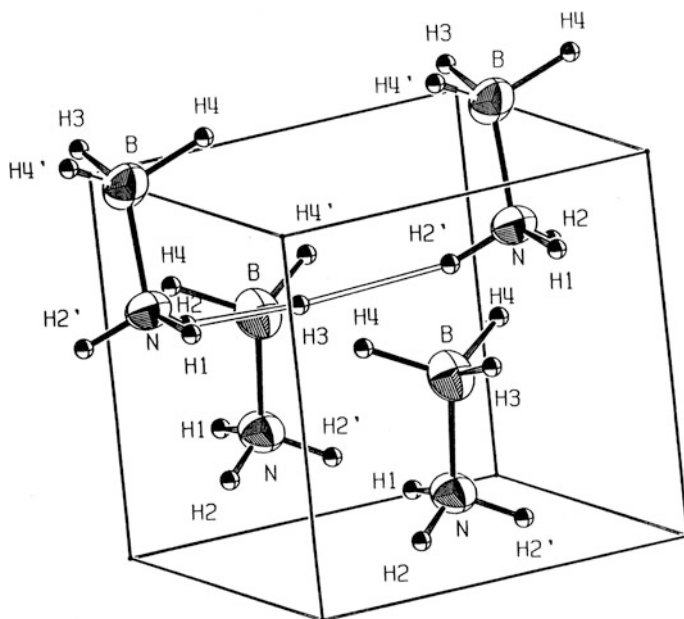
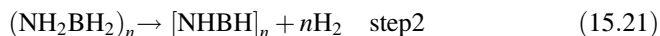
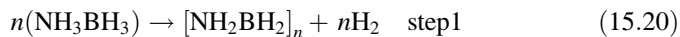


Fig. 15.12 Stereoview of the neutron diffraction structure of BH_3NH_3 with the shortest $\text{H}\cdots\text{H}$ with contacts $[\text{H2}-\text{H3}, 2.02(3) \text{ \AA}]$ indicated [127] (used with permission from American Chemical Society, Copyright 1999)

the tetragonal $I4mm$ space group with crystal parameters of $a = 5.234 \text{ \AA}$ and $c = 5.027 \text{ \AA}$ at room temperature [125]. However, at temperature as low as 110 K, it exhibits an orthorhombic $Pmn21$ space group with crystal lattice parameters of $a = 5.517 \text{ \AA}$, $b = 4.742 \text{ \AA}$ and $c = 5.020 \text{ \AA}$ [126], as shown in Fig. 15.12. Although AB is an isoelectronic species to ethane, its similarity to ethane is tenuous since AB is a solid and ethane is a gas at room temperature. This can be attributed to the highly polar nature of the B–N bond and the existence of dihydrogen bonds (Fig. 15.12) in the structure.

The thermal decomposition of AB in the solid state is a complex process depending on the heating rate, which will generate hydrogen during decomposition. The simplified form of the dehydrogenation of AB is a three-step reaction, releasing around 1 equiv. hydrogen at each step, as shown in Eqs. 15.20–15.22 [128–130]. According to the DTA result, AB melts at around $114 \text{ }^\circ\text{C}$, followed by the first and second dehydrogenation steps at around 120 and $150 \text{ }^\circ\text{C}$, forming amorphous polyaminoborane $((\text{NH}_2\text{BH}_2)_n, \text{PAB})$ and polyiminoborane $((\text{NHBH})_n, \text{PIB})$, respectively. However, the third step requires a temperature higher than $500 \text{ }^\circ\text{C}$, which is too high to be used for hydrogen storage. During dehydrogenation, other volatile by-products, i.e., ammonia, diborane and borazine et al., are produced, which are poisons to the proton exchange membrane fuel cell (PEFC). Since the

exothermic behavior of decomposition of AB, the direct hydrogenation of spent fuel from AB pyrolysis is infeasible.



It is widely accepted that the combination of proton and hydride in AB is the main driving force for the dehydrogenation. However, experimental results have shown that the proton and hydride arise from intermolecular interactions. A detailed mechanistic model for the dehydrogenation of AB was proposed, which comprised of three distinct steps: introduction, nucleation, and growth, as shown in Fig. 15.13 [131]. In the introduction period, a mobile phase of AB was generated, leading to a perturbed dihydrogen bonding network. After that, the diamoniato of diborane ($[\text{NH}_3\text{BH}_2\text{NH}_3]^+[\text{BH}_4]^-$ DADB for short) was generated in the nucleation step, which can further react with AB to form a dimer, oligomer, and polymer, or isomerize to form cyclic products. Nevertheless, the mechanism for the dehydrogenation of AB in solution is different from that in solid state, as shown in Fig. 15.14 [132]. It is proposed that AB reacted in an intermolecular reaction to give the instable DADB followed by hydrogen loss with the formation of cyclodiborazane (CDB). Then, CDB will further react with another equiv. AB to form hydrogen and B-(cyclodiborazanyl) aminoborohydride (BCDB). Both CDB and BCDB may convert into cyclotriborazane (CTB), which is a stable product in the dehydrogenation of AB in glyme solution. Although the dehydrogenations of

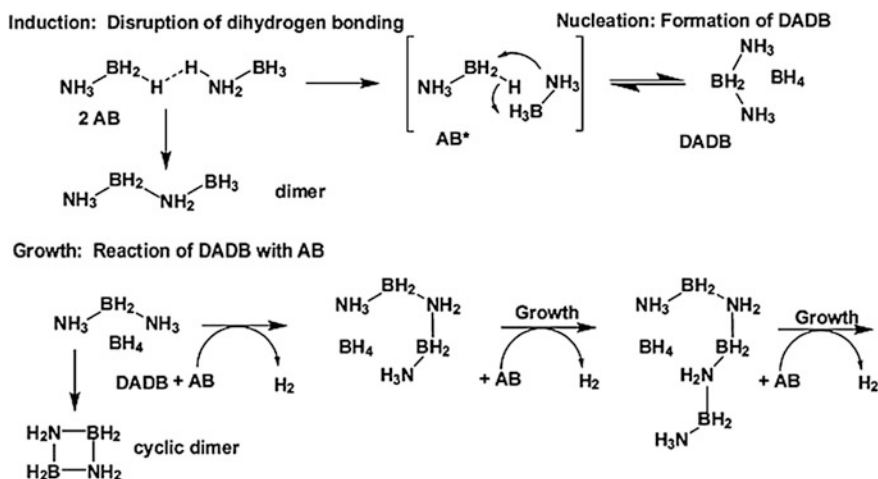


Fig. 15.13 The proposed thermal dehydrogenation mechanism of AB showing discrete induction, nucleation and growth steps leading to hydrogen release [131] (used with permission from the Royal Society of Chemistry, Copyright 2007)

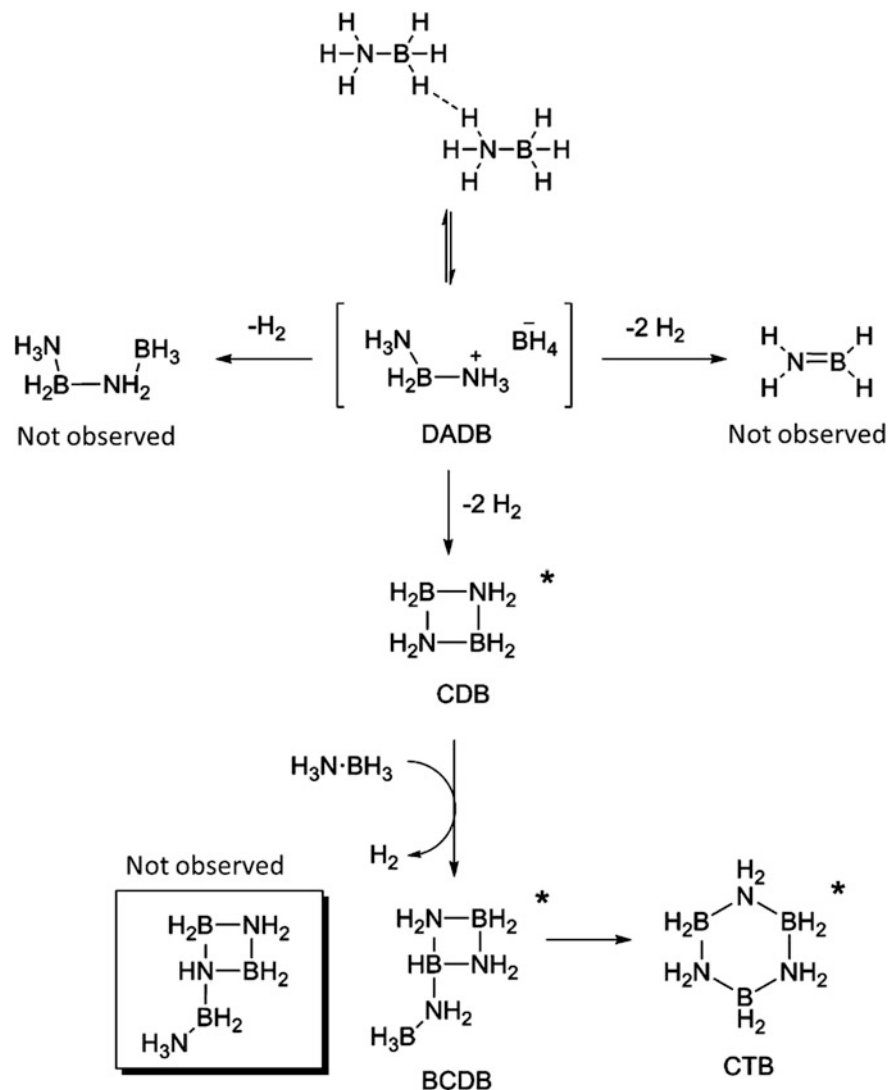


Fig. 15.14 Initial decomposition pathways of AB based on the results of in situ NMR spectroscopy. DADB was only observed at very low concentrations in the thermolysis study at 50 °C [132] (used with permission from John Wiley and Sons, Copyright 2008)

AB are different in solid state and in solution, it is obvious that DADB plays a very important role in the dehydrogenation of AB, which is supported by the experiment that adding a little amount of DADB will significantly facilitate the dehydrogenation of AB [133].

15.6.2 Modifications on Dehydrogenation of AB

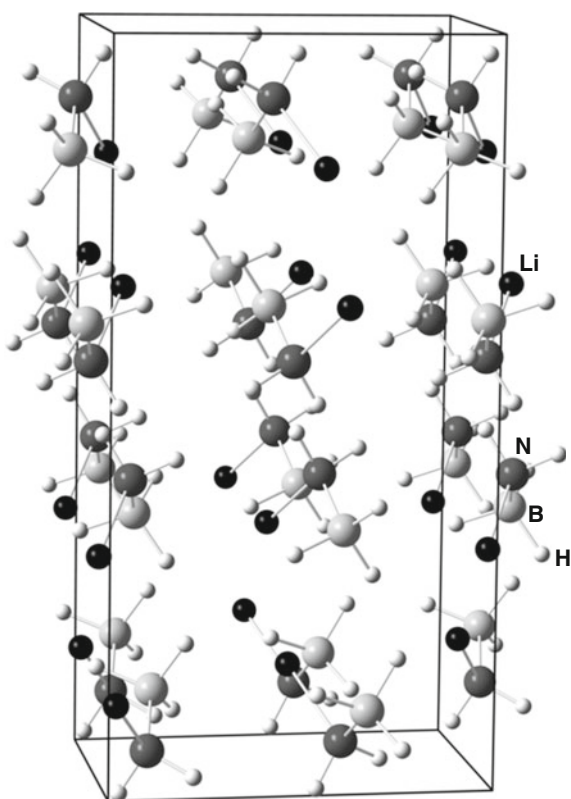
Due to the high kinetic barrier for the dehydrogenation of AB, lots of methods have been employed to overcome this drawback. One of the most important options is catalysis, including transitional metals [134, 135], and acid or base catalysis [136, 137]. Usually, catalytic dehydrogenation of AB using transition metals will produce two kinds of products: soluble borazine or polyborazylene and an insoluble compound [134, 138]. The insoluble compound was identified as cyclopentaborazane $[\text{NH}_2\text{BH}_2]_5$ by Böddeker et al. [139]. However, it can't be concluded that the insoluble product was not linear and oligomeric or polymeric in nature [138]. Manners et al. firstly reported the catalytic dehydrogenation of AB using Rh based catalyst with the formation of product borazine and poorly soluble product [140]. In 2006, Goldberg and Heinekey et al. demonstrated that an iridium pincer complex (POCOP)Ir(H)₂ (POCOP=[K³-1,3-(OPtBu₂C₆H₃)]) showed remarkable properties on the catalytic dehydrogenation of AB in THF solution with the formation of insoluble compound [134]. They believed that the formation of (POCOP)Ir(H)₂(BH₃) is the key step for the activation of AB molecule. The nonprecious Ni-N-heterocyclic carbene (Ni-NHC) catalyst resulted in the formation of soluble cross-linked borazine-type species in benzene solvent [141]. However, the Fe, Co and Ni based catalysts will produce crystal PAB in solid state catalysis [142, 143], which was identical to the insoluble polymer generated by Ir based catalyst. Until now, little evidence to fully understand the selectivity was found. It is possible that the active center, sterically crowded by different ligands, may hinder the further dehydrogenation of secondary amine-boranes, resulting in insoluble PAB. Apart from transition metals, Lewis acids including B(C₆F₅)₃, and HOSO₂CF₃ etc. could catalyze the dehydrogenation of AB to release more than 1 equiv. hydrogen at 60 °C [136].

Another important method to decrease the dehydrogenation temperature of AB is to disperse AB on support with large surface area, i.e., silicon [144], carbon-based materials [145], and MOFs [146] etc. It is well known that material reduced into nano size will show different physical and chemical properties compared with bulk material. Autrey et al. firstly introduced AB into the pores of SBA-15 and found the decreased temperature of AB dehydrogenation [144]. Subsequently, numerous porous supports were investigated to enhance the dehydrogenation of AB. The surface area of AB will considerably increase after being dispersed on the support or being forced into the nanoscale pores, which inevitably lowers the phase transition temperature, thereby, leading to lower temperature of AB dehydrogenation. Another important issue is that the presence of functional groups, such as hydroxide or carboxylic acids etc. could be observed on the surface of support. It is well known that these kinds of group could facilitate the dehydrogenation of AB.

15.6.3 Metal Amidoboranes

Syntheses of sodium amidoborane (NaAB) [147] and lithium amidoborane (LiAB) [148], the roles of which were always limited to reducing agent in the past few decades, using wet chemical method has been reported in 1938 and 1996. Recently, metal amidoboranes obtained from the interaction of metal hydrides and AB are considered as potential hydrogen storage materials due to the high hydrogen content and superior dehydrogenation properties to AB. $\text{Ca}(\text{NH}_2\text{BH}_3)_2$ (CaAB) was successfully synthesized by Burrell and co-workers through the interaction of CaH_2 and AB in the molar ratio of 1:2 [149]. At the same time, Chen et al. used LiH or NaH to react with AB in ratios of 1:1, resulting in 1 equiv. hydrogen and desired products lithium amidoborane (LiNH_2BH_3) and sodium amidoborane (NaNH_2BH_3) [150], as shown in Fig. 15.15. LiAB and NaAB released hydrogen at considerably lower temperatures, 92 and 89 °C, respectively, without formation of byproduct borazine. It is suggested that a stronger dative bond is being formed, as evidenced by a shorter B–N bond distance. In the following investigations, other main group metal-amidoboranes and dual-metal amidoboranes with superior dehydrogenation

Fig. 15.15 Schematic diagram of the crystal structure of LiNH_2BH_3 and NaNH_2BH_3 determined from high-resolution X-ray powder diffraction data at room temperature. Li (or Na), B, N and H are represented by black, grey, dark grey and white spheres, respectively [150] (used by permission from Macmillan Publishers Ltd: [Nature Materials], Copyright 2008)



properties to AB were developed, including K [151], Mg [152], Sr [153], Y [154], Li–Na [155], and Na–Mg [156]. Meanwhile, the other important amidoborane derivatives, amidoborane ammoniates, were also synthesized, such as LiAB · NH₃ [157], CaAB · nNH₃ [158, 159], and MgAB · nNH₃ [160, 161].

References

1. Bogdanović B, Schwickardi M (1997) Ti-doped alkali metal aluminum hydrides as potential novel reversible hydrogen storage materials. *J Alloys Compd* 253–254:1–9
2. Fichtner M, Fuhr O, Kircher O (2003) Magnesium alanate—a material for reversible hydrogen storage. *J Alloys Compd* 356–357:418–422
3. Ashby EC, Brendel GJ, Redman HE (1963) Direct synthesis of complex metal hydrides. *Inorg Chem* 2:499–506
4. Sato T, Ikeda K, Li H-W, Yukawa H, Morinaga M, Orimo S (2009) Direct dry syntheses and thermal analyses of a series of aluminum complex hydrides. *Mater Trans* 50:182–186
5. Lauher JW, Dougherty D, Herley PJ (1979) Sodium tetrahydroaluminate. *Acta Crystallogr B* 35:1454–1456
6. Hauback BC, Brinks HW, Jensen CM, Murphy K, Maeland AJJ (2003) Neutron diffraction structure determination of NaAlD₄. *J Alloys Compd* 358:142–145
7. Bogdanović B, Brand RA, Marjanović A, Schwickardi M, Tölle J (2000) Metal-doped aluminium hydrides as potential new hydrogen storage materials. *J Alloys Compd* 302:36–58
8. Ashby EC, Kobetz P (1966) The direct synthesis of Na₃AlH₆. *Inorg Chem* 5:1615–1617
9. Dymova TN, Eliseeva NG, Bakum SI, Dergachev YM (1974) Direct synthesis of alkali metal aluminum hydrides in the melt. *Dokl Akad Nauk SSSR* 215:1369–1372
10. Block J, Gray AP (1965) The thermal decomposition of lithium aluminum hydride. *Inorg Chem* 4:304–305
11. Jang J-W, Shim J-H, Cho YW, Lee BJ (2006) Thermodynamic calculation of LiH ↔ Li₃AlH₆ ↔ LiAlH₄ reactions. *J Alloys Compd* 420:286–290
12. Wang J, Ebner AD, Ritter JA (2006) Physicochemical pathway for cyclic dehydrogenation and rehydrogenation of LiAlH₄. *J Am Chem Soc* 128:5949–5954
13. Anton DL (2003) Hydrogen desorption kinetics in transition metal modified NaAlH₄. *J Alloys Compd* 356–357:400–404
14. Gross KJ, Majzoub EH, Spangler SW (2003) The effects of titanium precursors on hydriding properties of alanates. *J Alloys Compd* 356–357:423–428
15. Graetz J, Reilly JJ, Johnson J, Ignatov AY, Tyson TA (2004) X-ray absorption study of Ti-activated sodium aluminum hydride. *Appl Phys Lett* 85:500–502
16. Moisés Araújo C, Li S, Ahuja R, Jena P (2005) Vacancy-mediated hydrogen desorption in NaAlH₄. *Phys Rev B* 72:165101
17. Gunaydin H, Houk KN, Ozolinš V (2008) Vacancy-mediated dehydrogenation of sodium alanate. *PNAS* 105:3673–3677
18. Balde CP, Mijovilovich AE, Koningsberger DC, van der Eerden AMJ, Smith AD, de Jong KP, Bitter JH (2007) XAFS study of the Al K-edge in NaAlH₄. *J Phys Chem C* 111:2797–2802
19. Kadono R, Shimomura K, Satoh KH, Takeshita S, Koda A, Nishiyama K, Akiba E, Ayabe RM, Kuba M, Jensen CM (2008) Hydrogen bonding in sodium alanate: a muon spin rotation study. *Phys Rev Lett* 100:26401
20. Frankcombe TJ (2012) Proposed mechanisms for the catalytic activity of Ti in NaAlH₄. *Chem Rev* 112:2164–2178
21. Johnson TA, Jorgensen SW, Dedrick DE (2011) Performance of a full-scale hydrogen-storage tank based on complex hydrides. *Faraday Discuss* 151:327–352

22. Bellosta von Colbe JM, Metz O, Lozano GA, Pranzas PK, Schmitz HW, Beckmann F, Schreyer A, Klassen T, Dornheim M (2012) Behavior of scaled-up sodium alanate hydrogen storage tanks during sorption. *Int J Hydrogen Energy* 37:2807–2811
23. Gay-Lussac JL, Thénard IJ (1809) Notiz über das Kali - und das Natron – Metall. *Ann Phys* 32:23–39
24. Chen P, Xiong ZT, Luo JZ, Li JY, Tan KL (2002) Interaction of hydrogen with metal nitrides and imides. *Nature* 420:302–304
25. Greenlee KW, Henne AL, Fernelius WC (1946) *Inorganic syntheses*, vol II. Wiley, Hoboken, pp 128–135
26. Bergstrom FW (1955) Sodium amide. *Org Synth CV* 3, P 778
27. Xiong ZT, Hu JJ, Wu GT, Chen P, Luo WF, Gross K, Wang J (2005) Thermodynamic and kinetic investigations of the hydrogen storage in the Li-Mg-N-H system. *J Alloys Compd* 398:235–239
28. Hu YH, Ruckenstein E (2006) Hydrogen storage of Li_2NH prepared by reacting Li with NH_3 . *Ind Eng Chem Res* 45:182–186
29. Nakamori Y, Kitahara G, Ninomiya A, Aoki M, Noritake T, Towata S, Orimo S (2005) Guidelines for developing amide-based hydrogen storage materials. *Mater Trans* 46:2093–2097
30. Kojima Y, Ichikawa T, Fujii H (2009) *Fuels-hydrogen storage | complex hydrides*, Elsevier, *Encyclopedia of Electrochemical Power Sources*. pp 473–483
31. Hu YH, Ruckenstein E (2003) Ultra-fast reaction between LiH and NH_3 during H_2 storage in Li_3N . *J Phys Chem A* 107:9737–9739
32. Leng HY, Ichikawa T, Hino S, Hanada N, Isobe S, Fujii H (2004) New metal-NH system composed of $\text{Mg}(\text{NH}_2)_2$ and LiH for hydrogen storage. *J Phys Chem B* 108:8763–8765
33. Nakamori Y, Kitahara G, Orimo S (2004) Synthesis and dehydriding studies of Mg–N–H systems. *J Power Sources* 138:309–312
34. Dafert FW, Miklanz R (1910) Über einige neue verbindungen von stickstoff und wasserstoff mit lithium. *Manotsh Chem* 31:981–996
35. Ruff O, Geoges H, Über das lithium-imid und einige Bemerkungen zu der arbeit von dafert und miklauz: “Über einige neue verbindungen von stickstoff und wasserstoff mit lithium”. *Ber Dtsch Chem Ges* 44:502–506
36. Orimo S, Nakamori Y, Kitahara G, Miwa K, Ohba N, Noritake T, Towata S (2004) Destabilization and enhanced dehydriding reaction of LiNH_2 . *Appl Phys A* 79:1765–1767
37. Kojima Y, Kawai Y (2004) Hydrogen storage of metal nitride by a mechanochemical reaction. *Chem Commun* 2210–2211
38. Wang J, Li H-W, Chen P (2013) Amides and borohydrides for high-capacity solid-state hydrogen storage-materials design and kinetic improvements. *MRS Bull* 38:480–487
39. Pinkerton FE, Meisner GP, Meyer MS, Balogh MP, Kundrat MD (2005) Hydrogen desorption exceeding ten weight percent from the new quaternary hydride $\text{Li}_3\text{BN}_2\text{H}_8$. *J Phys Chem B* 109:6–8
40. Vajo JJ, Mertens F, Ahn CC, Bowman RC, Fultz B (2004) Altering hydrogen storage properties by hydride destabilization through alloy formation: LiH and MgH_2 destabilized with Si. *J Phys Chem B* 108:13977–13983
41. Gosawlit-Utke R, Colbe J, Gornheim M, Jensen TR, Cerenius Y, Bonatto CM, Peschke M, Bormann R (2010) LiF-MgB₂ system for reversible hydrogen storage. *J Phys Chem C* 114:10291–10296
42. Chen P, Xiong ZT, Yang LF, Wu GT, Luo WF (2006) Mechanistic investigations on the heterogeneous solid-state reaction of magnesium amides and lithium hydrides. *J Phys Chem B* 110:14221–14225
43. Shaw LL, Ren R, Markmaitree T, Osborn W (2008) Effects of mechanical activation on dehydrogenation of the lithium amide and lithium hydride system. *J Alloys Compd* 448:263–271

44. Liu YF, Zhong K, Luo K, Gao MX, Pan HG, Wang QD (2009) Size-dependent kinetic enhancement in hydrogen absorption and desorption of the Li–Mg–N–H System. *J Am Chem Soc* 131:1862–1870
45. Wang JH, Liu T, Wu GT, Li W, Liu YF, Araujo CM, Scheicher RH, Blomqvist A, Ahuja R, Xiong ZT, Yang P, Gao MX, Pan HG, Chen P (2009) Potassium-modified Mg(NH₂)₂/2 LiH system for hydrogen storage. *Angew Chem Int Ed* 48:5828–5832
46. Li H-W, Yan Y, Orimo S, Züttel A, Jensen CM (2011) Recent progress in metal borohydrides for hydrogen storage. *Energies* 4:185–214
47. Rude LH, Nielsen TK, Ravnsbæk DB, Bösenberg U, Ley MB, Richter B, Arnbjerg LM, Dornheim M, Filinchuk Y, Besenbacher F, Jensen TR (2011) Tailoring properties of borohydrides for hydrogen storage: a review. *Phys Status Solidi A* 208:1754–1773
48. Schlesinger HI, Brown HC, Metallo borohydrides. (1940) III. Lithium borohydride. *J Am Chem Soc* 62:3429–3435
49. Schlesinger HI, Brown HC, Hoekstra HR, Rapp LR (1953) New developments in the chemistry of diborane and the borohydrides. *J Am Chem Soc* 75:199–204
50. Friedrichs O, Borgschulte A, Kato S, Buchter F, Gremaud R, Remhof A, Züttel A (2009) Low-temperature synthesis of LiBH₄ by gas-solid reaction. *Chem Eur J* 15:5531–5534
51. Konoplev VN, Bakulina VM (1971) Some properties of magnesium borohydride. *Rus Chem Soc* 20:136–138
52. Li H-W, Kikuchi K, Nakamori Y, Miwa K, Towata S, Orimo S (2007) Effects of ball milling and additives on dehydrogenating behaviors of well-crystallized Mg(BH₄)₂. *Scripta Mater* 57:679–682
53. Matsunaga T, Buchter F, Miwa K, Towata S, Orimo S, Züttel A (2008) Magnesium borohydride: a new hydrogen storage material. *Renewable Energy* 33:193–196
54. Černý R, Filinchuk Y, Hagemann H, Yvon K (2007) Magnesium borohydride: synthesis and crystal structure. *Acta Mater* 46:5765–5767
55. Sato T, Miwa K, Nakamori Y, Ohoyama K, Li H-W, Noritake T, Aoki M, Towata S, Orimo S (2008) Experimental and computational studies on solvent-free rare-earth metal borohydrides R(BH₄)₃ (R=Y, Dy, and Gd). *Phys Rev B* 77:104114
56. Yan Y, Li H-W, Sato T, Umeda N, Miwa K, Towata S, Orimo S (2009) Dehydrogenating and rehydrogenating properties of yttrium borohydride Y(BH₄)₃ prepared by liquid-phase synthesis. *Int J Hydrogen Energy* 34:5732–5736
57. Köster R, Schoeller K (1957) Neue herstellungsmethoden für metallborhydride. *Angew Chem* 69:94
58. Harris PM, Meibohm EP (1947) The crystal structure of lithium borohydride LiBH₄. *J Am Chem Soc* 69:1231–1232
59. Soulie J-Ph, Renaudin G, Cerny R, Yvon K (2002) Lithium boro-hydride LiBH₄ I. crystal structure. *J Alloys Compd* 346:200–205
60. Filinchuk Y, Chernyshov D, Cerny R (2008) Lightest borohydride probed by synchrotron X-ray diffraction: experiment calls for a new theoretical revision. *J Phys Chem C* 112:10579–10584
61. Tekin A, Caputo R, Züttel A (2010) First-principles determination of the ground-state structure of LiBH₄. *Phys Rev Lett* 104:215501
62. Li H-W, Kikuchi K, Nakamori Y, Ohba N, Miwa K, Towata S, Orimo S (2008) Dehydrogenating and rehydrogenating processes of well-crystallized Mg(BH₄)₂ accompanying with formation of intermediate compounds. *Acta Mater* 56:1342–1347
63. Hwang SJ, Bowman RC, Reiter JW, Rijssenbeek J, Soloverchik GL, Zhao J-C, Kabbour H, Ahn CC (2008) NMR confirmation for formation of [B₁₂H₁₂]²⁻ complexes during hydrogen desorption from metal borohydrides. *J Phys Chem C* 112:3164–3169
64. Ozolin V, Majzoub EH, Wolverson C (2009) First-principles prediction of thermodynamically reversible hydrogen storage reactions in the Li-Mg-Ca-B-H System. *J Am Chem Soc* 131:230–237

65. Chong M, Karkamkar A, Autrey T, Orimo S, Jalisatgi S, Jensen CM (2011) Reversible dehydrogenation of magnesium borohydride to magnesium triborane in the solid state under moderate conditions. *Chem Commun* 47:1330–1332
66. Yan Y, Li H-W, Maekawa H, Aoki M, Noritake T, Matsumoto M, Miwa K, Towata S, Orimo S (2011) Formation process of $[B_{12}H_{12}]^{2-}$ from $[BH_4]^-$ during the dehydrogenation reaction of $Mg(BH_4)_2$. *Mater Trans* 52:1443–1446
67. Orimo S, Nakamori Y, Kitahara G, Miwa K, Ohba N, Towata S, Züttel A (2005) Dehydrogenating and rehydrogenating reactions of $LiBH_4$. *J Alloys Compd* 404:427–430
68. Li H-W, Akiba E, Orimo S (2013) Comparative study on the reversibility of pure metal borohydrides. *J Alloy Compd* 580:S292–S295
69. Nakamori Y, Miwa K, Ninoyiya A, Li H-W, Ohba N, Towata S, Züttel A, Orimo S (2006) Correlation between thermodynamical stabilities of metal borohydrides and cation electronegativities: first-principles calculations and experiments. *Phys Rev B* 74:045126
70. Li H-W, Orimo S, Nakamori Y, Miwa K, Ohba N, Towata S, Züttel A (2007) Materials designing of metal borohydrides: viewpoints from thermodynamical stabilities. *J Alloys Compd* 446–447:315–318
71. Vajo JJ, Olson GL (2007) Hydrogen storage in destabilized chemical systems. *Scripta Mater* 56:829–834
72. Vajo JJ, Skeith SL, Mertens F (2005) Reversible storage of hydrogen in destabilized $LiBH_4$. *J Phys Chem B* 109:3719–3722
73. Bösenberg U, Doppiu S, Mosegaard L, Barkhordarian G, Eigen N, Borgschulte A, Jensen TR, Cerenius Y, Gutfleisch O, Klassen T, Dornheim M, Bormann R (2007) Hydrogen sorption properties of $MgH_2 + 2LiBH_4$. *Acta Mater* 55:3951–3958
74. Pinkerton FE, Meyer MS, Meisner GP, Balogh MP, Vajo JJ (2007) Phase boundaries and reversibility of $LiBH_4/MgH_2$ hydrogen storage material. *J Phys Chem C* 111:12881–12885
75. Yan Y, Li H-W, Maekawa H, Miwa K, Towata S, Orimo S (2011) Formation of intermediate compound $Li_2B_{12}H_{12}$ during the dehydrogenation process of the $LiBH_4$ - MgH_2 system. *J Phys Chem C* 115:19419–19423
76. Price TE, Grant DM, Weston D, Hansen T, Arnbjerg LM, Ravnsbæk DB, Jensen TR, Walker GS (2011) The effect of H_2 partial pressure on the reaction progression and reversibility of lithium-containing multicomponent destabilized hydrogen storage systems. *J Am Chem Soc* 133:13534–13538
77. Shim JH, Lim JH, Rather SU, Lee YS, Reed D, Kim Y, Book D, Cho YW (2010) Effect of hydrogen back pressure on dehydrogenation behavior of $LiBH_4$ -based reactive hydride composites. *J Phys Chem Lett* 1:59–63
78. Jin SA, Lee YS, Shim JH, Cho YW (2008) Reversible hydrogen storage in $LiBH_4$ - MH_2 ($M=Ce, Ca$) composites. *J Phys Chem C* 112:9520–9524
79. Spatz P, Aebischer HA, Krozer A, Schlapbach L (1993) The diffusion of H in Mg and the nucleation and growth of MgH_2 in thin films. *Z Phys Chem* 181:393–397
80. Bogdanovic B (1985) Catalytic synthesis of organo-lithium and organomagnesium compounds and of lithium and magnesium hydrides—applications in organic-synthesis and hydrogen storage. *Angew Chem Int Edit* 24:262–273
81. Uesugi H, Sugiyama T, Nii H, Ito T, Nakatsugawa I (2011) Industrial production of MgH_2 and its application. *J Alloys Compd* 509:S650–S653
82. Vajeeston P, Ravindran P, Kjekshus A, Fjellvåg H (2002) Pressure-induced structural transitions in MgH_2 . *Phys Rev Lett* 89:175506
83. Noritake T, Aoki M, Towata S, Seno Y, Hirose Y, Nishibori E, Takata M, Sakata M (2002) Chemical bonding of hydrogen in MgH_2 . *Appl Phys Lett* 81:2008–2010
84. Zhu M, Lu Y, Ouyang L, Wang H (2013) Thermodynamic tuning of Mg-based hydrogen storage alloys: a review. *Materials* 6:4654–4674
85. Wagemans RWP, van Lenthe JH, de Jongh PE, van Dillen AJ, de Jong KP (2005) Hydrogen storage in magnesium clusters: quantum chemical study. *J Am Chem Soc* 127:16675–16680
86. Huot J, Liang G, Boily S, Van Nesteb A, Schulza R (1999) Structural study and hydrogen sorption kinetics of ball-milled magnesium hydride. *J Alloys Compd* 293–295:495–500

87. Nielsen TK, Manickam K, Hirscher M, Besenbacher F, Jensen TR (2009) Confinement of MgH₂ nanoclusters within nanoporous aerogel scaffold materials. *ACS Nano* 3:3521–3528
88. Barkhordarian G, Klassen T, Bormann R (2003) Fast hydrogen sorption kinetics of nanocrystalline Mg using Nb₂O₅ as catalyst. *Scr Mater* 49:213–217
89. Barkhordarian G, Klassen T, Bormann R (2004) Effect of Nb₂O₅ content on hydrogen reaction kinetics of Mg. *J Alloys Compd* 364:242–246
90. Finholt AE, Bond AC, Schlesinger HI (1947) Lithium aluminum hydride, aluminum hydride and lithium gallium hydride, and some of their applications in organic and inorganic chemistry. *J Am Chem Soc* 69:1199–1203
91. Chizinsky G, Evans GG, Gibb Jr TPP, Rice Jr MJ (1955) Non-solvated aluminum hydride. *J Am Chem Soc* 77:3164–3165
92. Brower FM, Matzek NE, Reigler PF, Rinn HW, Roberts CB, Schmidt DL, Snover JA, Terada K (1976) Preparation and properties of aluminum hydride. *J Am Chem Soc* 98:2450–2453
93. Bulychev BM, Verbetskii VN, Storozhenko PA (2008) “Direct” synthesis of unsolvated aluminum hydride involving Lewis and Bronsted acids. *Russ J Inorg Chem* 53:1000–1005
94. Bulychev BM, Storozhenko PA, Fokin VN (2009) “One-step” synthesis of nonsolvated aluminum hydride. *Russ Chem Bull Inter Ed* 58:1817–1823
95. Graetz J, Reilly JJ, Yartys VA, Maehlen JP, Bulychev BM, Antonov VE, Tarasov BP, Gabis IE (2011) Aluminum hydride as a hydrogen and energy storage material: past, present and future. *J Alloys Compd* 509:S517–S528
96. Saitoh H, Machida A, Katayama Y, Aoki K (2008) Formation and decomposition of AlH₃ in the aluminum-hydrogen system. *Appl Phys Lett* 93:151918
97. Clasen H (1962) German Patent 1141:623
98. Zidan R, Garcia-Diaz BL, Fewox CS, Stowe AC, Gray JR, Harter AG (2009) Aluminium hydride: a reversible material for hydrogen storage. *Chem Commun* 25:3717–3719
99. Murib JH, Horvitz D (1972) US Patent 3,642,853
100. Stecher O, Wiberg E (1942) Über einen nichtflüchtigen, polymeren aluminiumwasserstoff (AlH₃)_x und einige flüchtige verbindungen des monomeren AlH₃. *Ber Dtsch Chem Ges* 75B:2003–2012
101. Graetz J, Chaudhuri S, Wegrzyn J, Celebi Y, Johnson JR, Zhou W, Reilly JJ (2007) Direct and reversible synthesis of AlH₃-triethylenediamine from Al and H₂. *J Phys Chem C* 111:19148–19152
102. Lacina D, Wegrzyn J, Reilly J, Celebi Y, Graetz J (2010) Characterization of dimethylethylamine-alane and the regeneration of aluminum hydride. *Energy Environ Sci* 3:1099–1105
103. Turley JW, Rinn HW (1969) The crystal structure of aluminum hydride. *Inorg Chem* 8:18–22
104. Brinks HW, Istad-Lem A, Hauback BC (2006) Mechanochemical synthesis and crystal structure of alpha'-AlD₃ and alpha-AlD₃. *J Phys Chem B* 110:25833–25837
105. Brinks HW, Langley W, Jensen CM, Graetz J, Reilly JJ, Hauback BC (2007) Synthesis and crystal structure of beta'-AlD₃. *J Alloys Compd* 433:180–183
106. Yartys VA, Denys RV, Maehlen JP, Frommen C, Fichtner M, Bulychev BM, Emerich H (2007) Double-bridge bonding of aluminium and hydrogen in the crystal structure of gamma-AlH₃. *Inorg Chem* 46:1051–1055
107. Brinks HW, Brown C, Jensen CM, Graetz J, Reilly JJ, Hauback BC (2007) The crystal structure of gamma-AlD₃. *J Alloys Compd* 441:364–367
108. Sartori S, Opalka SM, Løvvik OM, Guzik MN, Tang X, Hauback BC (2008) Experimental studies of alpha-AlD₃ and alpha'-AlD₃ versus first-principles modelling of the alane isomorphs. *J Mater Chem* 18:2361–2370
109. Graetz J, Reilly JJ (2006) Thermodynamics of the alpha, beta and gamma polymorphs of AlH₃. *J Alloys Compd* 424:262–265
110. Sinke GC, Walker LC, Oetting FL, Stull DR (1967) Thermodynamic properties of aluminum hydride. *J Chem Phys* 47:2759–2761

111. Tkacz M, Filipek S, Baranowski B (1983) High pressure synthesis of aluminium hydride from the elements. *Pol J Chem* 57:651–653
112. Baranowski B, Tkacz M (1983) The equilibrium between solid aluminium hydride and gaseous hydrogen. *Z Phys Chem NF* 135:27–38
113. Kononov SK, Bulychev BM (1995) The P, T-state diagram and solid phase synthesis of aluminum hydride. *Inorg Chem* 34:172–175
114. Herley PJ, Christofferson O, Irwin R (1981) Decomposition of α -aluminum hydride powder. 1. Thermal decomposition. *J Phys Chem* 85:1874–1881
115. Graetz J, Reilly JJ (2005) Decomposition kinetics of the AlH_3 polymorphs. *J Phys Chem B* 109:22181–22185
116. Graetz J, Reilly JJ, Kulleck JG, Bowman RC (2007) Kinetics and thermodynamics of the aluminum hydride polymorphs. *J Alloys Compd* 446–447:271–275
117. Maehlen JP, Yartys VA, Denys RV, Fichtner M, Frommen C, Bulychev BM, Pattison P, Emerich H, Filinchuk YE, Chernyshov D (2007) *J Alloys Compd* 446–447:280–289
118. Sandrock G, Reilly J, Graetz J, Zhou WM, Johnson J, Wegrzyn J (2005) Accelerated thermal decomposition of AlH_3 for hydrogen-fueled vehicles. *Appl Phys A* 80:687–690
119. Sandrock G, Reilly J, Graetz J, Zhou WM, Johnson J, Wegrzyn J (2006) Alkali metal hydride doping of α - AlH_3 for enhanced H_2 desorption kinetics. *J Alloys Compd* 421:185–189
120. Orimo S, Nakamori Y, Kato T, Brown C, Jensen CM (2006) Intrinsic and mechanically modified thermal stabilities of α -, β - and γ -aluminum trihydrides AlH_3 . *Appl Phys A* 83:5–8
121. Kato S, Biemann M, Ikeda K, Orimo S, Borgschulte A, Zuttel A (2010) Surface changes on AlH_3 during the hydrogen desorption. *Appl Phys Lett* 96:051912
122. Staubitz A, Robertson APM, Manners I (2010) Ammonia—borane and related compounds as dihydrogen sources. *Chem Rev* 110:4079–4124
123. Stephens FH, Pons V, Baker RT (2007) Ammonia-borane, the hydrogen storage source par excellence. *Dalton Trans* 25:2613–2626
124. Shore SG, Parry RW (1955) The crystalline compound ammonia-borane, H_3NBH_3 . *J Am Chem Soc* 77:6084–6085
125. Lippert EL, Lipscomb WN (1956) The structure of H_3NBH_3 . *J Am Chem Soc* 78:503–504
126. Hoon CF, Reynhardt EC (1983) Molecular-dynamics and structures of amine boranes of the type $\text{R}_3\text{N BH}_3$. I. X-ray investigation of $\text{H}_3\text{N BH}_3$ at 295 K and 110 K. *J Phys C* 16:6129–6136
127. Klooster WT, Koetzle TF, Siegbahn PEM, Richardson TB, Crabtree RH (1999) Study of the N–H H–B dihydrogen bond including the crystal structure of BH_3NH_3 by neutron diffraction. *J Am Chem Soc* 121:6337–6343
128. Hu MG, Geanangel RA, Wendlandt WW (1978) The thermal decomposition of ammonia borane. *Thermochim Acta* 23:249–255
129. Wolf G, Baumann J, Baitalow F, Hoffmann FP (2000) Calorimetric process monitoring of thermal decomposition of B–N–H compounds. *Thermochim Acta* 343:19–25
130. Baitalow F, Baumann J, Wolf G, Jaenicke-Röbber K, Leitner G (2002) Thermal decomposition of B–N–H compounds investigated by using combined thermoanalytical methods. *Thermochim Acta* 391:159–168
131. Stowe AC, Shaw WJ, Linehan JC, Schmid B, Autrey T (2007) In situ solid state ^{11}B MAS-NMR studies of the thermal decomposition of ammonia borane: mechanistic studies of the hydrogen release pathways from a solid state hydrogen storage material. *Phys Chem Chem Phys* 9:1831–1836
132. Shaw WJ, Linehan JC, Szymczak NK, Heldebrant D, Yonker C, Camaioni D, Baker RT, Autrey T (2008) In situ multinuclear NMR spectroscopic studies of the thermal decomposition of ammonia borane in solution. *Angew Chem Int Ed* 47:7493–7496
133. Heldebrant DJ, Karkamkar A, Hess NJ, Bowden M, Rassat S, Zheng F, Rappe K, Autrey T (2008) The effects of chemical additives on the induction phase in solid-state thermal decomposition of ammonia borane. *Chem Mater* 20:5332–5336
134. Denney MC, Pons V, Hebden TJ, Heinekey DM, Goldberg KI (2006) Efficient catalysis of ammonia borane dehydrogenation. *J Am Chem Soc* 128:12048–12049

135. Paul A, Musgrave C (2007) Catalyzed dehydrogenation of ammonia–borane by iridium dihydrogen pincer complex differs from ethane dehydrogenation. *Angew Chem Int Ed* 46:8153–8156
136. Stephens FH, Baker RT, Matus MH, Grant DJ, Dixon DA (2007) Acid initiation of ammonia–borane dehydrogenation for hydrogen storage. *Angew Chem Int Ed* 46:746–749
137. Himmelberger DW, Yoon CW, Bluhm ME, Carroll PJ, Sneddon LG (2009) Base-promoted ammonia borane hydrogen-release. *J Am Chem Soc* 131:14101–14110
138. Staubitz A, Soto AP, Manners I (2008) Iridium-catalyzed dehydrocoupling of primary amine–borane adducts: a route to high molecular weight polyaminoboranes, boron–nitrogen analogues of polyolefins. *Angew Chem Int Ed* 47:6212–6215
139. Boddeker KW, Shore SG, Bunting RK (1966) Boron-nitrogen chemistry. 1. Syntheses and properties of new cycloborazanes, $(\text{BH}_2\text{NH}_2)_n$. *J Am Chem Soc* 88:4396–4401
140. Jaska CA, Temple K, Lough AJ, Manners I (2001) Rhodium-catalyzed formation of boron–nitrogen bonds: a mild route to cyclic aminoboranes and borazines. *Chem Commun* 11:962–963
141. Keaton RJ, Blacquiere JM, Baker RT (2007) Base metal catalyzed dehydrogenation of ammonia–borane for chemical hydrogen storage. *J Am Chem Soc* 129:1844–1845
142. He T, Xiong Z, Wu G, Chu H, Wu C, Zhang T, Chen P (2009) Nanosized Co- and Ni-catalyzed ammonia borane for hydrogen storage. *Chem Mater* 21:2315–2318
143. He T, Wang J, Liu T, Wu G, Xiong Z, Yin J, Chu H, Zhang T, Chen P (2011) Quasi in situ Mössbauer and XAS studies on FeB nanoalloy for heterogeneous catalytic dehydrogenation of ammonia borane. *Catal Today* 170:69–75
144. Gutowska A, Li L, Shin Y, Wang CM, Li XS, Linehan JC, Smith RS, Kay BD, Schmid B, Shaw W, Gutowski M, Autrey T (2005) Nanoscaffold mediates hydrogen release and the reactivity of ammonia borane. *Angew Chem Int Ed* 44:3578–3582
145. Feaver A, Sephiri S, Shamberger P, Stowe A, Autrey T, Cao G (2007) Coherent carbon cryogel-ammonia borane nanocomposites for H_2 storage. *J Phys Chem B* 111:7469–7472
146. Li Z, Zhu G, Lu G, Qiu S, Yao X (2010) Ammonia Borane Confined by a Metal–organic framework for chemical hydrogen storage: enhancing kinetics and eliminating ammonia. *J Am Chem Soc* 132:1490–1491
147. Schlesinger HI, Burg AB (1938) Hydrides of boron. VIII. The structure of the diammoniate of diborane and its relation to the structure of diborane. *J Am Chem Soc* 60:290–299
148. Myers AG, Yang BH, David KJ (1996) Lithium amidotrihydroborate, a powerful new reductant. Transformation of tertiary amides to primary alcohols. *Tetrahedron Lett* 37:3623–3626
149. Diyabalanage HVK, Shrestha RP, Semelsberger TA, Scott BL, Bowden ME, Davis BL, Burrell AK (2007) Calcium amidotrihydroborate: A hydrogen storage material. *Angew Chem Int Ed* 46:8995–8997
150. Xiong Z, Yong CK, Wu G, Chen P, Shaw W, Karkamkar A, Autrey T, Jones MO, Johnson SR, Edwards PP, David WIF (2008) High-capacity hydrogen storage in lithium and sodium amidoboranes. *Nat Mater* 7:138–141
151. Diyabalanage HVK, Nakagawa T, Shrestha RP, Semelsberger TA, Davis BL, Scott BL, Burrell AK, David WIF, Ryan KR, Jones MO, Edwards PP (2010) Potassium(I) amidotrihydroborate: structure and hydrogen release. *J Am Chem Soc* 132:11836–11837
152. Luo J, Kang X, Wang P (2013) Synthesis, formation mechanism, and dehydrogenation properties of the long-sought $\text{Mg}(\text{NH}_2\text{BH}_3)_2$ compound. *Energy Environ Sci* 6:1018–1025
153. Zhang QA, Tang CX, Fang CH, Fang F, Sun D, Ouyang LZ, Zhu M (2010) Synthesis, crystal structure and thermal decomposition of strontium amidoborane. *J Phys Chem C* 114:1709–1714
154. Genova RV, Fijalkowski KJ, Budzianowski A, Grochala W (2010) Towards $\text{Y}(\text{NH}_2\text{BH}_3)_3$: Probing hydrogen storage properties of $\text{YX}_3/\text{MNH}_2\text{BH}_3$ ($\text{X}=\text{F}, \text{Cl}$; $\text{M}=\text{Li}, \text{Na}$) and $\text{YH}_{x\sim 3}/\text{NH}_3\text{BH}_3$ composites. *J Alloys Compd* 499:144–148

155. Fijalkowski KJ, Genova RV, Filinchuk Y, Budzianowski A, Derzsi M, Jaron T, Leszczynski PJ, Grochala W (2011) Na[Li(NH₂BH₃)₂]⁺—the first mixed-cation amidoborane with unusual crystal structure. *Dalton Trans* 40:4407–4413
156. Wu H, Zhou W, Pinkerton FE, Meyer MS, Yao Q, Gadipelli S, Udovic TJ, Yildirim T, Rush JJ (2011) Sodium magnesium amidoborane: the first mixed-metal amidoborane. *Chem Commun* 47:4102–4104
157. Xia G, Yu X, Guo Y, Wu Z, Yang C, Liu H, Dou S (2010) Amminelithium amidoborane Li(NH₃)NH₂BH₃: a new coordination compound with favorable dehydrogenation characteristics. *Chem Eur J* 16:3763–3769
158. Chua YS, Wu G, Xiong Z, He T, Chen P (2009) Calcium amidoborane ammoniate—synthesis, structure, and hydrogen storage properties. *Chem Mater* 21:4899–4904
159. Chua YS, Li W, Shaw WJ, Wu G, Autrey T, Xiong Z, Wong MW, Chen P (2012) Mechanistic investigation on the formation and dehydrogenation of calcium amidoborane ammoniate. *ChemSusChem* 5:927–931
160. Chua YS, Wu G, Xiong Z, Karkamkar A, Guo J, Jian M, Wong MW, Autrey T, Chen P (2010) *Chem Commun* 46:5752–5754
161. Luo J, Kang X, Fang Z, Wang P (2011) Promotion of hydrogen release from ammonia borane with magnesium nitride. *Dalton Trans* 40:6469–6474

Chapter 16

Solid Hydrogen Storage Materials: High Surface Area Adsorbents

Huaiyu Shao and Stephen M. Lyth

Abstract This chapter describes main hydrogen adsorption characteristics and key parameters closely related to the sorption mechanism of high surface area sorbent materials by highlighting two promising materials of nanostructured carbon and metal-organic-frameworks (MOFs).

Keywords Adsorption · Nanostructure · Surface area · Pore size · Binding energy · Spillover · Carbon · MOF · Hydrogen storage

Hydrogen storage via physisorption on high specific surface area materials is a promising field that offers an alternative to chemical storage of hydrogen in hydrides. Sorbents are materials that can adsorb gases or liquids onto their surface via weak van der Waals interactions. This enables more hydrogen to be stored in a given volume compared with the case where no sorbent material is present. Indeed, multiple layers of hydrogen can be physisorbed onto a surface, while chemisorption is limited to a monolayer.

Hydrogen uptake in sorbent materials is dominated by binding energy, temperature, pressure, surface area, and pore-size distribution. Additionally for practical applications, cost is a hugely important factor. The binding energies of pure sorption materials are typically in the range of 5–30 kJ/mol (much lower than in the case of chemisorption), and there is negligible activation energy (whereas significant activation energy must be overcome to form hydrides). Physisorption is therefore highly reversible and hydrogen can be desorbed with ease, compared with chemisorption in which hydrogen is not so easily recovered. The result is that faster charge and discharge rates are observed, thermal management is simplified, charging/discharging efficiencies are high, and the engineering aspects of the

H. Shao (✉) · S.M. Lyth
International Institute for Carbon-Neutral Energy Research, Kyushu University,
Fukuoka 819-0395, Japan
e-mail: h.shao@i2cner.kyushu-u.ac.jp

S.M. Lyth
e-mail: lyth@i2cner.kyushu-u.ac.jp

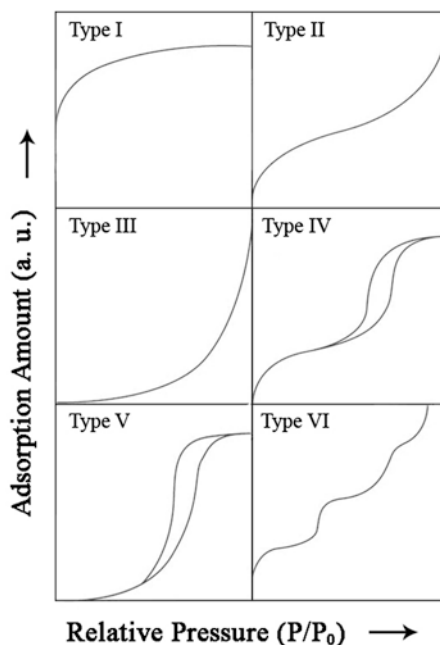
system are simplified. The above factors can potentially lead to a significant cost reduction if sorbent-based hydrogen storage systems are utilized. However, due to the low binding energy, physisorption generally requires large surface area and low temperature in order to adsorb useful amounts of hydrogen.

16.1 Adsorption Isotherms

The dependence of the amount of adsorbed gas on the partial pressure at fixed temperature is called an *adsorption isotherm*. There are six main types of isotherm classified by IUPAC [1, 2], the features of which are determined by the pore size and surface properties of the materials (Fig. 16.1).

- Type I: Microporous adsorbents (e.g. N_2 on activated carbon). Saturation is observed at high relative pressure.
- Type II: Nonporous adsorbents. After monolayer coverage, multilayer adsorption is observed at high relative pressure.
- Type III: Nonporous adsorbents with weak binding energy. Low adsorption is observed at low relative pressure.
- Type IV: Mesoporous adsorbents. Hysteresis is observed, resulting from capillary condensation.

Fig. 16.1 Six typical examples of physisorption isotherms for different adsorbents. P_0 is the saturation pressure of adsorbate gas at the measurement temperature. Type I (microporous); Type II (nonporous); Type III (weak adsorption); Type VI (mesoporous); Type V (mesoporous with weak adsorption); and Type VI (multilayer adsorption) [1, 2]



- Type V: Mesoporous adsorbents with weak binding energy. Hysteresis and low adsorption at low relative pressure is observed.
- Type VI: Nonporous adsorbents with homogeneous surface. Formation of multiple monolayers is observed.

Hydrogen storage on sorbent materials is a highly active field of research. In 2010, the U. S. Department of Energy (DOE) Hydrogen Sorption Center of Excellence (HSCoE) published the findings of a seminal 5-year project to develop sorbent materials for hydrogen storage [3]. Four important sorption mechanisms were identified: (1) nanostructure, (2) heteroatom substitution, (3) coordinated metal centers, and (4) spillover. In particular, two promising materials with high potential were highlighted for further development; nanostructured carbon, and metal-organic-frameworks (MOFs).

16.2 Nanostructured Carbon

Carbons have been a popular choice as hydrogen sorption materials due to their low cost, abundance, stability, varied microstructure, large surface area, and the low atomic mass. However, the very low binding energy between hydrogen gas molecules and the pure carbon surface necessitates the use of relatively low cryogenic temperatures, higher relative pressures, and specific surface area in excess of 3000 m²/g in order to satisfy DOE targets for on-board hydrogen storage [3]. Additionally, the pore size is of crucial importance, and should be large enough to be accessible to dihydrogen, but not so large as to reduce the bulk density and lower the volumetric capacity. The optimal pore size should therefore be in the range 0.6–0.8 nm [4, 5].

16.2.1 Nanostructure

One of the most crucial aspects of optimizing hydrogen adsorption on carbon is the surface area and pore size [6, 7]. There is a simple relationship between surface area of carbon and uptake capacity at 77 K, which states that for every 500 m²/g of surface area measured by nitrogen adsorption, the hydrogen uptake capacity will be 1 wt% (the Chahine rule) [8]. If a monolayer of hydrogen were physisorbed on both sides of a graphene sheet, the gravimetric capacity would be 6.6 wt% [9]. Therefore, maximizing the surface area is of paramount importance. There are many different varieties of carbon, from graphite with very low available surface area, to activated or templated carbons with extremely large surface area. In terms of hydrogen sorption, carbon nanotubes [10–14], activated carbons [8, 15–18], carbon aerogels [19, 20], carbon blacks [21], carbon nanohorns [22], templated carbons [23, 24], and graphene [25–29] have been studied as potentially useful powders for physisorption. One of the best results to date is on zeolite-templated

carbon with a surface area of 3189 m²/g, and hydrogen uptake of 6.9 wt% at 77 K and 2 MPa [24].

Graphene (a term here encompassing single layer graphene, few layer graphene, reduced graphene oxide and related graphenic materials) is particularly interesting since it is a single atomically thin layer of carbon, and therefore there is a large available surface area for hydrogen adsorption. However, in practice it is difficult to obtain single-layer graphene materials at the scale required for hydrogen uptake measurements. High quality, single-layer graphene is generally grown on a substrate, whereas freestanding graphene powders are required for hydrogen storage. Such powders can now be produced at sufficient scale by exfoliation via sonication, or sheer force. However, the surface area is generally relatively low in commercially available graphene powders. This is due to an effect called restacking, in which the individual graphene sheets tend to stick back together forming multilayer structures. Graphene has emerged as one of the best hydrogen adsorption materials, especially at low temperature.

In theoretical studies, Patchkovskii et al. [30] first calculated that the hydrogen storage capacity of perfect isolated graphene sheets is 4 wt% at 10 MPa and room temperature; and 6.5 wt% at 200 K and 5 MPa. Few experimental results have been published on the hydrogen adsorption properties of graphene. Cunning et al. synthesized few-layer graphene powder via combustion of Mg metal in CO₂. This material had a surface area of 235.5 m²/g and resulted in an excess hydrogen uptake of 0.9 wt% at ambient temperature (30 MPa) and 0.85 wt% at 77 K (6.5 MPa) [25]. Jin et al. tailored the spacing between graphene sheets (and thereby the pore size and surface area) via chemical functionalization. This resulted in a maximum hydrogen storage capacity of 1.4 wt% at 77 K and 0.2 MPa [31]. Rapid thermal expansion of graphite oxide followed by activation was used by Klechikov et al. to produce graphene-like material with surface area of up to 2300 m²/g. The hydrogen uptake was 1 wt% at ambient temperature (12 MPa) and 5 wt% at 77 K (12 MPa) [6]. Similar work by a different group resulted in 4.8 wt% at 77 K (9 MPa) and 0.5 wt% at ambient temperature (9 MPa) [4]. Lyth et al. produced graphene powder at gram scale via a low-cost, template-free method. The three-dimensional open-cell porous structure led to a large surface area of 1650 m²/g (Fig. 16.2). The excess hydrogen uptake at 77 K was 2.1 wt% [32]. Ultimately, the surface area of graphene powder materials needs to be increased and the cost needs to come down significantly for it to be used commercially in hydrogen storage applications.

16.2.2 Binding Energy

While tailoring the nanostructure of carbon can enhance hydrogen uptake to a point, the low binding energy fundamentally limits uptake. Although there are some advantages in the low binding energy associated with physisorption, it also means that less hydrogen can be stored at nominal temperature and pressure. Increasing the binding energy slightly to, e.g., 10–40 kJ/mol is therefore desirable. Pure carbon

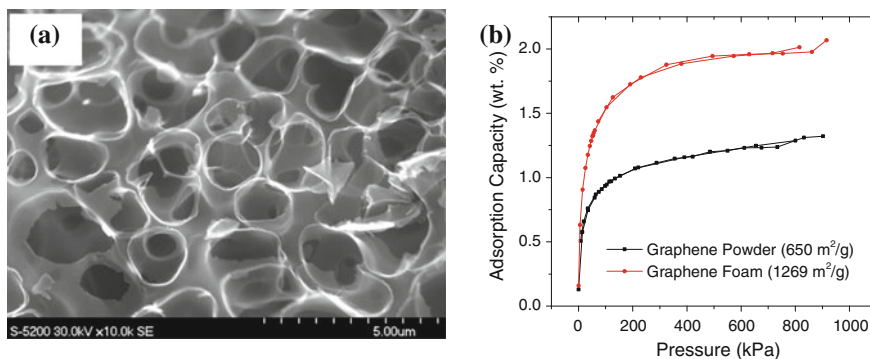


Fig. 16.2 a Porous graphene foam with large surface area produced by decomposition of sodium ethoxide. b Hydrogen uptake isotherm [32]

presents a homogeneous sp^2 lattice to the hydrogen molecule. Substituting some carbon atoms with heteroatoms (such as boron or nitrogen) induces inhomogeneity and therefore enhanced electronic interactions with the target hydrogen molecule. This is manifested as an increase in binding energy. The 2010 DOE report on hydrogen sorption concluded that boron-substitution in the carbon lattice was the only heteroatom to have a positive effect on uptake measurements [3]. Boron doping has been shown to improve hydrogen uptake in various theoretical studies [33, 34], but very few experimental works. For example, Chung et al. [35] demonstrated higher binding energy of ca. 11 kJ/mol, higher than the 4 kJ/mol reported on most carbon surfaces. Despite the DOE findings, nitrogen doping has also been shown to be effective in increasing hydrogen uptake capacity [36–39].

16.2.3 Strong Binding on Metal Sites

If the binding energy is further increased, multiple hydrogen molecules can be absorbed onto a single site via forward- and back-electron donation between the carbon and the hydrogen. This results in binding energies in the range of 20–120 kJ/mol [5, 40]. Metal atoms coordinated to the carbon lattice can be utilized to achieve this effect. Although much theoretical work has been done in this area [26, 29, 41, 42], very little has been verified experimentally, possibly due to the difficulty of obtaining stable metal sites without contamination.

16.2.4 Spillover

In general, physisorption is a precursor to chemisorption processes. The co-existence of these two processes is the basis of the useful spillover phenomenon.

Since spillover is relatively reversible compared to standard chemisorption, it is included here for completion. In this case, a catalyst on the carbon surface reversibly dissociates hydrogen molecules into atomic hydrogen, which then forms C–H bonds. The maximum amount of hydrogen that could be adsorbed onto the surface of a graphene sheet in this case is 8.3 wt% (compared with 6.6 wt% for physisorption) [5]. In general, metal catalyst nanoparticles such as Pt or Ni are utilized, although there is a trade-off in that these are relatively heavy (and expensive) elements. The major advantage of spillover is that it works well at ambient temperature. Spillover has been investigated in graphene-based systems with varying results. A capacity of 1.2 wt% at room temperature and 3.2 MPa was measured in Pt and Pd-decorated graphene [43]. Pd-decorated reduced graphene oxide increased the storage capacity from 0.6–2.5 wt% at 3 MPa and ambient temperature [44]. Recently, this concept has been taken to the extreme and hydrogen chemisorption in graphene has been achieved via Birch reduction, resulting in 5 wt% hydrogen stored stably as graphene [45]. Similarly, the Benkeser reaction was used on graphene to achieve a reported 14.67 wt% hydrogen, although this is much higher than the theoretical limit [46].

In conclusion, increasing surface area alone is not sufficient to meet the required uptake capacities for nanostructured carbon materials. Doping carbon with nitrogen or boron can be used to increase binding energy and therefore increase the hydrogen uptake capacity. Third, metal centers can be used to bind multiple hydrogen molecules on single adsorption sites. Finally, the spillover effect can form strong C–H bonds further by increasing uptake. Combining these different mechanisms via suitable chemical engineering of carbon may lead to the mass production of hydrogen sorption materials with capacities suitable for practical applications.

16.3 Metal Organic Frameworks (MOFs)

MOFs, or porous coordination polymers (PCPs), are an emerging material and one of the youngest classes of porous materials. MOFs are built from metal-containing nodes as secondary building units and organic ligands as linkers [47]. Due to the extremely high-specific surface area and chemically tunable structures in this type of material, MOFs have attracted great attention as hydrogen storage materials, and hydrogen storage on MOFs is a physical adsorption process. Therefore, the hydrogen adsorption capacity is much higher at cryogenic temperature than at room temperature. The hydrogen adsorption process on MOFs is totally reversible with fast kinetics. Research on MOFs as possible hydrogen storage solutions has been financially supported by the US DOE for a long period [48–50].

The first study of hydrogen storage on MOFs was performed by the Yaghi group in 2003 [51] (Fig. 16.3). This group also reported one of the MOFs with the highest specific surface area measured to date, MOF-210, with Brunauer-Emmett-Teller (BET) and Langmuir surface areas of 6240 and 10,400 m²/g, respectively [52]. So far, the best hydrogen storage capacity has been recorded in MOF-177 (Zn₄O

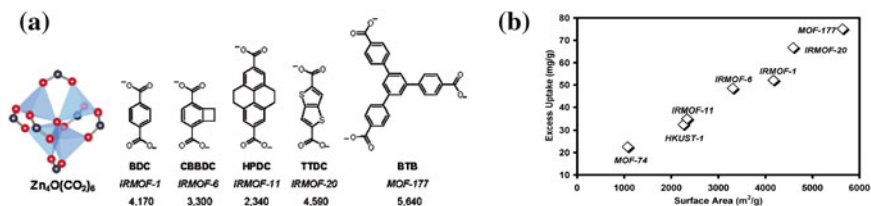


Fig. 16.3 **a** Zn₄O(CO₂)₆-based MOFs in italics derived from the link in parentheses: IRMOF-1 (BDC), IRMOF-6 (CBBDC), IRMOF-11 (HPDC), IRMOF-20 (TTDC), and MOF-177 (BTB). The numbers are Langmuir surface area (m²/g). **b** Hydrogen uptake amount against Langmuir surface area [53] (used with permission from American Chemical Society, Copyright 2006)

(CO₂)₆ clusters with benzene tribenzoate linkers) with a Langmuir surface area of 5640 m²/g and a hydrogen adsorption capacity of 7.6 wt% (32 g/L) at 77 K, under a hydrogen pressure up to 6.6 MPa [53] (Fig. 16.3). These numbers were also confirmed independently by gravimetric and volumetric methods [54]. The absolute hydrogen uptake is around 11 wt% at 77 K under a hydrogen pressure of 7 MPa including both the excess adsorption amount and the part of hydrogen gas molecules occupying the voids inside the MOF-177 sample.

Although these MOFs show impressive hydrogen storage capacities, these compounds still face several challenges before they can be really commercialized. These challenges include gravimetric and volumetric capacities for the system, hydrogen binding energy of materials and scaling-up of synthesis of MOFs for future applications. Great efforts have been taken to further improve the hydrogen uptake capacity, especially at ambient temperature. Here, several strategies adopted by researchers in order to improve hydrogen storage performance in MOFs, especially at ambient temperature are introduced [55, 56].

16.3.1 Surface Area and Pore Volume

For MOFs, there is a positive relationship between surface area of the material and the pore volume of the samples. Since, hydrogen adsorption is on the surface of the MOFs compounds, large surface area and pore volume are essential for MOFs to achieve high hydrogen adsorption capacity.

16.3.2 Pore Size and Geometry

Hydrogen adsorption is by weak van der Waals forces between hydrogen molecules and MOFs compounds. Therefore, the hydrogen adsorption capacity is greatly related to the pore sizes of the MOFs samples. Calculation shows that the optimum

pore size for good hydrogen adsorption performance at 77 K will be around 7 Å, in which case two layers of hydrogen molecules will be adsorbed on the pore surface of MOFs samples [57, 58].

16.3.3 Open Metal Sites

The interaction between hydrogen molecules and inorganic (usually metal) nodes is much stronger than between hydrogen and organic linkers. Structural analysis of MOF-5 shows that metal nodes usually are the first adsorption sites for hydrogen storage. This brings an approach of design of unsaturated metal sites in order to enhance the hydrogen uptake ability. These sites may help the hydrogen binding and retain high hydrogen uptake capacity even under low hydrogen pressures.

16.3.4 Catenation

Catenation is a method to form interweaving or interpenetrating networks from two different MOFs. The direct effects resulting from the catenation process include simultaneously decrease of pore size, increase of open metal sites, and reduction of pore volume. Therefore, whether catenation is a practical method for improvement of hydrogen adsorption performance on MOFs depends much on the specific MOFs cases and the measurement conditions for hydrogen adsorption.

Besides research on MOFs for hydrogen storage application, some other potential applications [47] for MOFs include energy transfer and photocatalysis, heterogeneous catalysis, proton and ion conductors [59, 60], liquid separation and purification, gas capture and degradation, gas storage (methane, CO₂), etc.

References

1. Brunauer S, Deming LS, Deming WE, Teller E (1940) On a theory of the van der Waals adsorption of gases. *J Am Chem Soc* 62:1723–1732
2. Sing KSW, Everett DH, Haul RAW, Moscou L, Pierotti RA, Rouquerol J, Siemieniewska T (1985) Reporting physisorption data for gas solid systems with special reference to the determination of surface-area and porosity (Recommendations 1984). *Pure Appl Chem* 57:603–619
3. Simpson L (2010) HSCoE final report executive summary. http://www1.eere.energy.gov/hydrogenandfuelcells/pdfs/hydrogen_sorption_coe_final_report.pdf. Accessed 27 Oct 2015
4. Kim BH, Hong WG, Yu HY, Han YK, Lee SM, Chang SJ, Moon HR, Jun Y, Kin HJ (2012) Thermally modulated multilayered graphene oxide for hydrogen storage. *Phys Chem Chem Phys* 14:1480–1484

5. Tozzini V, Pellegrini V (2013) Prospects for hydrogen storage in graphene. *Phys Chem Chem Phys* 15:80–89
6. Klechikov AG, Mercier G, Merino P, Blanco S, Merino C, Talyzin AV (2015) Hydrogen storage in bulk graphene-related materials. *Microporous Mesoporous Mater* 210:46–51
7. Dillon AC, Heben MJ (2001) Hydrogen storage using carbon adsorbents: past, present and future. *Appl Phys A* 72:133–142
8. Bénard P, Chahine R (2007) Storage of hydrogen by physisorption on carbon and nanostructured materials. *Scr Mater* 56:803–808
9. Schlapbach L, Züttel A (2001) Hydrogen-storage materials for mobile applications. *Nature* 414:353–358
10. Dillon AC, Jones KM, Bekkedahl TA, Kiang CH, Bethune DS, Heben MJ (1997) Storage of hydrogen in single-walled carbon nanotubes. *Nature* 386:377–379
11. Liu C (1999) Hydrogen storage in single-walled carbon nanotubes at room temperature. *Science* 286:1127–1129
12. Cheng HM, Yang QH, Liu C (2001) Hydrogen storage in carbon nanotubes. *Carbon* 39:1447–1454
13. Darkrim FL, Malbrunot P, Tartaglia GP (2002) Review of hydrogen storage by adsorption in carbon nanotubes. *Int J Hydrogen Energy* 27:193–202
14. Wang Q, Johnson JK (1999) Optimization of carbon nanotube arrays for hydrogen adsorption. *J Phys Chem B* 103:4809–4813
15. Wang H, Gao Q, Hu J (2009) High hydrogen storage capacity of porous carbons prepared by using activated carbon. *J Am Chem Soc* 131:7016–7022
16. Jordá-Beneyto M, Suárez-García F, Lozano-Castelló D, Cazorla-Amorós D, Linares-Solano A (2007) Hydrogen storage on chemically activated carbons and carbon nanomaterials at high pressures. *Carbon* 45:293–303
17. Noh J, Agarwal R, Schwarz J (1987) Hydrogen storage systems using activated carbon. *Int J Hydrogen Energy* 12:693–700
18. de la Casa-Lillo MA, Lamari-Darkrim F, Cazorla-Amorós D, Linares-Solano A (2002) Hydrogen storage in activated carbons and activated carbon fibers. *J Phys Chem B* 106:10930–10934
19. Tian HY, Buckley CE, Wang SB, Zhou MF (2009) Enhanced hydrogen storage capacity in carbon aerogels treated with KOH. *Carbon* 47:2128–2130
20. Kabbour H, Baumann TF, Satcher JH, Saulnier A, Ahn CC (2006) Toward new candidates for hydrogen storage: high-surface-area carbon aerogels. *Chem Mater* 18:6085–6087
21. Hynek S (1997) Hydrogen storage by carbon sorption. *Int J Hydrogen Energy* 22:601–610
22. Tanaka H, Kanoh H, Yudasaka M, Iijima S, Kaneko K (2005) Quantum effects on hydrogen isotope adsorption on single-wall carbon nanohorns. *J Am Chem Soc* 127:7511–7516
23. Nishihara H, Hou PX, Li LX, Ito M, Uchiyama M, Kaburagi T, Ikura A, Katamura J, Kawarada T, Mizuuchi K, Kyotani T (2009) High-pressure hydrogen storage in zeolite-templated carbon. *J Phys Chem C* 113:3189–3196
24. Yang Z, Xia Y, Mokaya R (2007) Enhanced hydrogen storage capacity of high surface area zeolite-like carbon materials. *J Am Chem Soc* 129:1673–1679
25. Cuning BV, Pyle DS, Merritt CR, Brown CL, Webb CJ, Gray EMA (2014) Hydrogen adsorption characteristics of magnesium combustion derived graphene at 77 and 293 K. *Int J Hydrogen Energy* 39:6783–6788
26. Wang L, Lee K, Sun YY, Lucking M, Chen Z, Zhao JJ, Zhang SB (2009) Graphene oxide as an ideal substrate for hydrogen storage. *ACS Nano* 3:2995–3000
27. Yuan W, Li B, Li L (2011) A green synthetic approach to graphene nanosheets for hydrogen adsorption. *Appl Surf Sci* 257:10183–10187
28. Ma LP, Wu ZS, Li J, Wu ED, Ren WC, Cheng HM (2009) Hydrogen adsorption behavior of graphene above critical temperature. *Int J Hydrogen Energy* 34:2329–2332
29. Dimitrakakis GK, Tylianakis E, Froudakis GE (2008) Pillared graphene: a new 3-D network nanostructure for enhanced hydrogen storage. *Nano Lett* 8:3166–3170

30. Patchkovskii S, Tse JS, Yurchenko SN, Zhechkov L, Heine T, Seifert G (2005) Graphene nanostructures as tunable storage media for molecular hydrogen. *Proc Natl Acad Sci* 102:10439–10444
31. Jin Z, Lu W, O'Neill KJ, Parilla PA, Simpson LJ, Kittrell C, Tour JM (2011) Nano-engineered spacing in graphene sheets for hydrogen storage. *Chem Mater* 23:923–925
32. Lyth SM, Shao H, Liu J, Sasaki K, Akiba E (2014) Hydrogen adsorption on graphene foam synthesized by combustion of sodium ethoxide. *Int J Hydrogen Energy* 39:376–380
33. Li J, Wang X, Liu K, Sun Y, Chen L (2012) High hydrogen-storage capacity of B-adsorbed graphene: first-principles calculation. *Solid State Commun* 152:386–389
34. Zhou YG, Zu XT, Gao F, Nie JL, Xiao HY (2009) Adsorption of hydrogen on boron-doped graphene: a first-principles prediction. *J Appl Phys* 105:014309
35. Chung TCM, Jeong Y, Chen Q, Kleinhammes A, Wu Y (2008) Synthesis of microporous boron-substituted carbon (b/c) materials using polymeric precursors for hydrogen physisorption. *J Am Chem Soc* 130:6668–6669
36. Jiang J, Gao Q, Zheng Z, Xia K, Hu J (2010) Enhanced room temperature hydrogen storage capacity of hollow nitrogen-containing carbon spheres. *Int J Hydrogen Energy* 35:210–216
37. Yang SJ, Cho JH, Oh GH, Nahm KS, Park CR (2009) Easy synthesis of highly nitrogen-enriched graphitic carbon with a high hydrogen storage capacity at room temperature. *Carbon* 47:1585–1591
38. Badzian A, Badzian T, Breval E, Piotrowski A (2001) Nanostructured, nitrogen-doped carbon materials for hydrogen storage. *Thin Solid Films* 398–399:170–174
39. Chen L, Xia K, Huang L, Li L, Pei L, Fei S (2013) Facile synthesis and hydrogen storage application of nitrogen-doped carbon nanotubes with bamboo-like structure. *Int J Hydrogen Energy* 38:3297–3303
40. Kubas GJ (2001) Metal–dihydrogen and σ -bond coordination: the consummate extension of the Dewar–Chatt–Duncanson model for metal–olefin π bonding. *J Organomet Chem* 635: 37–68
41. Lee H, Ihm J, Cohen ML, Louie SG (2010) Calcium-decorated graphene-based nanostructures for hydrogen storage. *Nano Lett* 10:793–798
42. Ataca C, Aktürk E, Ciraci S (2009) Hydrogen storage of calcium atoms adsorbed on graphene: first-principles plane wave calculations. *Phys Rev B* 79:041406
43. Parambath VB, Nagar R, Ramaprabhu S (2012) Effect of nitrogen doping on hydrogen storage capacity of palladium decorated graphene. *Langmuir* 28:7826–7833
44. Parambath VB, Nagar R, Sethupathi K, Ramaprabhu S (2011) Investigation of spillover mechanism in palladium decorated hydrogen exfoliated functionalized graphene. *J Phys Chem C* 115:15679–15685
45. Subrahmanyam KS, Kumar P, Maitra U, Govindaraj A, Hembram KPSS, Waghmare UV, Rao CNR (2011) Chemical storage of hydrogen in few-layer graphene. *Proc Natl Acad Sci* 108:2674–2677
46. Sarkar AK, Saha S, Ganguly S, Banerjee D, Kargupta K (2014) Hydrogen storage on graphene using Benkeser reaction. *Int J Energy Res* 38:1889–1895
47. Zhou HC, Kitagawa S (2014) Metal-organic frameworks (MOFs). *Chem Soc Rev* 43: 5415–5418
48. http://www.hydrogen.energy.gov/pdfs/review06/st_22_yaghi.pdf. Accessed 21 April 2015
49. http://www.hydrogen.energy.gov/pdfs/review09/st_33_doonan.pdf. Accessed 21 April 2015
50. http://www.hydrogen.energy.gov/pdfs/progress14/iv_b_7_veenstra_2014.pdf. Accessed 21 April 2015
51. Rosi NL, Eckert J, Eddaoudi M, Vodak DT, Kim J, O'Keeffe M, Yaghi OM (2003) Hydrogen storage in microporous metal-organic frameworks. *Science* 300:1127–1129
52. Furukawa H, Ko N, Go YB, Aratani N, Choi SB, Choi E, Yazaydin AO, Snurr RQ, O'Keeffe M, Kim J, Yaghi OM (2010) Ultrahigh porosity in metal-organic frameworks. *Science* 329:424–428
53. Wong-Foy AG, Matzger AJ, Yaghi OM (2006) Exceptional H₂ saturation uptake in microporous metal-organic frameworks. *J Am Chem Soc* 128:3494–3495

54. Furukawa H, Miller MA, Yaghi OM (2007) Independent verification of the saturation hydrogen uptake in MOF-177 and establishment of a benchmark for hydrogen adsorption in metal-organic frameworks. *J Mater Chem* 17:3197–3204
55. Zhao D, Yuan DQ, Zhou HC (2008) The current status of hydrogen storage in metal-organic frameworks. *Energy Environ Sci* 1:222–235
56. Sculley J, Yuan DQ, Zhou HC (2011) The current status of hydrogen storage in metal-organic frameworks—updated. *Energy Environ Sci* 4:2721–2735
57. Rzepka M, Lamp P, de la Casa-Lillo MA (1998) Physisorption of hydrogen on microporous carbon and carbon nanotubes. *J Phys Chem B* 102:10894–10898
58. Murray LJ, Dinca M, Long JR (2009) Hydrogen storage in metal-organic frameworks. *Chem Soc Rev* 38:1294–1314
59. Sadakiyo M, Yamada T, Honda K, Matsui H, Kitagawa H (2014) Control of crystalline proton-conducting pathways by water-induced transformations of hydrogen-bonding networks in a metal-organic framework. *J Am Chem Soc* 136:7701–7707
60. Sadakiyo M, Kasai H, Kato K, Takata M, Yamauchi M (2014) Design and synthesis of hydroxide ion-conductive metal-organic frameworks based on salt inclusion. *J Am Chem Soc* 136:1702–1705

Chapter 17

Liquid Hydrogen Carriers

Hai-Wen Li

Abstract This chapter describes key technologies for typical liquid hydrogen carriers, including the liquefaction process and storage vessel of liquid hydrogen, de-/re-hydrogenation properties of cycloalkane and heterocycle-based organic hydrides, as well as production process and thermal decomposition of ammonia.

Keywords Hydrogen carrier · Liquid hydrogen · Liquefaction · Organic hydride · Ammonia · Hydrogen storage

17.1 Liquid Hydrogen

Liquid hydrogen is a cryogenic hydrogen storage technology. Hydrogen cannot be liquefied above the critical point (30 K) and liquid hydrogen can be stored at 21.2 K at ambient pressure. The volume of gaseous hydrogen at ambient temperature and pressure can be reduced to 1/800 by liquefaction. However, around 1/3 of the heating value ($33.33 \text{ kWh kg}^{-1}$) that hydrogen possesses will be consumed by the liquefaction process. Since the boil-off losses due to heat leakage are proportional to the ratio of surface area to volume, liquid hydrogen had the greatest advantages in large-scale storage. Liquid hydrogen, therefore, was considered as a promising energy carrier to realize a hydrogen economy by the World Energy Network (WE-NET, see Fig. 17.1) project carried out from 1993 to 2002 [1]. Furthermore, liquid hydrogen has been widely used in space exploration.

H.-W. Li (✉)

International Research Center for Hydrogen Energy, Kyushu University, Fukuoka 819-0395, Japan

e-mail: li.haiwen.305@m.kyushu-u.ac.jp

© Springer Japan 2016

K. Sasaki et al. (eds.), *Hydrogen Energy Engineering*,

Green Energy and Technology, DOI 10.1007/978-4-431-56042-5_17

253

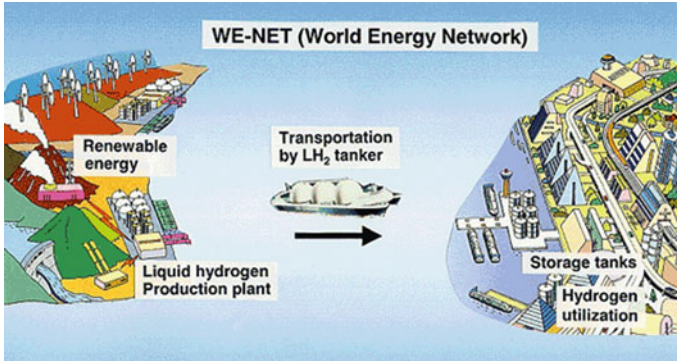


Fig. 17.1 World energy network concept in which liquid hydrogen is considered as an energy carrier for large-scale transportation [1]

17.1.1 The Joule–Thomson Effect

The Joule–Thomson effect, widely used in the liquefaction process of gases, describes the temperature change that accompanies expansion of a gas without production of work or transfer of heat with the environment. The Joule–Thomson effect depends crucially on the interactions between gas molecules, therefore, such effect is not observed for the ideal gases at all. At ambient temperature, all real gases except hydrogen, helium, and neon cool upon such expansion.

The coefficient, i.e., the rate of change of temperature with respect to pressure, in a Joule–Thomson process (at constant enthalpy) can be expressed as

$$\mu \equiv \left(\frac{\partial T}{\partial P} \right)_H = \frac{V}{C_p} (T\alpha - 1) \quad (17.1)$$

where T is the temperature, P is the pressure, V is the volume, C_p is the heat capacity at constant pressure, and α is the thermal expansion coefficient. For any given pressure, only when $\mu > 0$, i.e., below the inversion temperature (202 K for hydrogen, see Fig. 17.2), the Joule–Thomson expansion causes cooling. Before the first expansion step occurs, hydrogen is usually precooled using liquid nitrogen (77 K).

17.1.2 Liquefaction Process

The simplest liquefaction cycle is the Joule–Thomson cycle (Linde cycle, Fig. 17.3) [2]. In this process, hydrogen gas is first compressed, and then cooled in a heat exchanger using liquid nitrogen to below its inversion temperature (202 K),

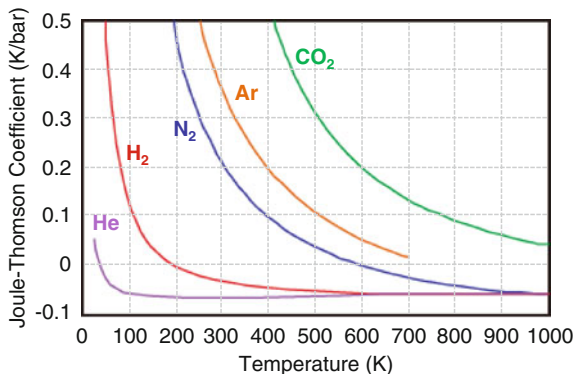


Fig. 17.2 Joule–Thomson coefficients for various gases at atmospheric pressure

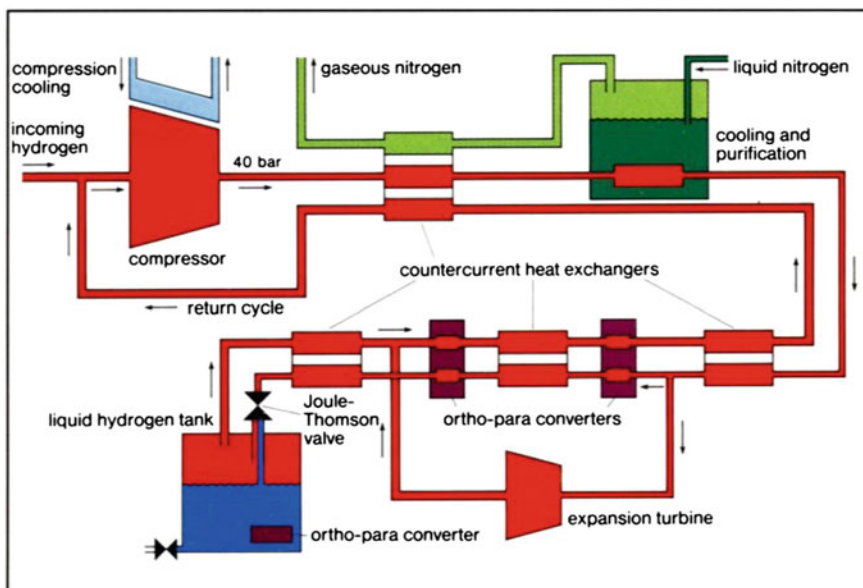


Fig. 17.3 The Joule–Thomson cycle (Linde cycle) [2]

before it passes through a throttle valve where it undergoes a Joule–Thomson expansion, producing some liquid hydrogen. The cooled hydrogen gas is separated from the liquid and returned to the compressor via the heat exchanger [2]. It is worth emphasizing that the conversion of orthohydrogen to parahydrogen is included in the liquefaction process, in order to minimize the storage boil-off losses caused by the heat released from the ortho-para-hydrogen conversion.

17.1.3 Storage Vessel

A liquid hydrogen tank usually consists of an inner vessel and an outer vessel, with an insulation vacuum layer inbetween, as shown in Fig. 17.4 [3]. The vacuum layer is of crucial importance to prevent heat transfer into tank via conduction, convection, and radiation. An approach to reduce heat transfer from the high temperature surface of the outer tank is to insert thin aluminum spacers with a thickness of 100 μm , or aluminum-evaporated films having a high reflection factor, with a thickness of 10 μm [4]. Nevertheless, boil-off is inevitable due to the inward heat leakage, which results in an increase in pressure. The liquid hydrogen tank must be equipped with a pressure relief system and safety valve. Boil-off losses can be diminished by using a larger storage vessel with lower surface-area-to-volume ratio [5]. In February 2014, Kawasaki Heavy Industries, Ltd. announced that it obtained approval in principle (AiP) from the Nippon Kaiji Kyokai, one of the major

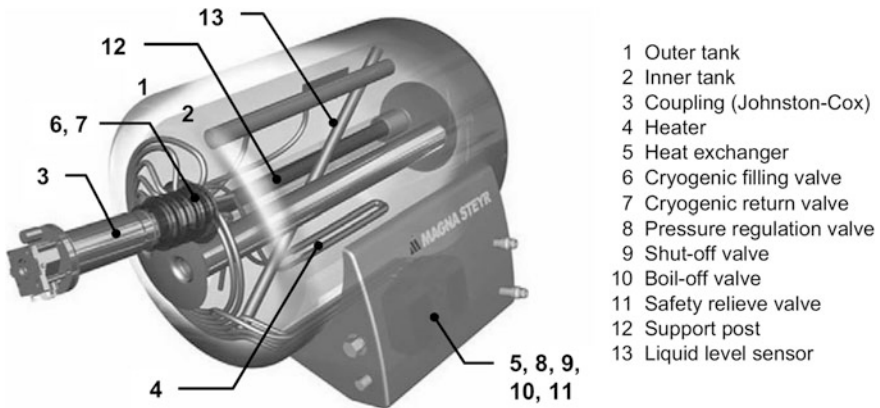


Fig. 17.4 Liquid hydrogen tank [3] (used with permission from Elsevier, Copyright 2009)

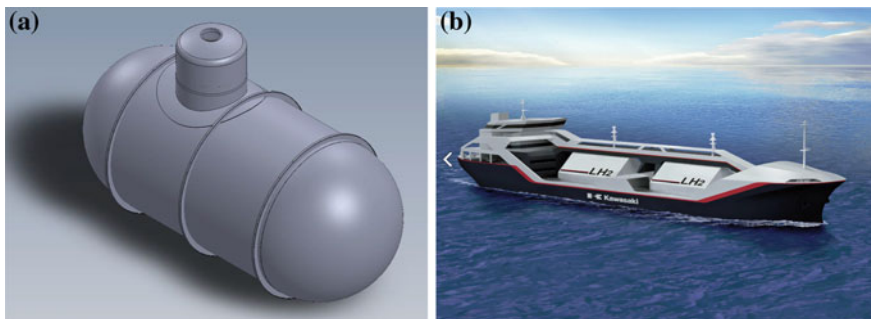


Fig. 17.5 **a** Liquefied hydrogen carrier cargo containment system, and **b** ship carrying liquefied gases in bulk (total carrying capacity: 2500 m^3) [6]

Classification Societies in the world also known as ClassNK, for its new cargo containment system (CCS) for ships that carry liquefied hydrogen in bulk. The CCS, which is equipped with a pressure build-up (accumulation) system, has a capacity to store 1250 m³ of cryogenic liquefied hydrogen (see Fig. 17.5) [6].

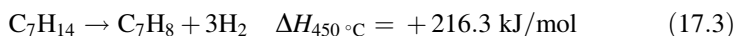
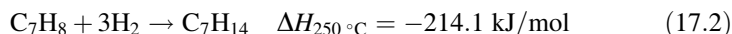
17.2 Organic Hydrides

Liquid organic hydrogen carriers (LOHCs) use unsaturated organic compounds to store hydrogen at ambient temperature. For example, toluene (C₇H₈) can be hydrogenated to form methylcyclohexane (MCH: C₇H₁₄), which can be returned back to toluene by dehydrogenation and reused. The idea of using methylcyclohexane as a recyclable liquid carrier in automotive applications was first proposed by Sultan and Shaw in 1975. However, at that time the method was not favorable compared to gasoline systems [7]. LOHC, like toluene, is a component of gasoline, therefore, is able to be transported using current infrastructure such as chemical tankers, suggesting advantages for large-scale, long-term, and long-distance hydrogen transport under ambient temperature and pressure.

17.2.1 Cycloalkanes

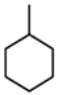
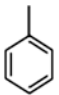


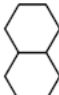

Table 17.1 shows some typical cycloalkane-based organic hydrides systems [8]. One mole of cycloalkane has the potential to store 3–5 mol of hydrogen. The MCH-toluene system exists in a liquid state over a wider temperature range (–95 to 100.9 °C) than cyclohexane-benzene (5.5–80.1 °C) and decalin-naphthalene (naphthalene is solid below 80.3 °C).

The hydrogenation of toluene to MCH proceeds exothermically, and accordingly the dehydrogenation of MCH to toluene is an endothermic reaction, according to following relations.



Hydrogenation of toluene was found to be first order with respect to hydrogen, and of a low fractional order in toluene, increasing slightly with temperature [9]. The hydrogenation was improved at 225 °C under 2.0 MPa of hydrogen using a zirconium-modified hexagonal molecular sieve-supported platinum and palladium catalyst [10]. The endothermic nature makes the dehydrogenation of MCH much more challenging, because it normally occurs between 400 and 500 °C [11]. The dehydrogenation temperature can be reduced to 350 °C using the S(0.8 %)-Pt (1.0 %)/Al₂O₃ catalyst, recently developed by Chiyoda Corporation [8]. In this

Table 17.1 Typical cycloalkane-based organic hydrides systems [8]

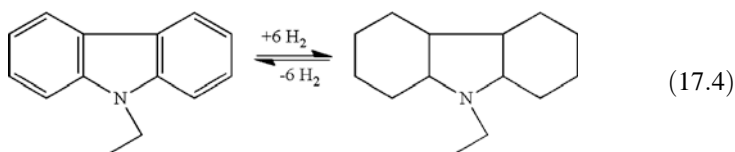
						
	MCH-Toluene		Cyclohexane-Benzene		Decalin-Naphthalene	
Formula	Methylcyclohexane	Toluene	Cyclohexane	Benzene	Decalin	Naphthalene
M.W.	C ₇ H ₁₄	C ₇ H ₈	C ₆ H ₁₂	C ₆ H ₆	C ₁₀ H ₁₈	C ₁₀ H ₈
State at room temp.	98.19	92.14	84.16	78.11	138.25	128.17
Density (g/cm ³)	Liquid	Liquid	Liquid	Liquid	Liquid	Solid
mp. (°C)	0.7694	0.8669	0.7791	0.8737	0.8963	0.9752
	-126.6	-95.0	6.5	5.5	<i>cis</i> : -43.0	80.3
					<i>trans</i> : -30.4	
bp. (°C)	100.9	110.6	81.0	80.1	<i>cis</i> : 194.6	218.0
					<i>trans</i> : 185.5	
Hydrogen storage density (wt%)	6.2		7.2		7.3	
(kg H ₂ /m ³)	47.4		56.0		65.4	

catalyst, Pt clusters (<1 nm) are uniformly impregnated into the alumina support with well-controlled pore size, and the Pt cluster is partially modified by sulfur to prevent coking. This dehydrogenation catalyst is known so far to show the best performance: the MCH conversion yield is greater than 95 %; toluene selectivity is over 99.99 %; and the hydrogen yield is greater than 95 % below 350 °C, 0.3 MPa, and a liquid hourly space velocity (LHSV) of 2.0 h⁻¹ [8].

17.2.2 Heterocycles

In 2006, Pez at Air Products first proposed organic heterocycle hydrides for hydrogen storage [12]. Partial substitution of C in the ring by N could lower the dehydrogenation enthalpy as it significantly reduces the aromaticity of the dehydrogenated molecules [13].

The *N*-ethylcarbazole-perhydro-*N*-ethylcarbazole system is a good example. The fully hydrogenated perhydro-*N*-ethylcarbazole has a hydrogen capacity of 5.8 wt% as shown in Eq. 17.4. The hydrogenation of *N*-ethylcarbazole occurs at 130–160 °C with 7.0 MPa pressure using noble metal catalysts like ruthenium supported on alumina. The dehydrogenation of perhydro-*N*-ethylcarbazole usually occurs at 200–230 °C and pressures slightly above ambient pressure, using the supported Pt or Pd catalysts [14]. The melting point of fully dehydrogenated *N*-ethylcarbazole is 68 °C, i.e., it is a solid at ambient temperature. To achieve full liquid handling, technical solutions such as partial dehydrogenation or blending are necessary, which reduce the overall storage capacity [15].



By substituting the organic CC unit with a BN unit, Liu et al. recently synthesized a 3-Methyl-1,2-BN-cyclopentane compound that is air- and water-stable with a melting point of -18 °C [16]. 3-Methyl-1,2-BN-cyclopentane has a hydrogen density of 4.7 wt% and 42 g H₂/L. Upon heating at 150 °C for 1 h in the absence of solvent, it releases 2 equiv. of H₂ in forming trimer 2, which is a liquid at room temperature (m.p.: 9 °C). Thus this system remains in the liquid phase throughout the process. The dehydrogenation can be significantly enhanced by the addition of 5 mol% of FeCl₂ catalyst, and it proceeds completely at 80 °C within 20 min as a result (see Fig. 17.6). Furthermore, the spent fuel of trimer 2 can be converted back to the charged fuel 1 (3-Methyl-1,2-BN-cyclopentane) with a good yield of 92 % [16].

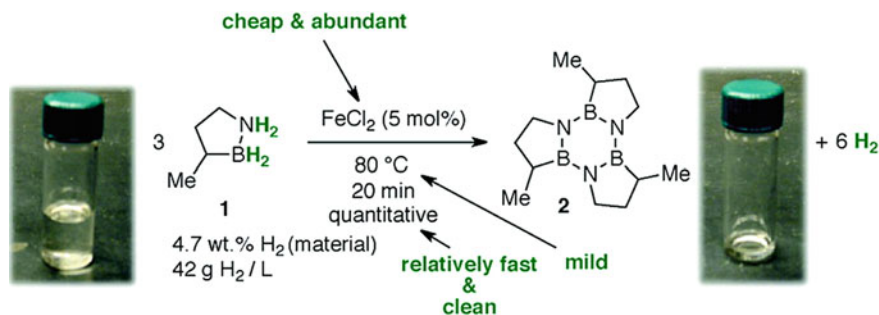


Fig. 17.6 Schematic illustration of the dehydrogenation of 3-Methyl-1,2-BN-cyclopentane [16] (used with permission from American Chemical Society, Copyright 2011)

17.3 Ammonia

Ammonia (NH₃), has been widely used as a precursor for fertilizer and nitrogenous compounds. The idea of using NH₃ as a hydrogen carrier or direct gasoline replacement has been discussed for more than 70 years [17].

17.3.1 Ammonia Properties

Ammonia has several desirable properties for use as a hydrogen (energy) carrier (see Table 17.2). Anhydrous ammonia is easily liquefied under mild condition because of its low vapor pressure of 8.88 bar at 21 °C, which is similar to propane gas. This means that ammonia can be easily stored and transported under moderate pressure using simple, inexpensive pressure vessels. Ammonia contains of 17.65 wt % of hydrogen. A volumetric density of hydrogen in liquid ammonia is about 45 % higher than that of liquid hydrogen [18]. It can be also burned directly to generate electricity without CO₂ emission, converted to electricity in an alkaline fuel cell, or decomposed to provide hydrogen for non-alkaline fuel cells [18].

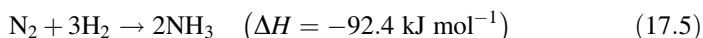
Furthermore, ammonia is easily detectable due to its characteristic pungent smell. Humans can smell anhydrous ammonia at 3–5 ppm that is 100 times lower than the alarmingly labeled “immediately dangerous to life of death” (IDLH) concentration stipulated by the National Institute for Occupational Safety and Health (NIOSH) [17]. In addition, the currently established infrastructures may help largely the widespread application of ammonia as hydrogen carrier.

17.3.2 Ammonia Production

Ammonia is normally produced through catalyzed reaction between hydrogen and nitrogen (see Eq. 17.5), based on the process developed by Haber and Bosch in the 1910s.

Table 17.2 Physical and chemical properties of ammonia [18]

<i>Hydrogen content</i>					
H ₂ weight fraction	17.65	wt%	H ₂ volume density	0.105	kg/l
<i>Solid phase</i>					
Melting point	-78	°C	Latent heat of fusion (1 atm at triple point)	-337.37	kJ/kg
<i>Liquid phase</i>					
Vapor pressure (21 °C)	8.88	bar	Liquid density (1 atm @ boiling point)	682	kg/m ³
Boiling point (@ 1.0 atm)	-33.5	°C	Liquid/gas equivalent (1 atm and 15 °C)	947	vol/vol
Latent heat of vaporization (1 atm @ boiling point)	1371.2	kJ/kg			
Critical temperature	132.4	°C	Critical pressure	112.8	bar
<i>Gas phase</i>					
Gas density (1 atm at boiling point)	0.86	kg/m ³	Gas density (1 atm at 15 °C)	0.73	kg/m ³
Compressibility (Z) (1 atm at 15 °C)	0.9929		Specific gravity (air = 1) (1 atm at 20 °C)	0.597	
Specific volume 1 atm at 20 °C)	1.411	m ³ /kg	Viscosity	0.000098	Poise
Heat capacity at constant pressure (Cp) (1 atm at 15 °C)	0.037	kJ/(mol K)	Heat capacity at constant pressure (Cv) (1 atm at 15 °C)	0.028	kJ/(mol K)
Critical density	0.24	g/ml	Entropy, gas @ 25 °C., 1 atm	45.97	cal/mol °C
Thermal conductivity	22.19	mW/(mK)			
<i>Misc</i>					
Water solubility (1 atm at 0 °C)	862	vol/vol	Autoignition temperature	630	°C
Lower flammable limit in air	15 %	By volume	Upper flammable limit in air	28 %	By volume
Molecular Weight	17.03				



This reaction typically occurs under high pressures of 20–40 MPa at temperatures of 400–600 °C, over a Fe catalyst [18].

Ammonia production, in fact, is coupled with hydrogen production through steam reforming of natural gas. The hydrogen is typically produced from natural

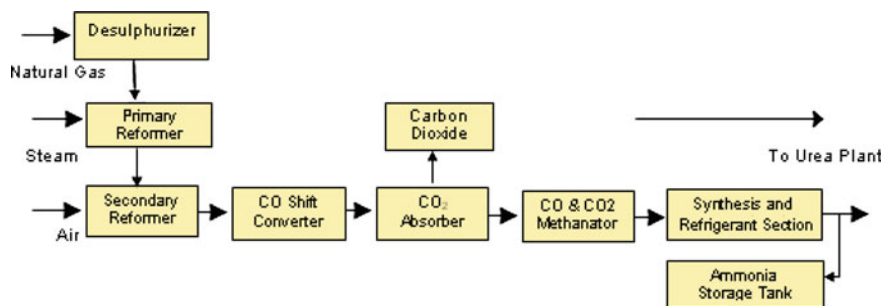
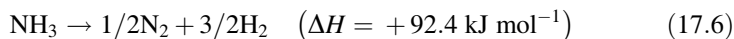


Fig. 17.7 Block flow diagram of the ammonia production processes [19]

gas, but it also can be produced using other sources like coal or coke. The first step of this process (see Fig. 17.7) is the steam reforming of natural gas over a catalyst, providing hydrogen-rich gas. Next, air is added and carefully regulated to provide the exact amount of nitrogen needed for ammonia catalyst. After a series of processes to remove CO and CO₂, the remaining high purity gas (high in nitrogen content) is compressed under extreme pressure and sent to reactor vessel where ammonia is synthesized. The anhydrous ammonia is then liquefied and stored at -33 °C [19].

17.3.3 Ammonia Decomposition

Decomposition of ammonia to produce nitrogen and hydrogen is the reverse reaction of the synthesis.



Due to the endothermic nature, the decomposition temperature largely depends on the catalyst. Among metal catalysts, Ru is the most active for NH₃ decomposition, which requires a temperature above 600 °C [20]. The supported Ni has been widely used in industry but the required temperature is as high as 1000 °C [20].

Recently, sodium amide NaNH₂ was demonstrated as an effective ammonia decomposition catalyst that involves the stoichiometric decomposition and formation of NaNH₂ from Na metal. 90 % NH₃ decomposition efficiency is obtained at 500 °C using NaNH₂, relative to 82 % and 58 % conversion at this temperature using the ruthenium and nickel catalysts, respectively, as shown in Fig. 17.8. This approach represents a significant departure in reaction mechanism compared with traditional surface catalysts [21].

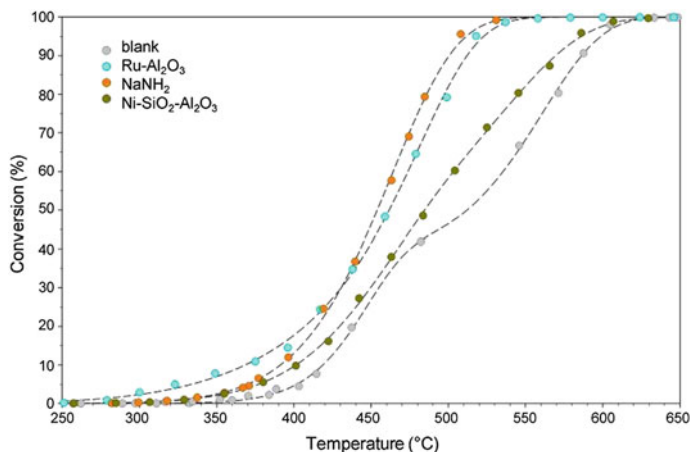


Fig. 17.8 Comparison of NH_3 conversion as a function of reaction temperature (between 250 and 650 °C) for the blank 46.9 cm^3 reactor and 0.5 g of NaNH_2 , silica/alumina-supported nickel, and alumina-supported ruthenium, at an NH_3 flow rate of 60 sccm [21]

References

1. https://www.ena.or.jp/WE-NET/newinfo/station_taka_e.html. Accessed 1 May 2015
2. <http://hydropole.ch/en/hydrogen/storage/>. Accessed 1 May 2015
3. Mori D, Hirose K (2009) Recent challenges of hydrogen storage technologies for fuel cell vehicles. *Int J Hydrogen Energy* 34:4569–4574
4. Hanada T, Takahashi K (2009) Liquid-hydrogen storage. In: Ohta T, Veziroglu TN (eds) *Energy carriers and conversion systems*. UNESCO-EOLSS
5. Züttel A (2003) Materials for hydrogen storage. *Mater Today* 6:24–33
6. http://global.kawasaki.com/en/corp/newsroom/news/detail/20140106_1e.html. Accessed 2 May 2015
7. Sultan O, Shaw M (1975) Study of automotive storage of hydrogen using recyclable chemical carriers. ERDA, Ann Arbor, MI, TEC-75/003
8. Okada Y, Mitsunori S (2013) Development of large-scale H_2 storage and transportation technology with liquid organic hydrogen carrier (LOHC). GCC-JAPAN environment symposia 2013. <https://www.chiyoda-corp.com/technology/files/Joint%20GCC-JAPAN%20Environment%20Symposia%20in%202013.pdf>. Accessed 2 May 2015
9. Karanth NG, Hughes R (1972) The kinetics of the catalytic hydrogenation of toluene. *J appl Chem Bwtechnol* 23:817–827
10. Roy S, Datta S (2013) Hydrogenation of toluene on zirconium-modified hexagonal molecular sieve supported platinum and palladium catalysts. *Ind Eng Chem Res* 52:17360–17368
11. Alhumaidan F, Cresswell D, Garforth A (2011) Hydrogen storage in liquid organic hydride: producing hydrogen catalytically from methylcyclohexane. *Energy Fuels* 25:4217–4234
12. Pez GP, Scott AR, Cooper AC, Cheng H (2006) Hydrogen storage by reversible hydrogenation of pi-conjugated substrates. US Patent 7,101,530, 5 Sep 2006
13. Clot E, Eisenstein O, Crabtree RH (2007) Computational structure–activity relationships in H_2 storage: how placement of N atoms affects release temperatures in organic liquid storage materials. *Chem Commun* 2231–2233
14. Teichmann D, Arlt W, Wasserscheid P, Freymann R (2011) A future energy supply based on liquid organic hydrogen carriers (LOHC). *Energy Environ Sci* 4:2767–2773

15. Zhu Q, Xu Q (2015) Liquid organic and inorganic chemical hydrides for high-capacity hydrogen storage. *Energy Environ Sci* 8:478–512
16. Luo W, Campbell PG, Zakharov LN, Liu S-Y (2011) A single-component liquid-phase hydrogen storage material. *J Am Chem Soc* 133:19326–19329
17. Ammonia. <http://www.elucidare.co.uk/news/Ammonia%20as%20H2%20carrier.pdf>. Accessed 2 May 2015
18. Potential roles of ammonia in a hydrogen economy. http://www.hydrogen.energy.gov/pdfs/nh3_paper.pdf. Accessed 2 May 2015
19. <http://www.safco.com.sa/en/products/ammonia>. Accessed 2 May 2015
20. Yin SF, Xu BQ, Zhou XP, Au CT (2004) A mini-review on ammonia decomposition catalysts for on-site generation of hydrogen for fuel cell applications. *Appl Catal A Gen* 277:1–9
21. David WIF, Makepeace JW, Callear SK, Hunter HMA, Taylor JD, Wood TJ, Jones MO (2014) Hydrogen production from ammonia using sodium amide. *J Am Chem Soc* 136:13082–13085

Chapter 18

Compressed Hydrogen: Thermophysical Properties

Naoya Sakoda

Abstract This chapter describes PVT properties of compressed normal hydrogen (75 % orthohydrogen and 25 % parahydrogen) up to 100 MPa and its equation of state (EOS) derived from the measurement data of the Burnett method, along with the measurement methods and correlation of viscosity and thermal conductivity for compressed hydrogen.

Keywords Compressed hydrogen · PVT property · Equation of state (EOS) · Burnett method · Viscosity · Thermal conductivity · Thermophysical property · Hydrogen storage

Fundamental information about the thermophysical properties of hydrogen is critical for the development of hydrogen utilization systems. These properties are of great importance at high temperatures and high pressures, especially in the efficient design of fuel cell vehicles (FCVs) and hydrogen refueling stations, which require compressed hydrogen up to 87.5 MPa. Figure 18.1 shows the PVT property surface of normal hydrogen (75 % orthohydrogen + 25 % parahydrogen) in which the relation of pressure, density, and temperature is described. The critical temperature of hydrogen is extremely low (33.145 K [1]), and liquefaction is not observed above a room temperature even if compressed at pressures over 100 MPa. Therefore, the thermophysical properties of compressed hydrogen are often derived assuming ideal gas behavior. However, for example, the density of hydrogen at 300 K and 100 MPa, calculated from the equation of state (EOS) for real-fluid hydrogen, is by 40 % smaller than that calculated from the ideal gas EOS. The properties of compressed hydrogen deviate significantly from the ideal gas state.

In spite of the simple structure of the hydrogen molecule, there are some unique characteristics in the thermophysical properties, unlike those observed for other

N. Sakoda (✉)

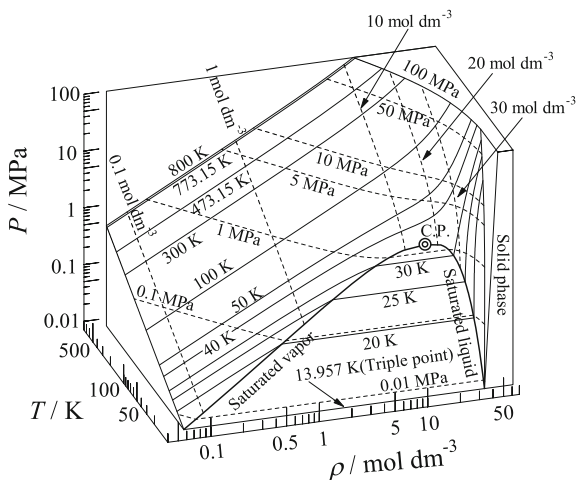
Department of Mechanical Engineering, Faculty of Engineering,
Kyushu University, Fukuoka 819-0395, Japan
e-mail: sakoda@mech.kyushu-u.ac.jp

© Springer Japan 2016

K. Sasaki et al. (eds.), *Hydrogen Energy Engineering*,
Green Energy and Technology, DOI 10.1007/978-4-431-56042-5_18

265

Fig. 18.1 PVT property surface of normal hydrogen: Calculated from the EOS Leachman [1] C.P. is the critical point (used with permission from Springer, Copyright 2009)



fluids. Hydrogen has two isomers, that is, orthohydrogen and parahydrogen [2], and the caloric properties (such as heat capacity and thermal conductivity) of these isomers show a maximum difference of 30 % near 150 K, while the PVT properties display little difference apart from the critical points and saturated properties. The equilibrium ratio of ortho- and parahydrogen depends on temperature. The conversion between ortho- and parahydrogen takes several months without catalysts in some cases, and the caloric properties of the isomers should be treated separately. In the liquid phase, hydrogen consists almost entirely of parahydrogen, and the equilibrium ratio above room temperature is 75 % ortho- and 25 % parahydrogen. This condition is called normal hydrogen. At very low temperatures, where hydrogen is liquefied, a quantum effect appears, and the heat capacity of the saturated liquid is lower than that of saturated vapor and the ideal gas heat capacity (also observed in helium). On the other hand, high-temperature hydrogen has a different feature in that it easily permeates through metals. The airtightness of vessels in hydrogen utilization systems is necessary for safety. However, hydrogen permeation through the vessel wall becomes apparent at temperatures above 573 K, where the perfect airtightness is no longer maintained. The permeation continues until the vessel containing hydrogen is finally evacuated even though the surrounding environment is at atmospheric pressure [3].

18.1 PVT Property

Systematic studies of the thermophysical properties of hydrogen were made by the NIST(NBS)-NASA group, mainly focusing on the low temperature region, including the liquid phase, in the 1970s. A review of the thermodynamic properties

of hydrogen, based on existing EOSs has been summarized [4]. Many EOSs for hydrogen have been developed since the 1970s. A modified Benedict–Webb–Rubin (mBWR) EOS by Younglove [5] for parahydrogen in 1982 is notable as it was used for a long time, until the Helmholtz-type EOSs for ortho-, para-, and normal hydrogen were developed by Leachman et al. [1] in 2009. These EOSs represent existing experimental data more accurately, but no new experimental data were given. The EOSs cover the whole fluid region including the vapor, liquid, and supercritical fluid phases. In 2012, the PVT properties of normal hydrogen from 353 to 473 K and up to 100 MPa were measured by the Burnett method, and a virial-type EOS was developed based on the experimental data with an uncertainty less than 0.24 % [6]. This EOS has a simple functional form for the compressed hydrogen and is available in the temperature range from 220 to 473 K and at pressures up to 100 MPa. The virial-type EOS is formulated by

$$Z = 1 + B(T)\rho + C(T)\rho^2 + D(T)\rho^3 \quad (18.1)$$

$$B(T) = b_1 + b_2 \exp(T_r^{-1}) + b_3 T_r^{-k_1} + b_4 T_r^{-k_2} \quad (18.2)$$

$$C(T) = c_1 + c_2 T_r^{-k_3} + c_3 T_r^{-k_4} \quad (18.3)$$

$$D(T) = d_1 T_r^{-k_5} \quad (18.4)$$

where $Z (= P/\rho RT$, P : pressure, ρ : density, T : temperature) is the compressibility factor. B , C , and D are the second, third, and fourth virial coefficients, respectively, and $T_r = T/T_c$, where T_c is the critical temperature. k_1 – k_5 , b_1 – b_4 , c_1 – c_3 , and d_1 are coefficients, and these numerical values are tabulated in Table 18.1 [6]. The other thermodynamic properties such as heat capacity, speed of sound, enthalpy, and entropy are calculated using thermodynamic relations. Accurate EOSs are generally obtained by fitting experimental data both for the PVT properties, as well as the other thermodynamic properties. However, the currently available data for heat capacity and speed of sound are limited up to 100 K, and the thermodynamic properties of the compressed hydrogen largely depend on the PVT property behavior.

Figure 18.2 shows the Burnett apparatus for the PVT property measurements of compressed hydrogen up to 100 MPa [7]. This apparatus utilizes two vessels; a

Table 18.1 Coefficients in the virial EOS for Eqs. 18.1–18.4 [6]

b_1	0.161777×10^{-1}	k_1	0.0612
b_2	-0.102798×10^0	k_2	2.71
b_3	0.129501×10^0	k_3	2.53
b_4	0.628764×10^{-1}	k_4	4.85
c_1	0.288234×10^{-3}	k_5	1.09
c_2	0.203867×10^{-2}		
c_3	-0.779969×10^{-3}		
d_1	0.716809×10^{-4}		

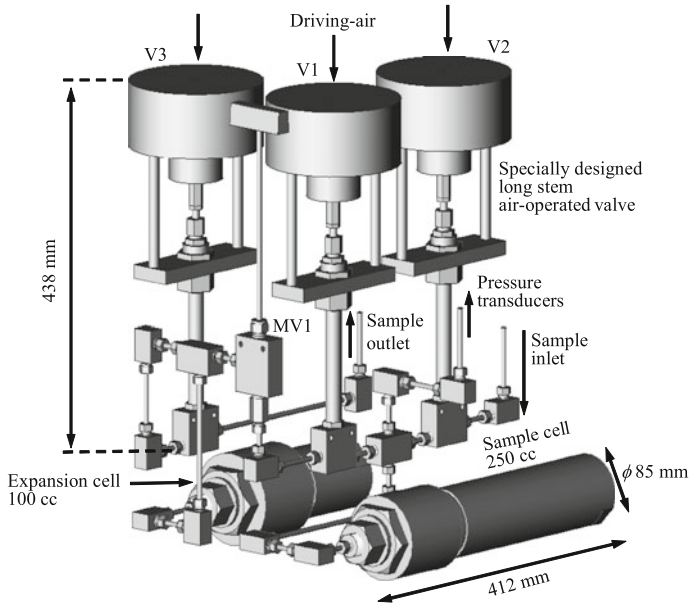


Fig. 18.2 Burnett apparatus for PVT property measurement of the compressed hydrogen [7]

sample cell (250 cm^3), and an expansion cell (100 cm^3). The high-pressure sample is filled in the sample cell, and the sample is isothermally expanded into the evacuated expansion cell. By a number of repeated isothermal expansions, the sample is considered to be an ideal gas, whose compressibility factor is unity. The volume ratio of the sample cell and expansion cell is related to the densities before and after expansion. The densities are evaluated from the equilibrium pressure measured at each expansion. This method does not need the sample mass, and is adequate for measuring low-density fluids such as hydrogen. A careful treatment of high-pressure hydrogen is required, and the experiment is remotely operated with specially designed air-operated valves applicable up to 100 MPa.

18.2 Viscosity and Thermal Conductivity

Transport properties of compressed hydrogen, such as viscosity and thermal conductivity, are also crucial for the design of hydrogen refueling stations, especially in the process of rapid filling of precooled high-pressure hydrogen to FCVs. The transport properties cannot be derived from thermodynamic relations, and the correlations for viscosity and thermal conductivity are separately developed. There were few reliable experimental data of the transport properties of the compressed hydrogen, and the revision of the correlations was required. Yusibani et al. [8] developed a correlation of the compressed hydrogen viscosity available from 100 to

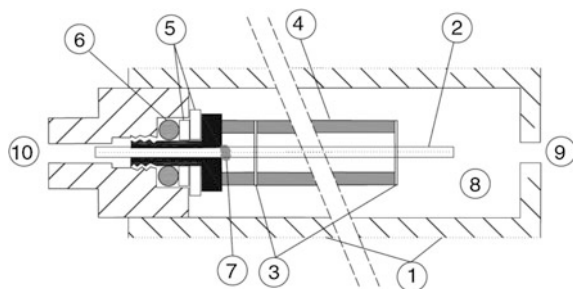


Fig. 18.3 Details of the test section of the capillary tube method for the viscosity measurement for normal hydrogen: 1 pressure vessel; 2 quartz capillary tube; 3 spacer; 4 support for capillary tube; 5 washer; 6 silicon o-ring; 7 ThreeBond-1209 sealant; 8 chamber ($\approx 40 \text{ cm}^3$); 9 gas inlet port; 10 gas outlet port. Reprinted from Yusibani et al. [9] (used with permission from Springer, Copyright 2011)

990 K and at pressures up to 220 MPa by using existing data based on the Chapman–Enskog solution in 2010. Moreover, the viscosity of normal hydrogen from 295 to 400 K and up to 99 MPa was measured by the capillary tube method [9]. The detailed structure of the capillary tube and the pressure vessel is shown in Fig. 18.3. In this method, compressed hydrogen flows in laminar flow conditions into the quartz capillary tube, whose length and inner diameter are 502 and 0.1 mm, respectively. The viscosity is evaluated from the flow rate of the sample and the pressure difference between the inlet and outlet of the capillary tube. At higher temperatures, this method is hard to apply because the sealing part of the capillary tube becomes fragile. Therefore, the vibrating wire method was performed [10]. In 2013, Muzny et al. [11] developed a correlation of normal hydrogen using the data by Yusibani et al. and others.

The thermal conductivity of normal hydrogen was measured by Moroe et al. [12] with a transient short hot-wire method from 323 to 773 K and up to 99 MPa. The apparatus is shown in Fig. 18.4. A constant current is supplied to a platinum wire 10 μm in diameter and 15 mm in length set in the pressure vessel to heat a sample fluid, and the transient temperature rise is measured. The thermal conductivity of the sample fluid strongly influences the temperature rise, and is obtained from the measured temperature via solution of the unsteady heat conduction equation. In the same period, Perkins [13] also measured the thermal conductivity from 301 to 601 K and up to 70 MPa. In 2011, Assael et al. [14] developed a correlation of thermal conductivity of normal and parahydrogen using these data.

The correlations of viscosity and thermal conductivity by Muzny et al. and by Assael et al. are formulated by

$$\eta(T, \rho) = \eta_0(T) + \eta_1(T)\rho + c_1\rho_r^2 \times \exp\left[c_2T_r + c_3/T_r + \frac{c_4\rho_r^2}{c_5 + T_r} + c_6\rho_r^6\right] \quad (18.5)$$

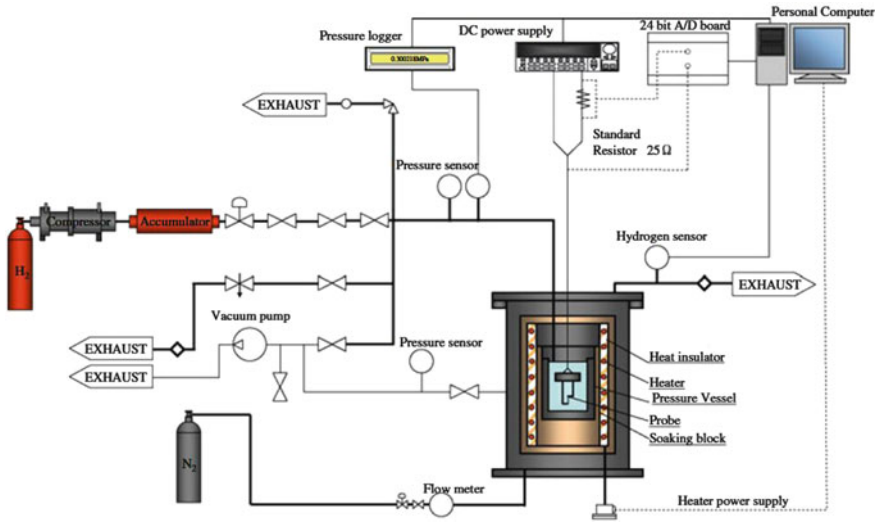


Fig. 18.4 Experimental setup of the transient short hot-wire method for the thermal conductivity measurement of compressed hydrogen: Reprinted from Moroe et al. [12] (used with permission from Springer, Copyright 2011)

$$\lambda(T, \rho) = \lambda_0(T) + \Delta\lambda(T, \rho) + \Delta\lambda_c(T, \rho) \tag{18.6}$$

respectively. In Eq. 18.5, $\rho_r = \rho/\rho_{sc}$ ($\rho_{sc} = 90.5 \text{ kg m}^{-3}$), $T_r = T/T_c$ (T_c : critical temperature), and c_1 – c_6 are the coefficients (tabulated in Ref. [11]). Both of the correlations consist of the dilute-gas limit term (η_0 and λ_0), and the excess term. In the thermal conductivity, a relatively large divergence is observed at the critical point, and the critical enhancement term, $\Delta\lambda_c$, is introduced. Figures 18.5 and 18.6 are viscosity and thermal conductivity surface of the compressed hydrogen calculated from Eqs. 18.5 and 18.6, respectively, via a NIST database, REFPROP [15], in the temperature range from 150 to 800 K and at pressures up to 100 MPa. The

Fig. 18.5 Viscosity surface of compressed hydrogen

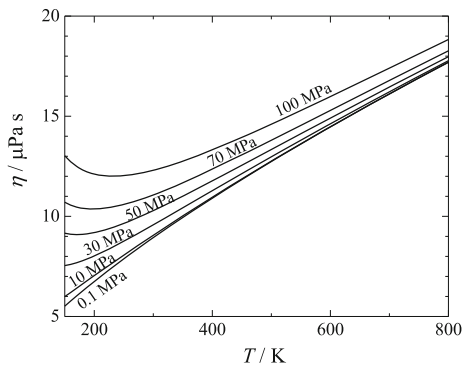
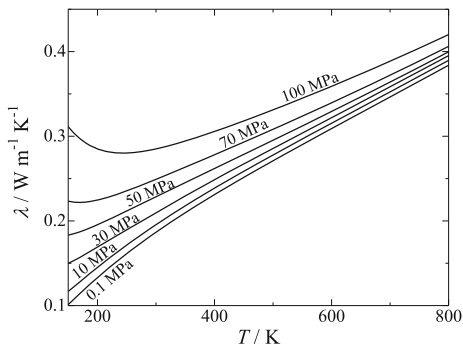


Fig. 18.6 Thermal conductivity surface of compressed hydrogen



uncertainty of the viscosity and thermal conductivity of the compressed hydrogen calculated from these correlations is 4 %. The behavior of the viscosity and thermal conductivity is very similar to each other, and as temperature increases, the pressure dependence is reduced.

References

1. Leachman JW, Jacobsen RT, Penoncello SG, Lemmon EW (2009) Fundamental equations of state for parahydrogen, normal hydrogen, and orthohydrogen. *J Phys Chem Ref Data* 38:721–748
2. Farkas A (1935) Orthohydrogen, parahydrogen and heavy hydrogen. Cambridge University Press
3. Sakoda N, Kumagai R, Ishida R, Shinzato K, Kohno M, Takata Y (2014) Vacuum generation by hydrogen permeation to atmosphere through austenitic and nickel-base-alloy vessel walls at temperatures from 573 K to 773 K. *Int J Hydrogen Energy* 39:11316–11320
4. Sakoda N, Shindo K, Shinzato K, Kohno M, Takata Y, Fujii M (2010) Review of the thermodynamic properties of hydrogen based on existing equations of state. *Int J Thermophys* 31:276–296
5. Younglove BA (1982) Thermophysical properties of fluids. I. Argon, ethylene, parahydrogen, nitrogen, nitrogen trifluoride, and oxygen. *J Phys Chem Ref Data* 11:S1
6. Sakoda N, Shindo K, Motomura K, Shinzato K, Kohno M, Takata Y, Fujii M (2012) Burnett PVT measurements of hydrogen and the development of a virial equation of state at pressures up to 100 MPa. *Int J Thermophys* 33:381–395
7. Sakoda N, Shindo K, Shinzato K, Kohno M, Takata Y, Fujii M (2010) Development of a PVT property measurement apparatus by the Burnett method for high pressure hydrogen. *Jpn J Thermophys Prop* 24:28–34
8. Yusibani E, Woodfield PL, Shinzato K, Kohno M, Takata Y, Fujii M (2010) Prediction of hydrogen gas viscosity at high pressure and high temperature. *Jpn J Thermophys Prop* 24:21–27
9. Yusibani E, Nagahama Y, Kohno M, Takata Y, Woodfield PL, Shinzato K, Fujii M (2011) A capillary tube viscometer designed for measurements of hydrogen gas viscosity at high pressure and high temperature. *Int J Thermophys* 32:1111–1124
10. Sakoda N, Hisatsugu T, Furusato K, Shinzato K, Kohno M, Takata Y (2015) Viscosity measurements of hydrogen at high temperatures up to 573 K by a curved vibrating wire method. *J Chem Thermodyn* 89:22–26

11. Muzny CD, Huber ML, Kazakov AF (2013) Correlation for the viscosity of normal hydrogen obtained from symbolic regression. *J Chem Eng Data* 58:969–979
12. Moroe S, Woodfield PL, Kimura K, Kohno M, Fukai J, Fujii M, Shinzato K, Takata Y (2011) Measurements of hydrogen thermal conductivity at high pressure and high temperature. *Int J Thermophys* 32:1887–1917
13. Perkins RA (2011) cited in Assael MJ, Assael JAM, Huber ML, Perkins RA, Takata Y (2011) Correlation of the thermal conductivity of normal and parahydrogen from the triple point to 1000 K and up to 100 MPa. *J Phys Chem Ref Data* 40:033101-1-13
14. Assael MJ, Assael JAM, Huber ML, Perkins RA, Takata Y (2011) Correlation of the thermal conductivity of normal and parahydrogen from the triple point to 1000 K and up to 100 MPa. *J Phys Chem Ref Data* 40:033101-1-13
15. Lemmon EW, Huber ML, McLinden MO (2013) NIST reference fluid thermodynamic and transport properties database-REFPROP: version 9.1, standard reference data. National Institute of Standards and Technology, Gaithersburg, MD

Chapter 19

Compressed Hydrogen: High-Pressure Hydrogen Tanks

Hai-Wen Li and Kiyooki Onoue

Abstract This chapter describes development history and composition of four types of high-pressure tanks and their applications for stationary storage like hydrogen filling station and portable storage such as hydrogen trailer and fuel cell vehicle onboard storage, followed with a hybrid tank system that combines a high-pressure tank and hydrogen storage materials.

Keywords Compressed hydrogen · High-pressure tank · Hydrogen filling station · Hydrogen trailer · Onboard storage · Hybrid tank · Hydrogen storage

The high-pressure tank is the most common and convenient way to store hydrogen. As described by the PVT properties of high-pressure hydrogen in Chap. 18, the compressibility factor increases with pressure at room temperature, giving rise to a larger volume than expected from the ideal gas equation. In other words, the volumetric hydrogen density inside a high-pressure tank increases with pressure, but shows a much smaller value than for an ideal gas (Fig. 19.1). Since the repulsive interactions between H₂ molecules become dominant at high pressure, the volumetric density is not comparable to that of liquid hydrogen.

H.-W. Li (✉)

International Research Center for Hydrogen Energy,
Kyushu University, Fukuoka 819-0395, Japan
e-mail: li.haiwen.305@m.kyushu-u.ac.jp

K. Onoue

Office for the Promotion of Safety and Health, Kyushu University,
Fukuoka 819-0395, Japan
e-mail: onoue.kiyooki.852@m.kyushu-u.ac.jp

© Springer Japan 2016

K. Sasaki et al. (eds.), *Hydrogen Energy Engineering*,
Green Energy and Technology, DOI 10.1007/978-4-431-56042-5_19

273

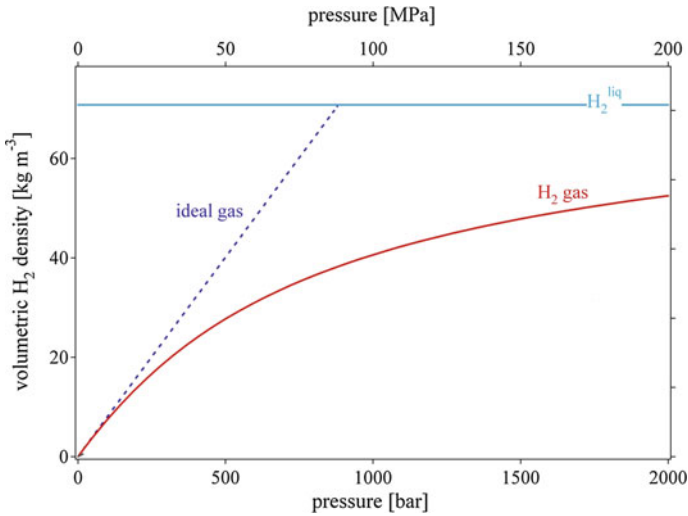


Fig. 19.1 Volumetric density of compressed hydrogen gas as a function of gas pressure including the ideal gas and liquid hydrogen [1] (used with permission from Springer, Copyright 2004)

19.1 Tank Development

Hydrogen can be stored in four types of high-pressure tank, as shown in Fig. 19.2. Type V1 is the oldest form, made of seamless steel and was introduced in 1870–1880. Type V2 is made of metallic liner (steel or Al) with hoop reinforcement on the hoop part with a glass fiber composite, and can withstand higher pressure than Type V1. Type V3 is made of aluminum liner fully wrapped by carbon fibers, and was developed for space/military applications in the 1980s. Type V4 is made of plastic liner fully wrapped by carbon fibers. Type V3 and Type V4 are widely accepted for portable applications, because of their light-weight properties compared to type V1 and V2 (see Fig. 19.2). However, they are much more expensive, which is one of the key issues for widespread applications.

19.2 Stationary Storage

Most of the type V1 high-pressure hydrogen tanks in Japan are made of CrMo steel, painted red, and the storage pressure is usually 14.7 MPa (Fig. 19.3a). Due to their weight, the type V1 is not appropriate for portable applications. However, they can be used as a high-pressure buffer/storage system in hydrogen filling stations, as shown in Fig. 19.3b. In the demonstration hydrogen filling station at Kyushu University, the tank was designed to serve for 40 MPa with a volume of 300 L.

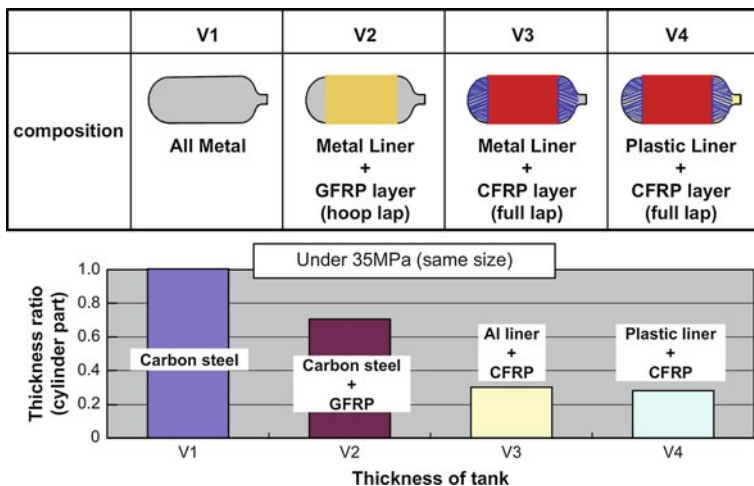


Fig. 19.2 Four types of high-pressure tank [2]. GFRP means glass fiber reinforced plastics, CFRP indicates carbon fiber reinforced plastics (used with permission from Elsevier, Copyright 2009)

Recently, a much longer version (6 m) of the type V3 tank, using Al liner (Fig. 19.3c) is being developed to withstand 80 MPa for hydrogen filling station applications.

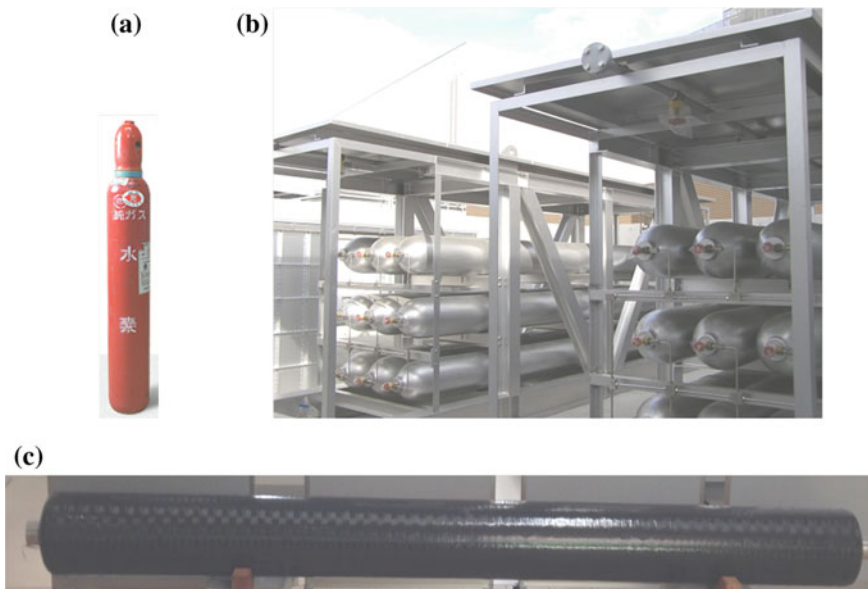


Fig. 19.3 a Type V1 high-pressure hydrogen tank used in the laboratories, b high-pressure hydrogen tanks used in the hydrogen filling station at Kyushu University, and c 6 m long type-V3 hydrogen tank

19.3 Portable Storage

19.3.1 Hydrogen Trailer

Hydrogen gas can be transported using a truck or semi-trailer consisting of a cluster of high-pressure hydrogen tanks. One challenge is that the total weight of a vehicle is regulated by the road law, and the road transport vehicle law. Currently the total weight for a truck or semi-trailer is limited to below 25 or 28 t, respectively, in order to prevent excessive damage to roads and bridges. Under such conditions, a hydrogen trailer using 24-type V3 tanks (45 MPa, 306 L, see Fig. 19.4) was recently developed to transport approximately 210 kg of hydrogen at 25 °C in order to improve the hydrogen transport efficiency.

19.3.2 FCV Onboard Storage

Onboard hydrogen storage is one of the most challenging issues for widespread fuel cell vehicles applications. Approximately 5 kg of hydrogen is required to reach a driving range (500 km) of current internal combustion engine vehicles. Taking into account the gravimetric and volumetric hydrogen density as well as filling time, type V4 tanks withstanding 70 MPa are regarded as a good candidate for onboard storage. Figure 19.5 shows a cutaway of the high-pressure hydrogen tanks equipped in the Toyota MIRAI FCV. The tank has three layers; a plastic liner to retain compressed hydrogen, a carbon fiber-reinforced plastic layer, and a glass fiber-reinforced plastic layer to protect the surface [4]. The two tanks have a total internal volume of 122.4 L (front tank 60.0 L and rear tank 62.4 L), and can store approximately 5.0 kg of hydrogen using the normal operation pressure of 70 MPa. The system has a gravimetric storage density of 5.7 wt%.



Fig. 19.4 Hydrogen trailer using 45 MPa high-pressure tanks [3]

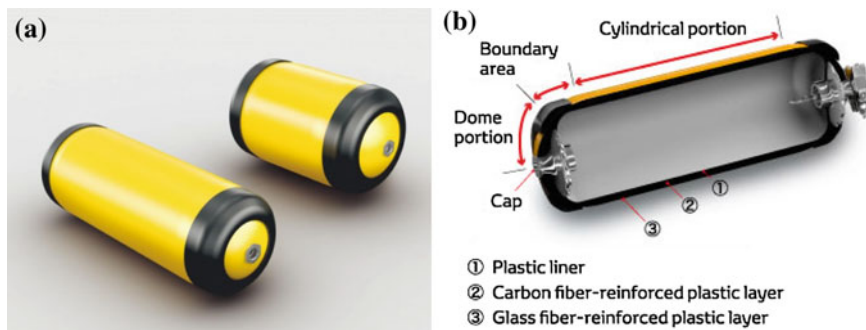


Fig. 19.5 **a** Two high-pressure hydrogen tanks as used in the Toyota MIRAI. **b** Schematic cross-section of their structure. One is located under the rear seats, and the other is located in the rear, under the trunk [4]

19.3.3 Hybrid MH Tank System

A hybrid tank system (see Fig. 19.6), combining a high-pressure tank and hydrogen storage materials with high equilibrium pressure, has been proposed in order to increase the volumetric storage density. In this system, a type V3 tank is adopted for withstanding 35 MPa, and a heat exchanger is used for thermal management during the hydrogen charge/discharge processes. Figure 19.7 shows the hybrid tank system, in which four tanks with outside volume of 180 L, and 75 kg of $Ti_{1.1}CrMn$ is filled in the divided space of each tank. The maximum storage capacity of this hybrid system is 7.3 kg of hydrogen. This is more than 2.5 times the storage capacity of high-pressure tanks with the same volume and hydrogen pressure (35 MPa), and approximately 1.7 times that of the same volume tank using 70 MPa hydrogen. Furthermore, the tank can be charged up to 80 % within 5 min, which is comparable to that of a high-pressure tank [2]. These attractive hydrogen storage properties indicate the high potentiality of hybrid tank systems for onboard hydrogen storage applications. The gravimetric density using alloys in the hybrid tank system, however, is a critical issue needed to overcome for practical applications. Continuous efforts are thus expected to put into the development of advanced hydrogen storage materials with high gravimetric and volumetric hydrogen density.

Despite the significant progress on compressed hydrogen storage systems, continuous efforts of research and development are still required to reduce cost and improve the volumetric and gravimetric storage density, reliability, and durability of high-pressure tanks for stationary and portable hydrogen storage applications.

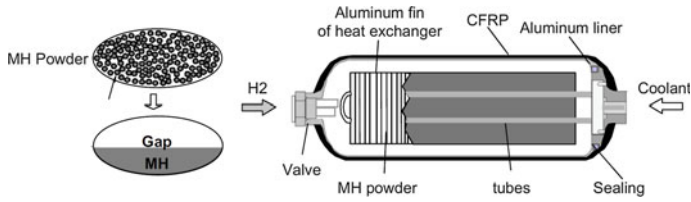
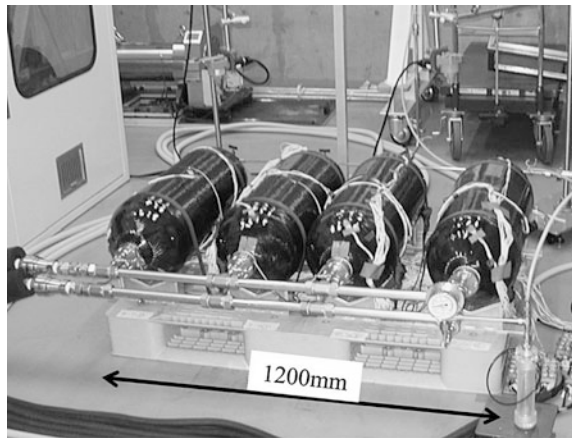


Fig. 19.6 Schematic illustration of a hybrid MH tank system combining a high-pressure tank with metal hydride (MH) powders [2] (used with permission from Elsevier, Copyright 2009)

Fig. 19.7 Illustration of a hybrid tank system combined with high-pressure tank and hydrogen storage materials (e.g., MH powder) [5]



Mechanistic clarification of hydrogen-induced degradation of metals and rubbers and exploration of new materials for high-pressure hydrogen applications are well summarized in Part V.

References

1. Züttel A (2004) Hydrogen storage methods. *Naturwissenschaften* 91:157–172
2. Mori D, Hirose K (2009) Recent challenges of hydrogen storage technologies for fuel cell vehicles. *Int J Hydrogen Energy* 34:4569–4574
3. <http://www.meti.go.jp/press/2013/03/20140331002/20140331002-1.pdf>. Accessed 5 May 2015
4. http://www.toyota-global.com/innovation/environmental_technology/technology_file/fuel_cell_hybrid.html. Accessed 5 May 2015
5. Mori D, Kobayashi N, Shinozawa T, Matsunaga T, Kubo H, Toh K, Tsuzuki M (2005) Hydrogen storage materials for fuel cell vehicles high-pressure MH system. *J Jpn Inst Met* 69:308–311

Chapter 20

Hydrogen Storage: Conclusions and Future Perspectives

Hai-Wen Li and Etsuo Akiba

Abstract This chapter summarizes the preceding chapters on hydrogen storage, and provides an outlook for the future of these technologies in the larger hydrogen society landscape.

Keywords Hydrogen storage · Interstitial hydride · Non-interstitial hydride · Adsorption · Absorption · Liquid hydrogen · Compressed hydrogen

Hydrogen has been extensively regarded as a clean energy carrier. The energy density of hydrogen per unit volume at ambient temperature and pressure is no more than 1/3000 of gasoline, which means that storage of hydrogen in a limited space is a big challenge. Therefore, storage and transport of hydrogen in a safe, compact, and economic way is indispensable for realizing a sustainable hydrogen society.

Hydrogen can be stored in gaseous, liquid, and solid states. The volumetric and gravimetric density in various systems are shown in Fig. 20.1.

Compressed hydrogen using high pressure tanks has been widely used as the most convenient way to supply hydrogen as chemical raw material or process gas in many fields, with the pressure lower than 20 MPa. Since hydrogen has been considered as an energy carrier, much higher pressure is required to increase the volumetric energy density, e.g., 70 MPa is adopted for onboard storage in the commercialized FCV MIRAI. Further improvement of the compression efficiency

H.-W. Li (✉)

International Research Center for Hydrogen Energy, Kyushu University,

Fukuoka 819-0395, Japan

e-mail: li.haiwen.305@m.kyushu-u.ac.jp

E. Akiba

Department of Mechanical Engineering, Faculty of Engineering, Kyushu University,

Fukuoka 819-0395, Japan

e-mail: e.akiba@mech.kyushu-u.ac.jp

© Springer Japan 2016

K. Sasaki et al. (eds.), *Hydrogen Energy Engineering*,

Green Energy and Technology, DOI 10.1007/978-4-431-56042-5_20

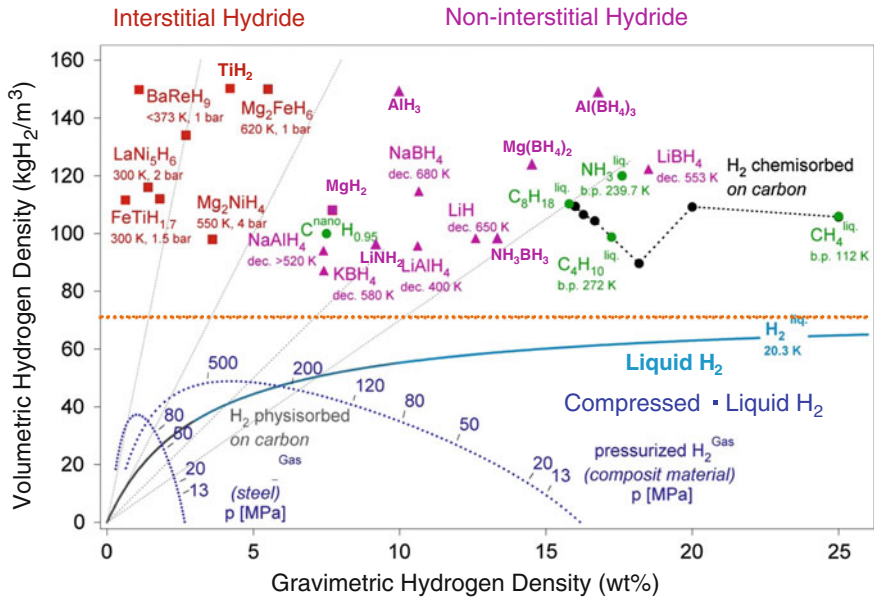


Fig. 20.1 Volumetric and gravimetric hydrogen density of some hydrogen storage systems [1] (used with permission from Elsevier, Copyright 2004)

and the development of low cost materials that can withstand the high pressure hydrogen under practical temperatures are crucial for widespread adoption of hydrogen energy applications.

Hydrogen can be stored in liquid carriers, such as liquid hydrogen, organic hydrides, and ammonia, which are assumed for large-scale hydrogen storage and transport in Japan. Liquid hydrogen is commonly used as liquid rocket fuel for space applications. The liquefaction of hydrogen needs an extremely low temperature of 20 K, which consumes approximately 30 % of the energy that hydrogen possesses. Development of high efficiency liquefaction processes and highly insulating systems to reduce the amount of boil off gas are therefore expected for use of liquid hydrogen for large-scale hydrogen storage and transport. Organic hydrides like methylcyclohexane (C_7H_{14}) keep their liquid state during hydrogen release and reabsorption processes, and are therefore potential hydrogen transport media. Such kinds of organic hydrides have similar chemical properties to gasoline, and therefore, can be transported using the current infrastructure. Development of advanced catalysts that reduce the hydrogen absorption and desorption temperature and separation technology of hydrogen from the organic hydrides are expected for the practical applications of organic hydrides for large-scale hydrogen storage. Ammonia, which can be readily liquefied by pressurizing to approximately 1.2 MPa at room temperature, is therefore also considered as a potential liquid energy carrier. It is well known that the performance of a proton exchange membrane fuel cell (PEFC) is seriously decreased by exposure to NH_3 as an impurity with ppm

concentration. For this reason, development of solid oxide fuel cell that is robust to NH_3 and combustion technology of NH_3 for power generation are expected for the realization of ammonia as a clean energy carrier.

Solid-state hydrogen storage can be divided into two groups of physical adsorption and chemical storage using hydrides. Physical adsorption uses high-surface materials like activated carbon, zeolite, metal organic framework (MOF), etc. Molecular hydrogen is physically adsorbed on the material surface via van der Waals forces with a binding energy of 5–10 kJ/mol, therefore, higher hydrogen storage density can only be realized at lower temperature such as 77 K. According to the empirical Chahine's rule, approximately 1 wt% of hydrogen at maximum can be adsorbed at 77 K per 500 m^2/g , suggesting higher surface area enables the storage of more hydrogen. Hydrogen can be also chemically stored through making chemical bonds with neighboring atoms by formation of interstitial hydrides and non-interstitial hydrides. Hydrogen occupies tetrahedral and octahedral sites to form a metallic bond in the interstitial hydrides (i.e., hydrogen storage alloys) that are usually comprised of transition metals. Most of the interstitial hydrides can reversibly store hydrogen near room temperature with reasonable reaction rates. Hydrogen tends to form covalent bonds (sometime mixed with ionic bonding nature) in the non-interstitial hydrides of which most are comprised of light elements so that exhibit high gravimetric hydrogen density than that of interstitial hydrides.

Each hydrogen storage method as mentioned above, has its own unique characteristics, therefore, systematic and thorough investigations are expected to explore and develop the right applications for each method. With regard to the most

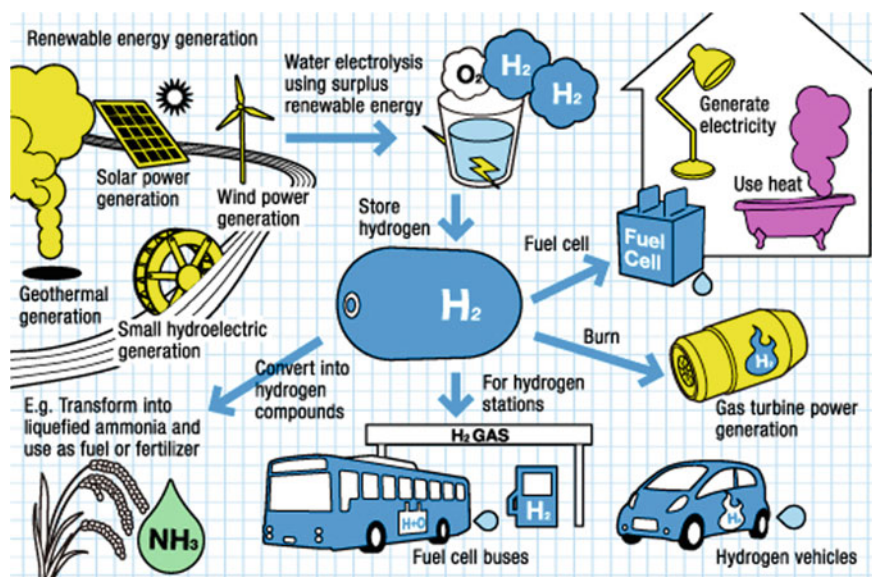


Fig. 20.2 An image of a sustainable hydrogen society [2]

challenging onboard hydrogen storage for FCV, due to the limited volumetric hydrogen density in the well-established compressed hydrogen and liquid hydrogen, solid-state hydrides comprised of light elements possessing high volumetric and gravimetric densities are highly expected for the realization of paradigm shift of hydrogen storage. Establishment of a *hydrogen materials science* based on further intensive fundamental researches will bring breakthrough in the development of hydrogen storage materials as well as structural materials for hydrogen infrastructure. Integration of several hydrogen storage methods is also expected from the engineering point of view to figure out a safe, compact, and economic way for storage and transport of hydrogen, aiming at the acceleration of the wide spread of a sustainable hydrogen society (see Fig. 20.2), as shown in the Strategic Road Map for Hydrogen and Fuel Cells compiled by the Ministry of Economy, Trade and Industry (METI) in Japan [3].

References

1. Züttel A, Wenger P, Sudan P, Mauron P, Orimo S (2004) Hydrogen density in nanostructured carbon, metals and complex materials. *Mater Sci Eng B* 108:9–18
2. <http://www.thinktheearth.net/thinkdaily/report/2010/08/rpt-53.html#page-2>. Accessed 1 Oct 2015
3. http://www.meti.go.jp/english/press/2014/pdf/0624_04a.pdf. Accessed 1 Oct 2015

Part IV

Hydrogen Utilization

Akari Hayashi

International Research Center for Hydrogen Energy, Kyushu University, Fukuoka, Japan

Part IV describes the process of converting hydrogen to energy. In this part, the details of fuel cell systems are discussed. First, Chap. 21 discusses the fundamentals of fuel cell reactions. In the following Chaps. 22–24, polymer electrolyte fuel cell (PEFC), solid oxide fuel cell (SOFC), and alkaline electrolyte fuel cell (AFC) are focused in terms of their principles and major material components. In addition, a hydrogen combustion system, converting hydrogen to energy through combustion, is discussed in Chap. 25.

Chapter 21

Fundamentals

Akari Hayashi and Kazunari Sasaki

Abstract This chapter describes fundamental science to understand fuel cells from the viewpoint of electrochemistry and material science. Related experimental techniques and procedures which can be used in laboratories are also explained.

Keywords Fuel cell · Electrochemistry · Overpotential · Defect chemistry · Experimental techniques · Microscopic analysis · Hydrogen utilization

21.1 Electrochemistry and Overpotential

In the fuel cell reaction, simply, hydrogen and oxygen react and produce water. This simple reaction is same for PEFCs, SOFCs, and also AFCs. Even though the overall reaction results in the same net process, each sub-reaction occurring at the anode and the cathode and ion transfer is slightly different. In the case of a PEFC, categorized as an acid-type fuel cell (Fig. 21.1), hydrogen gas is ionized to H^+ ions and releases electrons at the anode. Then, at the cathode, oxygen gas, electrons coming from the electric circuit, and H^+ ions coming from the electrolyte react and produce water. Although SOFCs and AFCs have slightly different reaction mechanisms, in all the cases, current (electricity) can be extracted during this simple reaction. Therefore, it is possible to directly convert chemical energy to electricity using hydrogen as a fuel.

In the fuel cell reaction, even though energy is spontaneously obtained from a thermodynamic standpoint, the reaction does not proceed continuously from a kinetic point of view. As shown in the classical energy diagram for exothermic (spontaneous) reactions (Fig. 21.2), enough energy to go over the hill in the

A. Hayashi (✉) · K. Sasaki
International Research Center for Hydrogen Energy, Kyushu University,
Fukuoka 819-0395, Japan
e-mail: hayashi.akari.500@m.kyushu-u.ac.jp

K. Sasaki
e-mail: sasaki@mech.kyushu-u.ac.jp

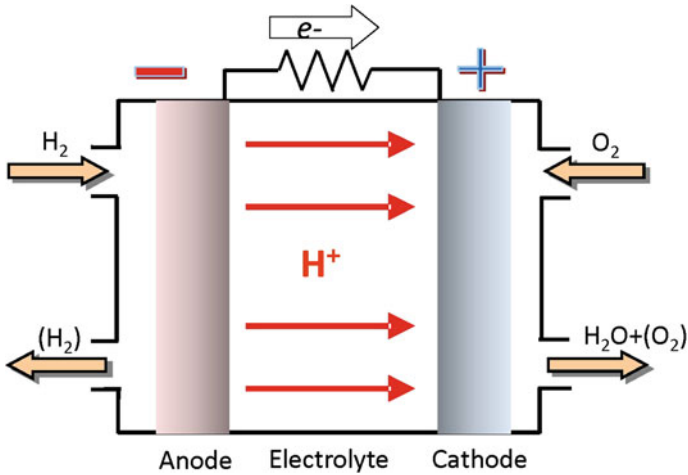


Fig. 21.1 Reactions and charge flow in PEFC

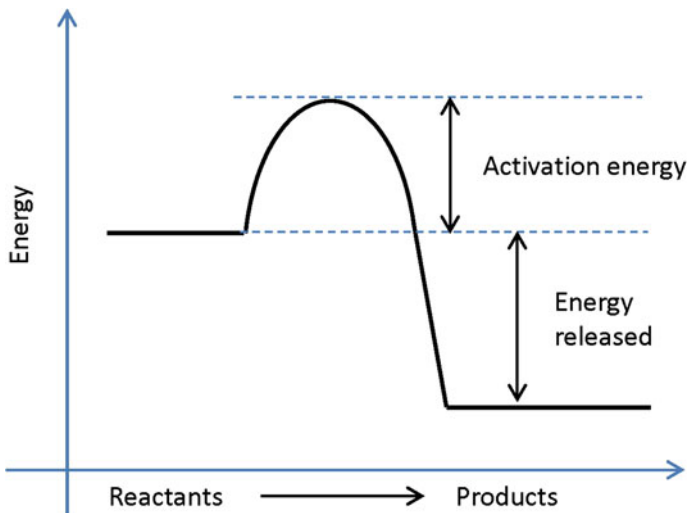


Fig. 21.2 Energy diagram for a simple exothermic reaction

diagram is required. If the probability to go over the hill is low, reactions occur only slowly. Except for reactions at very high temperature, such as over $800\text{ }^\circ\text{C}$, reactions occur slowly in real fuel cell systems. As shown in Fig. 21.3, because of this slow reaction, in reality, the open-circuit voltage is lower than the theoretical value. The cell voltage drops rapidly at the initial stage of current increase. Then, the current goes down gradually and linearly. Furthermore, when larger current is applied, the voltage rapidly drops.

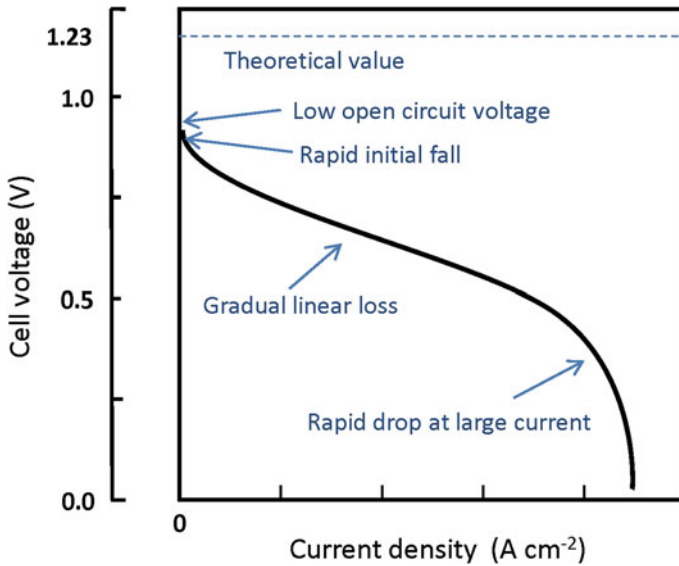


Fig. 21.3 A typical current–voltage curve for PEFC

The difference between the theoretical voltage and actual voltage is called overvoltage, overpotential, or losses. Then, such losses can be explained in the following ways [1].

Activation losses: This occurs owing to slow reactions at the electrode surface. A part of the generated voltage is lost enabling chemical reactions to proceed, in order to transfer electrons either from or to the electrode. This voltage loss rapidly occurs at the initial stage of current increase and results in nonlinear behavior. Activation losses can be reduced by increasing the roughness of electrodes, reactant concentration, temperature, and pressure. Usage of more active catalysts is another possibility but a more challenging approach.

Fuel crossover and internal currents: This loss mainly occurs by wasting fuels, which slightly permeate into the electrolyte, but also by conducting electrons through the electrolyte. Even though a role necessary for the electrolyte is transferring only ions, fuel diffusion and electron transfer to a certain degree cannot be completely avoided. This type of loss is usually small and can be ignored, but the open-circuit voltage in low temperature fuel cells is affected very much.

Ohmic losses: This is caused by the resistance of the ion transfer through the electrolyte and also the electron flow through the electrode and the interface between electrodes and other parts of fuel cells. Such a voltage loss results in linear behavior. Ohmic losses can be reduced by using electrodes with the highest possible conductivity, appropriate designs and materials for the cell interconnects, and an electrolyte as thin as possible.

Concentration losses or mass transport losses: This is caused by the change in concentration of reactants when fuels are consumed at the electrode surface. Since the change in concentration occurs when not enough reactants are delivered to the electrode surface, it is also called a mass transfer loss. When a large current is applied, concentration loss significantly occurs.

21.2 Defect Chemistry

In order to promote electrochemical reactions in fuel cells, efficient transfer of ions and electrons is crucial. The fuel cell components responsible for transferring ions and electrons are often called electrolytes and electrodes, respectively. Their transport properties depend on their concentrations and mobilities of ions and electrons. Especially, types of inorganic materials vary from insulators to semiconductors, metallic conductors, and even to superconductors owing to their different electronic properties. The electronic conductivity of a given metal oxide sometimes changes by a few orders of magnitude depending on the synthesis procedures or the presence of a small amount of dopants. Therefore, controlling the concentration of point defects (ionic defects and electronic defects), which determine the origin of ionic conductivity and electronic conductivity, is a key to fundamental materials design. In other words, defect chemistry can quantitatively indicate the relationship between defect concentration and physical properties or parameters of materials, leading to the fundamentals of quantitative control, prediction, and optimization of material properties.

Since the difference between a perfect crystal and an actual crystal often determines physical properties such as conductivity (Fig. 21.4), it is important to be able to denote the deviation from a perfect crystal in writing. The notation developed by Kröger and Vink [2, 3] as shown in Fig. 21.5 is usually used. This allows one to clearly indicate relative charge, the sites of defects, and also types of defects, compared to a perfect crystal. Furthermore, a defect equilibrium equation can be written using the notation, and so the defect equilibrium constant can be defined. Electrochemical reactions including defects can also be written [4].

At relatively high temperature where there is almost no kinetic limitation, reactions where ions, electrons, and molecules transfer within the materials or at the surface of materials often reach the equilibrium state. The relationship of defect concentrations is primarily determined under the consideration of defect equilibria, a mass conservation law, and electrically neutral conditions. On the other hand, when temperature decreases, equilibria in some reactions are never reached from a kinetic point of view. Especially, an oxygen exchange equilibrium reaction, which is important for electronic oxide materials, does not occur under 400–800 °C, resulting in failure in the oxygen exchange equilibrium equation. However, by adding a relative equation of oxygen concentration conservation within the materials, an equation for defect concentrations can in principle be determined [5, 6].

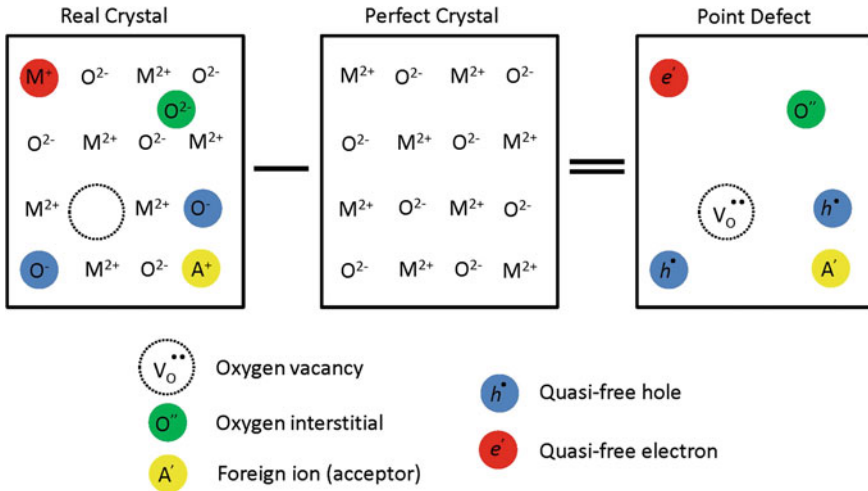


Fig. 21.4 Perfect crystal versus real crystal (Oxide “MO” as an example)

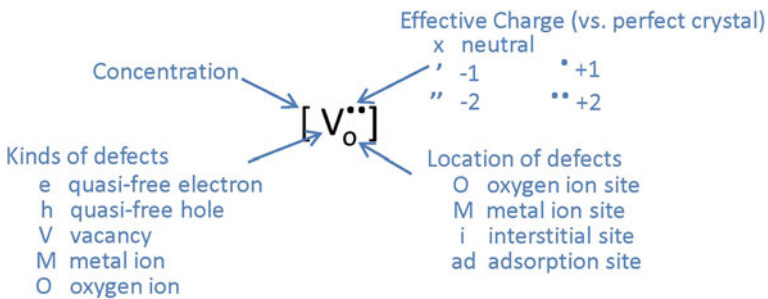


Fig. 21.5 Kröger-Vink notations (oxygen vacancy as an example)

In the case of SOFC, since the operating temperature is high enough (e.g., 800 °C), equilibrium is assumed to be achieved. On the other hand, if oxides are used in PEFCs, they are probably used under such conditions that defect equilibria are never achieved.

In order to find out numerical constants and coefficients, for example, in the equations of defect concentrations, material analyses based on solid-state electrochemistry and solid-state physics are essential, and typical methods are listed in Table 21.1. Since materials are often polycrystalline in reality, quantitative analyses excluding the effects of grain boundaries, interfaces between different phases of composites, and surfaces become important. Although solid-state electrochemical methods allow one to analyze macroscopic properties based on measured resistance, voltage, and current, further microscopic properties can be also obtained by directly detecting defects through electron spin resonance techniques and optical

Table 21.1 Characterization procedures in solid-state electrochemistry

Electrochemistry (steady-state/transient, reversible/blocking electrode)	<ul style="list-style-type: none"> • DC measurements • AC impedance • Transference number measurements • Permeation measurements • Point electrode technique (AFM, STM)
Defect and transport	<ul style="list-style-type: none"> • Tracer diffusion (^2D, ^{18}O) (SIMS, TG) • EPR/ESR (low/high temp.) • Optical absorption (UV, VIS, NIR) • NMR(PFG) • Half-effect measurements • Thermoelectric effect measurements • Thermal analysis (DSC, DTA, TG) • Gas Analysis (MS, FTIR, GC)
Material	<ul style="list-style-type: none"> • Microstructural characterization (SEM, TEM, AFM, STM) • Diffraction technique (XRD, Neutron diffraction) • Surface analysis (SIMS, LEIS)

DC Direct current, *AC* Alternating current, *AFM* Atomic force microscope, *STM* Scanning tunneling microscope, *SIMS* Secondary ion mass spectroscopy, *TG* Thermogravimetry, *EPR* Electron paramagnetic resonance, *ESR* Electron spin resonance, *UV* Ultraviolet, *VIS* Visible, *NIR* Near-infrared, *NMR* Nuclear magnetic resonance, *PFG* Pulsed field gradient, *DSC* Differential scanning calorimetry, *DTA* Differential thermal analysis, *MS* Mass spectrometry, *FTIR* Fourier transform infrared spectroscopy, *GC* Gas chromatography, *SEM* Scanning electron microscope, *TEM* Transmission electron microscope, *XRD* X-ray diffraction, *LEIS* Low-energy ion scattering

absorption methods. Such evaluation can be done even at high temperature, where ions can more actively move, leading to determination of quantities such as chemical diffusion coefficients and surface exchange reaction coefficients through in situ measurements [7, 8].

21.3 Experimental Procedures

In this section, experimental evaluation procedures for fuel cells are introduced. Since the cell voltage (performance) is the most important issue, and the most significant component to decide cell voltage is actually an electrocatalyst (electrode), this electrode can be examined separately using a method called a half-cell evaluation. This section starts by introducing techniques for a half-cell and then moves on to full cell evaluation. Furthermore, additional advanced techniques to evaluate materials constructing fuel cells are introduced.

The half-cell evaluation technique is a simple and useful method especially for fuel cells operating at low temperature, like PEFC and AFC [9]. By selecting a suitable electrolyte solution, for example, 0.1 M HClO_4 for PEFC and 0.1 M KOH for AFC, this technique is useful for various types of fuel cells. Here, a general half-cell method in the acidic condition like PEFC is explained as one example. In a

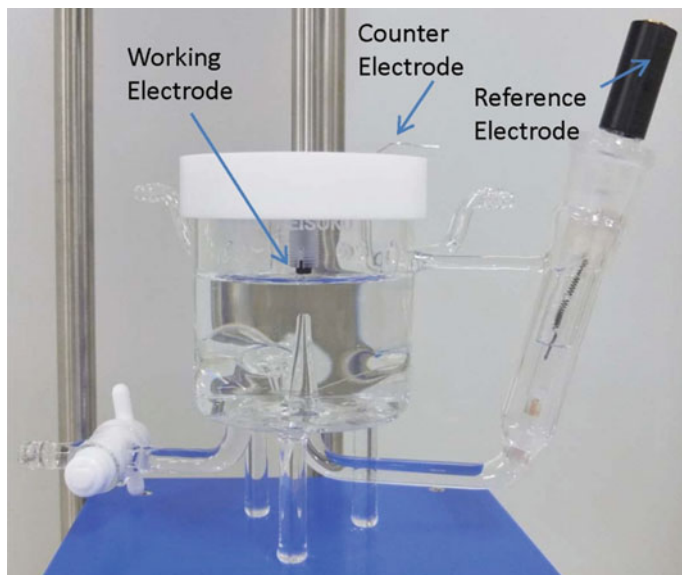


Fig. 21.6 A typical electrochemical cell with three electrodes

half-cell evaluation, a typical electrochemical cell of three electrodes with a solution electrolyte is used (Fig. 21.6). The cyclic voltammetry technique is used to evaluate the activity of electrocatalysts. A rotating disk electrode is useful as a working electrode. For counter and reference electrodes, Pt wire and Ag/AgCl are commonly used, respectively, but they are not limited to those materials. For the electrolyte solution, 0.1 M HClO₄ or H₂SO₄ is used. In order to evaluate the activity of anode and cathode electrocatalysts, the electrolyte solutions are saturated by hydrogen and oxygen, respectively. As a pretreatment step of electrochemical measurements, in order to clean the surface of electrocatalysts, especially for Pt metal, cyclic voltammetry is performed between 0.05–1.20 V at 50 mV/s under inert atmosphere, such as argon or nitrogen, until the profile of hydrogen adsorption/desorption shown in Fig. 21.7 is clearly obtained. From the hydrogen adsorption/desorption peak, the electrochemical surface area (ECA) of Pt can be evaluated. The electric charge (Q) of the hydrogen adsorption peak (shaded area in Fig. 21.7) is calculated. Then, the obtained electric charge can be divided by 210 $\mu\text{C}/\text{cm}^2$, which is the electric charge from one layer of hydrogen adsorbed on a Pt surface [10].

After electrochemical cleaning of the catalyst's surface, the electrolyte solution is saturated by oxygen or hydrogen for oxygen reduction or hydrogen oxidation reactions, respectively, and then linear sweep voltammetry is performed. In Fig. 21.8, a typical linear sweep voltammogram for the oxygen reduction reaction is shown. Commonly, mass activity (A/g-Pt) and specific activity (A/m²-Pt) at a certain voltage (usually 0.9 V vs. reversible hydrogen electrode (RHE)) are compared between various electrocatalysts for evaluating catalytic activity.

Fig. 21.7 A typical cyclic voltammogram of Pt dispersed on carbon support

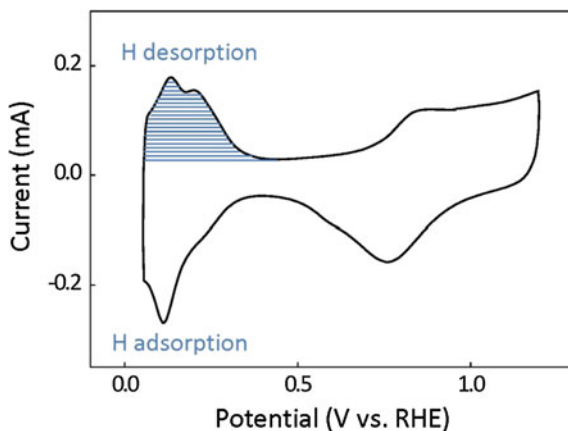
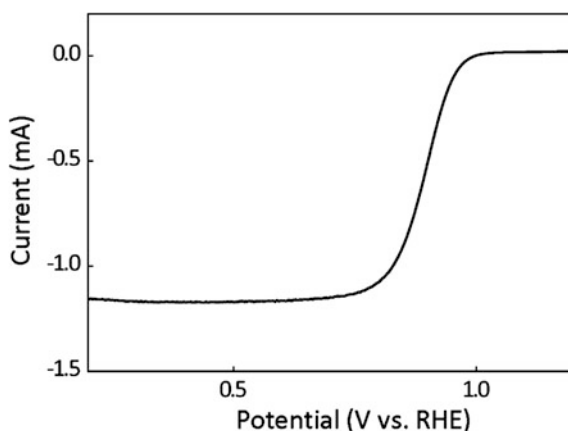


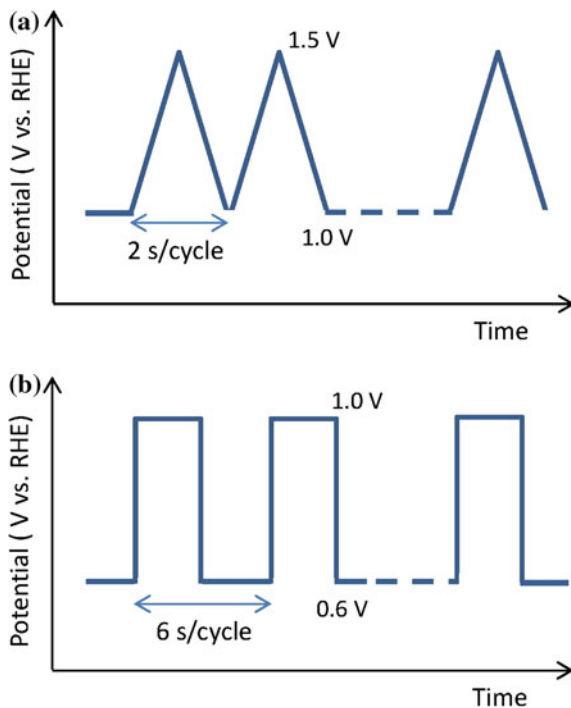
Fig. 21.8 A typical linear sweep voltammogram of Pt dispersed on carbon (electrode area: 0.2 cm², rotation speed: 1600 rpm)



Besides measuring the initial activity of electrocatalysts, protocols to evaluate durability are developed in many ways. Here, protocols simulating the operation of fuel cell vehicles given by Fuel Cell Commercialization Conference of Japan (FCCJ) are introduced [11]. For the simulation of stop/start cycles, cycles of the triangle wave between 1.0 and 1.5 V under nitrogen atmosphere with the rate of 2 s per cycle can be performed (Fig. 21.9a). In the case of simulating the potential change occurring during driving cycles, potential cycles of the square wave between 0.6 and 1.0 V under nitrogen atmosphere with the rate of 6 s per cycle can be carried out (Fig. 21.9b).

After high enough activity of each cell component is confirmed, an actual fuel cell should be fabricated with the electrocatalysts and other materials, and then, its performance can be evaluated. Even though details about each type of fuel cell are explained in the following chapters, Chaps. 22–24, here a general method of cell preparation is briefly explained. For example, a PEFC or anion-exchange

Fig. 21.9 Potential cycles for accelerating degradation based on FCCJ protocol [9]. **a** Simulating stop/start cycles of FCVs. **b** Simulating driving cycles of FCVs



membrane-based AFC can be prepared by printing electrocatalyst layers on both sides of a polymer electrolyte membrane (Fig. 21.10a) [12]. Regarding SOFCs, similarly, electrode materials are pasted on both sides of the electrolyte, but an additional sintering process is necessary (Fig. 21.10b) [13, 14]. Each prepared cell

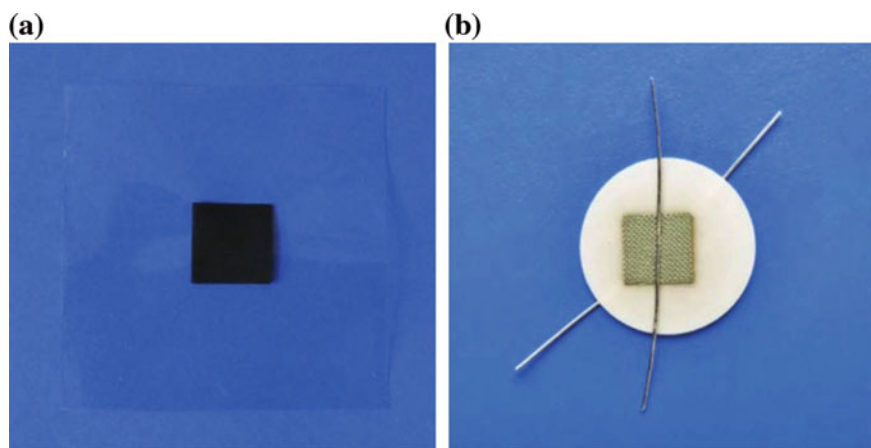


Fig. 21.10 Photographs of actual fuel cells (electrode: 1 cm^2). **a** PEFC. **b** SOFC

can be combined with the current collector, set into the gas supplying setup, and then operated at the appropriate temperature. Owing to a characteristic of polymer membranes, humidification is also required for PEFCs and AFCs.

Regarding the evaluation of cells, current–voltage (I – V) characteristics are evaluated. In addition, the ohmic resistance of cells can be evaluated using the current interrupt method or impedance measurements. Furthermore, the activation overpotential and concentration overpotential can be separated based on Tafel plot analyses after correcting for the ohmic portion from the actually obtained current (Fig. 21.11) [15]. Such electrochemical methods can be useful for various electrochemical devices including PEFCs, SOFCs, and AFCs.

Durability analyses for the cell are important issues. Regarding PEFCs, accelerating degradation protocols including stop/start cycles or load cycles explained above can be applied to the cell. Since the operation condition (temperature and humidity) is much more severe than that of the solution half-cell evaluation, durability evaluation of the full cells is highly recommended. For SOFCs, particularly for stationary purposes, durability over time, temperature cycles, and redox cycles can be evaluated by simulating real operation conditions [14].

In addition to electrochemical methods, recently, advanced techniques to evaluate materials constructing fuel cells have become available. Evaluation of material structures at the nanometer level or even at the atomic level is important since the reactivity of materials in fuel cells largely depends on such nanostructures. Elemental analyses of materials and valence state analyses of atoms are key techniques alongside nanostructure observation. Fundamentals of electrochemistry including catalytic activity largely depend on grain boundaries, surfaces, or

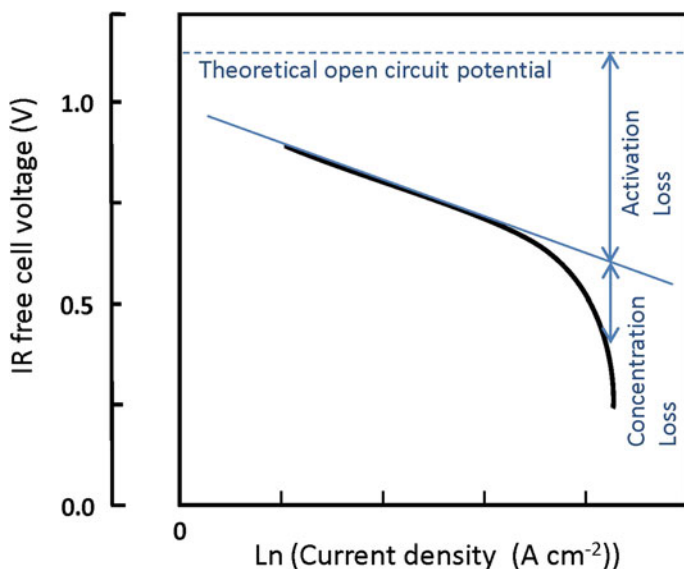


Fig. 21.11 Separation of activation overpotential and concentration overpotential

heterointerfaces between materials. Observation of such sites is essential and can be achieved by advanced analytic techniques such as electron microscopes. Major microscopic observation apparatus are summarized in the following.

X-ray computed tomography (X-ray CT) (Fig. 21.12): It is a nondestructive technique for visualizing interior features within solid objects, such as the whole unit of cells, devices, etc. X-rays are directed at the object from multiple orientations, and the decrease in intensity is basically measured.

Scanning electron microscope (SEM) (Fig. 21.13): It is often used along with elementary analyses by an energy-dispersive x-ray (EDX) spectrometer or a wavelength-dispersive x-ray (WDX) spectrometer and is a useful technique to analyze structure at nanometer to micrometer scales. More recently, SEM with surface cutting apparatus using a focused ion beam (FIB) is available and often called FIB-SEM. With FIB-SEM, many slices of pictures taken after FIB processing can be reconstructed into a three-dimensional image afterward, which allows quantitative analyses of the three-dimensional structure [13, 16].

Transmission electron microscope (TEM) and scanning transmission electron microscope (STEM) (Fig. 21.14): TEM is a powerful technique to analyze materials at the nanometer level after processing the sample to small pieces of several tens of nanometers thickness. STEM further has the function of focusing an electron beam, leading to possible observation at the atomic resolution level (<0.1 nm). A special sample holder may be applied to expose the TEM sample in a defined atmosphere and/or at an elevated temperature, for in situ or in operando observations, which is often called environmental TEM (ETEM) (Fig. 21.14c).



Fig. 21.12 X-ray computed tomography (X-ray CT)

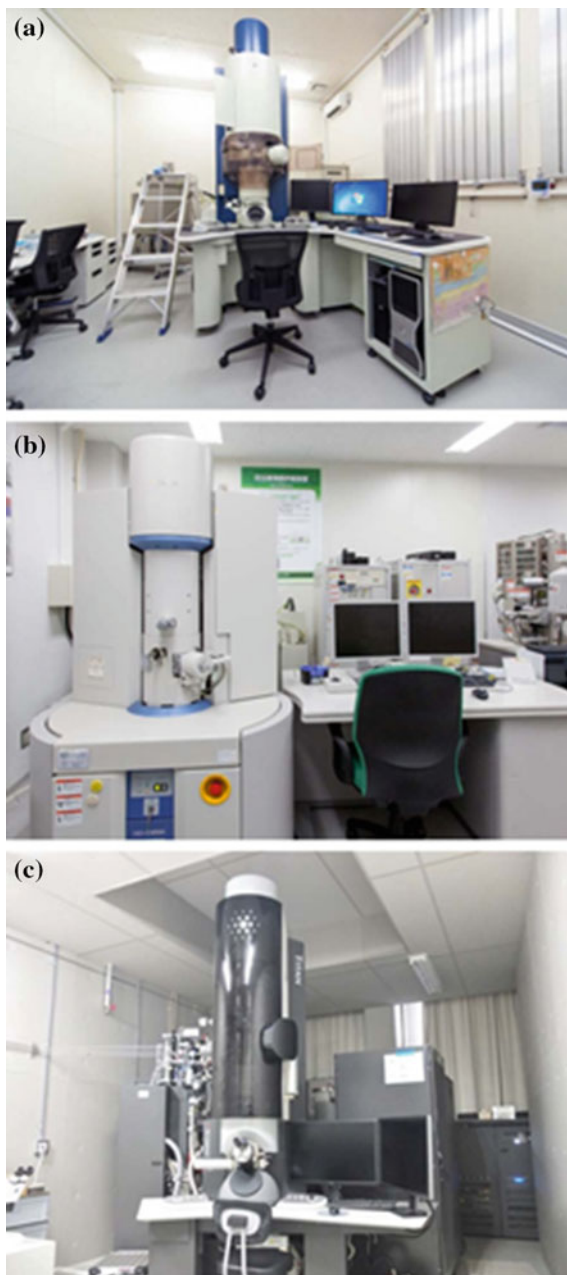


Fig. 21.13 Scanning electron microscope (*SEM*) equipped with **a** energy-dispersive *x*-ray (*EDX*) spectrometer and **b** focused ion beam (*FIB*)

Secondary ion mass spectroscopy (SIMS) (Fig. 21.15): It is a surface-sensitive analytical technique. With SIMS, elemental analyses of surfaces are possible based on secondary ions ejected from the sample surface when impacted by a primary beam of heavy particles. Profiles along the depth direction of materials are possible.

Low-energy ion scattering (LEIS) (Fig. 21.16): It is one of most useful techniques for outermost surface analyses. The concentrations of elements in the outermost surface can be evaluated from the change in kinetic energy of a low-energy primary ion that is scattered elastically from the sample surface when it impinges on the material surface [17].

Fig. 21.14 **a** Transmission electron microscope (*TEM*), **b** scanning transmission electron microscope (*STEM*), and **c** environmental transmission electron microscope (*ETEM*)



Recent advance in microscopic analyses is accompanied by in situ techniques. Combination of above techniques with control of the observation environments (temperature and gas atmosphere) leads to analyses in more practical conditions of cells and devices [18, 19].



Fig. 21.15 Secondary ion mass spectroscopy (SIMS)



Fig. 21.16 Low-energy ion scattering (LEIS)

References

1. Larminie J, Dicks A (2003) Fuel Cell Systems Explained, 2nd edn. Wiley, Chichester
2. Kröger FA, Vink HJ (1956) Relations between the concentrations of imperfections in crystalline solids. *Solid State Physics* 3:307–435
3. Maier J (2004) Physical chemistry of ionic materials. Wiley, Chichester
4. Hosoi T, Yonekura T, Sunada K, Sasaki K (2015) Exchange current density of SOFC electrode: theoretical relations and partial pressure dependencies rate-determined by electrochemical reactions. *J Electrochem Soc* 162:F136–F152

5. Sasaki K, Maier J (1999) Low temperature defect chemistry of oxides: I. General aspects and numerical calculations. *J Appl Phys* 86:5422–5433
6. Sasaki K, Maier J (1999) Low temperature defect chemistry of oxides: II. Analytical relations. *J Appl Phys* 86:5434–5443
7. Bieger T, Yugami H, Nicoloso N, Maier J, Waser R (1994) Optical absorption relaxation applied to SrTiO₃ and ZrO₂: an in-situ method to study trapping effects on chemical diffusion. *Solid State Ionics* 72:41–46
8. Sasaki K, Maier J (2000) In situ EPR studies of chemical diffusion in oxides. *Phys Chem Chem Phys* 2:3055–3061
9. Iiyama A, Hamada A (2011) Proposals of the development targets, research and development challenges and evaluation methods concerning PEFCs. Fuel cell commercialization conference of Japan, Tokyo
10. Biegler T, Rand DAJ, Woods R (1971) Limiting oxygen coverage on platinumized platinum; Relevance to determination of real platinum area by hydrogen adsorption. *J Electroanal Chem* 29:269–277
11. Ohma A, Shinohara K, Iiyama A, Yoshida T, Daimaru A (2011) Membrane and catalyst performance targets for automotive fuel cells by FCCJ membrane, catalyst, MEA WG. *ECS Trans* 41:775–784
12. Zhao X, Hayashi A, Noda Z, Sasaki K (2014) Evaluation of MEAs prepared by Pt/C electrocatalysts with improved durability through the heat treatment. *ECS Trans* 58:7–13
13. Haga K, Shiratori Y, Ito K, Sasaki K (2008) Chlorine poisoning of SOFC Ni-cermet anodes. *J Electrochem Soc* 155:B1233–B1239
14. Hanasaki M, Uryu C, Daio T, Kawabata T, Tachikawa Y, Lyth SM, Shiratori Y, Taniguchi S, Sasaki K (2014) SOFC durability against standby and shutdown cycling. *J Electrochem Soc* 161:F850–F860
15. Daimaru A (2014) The cell evaluation protocol. The New Energy and Industrial Technology Development Organization, Tokyo
16. Ni M, Zhao TS (eds) (2013) Solid oxide fuel cells: from materials to system modeling. Royal Society of Chemistry, Abingdon
17. Kilner JA, Skinner SJ, Brongersma HH (2011) The isotope exchange depth profiling (IEDP) technique using SIMS and LEIS. *Solid-State Lett* 15:861–876
18. Yaguchi T, Kanemura T, Shimizu T, Imamura D, Watabe A, Kamino T (2012) Development of a technique for in situ high temperature TEM observation of catalysts in a highly moisturized air atmosphere. *J Electron Microsc* 61:199–206
19. Matsumoto H, Konno M, Sato T, Nagaoki I, Yaguchi T, Howe JY (2013) Simultaneous in situ SEM and STEM analysis of gas/catalyst reaction in a cold field-emission environmental TEM. *Microsc Anal* 27:13–18

Chapter 22

Polymer Electrolyte Fuel Cells (PEFCs)

Akari Hayashi, Masamichi Nishihara, Junko Matsuda
and Kazunari Sasaki

Abstract This chapter describes operating principles of polymer electrolyte fuel cells. The fundamental components (electrolyte, electrode, and gas diffusion layer) are explained from the viewpoint of material science, followed by a description of cells and stack structures.

Keywords PEFC · MEA · Proton conductivity · Nafion · Pt · Carbon · FCV · Hydrogen utilization

22.1 Operating Principles of the PEFC [1]

PEFCs are well known for their commercialization for residential and automobile purposes. The fundamental structure of a PEFC is explained in Fig. 22.1. A PEFC is generally composed of a H^+ -conducting electrolyte membrane, electrodes, gas diffusion layers, and separators (bipolar plates). In particular, the electrocatalyst membrane sandwiched by two electrodes, made by highly dispersed precious metal particles on carbon with proton conducting ionomers, is called the membrane electrode assembly (MEA). Hydrogen and air are used as a fuel and an oxidant, respectively. Humidified hydrogen and air (close to relative humidity (RH) of

A. Hayashi (✉) · K. Sasaki
International Research Center for Hydrogen Energy, Kyushu University,
Fukuoka 819-0395, Japan
e-mail: hayashi.akari.500@m.kyushu-u.ac.jp

K. Sasaki
e-mail: sasaki@mech.kyushu-u.ac.jp

M. Nishihara · J. Matsuda
International Institute for Carbon-Neutral Energy Research (WPI-I2CNER),
Kyushu University, Fukuoka 819-0395, Japan
e-mail: nishihara@i2cner.kyushu-u.ac.jp

J. Matsuda
e-mail: junko.matsuda@i2cner.kyushu-u.ac.jp

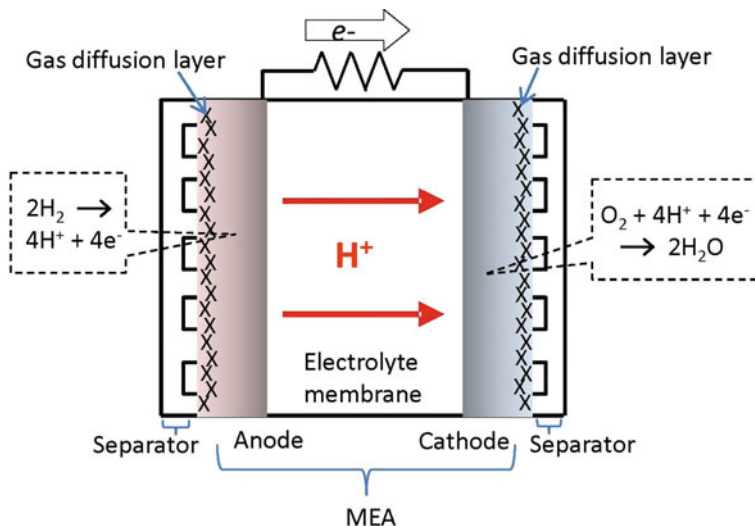
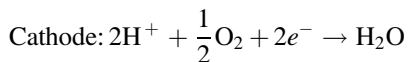
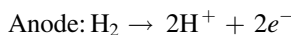


Fig. 22.1 Fundamental structure of a PEFC

100 %) are supplied, and the PEFC operates under 100 °C. Reactions at the cathode and the anode are given below.



The theoretical open-circuit voltage near room temperature is 1.23 V. The theoretical thermodynamic efficiency derived from the ratio of $\Delta G/\Delta H$ is about 84 %. At the anode, the overpotential of the reaction is small, and the reaction quickly occurs. On the other hand, at the cathode, the reaction occurs slowly under oxidizing atmosphere, which leads to a major voltage loss in PEFC (see *Electrochemistry and Overpotential* in Sect. 21.1). In reality, the open-circuit potential under atmospheric pressure is about 1 V, which is much lower than theoretical value of 1.23 V. Major reasons for that come from fuel crossover and internal current generation. In the following sections, the fundamental components of a PEFC (electrolyte, electrode, and gas diffusion layer), and cell and stack structures are explained.

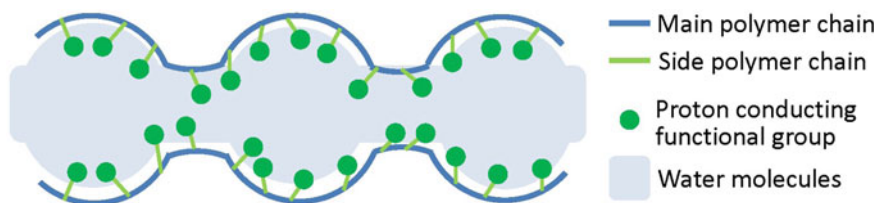


Fig. 22.2 Schematic drawing of hydrophilic channels made by Nafion

22.2 Electrolytes

For PEFCs, a polymer electrolyte membrane (PEM) has been used as an electrolyte material. The role of a PEM is to transfer protons. Generally, the thickness of membranes is 20–50 μm . In addition to transferring protons produced at the anode to the cathode, the abilities of preventing electron transfer between the two electrodes as an (electronic) insulator and blocking either hydrogen or air from leaking into the counter side of each electrode are required.

Proton conductivity is derived from functional groups which transfer protons within the PEM; these groups are strong acids like a sulfonic acid. Usually, polymers with many hydrophilic functional groups have high solubility in water and also low mechanical strength, compared to polymers without such functional groups. Therefore, it is necessary to introduce hydrophobic functional groups, while retaining enough proton conductivity. Also, for most PEMs, the proton conducting mechanism is explained by proton transfer through hydrophilic channels made by proton conducting functional groups and water molecules as shown in Fig. 22.2 [2]. Therefore, a certain degree of humidification is essential for proton transfer.

The most typical PEM is a perfluorohydrocarbon electrolyte membrane, called Nafion[®] (Dupont) [3] as shown in Fig. 22.3. Nafion has a framework of polytetrafluoroethylene (PTFE), where the hydrogen of the ethylene part is replaced by fluorine. In addition, the end of the side chains is composed of sulfonic acid (HSO_3) groups. Although the main chain has a hydrophobic character, the side chains

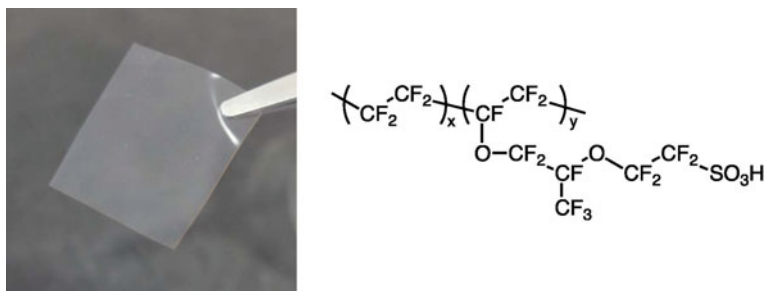


Fig. 22.3 A photograph of Nafion and its chemical structure

reveal hydrophilic regions since the end HSO_3 group is ionized to SO_3^- and H^+ , attracting water molecules. The presence of SO_3^- and H^+ leads to strong mutual attraction between positive and negative ions from different side chains, and then side chain molecules tend to form clusters within the overall structure. The hydrophilic regions around clusters of sulfonated side chains can adsorb large quantities of water, and then protons can move more efficiently between the two electrodes. Consequently, the power density largely depends on humidity. Since Nafion has high chemical stability and proton conductivity, it is commonly used for PEFC. On the other hand, humidification is essential, and so it is not suitable for operation above $100\text{ }^\circ\text{C}$, which is part of the future directions of PEFC research.

For the next generation electrolyte, the challenge includes the development of new PEMs in place of Nafion. For alternative PEMs, sulfonated aromatic electrolyte membranes are under study for high chemical and thermal stability. For example, sulfonated polyimides (SPI), sulfonated polyetheretherketone (SPEEK), sulfonated poly(phenylsulfone), sulfonated polyethersulfone (SPES), and also the combination of these can be candidates (Fig. 22.4) [4–8]. Even so, since these polymers have high ion exchange capacity (IEC: moles of acid per polymer unit), balancing water solubility and proton conductivity becomes a key issue. For example, increasing the resistance to water solubility by introduction of a monomer unit, which is not much affected by crosslinking and decomposition reactions, is underway [9]. Also, for the purpose of separating hydrophobic and hydrophilic regions at the macroscale and increasing the formation of hydrophilic cluster regions, the use of block polymers or graft polymers is under consideration [10, 11]. Moreover, besides the proton

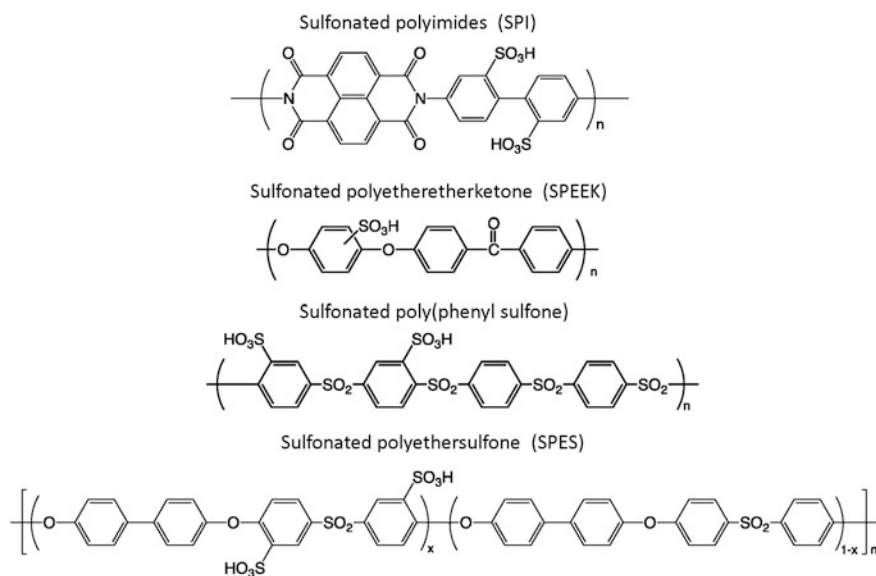


Fig. 22.4 Chemical structures of alternative PEMs

conducting process through water clusters, phosphoric acid-doped polybenzimidazole (PBI) membrane [12] or membranes using ionic liquids [13] are also studied.

In order to develop practical electrolyte membranes using such new electrolyte materials, high enough proton conductivity, stability, and durability under the real PEFC operating conditions (high temperature, low humidification, or low temperature like under the freezing point) are required. Since there is usually a trade-off between proton conductivity and durability, optimization of the polymer composition is essential.

22.3 Electrodes (Electrocatalysts)

The electrode is composed of a layer of electrocatalysts and ionomers with the thickness of several tens of micrometers. Such a catalyst layer requires high catalytic activity even around room temperature, both electronic conductivity and proton conductivity, and also high mass transfer properties in order to supply reactant gases and remove reaction products. A schematic figure of the electrode (cathode) cross section is shown in Fig. 22.5. In order to utilize all the electrocatalysts along the thickness of the layer, efficient development of a triple phase boundary, formed by the electrocatalyst-electrolyte (ionomer)-reactant gas interface, is essential. Therefore, electrocatalysts are desired to be covered by a thin layer of ionomers with the thickness of a few to several tens of nanometers. In the presence of a triple-phase boundary, hydrogen gas reaches the anode electrocatalyst through the ionomer layer and produces protons at the anode. These protons are allowed to transfer toward the surface of a cathode electrocatalyst first through the ionomer at the anode, then through the electrolyte membrane, and finally through the ionomer layer in the cathode. At the same time, oxygen in the air supplied at the cathode reaches the cathode electrocatalyst through its ionomer layer. Consequently, water is produced as a product.

For electrocatalysts, highly dispersed precious metal catalysts are usually used. Owing to the high acidity of perfluorosulfonic acid, Pt, which is stable in such a severe condition and also able to reduce the overpotential of reactions, is used for

Fig. 22.5 Schematic drawing of cathode cross section

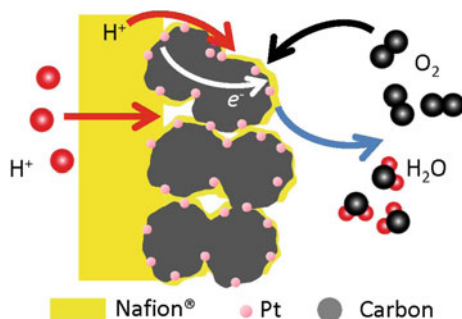
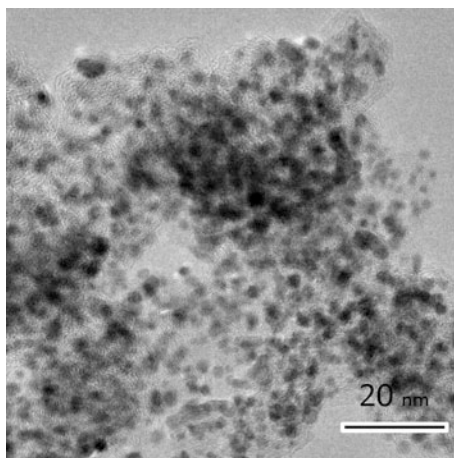


Fig. 22.6 A TEM image of a typical electrocatalyst, Pt deposited carbon black (Black spots: Pt nanoparticles)



both the anode and the cathode. Since Pt is expensive, it is essential to produce the cell voltage by keeping the amount of Pt as small as possible. Therefore, as shown in Fig. 22.6, Pt nanoparticles are dispersed on carbon black powder with high electronic conductivity. 10–50 wt% of Pt is deposited on the carbon black. The Pt particle size is usually 1–5 nm and its surface area is typically 50–100 m²/g. Since Pt nanoparticles have a tendency to grow and form larger particles when the percentage of Pt increases on the carbon support, carbon black with a large surface area is used to effectively disperse the Pt nanoparticles. Commonly, Vulcan (around 250 m²/g) and Ketjen Black (800–1300 m²/g) are used, and their primary particle size is 10–100 nm (Fig. 22.7).

Recently, in order to further improve the activity and durability of electrocatalysts, and also to reduce the high loading of Pt, thereby lowering the cost, alloys of Pt and other precious metals have been studied. Regarding the anode catalysts,

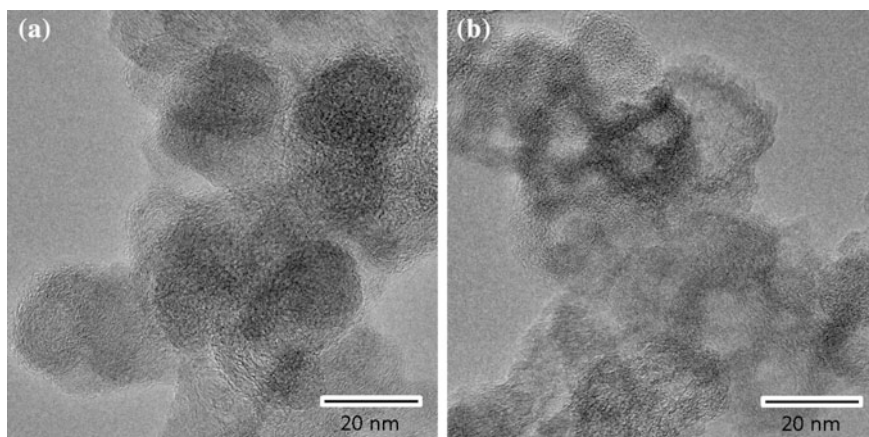


Fig. 22.7 TEM images of carbon black, **a** Vulcan and **b** Ketjen black

since hydrogen fuel is often made from reforming hydrocarbon gases like natural gas, a small amount of CO (a few ppm) may be included in the fuel. Such CO adsorbs on the Pt surface and reduces the number of catalytically active sites. To mitigate CO poisoning, a PtRu alloy catalyst is considered as one of the most promising commercially available catalysts. Its CO tolerance characteristics are attributed to a combination of its electronic properties and bifunctional mechanism. In terms of the electronic properties, because of the electron transfer between Pt and added metals, the Pt–CO bond is weakened. In terms of the bifunctional mechanism, oxygen species adsorbed on Ru sites help oxidation of the CO adsorbed on Pt sites. Since there is still room for further improvement, Pt-based binary and ternary electrocatalysts are also being developed [14, 15].

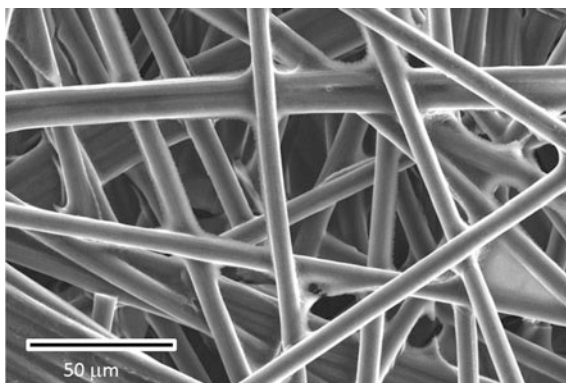
Similarly, for the cathode, in order to reduce the overpotential produced by the slow oxygen reduction reaction, alloying with various metals has been tried [16]. In this case, the surface electronic structure can be controlled to increase the reactivity toward oxygen reduction. Pt–Co- and Pt–Ni-based alloys are known to have high reactivity. Since the surface electronic structure changes, the adsorption of species other than O₂, such as OH[−], is reduced, and then more Pt sites remain available for O₂. This reaction mechanism is believed to be a reason for promotion of the oxygen reduction reaction, resulting in higher reactivity. Recently, Pt monolayer-based catalysts have been under development in order to control the surface electronic structure. The most typical example is a core–shell catalyst, where the shell is made by Pt, but for the core Au or Pd is often used. Usage of nonprecious metals for the core is desired as a topic for further study in terms of cost.

One of the problems for electrocatalysts to overcome is durability. Suppressing the degradation of catalysts is necessary to extend the lifetime of PEFC. During long-term operation, Pt nanoparticles agglomerate and grow. Thermodynamically unstable carbon supports are oxidized, leading to the promotion of Pt agglomeration, dissolution, and detachment. Especially, these phenomena are accelerated under the conditions of high temperature and high voltage. Recently, in order to improve carbon durability, carbon with the surface graphitic structure, showing increased oxidation resistance, has been applied [17, 18]. Even non-carbon materials like metal oxides have been recently introduced as support materials [19–21].

22.4 Gas Diffusion Layer [22, 23]

In order to supply reactant gases (hydrogen and air) to the electrode layers homogeneously, a gas diffusion layer is attached at the outer part of each electrode. This gas diffusion layer has a role of current collecting, and is made of carbon with a highly porous structure. Specifically, carbon fibers, whose pore diameter is several micrometers, make a paper-like structure with binder, called carbon paper. Carbon cloth and felts are also often used. Owing to water supplied along with the fuels, and water produced in the cathode reaction, water management is essential. Therefore, the gas diffusion layer has an important role to efficiently remove excess

Fig. 22.8 A SEM image of carbon paper



water. Hydrophobic PTFE is usually blended with the carbon fibers to form PTFE bridges across the pores of several tens to hundreds of micrometers made by the carbon fiber (Fig. 22.8). Particularly for the cathode side, a microporous layer (MPL) is commonly used as an additional layer on carbon paper. The MPL possesses smaller pores suitable for gas transfer and reducing water retention.

Besides their role of water management, gas diffusion layers need high thermal conductivity to remove the heat produced by reactions, and also high mechanical strength to support electrocatalyst layers that are several tens of micrometers thick.

22.5 Cell and Stack

A cell voltage commonly used for PEFC is 0.6–0.8 V, and several tens to several hundreds of cells are stacked up for the practical use depending on the required power density. The structure of stacked cells is conveniently called a stack. Usually 700 W or 100 kW are available for residential or automobile uses by stacking.

In order to stack cells, separators, where gas flow channels are two dimensionally arranged (Fig. 22.9), are further attached at the outside of the gas diffusion layers, in order to supply hydrogen and air to the MEA through the gas diffusion layers. The separator for PEFC is often called a bipolar plate and has a role to separate the two adjacent reactant gases when cells are stacked up (Fig. 22.10). Furthermore, the separator has the important roles of quickly getting rid of produced water and collecting current. Especially at high power densities, optimization of the channel structure and the thickness of separators become important. Homogenous supply of gases to the cell with high accuracy is required.

In terms of mass production and cost, development of carbon and metal separators is mainly considered [24]. Carbon has high chemical stability, but its electronic conductivity or stability varies depending on its original synthesis processes

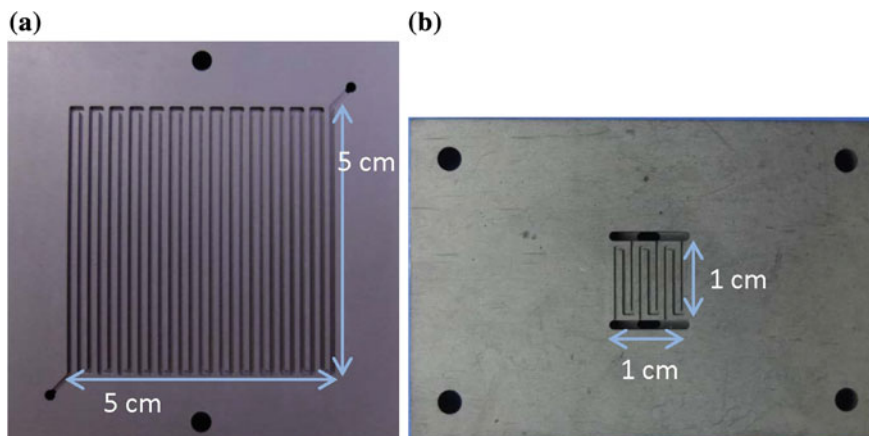


Fig. 22.9 Photographs of separators with **a** 5 cm \times 5 cm flow field of one serpentine pattern developed by JARI and **b** 1 cm \times 1 cm flow field of three serpentine patterns developed in a New Energy and Industrial Technology Development Organization (NEDO) project

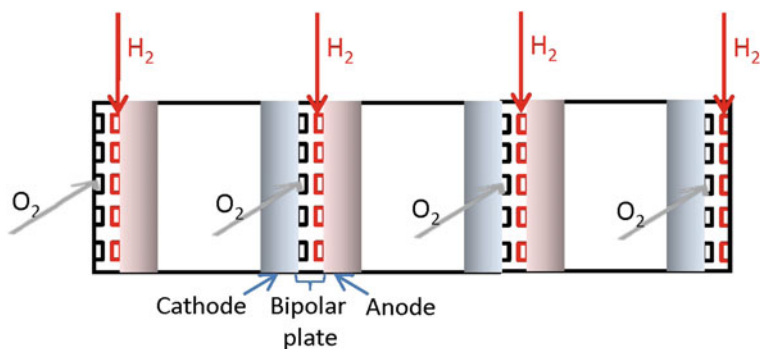


Fig. 22.10 PEFC single cells connected by bipolar plates

or the conditions of its posttreatments. Regarding making gas flow channels, each side of the separator can be patterned individually, leading to the flexibility of patterning.

On the other hand, in the case of metals, they have high electronic conductivity and mechanical strength and thereby an advantage upon thinning. The flow channels are made by pressing a template pattern, and so it takes only several seconds to make the flow channel. Since the patterning at one side is affected by the other side because of the pressing process, the flow channels should be well designed in order not to be affected by the other side of patterning. Since leaching of metal ions may contaminate the electrodes and electrolyte, leading to lowering the power density, careful selection of metal materials and also surface coatings are essential for preventing metal ion leaching. Among various metals, titanium has high corrosion

resistance, and almost no leaching is observed [25]. For this reason, titanium is well used as a material for separators. Since an insulating layer is easily formed on the surface of titanium, coating by Au is used to maintain high electronic conductivity.

22.6 Practical Materials and Applications of PEFCs

The latest practical PEFCs developed for automobile application are briefly introduced in this section. Fuel cell vehicles (FVCs) were commercialized in December 2014 after overcoming many problems as explained in Sects. 22.1–22.5. In Chap. 34, the TOYOTA MIRAI will be introduced as an automobile application in detail, but ahead of that the materials used for the PEFC within the MIRAI are focused on here [26]. For the electrolyte membrane, the thickness is reduced to one third of the original, leading to a threefold increase in proton conductivity. For electrocatalysts, Pt/C is still used at the anode, but for the cathode with a slow reaction, a more active PtCo/C is introduced, resulting in 1.8 times higher oxygen reduction activity. The gas diffusion layer is made more porous and thinner in order to increase gas diffusion ability, leading to twice higher gas diffusivity. Regarding the separators, for the cathode side, titanium separators with a 3D fine mesh flow channel are used in order to increase the hydrophobicity and promote oxygen gas diffusion, resulting in homogeneous power generation over the planar direction of the cells. Along with all these improvements to the materials, the power density of MIRAI becomes 2.4 times higher compared to TOYOTA FCHV-adv (2008 model). Please see Chap. 34 for more details.

References

1. Larminie J, Dicks A (2003) Fuel cell systems explained, 2nd edn. John Wiley & Sons, Chichester
2. Jiao K, Li X (2011) Water transport in polymer electrolyte membrane fuel cells. *Prog Energy Combust Sci* 37:221–291
3. Grot W (2011) Fluorinated Ionomers, 2nd edn. William Andrew, Waltham
4. Zhang H, Shen PK (2012) Advances in the high performance polymer electrolyte membranes for fuel cells. *Chem Soc Rev* 41:2382–2394
5. Vallejo E, Pourcelly G, Gavach C, Mercier R, Pineri M (1999) Sulfonated polyimides as proton conductor exchange membranes. Physicochemical properties and separation H^+/M^{z+} by electro dialysis comparison with a perfluorosulfonic membrane. *J Membr Sci* 160:127–137
6. Zaidi SMJ, Mikhailenko SD, Robertson GP, Guiver MD, Kaliaguine S (2000) Proton conducting composite membranes from polyether ether ketone and heteropolyacids for fuel cell applications. *J Membr Sci* 173:17–34
7. Dyck A, Fritsch D, Nunes SP (2002) Proton-conductive membranes of sulfonated polyphenylsulfone. *J Appl Polym Sci* 86:2820–2827
8. Wang F, Hickner M, Kim YS, Zawodzinski TA, McGrath JE (2002) Direct polymerization of sulfonated poly(arylene ether sulfone) random (statistical) copolymers: candidates for new proton exchange membranes. *J Membr Sci* 197:231–242

9. Tanaka M, Koike M, Miyatake K, Watanabe M (2011) Synthesis and properties of anion conductive ionomers containing fluorenyl groups for alkaline fuel cell applications. *Polym Chem* 2:99–106
10. Nasef MM (2014) Radiation-grafted membranes for polymer electrolyte fuel cells: current trends and future directions. *Chem Rev* 114:12278–12329
11. Elabd YA, Hickner MA (2011) Block copolymers for fuel cells. *Macromolecules* 44:1–11
12. Zeis R (2015) Materials and characterization techniques for high-temperature polymer electrolyte membrane fuel cells. *Beilstein J Nanotechnol* 6:68–83
13. Díaz M, Ortiz A, Ortiz I (2014) Progress in the use of ionic liquids as electrolyte membranes in fuel cells. *J Membr Sci* 469:379–396
14. Antolini E (2003) Formation of carbon-supported PtM alloys for low temperature fuel cells: a review. *Mater Chem Phys* 78:563–573
15. Ehteshami SMM, Chan SH (2013) A review of electrocatalysts with enhanced CO tolerance and stability for polymer electrolyte membrane fuel cells. *Electrochim Acta* 93:334–345
16. Wang YJ, Zhao N, Fang B, Li H, Bi XT, Wang H (2015) Carbon-supported Pt-based alloy electrocatalysts for the oxygen reduction reaction in polymer electrolyte membrane fuel cells: particle size, shape, and composition manipulation and their impact to activity. *Chem Rev* 115:3433–3467
17. Zhang S, Yuan XZ, Hin JNC, Wang H, Friedrich KA, Schulze M (2009) A review of platinum-based catalyst layer degradation in proton exchange membrane fuel cells. *J Pow Sour* 194:588–600
18. Zhao X, Hayashi A, Noda Z, Sasaki K (2014) Evaluation of MEAs prepared by Pt/C electrocatalysts with improved durability through the heat treatment. *ECS Trans* 58:7–13
19. Kocha SS (2012) *Polymer electrolyte fuel cell degradation*. Elsevier academic press, San Diego
20. Zhang Z, Liu J, Gu J, Su L, Cheng L (2014) An overview of metal oxide materials as electrocatalysts and supports for polymer electrolyte fuel cells. *Energy Environ Sci* 7:2535–2558
21. Takabatake Y, Noda Z, Lyth SM, Hayashi A, Sasaki K (2014) Cycle durability of metal oxide supports for PEFC electrocatalysts. *Int J Hydro Ener* 39:5074–5082
22. Arvay A, Yli-Rantala E, Liu CH, Peng XH, Koski P, Cindrella L, Kauranen P, Wilde PM, Kannan AM (2012) Characterization techniques for gas diffusion layers for proton exchange membrane fuel cells—a review. *J Pow Sour* 213:317–337
23. Park S, Lee JW, Popov BN (2012) A review of gas diffusion layer in PEM fuel cells: materials and designs. *Int J Hydro Energy* 37:5850–5865
24. Antunes RA, Oliveira MCL, Ett G, Ett V (2011) Carbon materials in composite bipolar plates for polymer electrolyte membrane fuel cells: a review of the main challenges to improve electrical performance. *J Pow Sour* 196:2945–2961
25. Netwall CJ, Gould BD, Rodgers JA, Nasello NJ, Swider-Lyons KE (2013) Decreasing contact resistance in proton-exchange membrane fuel cells with metal bipolar plates. *J Pow Sour* 227:137–144
26. Kawai T (2015) Abstract: fuel cell vehicle development and initial market creation. FC EXPO 2015—11th Int'l Hydrogen & Fuel Cell Expo

Chapter 23

Solid Oxide Fuel Cells (SOFCs)

Kazunari Sasaki, Yusuke Shiratori, Shunsuke Taniguchi
and Akari Hayashi

Abstract This chapter describes the operating principles of solid oxide fuel cells. The fundamental components (electrolyte and electrode) are explained from the viewpoint of material science. Typical types of cell and stack structures are also described.

Keywords SOFC · O^{2-} ion conductivity · High temperature · Ceramic · Chemical degradation · Hydrogen utilization

23.1 Operating Principles of the SOFC [1]

SOFCs are well-known power generation devices for large-scale applications, and have been commercially available for residential use since 2011 in Japan. In addition, large power plant applications are also expected in the future. SOFCs operate at high temperature such as 800 °C. A schematic of the simplified SOFC structure is shown in Fig. 23.1. It is composed of a ceramic ionic conductor as an electrolyte, ceramic electronic conductors (or cermet) as electrodes, and interconnects (separators). Due to the high operation temperature, it consists of mostly ceramic materials, which are stable even at high temperature. At the cathode,

K. Sasaki (✉) · S. Taniguchi · A. Hayashi
International Research Center for Hydrogen Energy, Kyushu University,
Fukuoka 819-0395, Japan
e-mail: sasaki@mech.kyushu-u.ac.jp

S. Taniguchi
e-mail: taniguchi.shunsuke.330@m.kyushu-u.ac.jp

A. Hayashi
e-mail: hayashi.akari.500@m.kyushu-u.ac.jp

Y. Shiratori
Department of Mechanical Engineering, Faculty of Engineering,
Kyushu University, Fukuoka 819-0395, Japan
e-mail: y-shira@mech.kyushu-u.ac.jp

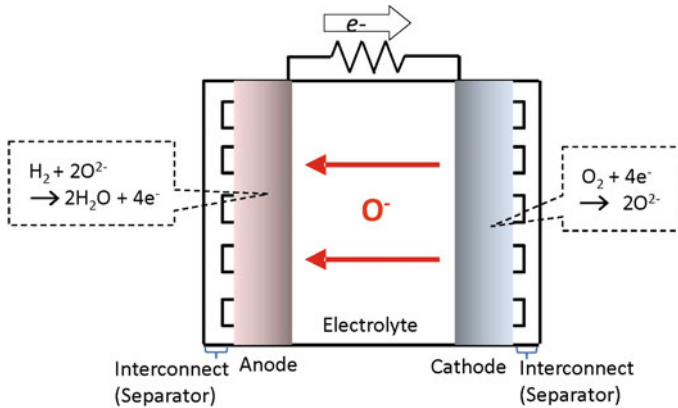
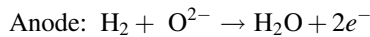
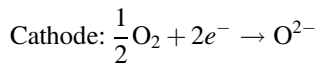


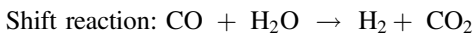
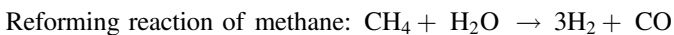
Fig. 23.1 Fundamental structure of a SOFC

oxygen molecules receive electrons to become O^{2-} ions. Unlike PEFCs, ions move from the cathode to the anode, where hydrogen reacts with the O^{2-} ions to produce water. The reactions at each electrode are the following:



Also, in addition to operating on pure hydrogen, hydrogen may be produced by the following reforming reactions of hydrocarbon fuels such as methane or a shift reaction of CO with water at the high operation temperatures [1–3].

Hence, SOFCs offer a wide range of fuel flexibility.



One of the advantages of SOFCs amongst other types of fuel cells is the relatively small overpotential of electrode reactions owing to high operation temperature. Another advantage comes from the fact that heat generated from the electrode reactions and exhaust heat in the system can be effectively used for endothermic internal reforming reactions. Therefore, power generation with higher efficiency can be achieved. On the other hand, SOFCs need much longer start-up times since the difference between room temperature and operation temperature is large. Unreasonable heating rates often lead to biased heat distribution within the cell stacks, resulting in crack formation.

In the following sections, the typical components of SOFC cells (electrolyte and electrode), and SOFC stack structure are described.

23.2 Electrolytes

Ceramic ionic conductors are used as electrolytes for the transfer of O^{2-} ions, and typically have a thickness from several tens to a few hundred micrometers. The electrolyte requires high O^{2-} ion conductivity (over 0.1 S/cm), negligible electronic conductivity, and a dense structure with minimized gas leakage as seen in Fig. 23.2. Furthermore, since one side of the cell is under oxidizing atmosphere but the other side under reducing atmosphere, the above requirements should be fulfilled over a large range of oxygen partial pressures. In addition, minimal expansion under a reducing atmosphere is also required for the electrolyte. Figure 23.3 shows the temperature dependence of O^{2-} ion conductivity in a number of ceramic electrolyte materials [4].

Figure 23.3 shows the ionic conductivity of various electrolyte materials as a function of temperature in the range at which SOFC devices operate (600–1000 °C). One of the most commonly used materials is Y_2O_3 -stabilized (or partially stabilized) ZrO_2 (referred to as YSZ), not only due to its relatively high ionic conductivity but also because of its stability in reducing atmospheres, as mentioned above. Other electrolytes under consideration in order to reduce the operating temperature, shorten start-up times, and improve fuel flexibility are Sc_2O_3 -stabilized ZrO_2 , and those based on $LaGaO_3$ [5] or CeO_2 [6, 7] O^{2-} ion conductors, as well as proton conducting materials [8, 9].

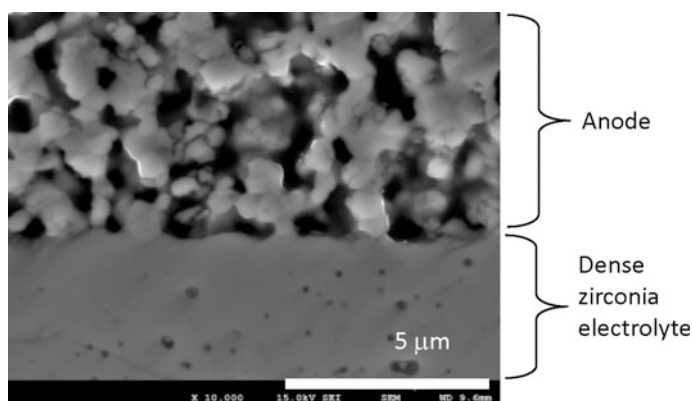
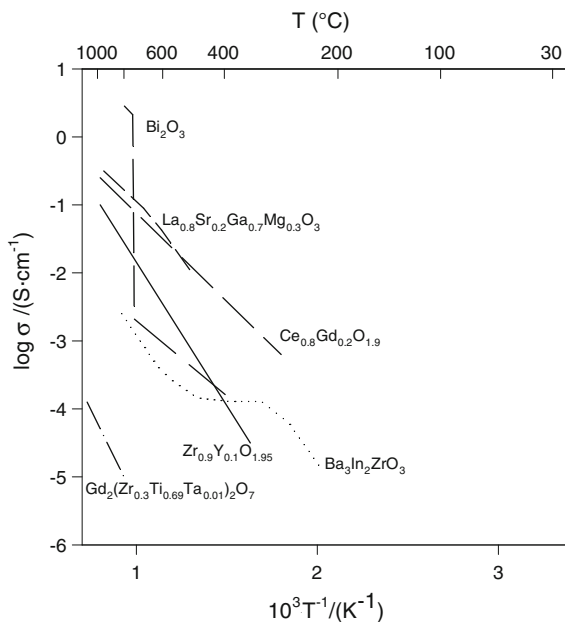


Fig. 23.2 An SEM image showing the cross section of dense zirconia electrolyte with a porous anode layer

Fig. 23.3 Dependence of oxygen ion conductivity of major electrolyte materials against temperature [4] (reproduced with permission from WILEY, Copyright 2004)



23.3 Electrode

Ceramic materials are used for both the anode and the cathode. A cross-section image of a typical SOFC is shown in Fig. 23.4 [10, 11]. Each electrode usually has a thickness of several tens of micrometers, must have good catalytic activity, may be both an electronic and ionic conductor, and have high porosity for mass transport of reactant and product gases. Materials with both high ionic conductivity and high electronic conductivity are called mixed conductors. From Fig. 23.5, one may see that the active electrode area is increased to the entire surface of the electrode when using a mixed conductor, compared to just the triple-phase boundary when using an electronic conductor.

As shown in Fig. 23.4, two-layer or even three-layer structures are often applied for both the cathode and the anode in order to further improve electronic transport within the direct electrode layer. The composition of the first layer in contact with the electrolyte is designed for maximizing triple-phase boundary formation, such that electronic conductivity, ionic conductivity, and porosity are optimized. The second and the third layers are not considered as reaction sites and rather as a current-collecting layer. Therefore, the composition of the first layer is designed to increase reactivity as well as reducing the difference in thermal expansion between the electrolyte and electrode layers.

Cathode: Since cathode materials stay under the high temperature and oxidizing conditions, chemical stability in such an environment is essential. Also, good compatibility with neighboring materials, such as a similar thermal expansion

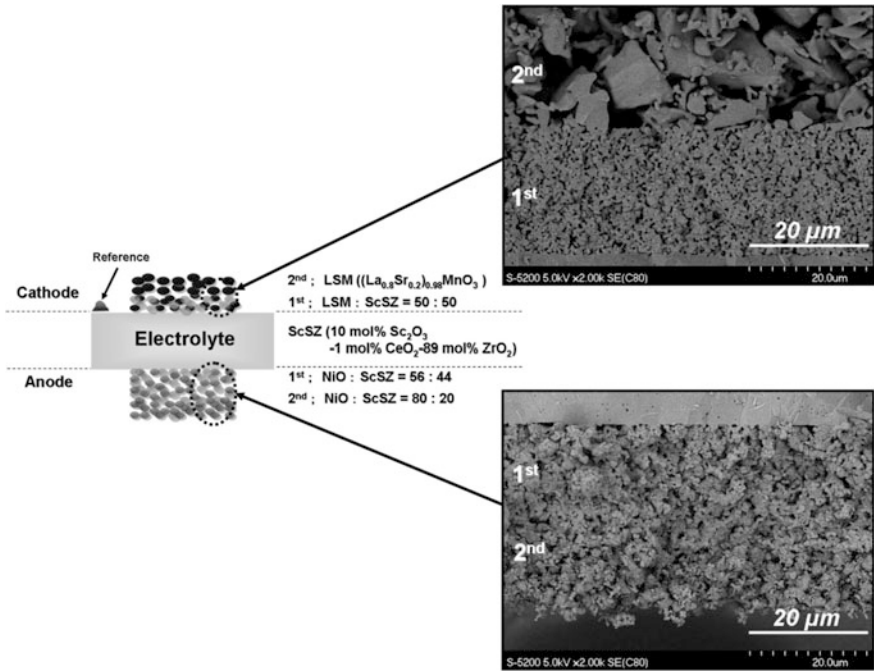


Fig. 23.4 A cross-section image of a typical SOFC [10, 11] (reproduced with permission from Springer Sciences+Business Media, Copyright 2012 and also from Dr. Kengo Haga)

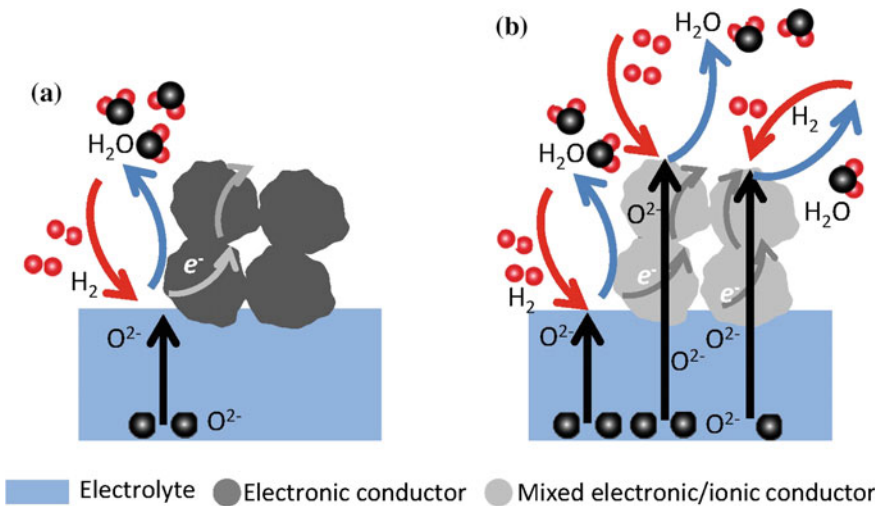
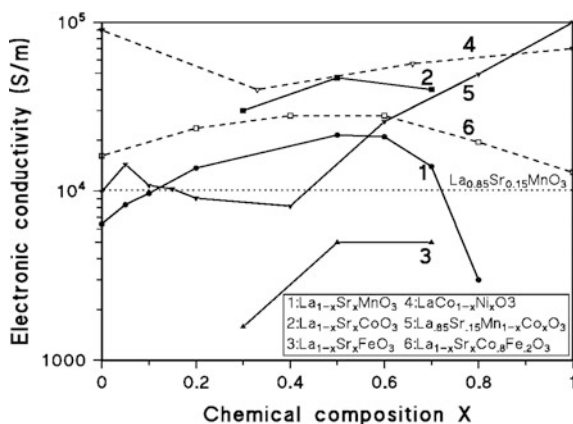


Fig. 23.5 Schematic diagrams of triple-phase boundary regions made from a electronic conductor and b mixed electronic/ionic conductor (anode)

Fig. 23.6 Electronic conductivity of various oxides at 800 °C [12] (reproduced with permission from European Fuel Cell Forum, Copyright 1994)



coefficient with the electrolyte and interconnects, is required [2, 3]. The electronic conductivity of common oxides for high-temperature electrodes is summarized in Fig. 23.6 [12]. Although Sr-doped LaMnO_3 -based materials are widely used, LaCoO_3 - and LaFeO_3 -based materials also exhibit high electronic conductivity. When stabilized zirconia is used as an electrolyte, cathode materials could face problems due to a mismatch of the thermal expansion coefficient and undesirable chemical reactions between the cathode and electrolyte materials. However, these problems can be solved by the addition of a CeO_2 -based thin buffer layer between the cathode and the zirconia electrolyte, which is frequently practiced today.

In the case of $\text{La}(\text{Sr})\text{MnO}_3$ -based cathode materials, the electronic conductivity dominates the electrical properties. Therefore, in comparison to mixed ionic–electronic conductors, reaction sites are limited and are likely to occur only at the triple-phase boundaries, formed by the electrolyte, cathode, and a reactant gas. In order to increase the number of triple-phase boundaries, sometimes zirconia electrolyte particles are mixed into $\text{La}(\text{Sr})\text{MnO}_3$. In addition, the $\text{La}(\text{Sr})\text{MnO}_3$ will have a porous microstructure in order to increase the number of reaction sites through improved gas transfer. Other cathode materials such as $\text{La}(\text{Sr})\text{Fe}(\text{Co})\text{O}_3$ are good mixed ionic–electronic conductors [13], and therefore reaction sites are increased, resulting in high electrocatalytic activity.

Anode: Ceramic composites consisting partially of electrolyte materials, such as zirconia (YSZ) and NiO are widely used. Under operation conditions, NiO is reduced to Ni metal, such that the anode is a cermet made of metallic nickel and YSZ, usually called a Ni cermet. The nickel works as a catalyst and the zirconia serves to inhibit sintering of the metal particles and provide a thermal expansion coefficient comparable to that of the electrolyte.

As explained in Sect. 23.1, since various fuels other than hydrogen can be used, understanding the characteristics of power generation directly using natural gas (mostly CH_4), gasified coal (mostly $\text{CO} + \text{H}_2$), hydrocarbon gas, biogas (mostly $\text{CH}_4 + \text{CO}_2$), and alcohol is very important [2, 3, 14, 15]. Except for when operating with pure hydrogen, anode materials could face problems, such as poisoning

by impurities and carbon deposition. Since carbon deposition is a result of the good catalytic activity of Ni for decomposition of hydrocarbon fuels, in place of Ni, Cu-based cermet and electronic conducting oxides are under study because of lower catalytic activity [14]. However, lower catalytic activity increases the anode overpotential, and therefore, there are still issues to be overcome regarding fuel flexibility.

23.4 Chemical Degradation

Long-term durability is an important requirement for SOFC commercialization. Chemical degradation phenomena occur over longer operation, such as interdiffusion from neighboring components and associated interfacial chemical reactions. Figure 23.7 summarizes typical chemical degradation phenomena revealed by post analyses of cells after long-term durability tests up to 10,000 h [16, 17].

Figure 23.7a shows interdiffusion where fast-diffusive species like Ca ions have diffused through the porous LSM cathode layer and then to grain boundaries in the dense YSZ electrolyte. This changes grain boundary resistivity in the electrolyte. Figure 23.7b shows a solid-state reaction where an insulating phase of $(\text{Ca}, \text{Sr})\text{ZrO}_3$ has formed at the interface between the LSM cathode and the YSZ electrolyte. Figure 23.7c displays sintering of Ni at the anode caused by grain growth. Figure 23.7d suggests phase transformation from the cubic zirconia phase to the tetragonal zirconia phase and further to the monoclinic zirconia phase. Such phase transition is caused by dissolution and reprecipitation of Y dopants from YSZ grains to the grain boundaries. This leads to a decrease in the dopant concentration and then substantial volume change when cooling down to room temperature. Figure 23.7e reveals precipitation of MnO_x as a secondary phase where Mn ions diffuse from the cathode to zirconia electrolyte during sintering. Figure 23.7f shows densification where fast-diffusive species are transported through the surface, the grain boundaries, and the gas phase to form condensed phases in the porous electrode. In order to improve durability, each of these possible degradation phenomena must be avoided. In addition, for practical applications, the extrinsic degradation associated with impurities in the SOFC fuels also has to be considered.

23.5 Cell and Stack

In order to reduce ohmic resistance in the perpendicular direction to the cell plane, the anode, the electrolyte, and the cathode, should be as thin as possible. However, thin assemblies of ceramic materials need support materials. Unlike PEFC, there are many possibilities for materials and shapes of supports, and various types of SOFC cell are available. In terms of SOFCs with different types of support components, anode-, electrolyte-, cathode-, porous metal oxide substrate-, and metal (interconnect)-supported

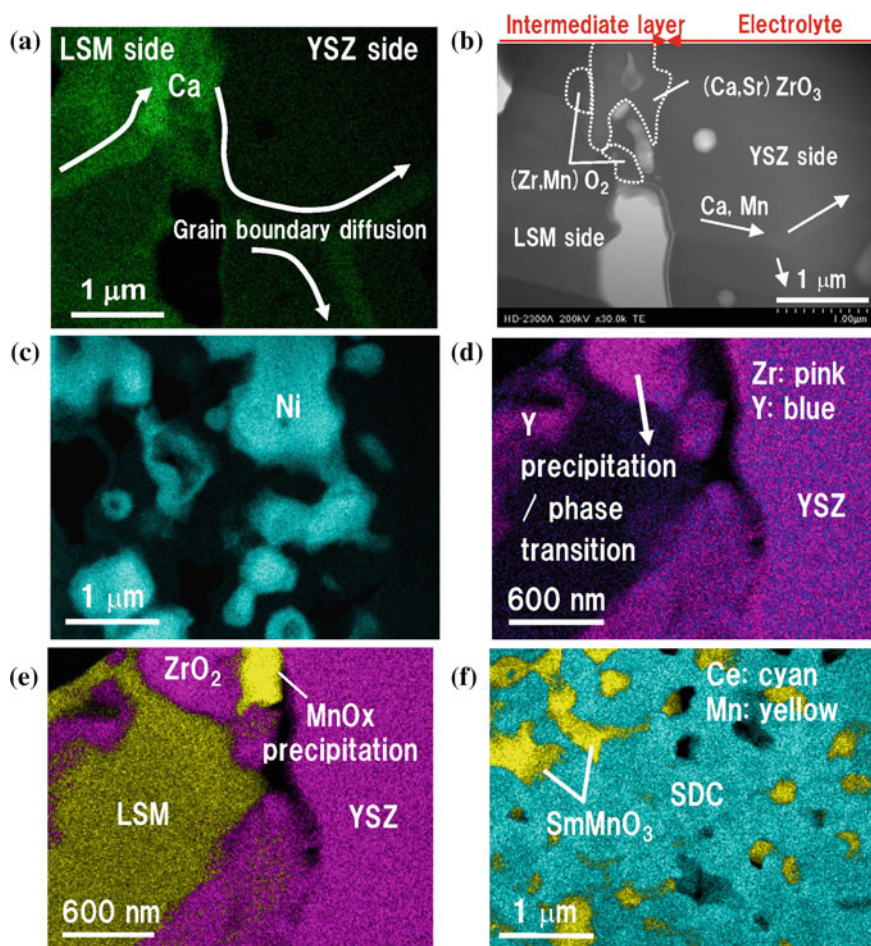
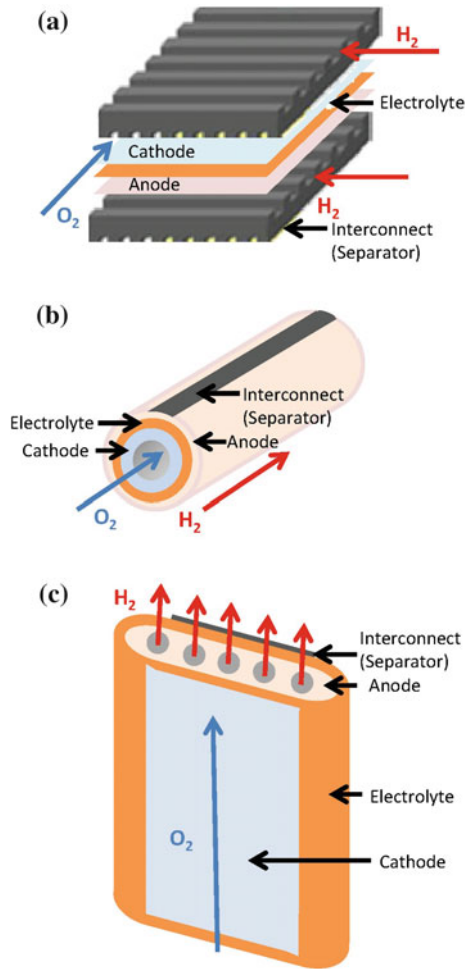


Fig. 23.7 Possible chemical degradation in SOFCs: **a** interdiffusion; **b** solid-state reaction; **c** sintering; **d** phase transition; **e** precipitation; and **f** densification. [17] (reproduced with permission from The Electrochemical Society, Copyright 2013)

cells are possible. Regarding the cell structure, there are planar (flat sheet), tubular, and flat tubular designs as shown in Fig. 23.8 [2, 3].

Cell fabrication is based on common ceramic manufacturing techniques. Molding of support materials is usually done by casting molding, extrusion molding, or injection molding. Thin film electrodes and electrolytes are often prepared by tape casting, screen printing, or dip coating techniques. The resulting assembly is sintered at high temperature. In general, to obtain a dense structure, a heat treatment over 1300 $^{\circ}\text{C}$ is necessary. It is desirable for cells to be sintered as a whole, but owing to differences in thermal shrinkage or undesirable solid phase

Fig. 23.8 Typical cell structures: **a** planar, **b** tubular, **c** flat tubular

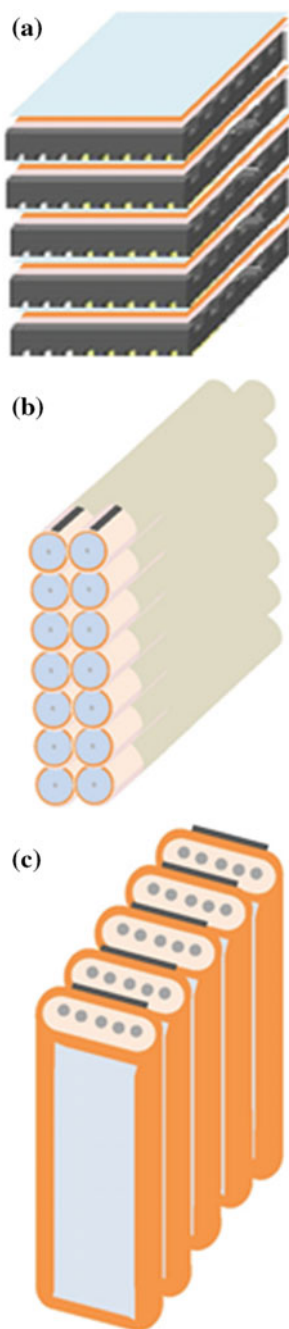


reactions among different component materials, heat treatments are often performed in several steps.

A key issue for cell fabrication, especially of planar-type cells, is sealing the ceramic components to obtain gas tightness. A common approach for sealing is to use glass whose transition temperature is close to the operating temperature of the SOFC. Glass is softened at high temperature and used to seal around the cell. However, a problem remains due to the migration of silica, which causes degradation in cell performance.

Since the operation voltage of SOFCs is between 0.7 and 0.9 V and the power density is about 0.2 and 1 W/cm², many cells are stacked together in order to get practical voltages and power densities. In an SOFC stack, each cell is connected using an interconnect. In addition to conducting electricity between the anode of one cell and the cathode of an adjacent cell, interconnects also prevent the mixing of the gases

Fig. 23.9 Typical stack structures: **a** planar, **b** tubular, **c** flat tubular



supplied to the anode and the cathode. Therefore, interconnects require good electronic conductivity and a dense structure in addition to being stable under the reducing/oxidizing atmospheres at high temperature. LaCrO_3 -based electronic conducting ceramics or thermally stable metal alloys, such as Ni-based superalloy and Fe-based stainless steel, are commonly used for interconnects. However, depending on operation conditions, oxidation of such materials or Cr migration from the interconnects to the electrodes over long operation times becomes a problem [18].

As shown in Fig. 23.9, stack structures are varied depending on the type of cells used. Characteristics of each stack [1] are summarized in the following.

Planar: Cells are connected along the direction of current flow minimizing the length of the current path, resulting in high power density. Also, simple and low-cost methods, such as screen printing and tape casting, can be applied. However, gas-tight sealing becomes a problem since relatively large amount of sealing materials are necessary around the cell (four sides). Mechanical degradation is also an issue caused by different thermal expansion coefficients between the cell and stack materials.

Tubular: The original design uses a porous ceramic tubular substrate. Along the tube, a cylindrical anode is deposited, followed by the electrolyte, the cathode, and the interconnect through masking processes. In a recent design, the process is sometimes reversed. An advantage is that only small amounts of gas-tight sealing are necessary for the two ends of the tubes. Also, since the interconnect is incorporated into the cell, cells are relatively easily bundled together and constructed into a large stack. However, the complicated and high-cost processes of electrolyte and electrode deposition become disadvantageous. Since a typical path of electrons from the anode of one cell to the cathode of the next cell is long, relatively low power density is a weakness of this type of design.

Flat tubular: Similar to the planar design, high power density is available. In addition, there is an advantage due to the fact that a relatively small amount of gas-tight sealing is necessarily. Only the two ends of the tubes should necessary be sealed. However, owing to volume expansion of the interconnects under the reducing atmosphere, this type of design may not be suitable for large-scale SOFCs.

References

1. Larminie J, Dicks A (2003) Fuel cell systems explained, 2nd edn. John Wiley & Sons, Chichester
2. Minh NQ, Takahashi T (1995) Science and technology of ceramic fuel cells. Elsevier, Amsterdam
3. Singhal SC, Kendal K (2003) High temperature fuel cells: fundamentals. Design and Applications, Elsevier, Oxford
4. Maier J (2004) Physical chemistry of ionic materials: ions and electrons in solids. John Wiley & Sons, Chichester
5. Ishihara T, Matsuda H, Takita Y (1994) Doped LaGaO_3 perovskite type oxide as a new oxide ionic conductor. J Am Chem Soc 116:3801–3803

6. Tuller HL, Nowick AS (1975) Doped ceria as a solid oxide electrolyte. *J Electrochem Soc* 122:255–259
7. Kilner J, Steele BCH (1981) *Nonstoichiometric oxides*. Academic Press, New York
8. Takahashi T, Iwahara H (1971) Ionic conduction in perovskite-type oxide solid solution and its application to the solid electrolyte fuel cell. *Energy Convers* 11:105–111
9. Kreuer KD, Paddison SJ, Spohr E, Schuster M (2004) Transport in proton conductors for fuel-cell applications: simulations, elementary reactions, and phenomenology. *Chem Rev* 104:4637–4678
10. Meyers RA (2012) *Encyclopedia of sustainability science and technology*, vol 6. Springer, Heidelberg
11. Haga K (2010) *Chemical degradation of Ni-based anode materials in solid oxide fuel cells*. Dissertation, Kyushu University, Fukuoka Japan
12. Sasaki K, Wurth JP, Gödickemeier M, Mitterdorfer A, Gauckler LJ (1994) Processing microstructure-property relations of solid oxide fuel cell cathodes. In: *First European solid oxide fuel cell forum proceedings*, vol 1, pp 475–492
13. Teraoka Y, Zhang HM, Okamoto K, Yamazoe N (1988) Mixed ionic-electronic conductivity of $\text{La}_{1-x}\text{Sr}_x\text{Co}_{1-y}\text{Fe}_y\text{O}_{3-\delta}$ perovskite-type oxides. *Mater Res Bull* 23:51–58
14. Lu C, An S, Worrell WL, Vohs JM, Gorte RJ (2004) Development of intermediate-temperature solid oxide fuel cells for direct utilization of hydrocarbon fuels. *Solid State Ion* 175:47–50
15. Atkinson A, Barnett S, Gorte RJ, Irvine JTS, McEvoy AJ, Mogensen M, Singhal SC, Vohs J (2004) Advanced anodes for high-temperature fuel cells. *Nat Mater* 3:17–27
16. Sasaki K, Haga K, Yoshizumi T, Minematsu D, Yuki E, Liu RR, Uryu C, Oshima T, Ogura T, Shiratori Y, Ito K, Koyama M, Yokomoto K (2011) Chemical durability of solid oxide fuel cells: influence of impurities on long-term performance. *J Pow Sour* 196:9130–9140
17. Sasaki K, Yoshizumi T, Haga K, Yoshitomi H, Hosoi T, Shiratori Y, Taniguchi S (2013) Chemical degradation of SOFCs: external impurity poisoning and internal diffusion-related phenomena. *ECS Trans* 57:315–323
18. Taniguchi S, Kadowaki M, Kawamura H, Yasuo T, Akiyama Y, Miyake Y, Saitoh T (1995) Degradation phenomena in the cathode of a solid oxide fuel cell with an alloy separator. *J Pow Sour* 55:73–79

Chapter 24

Alkaline Electrolyte Fuel Cells (AFCs)

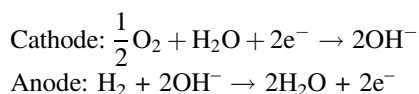
Akari Hayashi, Tsuyohiko Fujigaya and Naotoshi Nakashima

Abstract This chapter describes the operating principles of alkaline electrolyte fuel cells. The fundamental components (electrolyte and electrode) are explained from the viewpoint of materials, followed by description of cell and stack structures.

Keywords AFC · AEM · OH⁻ ion conductivity · CO poisoning · Space exploration applications · Hydrogen utilization

24.1 Operating Principles of the AFC

Historically, AFCs were developed prior to PEFCs. The fundamental assembly of anode–electrolyte–cathode is similar to that of PEFCs as shown in Fig. 24.1. Hydrogen and air are supplied as reactants for the anode and the cathode, respectively. However, the direction of ion transfer is different. Hydroxide ions move from the cathode side to the anode side, through the electrolyte. Reactions at the cathode and the anode are described by the following:



A. Hayashi (✉)
International Research Center for Hydrogen Energy, Kyushu University,
Fukuoka 819-0395, Japan
e-mail: hayashi.akari.500@m.kyushu-u.ac.jp

T. Fujigaya · N. Nakashima
Department of Applied Chemistry, Kyushu University,
Fukuoka 819-0395, Japan
e-mail: fujigaya-tcm@mail.cstm.kyushu-u.ac.jp

N. Nakashima
e-mail: nakashima-tcm@mail.cstm.kyushu-u.ac.jp

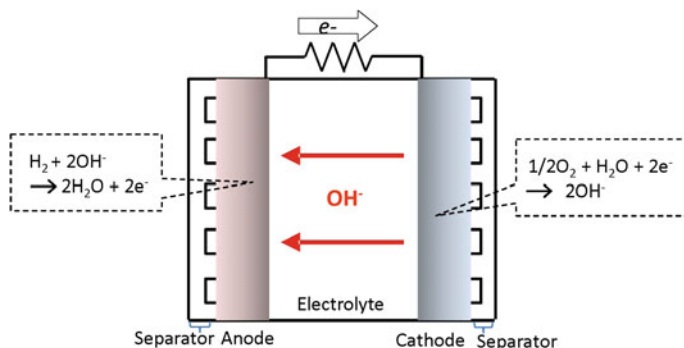


Fig. 24.1 Fundamental structure of an AFC

Even though the direction of ion transfer within the electrolyte is opposite to the direction in PEFCs, the overall reactions are the same, and so the theoretical open-circuit voltage near room temperature results in 1.23 V. However, in terms of classical AFCs, the cell and stack design is very different from those of PEFCs and SOFCs. A liquid electrolyte is usually used, and the structure is rather similar to standard primary batteries. Depending on the design of the cell and stack, the operation temperature can be up to around 250 °C [1, 2]. In AFCs, the overvoltage on the oxygen reduction reaction can be reduced mainly owing to the decreased extent of anion adsorption on the electrocatalysts [3], resulting in high current density, which is an advantage over PEFCs.

A single AFC usually operates at over 0.85 V, which is higher than PEFCs. However, a problem arises due to CO_2 in the fuel gases, as well as in the ambient air. CO_2 reacts with the alkaline electrolyte and carbonate ions (CO_3^{2-}) are produced in the liquid electrolyte solution. This leads to a reduction in the ionic conductivity of the electrolyte solution and finally a decrease in the power density of the AFC.

In the long history of fuel cells, owing to the great success of PEFCs, AFCs have received less attention. However, since the development of non-Pt catalysts has not yet been successfully commercialized in PEFCs, AFCs have been receiving increasing attention, especially in the area of anion exchange membranes. In the following sections, the fundamental materials used in AFCs as well as cell and stack structures are introduced.

24.2 Electrolytes

For practical AFCs, liquid electrolytes consisting of a 30–50 % potassium hydroxide (KOH) solution have commonly been used. In the liquid electrolyte AFC, a problem arises when reactant gases are contaminated by CO_2 . A high concentration KOH solution reacts with CO_2 contamination, leading to K_2CO_3 precipitation, blocking the surface of the electrocatalyst layers, and resulting in a

lower power density. In order to solve this problem, the electrolyte solution can be circulated. This mobile electrolyte also has advantages on the removal of heat and produced water. However, as the layer of electrolyte becomes thick, this will result in increased resistance, especially in the high current density region. A circulation pump is a necessary additional accessory for this system. Finally, this system cannot be tilted, and therefore is not suitable for portable applications.

The latest designs of AFCs are based on a solid electrolyte membrane, which is advantageous in terms of compactness, portability, and sealing. Similar to PEFCs, polymer electrolytes with anion (OH^-) conductivity have been developed as anion exchange membranes (AEMs). With AEMs, there is no cation, such as K^+ , and so the reduction of the power density owing to precipitation of a carbonate salt is avoided. Similar to PEMs, functional properties such as the ability to transfer OH^- produced at the cathode to the anode as well as good electronic insulation between two electrodes, are required for AEMs. However, in reality, there are no AEMs developed satisfying both a high anion conductivity over 1×10^{-2} S/cm as well as demonstrating high chemical and mechanical stability. Hence, AEMs are still under development.

AEMs under study [4, 5] are often composed of cation exchange functional groups at either the main chain or the side chain of polymers. As shown in Fig. 24.2, for example, cation exchange functional groups can be pyridinium, ammonium, phosphonium, sulfonium, and guanidium, or imidazolium groups. Among these cation exchange groups, AEMs with quaternary ammonium groups have received the most attention. Though there is still a problem with the properties at high temperature, the OH^- conductivity can often reach the level of proton conductivity in Nafion. Regarding the tolerance to CO_2 , even though precipitation of carbonate salts is avoided, CO_2 is still absorbed into AEM. In that case, the OH^- ion is converted to a HCO_3^- ion, leading to reduced ionic conductivity. However, it has been reported that OH^- is replenished within the AEM during operation mode [6]. This mechanism is called “self-purging”. Even though the process of self-purging is recognized, the details are still not entirely clear. Therefore,

Fig. 24.2 Examples of cation exchange functional groups for AEMs

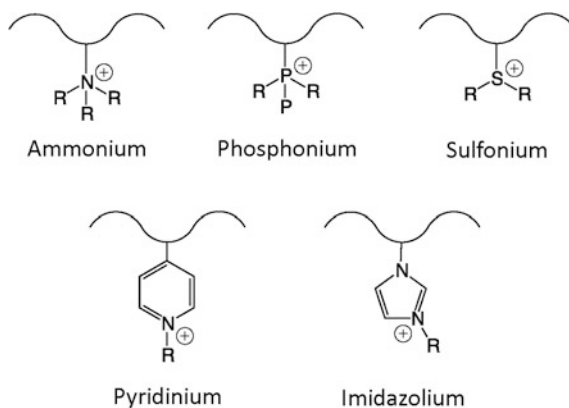
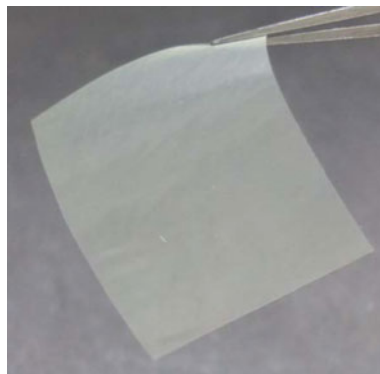


Fig. 24.3 A photograph of a sheet of AEM (developed by Tokuyama Corporation)



understanding the mechanism involved will be a key for further development of AEMs.

Even though there are no practical implementations of AEM-based AFCs yet, AEMs developed by Tokuyama Corporation (Japan) [2] (Fig. 24.3) are widely used to develop AFCs in labs in many places beyond Japan. Development of practical AFCs with the Tokuyama Corporation AEM is expected in the future.

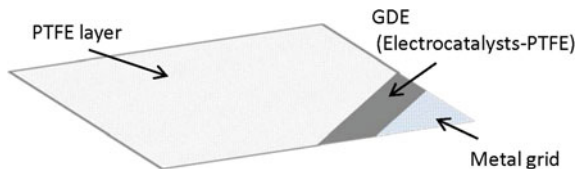
24.3 Electrodes (Electrocatalysts)

In classical AFCs using a liquid electrolyte, the anode and the cathode are directly in contact with the electrolyte solution, and so electrodes have a role to transfer both reactant gases and liquid electrolytes. Therefore, two different types of pores, hydrophobic and hydrophilic pores, are necessary in the electrode structure. The coexistence of hydrophilic and hydrophobic pores is also necessary for PEFCs, owing to the liquid water produced at the cathode. However, in case of liquid electrolyte AFCs, the control of such pores becomes a serious issue.

Polytetrafluoroethylene (PTFE)-bonded gas diffusion electrodes (GDEs) are often used in AFCs. In PTFE-bonded GDEs, the PTFE acts as a binder for the electrocatalyst, and also contributes to hydrophobic pore formation. The PTFE-bonded GDEs are commonly supported by metal grids (Fig. 24.4) [1, 7], resulting in high conductivity and mechanical strength. Furthermore, a thin layer of PTFE is coated on the gas-side surface of the electrode to control the porosity.

Unlike PEFCs, electrocatalysts remain under alkaline conditions, and so it is advantageous to reduce the overpotential of the oxygen reduction reaction at the cathode, owing to the decreased extent of anion adsorption on the electrocatalysts. In addition, relatively cheap metal catalysts (for examples, Ni and Ag), oxides, and organometallic complexes are stable in alkaline media and can be used as cathode materials.

Fig. 24.4 Schematic diagram of a PTFE-bonded GDE supported by a metal grid



In reality, the performance of AFCs dramatically increases if Pt is used for both anode and cathode catalysts. Generally, for the anode, Pt or Pt-Pd nanoparticles deposited on carbon are used. As a non-noble metal, a porous nickel catalyst called Raney nickel can also be commonly used.

Regarding the cathode, since the overpotential of the oxygen reduction reaction can be reduced in alkaline conditions, many catalyst materials are under investigation. Despite the reactivity of Pt being the highest, lithium-doped nickel oxide shows high enough activity for operation at above 150 °C [1]. Silver has also received attention, and much work has been done to further increase its activity [8, 9]. Since cobalt is stable in alkaline media, Pd-Co alloys are also possible candidates [10]. Manganese oxides are well studied as possible oxide catalysts [11]. Furthermore, iron(II) and cobalt(II) phthalocyanine, and other M-N4-macrocycles deposited on carbon supports result in high oxygen reduction activity [12, 13]. More recently, nitrogen-doped carbon has been found to have similar kinetics as Pt deposited on carbon and to be higher than silver deposited on carbon [14–16].

Regarding further development of AEM-based AFCs, similar electrocatalysts to those used in liquid electrolyte AFCs can essentially be used. However, additional requirements, such as high electrocatalytic activity, electron and proton conductivity, mass transfer ability for fueling gases and removing products similar to electrocatalysts in PEFC, should also be fulfilled.

24.4 Cell and Stack

Classical liquid electrolyte AFCs have a different cell structure compared to PEFCs or SOFCs and are rather similar to standard primary batteries. There are two types of liquid electrolyte AFCs, mobile electrolyte AFCs and static electrolyte AFCs [1]. The basic structure of a mobile electrolyte AFC is shown in Fig. 24.5. In this cell, KOH solution is pumped around the AFC. Hydrogen fuel is supplied to the anode and is also circulated. Since the water is produced at the anode during the AFC operation, it is evaporated from the circulated hydrogen and then condensed out at the cooling unit. Here, the circulating electrolyte is able to serve as a coolant for the AFC. For the cathode, air is used. As explained in Sect. 24.1, CO₂ poisoning can be reduced by flowing KOH.

Fig. 24.5 Diagram of an AFC with a mobile electrolyte

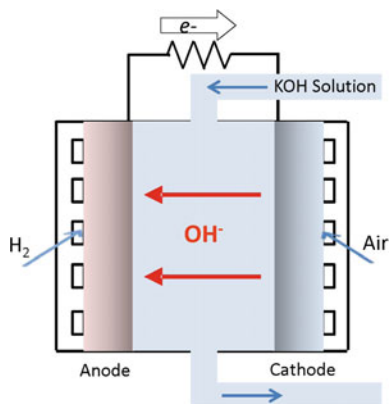
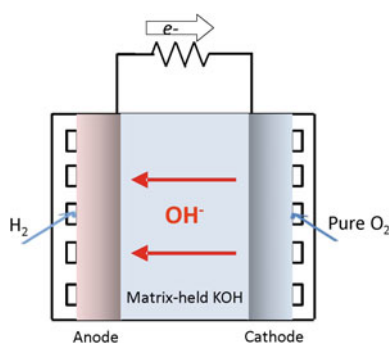


Fig. 24.6 Diagram of an AFC with a static electrolyte held in a matrix



The basic structure of a static electrolyte AFC is shown in Fig. 24.6. A matrix absorbing KOH is used as an electrolyte. Owing to its porosity, mechanical strength, and corrosion resistance, asbestos had commonly been used as a matrix. The basic structure is the same as that of a mobile electrolyte type, but pure oxygen has to be used for the cathode. Since the electrolyte cannot be replaced unlike the mobile electrolyte AFC, CO_2 poisoning becomes a serious problem. Therefore, CO_2 has to be removed from the reactant gases.

A single cell usually operates at around 0.85 V, while generally several tens of cells are stacked. When constructing a stack of liquid electrolyte AFCs, the face-to-face electronic contact between two electrodes is challenging, because an insulating PTFE layer generally covers the electrodes, as explained in Sect. 24.2. Therefore, bipolar plates such as those utilized in PEFCs are difficult to use. Since the electrodes are supported by metal grids, an edge-to-edge connection as seen in

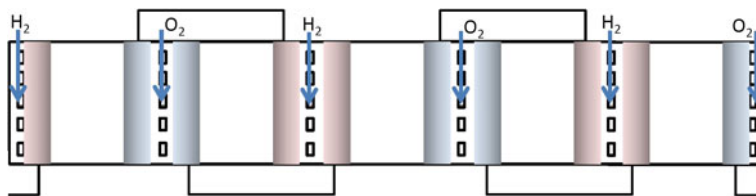


Fig. 24.7 Edge-to-edge connection of cells in an AFC stack

Fig. 24.7 is commonly made [17]. In this case, the connection between the cathode side of one cell to the anode side of an adjacent cell, which is seen for the stack structure using bipolar plates, is not necessary. In classical AFC stacks, the cathode of one cell faces the cathode of an adjacent cell. Air flows between these two cathodes, resulting in an AFC stack of cells connected by monopolar plates.

New AEM-based AFCs have a different structure. Even though AEM-based AFCs are still under development, the structure of cells and stack will be similar to that of PEFCs as shown in Sect. 22.5.

24.5 Practical Materials and Applications of AFCs

In early AFCs, developed for space exploration applications, a liquid electrolyte was used. From the 1960s, the National Aeronautics and Space Administration of the United States (NASA) used mobile electrolyte AFCs, with an 85 % KOH electrolyte solution as part of the Apollo missions (Fig. 24.8) [1]. This AFC is well known for having provided the electrical power and water for the craft that first took man to the moon. In terms of electrode materials, nickel and lithium-doped nickel oxide were used for the anode and the cathode, respectively.

The Apollo system was further developed and improved for the Space Shuttle Orbiter vehicles in the 1980s (Fig. 24.9) [1]. In this case, static electrolyte AFCs were used. PTFE-bonded Pt/Pd on an Ag grid was used for the anode, and PTFE-bonded Au/Pt on an Au grid was used for the cathode, and they were separated by a 32 % KOH solution held in an asbestos matrix.

Despite classical liquid electrolyte AFCs being used historically for space exploration applications, AEM-based AFCs have only recently been developed to rival liquid electrolyte AFCs. Additionally, PEFCs have been used for the more recent Space Shuttle Orbital vehicles. However, the development of practical AFCs with AEMs is highly desired for future space exploration and other applications.

Fig. 24.8 1.5-kW fuel cell from the Apollo spacecraft [1] (Reproduced with permission from WILEY, Copyright 2003)

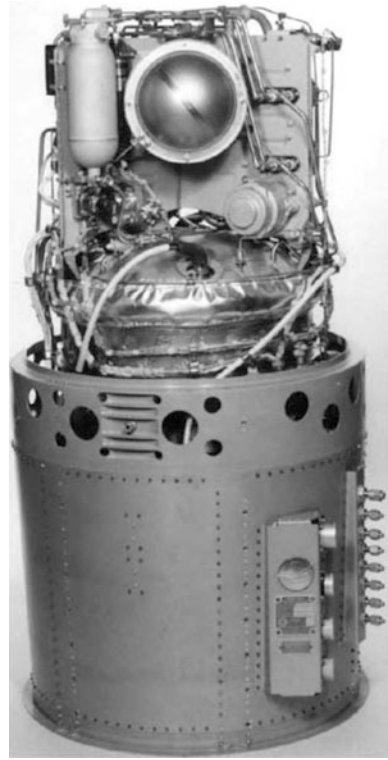
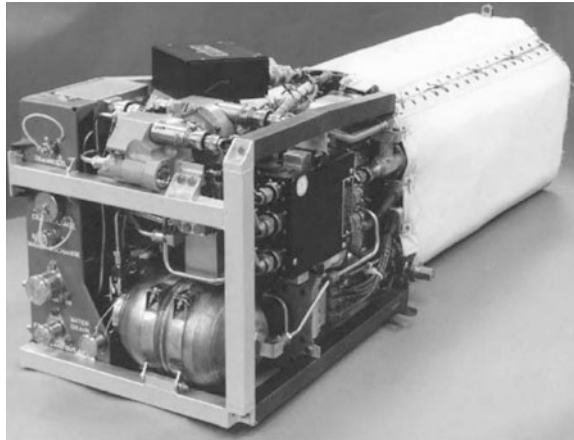


Fig. 24.9 12-kW fuel cell used on the Space Shuttle Orbiter [1] (Reproduced with permission from WILEY, Copyright 2003)



References

1. Larminie J, Dicks A (2003) Fuel cell systems explained, 2nd edn. Wiley, Chichester
2. Stolten D, Emonts B (2012) Fuel cell science and engineering: materials, processes, systems and technology, vol 1. Wiley-VCH, Weinheim
3. Spendelov JS, Wieckowski A (2007) Electrocatalysis of oxygen reduction and small alcohol oxidation in alkaline media. *Phys Chem Chem Phys* 9:2654–2675
4. Merle G, Wessling M, Nijmeijer K (2011) Anion exchange membranes for alkaline fuel cells: a review. *J Membrane Sci* 377:1–35
5. Couture G, Alaeddine A, Boschet F, Ameduri B (2011) Polymeric materials as anion-exchange membranes for alkaline fuel cells. *Prog Polym Sci* 36:1521–1557
6. Adams LA, Poynton SD, Tamain C, Slade RCT, Varcoe JR (2008) A carbon dioxide tolerant aqueous-electrolyte-free anion-exchange membrane alkaline fuel cell. *ChemSusChem* 1:79–81
7. Ur-Rahman S, Al-Saleh MA, Al-Zakri AS, Gultekin S (1997) Preparation of Raney–Ni gas diffusion electrode by filtration method for alkaline fuel cells. *J Appl Electrochem* 27:215–220
8. Guo J, Hsu A, Chu D, Chen R (2010) Improving oxygen reduction reaction activities on carbon-supported Ag nanoparticles in alkaline solutions. *J Phys Chem C* 114:4324–4330
9. Cheng Y, Li W, Fan X, Liu J, Xu W, Yan C (2013) Modified multi-walled carbon nanotube/Ag nanoparticle composite catalyst for the oxygen reduction reaction in alkaline solution. *Electrochim Acta* 111:635–641
10. Maheswari S, Karthikeyan S, Murugan P, Sridhar P, Pitchumani S (2012) Carbon-supported Pd-Co as cathode catalyst for APEMFCs and validation by DFT. *Phys Chem Chem Phys* 14:9683–9695
11. Cao YL, Yang HX, Ai XP, Xiao LF (2003) The mechanism of oxygen reduction on MnO₂-catalyzed air cathode in alkaline solution. *J Electroanal Chem* 557:127–134
12. Morozan A, Campidelli S, Filoramo A, Josselme B, Palacin S (2011) Catalytic activity of cobalt and iron phthalocyanines or porphyrins supported on different carbon nanotubes towards oxygen reduction reaction. *Carbon* 49:4839–4847
13. Kruusenberg I, Matisen L, Shah Q, Kannan AM, Tammeveski K (2012) Non-platinum cathode catalysts for alkaline membrane fuel cells. *Int J Hydrogen Energy* 37:4406–4412
14. Maldonado S, Stevenson KJ (2005) Influence of nitrogen doping on oxygen reduction electrocatalysis at carbon nanofiber electrodes. *J Phys Chem B* 109:4707–4716
15. Li H, Liu H, Jong Z, Qu W, Geng D, Sun X, Wang H (2011) Nitrogen-doped carbon nanotubes with high activity for oxygen reduction in alkaline media. *Int J Hydrogen Energy* 36:2258–2265
16. Wang DW, Su D (2014) Heterogeneous nanocarbon materials for oxygen reduction reaction. *Energy Environ Sci* 7:576–591
17. Vielstich W, Lamm A, Gasteiger HA (2003) Handbook of fuel cells-fundamentals, technology and applications, vol 4. Wiley, Chichester

Chapter 25

Hydrogen Combustion Systems

Koji Takasaki and Hiroshi Tajima

Abstract This chapter describes overviews of hydrogen utilization for closed-system internal combustion engines (C-ICE). Basic reactions are explained with a simple H_2 - O_2 combustion system, and hydrogen application to C-ICE is discussed in comparison to other conventional fuels, also followed by case studies of hydrogen combustion systems.

Keywords H_2 - O_2 combustion · Internal combustion engine (ICE) · Hydrogen-admixture · Spark ignition (SI) · Compression ignition (CI) · Hydrogen utilization

25.1 Overview

Hydrogen combustion is essentially a continuous chain of elementary reactions under high temperature conditions which releases the enthalpy drop of a water-forming reaction. It has been a widespread method for the utilization of hydrogen as a heat source. Steady or quasi-steady flame applications have a well-documented track record, especially in the case of hydrogen-mixed gases for burners and gas turbines [1], therefore these fields will not be given special attention here.

In this section, the review subject is focused on hydrogen utilization for closed-system internal combustion engines (C-ICEs, hereafter) where cyclic and non-steady hydrogen combustion systems are used. As already described briefly, hydrogen and other sub-generated combustible gases can be supplied from various

K. Takasaki (✉) · H. Tajima
Department of Energy and Environmental Engineering,
Faculty of Engineering Sciences, Kyushu University,
Fukuoka 816-8580, Japan
e-mail: takasaki@ence.kyushu-u.ac.jp

H. Tajima
e-mail: tasima@ence.kyushu-u.ac.jp

hydrogen carriers such as; methanol (CH₃OH) [2]; ethanol (CH₃CH₂OH) [3]; and ammonia (NH₃) [4]. They can be turned into more valuable fuels because their reforming process is endothermic and provides opportunities for the exhaust heat recovery or chemical energy regeneration in C-ICEs. Moreover, excessively rich mixture combustion has been recently been introduced into a certain cylinder of a C-ICE to generate exhaust gas including H₂ which is recirculated into other cylinders, realizing the low emission of nitric oxides and particulate matter, which is called “dedicated exhaust gas recirculation (EGR)” [5].

For simplification, the basic H₂–O₂ combustion system is described here, briefing mentioning hydrogen-methane (so-called hythane) mixture utilization. Although the thermal properties of hydrogen are discussed in detail in the previous chapters, it is beneficial to introduce the fundamentals of the chemical reactions in H₂–O₂ combustion for discussion of the characteristics of combustion systems for hydrogen-fueled C-ICEs.

While the H₂–O₂ combustion process progresses spontaneously with substantial heat release, it eventually results in a water-forming reaction in common with that of fuel cells. The overall reaction is described by $2\text{H}_{2(\text{g})} + \text{O}_{2(\text{g})} \rightarrow 2\text{H}_2\text{O}_{(\text{g})}$ except that the water formed is always in the gas phase. Therefore, the thermal efficiency of an ICE is usually evaluated on the lower heating value (LHV) of the fuel. However, its reaction rate is never proportional to the molar concentration of O₂ and to the squared molar concentration of H₂ (i.e., the stoichiometric coefficients) since the H₂–O₂ combustion process actually consists of more than 30 elementary reactions which obey the law of the reaction rate [6]. A set of elementary reactions for a particular overall reaction is usually called a reaction scheme and a number of reaction schemes have been proposed to some of the overall reactions of industrial importance.

25.2 Combustion Reactions and Analysis Approach

A reaction scheme provides a closed series of elementary reactions among reactants, products, and chain carriers to reproduce the combustion of its target fuel.

Equation 25.1 exemplifies an elementary reaction from reactants A and B to products P and Q where a , b , p , and q are the numbers of involved molecules, respectively.



The reaction rate r is described in Eq. 25.2, where the square brackets around a species refer to its molar concentration. k stands for the rate coefficient and its suffixes “f” and “r” stand for a forward reaction and a reverse reaction, respectively.

$$r = -\frac{1}{a} \frac{d[A]}{dt} = -\frac{1}{b} \frac{d[B]}{dt} = \frac{1}{p} \frac{d[P]}{dt} = \frac{1}{q} \frac{d[Q]}{dt} = k_f[A]^a[B]^b - k_r[P]^p[Q]^q \quad (25.2)$$

For versatility, the above equation is extended to a more universal expression as shown in Eq. 25.3 below which M types of the chemical species X are identified with an index “ i ” and N types of elementary reaction are identified with an index “ j ”. The stoichiometric coefficients in the j -th elementary reaction are given as F_{ij} and R_{ij} at the reactant side and the product side, respectively, and basically correspond to the order of reactions in the case of elementary reactions.

$$r_j = k_{fj} \prod_{i=1}^M [X_i]^{F_{ij}} - k_{rj} \prod_{i=1}^M [X_i]^{R_{ij}} \quad (j = 1, \dots, N) \quad (25.3)$$

As is well-known, the rate coefficients of elementary reactions can be expressed in the form of modified Arrhenius’ equations (Eq. 25.4) for j -th elementary reaction where T and \mathbf{R} denote temperature and a universal gas constant, respectively. A_{fj} , A_{rj} , E_{fj} , E_{rj} , β_{fj} , and β_{rj} stand for the pre-exponential constants, the activation energies of the reactions and the Arrhenius’ temperature exponent for both forward and reverse directions.

$$k_{fj} = A_{fj} T^{\beta_{fj}} \exp\left(\frac{-E_{fj}}{\mathbf{R}T}\right), \quad k_{rj} = A_{rj} T^{\beta_{rj}} \exp\left(\frac{-E_{rj}}{\mathbf{R}T}\right) \quad (25.4)$$

A reaction scheme is essentially a list of the elementary equations and the parameters with the suffix “ j ” in Eqs. 25.3 and 25.4. The overall molar production rate of i -th species is then calculated based on Eq. 25.5.

$$\dot{\omega}_i = \sum_{j=1}^N r_j (R_{ij} - F_{ij}) \quad (i = 1, \dots, M) \quad (25.5)$$

Specific expressions on mass basis on Eq. 25.6 are preferably used in computational fluid dynamics (CFD) codes instead of molar basis as

$$\frac{dY_i}{dt} = \nu \dot{\omega}_i W_i \quad (i = 1, \dots, M), \quad Y_i = \frac{m_i}{m}, \quad \nu = \frac{V}{m}, \quad m = \sum_{i=1}^M m_i \quad (25.6)$$

where t is time, Y_i is the mass fraction of the i -th species, V is the volume of the system, $\nu = V/m$ is the specific volume, W_i is the molecular weight of the i -th species, and m is the total mass of the mixture. V may vary with time in the case of C-ICEs, as $V = V(t)$.

Based on a reaction scheme, one can obtain ordinary differential equations (ODEs) closed about the rate constants of all the relevant chemical species. As for the combustion systems of C-ICEs, specialized matrix calculation packages have

been developed in order to solve these ODEs and to get non-conflict changes over all the relevant species during a controlled time step [7, 8].

For an adiabatic closed-system corresponding to the in-cylinder gas in the C-ICE's power strokes that is capable of changing its pressure and temperature, the energy balance of the system has to be introduced to determine the final conditions of the system and the local temperature of the mixture are renewed inside a control volume or a computing cell based on Eq. 25.7 as

$$c_v \frac{dT}{dt} + P \frac{dv}{dt} + v \sum_{i=1}^M u_i \dot{\omega}_i W_i = 0, \quad c_v = \sum_{i=1}^M Y_i c_{v,i} \quad (25.7)$$

where c_v is the mean specific heat of the mixture at constant volume, $c_{v,i}$ is the specific heat of the i -th species evaluated at constant volume, and P is the in-cylinder pressure.

This computational approach using an ODE solver has become standard in today's combustion analysis especially for fuels of smaller and simpler reaction mechanism represented by hydrogen, methane, and natural gas (NG, hereafter).

25.3 Low-Temperature Stage of the Hydrogen Combustion Reaction

Figure 25.1 shows the reaction chain paths of the low-temperature stage of H_2 - O_2 combustion on an elementary reaction basis [9]. The reaction's so-called chain initiation or hydrogen abstraction starts from the reaction described in Eq. 25.8. With a C-ICE application in mind, this reaction needs an ambient temperature of over 1000 K for the H_2 -Air mixture to obtain substantial reaction speeds.

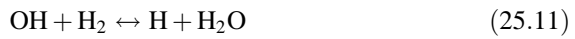
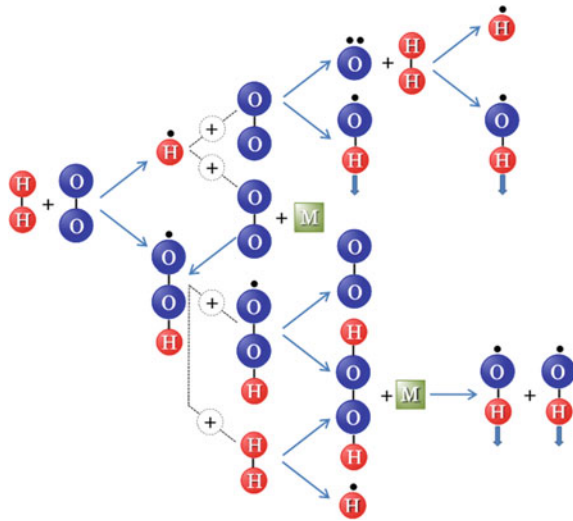
Although the H_2 - O_2 system has one of the simplest combustion processes, it actually consists of more than 30 elementary reactions up to a ternary level involving eight chemical species including free radicals or chain carriers [6].



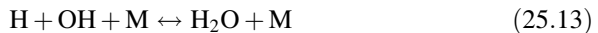
Resulting radicals H and HO_2 have chain branching reactions with O_2 , H_2 , and derive OH starting from Eqs. 25.9 to 25.11. Since Eq. 25.11 is duplicated, three Hs generated in the process and the above chain loop can circulate without the help of Eq. 25.8 if the ignition event ends in success.

At the same time, a recombination reaction shown in Eq. 25.12 generates HO_2 exothermically from H and O_2 . M in these equations means a third body. The early reaction rate of the H_2 - O_2 combustion tends to be controlled by a competition between the reactions in Eq. 25.12 with the branching reaction in Eq. 25.9.

Fig. 25.1 Chain paths of the low-temperature stage of H_2 - O_2 combustion



After the radicals H and OH accumulate sufficiently, they start deactivating themselves through the recombination reactions Eqs. 25.13 and 25.14 to generate H_2O . These reactions open up the final stage of the combustion process and release the effective heat to form a hot flame.



In general, an ignition source has to be externally supplied to raise the mixture temperature locally up to the level high enough to ensure the initiation and branching of these chain reactions. Moreover, in the case of the so-called auto-ignition, another completion becomes crucial between the recombination in Eqs. 25.15 and 25.16 from HO_2 to H_2O_2 and another branching in Eq. 25.17 from H_2O_2 to two OH s. They sustain the reaction loop under lower temperature conditions in the case of auto-ignition.

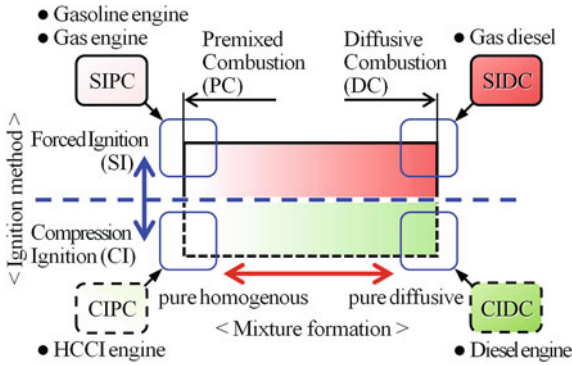
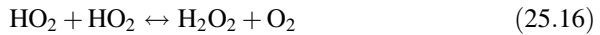


Fig. 25.2 Four example combustion types for C-ICEs



All in all, the ignition of the $\text{H}_2\text{-O}_2$ combustion system should satisfy two requirements. One is the field temperature for overcoming the barrier of the activation energy of the hydrogen abstraction reaction. The minimum level of the temperature is usually called “auto-ignition temperature” or “ignition point.” In spite of its significance for fire prevention, the ignition point (~ 850 K for $\text{H}_2\text{-Air}$ atmospheric mixture) proves to be much lower than the temperature (~ 1000 K for $\text{H}_2\text{-Air}$ mixture) needed to cause practical auto-ignition in Spark Ignition-Premixed Combustion (SIPC) type C-ICEs (see also Fig. 25.2 for various combustion types).

The other is the collision probability between H_2 and O_2 for sustaining a substantial reaction rate between them. This probability is usually evaluated based on the fuel concentration of the mixture. The minimum/maximum fuel concentration is called “lean/rich limit of combustion” or “flammable range.”

25.4 Combustion Methods for a Hydrogen-Fueled C-ICE

As is well-known, a thermodynamic cycle of a C-ICE using a crank mechanism consist of a power stroke; compression and expansion as a closed system, and a gas-exchanging stroke; exhaust and intake as a semi-open system. Ignition and combustion happen around the switchover timing from compression to expansion.

This cycle has characteristic features both in the in-cylinder conditions at the end of compression and in the possibility of involuntary forced ignition during the gas

exchange. As for the in-cylinder conditions, the compression temperature of C-ICEs is sufficiently low to avoid the low-temperature reactions of the H_2 -Air premixture, whereas the compression pressure frequently reaches as high as 10–15 MPa. Regarding the gas exchange process, an overlap period is normally needed between an exhaust process and an intake process in order to make the gas exchange more complete. This means that fresh gas in the intake ports may make contact with hot residual gas in the combustion chamber at the start of the intake stroke.

Figure 25.2 shows four exemplary combustion types for C-ICEs. The types are divided based on the formation and ignition of their fuel-air mixture. Combustion in C-ICEs is no exception in that it happens in the mixture within the above-mentioned flammable range and always progresses in the turbulent combustion mode.

An important point is that the methods of mixture formation largely determine the combustion characteristics including flame shape and luminance. In the case where a homogenous mixture fills the whole of a combustion chamber well before an ignition event, the combustion is categorized as premixed combustion abbreviated as PC shown in the figure. In the case where pressurized fuel is directly injected into a closed combustion chamber just before an ignition event, the combustion will happen in diffusive combustion mode as abbreviated as DC in the figure. In the diffusive combustion mode, liquid sprays or gaseous jets of the fuel should entrain the ambient air into themselves and form a flammable premixture around them.

As for the ignition methods in C-ICEs, they are divided into forced ignition or traditionally called Spark Ignition; SI, and auto-ignition or Compression Ignition; CI, respectively. So, the exemplary combustion types make four sets according to the combustion modes and the ignition methods.

The C-ICE usually called “Gasoline engine,” or Otto-cycle engine, is categorized as a SIPC type and the C-ICE called “Diesel engine” with conventional near-top-dead-center injection as a CIDC type. Although practical examples are much fewer in number than these two, the C-ICE called “Gas diesel” is categorized as a SIDC type in which high-pressure gas jets are ignited by forced ignition sources like pilot sprays of diesel oil. A CIPC type is rather identified as homogenous charge CI (HCCI [10]) and is partially used in the CIDC type engines owing to its low emission feature. As also shown in the figure, it should be noted that there is not a clear distinction between the two combustion modes and an intermediate combustion type actually exists especially in CIDC engines with multiple injections.

In C-ICEs, unburned premixture in a cylinder is always compressed not only by the piston motion but also by the expansion of hot burned gas regardless of the combustion types. Therefore, the possibility of unintended local CIPC occurrence always exists in the SIPC case. This CIPC occurrence in the SIPC mode is known as “knocking” and it strictly limits the power density and the maximum dimension of SIPC type engines.

Also in the case of SIPC application, its premixture has to be always within the flammable range previously mentioned without regard to the required engine load,

which forces to throttle the intake air flow according to the amount of fuel injection at lower load conditions. This causes deterioration of the engine efficiency called pumping loss.

25.5 Hydrogen Application Concept for C-ICE

Hydrogen or hydrogen-mixed gas can be applied to all the four combustion types mentioned in the last section and there exist practical examples for every one of the four types; but SIPC and SIDC will continue being major application targets for hydrogen-related gas fuels, thanks to their higher auto-ignition point. In principle, the SIPC type is favorably used in smaller high-speed engines and the SIDC type would be suited for larger low-speed engines. Practical examples are introduced in the next section.

Table 25.1 summarizes the evaluation results of hydrogen fuel used with a SIPC type C-ICE against its counterparts running on conventional fuels [11–14]. Some of the evaluation items are listed with relevant physical properties. Additional explanations are given as follows:

1. A higher ignition point is a major advantage of hydrogen over conventional gasoline fuel. Hydrogen can be applied to more efficient engines of a higher compression ratio or to larger dimension engines without fear of knocking. However, the ignition point of hydrogen is lower than that of methane by about 100 K as well as its start point of the low-temperature combustion stage; so it should be noted that hythane fuel used with natural gas engines may limit their knock-free operation. It is easily understood from Fig. 25.1 that the branching OHs from H_2-O_2 reaction system can also accelerate the initiation processes of methane combustion.
2. A broader flammable range especially on the leaner limit side is clearly one of the biggest advantages of hydrogen. This enables hydrogen-fueled SIPC engines to run without throttling their intake air and to be nearly free from pumping loss, which drastically improves the engine efficiency at lower load conditions.
3. A very high ignitibility of hydrogen due to the broader flammable range is clearly one of the biggest disadvantages. As explained in the second paragraph in the previous section, SIPC engines with low-pressure port injection usually have a direct connection between their fuel gas in the intake ports and their combustion chamber around the timing of top dead center (TDC). Hot residual gas, carbon sludge, hot spots, etc., inside the chamber can be an ignition source for backfire. Even faint spark of an ignition plug was once included, which was caused by cross talk among high-tension ignition cables. Fortunately, technologies like variable valve phasing and so-called “direct ignition coils” have greatly improving the situation regarding the backfire problem of hydrogen-fueled SIPC engines.

Table 25.1 Evaluation of hydrogen used in a SIPC type C-ICE versus other conventional fuels

Combustion type		SIPC		
Item	Fuel	Methane (NG)	Hydrogen	
(1) Anti-knocking	Gasoline ($C_{7.5}H_{13.5}$)	Excellent	Good	
ignition point [K]	Ref. (poor)	900–920	800–850	
(2) Anti-pumping loss & lean-burn stability	Ref. (poor)	Moderate	Excellent	
Flammable range; a [-]	0.71–2.5	0.48–1.43	0.10–6.67	
(3) Anti-backfiring	Ref.(moderate)	←	Very poor	
Min. ign. energy [mJ]	0.24	0.29	0.015	
(4) Other abnormal combustion	LSPF ^b with high pressure T/C	←	Pre-ignition rapid combustion	
Max. comb. speed [cm/s]	40–46	37–38	270–290	
(5) Anti-NOx emission	Ref.	←	Poor	
Max. adiabatic flame	2140	2240	2400	
Temperature [K]	($\phi = 1.0$, hexane)	($\phi = 1.05$)	($\phi = 1.07$)	
(6) Anti-GHG emission quenching distance [mm]	Ref.	Good (methane slip)	Excellent	
(7) Anti-PM emission	2.00 Ref. (GPF ^{b?})	2.03 Excellent	0.64 ←	

(continued)

Table 25.1 (continued)

Combustion type		SIPC
Item	Fuel	
(8) Specific power ^b	Gasoline (C _{7.5} H _{13.5})	
Ref.		Methane (NG) Poor
Relative evaluation [-]	1	Hydrogen Very poor
Vapor density ^c [kg/m ³]	5.1	0.86
LHV ^d [MJ/kg]	43.5	0.717
Stoichiometry [kg _{air} /kg _{fuel}]	14.7	50.0
Fuel vol. in 1L cylinder [cm ³]	17	17.2
(9) Ignition source		95
(10) Thermal load on wall	Ignition plug for small bore Ref.	Consideration for large bore Moderate
(11) Injector durability	Ref. (good)	Consideration
(12) Lub. oil deterioration	Dilution by fuel	Gentle
		Hydrogenation?

^aEquivalence ratio^bSee "7)" item in the text^cAt atmospheric conditions^dLower heating value^eLow-speed pre-ignition^fGasoline particulate filter

- 4, 5. The highest combustion speed and higher flame temperature of hydrogen could be theoretically strong points in achieving an ideal Otto cycle. However, these advantages and requirements in practical engine running are in the relationship of trade-off. Too high maximum combustion pressure and too rapid pressure increase must be avoided due to the limitations of mechanical strength, NO_x emission. Actually, considerable retardation of the ignition timing and a mixture setting below stoichiometric conditions are required to achieve peak combustion of hydrogen, and the theoretical efficacy of the hydrogen combustion almost disappears at higher load conditions. Although these situations are not serious, low-speed pre-ignition (LSPI) is often reported in today's gasoline and NG engines especially in the case of high charging pressure.
6. There can be no doubt about the near zero greenhouse gas (GHG) emission from hydrogen combustion at least on tank-to-wheel basis. Moreover, the shortest quenching distance of hydrogen is also advantageous in combustion efficiency, since unburned fuel emission originates mainly from the flame quenching zone on a chamber wall and in a crevice volume. Considering no effective oxidation catalyst is available for NG engines because of methane's inactivity at their typical exhaust temperature around 650 K or lower, hythane fuel has been repeatedly proven to be a remedy to control the flame quenching of NG engines and the worrying emission of unburned methane which reaches as high as 25 in global warming potential (GWP).
7. Hydrogen combustion is safely free from particulate matter (PM) emission except that a small amount of PM could originate from pilot sprays for the forced ignition of a H_2 -air mixture, whereas today's gasoline direct injection (GDI) engines are sometimes denounced as emitting smaller sized PM to be filtered by a gasoline particulate filter (GPF).
8. Specific power is clearly one of the largest disadvantages of hydrogen fuel in SIPC type C-ICEs where their fuel gas is admitted into the intake ports with the pressure slightly higher than the charging pressure in order to save the compression work for fuel injection. The specific power is simply evaluated here on the relative heat value of the sucked fuel in the stoichiometric mixture in the same cylinder volume. As shown in Table 25.1, a hydrogen-fueled engine can make only 86 % power of a corresponding gasoline-fueled one and outputs 4 % less even than a NG counterpart. It is evident that this drawback is derived from the lightest vapor density and the largest stoichiometry of the three fuels in spite of its highest LHV. Considering that hydrogen tends to need a leaner mixture setting than other fuels, a hydrogen engine needs larger dimension to tie with a gasoline engine of the same output and should have a heavier weight and larger friction loss.
- 9–12. A spark ignition system for a gasoline engine can be used for hydrogen-fueled engines although it requires some modifications. The hydrogen-air mixture has a higher break-down voltage than the other mixtures, which is easily predicted from the fact that high-pressure hydrogen is commonly used as an insulator as well as a coolant in a power plant

alternator. The spark plug gap is typically halved to handle this problem (example from 0.9 to 0.4 mm), but this results in greater cooling loss of ignition energy and smaller capacity for sludge formation between the electrodes. Fortunately, the carbon-free nature of hydrogen, as well as its easy ignition, minimizes these issues. In contrast, a NG engine needs a more powerful ignition source such as flame torches from a pre-combustion chamber to promote the combustion of methane–air mixtures especially in larger engine dimensions.

In general, the thermal load on the combustion chamber wall will be larger in hydrogen fuel engines than those in gasoline or NG engines owing to its shorter quenching distance and higher thermal conductivity.

As for the low-pressure gas injection into an intake port, there seems to exist no fatal problems regarding the injector durability, although the injector's so-called "gas admission valve" adopted in large-sized NG engines will have difficulty in stopping hydrogen leaks through its seat surface. After a long-term traveling test in a vehicle, the lubrication oil of the hydrogen-fueled engine was found to seriously lose its lubricating qualities. This is understandable because hydrogen breaks open the double C–C bonds of the oil components and harden the lubrication oil in atmospheric conditions. The primary cause of this deterioration should be attributed to the considerable blow-by of a hydrogen–air mixture from a combustion chamber down to crank case.

Table 25.2 summarizes evaluation results of hydrogen used in SIDC type C-ICEs against their NG counterpart and a CIDC engine on diesel oil [15, 16]. Additional explanations are given one by one as follows:

- 1–4. A distinct advantage of in-cylinder diffusive combustion (DC) is its self-regulating nature of the amount of mixture formed to burn along with the sprays or jets. It is free from the involuntary occurrence of local CIPC (knocking) and intake-flow throttling to keep the premixture within the flammable range, and avoids running instability near the mixture at the lean limit in the SIPC engines. Thanks to the direct fuel injection well after the intake valve closes, DC type hydrogen engines are also free from the troubles of backfiring, although earlier injection timing to optimally reduce the density of hydrogen may cause a pre-ignition problem.
5. Higher engine-out NO_x emissions are a well-known disadvantage of DC type engines where the fuel-air mixture formed around the spray or gas jets can always ignite and burn in the flammable range regardless of the amount of injected fuel and intake of air. To make matters worse, the overall equivalence ratio of DC type engines should be less than unity, or stoichiometrically lean to ensure better completion of the diffusive combustion, which implies a difficulty in the catalytic NO_x reduction in the exhaust pipe and has been promoting the introduction of EGR and selective catalytic reduction (SCR). A hydrogen-fueled DC engine has a potent NO_x emission rate because of its high combustion temperature. However, a unique attempt has been proposed to maximize the

Table 25.2 Evaluation of hydrogen used in a SIDC type C-ICE versus a counterpart on methane and CIDC engine on diesel oil

Combustion type	CIDC		SIDC
Item	Fuel		
	Diesel oil (C ₁₆ H ₃₀)	Methane (NG)	Hydrogen
(1) Anti-knocking	Ignition point [K] 620–670		
(2) Anti-pumping loss & lean-burn stability	Diffusive combustion with direct injection mode is basically free from knocking, pumping loss, lean-burn instability and backfiring		
(3) Anti-backfiring			
(4) Other abnormal combustion			Pre-ignition w/h earlier inj. timing
(5) Anti-NOx emission	Poorer than SIPC	≈ SIPC	Very poor
	EGR, SCR ^c , etc.	(on ign. method)	H ₂ -O ₂ -Ar system
(6) Anti-GHG emission	Better than SIPC	Better than SIPC	Excellent
(7) Anti-PM emission	DPF ^d needed	Good (on ign. method)	Excellent
(8) Specific power evaluated on BMEP ^a	Better than SIPC (P _{max} ^e controlled)	←	←
Power to weight ratio	Poorer than SIPC	←	←
Specific heat ratio [-]	–	1.30	1.41
Specific heat at constant volume [kJ/(kg·K)]	–	1.71	10.1
LHV [MJ/kg]	43.0	50.0	122
Molecular weight [-]	222.4	16.043	2.016
Typical inj. pressure [MPa]	180–220	30	30–40
Compression work ^b [%]	Negligible	1.5~	5.0~
(9) Ignition source	Unnecessary (glow plug)	Pilot sprays	Modified ignition plug, laser ignition
(10) Thermal load on wall	Severer on piston cavity	Moderate	←
(11) Injector durability	Ref. (good)	Bad, yet to be established	
(12) Lub. oil deterioration	PM, sludge	Gentle	←

^aBrake mean effective pressure^bSee “8)” item in the text^cSelective catalytic reduction^dDiesel particulate filter^eMaximum combustion pressure

engine performance without the fear of NO_x emission. In the attempt, an inert substituent of nitrogen in the air is mixed with pure oxygen and supplied to a hydrogen-fueled SIDC engine as an artificial air. The inert component can be fully recycled through a cooled EGR system because H_2O is a sole major product of the $\text{H}_2\text{-O}_2$ reaction and also a sole exhaust gas component that can be liquefied at room temperature thanks to its high condensation point. The substituent should be inert enough not to make any oxides and should be useful to improve the engine performance. Since it is well-known, the theoretical efficiency of C-ICEs increases monotonously with respect to the ratio of working gas's specific heat at constant pressure to its specific heat at constant volume, monoatomic-molecule rare gases are logical choice for the substituent. In the attempt, an Ar- O_2 substitute for air was supplied to a hydrogen-fueled SIDC engine and its exhaust gas was strongly cooled down to separate out the liquid water. The residual Ar gas was mixed with fresh O_2 to make a new substitute air and recirculated to the engine once again. This system could suit the hydrogen production from water electrolysis.

6. Less emissions of unburned fuel components are usually regarded as another advantage of DC type engines except that gas diesel engines are often reported to emit relatively higher unburned fuel (methane) than their counterparts.
7. High PM emission is another distinctive disadvantage of CIDC type engines with direct injection of diesel oil, which originates from richer and cooler regions of the fuel-air mixture. Hence, the engine-out PM should be purified by a diesel particulate filter (DPF). Gaseous fuels are thought to be too light to polymerize into heavy solid molecules in their combustion processes, but gas diesel engines burning methane need a volumetric and strong ignition source like pilot sprays of diesel oil, which can be an additional PM source (and NO_x too).
8. For specific power evaluation of DC type C-ICEs, it is challenging to obtain a proper explanation. Thanks to its knock-free nature and great progresses in turbocharger technologies, today's CIDC engines or diesel engines can output even larger brake mean effective pressure (BMEP) than SIDC counterparts. Because the overall equivalence ratio remains lean, this high BMEP means higher charge pressure and larger mechanical strength are required of modern diesel engines than of gasoline ones, which sacrifices the power to weight ratio of the CIDC motors. All in all, the DC concept may seem more suitable for hydrogen-fueled C-ICEs, but in reality SIDC type engines are far behind the SIPC types in popularity for practical implementation. Again, the reason is the near unacceptable compression work and the weight-increasing compressor system for the hydrogen direct injection. Although the details were already discussed in the hydrogen storage-relating chapters, the compression for the gas direct injection is different in that the injection pressure has to be kept high throughout the engine operation regardless of the internal pressure in the tank. The work may vary significantly according to the phase of the fuel to compress and to the pressure ratio before and after the compression. Considering hydrogen is awfully difficult to compress in the liquid phase, we simply

assume here gaseous compression from room temperature (300 K) with a probable pressure ratio in actual engines. The corresponding adiabatic and isothermal compression work can be calculated using Eqs. 25.18 and 25.19 as

$$w_{\text{adv}} = \frac{c_v T_1}{LHV} \left\{ 1 - (P_2/P_1)^{\frac{1-\kappa}{\kappa}} \right\} < 0 \quad (25.18)$$

$$w_{cT} = \frac{RT_1}{LHV} \ln(P_1/P_2) < 0 \quad (25.19)$$

where LHV is the lower heating value of the fuel, κ is the specific heat ratio, R is the gas constant of the fuel gas, and the suffixes “1” and “2” are for the states before and after the compression. Both equations show how much compression work has to be done to get the same amount of heat released from certain gaseous fuel.

The pressure ratio is set to 60 from an inline pressure of 0.5 MPa to an injection pressure of 30 MPa. The adiabatic compression from room temperature results in gaseous fuel so hot that intercooling is necessary, and that the isothermal compression needs huge heat exchangers to keep the gas temperature constant. So, the actual compression work should lie somewhere in between depending on the compressor design. In Table 25.2, simple averages of the two compression work are shown only for estimation and comparison of the minimum value.

In spite of its higher LHV, hydrogen needs three times more compression work than methane for the direct injection in SIDC engines. The work is found to be equal to at least as much as 5 % of the supplied fuel energy. Even if a high-pressure compressor of a SIDC engine marks 40 % as the total driving efficiency, this compression work should be 2.5 times more on the engine power basis, which is quite enough to abandon the practical use of the direct injection. However, Eqs. 25.18 and 25.19 indicate that the work is proportional to the initial temperature of the fuel gas, so that the compression work can be drastically reduced if fuel gas boils off from its liquid tank under low temperature. This is particularly suitable for methane-fueled engines in LNG carrying ships. High-pressure compression in the liquid phase could be an ultimate solution, but there exist several problems both in LNG and LH_2 compression.

- 9–12. A spark ignition system for a turbo-charged gasoline engine could be used for hydrogen-fueled SIDC engines, although the aforementioned modifications are necessary and the situation is severer due to their higher charging pressure. Since the pilot spray injection may spoil the GHG-free and PM-free characteristics of hydrogen combustion, a laser ignition system would be a potential solution thanks to no residual ignition sources in a cylinder and no ignition difficulty or even ignition easiness under high ambient gas density.

Injector durability under high-pressure conditions of the direct injection is the last and most worrying issue of hydrogen-fueled SIDC type C-ICEs. As is well-known, state-of-the-art injectors have minute metal structures consisting of an injector

needle and a nozzle body, which have to actuate to keep the clearance between them at a micron level. The higher the injection pressure is, the tighter the clearance is to minimize the leakage of the high-pressure fuel. The good thing about the liquid fuel injection is that the fuel serves as lubrication oil and a sealing film for the needle and the nozzle body. Although the injection pressure of hydrogen direct injection engines is only a fraction of the modern liquid injection, the gas injector cannot live long if it keeps the clearance tight enough to seal the leaky hydrogen under dry conditions. There is a slim chance that mechanical sealing such as an O-ring will work against the difference in internal and external pressure of the injector. Instead, pressurized “seal oil” is applied to the upper part of the needle to control the gas leakage from a gas passage in the lower part of the needle. It is very important to adjust the seal oil pressure to the proper level, which is normally lower than the gas injection pressure by a small margin. However, the seal oil pressure is sometimes set to the higher level especially in the case of hydrogen for safety reason. This may result in seal oil consumption and deterioration of the anti-knocking feature.

25.6 Case Studies of Hydrogen Combustion in Medium-Sized Internal Combustion Engines

Research on hydrogen combustion is conducted not only in small-sized engines for vehicles but also in medium-sized engines for power generation. Pure hydrogen combustion engines have not yet been developed practically, but research on burning natural gas mixed with hydrogen is currently being carried out. Some of the case studies are introduced as follows.

25.6.1 An Example of Research on a High-Powered Hydrogen Engine System [17]

In this study, a diesel engine for power generation whose principal particulars are shown in Table 25.3 has been converted to a pure hydrogen combustion engine for research purposes.

Figure 25.3 shows an outline of the system. As mentioned in the section about vehicle engines, the method of supplying hydrogen to the intake pipe sometimes causes a backfire phenomenon, which is disastrous to the engine. In this research, a similar combustion method to that of diesel engines has been adopted to solve the above problem. Only the air is induced into the cylinder and hydrogen is directly injected into the cylinder after the piston compression stroke. Therefore, hydrogen needs to be injected at high pressures such as 30 MPa.

Since hydrogen has a high self-ignition temperature, ignition sources such as an ignition plug or pilot injection, or a high temperature on the air side is necessary. Research is challenging on this point. The ignition plug is used during the starting

Table 25.3 Specifications of hydrogen-fueled engine

Elements	Specifications/size
Engine type	Four-strokes
Number of cylinders	6
Bore × stroke	Φ170 mm × 220 mm
Rated power output	600 kW/1500 rpm
Mean effective pressure	1.69 MPa

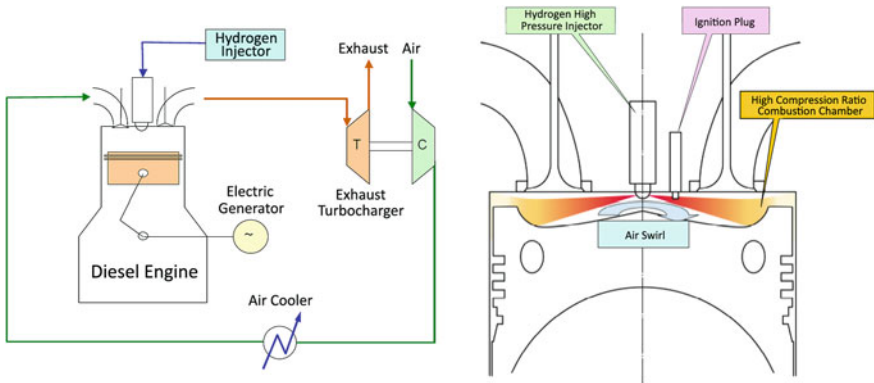


Fig. 25.3 System of a hydrogen-fueled engine

up time, but the self-ignition of hydrogen is attempted under high load. If this is possible, it shows the same combustion pattern as diesel. From the results, an air temperature of higher than 690 °C is necessary in order for the hydrogen to ignite by itself. This temperature is realized in the compression ratio of 18.3 and the intake air temperature of 100 °C for example.

Thermal efficiency when using hydrogen becomes higher than a diesel engine operated with diesel oil and reaches 49 % at full load. One reason for this comes from the difference of the theoretical air quantity/LHV in Table 25.4. Since the value of hydrogen is 15 % smaller than that of petroleum-based fuel, its intake air pressure can be set lower even when acquiring the same released heat under the same excess air ratio. Due to this, the compression ratio can be increased under the same cylinder maximum pressure (P_{max}), which improves the thermal efficiency accordingly. Moreover, the high air temperature at the end of compression due to

Table 25.4 Comparison of properties between hydrogen and petroleum-based fuel

	Hydrogen	Petroleum
Self-ignition temperature (atmospheric pressure)	571 °C	230 °C
Lower heating value (LHV)	120.0 MJ/kg	42.7 MJ/kg
Theoretical air quantity	34.3 kg/kg	14.3 kg/kg
Theoretical air quantity /LHV	0.286 g/kJ	0.335 g/kJ

the high compression ratio is favorable to the self-ignition of hydrogen as mentioned above. At maximum, a high compression ratio of 22 in this engine has been tested.

Naturally, CO_2 and SO_x are not emitted from hydrogen-fueled engines, but NO_x due to the high combustion temperature is emitted. This engine emits 835 ppm NO_x (O_2 : 0 %) at an EGR ratio of 24 %, but it can be reduced down to 100 ppm by combining the catalyst for after-treatment of the exhaust gas.

Test results are successful as mentioned above. However, there are many challenges to be solved such as the durability of the hydrogen injection system for long-term operation in practical applications.

25.6.2 A Fundamental Study on “Hydrogen-Admixture to Natural Gas” Combustion [18]

There are some studies on combustion of pure hydrogen as mentioned above. However, it is still far from practical use to apply it to an engine for power generation which requires several thousand hours operation in a year because many problems still remain such as reliability of the hydrogen injection system and stability of combustion itself. On the other hand, natural gas engines for power generation widely prevail. Research on injecting hydrogen-admixture to natural gas in a cylinder, which is more practical as hydrogen utilization for internal combustion engines, is introduced.

One of the experimental results using a visual combustion test apparatus is shown in Fig. 25.4. Hydrogen is added to methane in advance, and the admixture is

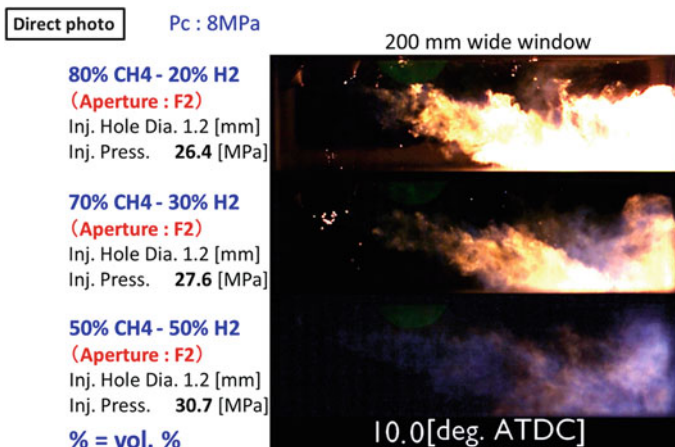


Fig. 25.4 Improvement of methane combustion by mixing hydrogen (ATDC: After Top Dead Center of piston)

injected at a pressure of >30 MPa into the chamber containing the air. The air pressure in the chamber is 10 MPa. At the left end of the rectangular chamber with a length of 200 mm in the figure, a gas injection nozzle and a diesel oil pilot injection nozzle are equipped. The combustion state of the methane + hydrogen jet is directly photographed. According to the photo, a case containing massive amounts of methane shows diffusive combustion with luminous flame, but the luminous flame changes to a blue flame as the hydrogen quantity increases and shows non-luminous diffusive combustion.

Figure 25.5 shows a comparison of the heat release rate and the emission. All three cases in this figure have injection duration between 0 to 10 ms, and the heat release rate in this period is apparently increased by hydrogen percentage, as shown in circle ①. Accordingly, after-burning after the injection ends at 10 ms, apparently shortens and it shows satisfactory burn-up (in the circle ②). According to the emission in the table in the figure, NO_x is increased because of a higher combustion temperature of hydrogen than that of methane. On the other hand, the amount of unburned hydrocarbon is decreased.

The maximum hydrogen quantity at the experiment is 50 vol.%. Even in that case, it is 11 mass% and 23 % by the released heat due to the low density of hydrogen. Although its quantity is not so large, it highly contributes to the combustion improvement as mentioned above.

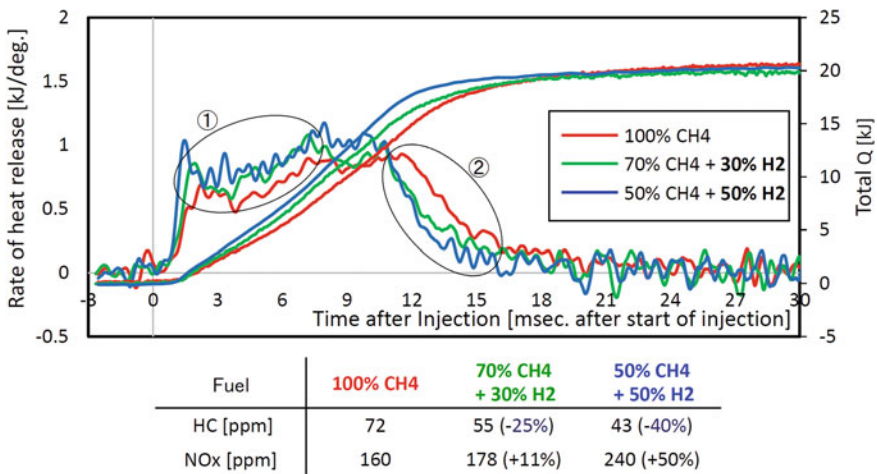


Fig. 25.5 Improvement of methane combustion by mixing hydrogen (heat release rate and emission)

25.6.3 A Case Study of Engine Operation with Hydrogen-Admixture to Natural Gas (Limit on Knocking/Misfiring) [19]

Research has been conducted using a medium-sized (170 mm bore) test engine. This gas engine does not inject gas into the cylinder but is called a lean-burn type engine. In the case of a lean-burn type engine, natural gas (+hydrogen) is provided to an intake pipe of the engine, where air-fuel mixture is produced. The air-fuel mixture is ignited by an ignition plug after the intake and piston compression stroke, and leads to combustion called premixed combustion or flame propagation. In this research, the addition of hydrogen of up to 30 vol.% to natural gas has been tested.

Since the ignition energy of hydrogen is extremely small, this method may easily cause pre-ignition in which the natural gas ignites earlier than the ignition plug due to so much hydrogen being added to the natural gas. On the other hand, the misfire limit of the air-fuel mixture expands by adding hydrogen, which prevents misfire even with a leaner air-fuel mixture than the conventional one. Although this is a completely opposite story to the NO_x increase by hydrogen addition which has been pointed out in the former section, leaner air-fuel mixture reduces NO_x further.

In Europe, research on preventing misfire by adding hydrogen to low calorie and low combustible gases such as coal-mine gas and bio-gas and activating combustion is being conducted. Moreover, if the hydrogen is produced from renewable energy, it contributes to a reduction of CO_2 emissions.

Another way to burn hydrogen more easily is to use it in steady combustion such as that in a gas turbine. It has been announced in Japan that the development of such a hydrogen burning gas turbine is in the R&D stage.

References

1. Chiesa P, Lozza G, Mazzocchi L (2003) Using hydrogen as gas turbine fuel. ASME Turbo Expo 3:163–171
2. Shudoa T, Shimab Y, Fujiic T (2009) Production of dimethyl ether and hydrogen by methanol reforming for an HCCI engine system with waste heat recovery—continuous control of fuel ignitability and utilization of exhaust gas heat. Int J Hydrogen Energy 34:7638–7647
3. Saxenaa S, Schneiderb S, Acevesc S, Dibbble R (2012) Wet ethanol in HCCI engines with exhaust heat recovery to improve the energy balance of ethanol fuels. Appl Energy 98:448–457
4. Zamfirescu C, Dincer I (2009) Ammonia as a green fuel and hydrogen source for vehicular applications. Fuel Process Technol 90:729–737
5. Alger T, Mangold B (2009) Dedicated EGR: a new concept in high efficiency engines. SAE Int J Engines 2(1):620–631
6. Frenklach M, Kazakov A (2013) Reduced reaction sets based on GRI-Mech 3.0. 06/19/2013. www.me.berkeley.edu/drm

7. Kee RJ, Rupley FM, Meeks E, Miller JA (1996) CHEMKIN-III: A FORTRAN chemical kinetics package for the analysis of gas-phase chemical and Plas-ma kinetics. Sandia National Laboratories, Albuquerque
8. Lutz AE, Kee RJ, Miller JA (1997) SENKIN: A Fortran program for predicting homogeneous gas phase chemical kinetics with sensitivity analysis. Sadia National Laboratories, Albuquerque
9. Sato P, Yamasaki Y, Kawamura H, Iida N (2005) Research on the infulence of hydrogen and carbon monoxide on methane HCCI combustion. *JSME Int J (Ser B)* 48–4:725–734
10. Kong SC, Marriott C, Reitz RD, Christensen M (2001) Modeling and experiments of HCCI engine combustion using detailed kinetics with multidimensional CFD. SAE Technical Paper 2001-01-1026
11. Cracknell R, Alcock J, Rowson J, Shirvill L et al (2002) Safety considerations in retailing hydrogen. SAE Technical Paper 2002-01-1928
12. Lide DR (ed) (1991) 72nd edition: CRC handbook of chemistry and physics. CRC Press, Boca Raton
13. Das LM (1996) Hydrogen-oxygen reaction mechanism and its implication to hydrogen engine combustion. *Int J Hydrogen Energy* 21–8:703–715
14. Karim GA (2003) Hydrogen as a spark ignition engine fuel. *Int J Hydrogen Energy* 28–5:569–577
15. Aleiferis PG, Rosati MF (2012) Controlled autoignition of hydrogen in a direct-injection optical engine. *Combust Flame* 159(7):2500–2515
16. Welch A, Mumford D, Munshi S, Holbery J et al (2008) Challenges in developing hydrogen direct injection technology for internal combustion engines. SAE Technical Paper 2008-01-2379
17. Takaishi T, Akagawa H (2006) Development of high-powered hydrogen engine system. *Hydrogen Energy Syst* 31:8–11 (in Japanese)
18. Takasaki K et al (2015) Visual study on GI (gas high-pressure injection) combustion for highly efficient gas engine. In: Conference ‘the working process of the internal combustion engines’ Graz, Austria
19. Kawauchi S, Korb B, Wachtmeister G (2015) Influence of H₂ addition on engine performance and emission characteristics in premixed lean burn natural gas engines at high specific loads. In: Conference ‘engine combustion processes—current problems and modern techniques’ Ludwigsburg, Germany

Part V

Hydrogen Safety

Junichiro Yamabe

International Research Center for Hydrogen Energy, Kyushu University, Fukuoka, Japan

Hydrogen degrades the tensile and fatigue properties of many metallic materials. This phenomenon is known as hydrogen embrittlement (HE). In general, high-strength materials are severely degraded by hydrogen. Many studies on HE have been performed. However, the mechanism of HE has not yet been clarified. High-pressure hydrogen exposure also degrades rubber materials because of decompression failure. In Part V of this book, the fundamental principles and recent progress regarding hydrogen safety in terms of hydrogen interaction of materials are reviewed. The effect of hydrogen on fretting fatigue is also reviewed in terms of practical importance. Moreover, hydrogen gas safety management and hydrogen safety in practice are reviewed.

Chapter 26

Hydrogen Safety Fundamentals

Junichiro Yamabe and Saburo Matsuoka

Abstract This chapter describes an overview of hydrogen safety related to hydrogen embrittlement (HE), hydrogen gas safety management, and hydrogen safety best practice. Blister fracture of rubbers caused by decompression of high-pressure gaseous hydrogen is also introduced.

Keywords Hydrogen embrittlement · Blistering · Hydrogen diffusion · Steel · Aluminum · Rubber · Hydrogen safety

26.1 Important Issues in Hydrogen Safety

For the safe operation of hydrogen-energy systems, in particular systems that use high-pressure hydrogen, the design should seriously consider hydrogen embrittlement (HE). In terms of strength design, the characteristics of hydrogen gas should be considered, including high diffusivity, fast leakage, and the wide range hydrogen concentrations within the explosion limit. This is hydrogen gas safety management. Moreover, it is important to reduce and eliminate issues such as human error (hydrogen safety best practice). Figure 26.1 shows a schematic illustration of hydrogen safety in a laboratory environment.

J. Yamabe (✉)

International Research Center for Hydrogen Energy, Kyushu University,
Fukuoka 819-0395, Japan
e-mail: yamabe.junichiro.575@m.kyushu-u.ac.jp

S. Matsuoka

Research Center for Hydrogen Industrial Use and Storage (HYDROEGNIUS),
Kyushu University, Fukuoka 819-0395, Japan
e-mail: matsuoka.saburo.204@m.kyushu-u.ac.jp

© Springer Japan 2016

K. Sasaki et al. (eds.), *Hydrogen Energy Engineering*,
Green Energy and Technology, DOI 10.1007/978-4-431-56042-5_26

359

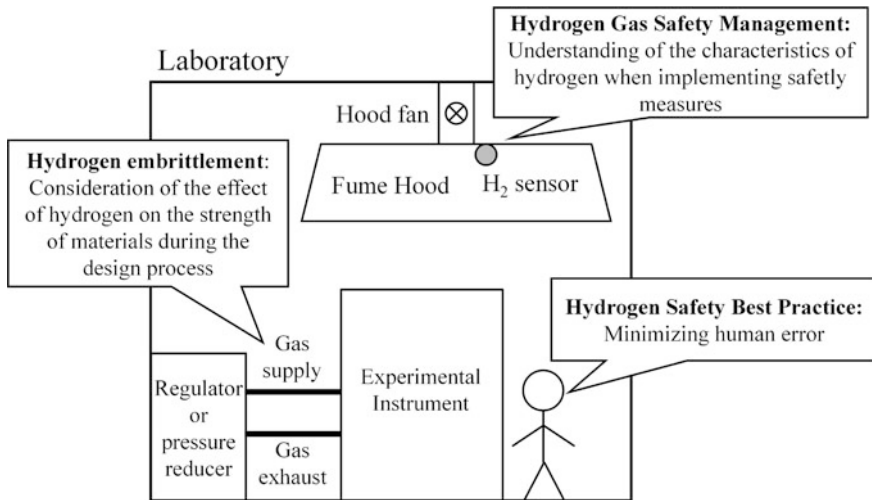


Fig. 26.1 Schematic illustration of hydrogen safety in a research environment

26.2 Recent Trends in Evaluation of Hydrogen Compatibility

Fuel-cell vehicles (FCVs) have recently been commercialized, and the necessary hydrogen filling stations are gradually being built. To ensure the safe and reliable use of metallic materials in a hydrogen environment, hydrogen-tolerant materials and systems must be employed to prevent accidents due to HE-related failure [1–5].

In the development of Japanese 35 MPa hydrogen stations beginning around 2000, only metallic materials that were not susceptible to HE could be used in hydrogen components. The following three requirements for the materials were imposed: (1) the yield and tensile strengths, elongation, and reduction of area (RA) for slow strain rate testing (SSRT) in gaseous hydrogen must be equal to or greater than those in air, (2) the fatigue life of the material in gaseous hydrogen must be nearly equal to that in air, and (3) the fatigue crack growth (FCG) in gaseous hydrogen must be nearly equal to that in air. To satisfy these requirements, Type 316L stainless steel and A6061-T6 aluminum alloy were mainly used for the hydrogen components.

On the other hand, in the development of high-pressure 70 MPa hydrogen stations in Japan from around 2010, metallic materials that were slightly susceptible to HE were permitted to be used in hydrogen-exposed components. The following two requirements for the materials were imposed: (1) the RA in SSRT must satisfy a judgment criterion; and (2) the fatigue life of the material in gaseous hydrogen must be nearly equal to that in air. The degradation of the RA correlates with the austenitic stability of materials [6], which can be quantified by a “nickel equivalent” [7, 8]. Thus, the nickel equivalent is used as an indicator to determine the degradation of RA, and selection of the material is based on chemical composition. As a result, Type 316 and Type 316L stainless steels,

which have nickel equivalents that satisfy the judgment criterion, can be used in hydrogen-exposed components [9].

However, these materials have lower strength and higher cost compared with conventional steels, such as carbon- and low-alloy steels. For the widespread commercialization of hydrogen energy systems in the near future, conventional steels with higher strength and lower cost will be required. Consequently, many experiments on the tensile strength, fatigue, and hydrogen diffusion properties of such materials in high-pressure hydrogen gas environment need to be performed. Appropriate design methods will have to be established based on the resulting scientific findings.

As well as metals, organic materials such as rubber are used in hydrogen systems. Rubber is used for making O-rings for high-pressure hydrogen gas seals. However, exposure to high-pressure hydrogen causes internal cracks in rubber materials, resulting in degradation. Thus, it is also imperative to clarify the mechanism of hydrogen-induced degradation of organic materials such as rubber.

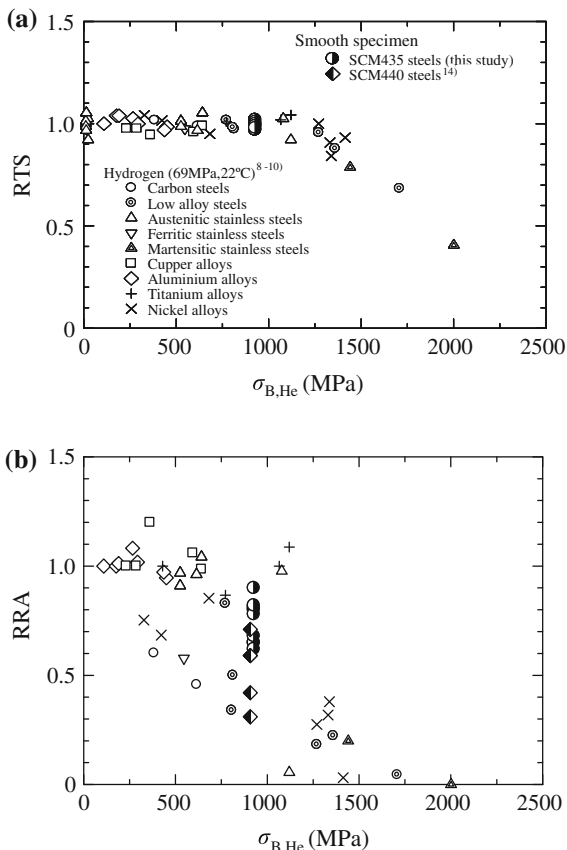
26.3 Tensile Behavior of Metals in the Presence of Hydrogen

The loss of tensile ductility is an indicator of HE susceptibility, and the relative reduction of area (RRA), i.e., the ratio of RA in hydrogen environment to that in an “inert” gas environment such as helium (or air), is often used as a measure of tensile ductility. In addition, tensile fracture surfaces change when exposed to hydrogen. This section explores the loss of tensile ductility in various metals, and gives examples of fracture surface morphologies. The details of the tensile properties in the presence of hydrogen will be discussed in Chap. 29.

26.3.1 *Effect of Hydrogen on the Loss of Tensile Ductility of Various Metals*

The tensile ductility of various metals in high-pressure gaseous hydrogen is provided in the NASA database [10]. To obtain these values, tensile tests of smooth and notched specimens were performed in helium and hydrogen gases at 69 MPa. The materials were then categorized into four grades: extremely embrittled; severely embrittled; slightly embrittled; and negligibly embrittled, according to their susceptibility to HE. Type 316L stainless steel and A6061-T6 aluminum alloy were found to be negligibly embrittled by exposure to high-pressure hydrogen, whereas carbon steels and low-alloy steels were found to be severely embrittled, or extremely embrittled. Figure 26.2a shows the relative tensile strength (RTS), i.e., the ratio of tensile strength in hydrogen ($\sigma_{B,H}$) to that in helium ($\sigma_{B,He}$), against the tensile strength in helium. Figure 26.2b also shows RRA versus $\sigma_{B,He}$, and it is observed that the RRA decreases with increasing σ_B ,

Fig. 26.2 Susceptibility to HE of various metals, as reported in the NASA database: **a** RTS, and **b** RRA as functions of $\sigma_{B,He}$ [10, 11]



In contrast, the RTS is largely unaffected by hydrogen for metals with $\sigma_{B,He} < 1200$ MPa. However, it decreases with increasing $\sigma_{B,He}$ for metals with $\sigma_{B,He} > 1200$ MPa. It is therefore clear that the susceptibility of a metal to HE is dependent on the tensile strength of the metal; high-strength steel with $\sigma_B > 1200$ MPa is particularly severely degraded by exposure to hydrogen.

26.3.2 Change in Void Morphology of Pipeline and Type 316L Steels

The characteristic ductile fracture morphology of metals subjected to tensile testing is the “cup-and-cone” fracture morphology. This fracture morphology consists of normal stress and shear stress fracture surfaces that are covered with voids. In materials that are negligibly, or slightly susceptible to HE, the hydrogen often does not change the macroscopic fracture morphology. However, it does change the microscopic morphology (i.e., the void morphology). The change in void

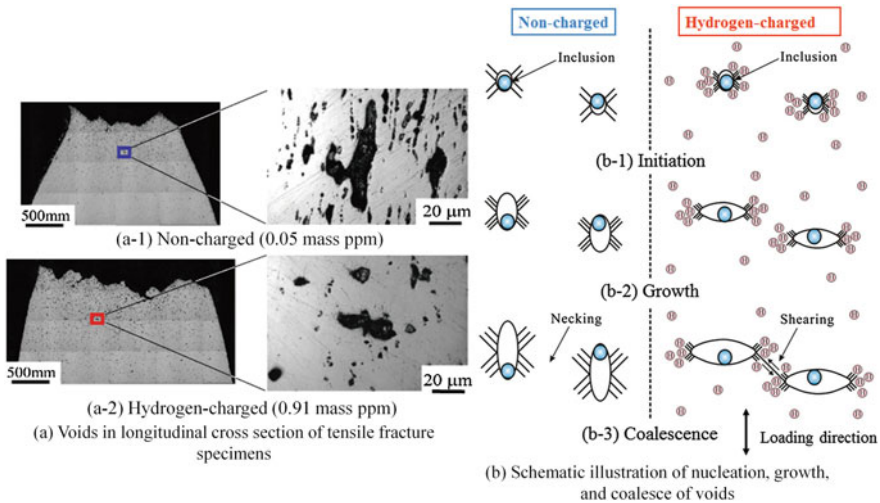


Fig. 26.3 Development of voids in a tensile strength test of a hydrogen-charged pipeline steel specimen, JIS-SGP (0.078 % C) [14]

morphology of various steels in the presence of hydrogen is summarized in Ref. [12]. In contrast, in materials that are extremely, or severely susceptible to HE, surface cracks associated with quasi-cleavage are initiated. Consequently, cup-and-cone fracture is often not observed [6, 13].

Figure 26.3 shows an interesting difference in void growth behavior between the non-charged and hydrogen-charged specimens of a pipeline steel. In the non-charged specimen, voids are elongated in the tensile direction (Fig. 26.3a-1). In the hydrogen-charged specimen, voids grow in the lateral direction in pipeline steel (Fig. 26.3a-2) [14]. The hydrogen charging was performed electrochemically. The difference in void morphology between the non-charged and hydrogen-charged specimens is attributed to enhancement of localized slip deformation by hydrogen.

The mechanisms of HE are broadly classified into: (i) hydrogen-enhanced decohesion (HEDE) [15–17], and (ii) hydrogen-enhanced localized plasticity (HELP) [18–20] (although another model associated with hydrogen-induced void nucleation has been recently proposed [21–23]). In the HEDE model, hydrogen weakens interatomic bonds. Consequently, the fracture is both microscopically and macroscopically brittle. Conversely, in the HELP model, hydrogen enhances local slip, and consequently this model results in microscopic ductile fracture, even though the macroscopic fracture looks like a brittle fracture. The present results shown in Fig. 26.3 can be explained by the HELP model rather than by the HEDE model.

Furthermore, the basic mechanisms of void growth lateral to the tensile axis in the hydrogen-charged specimen (Figs. 26.3a-2, b) can be considered consistent with that of FCG, as shown later in Fig. 26.10.

In contrast to the hydrogen-induced increase in void size for pipeline steel shown in Fig. 26.3, hydrogen causes a reduction in void size in Type 316L stainless steel [24]. It is presumed that localized slip deformation is enhanced by hydrogen. As a result, small voids associated with void sheets are formed [25, 26]. The void sheets are attributed to severe plastic deformation; therefore the phenomenon observed in Type 316L stainless steel can also be explained in terms of the HELP model rather than the HEDE model. The difference in these void morphologies is believed to be related to a large difference in hydrogen diffusivity. Indeed, the hydrogen diffusivity of pipeline steel is approximately 6 orders of magnitude larger than that of Type 316L stainless steel, as discussed further in Sect. 26.5.

26.4 Fatigue Behavior of Metals in the Presence of Hydrogen

The effects of hydrogen are often investigated by using a hydrogen-charged specimen tested in air (internal hydrogen), or a non-charged specimen tested in gaseous hydrogen (external hydrogen). This section reports the fatigue behavior of metals charged electrochemically, i.e., hydrogen-charged metals, and the basic mechanism of HE based on these results. The behavior of these metals in high-pressure gaseous hydrogen will be discussed in Chap. 30.

26.4.1 *General Types of Hydrogen-Assisted FCG Behavior*

Hydrogen often causes acceleration of the FCG rate of various metals. In general, hydrogen-assisted FCG behaviors are classified into three types [5]: (i) true-corrosion fatigue; (ii) stress-corrosion fatigue; and (iii) mixed behavior. In the case of stress-corrosion fatigue, FCG acceleration occurs when the maximum stress intensity factor exceeds the threshold stress intensity factor for hydrogen-induced cracking under a sustained load. This type of fracture has been observed mainly in high-strength steels. In contrast, true-corrosion fatigue and mixed behavior are often observed in low- and medium-strength steels. Several examples of FCG behavior in the presence of hydrogen are given below.

26.4.2 *Fatigue Behavior of Pipeline and Cr–Mo Steels*

Figure 26.4 shows the morphology of slip bands at crack tips for hydrogen-charged specimens tested at different frequencies [27]. The hydrogen charging was performed electrochemically. The morphology of the slip bands for the non-charged

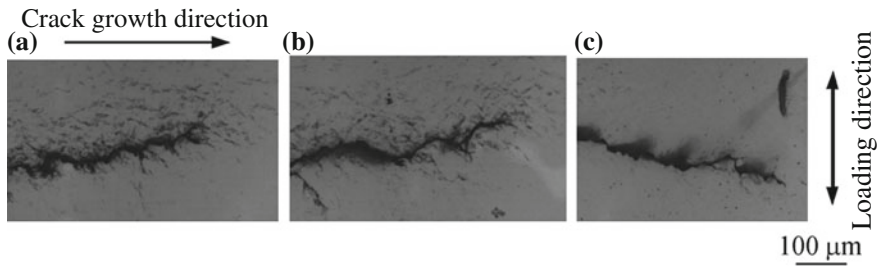


Fig. 26.4 Crack tip of a hydrogen-charged specimen. The residual hydrogen content after the test ($C_{H,R}$) is 1.1 ppm [27]. **a** $f = 10$ Hz, **b** $f = 0.1$ Hz, **c** $f = 0.01$ Hz

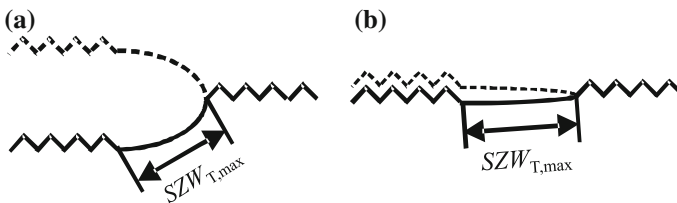


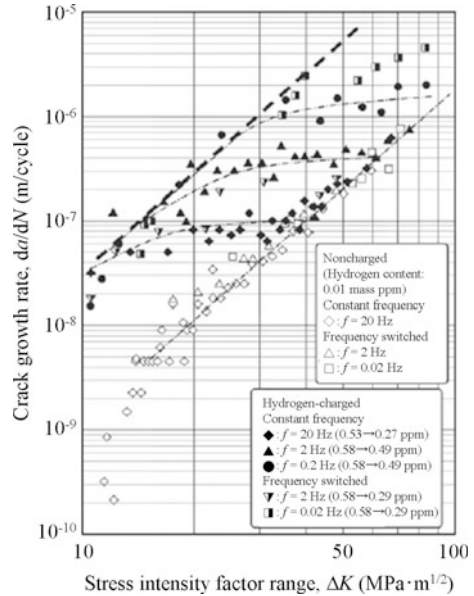
Fig. 26.5 Difference in morphology of stretch zone for non-charged (uncharged) and hydrogen-charged specimens [27]. **a** Uncharged. **b** Hydrogen-exposed

specimen was almost the same as that for the hydrogen-charged specimen tested at 10 Hz (Fig. 26.4a), regardless of test frequency. The slip bands for the hydrogen-charged specimen tested at 0.01 Hz were localized near the crack tip. Nevertheless, the FCG rate of the hydrogen-charged specimen was significantly accelerated, showing an FCG rate that was 10 times faster than that of the non-charged specimen at low frequency.

In order to investigate the mechanism of crack growth acceleration, the morphology of the stretch zone (Fig. 26.5) was compared between the non-charged and hydrogen-charged specimens. The maximum size of the stretch zone ($SZW_{T,max}$) was measured by tilting the fracture surface. If crack tip blunting is large, a large tilting angle is needed to obtain $SZW_{T,max}$. The measured tilt angles in the non-charged and hydrogen-charged specimens revealed a peculiar crack growth mechanism in the presence of hydrogen, as illustrated in Fig. 26.5b, which is consistent with the void growth shown in Fig. 26.3.

The crack growth rates of Cr–Mo steel with a tensile strength less than 900 MPa in the presence of hydrogen were 30 times higher than those of the non-charged specimens, as shown in Fig. 26.6 [28]. The hydrogen caused acceleration of the FCG rate; however, there was an upper bound to the FCG acceleration. The slip bands of the hydrogen-charged specimens were restricted at a very narrow area beside the crack line. These characteristics have been commonly observed in hydrogen-charged specimens of other materials [28]. This FCG acceleration in the presence of hydrogen can be explained in terms of the HELP model. However, as

Fig. 26.6 Relationship between fatigue crack growth rate, da/dN , and stress intensity factor, ΔK (Material: JIS-SCM435) [28]



shown in Fig. 26.11 later, there is no upper bound of FCG acceleration in the presence of hydrogen for high-strength steel with tensile strengths of approximately 1900 MPa. Thus, a mechanism different from that of the HELP model causes the FCG behavior [29]. Also, Cr–Mo steel with tensile strength higher than 900 MPa often has no upper bound of FCG acceleration [30].

26.4.3 Fatigue Behavior of Austenitic Stainless Steels

26.4.3.1 Effect of Hydrogen and Test Frequency on FCG Behavior

Figure 26.7 shows FCG curves for cracks starting from a 100 μm hole in the non-charged and hydrogen-charged specimens of Type 304, Type 316, and Type 316L steels [31]. Hydrogen charging was carried out via cathodic charging. For Type 304 and Type 316 steels, the hydrogen clearly causes FCG acceleration. The FCG rate in the hydrogen-charged Type 316L stainless steel, however, is only slightly higher than that of the non-charged Type 316L steel. It must be noted that the fatigue tests were performed at frequencies of 1.2–5 Hz.

The crack growth curves for Type 304 and Type 316L steels are shown in Fig. 26.8a, b, respectively [32]. Figure 26.8c shows the relationship between da/dN and ΔK for Type 316L stainless steel. In Type 316L stainless steel tested at a frequency of 1.5 Hz, there was no pronounced difference between the non-charged and hydrogen-charged specimens. The FCG rate of the hydrogen-charged Type

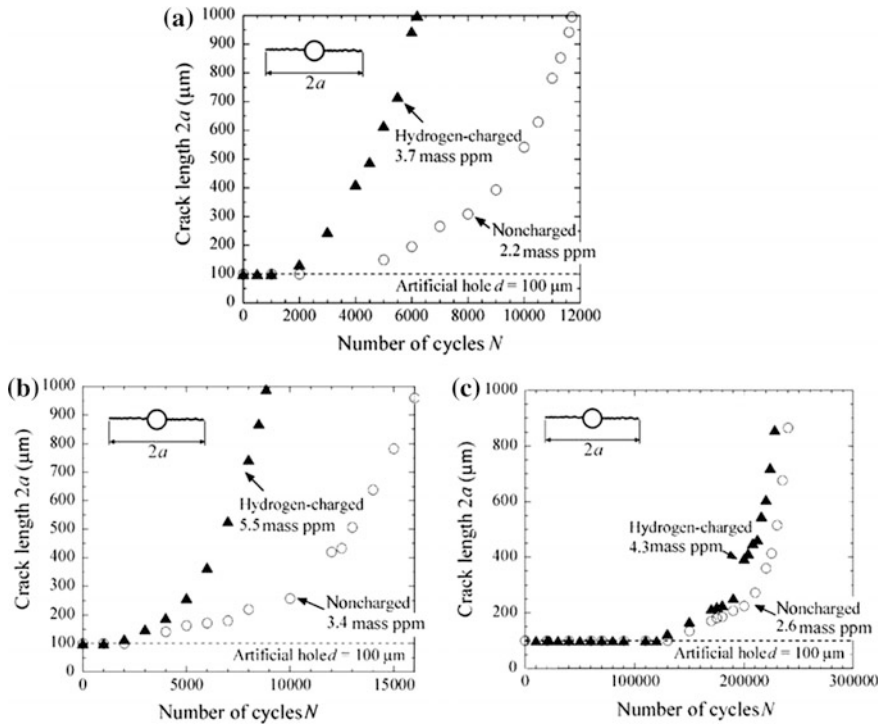


Fig. 26.7 Influence of hydrogen charging on crack growth from $100 \mu\text{m}$ hole for Type 304, Type 316, and Type 316L austenitic stainless steels. Hydrogen charging was carried out by cathodic charging at $50 \text{ }^\circ\text{C}$ for 672 h [31]. **a** Type 304 ($\sigma = 280 \text{ MPa}$, $f = 1.2 \text{ Hz}$), **b** Type 316 ($\sigma = 260 \text{ MPa}$, $f = 1.2 \text{ Hz}$), **c** Type 316L ($\sigma = 260 \text{ MPa}$, $f = 5 \text{ Hz}$)

316L tested at 0.0015 Hz was two to three times higher than that of Type 316L tested at 1.5 Hz . Surprisingly, the non-charged specimen also exhibited an increase in the FCG rate as the test frequency decreased from 1.5 to 0.0015 Hz .

As mentioned above, the hydrogen-accelerated FCG rate of austenitic stainless steels correlates with their austenitic stability [6], which can be quantified using the nickel equivalent [7, 8]. Austenitic stainless steel with higher austenitic stabilities provides excellent resistance to HE. The tensile and FCG behaviors of austenitic stainless steels with various nickel equivalents in high-pressure gaseous hydrogen are discussed in Chaps. 29 and 30, respectively. The selection of Types 316 and 316L steels in the current study was based on their respective nickel equivalents (see Chap. 29) [9]. Recently, new stainless steels having a high resistance to HE have been developed by adding small amounts of elements such as nitrogen and niobium, which lead to a high nickel equivalent [6].

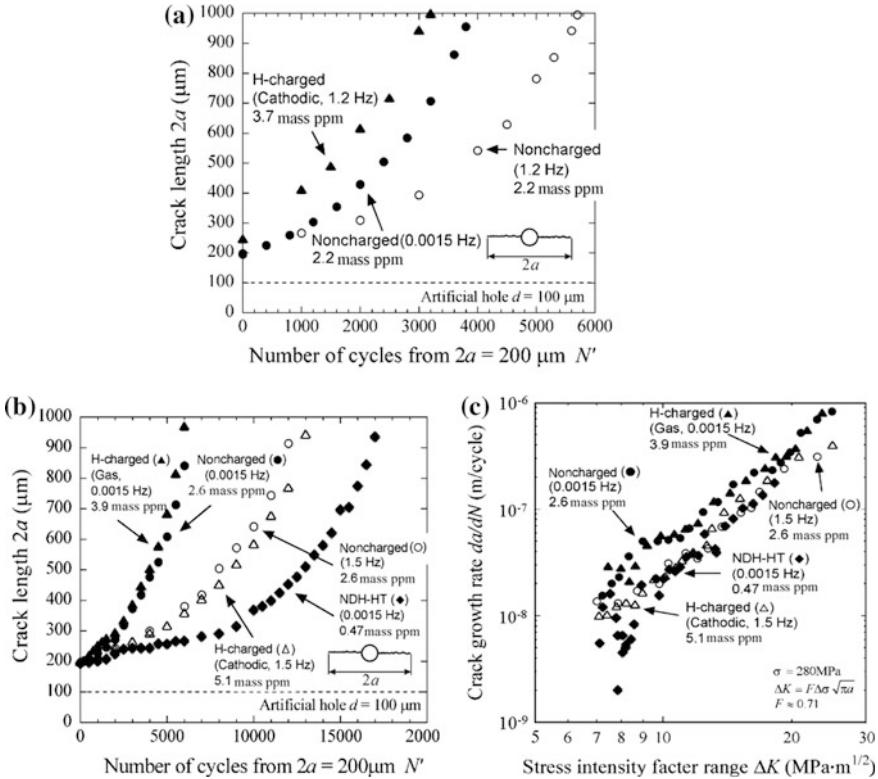


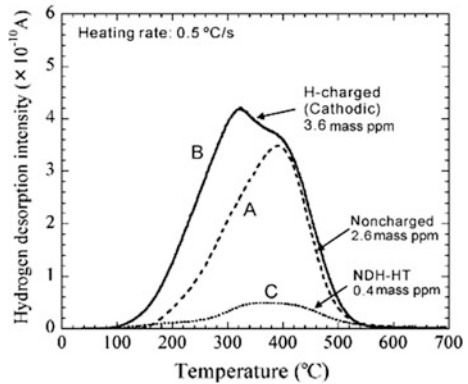
Fig. 26.8 Influence of hydrogen and test frequency on FCG from $2a = 200 \mu\text{m}$ [32]. **a** Type 304 ($\sigma = 280 \text{ MPa}$), **b** Type 316L ($\sigma = 280 \text{ MPa}$), **c** Type 316L

26.4.3.2 FCG Behavior of Type 316L by Removing Non-diffusible Hydrogen

Hydrogen is unavoidably trapped during the steel making process, and this is known as non-diffusible hydrogen (NDH). In order to investigate the influence of NDH on FCG, a special heat treatment (NDH-HT) was applied to remove it. The effect of NDH-HT is clearly shown in Fig. 26.9 [32], in which the hydrogen content in an ordinarily heat treated Type 316L was 2.6 mass ppm, whilst in the sample subjected to NDH-HT the hydrogen content was just 0.4 mass ppm.

The FCG behavior of NDH-HT specimens is shown in Fig. 26.8b. Surprisingly, the FCG rate is substantially decreased in comparison with a hydrogen-charged specimen, and even in comparison with a non-charged specimen. Further evidence of the effect of NDH-HT on the FCG rate is seen in the striation height-spacing ratios (H/s), which are shifted to higher values [32]. The above facts are definite proof that even so-called non-diffusible hydrogen contained in ordinary solution-treated austenitic stainless steels influences FCG rates.

Fig. 26.9 Hydrogen thermal desorption spectra of Type 316L steel [32]



26.4.3.3 Hydrogen-Induced Striation Formation Mechanism and FCG Mechanism

The effect of hydrogen on the crack closure mechanism during one load cycle is illustrated in Fig. 26.10a, b. Figure 26.10 ((a-1) \rightarrow (a-4)) shows the crack opening behavior with increasing load, in the absence of hydrogen. The crack tip opening displacement reaches its saturated value at a given load level, and crack growth ceases. However, hydrogen concentrates near the crack tip in the presence of hydrogen, as shown in Fig. 26.10((b-1) \rightarrow (b-2)). Hydrogen concentration enhances further crack opening via slip, and crack growth continues. Since the corresponding plastic zone at the crack tip does not become large, the wake of the plastic zone, which remains on the fracture surface, is shallow. The difference in crack tip blunting mechanism with and without hydrogen is essentially the same as Fig. 26.3. Figure 26.10c, d show schematic illustrations of plastic zone wakes with and without hydrogen. This phenomenon results in both a decrease in the height of striation [32], and a decrease in the crack opening load (i.e., a decrease in ΔK_{op} and an increase in ΔK_{eff}).

26.4.4 Fatigue Behavior of High-Strength Steel

26.4.4.1 Effect of Hydrogen on FCG Rate

Figure 26.11 shows the relationship between da/dN and ΔK of the high-strength steel ($HV = 568$) and the effect of test frequency on the FCG acceleration in the presence of hydrogen [29]. In the figure, $C_{H,R}$ is the residual hydrogen content after the tests. The FCG rates of the hydrogen-charged specimens are much faster than those of non-charged specimens. The open symbols for the non-charged specimens show little difference in FCG rate at 0.2 and 20 Hz at $R = 0.1$. On the other hand, the FCG rates of the hydrogen-charged specimens are strongly dependent on the frequency, as shown by the solid symbols. In this case, there is no upper bound of

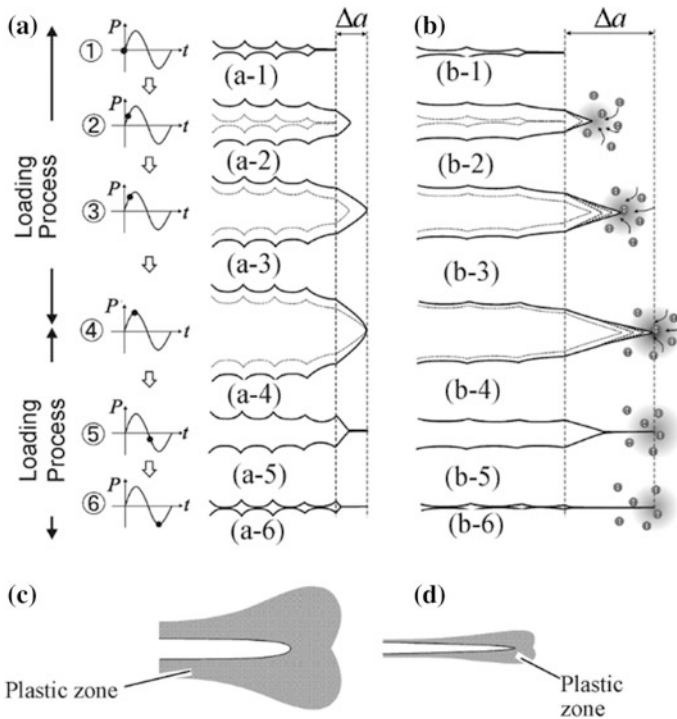


Fig. 26.10 Crack tip opening and striation formation mechanism in fatigue [32]. **a** No hydrogen effect on striation formation. **b** Hydrogen effect on striation formation. **c** No hydrogen effect on plastic zone. **d** Hydrogen effect on plastic zone

accelerated FCG rate (see Fig. 26.11b), and this behavior is completely different from that of the Cr–Mo steel shown in Fig. 26.6.

Figure 26.12 shows the relationship between crack increment, Δa , and increment cycles, ΔN , of the hydrogen-charged specimen obtained from a frequency-switching test from 0.02 to 20 Hz. Crack growth is accelerated immediately after switching to 20 Hz. The size of the zone in which crack growth is accelerated, known as a hydrogen-affected FCG zone (HAFCG zone), increases with decreasing initial test frequency (0.02, 0.2, or 2 Hz). The HAFCG zone sizes are much larger than the monotonic plastic zone sizes under plane-strain conditions. The FCG acceleration of the hydrogen-charged specimens, which is observed as time-dependent crack growth of high-strength steel, cannot be simply related to the plastic deformation at the fatigue crack tip.

26.4.4.2 Initiation and Cause of Secondary Cracks

Figure 26.13 shows fatigue cracks of a hydrogen-charged specimen tested at 0.2 Hz, $R = 0.1$, obtained by scanning electron microscopy (SEM). Secondary

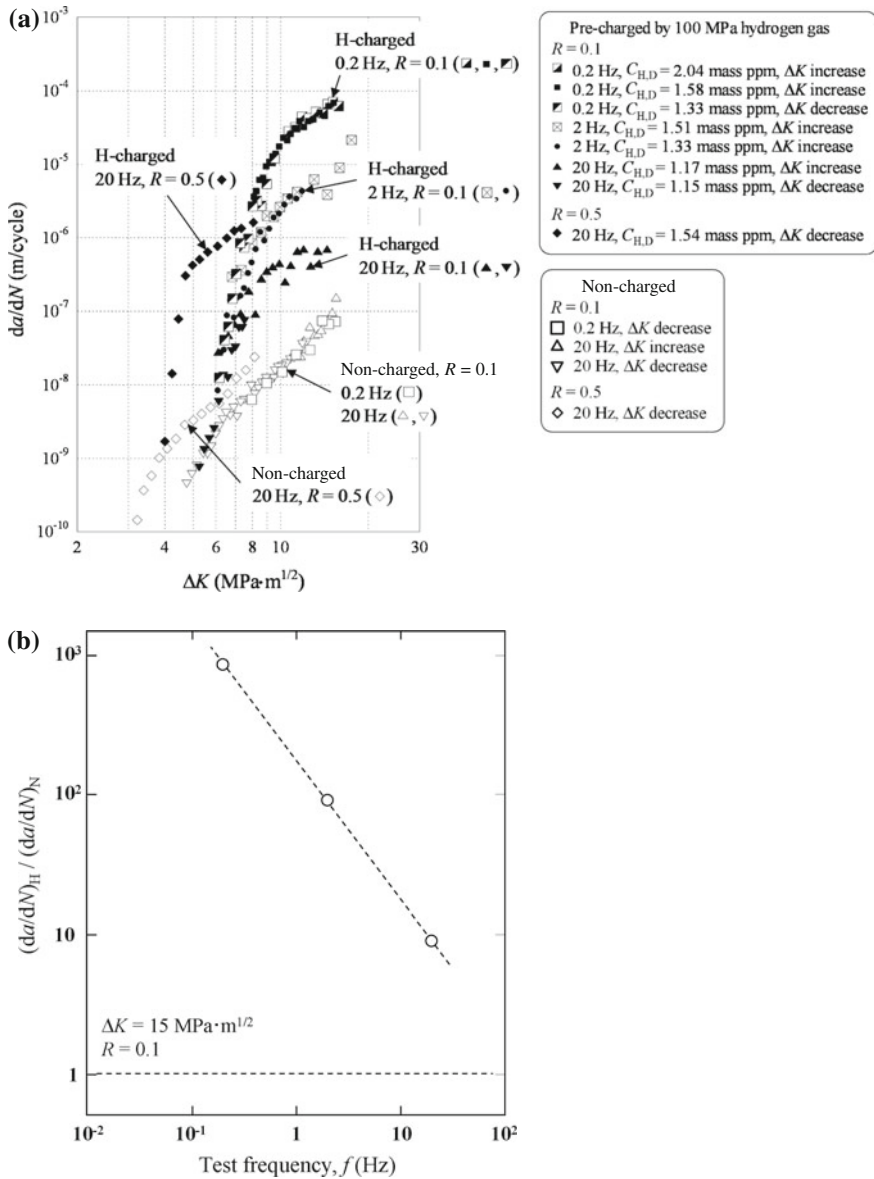


Fig. 26.11 Effects of hydrogen and frequency on FCG of high-strength steel ($HV = 568$). Hydrogen content is measured after tests [29]. **a** da/dN - ΔK curves. **b** Effect of test frequency of FCG acceleration in presence of hydrogen

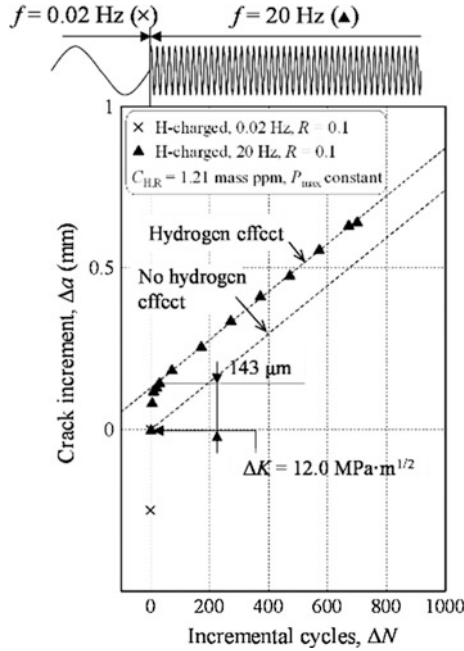


Fig. 26.12 Size of the hydrogen-affected fatigue crack growth zone (HAFCG zone) of a high-strength steel ($HV = 568$) [29]

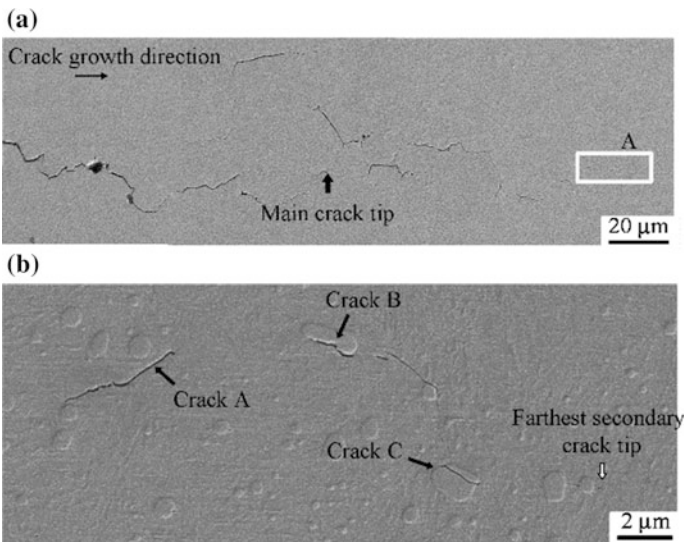


Fig. 26.13 SEM micrographs of the fatigue cracks at the middle section of the hydrogen-charged specimen ($f = 0.2$ Hz, $R = 0.1$, $\Delta K = 12.2$ MPa m^{1/2}, $C_{H,R} = 1.21$ mass ppm, $da/dN \approx 40$ μm/cycle) [29]. **a** SEM micrographs of the fatigue cracks at the middle section of the H-charged specimen. **b** Magnification of A

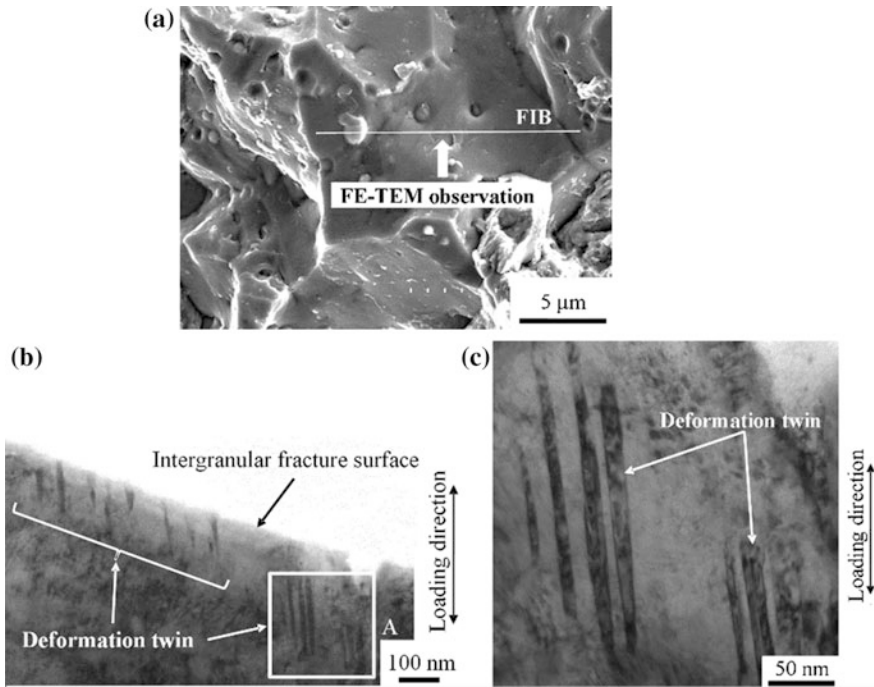


Fig. 26.14 FE-TEM micrographs at the cross section of the IG fracture surface for a hydrogen-charged specimen ($f = 20$ Hz, $R = 0.1$, $\Delta K = 11.6$ MPa $m^{1/2}$, $C_{H,R} = 1.17$ mass ppm) [29]. **a** IG surface for TEM. **b** Cross section of IG fracture surface. **c** Magnification of A

cracks are formed ahead of the main crack tip. Such secondary cracks are not formed in the non-charged specimens.

All secondary cracks are observed in the HAFCG zone. However, this result was obtained by two-dimensional (2D) observation. The fatigue cracks in the hydrogen-charged specimens have a complicated, three-dimensional (3D) shape, and most of the secondary cracks are connected in three dimensions to the primary crack (although secondary cracks completely isolated from the primary crack were also observed). The 2D isolated cracks shown in Fig. 26.13b are formed either along the original austenite grain boundaries (crack A) and carbide boundaries (crack B) or by direct cracking of carbides (crack C).

Figure 26.14b, c show magnified images of the intergranular (IG) fracture surface shown in Fig. 26.14a, obtained by field emission transmission electron microscopy (FE-TEM). The linear bands observed in the high magnification images are deformation twins. It is presumed that IG fractures of secondary cracks are formed by stress concentration due to the deformation twins coming into contact with the original austenite or carbide boundaries. Figure 26.15 illustrates the mechanism for three typical secondary crack initiation modes caused by deformation twins [29]. Because this hydrogen-induced deformation twin model is

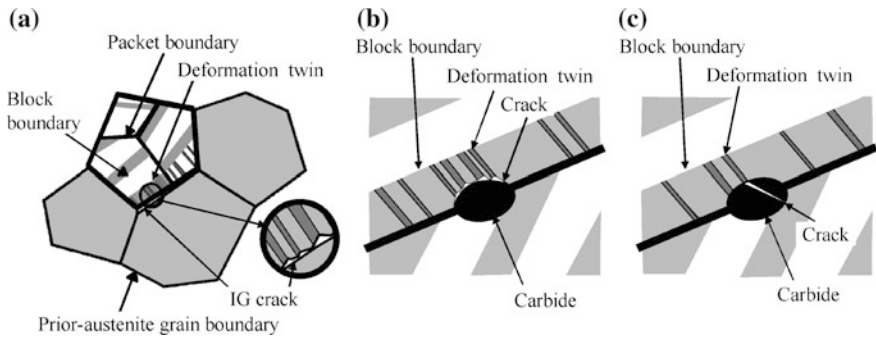


Fig. 26.15 Schematic of the formation of **a** an IG crack, **b** a carbide boundary crack, and **c** a carbide crack due to stress concentration by deformation twins [29]

different from the HELP model, it is recognized that the FCG behavior of the present high-strength steel in the presence of hydrogen was different from that of the Cr–Mo steel shown in Fig. 26.5, which had an upper bound for the accelerated FCG rate.

A few different fracture processes are presumed to be coupled in IG fracture in the presence of hydrogen. Therefore, the mechanism of hydrogen-induced IG fracture is complicated. Novak et al. recently reported a coupled HEDE and HELP model to explain the hydrogen-induced IG fracture of high-strength steel [33].

26.4.5 Fatigue Behavior of Aluminums

Aluminum is categorized as “negligibly embrittled” in the NASA database, and thus it has a high resistance to HE [10]. FCG tests of an A6061-T6 aluminum alloy in gaseous hydrogen (shown in Chap. 30) provide the following results [34]: (i) the FCG rate in gaseous hydrogen is equal to that in nitrogen gas; and (ii) the FCG rate in gaseous hydrogen is less than that in air at ≥ 1 Hz, but equal to that in air at <1 Hz. The FCG behavior of aluminum is affected by humidity, and it seems that a small amount of moisture in the environment has a significant impact on the FCG behavior [35].

26.5 Hydrogen Diffusivity and Solubility

HE is caused by hydrogen dissolved in metallic materials. In gaseous hydrogen, the following transport processes should be considered in order to understand the HE mechanism [36]: gas-phase transport; physical adsorption; dissociative chemical adsorption; hydrogen entry; and diffusion. It is known that oxide layers prevent

entry of hydrogen into metals, and these exist in low-pressure gaseous hydrogen or at near-ambient temperatures [37–39]. However, the surface effect of oxide layers decreases in high-pressure gaseous hydrogen or at high temperature [40, 41]. The susceptibility to HE of metals is related to the distribution of dissolved hydrogen. The macroscopic hydrogen concentration in a material in an unloaded condition can be calculated by using the hydrogen diffusivity and saturated hydrogen content if hydrogen entry and exit occur by a diffusion-controlled process. The hydrogen diffusivity and solubility can be determined with several methods, such as hydrogen permeation, entry, and desorption (release) methods. The hydrogen diffusivity of various metallic materials is provided in Refs. [42, 43]. This section reviews the hydrogen diffusion properties of the metallic materials.

26.5.1 Iron and Steels

The hydrogen diffusivity of lattice hydrogen in body-centered cubic (bcc) iron is expressed as follows [44]:

$$\begin{aligned} & [233 \text{ to } 353 \text{ K } (-40 \text{ to } 80^\circ\text{C})] \\ D_L &= 7.23 \times 10^{-8} \exp\left(-\frac{5690}{RT}\right) \end{aligned} \quad (26.1)$$

$$\begin{aligned} & [323 \text{ to } 823\text{K } (50 \text{ to } 550^\circ\text{C})] \\ D_L &= (1 \text{ to } 2.52) \times 10^{-7} \exp\left(-\frac{6700 \text{ to } 7120}{RT}\right) \end{aligned} \quad (26.2)$$

where D_L is the lattice hydrogen diffusivity in bcc iron with no traps ($\text{m}^2 \text{s}^{-1}$), R is the gas constant ($=8.314 \text{ J mol}^{-1} \text{ K}^{-1}$), and T is the absolute temperature (K). The saturated hydrogen content of lattice hydrogen in the bcc iron can be expressed as follows [38]:

$$C_{LS} = 104.47\sqrt{f} \exp\left(-\frac{3440}{T}\right) \quad (26.3)$$

where C_{LS} is the saturated hydrogen content in the bcc iron (mass ppm) and f is the fugacity (MPa). The hydrogen diffusivity and saturated hydrogen content of practical carbon and low-alloy steels (shown previously in Fig. 26.16), are significantly different from those calculated by Eqs. (26.1)–(26.3) [39, 45–48]. These differences are responsible for hydrogen trapping. The average hydrogen diffusivity and saturated content of Materials A–E having the chemical composition and Vickers

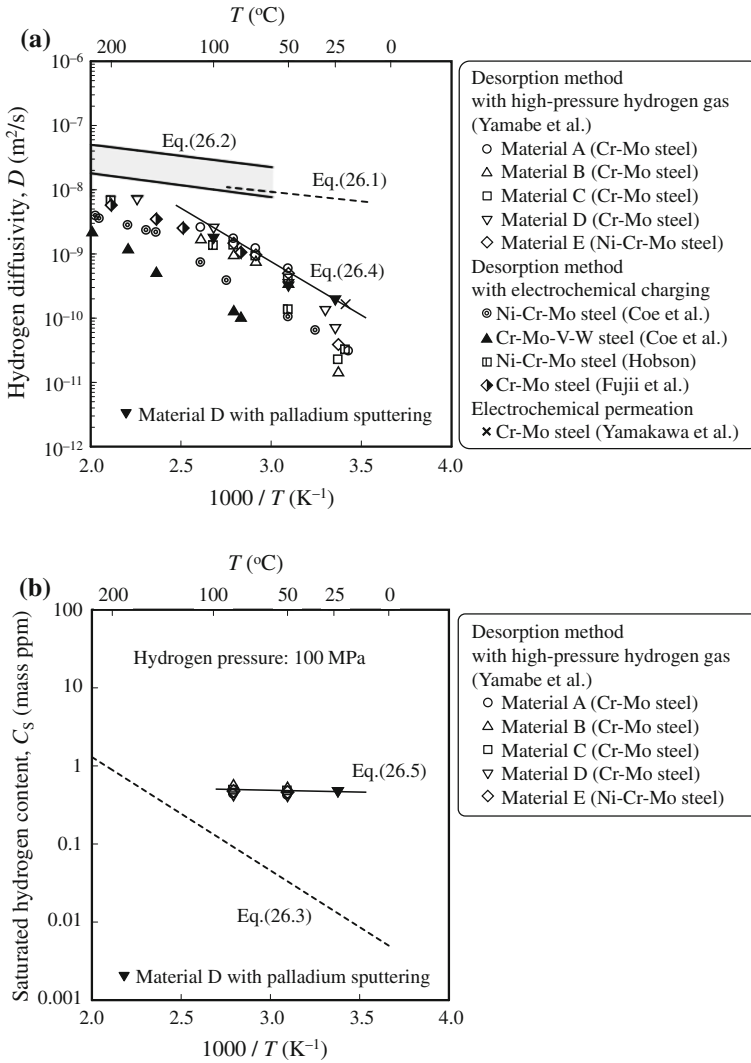


Fig. 26.16 **a** Hydrogen diffusivity and **b** saturated hydrogen content of various low-alloy steels [39, 45–48]

hardness in Table 26.1 can be approximated in terms of the Oriani’s equilibrium theory [49] as follows:

$$D = \frac{D_L}{1 + \frac{N_X}{N_L} \exp\left(\frac{E_B}{RT}\right)} = \frac{7.23 \times 10^{-8}}{1 + \frac{N_X}{N_L} \exp\left(\frac{E_B}{RT}\right)} \exp\left(-\frac{5690}{RT}\right) \quad (26.4)$$

Table 26.1 Chemical composition (mass%) and Vickers hardness (*HV*)

Material	Symbol	C	Si	Mn	P	S	Cr	Mo	Ni	<i>HV</i>
Cr–Mo ^a	A	0.38	0.22	0.79	0.006	0.004	1.10	0.23	– ^c	256
	B	0.37	0.21	0.77	0.012	0.007	1.07	0.23	– ^c	289
	C	0.35	0.25	0.74	0.011	0.004	1.08	0.26	– ^c	275
	D	0.36	0.18	0.78	0.013	0.005	1.04	0.20	– ^c	258
Requirement (JIS G 3441)		0.33–0.38	0.15–0.35	0.60–0.85	≤ 0.030	≤ 0.030	0.90–1.20	0.15–0.30	≤ 0.25	– ^d
Ni–Cr–Mo ^b	E	0.43	0.27	0.82	0.005	0.002	0.91	0.23	1.95	292
Requirement (JIS G 4053)		0.36–0.43	0.15–0.35	0.60–0.90	≤ 0.030	≤ 0.030	0.60–1.00	0.15–0.30	1.60–2.00	– ^d

^aJIS–SCM435^bJIS–SNM439^cNot measured^dNot regulated

$$\begin{aligned}
 C_S &= \left\{ 1 + \frac{N_X}{N_L} \exp\left(\frac{E_B}{RT}\right) \right\} C_{LS} \\
 &= 104.47 \left\{ 1 + \frac{N_X}{N_L} \exp\left(\frac{E_B}{RT}\right) \right\} \sqrt{f} \exp\left(\frac{-3440}{T}\right)
 \end{aligned} \tag{26.5}$$

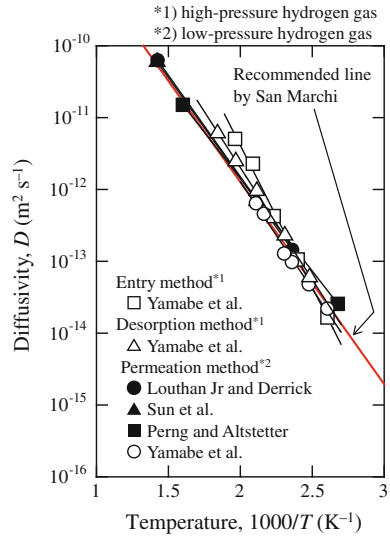
where D is the hydrogen diffusivity ($\text{m}^2 \text{s}^{-1}$), C_S is the saturated hydrogen content (mass ppm), N_L is the number of lattice sites per the unit volume, N_X is the number of trap sites per unit volume, and E_B is the binding energy. According to San Marchi et al. [50], the fugacity, f , is expressed by using the hydrogen gas pressure as follows:

$$f = p \exp\left(\frac{bp}{RT}\right) \tag{26.6}$$

where p is the hydrogen gas pressure (MPa) and b is a constant ($1.584 \times 10^{-5} \text{ m}^3 \text{ mol}^{-1}$ [50]). The fitted parameters of the present case were as follows: $N_X/N_L = 2.1 \times 10^{-4}$ and $E_B = 29.6 \text{ kJ/mol}$. From the binding energy determined by the least squares method, it was recognized that the hydrogen dissolved in low-alloy steels is mainly trapped at dislocations [51]. In general, there are many trap sites in steels [52], and their activation energies can be obtained by thermal desorption analysis (TDA) under a different heating rate [53].

Matsuoka et al. [7] reported that the saturated hydrogen contents of Cr–Mo steel obtained with electrochemical charging were 0.85 mass ppm (an immersed charge with a NH_4SCN solution at 40 °C for 12 h), whereas Takeuchi et al. [54] reported a value of 1.20 mass ppm (a cathode charge with a mixed solution of NH_4SCN and NaCl at a current density of 0.3 mA/cm^2 for 24 h). The corresponding pressures of gaseous hydrogen at room temperature were estimated to be 190 and 250 MPa, respectively, from Eq. 26.5. It therefore follows that ordinary electrochemical

Fig. 26.17 Hydrogen diffusivity of 300-series austenitic stainless steel [50, 55–57]



charging is a more severe condition than exposure to hydrogen gas at a high pressure such as 100 MPa.

Figure 26.17 shows the hydrogen diffusivity of 300-series austenitic stainless steels [50, 55–57]. There is no significant difference in the hydrogen diffusivity, regardless of researcher and test method. The recommended hydrogen diffusivity of 300-series steel is provided by San Marchi et al. [50] as follows:

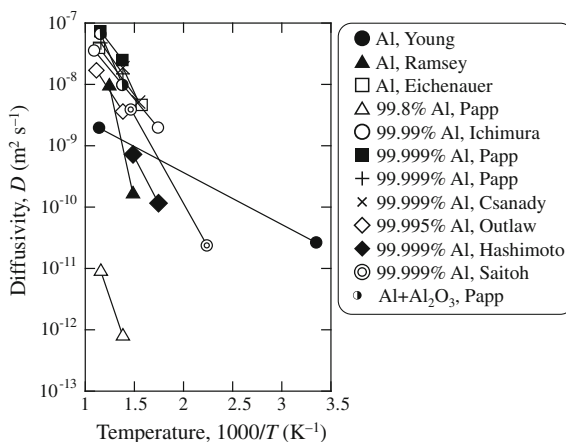
$$D = 8.9 \times 10^{-7} \exp\left(-\frac{53900}{RT}\right) \quad (26.7)$$

where D is the recommended hydrogen diffusivity ($\text{m}^2 \text{s}^{-1}$). Similarly, the recommended hydrogen solubility of the 300-series stainless steel is provided by San Marchi et al. [50] as follows:

$$S = 135 \exp\left(-\frac{5900}{RT}\right) \quad (26.8)$$

where S is the recommended hydrogen solubility ($\text{mol H}_2 \text{ m}^{-3} \text{ MPa}^{-1/2}$). In steels, 1 mass ppm $\text{MPa}^{-1/2}$ is converted into $3.9 \text{ mol H}_2 \text{ m}^{-3} \text{ MPa}^{-1/2}$ [50]. The recommended values of D and S for other stainless steels are also shown in Ref. [50].

Fig. 26.18 Hydrogen diffusivity of various pure aluminums [59]



26.5.2 Aluminums

The hydrogen diffusion behavior of pure aluminum is discussed by Young and Scully in Ref. [58], and its temperature dependence is summarized in Ref. [59]. Figure 26.18 shows Arrhenius plots of the hydrogen diffusivity of various pure aluminum metals. There is significant variation in the experimental results; thus, it is difficult to quantify the temperature dependence of hydrogen diffusivity of pure aluminum metals; their temperature dependence seems to be influenced by their microstructure and purity. Surface effects may affect the experimental data. Apart from the pure aluminum (99.8 %) reported by Papp [60], the hydrogen diffusivity of pure aluminum is larger than that of the 300-series austenitic stainless steels shown in Fig. 26.17. The hydrogen diffusivities of aluminum alloys are summarized in Ref. [61].

26.6 Hydrogen-Induced Fracture of Rubbers

Decompression of various high-pressure gases often causes internal cracks in rubber materials [62–66]. These are referred to as blisters. Figure 26.19 shows the blisters in transparent cylindrical rubber (ϕ 29 mm \times 12.5 mm) exposed to 10 MPa hydrogen gas at room temperature. Decompression failure occurs even with high-pressure hydrogen gas [67]. The damage caused in rubber by high-pressure hydrogen gas decompression is influenced by the materials used, the seal, and the environmental conditions [67–69]. Crack damage by blistering becomes more serious for rubber with higher hydrogen content and poorer tensile properties. Fillers such as carbon black and silica can be used to reinforce rubber materials, offering excellent tensile properties. However, carbon black increases the

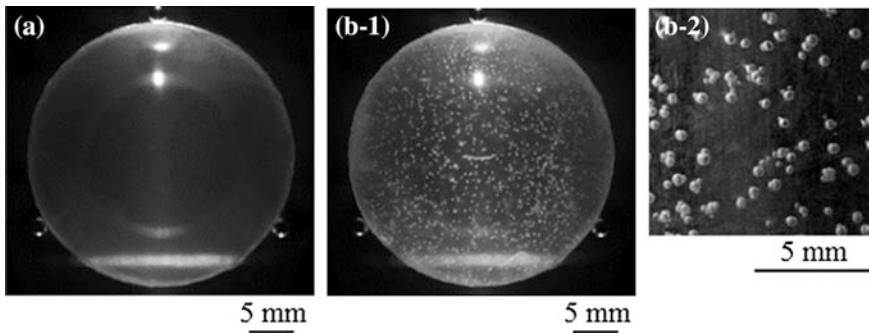


Fig. 26.19 Blister fracture of transparent cylindrical rubber **a** before and **b** after exposure to hydrogen at 10 MPa. **b-1** and **b-2** low and high magnifications

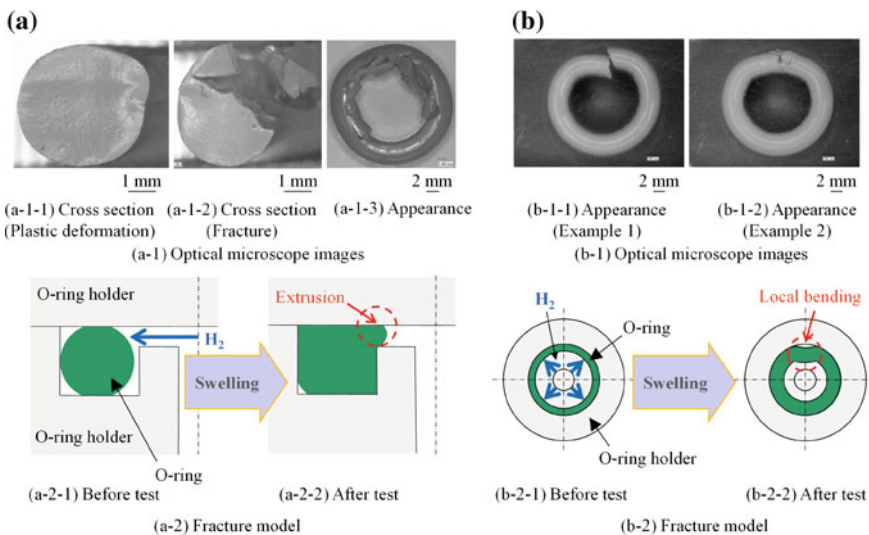


Fig. 26.20 Surface-crack initiation of O-rings with hydrogen-pressure cycling [69]. **a** Fracture at high filling ratio. **b**. Fracture at low filling ratio

hydrogen content of the rubber as compared to silica; thus, the addition of the carbon black is not necessarily effective for improving the resistance to blistering [67].

In practical rubber O-rings under high-pressure hydrogen gas, surface cracks caused by extrusion (Fig. 26.20a) or buckling (Fig. 26.20b) are sometimes observed in addition to blisters, because the high-pressure hydrogen gas causes a significant increase in the volume of the O-rings. This volume increase is referred to as swelling [69]. Hence, the sealing conditions significantly affect the durability of rubber O-rings in high-pressure hydrogen gas.

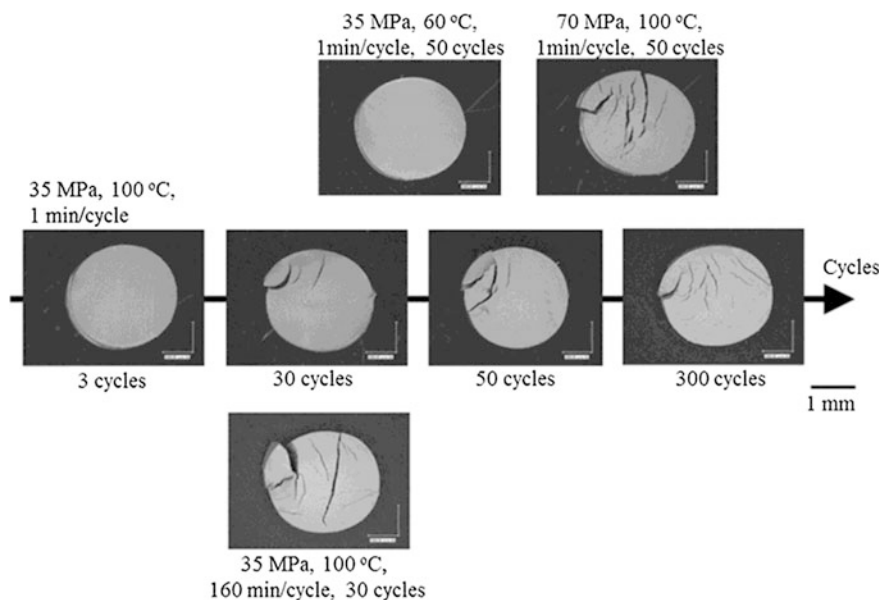


Fig. 26.21 Effects of pressure, temperature, and cycle pattern on damage to rubber O-rings subjected to hydrogen-pressure cycling [68]

Figure 26.21 shows the effect of pressure, temperature, and cycle pattern on the crack damage of rubber O-rings subjected to hydrogen-pressure cycling. Cross sections of the rubber O-rings were observed by optical microscopy. Both surface and inner cracks are observed in the O-rings. This result reveals that crack damage of the rubber O-rings is affected not only by hydrogen gas pressure but also by environmental temperature and cycle pattern. Details of the hydrogen-induced fracture of rubber are reviewed in Ref. [70].

References

1. Murakami Y, Matsuoka S, Kondo Y, Nishimura S (2012) Mechanism of hydrogen embrittlement and guide for fatigue design. Yokendo, Tokyo
2. Gangloff RP, Somerday BP (eds) (2012) Gaseous hydrogen embrittlement of materials in energy technologies. Woodhead Publishing, Cambridge
3. Nagumo M (2008) Fundamentals of hydrogen embrittlement. Uchida Rokakuho, Tokyo
4. Gangloff RP (2003) Hydrogen assisted cracking of high strength alloys. In: Milne I (ed) Comprehensive structural integrity. Elsevier Science, New York, pp 31–101
5. Suresh S, Ritchie RO (1982) Mechanistic dissimilarities between environmentally influenced fatigue-crack propagation at near-threshold and higher growth rates in lower strength steels. *Mater Sci Technol* 16:529–538
6. Itoga H, Matsuo T, Orita A, Matsunaga H, Matsuoka S, Hirofumi R (2014) SSRT and fatigue crack growth properties of high-strength austenitic stainless steels in high-pressure hydrogen

- gas (PVP2014-28640). In: Proceedings of PVP-2014: ASME pressure vessels and piping division conference, Anaheim, California, USA, July 20–24 2014, ASME, American Society of Mechanical Engineers, New York
7. Ogirima Hirayama T (1970) Influence of chemical composition on martensitic transformation in Fe-Cr-Ni stainless Steel. *J Japan Inst Met Mater* 34:507–510
 8. Sanga M, Yukawa N, Ishikawa T (2000) Influence of chemical composition on deformation-induced martensitic transformation in austenitic stainless steel. *J Jpn Soc Technol Plast* 41:64–68
 9. Yamada T, Kobayashi H (2012) Material selection used for hydrogen station. *J High Press. Gas Safety Inst Jpn* 49:885–893
 10. NASA (1997) Safety standard for hydrogen and hydrogen systems. NSS 1740.16, Washington DC
 11. Matsuoka S, Homma N, Tanaka H, Fukushima Y, Murakami Y (2006) Effect of hydrogen on tensile properties of 900-MPa-class JIS-SCM435 low-alloy-steel for use in storage cylinder of hydrogen station. *J Jpn Inst Met Mater* 70:1002–1011
 12. Thompson AW (1979) Ductile fracture topography: geometrical contributions and effects of hydrogen. *Metall Trans A* 10:727–731
 13. Matsunaga H, Yoshikawa M, Kondo R, Yamabe J, Matsuoka S (2015) Slow strain rate tensile and fatigue properties of Cr–Mo and carbon steels in a 115 MPa hydrogen gas atmosphere. *Int J Hydrogen Energy* 40:5739–5748
 14. Matsuo T, Homma N, Matsuoka S, Murakami Y (2008) Effect of hydrogen and prestrain on tensile properties of carbon steel SGP (0.078 C–0.012 Si–0.35 Mn, mass %) for 0.1 MPa hydrogen pipelines. *Trans JSME A* 74:1164–1173
 15. Morlet JG, Johnson HH, Triano AR (1958) A new concept of hydrogen embrittlement in steel. *J Iron Steel Inst* 189–1:37–41
 16. Troiano AR (1960) The role of hydrogen and other interstitials in the mechanical behavior of metals. *Trans ASM* 52:54–80
 17. Oriani RA, Josephic H (1974) Equilibrium aspects of hydrogen-induced cracking of steels. *Acta Metall* 22:1065–1074
 18. Sofronis P, McMeeking RM (1989) Numerical analysis of hydrogen transport near a blunting crack tip. *J Mech Phys Solids* 37:317–350
 19. Birnbaum HK, Sofronis P (1994) Hydrogen-enhanced localized plasticity: a mechanism for hydrogen-related fracture. *Mater Sci Eng A* 176:191–202
 20. Robertson IM, Birnbaum HK (1986) An HVEM study of hydrogen effects on the deformation and fracture of nickel. *Acta Metall* 34:353–366
 21. Nagumo M, Nakamura M, Takai K (2001) Hydrogen thermal desorption relevant to delayed-fracture susceptibility of high-strength steels. *Metall Mater Trans A* 32:339–347
 22. Nagumo M, Uyama H, Yoshizawa M (2001) Accelerated failure in high strength steel by alternating hydrogen-charging potential. *Scr Mater* 44:947–952
 23. Nagumo M, Ishikawa T, Endoh T, Inoue Y (2003) Amorphization associated with crack propagation in hydrogen-charged steel. *Scr Mater* 49:837–842
 24. Matsuo T, Yamabe J, Matsuoka S (2014) Effects of hydrogen on tensile properties and fracture surface morphologies of Type 316L stainless steel. *Int J Hydrogen Energy* 39:3542–3551
 25. Roger HC (1960) The tensile fracture of ductile metals. *Trans ASME* 218:498–506
 26. Cox TB, Low JR Jr (1974) An investigation of the plastic fracture of AISI 4430 and 18 Ni-200 grade maraging steels. *Metall Trans* 5:1457–1470
 27. Matsuoka S, Tsutsumi N, Murakami Y (2008) Effects of hydrogen on fatigue crack growth and stretch zone of 0.08 Mass% low carbon steel pipe. *Trans JSME A* 74:1528–1537
 28. Tanaka H, Homma N, Matsuoka S, Murakami Y (2007) Effect of hydrogen and frequency on fatigue behavior of SCM435 steel for storage cylinder of hydrogen station. *Trans JSME A* 73:1358–1365
 29. Yamabe J, Matsumoto T, Matsuoka S, Murakami Y (2012) A new mechanism in hydrogen-enhanced fatigue crack growth behavior of a 1900-MPa-class high-strength steel. *Int J Fract* 177:141–162

30. Yamabe J, Itoga H, Awane T, Matsuo T, Matsunaga H, Matsuoka S (2016) Pressure cycle testing of Cr-Mo steel pressure vessels subjected to gaseous hydrogen. *J Press Vess Technol ASME* 183–011401:1–13
31. Kanazaki T, Narazaki C, Mine Y, Matsuoka S, Murakami Y (2008) Effects of hydrogen on fatigue crack growth behavior of austenitic stainless steels. *Int J Hydrogen Energy* 33:2604–2619
32. Murakami Y, Kanazaki T, Mine Y, Matsuoka S (2008) Hydrogen embrittlement mechanism in fatigue of austenitic stainless steels. *Metall Mater Trans A* 39:1327–1339
33. Novak P, Yuan R, Somerday BP, Sofronis P, Ritchie RO (2010) A statistical, physical-based micro-mechanical mode of hydrogen-induced intergranular fracture in steel. *J Mech Phys Solids* 58:206–226
34. Itoga H, Watanabe S, Fukushima Y, Matsuoka S, Murakami Y (2013) Fatigue crack growth of aluminum alloy A6061-T6 in high pressure hydrogen gas and failure analysis on 35 MPa compressed hydrogen tanks VH3 for fuel cell vehicles. *Trans JSME A* 78:442–457
35. Ohnishi T (1989) Hydrogen in pure aluminum and in aluminum alloys. *J Jpn Inst Light Met.* 39:235–251
36. Wei RP, Simmons GW (1981) Recent progress in understanding environment assisted fatigue crack growth. *Int J Fract* 17:235–247
37. Swansiger WA, Bastasz R (1979) Tritium and deuterium permeation in stainless steel: influence of thin oxide films. *J Nucl Mater* 85–6:335–339
38. Hirth JP (1980) Effects of hydrogen on the properties of iron and steel. *Metall Trans A* 11:861–890
39. Yamabe J, Awane T, Matsuoka S (2015) Investigation of hydrogen transport behavior of various low-alloy steels with high-pressure hydrogen gas. *Int J Hydrogen Energy* 40:11075–11086
40. Yamabe J, Matsuoka S, Murakami Y (2013) Surface coating with a high resistance to hydrogen entry under high-pressure hydrogen-gas environment. *Int J Hydrogen Energy* 38:10141–10154
41. Yamabe J, Matsuoka S, Murakami Y (2014) Development of high-performance hydrogen barrier coating for steels. In: *Proceedings of SteelyHydrogen2014 conference*, Ghent, Belgium, May 5–7 2014
42. Iijima Y, Hirano K (1975) Diffusion of hydrogen in metals. *Bull Jpn Inst Met* 14:599–620
43. San Marchi C, Somerday BP (2012) Technical reference for hydrogen compatibility of materials. Sandia report
44. Kiuchi K, McLellan RB (1983) The solubility and diffusivity of hydrogen in well-annealed and deformed iron. *Acta Metall* 31:961–984
45. Hobson JD (1958) The diffusivity of hydrogen in steel at temperatures of -78 to 200 °C. *J Iron Steel Inst* 189:315–321
46. Coe FR, Moreton J (1966) Diffusion of hydrogen in low-alloy steel. *J Iron Steel Inst* 204:366–370
47. Yamakawa K, Minamino Y, Matsumoto K, Yonezawa S, Yoshizawa S (1980) Hydrogen absorbability of SCM steels and its effect on cracking behavior. *J Soc Mater Sci Jpn* 29:1101–1107
48. Fujii T, Nomura K (1984) Temperature dependence of hydrogen diffusivity of 2 1/4Cr-1Mo steel. *Tetsu-to-Hagane* 70:104–111
49. Oriani RA (1970) The diffusion and trapping of hydrogen in steel. *Acta Metall* 18:147–157
50. San Marchi C, Somerday BP, Robinson SL (2007) Permeability, solubility and diffusivity of hydrogen isotopes in stainless steels at high gas pressures. *Int J Hydrogen Energy* 32:100–116
51. Gibala R (1967) Hydrogen-dislocation interaction in iron. *Trans Met Soc AIME* 239:1574–1585
52. Takai K (2004) Hydrogen existing states in metals. *Trans JSME A* 70:1027–1035
53. Choo WY, Lee JY (1982) Thermal analysis of trapped hydrogen in pure iron. *Metall Trans A* 13:135–140

54. Takeuchi E, Furuya Y, Hirukawa Y, Matso T, Matsuoka S (2013) Effect of hydrogen on fatigue crack growth properties of SCM435 steel used for storage cylinder in hydrogen station. *Trans JSME A* 79:1030–1040
55. Louthan MR Jr, Derrick RG (1975) Hydrogen transport in austenitic stainless steel. *Corros Sci* 15:565–577
56. Sun XK, Xu J, Li YY (1989) Hydrogen permeation behaviour in austenitic stainless steels. *Mater Sci Eng, A* 114:179–187
57. Perng T-P, Altstetter CJ (1986) Effects of deformation on hydrogen permeation in austenitic stainless steels. *Acta Metall* 34:1771–1787
58. Young GA Jr, Scully JR (1998) The diffusivity and trapping of hydrogen in high purity aluminum. *Acta Mater* 46:6337–6349
59. Scully JR, Young GA Jr, Smith SW (2012) Hydrogen embrittlement of aluminum and aluminum-based alloys. In: Gangloff RP, Somerday BP (eds) *Gaseous hydrogen embrittlement of materials in energy technologies*, vol 1. Woodhead Publishing Limited, Cambridge, pp 707–768
60. Papp K, Kovacs-Csetenyi E (1981) Diffusion of hydrogen in high purity aluminum. *Scr Metall* 15:161–164
61. Jia-He Ai, Lim MLC, Scully JR (2013) Effective hydrogen diffusion in aluminum alloy 5083-H131 as a function of orientation and degree of sensitization. *Corrosion* 69:1225–1239
62. Briscoe BJ, Savvas T, Kelly CT (1994) Explosive decompression failure of rubber: a review of the origins of pneumatic stress induced rupture in elastomer. *Rubber Chem Technol* 67:384–416
63. Gent AN, Tompkins DA (1969) Nucleation and growth of gas bubbles in elastomers. *J Appl Phys* 40:2520–2525
64. Gent AN, Lindley PB (1958) Internal rupture of bonded rubber cylinders in tension. *Proc R Soc LON Ser-A* 249:195–205
65. Zakaria S, Briscoe BJ (1990) Why rubber explodes. *ChemTech* 20:492–495
66. Briscoe BJ, Liatsis D (1992) Internal crack symmetry phenomena during gas-induced rupture of elastomers. *Rubber Chem Technol* 65:350–373
67. Yamabe J, Nishimura S (2009) Influence of fillers on hydrogen penetration properties and blister fracture of rubber composites for O-ring exposed to high-pressure hydrogen gas. *Int J Hydrogen Energy* 34:1977–1989
68. Yamabe J, Koga A, Nishimura S (2013) Failure behavior of rubber O-ring under cyclic exposure to high-pressure hydrogen gas. *Eng Fail Anal* 35:193–205
69. Koga A, Uchida K, Yamabe J, Nishimura S (2011) Evaluation on high-pressure hydrogen decompression failure of rubber O-ring using design of experiments. *Int J Automotive Eng* 2:123–129
70. Yamabe J, Nishimura S (2012) Hydrogen-induced degradation of rubber seals. In: Gangloff RP, Somerday BP (eds) *Gaseous hydrogen embrittlement of materials in energy technologies*, vol 1. Woodhead Publishing Limited, Cambridge, pp 769–817

Chapter 27

Hydrogen Gas Safety Management

Masahiro Inoue

Abstract This chapter describes the hydrogen gas safety management related to properties and combustion of hydrogen, hydrogen diffusion, and hydrogen sensor. Prevention method of hydrogen-related accidents and examples of the necessity of hydrogen dissipation are also introduced.

Keywords Safety · Hydrogen combustion · Diluent gas · Incident · Accident · Hydrogen diffusion · Hydrogen sensor · Hydrogen safety

27.1 Dangers Posed by Hydrogen

The word “hydrogen” is in common usage. However, most people do not have any actual experience of dealing with hydrogen, and do not realize how dangerous it can be. Many methods have been developed to safely use dangerous but useful materials, such as gasoline and city gas. Nonetheless, these materials still cause many accidents. Hydrogen is expected to find widespread use in the future. Thus, it is important to develop safe methods for handling hydrogen whilst minimizing the incidence of accidents.

From 1965 to 2005, 2.9 % of accidents involving high-pressure gases involved hydrogen, according to a report [1]. When the selection of accidents is limited to explosion or fire, the ratio increases to 5.6 %. These statistics indicate that hydrogen is more dangerous than other gases. Household fuel cells use hydrogen at pressures below 1 MPa. On the other hand, FCVs use hydrogen gas at, for example 70 MPa, which most people have no experience with. Therefore, it is important to confirm the usage conditions carefully for hydrogen gas safety management.

M. Inoue (✉)

Department of Earth Resources Engineering, Kyushu University,
Fukuoka, 819-0395, Japan
e-mail: inoue@mine.kyushu-u.ac.jp

© Springer Japan 2016

K. Sasaki et al. (eds.), *Hydrogen Energy Engineering*,
Green Energy and Technology, DOI 10.1007/978-4-431-56042-5_27

385

27.2 Properties of Hydrogen

Hydrogen is harmless to the human body. The main safety concerns are combustion and explosion. The properties of hydrogen are compared with methane (commonly used as city gas) in Table 27.1. Several properties of hydrogen important from a safety viewpoint are explained below.

Figure 27.1 shows the minimum ignition energy of various combustible gases [2]. The minimum ignition energy of hydrogen (0.02 mJ) is an order of magnitude lower than that of methane (0.28 mJ). Static electricity can cause sparks, and there are already some measures in place to minimize sparks in methane use. At 2 kV, electrical discharges occur which can be heard and felt as a small shock by humans. The electrical discharge energy is defined as $CE^2/2$, and the electric capacity C of the human body is thought to be ~ 100 pF [3]. Therefore, at 2 kV, the discharge energy is 0.2 mJ. This is insufficient for combustion of methane, but can ignite hydrogen. This suggests that conventional measures taken against static electricity that are effective for methane may not be sufficient for hydrogen.

Figure 27.2 shows the flammability limit of various combustible gases. The range of hydrogen combustion in air is 4–75 %. This is very wide compared with other combustible gases, and is therefore considered noteworthy. However, any combustible gas is dangerous if it leaks and accumulates. In fact, even powders such as flour explode in the right conditions. The three elements required for a fire are: oxygen; fuel; and an ignition source. Oxygen is present in the air. If there is an ignition source near hydrogen leak, combustion begins immediately.

Figure 27.3 shows the quenching distance of various combustible gases. The quenching distance is an index that shows how small a gap the combustion flame can pass through. This distance is 0.64 mm for hydrogen and 2.2 mm for methane. A flame arrester is applied to fuel gas supply pipes of a combustion device so that combustion cannot spread to the supply side of the gas due to some trouble and result in explosion. The essential point of the arrester is to pass the fuel gas through

Table 27.1 Properties of hydrogen and methane [2]

Properties	Unit	Hydrogen	Methane
Density (1 atm, 20 °C)	kg/m ³	0.0838	0.651
Dynamic viscosity (1 atm, 20 °C)	m ² /s	105×10^{-6}	16.6×10^{-6}
Ignition temperature (in air)	°C	572	580
Flammability limit (in air)	vol.%	4–75	5–15
Diffusion coefficient (in air)	m ² /s	6.66×10^{-5}	2.14×10^{-5}
Speed of sound (1 atm, 25 °C)	m/s	1308	449
Minimum ignition energy	mJ	0.02	0.28
Quenching distance	mm	0.64	2.2
Theoretical mixture ratio (in air)	vol.%	29.53	9.48
Burning velocity (in air)	m/s	2.65	0.4

Fig. 27.1 Minimum ignition energy of various combustible gases [2]

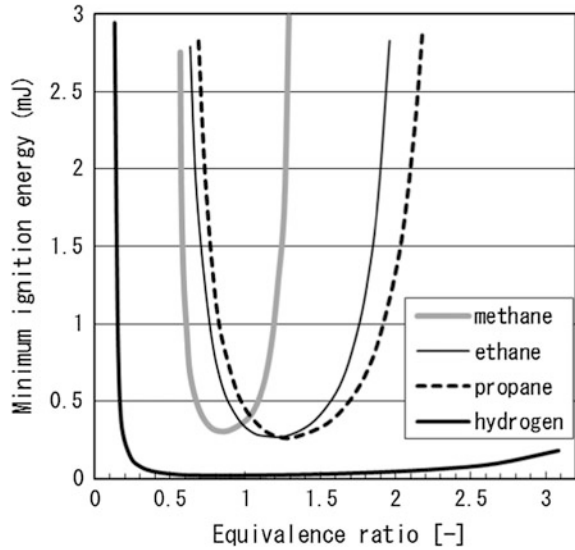
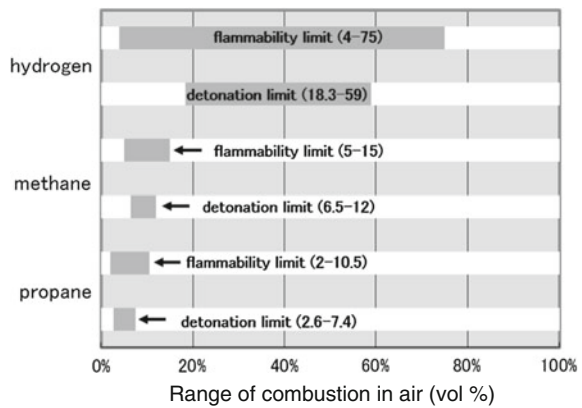


Fig. 27.2 Combustion limit of various gases [2]



narrow gaps to quench the flame at abnormal combustion. Essentially, a flame arrester designed for methane is useless for hydrogen because the gaps are too large.

Moreover, lighting units and sensors must not be able to be ignition sources in explosive atmosphere. Devices used in such environments must be explosion-proof. Many explosion-proof devices are designed such that if a flame ignites within them, it cannot spread to the outside, due to gaps smaller than the quenching distance (0.64 mm). Since the required gap is very small for hydrogen, advanced techniques are needed for explosion-proofing.

Figure 27.4 shows the burning velocity of various combustible gases. This is the velocity at which the combustible gas moves through a flame in a direction

Fig. 27.3 Quenching distance of various combustible gases [2]

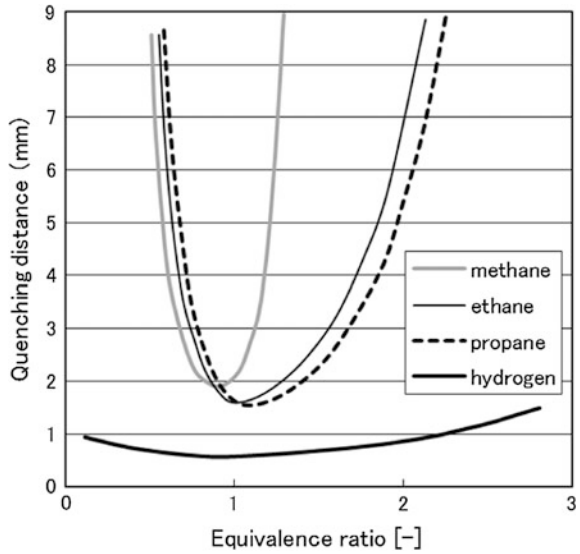
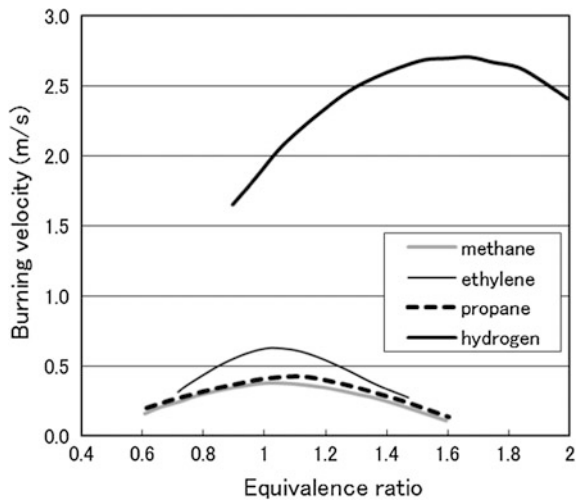
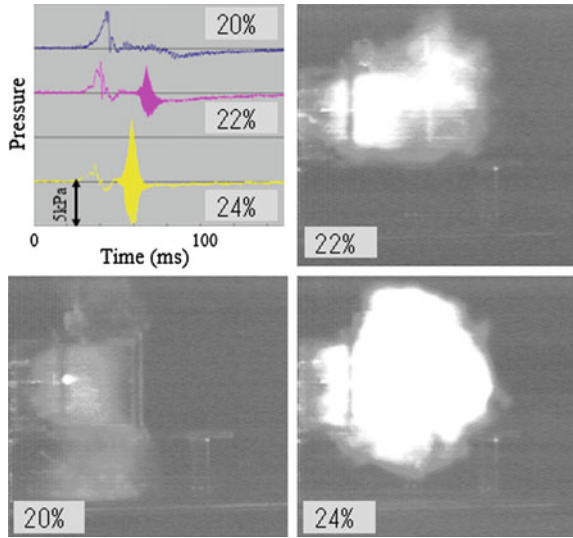


Fig. 27.4 Burning velocity of various combustible gases [2]



perpendicular to the flame surface. The velocity of hydrogen is 2.65 m/s, which is very high, whereas that of methane is 0.4 m/s. These values are obtained when the gases are stationary. Under a flow or turbulent conditions, the gases burn faster. The pressure increases when combustion is faster; consequently, the possibility of destroying surrounding materials increases.

Fig. 27.5 State of combustion and pressure change



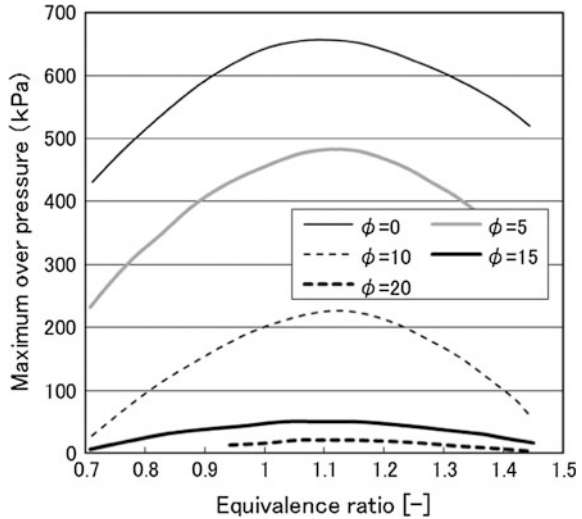
27.3 Combustion of Hydrogen

The combustion conditions of hydrogen are strongly dependent on the hydrogen concentration. At a hydrogen concentration of 8 %, the burning velocity is slow and not much sound is produced. When the concentration exceeds 20 %, hydrogen displays intense combustion. Figure 27.5 shows the state of combustion and the change in pressure when the hydrogen concentrations in a cubic container of 120 mm side length are 20, 22, and 24 %. The combustion condition significantly changes despite only a 2 % change in concentration. Furthermore, combustion propagation shows directionality. Combustion propagates largely upward if the concentration is greater than 4 %; upwards and horizontally at concentrations of greater than 6 %; and in all directions (upwards, horizontally, and downwards) at concentrations greater than 9 % [4].

27.4 Combustion Under Pressure

Figure 27.6 shows the maximum over-pressure when propane gas burns in a cylindrical container with a diameter of 100 mm and a height of 100 mm, and with a circular opening of 0, 5, 10, 15, or 20 mm diameter. It should be noted that hydrogen combustion *does not occur* in this case. The pressure is increased up to ~650 kPa when the container is completely sealed. The maximum pressure is considerably decreased when the opening diameter is large. If the pressure inside the equipment does not need to be maintained, it is preferable to install a rupture

Fig. 27.6 Over-pressure when propane gas burns in a container [2]



disk to release pressure. The maximum pressure is theoretically calculated to be ~ 820 kPa for hydrogen combustion under insulated constant volume conditions.

27.5 Effect of Diluent Gas

As mentioned above, the flammability limit for hydrogen mixed with air is 4–75 %. The flammability limit changes if another diluent gas such as carbon dioxide is mixed into the hydrogen–air mixture. Figure 27.7 shows the effects of the diluent gas on the flammability limit. Hydrogen does not burn when the concentration of carbon dioxide is ~ 59 % or higher and when the concentration of nitrogen is ~ 73 % or higher. Furthermore, hydrogen does not burn when the air concentration is ~ 18 % or lower irrespective of the type of diluent gas.

27.6 Prevention of Hydrogen-Related Accidents

Hydrogen-related incidents or accidents generally occur due to the following processes: leaks; diffusion; accumulation; ignition; fire; and explosion, as shown in Fig. 27.8. It is necessary to establish countermeasures for each stage of these incidents or accidents. These include leak prevention, leak detection, personnel evacuation, hydrogen dissipation systems, power shutdown, and combustion control. One Gas Company’s safety motto is “Don’t leak. Don’t accumulate. Don’t ignite.” It is preferable not to leak hydrogen at all. However, incident or accident reports suggest that it is not easy to prevent hydrogen leakage [1]. The next

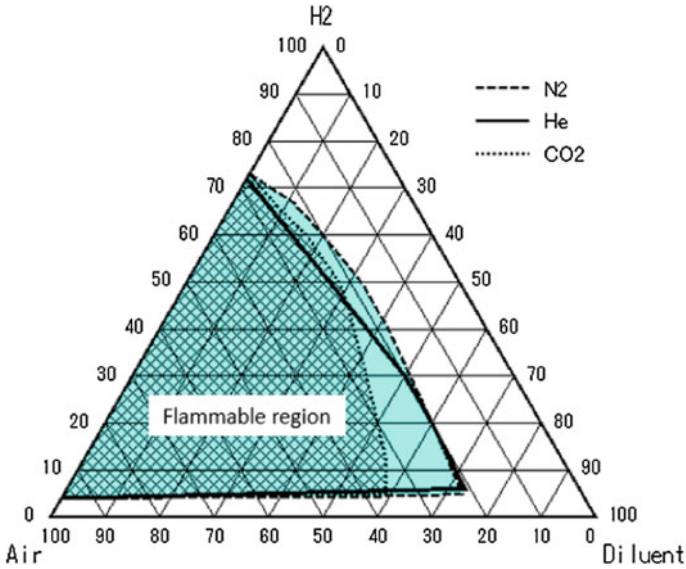
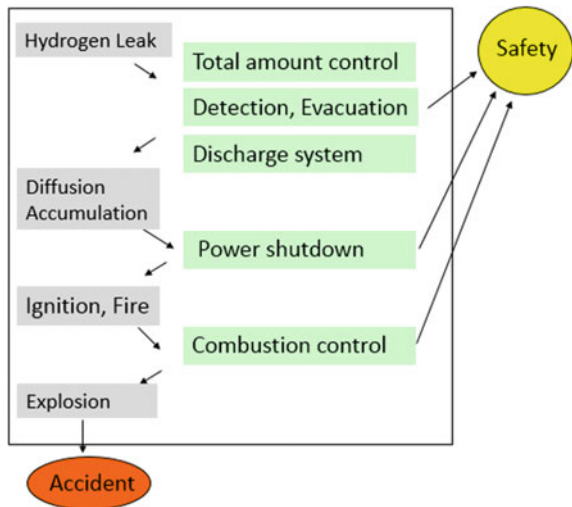


Fig. 27.7 Effects of diluent gas on flammability limit (vol.%) [4]

Fig. 27.8 Hydrogen disaster prevention



practical consideration is “Don’t accumulate.” One of the most dangerous cases is when hydrogen leaks in a room without good ventilation. In this case, it is effective to limit the maximum amount of hydrogen leakage to ensure safety. A conventional gas cylinder contains 7 m³ of hydrogen. The concentration of hydrogen in a room of 75 m³ would be ~8.5 % if all the hydrogen leaks out from the cylinder. This

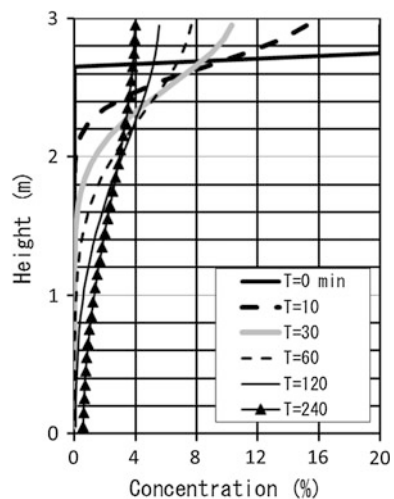
concentration is within the hydrogen flammable range, and therefore dangerous. In another case, with a smaller gas cylinder with a capacity of 1.5 m^3 leaks, the concentration of hydrogen in the same room will $\sim 2 \%$. This concentration is below the flammable range and therefore the room is relatively safe.

27.7 Hydrogen Diffusion

According to experiments, when hydrogen leaks in a room, it mixes with circumambient air. Consequently, the concentration drops to $\sim 20\text{--}30 \%$ in the vicinity of the ceiling [5]. Hydrogen at a concentration of $\sim 20 \%$ is formed in a 0.3 m -thick layer in the vicinity of the ceiling immediately after leakage, provided that 1.5 m^3 of hydrogen is leaked in a room of 75 m^3 . A concentration of 20% is in the combustion range. Subsequently, the hydrogen concentration decreases gradually and becomes uniform by molecular diffusion; finally, the hydrogen concentration reaches $\sim 2 \%$, which is the ratio of $1.5\text{--}75$, and is considered safe.

To estimate the time needed to reach a safe concentration, a diffusion equation was solved for this case, as shown in Fig. 27.9. The maximum concentration decreases with time. The concentration reaches 4% or lower at 240 min in the entire room, and the hydrogen in the room reaches a safe concentration. As seen from Fig. 27.9, hydrogen diffusion is extremely slow. The assumption that hydrogen is immediately released outside because the hydrogen diffusivity is large is erroneous. Although the hydrogen in a room finally reaches a safe concentration by hydrogen diffusion, it is preferable not to leave a room in dangerous conditions for a long time without taking any safety measures. It is necessary to dissipate the

Fig. 27.9 Change in hydrogen concentration by diffusion



leaked hydrogen by an air current, and the place where hydrogen is used should always be well-ventilated.

27.8 Example of the Necessity of Hydrogen Dissipation

In a parking lot in a building (as shown in Fig. 27.10), or a garage with a small opening, leaked hydrogen accumulates easily. Air currents in passageways or ventilation ducts are used for hydrogen dissipation. Such ventilation can be used to dissipate a small continuous hydrogen leak. However, a large leak rate cannot be dissipated in a short time irrespective of the air current.

27.9 Hydrogen Diffusion Near a Ceiling

An experiment was conducted in an idealized room (Fig. 27.11), with a horizontal circular ceiling with a radius of ~ 1.2 m. A hydrogen leak was simulated with a leak rate of 48 L/min, at 50 cm below the ceiling level. The figure shows the change in hydrogen concentration with time. If the radial distance r from the center of the leak is the same, the concentration at $h = 0$ cm is higher than that at $h = 8$ cm. In other words, a sensor nearer to the ceiling can detect hydrogen earlier than other sensors. Furthermore, it is difficult to detect a hydrogen leak by a sensor at $h = 8$ cm if the sensitivity is not better than $\sim 0.2\%$ for the amount of leaked hydrogen.

Fig. 27.10 Parking lot in a building

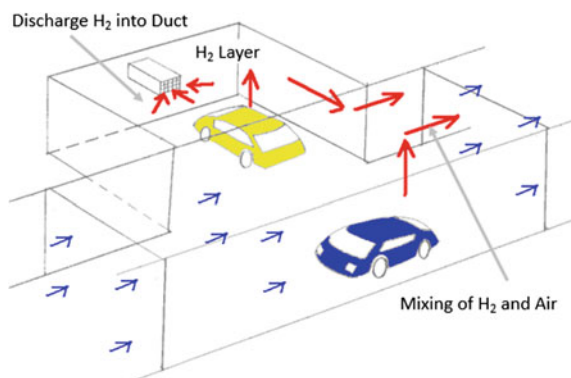
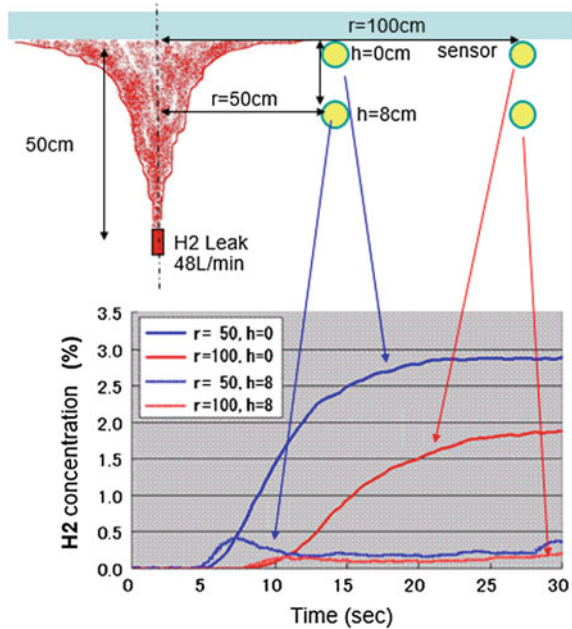


Fig. 27.11 Hydrogen concentration near the ceiling [5]



27.10 Hydrogen Sensors

There are many types of hydrogen sensors. Catalytic-combustion- or thermal-conductivity-type sensors are widely used practically. Neither sensor can selectively detect hydrogen. The measurement principle of the catalytic-combustion-type sensor is that the higher the hydrogen concentration in air, the higher is the combustion (catalyst oxidation) temperature of the sensor element. This sensor cannot be used in an environment without oxygen. Moreover, when another combustible gas exists, an accurate value is not obtained. In addition, the sensor consumes oxygen and hydrogen during the measurement; therefore, the concentration apparently decreases in a small closed space with time.

The principle of the thermal-conductivity-type sensor is that the heat radiation from the sensor element depends on the thermal conductivity of the surrounding gases. Therefore, oxygen is unnecessary for the measurement. However, when gases other than air are mixed, an accurate value is not obtained. It is necessary to understand the characteristics of the sensors to use them properly.

References

1. Accidents and incidents data base (2002) High Pressure Gas Safety Institute of Japan, Tokyo
2. Sato Y (2005) Hydrogen character relating safety. *J Jpn Soc Safety Eng* 44:378–385
3. Moriyama T (2007) Introduction for electric safety. *J Jpn Soc Safety Eng* 46:136–143
4. Yagyu S (1977) Flammable limits of gas and vapor. Japan Society for Safety Engineering, Tokyo
5. Inoue M, Tsukikawa H, Kanayama H, Matsuura K (2009) Experimental study on leaking hydrogen dispersion in a duct and under a ceiling. *J Hydrog Energy Syst Sci Jpn* 34:32–43

Chapter 28

Hydrogen Safety in Practice

Junichiro Yamabe and Nobuhiro Kuriyama

Abstract This chapter introduces the near miss reports at Kyushu University submitted from 2007 to 2013 in terms of system- or organization-related problems due to machine functions and safety measures and human errors due to unconscious behavior, impulsive behavior, incomplete recognition and knowledge, and disregard of rules.

Keywords Near miss · Incident · Accident · Hydrogen leak · Gas detector · O-ring · Hydrogen safety

28.1 Safety Measures and Devices for Hydrogen Facilities

For the safe operation of hydrogen energy systems in practice, which include various components such as pressure vessels and pipes, we must take into account hydrogen embrittlement (HE), hydrogen gas safety management, and hydrogen safety. When we treat high-pressure gaseous hydrogen, the components operated under high pressure must be designed based on the High Pressure Gas Safety Act, which are the Japanese regulations for high-pressure gas. Based on this act, components are manufactured by using materials with a high resistance to HE. Furthermore, annual inspections of the components are legally required to detect

J. Yamabe (✉)

International Research Center for Hydrogen Energy, Kyushu University,
Fukuoka 819-0395, Japan
e-mail: yamabe.junichiro.575@m.kyushu-u.ac.jp

N. Kuriyama

Research Institute of Electrochemical Energy Department of Energy and Environment,
National Institute of Advanced Industrial Science and Technology, Osaka 1-8-31, Japan
e-mail: kuriyama-n@aist.go.jp

© Springer Japan 2016

K. Sasaki et al. (eds.), *Hydrogen Energy Engineering*,
Green Energy and Technology, DOI 10.1007/978-4-431-56042-5_28

397

Fig. 28.1 Fume hood equipped in a laboratory

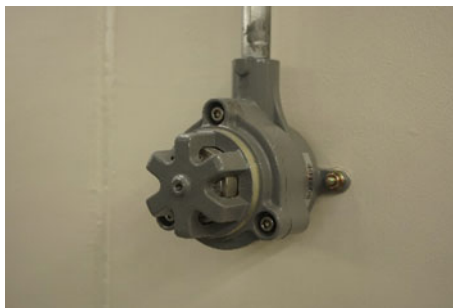


unexpected failure. It is important for hydrogen safety to be implemented in practice to prevent hydrogen leaks during operation. Thus, a system that enables the quick detection of hydrogen leaks and the release of hydrogen is required. Experiments have been carried out at two centers in Kyushu University, the International Research Center for Hydrogen Energy, and the Research Center for Hydrogen Industrial Use and Storage (HYDROGENIUS). Many experimental instruments and infrastructure for hydrogen are operated in these facilities. A fume hood (Fig. 28.1) is equipped in each room, and the relevant experimental instrument is installed below. In addition, explosion-proof lighting is equipped in the room, and a supervision panel is equipped on each floor to monitor the conditions of the instruments. Ventilation is usually performed through a fan installed in the fume hood. Any hydrogen leaking from the instruments is detected by a hydrogen gas detector in the fume hood fan (Fig. 28.2). An oxygen-gas detector is also installed in each room (Fig. 28.3) to prevent suffocation. The 1st stage alarm goes off when a hydrogen gas concentration of over 500 ppm or 1000 ppm is detected. The 1st and 2nd stage alarms comprise of a rotating warning light and a sound speaker. In addition to these alarms, when a hydrogen leak is detected, the hydrogen

Fig. 28.2 Hydrogen-gas detector installed in a laboratory



Fig. 28.3 Oxygen-gas detector installed in a laboratory



supply is stopped and ventilation is automatically performed. Hydrogen often leaks from the joints of pipes and the sealed parts of pressure vessels. Thus, hydrogen leaks need to be checked before experiments by using a portable gas detector.

28.2 Examples of Near Miss Reports

To avoid a large accident or repeat similar accidents from the past, we should publicize small incidents, near misses, and potential serious errors. Thus, submission of near miss reports is mandatory at Kyushu University. Annual safety training days and disaster drills are also conducted. Supervisors discuss near miss reports during health and safety meetings; then suitable safety measures are updated to reduce the chance of similar future incidents. We analyzed the near miss reports submitted from 2007 to 2013 in terms of system- or organization-related problems due to machine functions and safety measures and human errors due to unconscious behavior, impulsive behavior, incomplete recognition and knowledge, and disregard of rules. Table 28.1 shows the results of the near miss reports. To summarize these reports, the following tendencies are observed:

- (1) Technical staff are usually the most frequent operators of high-pressure hydrogen machines. Therefore, the ratio of near miss reports from these staff is relatively high.
- (2) Nearly half of the near miss reports originate from human error.
- (3) Initial problems in components tend to occur from 1 to 2 years after their installation, and degradation of components tends to become an issue 6 or more years after installation.
- (4) Problems in high-pressure hydrogen components occur 2–3 years after installation.
- (5) Many experts can cause human errors by ignoring relevant procedures.
- (6) Almost all human errors related to the vendors is caused by lack of sufficient communication or misunderstandings.
- (7) Nearly half of hydrogen leaks are attributed to sealing problems, and half of these problems are caused by O-rings.

Table 28.1 Result of near miss reports

Classification	Machine problem		Human error				Total	%
	Machine function	Safety measure	Disregard of rules	Incomplete recognition and knowledge	Impulsive behavior	Unconscious behavior		
Professor	4	2	2	0	0	0	8	9.6
Technical staff	21	8	3	4	0	0	36	43.4
Postdoc	0	0	0	0	0	0	0	0.0
Doctor course	0	0	1	2	0	0	3	3.6
Master course	5	1	8	8	0	0	22	26.5
Bachelor	1	0	0	0	0	0	1	1.2
Researcher	0	0	0	0	0	0	0	0.0
Vendors	3	1	7	1	1	0	13	15.7
Unknown	0	0	0	0	0	0	0	0.0
Total	34	12	21	15	1	0	83	100
%	41.0	14.5	25.3	18.1	1.2	0.0	100	-

Fig. 28.4 Rubber O-ring used to seal high-pressure gaseous hydrogen, shown after fracture



Figure 28.4 shows an example of the failure of a rubber O-ring used for high-pressure gaseous hydrogen. As mentioned in Chap. 26, the fast decompression of high-pressure gaseous hydrogen often causes a significant volume increase in the O-ring, resulting in the failure of the O-ring.

Chapter 29

Effect of Hydrogen on the Tensile Properties of Metals

Shigeru Hamada

Abstract This chapter describes the effect of hydrogen on tensile properties of metals, showing that the hydrogen-assisted fracture is more enhanced for a material with higher tensile strength. It is also demonstrated that the relative reduction of area of austenitic stainless steels strongly correlates with nickel equivalent.

Keywords Hydrogen · Hydrogen-assisted fracture · Slow strain rate tensile test · Reduction of area · Nickel equivalent · Austenitic stability · Steel · Hydrogen safety

29.1 Assessment of Tensile Properties in the Presence of Hydrogen

Tensile properties are often used to assess the effect of hydrogen on the strength of metals. In this chapter, the effect of hydrogen on the tensile properties of metals will be described. Many methods have been proposed for measuring the effect of hydrogen on the tensile properties of metals, with slow strain rate testing (SSRT) being among the most common. Because hydrogen concentration increases in regions of a material where stress is concentrated, especially with the occurrence of a fracture, the influence of hydrogen on the tensile properties is time-dependent. Therefore, SSRT emphasizes these time-dependent characteristics.

In general, the effect of hydrogen on the reduction of area (RA) appears to be strongly correlated with tensile strength, σ_B , σ_{uts} [1]. The effect of hydrogen on RA is captured through measurement of relative reduction of area (RRA).

S. Hamada (✉)
Department of Mechanical Engineering, Kyushu University,
Fukuoka 819-0395, Japan
e-mail: hamada@mech.kyushu-u.ac.jp

29.2 Notched and Unnotched Tensile Strength and Ductility in Hydrogen Environment

The values for the tensile strengths of notched and unnotched (smooth) specimens, as well as the tensile ductility of unnotched specimens, for various metallic materials in high-pressure gaseous hydrogen are provided in the NASA database, as mentioned in Chap. 26 [2]. Some of these data were also reported by Walter et al. [3, 4] and Chandler et al. [5]. Chandler et al. [5] designed special equipment for measuring the tensile ductility in high-pressure gas at 69 MPa. Figure 29.1 shows a schematic of this experimental setup. The specimens tested using this apparatus were 7.77 mm in diameter and 229-mm long. Unnotched specimens were marked with a gauge section that was 3.18 mm long and 6.35 mm in diameter. Notched specimens had a V-shaped notch with an angle of 60° at the midplane. Unnotched specimens were crosshead-paced, usually at a rate of 0.127 mm/min, while notched specimens were load-paced at a loading rate corresponding to a strain rate of 0.0007/min.

As mentioned in Chap. 26, materials are categorized into four grades in the database, according to their susceptibility to hydrogen embrittlement (HE). The arrangement of the NASA database is shown in Fig. 29.1. Table 29.1 shows a part of the database. All of the metals listed in Table 29.1 are “extremely embrittled.” However, the strength ratios (H_2/He) for some of the unnotched specimens were

Fig. 29.1 Specimen sealed in vessel for tension testing in high-pressure hydrogen [5]

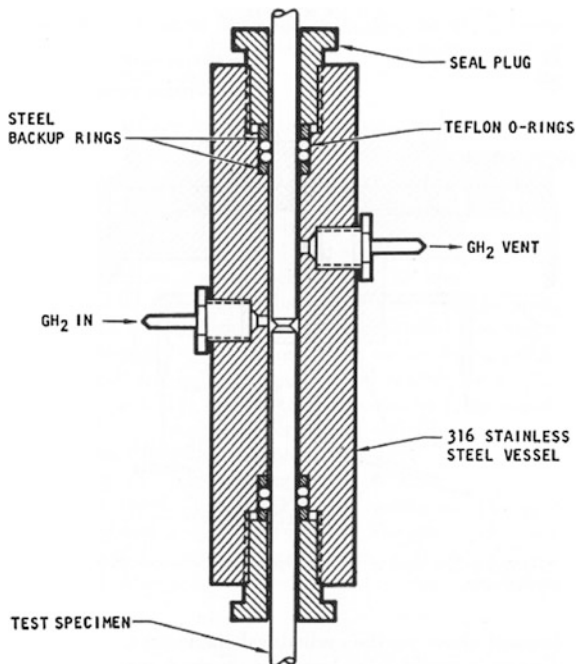


Table 29.1 Susceptibility of materials to embrittlement in hydrogen at 69 MPa and 22 °C [2]

Material	Strength ratio, H ₂ /He		Unnotched ductility			
			Elongation (%)		Reduction of area (%)	
	Notched ^a	Unnotched	He	H ₂	He	H ₂
<i>Extremely embrittled</i>						
I8Ni-250 maraging steel	0.12	0.68	8.2	0.2	55	2.5
410 stainless steel	0.22	0.70	15	1.3	60	12
1042 steel (quenched and tempered)	0.22	–	–	–	–	–
17-7 pH stainless steel	0.23	0.92	17	1.7	45	2.5
Fe-9Ni-4Co-0.20C	0.24	0.86	15	0.5	67	15
H-11	0.25	0.57	8.8	0	30	0
René 41	0.27	0.84	21	4.3	29	11
Electro-formed nickel	0.31	–	–	–	–	–
4140	0.40	0.96	14	2.6	48	9
Inconel 718	0.46	0.93	17	1.5	26	1
440C	0.50	0.40	–	–	3.2	0

^aStress concentration factor, $K_t = 8.4$

close to 1. Therefore, test conditions (including specimen shape, notched-type, or unnotched-type) need to be taken into account when conducting tests for metal selection based on test results.

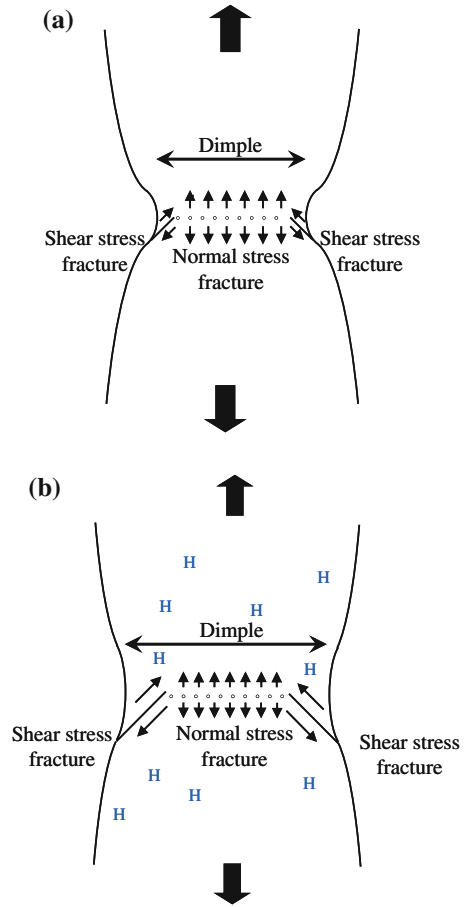
29.3 Mechanisms of HE in Tensile Tests

Matsuoka et al. [6] conducted tensile tests of hydrogen-charged and non-charged steel. They measured a 900 MPa class quenched and tempered Cr–Mo steel specimen (JIS-SCM435). Using scanning electron microscopy (SEM) to observe the fractured shape and surface, along with the tensile strength measurements, they proposed a mechanism for HE.

Figure 29.2a shows a vertical divisional cross-section of a non-charged steel specimen with tensile fracture. The corresponding schematic for a hydrogen-charged specimen is shown in Fig. 29.2b. Both are observed to have cup-and-cone fractures. In Fig. 29.2, although the normal stress fracture zones of non-charged and hydrogen-charged specimens are of the same approximate size, the shear stress fracture zone of the hydrogen-charged specimen is larger.

This demonstrates that hydrogen affects the formation of the shear fracture zone. During the necking process, the cross-section of a specimen reduces in area locally. In order for a shear stress fracture zone to increase in size in the necking process, it is necessary for the shear stress fracture to occur easily, and slip deformation by shear stress is promoted by hydrogen. Therefore, for JIS-SCM435, pre-charged

Fig. 29.2 Schematic representations of tensile fracture processes. **a** and **b** are the processes for non-charged and hydrogen-charged specimens, respectively, in a tensile test in air at room temperature [6]



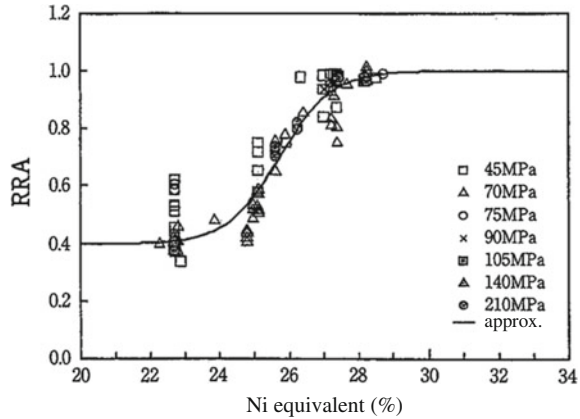
with hydrogen, the hydrogen-enhanced localized plasticity (HELP) model [7–9] can explain the tensile test results as a decreased RA owing to the presence of hydrogen under room temperature atmospheric conditions.

29.4 Effect of Hydrogen on Tensile Properties

29.4.1 *Effect of Nickel Equivalent on RRA in Hydrogen Atmosphere for Austenitic Stainless Steels*

Austenitic stainless steels exhibit good characteristics with respect to their resistance to HE. The tensile properties of austenitic stainless steels are closely related to a martensitic transformation. The effect of hydrogen on RRA is also closely related

Fig. 29.3 Relationship between RRA and Ni_{eq} at room temperature [12]



to a martensitic transformation, and depends on the austenite stabilization elements (Ni and Cr). Hirayama et al. [10, 11] discussed this issue from a thermodynamics viewpoint and proposed the following equation showing the stability of austenite with nickel equivalent, Ni_{eq}

$$Ni_{eq} = Ni + 0.65Cr + 0.98Mo + 1.05Mn + 0.35Si + 12.6C \quad (29.1)$$

Yamada et al. [12] studied the influence of hydrogen on RRA by using SSRT on various austenitic stainless steels, and using Eq. 29.1. Figure 29.3 shows the results of these studies at room temperature. From Fig. 29.3, a relationship between nickel equivalent and RRA (a measure of the effect of hydrogen) is observed.

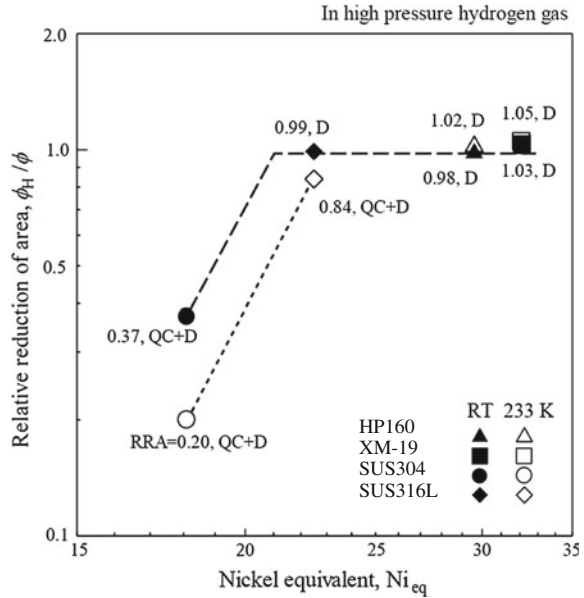
Although Eq. 29.1 does not account for nitrogen, it is known that the tractive characteristics improve with the addition of nitrogen. Therefore, by considering nitrogen, Sanga et al. [13] discussed this issue from a thermodynamics viewpoint and proposed the following equation:

$$Ni_{eq} = Ni + 12.93C + 1.11Mn + 0.72Cr + 0.88Mo - 0.27Si - 0.24Ti - 0.07Co + 0.19Nb + 0.53Cu + 0.90V + 0.70W - 0.69Al + 7.55N \quad (29.2)$$

Oshima et al. [14] studied and discussed the influence of alloying elements on the crystalline structure, mechanical characteristics, and austenite stability of a cold-rolled plate of five types of Cr–Mo–Ni steel, and proposed the following equation:

$$Ni_{eq} = Ni + Cu + 15.9(C + N) + 0.32Si + 0.28Mn + 0.64Mo + 0.47Cr + 2.3Nb \quad (29.3)$$

Fig. 29.4 Relationship between RRA and nickel equivalent. The numbers next to the data points show the RRA values [15, 16]



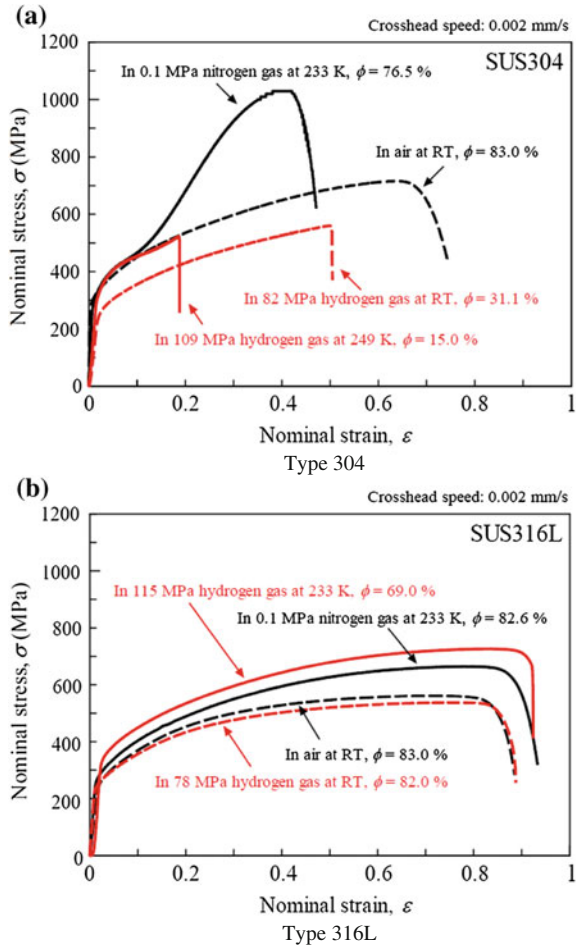
Using Eq. 29.3, Itoga et al. [15, 16] investigated the SSRT characteristics of high-strength austenitic stainless steels and obtained the relation to nickel equivalent. Figure 29.4 shows the result. The numbers associated with different data points in Fig. 29.4 are the values of RRA. The label D relates to the dimple on a fractured surface while the label QC denotes quasi cleavage (QC) on a fractured surface. As in Fig. 29.3, a relationship between nickel equivalent and RRA (a measure of the effect of hydrogen) is observed.

29.4.2 Effect of Hydrogen on Tensile Properties of Austenitic Stainless Steels

Itoga et al. [15, 16] used SSRT to examine the effect of temperature and gas environment on the tensile properties of Type 304 and Type 316L steels. Type 316L has good resistance against HE. Figure 29.5 shows the relationship between nominal stress and nominal strain. Significant difference between the nominal stress-strain diagrams of Type 304 and Type 316L was observed. These steels were fractured before reaching a maximum load point or not in presence of hydrogen.

For Type 304 (Fig. 29.5a), degradation of the tensile strength and the RA can be seen in 82 MPa hydrogen gas at room temperature, compared with those in room temperature atmosphere. In 0.1 MPa nitrogen gas at low temperature, an increase of the tensile strength by strain-induced martensitic transformation was confirmed. On the other hand, in 109 MPa hydrogen gas at low temperature, tensile failure

Fig. 29.5 Nominal stress-strain curves for Type 304 and Type 316L steels in 78–115 MPa hydrogen gas at room temperature, and at -40 to -27 °C [15, 16]. **a** Type 304. **b** Type 316L



occurred before strain-induced martensitic transformation, and remarkable degradations of the tensile strength and RA were observed.

For Type 316L (Fig. 29.5b), the tensile strength and RA in 78 MPa hydrogen gas at room temperature were almost the same as at atmospheric condition. On the other hand, although the tensile strength in 115 MPa hydrogen gas at low temperature (-40 °C) was increased, the RA decreased by about 16 % compared with that observed in 0.1 MPa nitrogen gas at low temperature (-40 °C). In addition, for Type 316L, which has good HE resistance characteristics, the RA was degraded by hydrogen exposure, and consequently HE occurred at low temperature (e.g., -40 °C).

References

1. Fukuyama S, Imade M, Iijima T, Yokogawa K (2008) Development of new material testing apparatus in 230 MPa hydrogen and evaluation of hydrogen gas embrittlement of metals. ASME Pressure Vessels and Piping Division (Publication) PVP2008-61849, pp 235–240
2. NASA (1997) Safety standard for hydrogen and hydrogen systems. Washington, DC, NSS 1740.16
3. Walter RJ, Chandler WT (1971) Influence of hydrogen pressure and notch severity on hydrogen-environment embrittlement at ambient temperatures. *Mater Sci Eng* 8:90–97
4. Walter RJ, Jewett RP, Chandler WT (1970) On the mechanism of hydrogen-environment embrittlement of iron- and nickel-base alloys. *Mater Sci Eng* 5:99–110
5. Chandler W, Walter R (1974) Testing to determine the effect of high-pressure hydrogen environments on the mechanical properties of metals. In: Raymond L (ed) Hydrogen embrittlement testing STP 543. ASTM Special Technical Publication, pp 170–197
6. Matsuoka S, Homma N, Tanaka H, Fukushima Y, Murakami Y (2006) Effect of hydrogen on tensile properties of 900-MPa-class JIS-SCM435 low-alloy-steel for use in storage cylinder of hydrogen station. *J Jpn Inst Met Mater* 70:1002–1011
7. Sofronis P, McMeeking RM (1989) Numerical analysis of hydrogen transport near a blunting crack tip. *J Mech Phys Solids* 37:317–350
8. Birnbaum HK, Sofronis P (1994) Hydrogen-enhanced localized plasticity: a mechanism for hydrogen-related fracture. *Mater Sci Eng A* 176:191–202
9. Robertson IM, Birnbaum HK (1986) An HVEM study of hydrogen effects on the deformation and fracture of nickel. *Acta Metall* 34:353–366
10. Hirayama T, Ogirima M (1970) Influence of chemical composition on martensitic transformation in Fe-Cr-Ni stainless steel. *J Jpn Inst Met Mater* 34:507–510
11. Hirayama T, Ogirima M (1970) Influence of martensitic transformation and chemical composition on mechanical properties of Fe-Cr-Ni stainless steel. *J Jpn Inst Met Mater* 34:511–516
12. Yamada T, Kobayashi H (2012) Criteria of selecting materials for hydrogen station equipments. *J High Press Gas Safety Inst Jpn* 49:885–893
13. Sanga M, Yukawa N, Ishikawa T (2000) Influence of chemical composition on deformation-induced martensitic transformation in austenitic stainless steel. *J Jpn Soc Technol Plast* 41:64–68
14. Oshima T, Habara Y, Kuroda K (2007) Effects of alloying elements on mechanical properties and deformation-induced martensite transformation in Cr-Mn-Ni austenitic stainless steels (transformations and microstructures). *Tetsu- to- Hagane* 93:544–551
15. Itoga H, Matsuo T, Orita A, Matsunaga H, Matsuoka S, Hirofumi R (2014) SSRT and fatigue crack growth properties of high-strength austenitic stainless steels in high-pressure hydrogen gas (PVP2014-28640). In: Proceedings of PVP-2014: ASME pressure vessels and piping division conference, Anaheim, California, USA, 20–24 July 2014, ASME, New York, NY
16. Itoga H, Matsuo T, Orita A, Matsunaga H, Matsuoka S (2013) SSRT and fatigue crack growth properties of two types of high strength austenitic stainless steels in high pressure hydrogen gas. *Trans JSME A* 79:1726–1740

Chapter 30

Effect of Hydrogen on Fatigue Properties of Metals

Hisao Matsunaga

Abstract This chapter describes the effects of hydrogen pressure and test frequency on fatigue life and fatigue crack growth (FCG) behaviors of carbon and low-alloy steels. FCG behaviors of austenitic stainless steels and aluminum alloy in high-pressure gaseous hydrogen are also introduced.

Keywords Hydrogen · Fatigue life property · Fatigue crack growth property · Non-propagating crack · Slip deformation · Striation · Steel · Aluminum · Hydrogen safety

30.1 Fatigue Life Properties in High-Pressure Hydrogen Gas

The fatigue-life property (S - N property) of smooth specimens is one of the most commonly quoted fatigue properties, widely used in both the finite-life fatigue design and infinite-life fatigue design (fatigue limit design) of mechanical components.

Recently, considerable efforts have been undertaken to identify the S - N properties of steels in high-pressure hydrogen gas. As representative examples, the results of tension-compression fatigue tests conducted on two steels, obtained in 115 MPa hydrogen gas at room temperature are introduced and discussed in this chapter [1]. One sample is a quenched and tempered Cr–Mo steel (JIS-SCM435), and the other is an annealed, low carbon steel (JIS-SM490B). Table 30.1 summarizes the mechanical properties of these steels. Figure 30.1 presents the S - N data. Past studies have reported that the degradation of fatigue life in hydrogen gas is more pronounced in a shorter life regime [1]. Further, in Fig. 30.1, the fatigue lives of both steels show a noticeable decrease in hydrogen gas in the short fatigue life regime (i.e., $N_f < 10^5$)

H. Matsunaga (✉)

Department of Mechanical Engineering, Kyushu University,
Fukuoka 819-0395, Japan
e-mail: matsunaga.hisao.964@m.kyushu-u.ac.jp

© Springer Japan 2016

K. Sasaki et al. (eds.), *Hydrogen Energy Engineering*,
Green Energy and Technology, DOI 10.1007/978-4-431-56042-5_30

411

Table 30.1 Mechanical properties of JIS-SCM435 and JIS-SM490B

	$\sigma_{0.2}$ (MPa)	σ_U	σ_B (MPa)	HV
JIS-SCM435	671	–	824	272
JIS-SM490B	–	360	537	153

$\sigma_{0.2}$ 0.2 % off-set yield strength, σ_U Upper yield point strength, σ_B Ultimate tensile strength, HV Vickers hardness

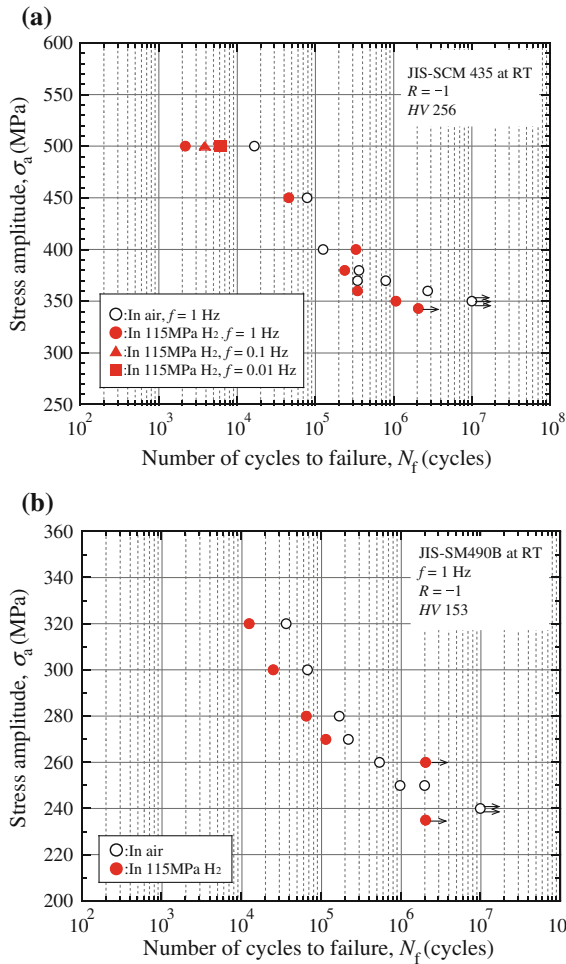


Fig. 30.1 $S-N$ data in air and 115 MPa hydrogen gas at room temperature. During the tests in air, if the specimen did not fail up to N of 2×10^6 cycles, the test frequency was increased to 5 Hz and the test was continued [1]. **a** JIS-SCM435. **b** JIS-SM490B

cycles). It can also be confirmed for JIS-SCM435 that the fatigue life is dependent on the test frequency at relatively high stress amplitude. This phenomenon can be understood from the frequency dependence of the fatigue crack growth (FCG) rate, to be described later in Sect. 30.2. Owing to a combination of fatigue life degradation and frequency dependence, great care must be observed when evaluating the effect of hydrogen on fatigue life in the short-life regime. In contrast, in the long-life regime (i.e., $N_f > 10^5$ cycles), there is no noticeable difference in the fatigue lives of specimens tested in air or in hydrogen gas. Similar fatigue-life properties in high-pressure hydrogen gas have also been reported for Type 316L stainless steel [2].

In general, steels of low or moderate strength (e.g., $\sigma_B < 1000$ MPa) show a definite fatigue limit in air [3], usually determined by testing up to $N = 10^7$ cycles. Therefore, the existence of a fatigue limit is the important element in infinite life design. However, with respect to fatigue testing in a high-pressure hydrogen gas atmosphere, O-rings are usually used in the testing machines, in the sliding parts between the high-pressure vessel and piston cylinder. This restricts the test frequency to a low value, e.g., 1 Hz. Thus, a test up to $N = 10^7$ cycles would be impractical in view of the testing costs and time. For this reason, in the results shown in Fig. 30.1, fatigue tests in hydrogen gas were considered as run-outs at $N = 2 \times 10^6$ cycles, in order to complete the series of tests within a reasonable timeframe. Even in such a situation, observation of the specimen surface provided important evidence to establish the existence of a fatigue limit for these steels in high-pressure hydrogen gas [4]. In order to establish the presence or absence of a fatigue limit for both steels in 115 MPa hydrogen gas, the surfaces of unbroken specimens were observed after the fatigue tests. Regarding the unbroken specimens of JIS-SCM435 tested at low stress amplitudes both in hydrogen and in air, no fatigue cracks were observed on the specimen surfaces. The result inferred that the fatigue limit was determined by the crack initiation limit, not only in air, but also in hydrogen gas. A similar phenomenon, i.e., the determination of the fatigue limit as a crack initiation limit, has been widely observed for smooth specimens of quenched and tempered steels in air [5]. In contrast, in unbroken specimens of JIS-SM490B at the stress amplitude, σ_a of 260 MPa, and the number of cycles, N of 2×10^6 , a number of cracks was observed on the surface of specimens tested in both atmospheres. The largest crack found in the specimen tested in hydrogen gas measured about 140 μm in length. In order to determine whether the cracks in hydrogen gas were propagating or non-propagating, two additional fatigue tests were carried out at the stress amplitude σ_a of 260 MPa in 115 MPa hydrogen gas. The tests were terminated at N of 2×10^5 and 10^6 , respectively, after which the specimen surface was observed again. A number of cracks were detected at both N of 2×10^5 and 10^6 .

Figure 30.2 shows optical micrographs of the cracks at different numbers of cycles. Figure 30.3 illustrates the lengths of the top ten largest cracks as a function of the number of cycles. The figure indicates that there was a certain amount of

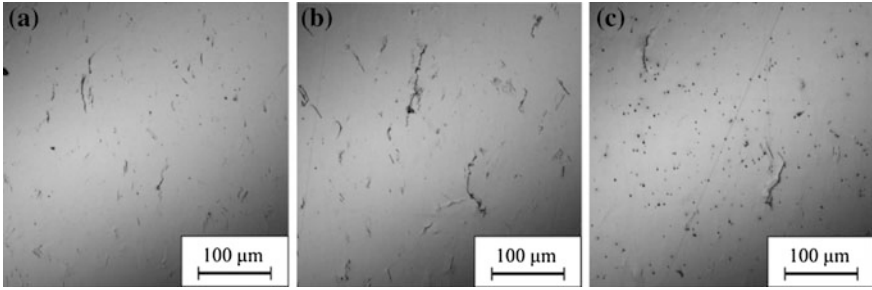
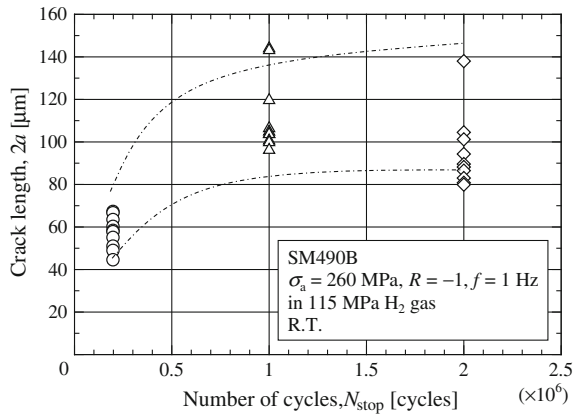


Fig. 30.2 Optical micrographs of the surfaces of JIS-SM490B specimens tested in 115 MPa hydrogen gas [4]. **a** $N = 2 \times 10^5$. **b** $N = 1 \times 10^6$. **c** $N = 2 \times 10^6$

Fig. 30.3 Relationship between crack lengths and the number of cycles during tension-compression fatigue tests of JIS-SM490B in 115 MPa hydrogen gas at $\sigma_a = 260$ MPa [4]



growth between $N = 2 \times 10^5$ and $N = 10^6$, but that there was little, if any, growth between $N = 10^6$ and $N = 2 \times 10^6$, although these data exhibit a scatter among the three different specimens. This result suggests that even in 115 MPa hydrogen gas there is a fatigue limit in JIS-SM490B, determined by the non-propagation condition of cracks initiated in the early stages of the fatigue process.

As previously shown, during the fatigue tests of JIS-SCM435 and JIS-SM490B in 115 MPa hydrogen gas, the fatigue strength did not deteriorate in the long-life regime, as compared to that in air, even though the NASA guidelines categorize these steels as being “severely-embrittled” or “extremely-embrittled” materials when exposed to hydrogen [6]. Moreover, the existence of a fatigue limit was inferred in both steels, even in 115 MPa hydrogen gas. The insights outlined earlier in this section can be the basis for the fatigue design of mechanical components used in high-pressure hydrogen gas.

30.2 Fatigue Crack Growth (FCG) Properties

30.2.1 FCG in Hydrogen Gas

The FCG property is necessary for evaluating crack growth life in finite-life fatigue design. When the FCG rate, da/dN , is given as a function of the stress intensity factor range, ΔK , the FCG life can be calculated by integrating the $da/dN - \Delta K$ curve. In general, the FCG rate is described by Paris' law [7]:

$$(da/dN) = C(\Delta K)^m \quad (30.1)$$

where, c and m are constants.

It has been reported for various steels that the FCG is accelerated in high-pressure hydrogen gas [8–14]. Therefore, to ensure the safe use of components in hydrogen gas atmospheres, the FCG data under design pressure at service temperatures are needed, as well as a proper understanding of the mechanisms of FCG acceleration. In this section, the FCG properties obtained in hydrogen gas at various pressures are introduced and discussed for the following steels and aluminum alloy: (i) annealed low carbon steel (JIS-SM490B) [8]; (ii) quenched and tempered Cr–Mo steel (JIS-SCM435) [9]; (iii) four types of austenitic stainless steels [10]; and (iv) A6061-T6 aluminum alloy [11].

Figure 30.4 shows the crack-growth rate, da/dN , as a function of the stress intensity factor range, ΔK , for JIS-SM490B in air, as well as the various pressures of hydrogen gas at the stress ratio, $R = 0.1$ [8]. In a low ΔK regime, i.e., $\Delta K < 20 \text{ MPa m}^{1/2}$, the rate of crack growth acceleration increased with an augmentation of ΔK . Conversely, in a higher ΔK regime, i.e., $\Delta K > 20 \text{ MPa m}^{1/2}$, the da/dN curves in hydrogen gas were parallel to the curves in air.

Figure 30.5 presents the relative FCG rate (RFCGR), $(da/dN)_{\text{H}_2}/(da/dN)_{\text{air}}$, as a function of the hydrogen pressure, p_{H_2} , obtained at $\Delta K = 30 \text{ MPa m}^{1/2}$ under $f = 1 \text{ Hz}$ and $R = 0.1$. Where, $(da/dN)_{\text{H}_2}$ and $(da/dN)_{\text{air}}$ are the growth rates in hydrogen and air, respectively. The RFCGR was nearly constant at $p_{\text{H}_2} = 0.7\text{--}90 \text{ MPa}$. The independence of $(da/dN)_{\text{H}_2}/(da/dN)_{\text{air}}$ against p_{H_2} in a high-pressure regime is crucially important for the fatigue life design of components, since the existence of the upper bound of acceleration allows for the provision of a fatigue life estimation for the worst case scenario.

Figure 30.6 exhibits the relationship between the RFCGR and the test frequency, f [8]. Under $p_{\text{H}_2} \leq 10 \text{ MPa}$, the RFCGR gradually increases with a reduction in f , and then suddenly decreases close to 1.0. Similar behavior has been reported for Cr–Mo steels [12, 15] and austenitic stainless steels [10]. It is to be noted that the peak of acceleration shifts towards the lower f with an increase in p_{H_2} . Under $p_{\text{H}_2} \geq 45 \text{ MPa}$, reduction of the RFCGR does not occur in the low-frequency regime down to the f of 0.001 Hz. It is also noteworthy that at the p_{H_2} of 45 MPa, the RFCGR saturated at about 30. On the other hand, at the p_{H_2} of 90 MPa, the upper bound of the FCG acceleration did not exist down to the f of 0.001 Hz.

Fig. 30.4 Relationship between da/dN and ΔK in 0.1–90 MPa hydrogen gas (JIS-SM490B) [8]

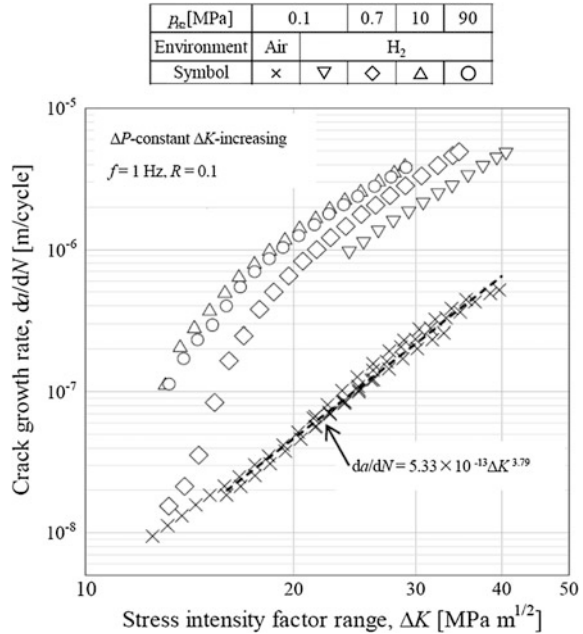
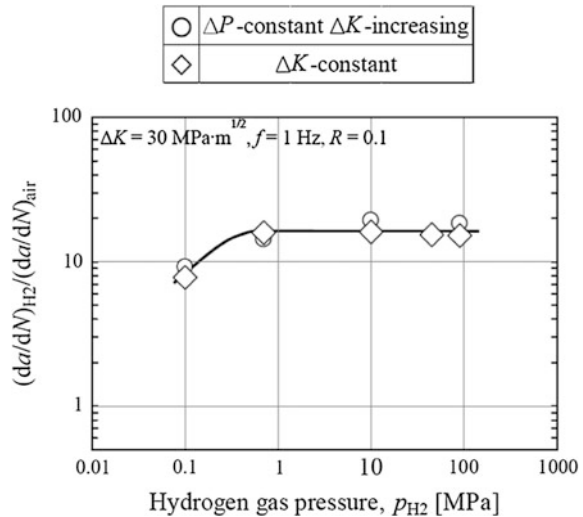
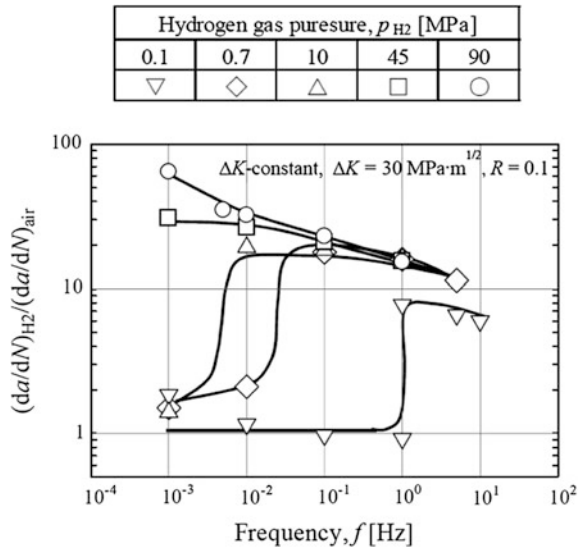


Fig. 30.5 Relationship between $(da/dN)_{H_2}/(da/dN)_{air}$ and hydrogen gas pressure, p_{H_2} (JIS-SM490B) [8]



Practically speaking, since some components are subjected to very slow stress cycles in service, the existence of the upper bound against the test frequency is necessary for the finite life fatigue design of components. In view of this, JIS-SM490B is eligible for use in hydrogen gas up to 45 MPa, but is not suitable for use in 90 MPa hydrogen, due to the absence of the upper bound of acceleration.

Fig. 30.6 Relationship between $(da/dN)_{H_2}/(da/dN)_{air}$ and test frequency, f (JIS-SM490B) [8]



In order to understand the peculiar frequency dependence of the FCG rate (e.g., Fig. 30.6), two mechanisms are proposed. Using the Cr–Mo steel JIS-SCM435, Matsuo et al. [16] performed FCG testing in 0.7 MPa hydrogen gas at various test frequencies, thereby detecting the peculiar frequency dependence of hydrogen-induced acceleration. They explained the acceleration mechanism based on a hydrogen-enhanced successive fatigue crack growth (HESFCG) model (cf. Fig. 26.10 in Chap. 26) [17, 18].

In this model, the acceleration is not determined by either the presence or absence of hydrogen at the crack tip, but is determined by the distribution of hydrogen near the tip of the fatigue crack. They suggested that a steep gradient of hydrogen at the crack tip causes a localization of plasticity which prevents crack tip blunting and sharpens the crack tip. As a result, the crack growth per cycle is increased.

Conversely, Somerday et al. [12] performed FCG testing on the pipeline steel X52, at various test frequencies in 21 MPa hydrogen gas containing 10, 100 and 1000 vol. ppm oxygen. They discovered that the frequency dependence of FCG acceleration in hydrogen was altered by the oxygen content. Based on these findings, they suggested that the oxygen covering the crack tip surface inhibits the diffusion of hydrogen into the material, thereby modifying the concentration of hydrogen near the crack tip.

Figure 30.7 illustrates the crack growth rate, da/dN , as a function of the stress intensity factor range, ΔK , for JIS-SCM435. The FCG rate is also strongly dependent on hydrogen pressure and test frequency in this material. Figure 30.8 shows the relationship between the RFCGR, $(da/dN)_{H_2}/(da/dN)_{air}$, and the test frequency, f [9]. In contrast to the low carbon steel, JIS-SM490B (cf. Fig. 30.6), this steel revealed an upper bound of FCG acceleration, even in 90 MPa hydrogen.

Fig. 30.7 da/dN - ΔK curves of JIS-SCM435 in air and in hydrogen gas [9]

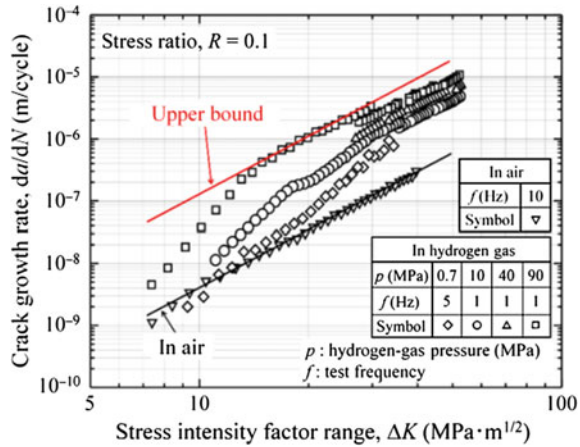
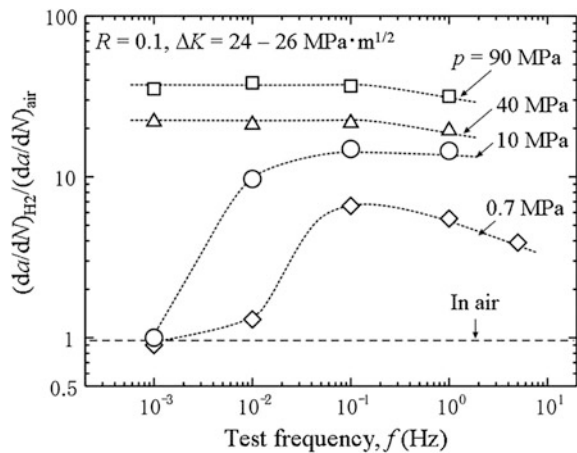


Fig. 30.8 Relationship between $(da/dN)_{\text{H}_2}/(da/dN)_{\text{air}}$ and the test frequency, f , (JIS-SCM435, $\Delta K \approx 25 \text{ MPa m}^{1/2}$) [9]



Based on these results, Yamabe et al. [9] suggested that JIS-SCM435 is appropriate for use in hydrogen gas up to 90 MPa under the design-by-rule (i.e., finite-fatigue life design), if the strength level and microstructure of the steel are properly controlled.

Figure 30.9 shows the crack growth rate, da/dN , as a function of the stress intensity factor range, ΔK , in four types of austenitic stainless steels (Types 304, 316L, XM19 and HP160) in air and in 95–115 MPa hydrogen gas at room temperature [10]. In Type 304, the FCG is markedly accelerated in hydrogen gas, whereas the acceleration rate is not so significant in Types 316L, XM19 and HP160. It should also be noted that, in air, XM19 and HP160 exhibits better FCG resistance than Types 304 and 316L, when compared at the same ΔK level. Measurement by the unloading elastic compliance method [19] revealed that the difference was caused by an enhanced crack closure [20].

Fig. 30.9 da/dN - ΔK curves of austenitic stainless steels, Types 304, 316L, XM-19 and HP160, in 95–115 hydrogen gas at room temperature [10]

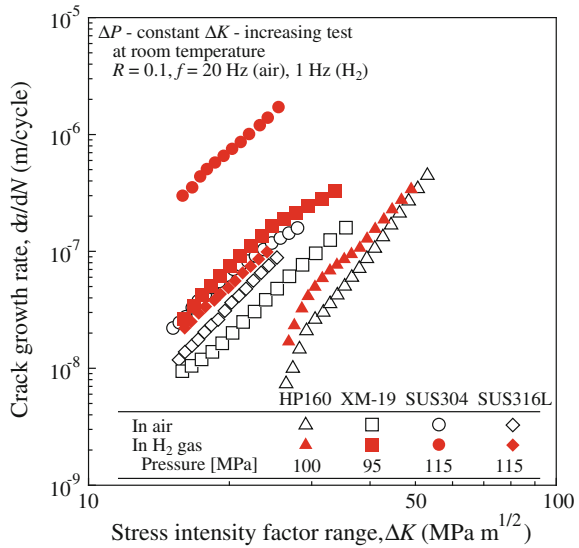


Fig. 30.10 Frequency dependence of the relative fatigue crack growth rate [10]

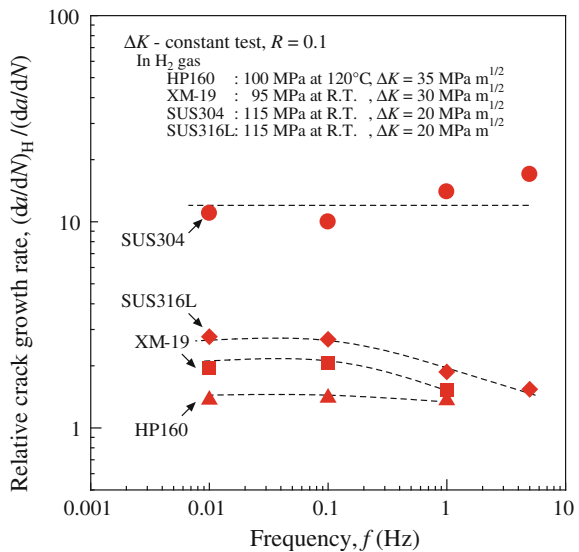
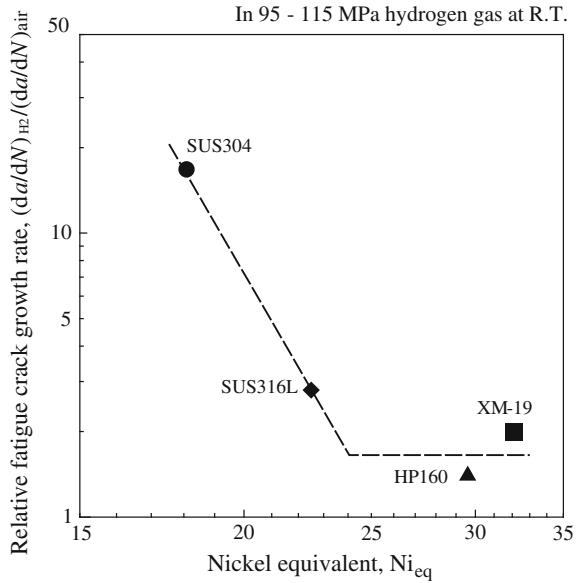


Figure 30.10 presents the RFCGR, $(da/dN)_{H_2}/(da/dN)_{air}$, as a function of the test frequency, f . In Type 304, the RFCGR is greater than 10, whereas the RFCGR remains at or below a maximum of 3 in Type 316L. With respect to Types XM19 and HP160, an even lower RFCGR is exhibited, remaining within a maximum range of 1.5–2. In Types XM19 and 316L, the RFCGR increases with a simultaneous decrease in f in the frequency range of 0.1–5 Hz. However, the RFCGR seems to plateau at an f of 0.01–0.1 Hz. As shown above, Types XM19 and HP160

Fig. 30.11 Relationship between the relative fatigue crack growth rate and the nickel equivalent in austenitic stainless steels [10]



demonstrate excellent FCG resistance, which is hardly degraded even in high-pressure hydrogen gas up to 95–100 MPa.

In austenitic stainless steels, it was reported that the susceptibility of the FCG to hydrogen can be correlated with their austenitic stabilities [10], quantifiable with the nickel equivalent [21]. As illustrated in Fig. 30.11, the steel with a higher austenitic stability possesses a higher FCG resistance to hydrogen. Therefore, the nickel equivalent can serve as an effective grading criterion in the selection of the austenitic stainless steels to be used in high-pressure hydrogen gas atmospheres.

Aluminum alloys are categorized as ‘negligibly-embrittled’ materials in the NASA guidelines [6] and are well known as materials that are highly resistant to hydrogen embrittlement (HE). Figure 30.12 shows the crack growth rate, da/dN , as a function of the stress intensity factor range, ΔK , for A6061-T6 aluminum alloy as obtained in air, 40 MPa hydrogen gas, 90 MPa hydrogen gas and deionized water [11]. Even in high-pressure hydrogen, there is no noticeable acceleration in the FCG rate. Rather, a small amount of moisture in the environment has a significant impact on the FCG acceleration in the alloy.

30.2.2 Morphology of FCG in Hydrogen Gas

In this section, some important features of FCG in hydrogen gas are demonstrated by using the example of the annealed low carbon steel, JIS-SM490B [8]. Clarification of the FCG behavior is necessary for a better understanding of the mechanisms of FCG acceleration, introduced previously in Sect. 30.2.1.

Fig. 30.12 da/dN - ΔK curves of A6061-T6 in air, 40 MPa hydrogen gas, 90 MPa hydrogen gas and deionized water [11]

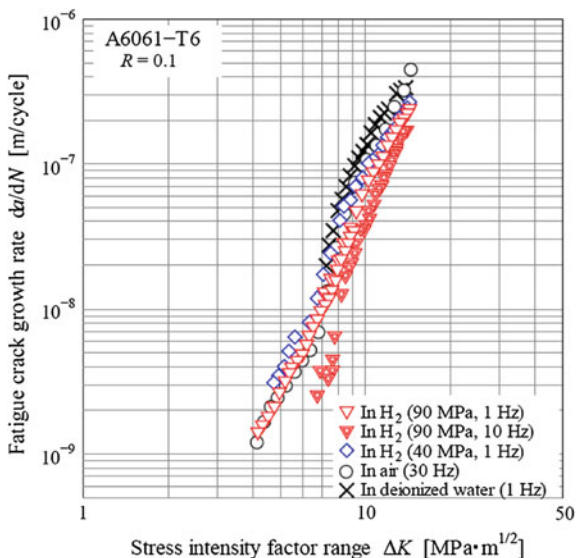


Figure 30.13 shows the striations observed on the fatigue fracture surface of compact tension (CT) specimens at $\Delta K = 30 \text{ MPa m}^{1/2}$ [8]. The tests were performed in air and in 0.7–90 MPa hydrogen gas at various test frequencies. The figure captions also explain the average striation spacing and da/dN , which nearly coincide with each other. In air, a typical ductile striation is observed (Fig. 30.13a). The striation is flat and blurred in the combination of 0.7 MPa hydrogen gas and the test frequency of 1 Hz, where the FCG growth is remarkably accelerated when compared with the growth in air (Fig. 30.13b). Similar striation morphologies are also observed under the influence of hydrogen in other steels [10, 22]. In contrast, in the combination of 0.7 MPa hydrogen gas and the test frequency of 0.001 Hz, where the FCG rate was nearly the same as that in air, the striation morphology is similar to that observed in air (cf. Fig. 30.13a, c). On the other hand, in 90 MPa hydrogen gas, striations are flat and blurred, irrespective of the test frequency used (Fig. 30.13d, e).

Figures 30.14 and 30.15 show laser microscope images of the crack morphology at the surface of the CT specimen, after a ΔK -constant test performed at $\Delta K = 30 \text{ MPa m}^{1/2}$. In Fig. 30.14, the test was initiated in air, after which the test atmosphere was switched to 0.7 MPa hydrogen gas. In air, extensive slip bands are observed along the fatigue crack (Fig. 30.14b). The same proves to be the case for the crack grown in 0.7 MPa hydrogen gas at the frequency of 0.001 Hz (Fig. 30.14d), where the crack growth rate is nearly equivalent to that observed in air. In contrast, in the test in 0.7 MPa hydrogen gas at the frequency of 1 Hz, where the FCG was accelerated by about a factor of 10, very few slip bands are observed along the crack (Fig. 30.14c). It is assumed that this is due to the localization of plastic deformation at the crack tip under the influence of hydrogen. Conversely, in

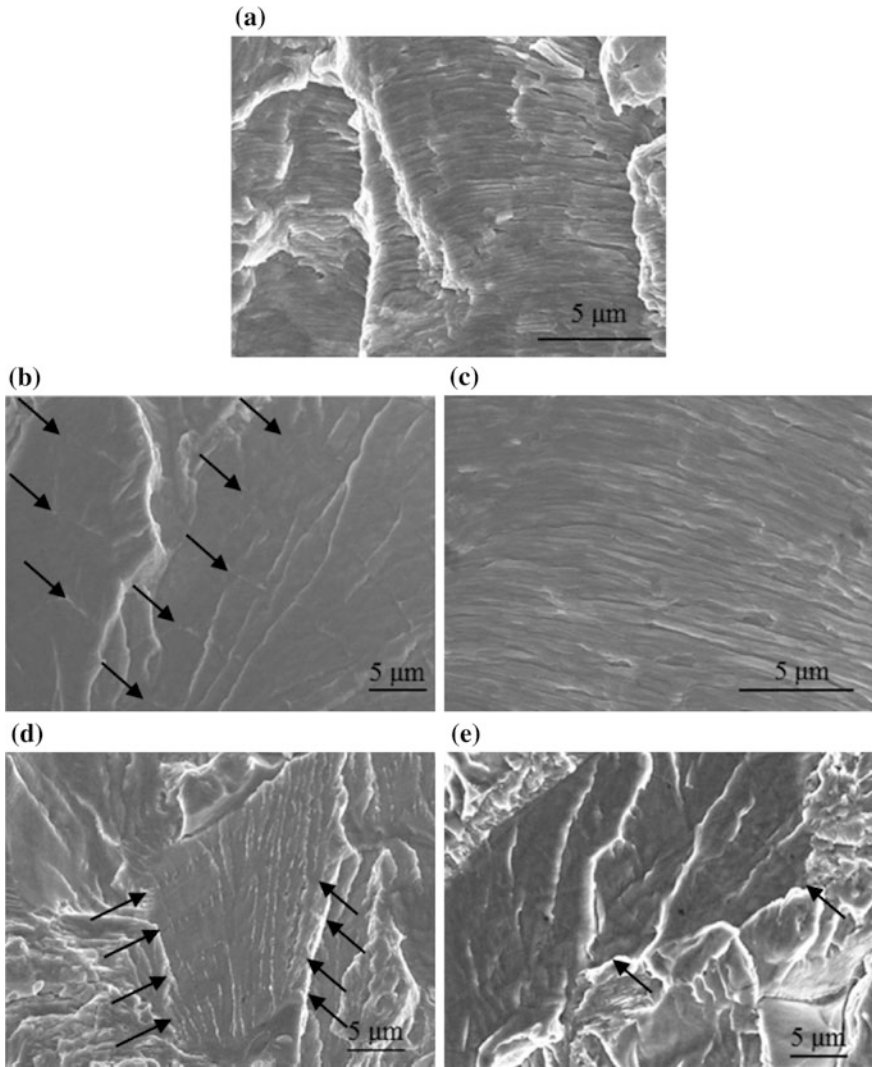


Fig. 30.13 Striations formed in air and in hydrogen gas on annealed low carbon steel, JIS-SM490B. Crack growth is from bottom to top [8]. **a** Air, $f = 10$ Hz, $s = 0.22$ μm , $da/dN = 1.9 \times 10^{-7}$ m/cycle. **b** 0.7 MPa H_2 , $f = 1$ Hz, $s = 6.3$ μm , $da/dN = 2.2 \times 10^{-6}$ m/cycle. **c** 0.7 MPa H_2 , $f = 0.001$ Hz, $s = 0.30$ μm , $da/dN = 3.2 \times 10^{-7}$ m/cycle. **d** 90 MPa H_2 , $f = 1$ Hz, $s = 3.6$ μm , $da/dN = 3.2 \times 10^{-6}$ m/cycle. **e** 90 MPa H_2 , $f = 0.001$ Hz, $s = 15.7$ μm , $da/dN = 1.4 \times 10^{-5}$ m/cycle

the test under 90 MPa hydrogen gas (Fig. 30.15), where growth accelerates at the test frequencies of 1 Hz and 0.001 Hz, very few slip bands are observed along the crack in both cases.

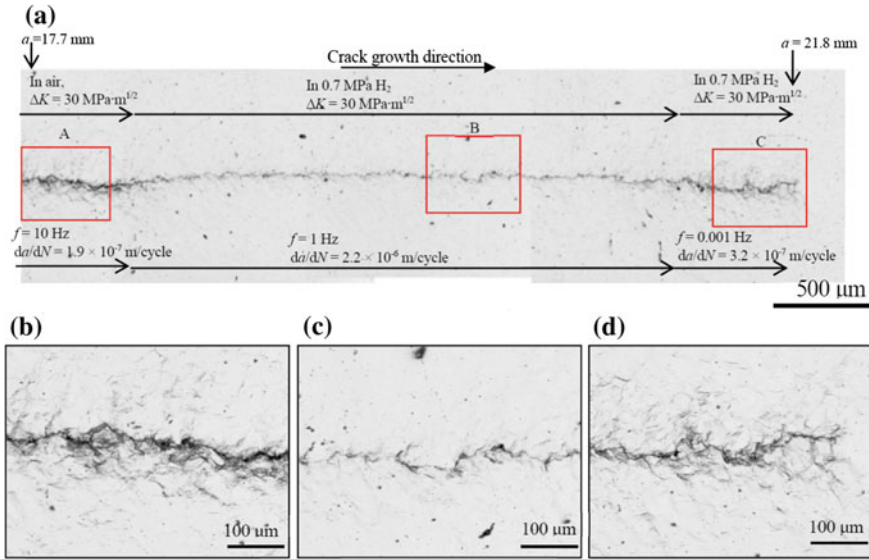


Fig. 30.14 Crack appearance at the specimen surface after the FCG test in 0.7 MPa hydrogen gas (JIS-SM490B) [8]. **a** Low magnification. **b** Enlargement of A. **c** Enlargement of B. **d** Enlargement of C

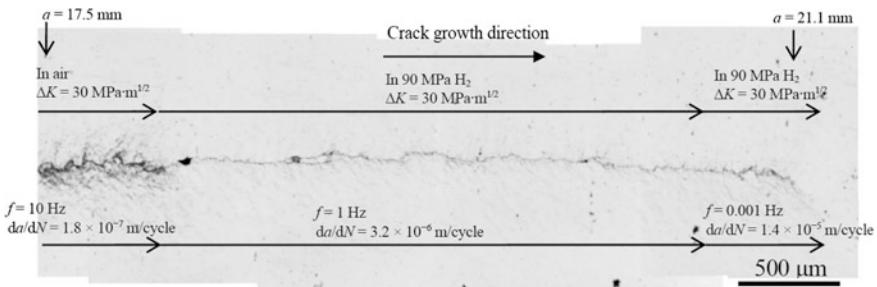


Fig. 30.15 Crack appearance at the specimen surface after the FCG test in 90 MPa hydrogen gas (JIS-SM490B) [8]

The aforementioned results indicate that FCG acceleration due to hydrogen is always accompanied by slip localization at the crack tip. Once again, it is important to note that, even in hydrogen gas, FCG acceleration does not occur when the slip deformation is not localized. Similar phenomena with respect to slip localization at the crack tip were also observed in JIS-SCM435 [16]. Based on these results, it can be concluded that slip localization at the crack tip is a determining factor in the occurrence or non-occurrence of crack growth acceleration, leading also to the difference in the striation morphologies shown in Fig. 30.13. This series of observations seems to support the HESFCG model [17, 18], as described in Chap. 26.

References

1. Matsunaga H, Yoshikawa M, Kondo R, Yamabe J, Matsuoka S (2015) Slow strain rate tensile and fatigue properties of Cr–Mo and carbon steels in a 115 MPa hydrogen gas atmosphere. *Int J Hydrogen Energy* 40:5739–5748
2. Yamada T, Kobayashi H (2012) *J High Press Gas Safety Inst Jpn* 49:885–893
3. Suresh S (1998) *Fatigue of materials*, 2nd edn. Cambridge University Press, Cambridge
4. Ogawa Y, Matsunaga H, Yoshikawa M, Yamabe J, Matsuoka S (2015) Effect of high-pressure hydrogen gas environment on fatigue life characteristics of low alloy steel SCM435 and carbon steel SM490B. In: *Proceedings of the eighth Japan conference on structural safety and reliability*
5. Murakami Y (2002) *Metal fatigue: Effects of small defects and nonmetallic inclusions*. Elsevier Science
6. NASA (1997) *Safety standard for hydrogen and hydrogen systems*. Washington, DC, NSS 1740.16
7. Paris PC, Erdogan F (1963) A critical analysis of crack propagation laws. *Trans ASME Ser D J Basic Eng* 85:528–534
8. Yoshikawa M, Matsuo T, Tsutsumi N, Matsunaga H, Matsuoka S (2014) Effects of hydrogen gas pressure and test frequency on fatigue crack growth properties of low carbon steel in 0.1–90 MPa hydrogen gas. *Trans JSME A* 80
9. Yamabe J, Itoga H, Awane T, Matsuo T, Matsunaga H, Matsuoka S (2016) Pressure cycle testing of Cr–Mo steel pressure vessels subjected to gaseous hydrogen. *J Press Vess Technol ASME* 183–011401:1–13
10. Itoga H, Matsuo T, Orita A, Matsunaga H, Matsuoka S, Hirofumi R (2014) SSRT and fatigue crack growth properties of high-strength austenitic stainless steels in high-pressure hydrogen gas (PVP2014-28640). In: *Proceedings of PVP-2014: ASME pressure vessels and piping division conference*, Anaheim, California, USA, July 20–24 2014 ASME, New York, NY
11. Itoga H, Watanabe S, Fukushima Y, Matsuoka S, Murakami Y (2013) Fatigue crack growth of aluminum alloy A6061-T6 in high pressure hydrogen gas and failure analysis on 35 MPa compressed hydrogen tanks VH3 for fuel cell vehicles. *Trans JSME A* 78:442–457
12. Somerday BP, Sofronis P, Nibur KA, San Marchi C, Kirchheim R (2013) Elucidating the variables affecting accelerated fatigue crack growth of steels in hydrogen gas with low oxygen concentrations. *Acta Mater* 61:6153–6170
13. Yamabe J, Matsunaga H, Furuya Y, Hamada S, Itoga H, Yoshikawa M, Takeuchi E, Matsuoka S (2014) Qualification of chromium–molybdenum steel based on the safety factor multiplier method in CHMC1-2014. *Int J Hydrogen Energy* 40:719–728
14. Macadre A, Artamonov M, Matsuoka S, Furtado J (2011) Effects of hydrogen pressure and test frequency on fatigue crack growth properties of Ni–Cr–Mo steel candidate for a storage cylinder of a 70 MPa hydrogen filling station. *Eng Fract Mech* 78:3196–3211
15. Matsuoka S, Tanaka H, Homma N, Murakami Y (2011) Influence of hydrogen and frequency on fatigue crack growth behavior of Cr–Mo steel. *Int J Fract* 168:101–112
16. Matsuo T, Matsuoka S, Murakami Y (2010) Fatigue crack growth properties of quenched and tempered Cr–Mo steel in 0.7 MPa hydrogen gas. In: *Proceedings of the 18th European conference on fracture (ECF18)*
17. Murakami Y, Kanazaki T, Mine Y, Matsuoka S (2008) Hydrogen embrittlement mechanism in fatigue of austenitic stainless steels. *Metall Mater Trans A* 39:1327–1339
18. Murakami Y, Matsuoka S, Kondo Y, Nishimura S (2012) *Mechanism of hydrogen embrittlement and guide for fatigue design*. Yokendo, Tokyo
19. Kikukawa M, Jono M, Tanaka K, Takatani M (1976) Measurement of fatigue crack propagation and crack closure at low stress intensity level by unloading elastic compliance method. *J Soc Mater Sci Jpn* 25:899–903

20. Orita A, Matsuo T, Matsuoka S, Murakami Y (2013) Tensile and fatigue crack growth properties of high strength stainless steel with high resistance to hydrogen embrittlement in 100 MPa hydrogen gas. In: Proceedings of the 19th European conference on fracture (ECF19)
21. Oshima T, Habara Y, Kuroda K (2007) Effects of alloying elements on mechanical properties and deformation-induced martensite transformation in Cr-Mn-Ni austenitic stainless steels (transformations and microstructures). *Tetsu- to- Hagane* 93:544–551
22. Matsuoka S, Tsutsumi N, Murakami Y (2008) Effects of hydrogen on fatigue crack growth and stretch zone of 0.08 mass % C low carbon steel pipe. *Trans JSME A* 74:1528–1537

Chapter 31

Effect of Hydrogen on the Fretting Fatigue Properties of Metals

Masanobu Kubota

Abstract This chapter describes fretting fatigue of austenitic stainless steels in presence of hydrogen. The fretting fatigue strength is degraded by hydrogen and its mechanisms are revealed based on surface analysis and observations of fretting fatigue cracks and microstructures changed due to adhesion.

Keywords Hydrogen · Fretting fatigue · Austenitic stainless steel · Adhesion · Strain-induced martensitic transformation · Oxide layer · Hydrogen safety

31.1 Fretting Fatigue

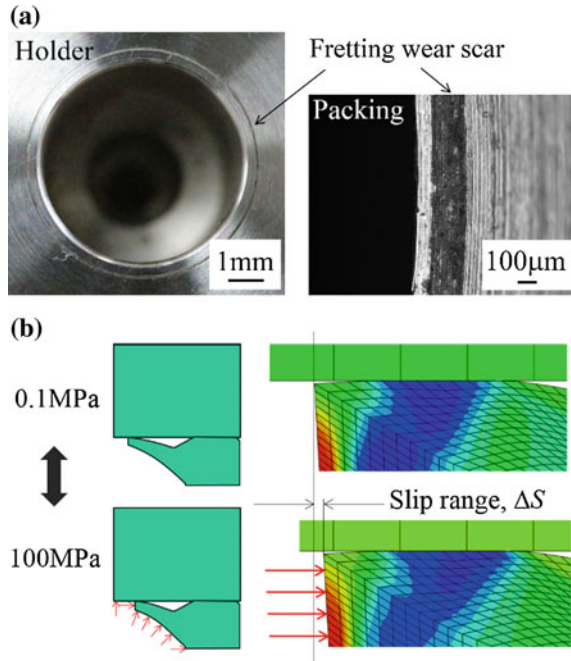
Fretting wear, which was found during the development of metal packing for sealing 100 MPa hydrogen gas is shown in Fig. 31.1 [1]. Fretting is the cyclic relative slip motion with a small slip range which can occur between two surfaces in contact. In the case of the packing, the tip of the packing moves backward several μm with an increase in the hydrogen pressure, and returns to the original position with a decrease in the hydrogen pressure. Thus, pressure cycling caused fretting between the tip of the packing and holder, which results in fretting wear as shown in the figure. The depth of the fretting wear is less than the surface roughness of the holder. However, fretting wear is considered as one of the key issues for the packing during the development, since it is related to the gas tightness.

Fretting is commonly induced by the fatigue loading of one of the members participating in the contact. Therefore, the fretted surface simultaneously suffers from fatigue. This case is termed fretting fatigue. Since the hydrogen environment or hydrogen can influence both the fretting [2, 3] and fatigue [4], it can be expected that the effects of hydrogen on the fretting fatigue properties are very complicated. Coupled with the fact that fretting fatigue results in a much reduced fatigue

M. Kubota (✉)

International Institute for Carbon-Neutral Energy Research (I2CNER),
Kyushu University, Fukuoka 819-0395, Japan
e-mail: kubota.masanobu.304@m.kyushu-u.ac.jp

Fig. 31.1 Fretting in packing for high-pressure hydrogen gas: **a** holder and tip of packing suffering from fretting wear; **b** mechanism causing fretting [1]



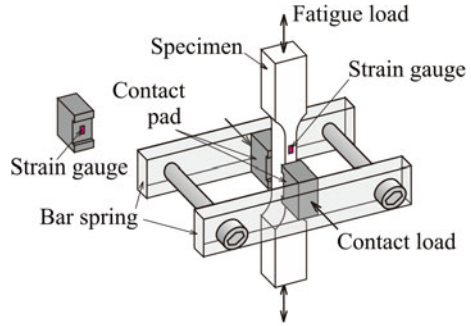
strength, characterization of the fretting fatigue in a hydrogen environment and elucidation of the mechanisms that cause changes in the fretting fatigue properties due to hydrogen are necessary to establish a safe design.

31.2 Fretting Fatigue Test Method

The fretting fatigue strength is strongly affected by the test method [5]. Therefore, the fretting fatigue test method used in this study is specified as shown in Fig. 31.2 [6]. Two contact pads are pressed onto the front and back surfaces of the fatigue test specimen. When a fatigue loading is applied to the specimen, fretting is induced between the contacting surfaces due to the difference in deformation between the specimen and the contact pad.

There are many factors influencing the fretting fatigue strength, such as the combination of materials [7], contact pressure [8], and relative slip range [9]. In addition, fretting fatigue failure can occur in the long life regime when the number of cycles is greater than 10^7 cycles [10]. On the other hand, in plain fatigue, the effect of hydrogen becomes more significant with a reduction in the fatigue loading frequency [11]. Pressure [12], temperature [13], and purity [14] of the hydrogen gas also influence the fatigue properties. As the boundary conditions for the results of the fretting fatigue test shown here, the following information is provided: the

Fig. 31.2 Fretting fatigue test method [6]



contact pad material was the same as that of the specimen, the contact pressure was 100 MPa, the pad length (which is related to the slip range) was 20 μm , the loading frequency was 20 Hz, the hydrogen gas pressure was 0.2 MPa in absolute pressure, the temperature was ambient, the fretting fatigue test was terminated at 10^7 cycles if no failure of the specimen occurred, and the purity of the supplied hydrogen gas was 99.9999 %.

31.3 Effect of Hydrogen on Fretting Fatigue Strength

The fretting fatigue strength of JIS-SUS304 austenitic stainless steel in hydrogen gas is shown in Fig. 31.3. The fretting fatigue strength of the JIS-SUS304 is significantly lower in hydrogen gas (black circles) than in air (white circles).

The effect of the hydrogen charge on the fretting fatigue strength of the JIS-SUS304 is shown in Fig. 31.4. Hydrogen charging was performed by a thermal method in which the specimen was exposed to high-pressure hydrogen gas at an elevated temperature for a specified time. The hydrogen concentration in the material is shown in the figure. The fretting fatigue strength in air (white circles) was significantly reduced by the hydrogen charge (half white/black circles). When the fretting fatigue test of the hydrogen-charged material was done in hydrogen gas, the reduction in the fretting fatigue strength was very significant (black circles).

Based on the above results, gaseous hydrogen and internal hydrogen independently reduced the fretting fatigue strength of the JIS-SUS304. In other words, gaseous hydrogen and internal hydrogen have different mechanisms to reduce the fretting fatigue strength. The mechanisms will be described in the following section.

The plain fatigue strength without fretting is also shown in Figs. 31.3 and 31.4. The plain fatigue limit of the JIS-SUS304 in hydrogen was the same as that in air, and the fatigue life was rather longer in the hydrogen gas than that in air (Fig. 31.3, white and black diamonds). There is a report that the high-cycle fatigue strength in hydrogen gas increases when loading frequency is relatively high [15]. One of the possible reasons is that the diffusion of hydrogen to the crack tip does not catch up

Fig. 31.3 Fretting fatigue strength of JIS-SUS304 in hydrogen gas (0.2 MPa abs)

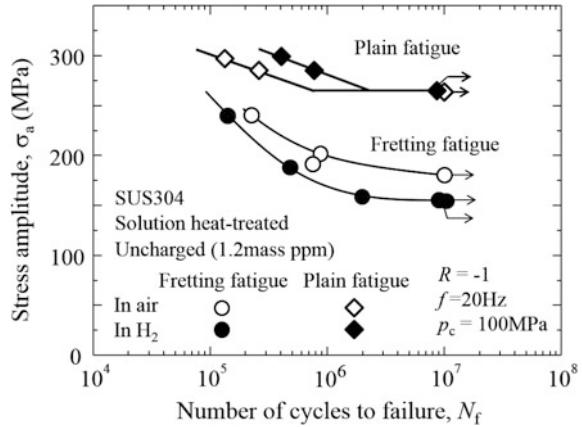
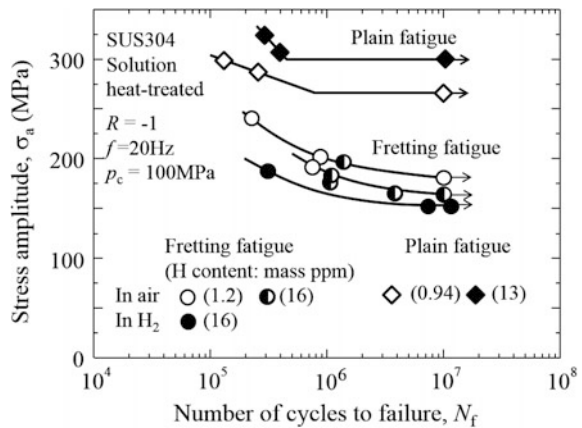


Fig. 31.4 Effect of hydrogen charge on the fretting fatigue strength of JIS-SUS304



with the critical hydrogen concentration, which causes the hydrogen-assisted failure.

The plain fatigue strength of the hydrogen-charged material was higher than that in air (Fig. 31.4). An increase in the crack growth resistance due to the hydrogen charge is reported in similar types of stainless steels [16]. The pertinent point is that the effect of the hydrogen on the samples is different or completely the opposite between the fretting fatigue test and the plain fatigue test. Fretting clearly has some effects that assist with hydrogen-assisted fatigue failure.

31.4 Mechanisms for the Hydrogen-Induced Reduction in Fretting Fatigue Strength

31.4.1 Local Adhesion Between Contacting Surfaces

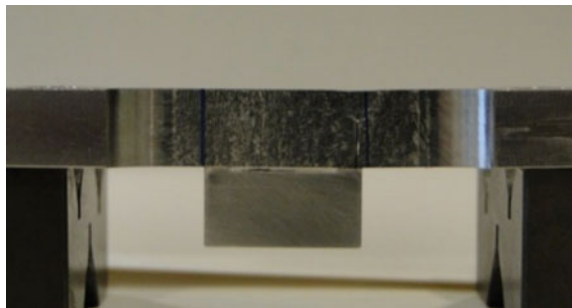
The specimen and contact pad after the fretting fatigue test in hydrogen gas is shown in Fig. 31.5 [17]. The specimen and pad did not separate when the contact load was removed. During the fretting in hydrogen gas, the protection layer on the stainless steel was removed by fretting, and no oxidation occurs from then on. Therefore, adhesion becomes dominant during the damaging process. On the other hand, adhesion similar to Fig. 31.5 did not occur during the fretting fatigue test in air, since the contact surfaces of the specimen and pad are separated by oxidized fretting wear particles.

The adhered specimen and pad were cut along the specimen axis without disassembling. The section is shown in Fig. 31.6 [18]. There are many small cracks at the interface between the specimen and pad. The small cracks propagate in two directions at which the small cracks make angles of approximately 45 or 135° to the contact surface. During the fretting fatigue in air, small oblique cracks and multiple small cracks are the typical characteristics [19]. However, the angle of the oblique small cracks is constant in the narrow region [20]. The morphology of the small fretting fatigue cracks in hydrogen gas is unique compared to that observed in air.

In the photograph, the interface between the specimen and pad is meandering and discontinuous at positions A, B, and C. This is evidence of adhesion. At position D where no adhesion occurs because the boundary is straight, there are no fretting fatigue cracks. Therefore, the formation of small cracks is associated with local adhesion. There is a major crack leading to specimen failure at position C. This major crack started to grow from one of the small cracks that emanated from the adhered spot. Therefore, adhesion and the subsequent formation of many small cracks are one of the root causes of reduced fretting fatigue strength in hydrogen gas.

The change in the damaging process causes a significant change in the morphology of the fretting damage, as shown in Fig. 31.7. Fretting wear dimples were observed after the fretting fatigue test in air, elongated in the slip direction.

Fig. 31.5 Adhered specimen and contact pad after fretting fatigue test in hydrogen gas (JIS-SUS316L, noncharged, $\sigma_a = 200$ MPa, $N_f = 5.4 \times 10^5$) [17]



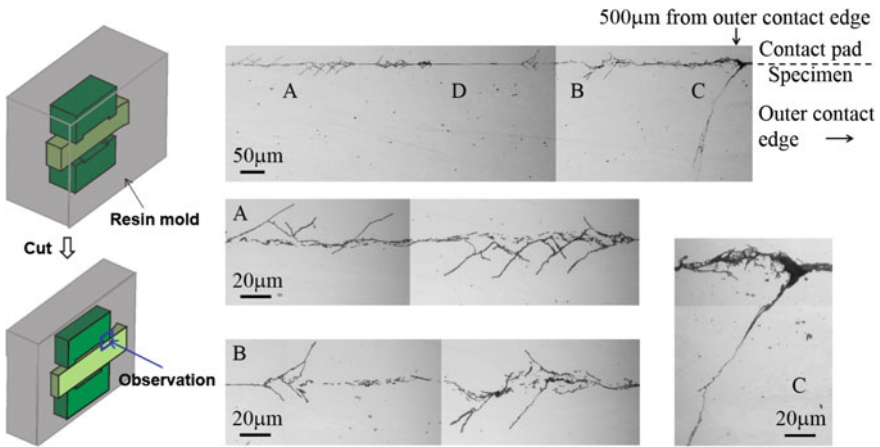


Fig. 31.6 Observation of adhered part at the longitudinal section of the specimen and pad after fretting fatigue test in hydrogen gas (JIS-SUS304, $\sigma_a = 180$ MPa, $N = 1.0 \times 10^6$) [18]

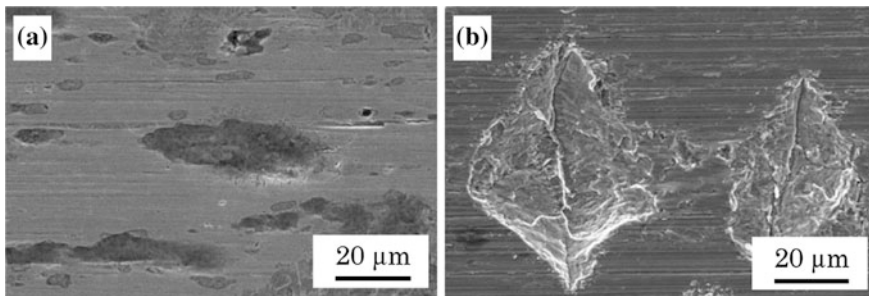


Fig. 31.7 Fretting damage of noncharged JIS-SUS304. Fretting occurred in horizontal direction: **a** in air, $\sigma_a = 183$ MPa, $N_f = 2.96 \times 10^6$; **b** in hydrogen gas, $\sigma_a = 188$ MPa, $N_f = 2.23 \times 10^6$ [18]

V-shaped grooves were observed after the fretting fatigue test in hydrogen gas, growing perpendicular to the slip direction. The inside surface of the grooves displays typical features of a fatigue fracture surface.

31.4.2 Hydrogen-Induced Reduction in Critical Stress to Crack Initiation

Adhesion causes crack initiation during the fretting fatigue in hydrogen gas. However, this is caused by an increase in the mechanical stress at the adhered spot. A similar mechanism can work in other non-oxidative environments or vacuum.

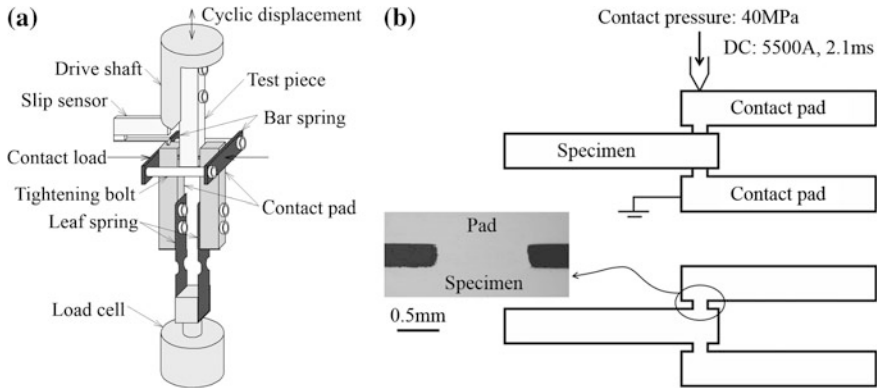


Fig. 31.8 Fatigue test method to simulate crack initiation during fretting fatigue test in hydrogen gas. The adhered spot is artificially produced by spot welding: **a** test apparatus; **b** spot-welded specimen [22]

For instance, there has been research in which fretting crack initiation in a vacuum is discussed in relation to the adhesion [21]. Therefore, the essential role of hydrogen in reducing the fretting fatigue strength was investigated. For fretting fatigue, crack propagation at the position distant from the contact surface is no different from that of plain fatigue. Thus, the effect of hydrogen on the crack initiation was investigated.

The fatigue test method for the characterization of the crack initiation from the adhered spot including the effect of hydrogen is shown in Fig. 31.8 [22]. As shown in Figs. 31.6 and 31.7, the size and position of the adhered spot during the fretting fatigue in hydrogen gas were random. Therefore, an adhesion spot was artificially produced by spot welding in order to avoid such a random event during the evaluation. This test is not classed as fretting because there is no relative slip. It is regarded as a kind of low-cycle fatigue test, but the crack initiation from the adhered spot was well reproduced. The fatigue test was interrupted at 10^5 cycles, and initiation of an approximately $100\ \mu\text{m}$ crack was identified.

The result is shown in Fig. 31.9 [22]. The critical stress to crack initiation is significantly lower in the hydrogen gas (Fig. 31.9b) than in air (Fig. 31.9a). The critical stress to crack initiation for the hydrogen-charged specimen (Fig. 31.9c) is also reduced compared to that of the noncharged specimen (Fig. 31.9a). These results clearly indicate that hydrogen gas or hydrogen charging assists with the crack initiation under adhesion conditions.

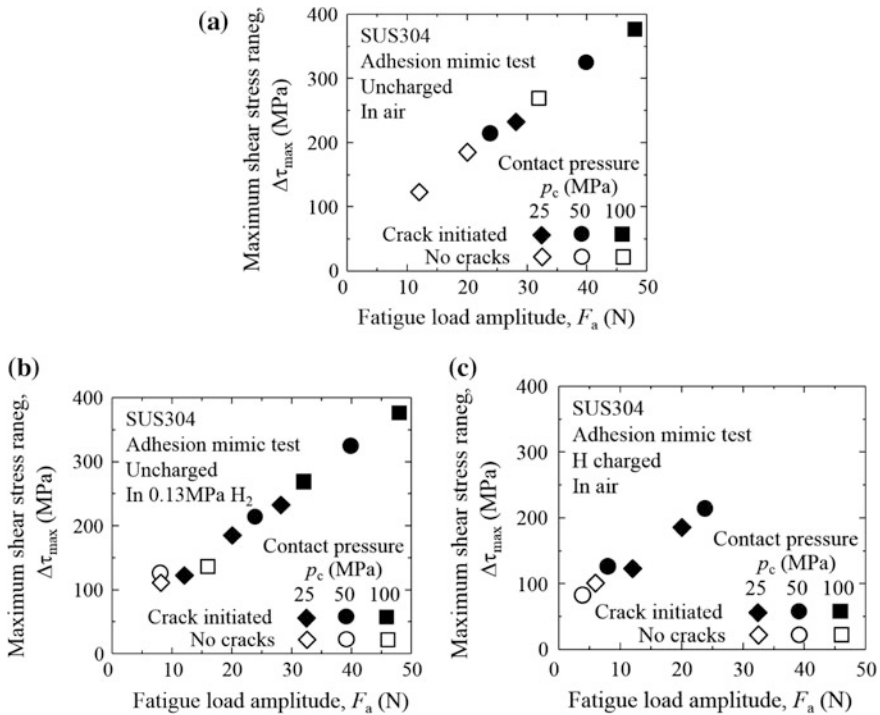


Fig. 31.9 Results of adhesion mimic fatigue test of JIS-SUS304: **a** noncharged in air; **b** noncharged in hydrogen gas; **c** hydrogen-charged in air [22]

31.4.3 Microstructure Change Due to Adhesion

As described in the previous sections, local adhesion during fretting fatigue in hydrogen is one of the root causes of reduced fretting fatigue strength in hydrogen gas. In this section, microstructural changes at the adhered spot are discussed in relation to the effects of hydrogen. The microstructure at the adhered spot during the fretting fatigue in hydrogen is shown in Fig. 31.10 [1]. The original grain size before the fretting fatigue test was several tens of μm . However, a very fine microstructure was found at the adhered spot. This indicates that an extremely high strain was cyclically produced in the material in the adhered spot. In addition to the fact that repeated higher strain simply causes fatigue cracks, hydrogen diffusion might be enhanced by the interaction between the dislocation motion and hydrogen [23]. Furthermore, assuming the hydrogen-enhanced localized plasticity (HELP) model [24], plastic deformation is essential for the hydrogen-assisted fatigue fracture.

The same position in Fig. 31.10 was observed by electron backscatter diffraction (EBSD), and a phase map of the adhered part is shown in Fig. 31.11 [25]. Alpha iron, which is considered to be strain-induced martensite (α'), was detected at the

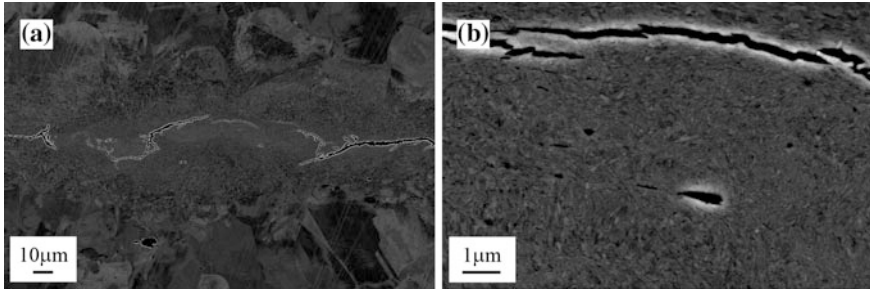
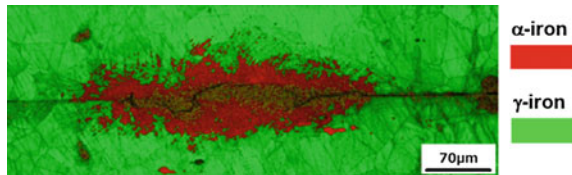


Fig. 31.10 Microstructure refinement at adhered spot during fretting fatigue in hydrogen gas. The material was JIS SUS316L. $\sigma_a = 182$ MPa, $N_f = 10^6$: **a** adhered spot; **b** enlargement of boundary between contact pad and specimen [1]

Fig. 31.11 EBSD observation of the adhered part between fretting surfaces, at the same position as shown in Fig. 31.10 [25]



adhered spot despite the material being a stable JIS-SUS316L austenitic stainless steel. In addition to the ultrafine microstructure, the presence of the strain-induced martensite also indicated that the material in the adhered spot underwent severe cyclic plastic deformation.

As a result of microstructure transformation from austenite to martensite, rapid diffusion of hydrogen into the material could occur, since the diffusivity of hydrogen is significantly greater in the martensitic phase than in the austenitic phase [26]. Furthermore, martensite is more vulnerable to hydrogen than austenite [27]. These are particular phenomena for fretting, and are also major reasons for the significant reduction in the fatigue strength.

Results of X-ray photoelectron spectroscopy (XPS) of the fretted JIS-SUS304 surface in high-purity hydrogen gas (0.088 vol. ppm O_2) are shown in Fig. 31.12 [28]. The vertical axis is the abundance ratio of pure iron and iron oxide. The horizontal axis is the depth below the surface. In the case of the unfretted surface, iron oxide is dominant at a very shallow depth. On the other hand, in the case of the fretted surface in high-purity hydrogen, the pure iron is dominant. It is therefore confirmed that fretting removes the original oxide layer of the stainless steel. Formation of a fresh surface is another function of fretting that activates the interaction between hydrogen and the test material.

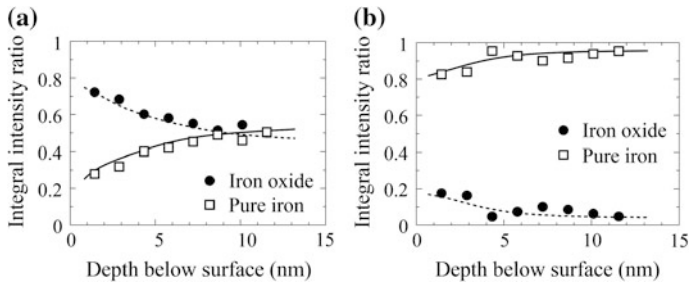


Fig. 31.12 XPS analysis of oxide on the fretted surface of JIS-SUS304 in hydrogen gas or air: **a** unfretted; **b** fretted in high-purity hydrogen gas (0.088 vol. ppm O₂) [28]

References

1. Kubota M, Komoda R (2015) Fretting fatigue in hydrogen environment. *Tribologist* 60: 651–657
2. Izumi N, Mimuro N, Morita T, Sugimura J (2009) Fretting wear tests of steels in hydrogen gas environment. *Tribol Online* 4:109–114
3. Izumi N, Morita T, Sugimura J (2011) Fretting wear of a bearing steel in hydrogen gas environment containing a trace of water. *Tribol Online* 6:148–154
4. Johnson WH (1874) On some remarkable changes produced in iron and steel by the action of hydrogen and acids. *Proc R Soc Lon* 23:168–179
5. Kondo Y, Bodai M (1997) Study on fretting fatigue crack initiation mechanism based on local stress at contact edge. *Trans JSME A* 63:669–676
6. Kubota M, Nishimura T, Kondo Y (2010) Effect of hydrogen concentration on fretting fatigue strength. *J Solid Mech Mater Eng* 4:1–14
7. Nagata K, Fukakura J (1992) Effect of contact materials on fretting fatigue strength of 3.5Ni–Cr–Mo–V rotor steel and life-prediction method. *Trans JSME A* 58:1561–1568
8. Nishioka K, Hirakawa K (1971) Fundamental investigation of fretting fatigue (part 6, effects of contact pressure and hardness). *Trans JSME* 3:1051–1058
9. Nishioka K, Hirakawa K (1969) Fundamental investigation of fretting fatigue (part 2, fretting fatigue testing machine and some test results). *Bull JSME* 12:180–187
10. Hirakawa K, Toyama K, Kubota M (1998) Analysis and prevention of failure in railway axles. *Int J Fat* 20:135–144
11. Hayakawa M, Takeuchi M, Matsuoka S (2014) Hydrogen fatigue-resisting carbon steels. *Procedia Mater Sci* 3:2011–2015
12. Macadre A, Artamonov M, Matsuoka S, Furtado J (2011) Effects of hydrogen pressure and test frequency on fatigue crack growth properties of Ni–Cr–Mo steel candidate for a storage cylinder of a 70 MPa hydrogen filling station. *Eng Fract Mech* 782:3196–3211
13. Fassina P, Brunella MF, Lazzari L, Reb G, Vergani L, Sciuccati A (2013) Effect of hydrogen and low temperature on fatigue crack growth of pipeline steels. *Eng Fract Mech* 103:10–25
14. Somerdar BP, Sofronis P, Nibur KA, San Marchi C, Kirchheim R (2013) Elucidating the variables affecting accelerated fatigue crack growth of steels in hydrogen gas with low oxygen concentrations. *Acta Mater* 61:6153–6170
15. Kubota M, Kawakami K (2014) High-cycle fatigue properties of carbon steel and work-hardened oxygen free copper in high pressure hydrogen. *Adv Mater Res* 891–892:575–580
16. Murakami Y, Kanezaki T, Mine Y (2010) Hydrogen effect against hydrogen embrittlement. *Metall Mater Trans A* 41:2548–2562

17. Furtado J, Komoda R, Kubota M (2013) Fretting fatigue properties under the effect of hydrogen and the mechanisms that cause the reduction in fretting fatigue strength. In: Proceedings of ICF13, Beijing, China, S16–003
18. Kubota M, Tanaka Y, Kuwada K, Kondo Y (2010) Mechanism of reduction of fretting fatigue limit in hydrogen gas in SUS304. *J Soc Mater Sci Jpn* 59:439–446
19. Endo K, Goto H (1976) Initiation and propagation of fretting fatigue cracks. *Wear* 38:311–324
20. Nishioka K, Hirakawa K (1969) Fundamental investigation of fretting fatigue (part 3, some phenomena and mechanisms of surface cracks). *Bull JSME* 12:397–407
21. Iwabuchi A, Kayaba T, Kato K (1983) Effect of atmospheric pressure of friction and wear of 0.45 %C steel in fretting. *Wear* 91:289–305
22. Komoda R, Yoshigai N, Kubota M, Furtado J (2014) Reduction in fretting fatigue strength of austenitic stainless steels due to internal hydrogen. *Adv Mater Res* 891–892:891–896
23. Sofronis P, McMeeking RM (1989) Numerical analysis of hydrogen transport near a blunting crack tip. *J Mech Phys Solid* 37:317–350
24. Birnbaum HK, Sofronis P (1994) Hydrogen-enhanced localized plasticity: a mechanism for hydrogen-related fracture. *Mater Sci Eng A* 176:191–202
25. Kubota M, Shiraishi Y, Komoda R, Kondo Y, Furtado J (2012) Considering the mechanisms causing reduction of fretting fatigue strength by hydrogen. In: Proceedings of ECF19, Kazan, Russia, p 281
26. Nelson HG, Stein JE (1973) Gas-phase hydrogen permeation through alpha iron, 4130 steel, and 304 stainless steel from less than 100 C to near 600 C. NASA TN D-7265
27. San Marchi C, Somerday BP, Tang X, Schiroky GH (2008) Effects of alloy composition and strain hardening on tensile fracture of hydrogen-precharged type 316 stainless steels. *Int J Hydrogen Energy* 33:889–904
28. Komoda R, Kubota M, Furtado J (2015) Effect of addition of oxygen and water vapor on fretting fatigue properties of an austenitic stainless steel in hydrogen. *Int J Hydrogen Energy* 40:16868–16877

Chapter 32

Structural Design and Testing

Junichiro Yamabe

Abstract This chapter describes various design methods of components in consideration for the detrimental effect of hydrogen. Based on the design method, fatigue life and leak before break assessments of Cr–Mo steel pressure vessels subjected to hydrogen-pressure cycling are performed.

Keywords Safety factor multiplier method · Design by rule · Design by analysis · Leak before break · Fracture toughness · Operation history · Pressure vessel · Hydrogen safety

32.1 Design Methods in Consideration of the Effects of Hydrogen

In anticipation of the commercialization of fuel cell vehicles (FCVs) and hydrogen stations, numerous components (e.g., vessels, valves, regulators, and metering devices) are being developed for use with high-pressure gaseous hydrogen. In the selection and qualification of materials for use with hydrogen gas, susceptibility to hydrogen embrittlement (HE) must be considered. This is dependent on various factors, such as the pressure of the hydrogen gas, the temperature, and the loading conditions [1, 2].

One of the design methods used in consideration of the hydrogen effect is Article KD-10 (Special Requirements for Vessels in High-Pressure Gaseous Hydrogen Transport and Storage Service) in ASME BPVC VIII-3, which is based on the fracture mechanics approach [3]. Furthermore, to permit evaluation of hydrogen compatibility and the suitability of materials for hydrogen service, the Canadian Standards Association (CSA) has published CHMC1-2014 (Test Method for Evaluating Material Compatibility in Compressed Hydrogen Applications—Phase I—Metals)

J. Yamabe (✉)

International Research Center for Hydrogen Energy, Kyushu University,
Fukuoka 819-0395, Japan
e-mail: yamabe.junichiro.575@m.kyushu-u.ac.jp

© Springer Japan 2016

K. Sasaki et al. (eds.), *Hydrogen Energy Engineering*,
Green Energy and Technology, DOI 10.1007/978-4-431-56042-5_32

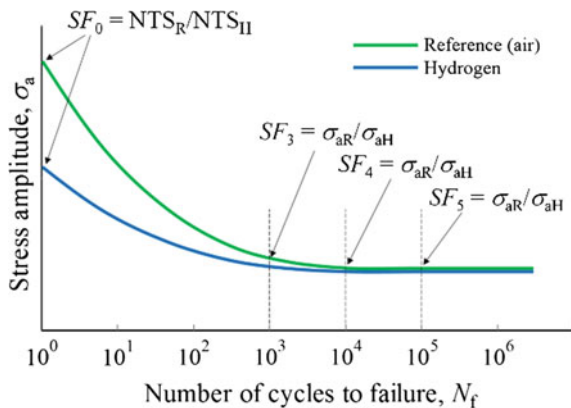
439

[4, 5], which standardizes materials qualification procedures and provides quantitative metrics as one option for qualification of a material for specific conditions of intended service. One option for qualification testing stipulated in CHMC1-2014 is the so-called “safety factor multiplier method,” in which tests of fatigue life are used to determine a safety factor to account for the effects of hydrogen on strength and fatigue. When a safety factor based on the safety factor multiplier method is introduced, the hydrogen components can be designed by using tensile and fatigue properties in air. Another option is to use any generally accepted design methodology based on design by rule or design by analysis [6–13]. This strength design is performed on the basis of tensile and fatigue data in hydrogen gas.

32.2 Safety Factor Multiplier Method

Figure 32.1 shows how the safety factor multiplier is determined [4, 5]. After appropriate statistical treatment of the data, the ratio of stress in the reference environment, σ_{aR} , relative to that in a hydrogen environment, σ_{aH} , is determined at 10^3 , 10^4 , and 10^5 cycles; and this ratio is generally greater than or equal to one. The ratio of the notch tensile strength (NTS) is also determined. The safety factor multiplier is the largest of these ratios, and it must be used as a multiplier for other safety factors considered in the design. The safety factor multipliers of various steels are given in Ref. [14]. The results confirm that the safety factor multiplier method provides overly conservative safety factors (for ex., 12 for design by rule and 7.2 for design by analysis in a Cr–Mo steel). The safety factor multiplier

Fig. 32.1 Schematic of the safety factor multiplier method from the CHMC1 standard [4, 5]



method provides a safe result for any application, but it is likely to be overly conservative for most. Thus, when possible, designers should always use a generally accepted design methodology based on design by rule or design by analysis for specific component application [14–16].

32.3 Design by Rule

The strength design of mechanical components used for high-pressure gases can be categorized into two methods: design by rule and design by analysis [6–13]. In design by rule, an infinite life design is applied by using a safety factor, S_R , as defined by the following equation:

$$S_R = \frac{\sigma_B}{\sigma_{\text{allowable}}}, \quad (32.1)$$

where σ_B is the tensile strength of the material and $\sigma_{\text{allowable}}$ is the allowable design stress. In some cases, the flow stress σ_{flow} is used instead of σ_B , as follows:

$$S_R = \frac{\sigma_{\text{flow}}}{\sigma_{\text{allowable}}}, \quad \sigma_{\text{flow}} = \frac{\sigma_Y + \sigma_B}{2}, \quad (32.2)$$

where σ_Y is the yield stress. In fatigue limit design, the value of S_R is specified to be 3.5–4.0 in existing design codes [6–8]. Such S_R values are justified by the presence of a fatigue limit in various types of steels with low or moderate strength (<1 GPa).

Figure 32.2 shows the slow strain rate testing (SSRT) properties of Cr–Mo steel in 115 MPa nitrogen or hydrogen gas at various temperatures [15]. The results evidently show that there is no degradation in the tensile strength obtained in SSRT, regardless of test temperature. The S – N curves of the same Cr–Mo steel at room temperature in 115 MPa hydrogen gas and in air are shown in Fig. 30.1. The fatigue limits in air and in 115 MPa hydrogen gas are nearly equal. Based on the definition of the safety factor (Eq. 32.1), it is proposed that a material is suitable for service in hydrogen gas by design by rule (which requires only material selection and the determination of wall thickness by stress analysis) if it fulfills the following two criteria at the maximum design pressure of hydrogen gas; (A) there is no degradation in the tensile strength in SSRT; and (B) there is no degradation in the fatigue limit. For example, according to the series of experimental findings in the present study, taken in conjunction with the above criteria, Cr–Mo steels with a moderate strength (tensile strength <900 MPa) are judged to be eligible for design by rule on the basis of a safety factor.

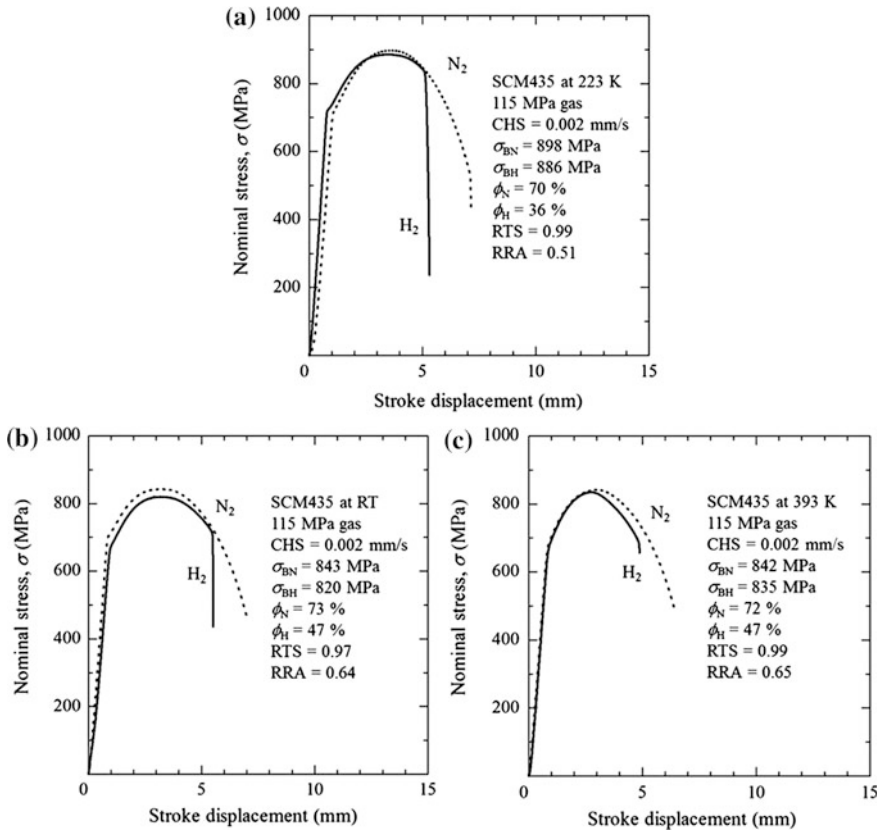


Fig. 32.2 SSRT properties of Cr–Mo steel in 115 MPa nitrogen or hydrogen gas at a 223 K, b room temperature, and c 393 K [15]

32.4 Design by Analysis

In design by analysis, safety factors (for example, $S_R = 2.4\text{--}3.0$) are used for finite life design [9–13], which additionally requires leak before break (LBB) assessment and fatigue life prediction using a stress-based approach or a fracture mechanics-based approach. The LBB assessment for hydrogen-service components should be performed by using the fracture toughness in air rather than that in gaseous hydrogen, as recommended in CHMC1-2014 [4]. Justification for using the fracture toughness in air has also been shown in terms of hydrogen-pressure cycle tests on Cr–Mo steel pressure vessels, as mentioned in Sect. 32.6.

The $S\text{--}N$ curve in gaseous hydrogen shown in Fig. 30.1 can be used for fatigue life prediction using a stress-based approach. Fatigue life prediction can also be conducted by means of a fracture mechanics approach, taking into consideration hydrogen-enhanced fatigue crack growth (FCG) acceleration [17, 18].

The FCG behavior of a Cr–Mo steel, JIS-SCM435, with a tensile strength less than 900 MPa, was previously shown in Figs. 30.7 and 30.8. In those figures, hydrogen-induced FCG acceleration is observed; however, there is an upper bound of the FCG acceleration, which is approximately 30 times the acceleration. Therefore, it is proposed that a material is eligible for hydrogen service under design by analysis if there is an upper bound on FCG acceleration in the hydrogen environment, such as the FCG behavior of the Cr–Mo steel shown in Figs. 30.7 and 30.8. On the basis of this criterion, Cr–Mo steels with moderate strength (for ex., tensile strength <900 MPa) and austenitic stainless steels of Types 304, 316, and 316L [19] are judged to be eligible for finite life design on the basis of a safety factor.

In contrast, bearing steel with $\sigma_B > 1900$ MPa showed a completely different FCG behavior from the present Cr–Mo steel, in that it had no upper bound of FCG acceleration, as shown in Fig. 26.11 [20].

32.5 Importance of Operation Histories

Figure 32.3 shows the fatigue lives for two hydrogen cylinders predicted using the fracture mechanics approach. One of the components is a transport cylinder with an outer diameter of 355 mm operated at a maximum pressure of 20 MPa and a stress ratio of 0.2. The other is a storage cylinder for a hydrogen station; the cylinder has an outer diameter of 355 mm and is operated at a maximum pressure of 106 MPa and a stress ratio of 0.8. These are both common operating conditions; storage cylinders for hydrogen stations generally operate at a high stress ratio, such as $R = 0.8$.

Calculations were performed for $\sigma_B = 900$ MPa and $S_R = 2.4$. As a result, the required wall thickness t was determined to be 9.25 mm for the transport cylinder and 44.75 mm for the storage cylinder. In these calculations, the allowable design stress, $\sigma_{\text{allowable}}$, was determined by the maximum hoop stress at the inner surface of the cylinder. It is also assumed that the initial crack depth, c_0 , with a length-to-depth ratio (l_0/c_0) of 3, was 0.5 mm for the transport cylinder with $t = 9.25$ and 1.1 mm for the storage cylinder with $t = 44.75$ mm, in accordance with the KHK S 0220 standard [13]. From experimental results obtained with real Cr–Mo steel pressure vessels [16], the length-to-depth ratio of the crack in the cylinders was also assumed to retain its initial value of 3 throughout the FCG life calculation.

The predicted FCG life, N_f , of the transport cylinder was approximately 4,000 cycles for a maximum pressure of 20 MPa at a stress ratio of 0.2; the N_f value for the storage cylinder for the hydrogen station was approximately 150,000 cycles for a maximum pressure of 106 MPa at a stress ratio of 0.8. In contrast, if these FCG lives were calculated without considering the operational histories ($R = 0$), the predicted value of N_f would be approximately 3,000 cycles for the transport cylinder and 1,500 cycles for the storage cylinder. Therefore, the predicted value of N_f for the storage cylinder with consideration of the operation history was two orders of magnitude longer than that without consideration of the operational history.

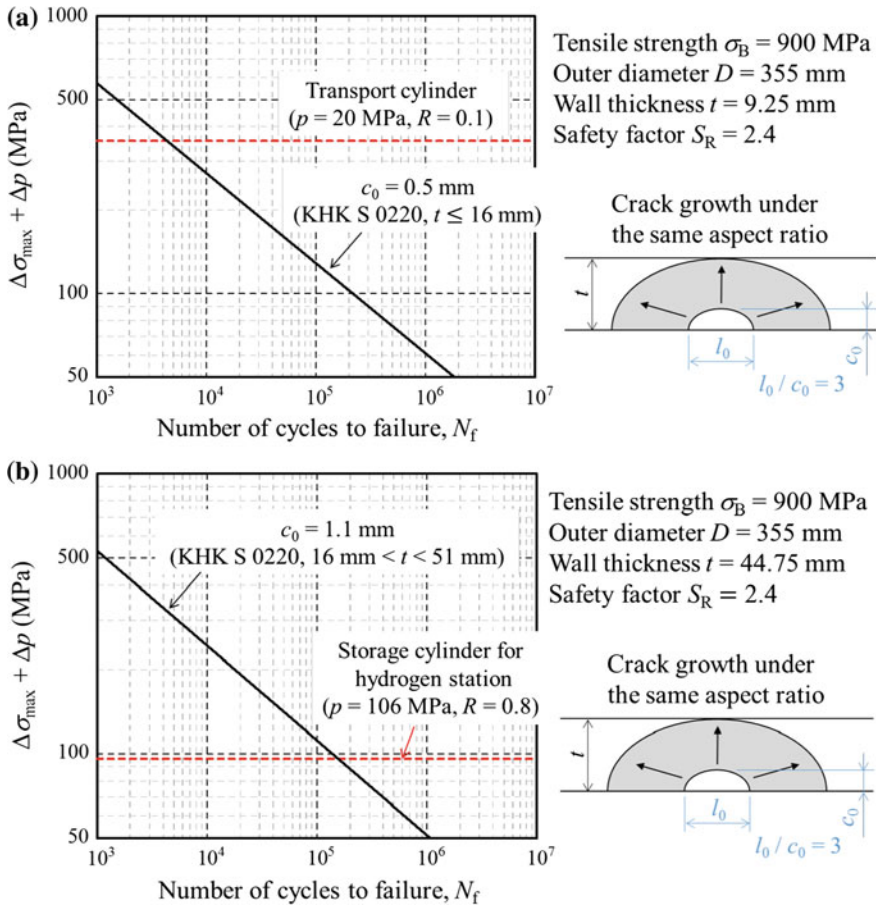


Fig. 32.3 Predicted FCG lives for a transport and b storage cylinders under high-pressure hydrogen gas

Therefore, it is concluded that consideration of the operational history is crucial for precise prediction of the FCG life of hydrogen-service components.

32.6 Pressure Cycling of Real Pressure Vessels

32.6.1 Materials and Pressure Vessels

Pressure cycle tests were performed on two types of Cr–Mo steel pressure vessels with respective inner diameters of 306 and 210 mm and notches machined on the internal surfaces under hydrogen gas pressures between 0.6 and 45 MPa at room temperature. One of the Cr–Mo steels had a fine microstructure with a tensile

strength of 828 MPa (steel A), whereas the other had a coarse microstructure with a tensile strength of 947 MPa (steel B). The chemical composition of A was 0.38 C, 0.22 Si, 0.79 Mn, 0.006 P, 0.004 S, 1.10 Cr, and 0.23 Mo (in mass%); the remainder was Fe. The chemical composition of B was 0.37 C, 0.21 Si, 0.77 Mn, 0.012 P, 0.007 S, 1.07 Cr, and 0.28 Mo; the remainder was Fe.

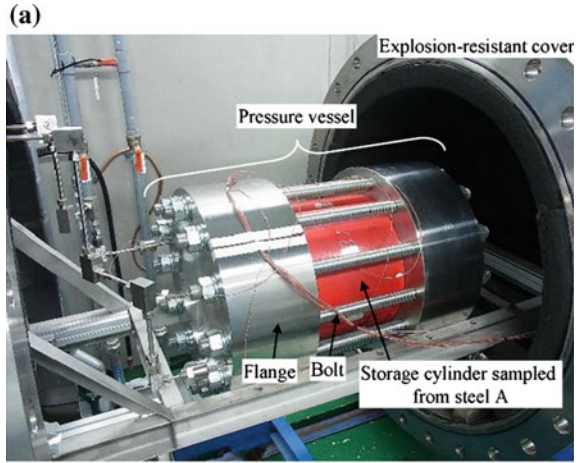
Figure 32.4a shows photographs of the Cr–Mo steel pressure vessels subjected to hydrogen-pressure cycling. The pressure vessels consisted of storage cylinders sampled from steels A and B, as shown in Fig. 32.4b, and jigs (flanges, bolts, O-rings, and aluminum filler). The aluminum filler was used to minimize the required volume of hydrogen. The pressure vessels with storage cylinders made of steels A and B are referred to as A pressure vessels and B pressure vessels, respectively. U-shaped, semi-elliptical notches with a length-to-depth ratio (l_0/c_0) of 3 were machined on the inner surfaces of the pressure vessels by electrical discharge machining. The B pressure vessels were also used for a hydraulic cycle test. Five pressure vessels labeled A-1, A-2, B-1, B-2, and B-3 were prepared. The tests of A-1, A-2, B-1, and B-2 were performed with gaseous hydrogen, whereas that of B-3 was performed with compressed water. The depth of the U-shaped notches of the A pressure vessels was 6.0 mm (24 % of the wall thickness) for A-1 and 18.0 mm (71 % of the wall thickness) for A-2, whereas that for the B pressure vessels was 12.0 mm (40 % of the wall thickness) for B-1 and 24.0 mm (80 % of the wall thickness) for B-2 and B-3. The width of the U-shaped notches was 0.3 mm ($c_0 = 6.0$ mm) or 0.5 mm ($c_0 = 12.0, 18.0,$ and 24.0 mm), where the notch width was the same as the notch diameter.

32.6.2 Fatigue Life and Failure Behavior

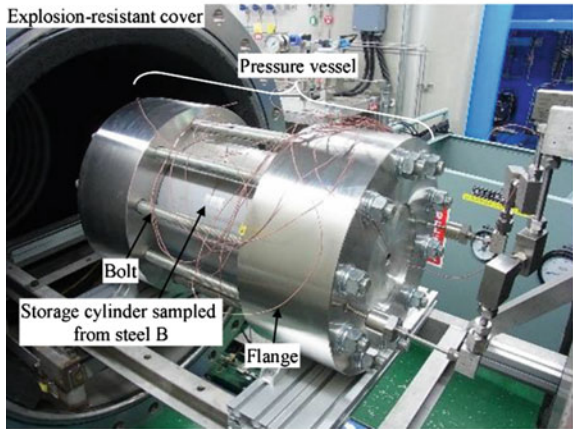
Four pressure vessels (A-1, A-2, B-1, and B-2) were subjected to hydrogen-pressure cycling at pressures varying between 0.6 and 45 MPa at room temperature, whereas one pressure vessel (B-3) was subjected to hydraulic cycling at pressures varying between 0.5 and 45 MPa at room temperature. The A-1 pressure vessel with a 6.0-mm-depth notch and the A-2 pressure vessel with an 18.0-mm-depth notch failed after 1760 and 177 cycles, respectively. The B-1 pressure vessel with a 12.0-mm-depth notch and the B-2 pressure vessel with a 24.0-mm-depth notch failed after 675 and 47 cycles, respectively. In contrast, the B-3 pressure vessel with a 24.0-mm-depth notch failed after 3621 cycles; accordingly, the high-pressure gaseous hydrogen caused a significant reduction in the fatigue life of the Cr–Mo steel pressure vessel.

Figure 32.5 shows photographs of the A-1, A-2, B-1, and B-2 pressure vessels after leakage. It is difficult to observe a through-wall crack under no-load conditions. Therefore, the crack was observed under pressurized nitrogen gas with a liquid form. The liquid form was used for easily detecting the crack under pressurization. The A-1, A-2, B-1, and B-2 pressure vessels failed by leaking from the through-wall cracks during the pressurization stage in the course of pressure

Fig. 32.4 Pressure-cycle testing of Cr–Mo steel pressure vessels with gaseous hydrogen [16]. **a** Photographs of pressure vessels subjected to hydrogen-pressure cycling. **b** Shapes and dimensions of storage cylinders sampled from steels A and B for pressure-cycle testing



(a-1) A pressure vessel



(a-2) B pressure vessel

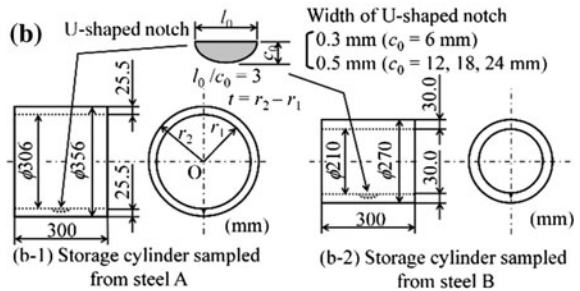
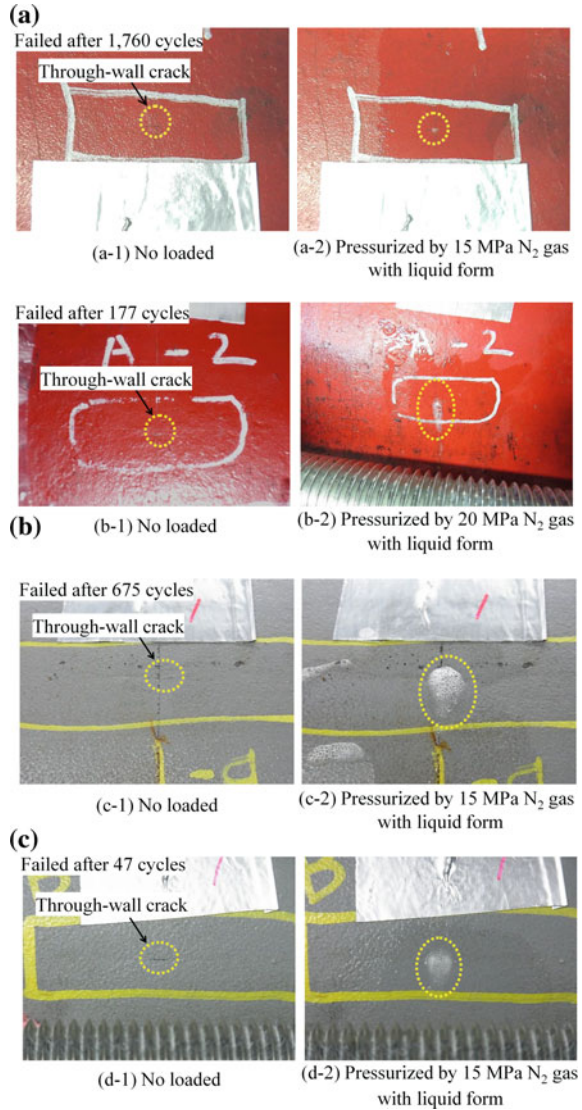


Fig. 32.5 Photographs of pressure vessels after hydrogen-pressure cycling at pressures between 0.6 and 45 MPa at room temperature [16]. **a** A-1 pressure vessel (notch depth: 6.0 mm, wall thickness: 25.5 mm). **b** A-2 pressure vessel (notch depth: 18.0 mm, wall thickness: 25.5 mm). **c** B-1 pressure vessel (notch depth: 12.0 mm, wall thickness: 30.0 mm). **d** B-2 pressure vessel (notch depth: 24.0 mm, wall thickness: 30.0 mm)



cycling; namely, these pressure vessels failed by LBB. Similarly, the B-3 pressure vessel subjected to compressed water also failed by LBB.

The maximum stress intensity factor of a near-through wall crack, K_{max} , of the B-2 pressure vessel actually exceeded the fracture toughness in hydrogen gas, $K_{IC,H}$. Therefore, it is expected that the failure of the B-2 pressure vessel was not by LBB, since $K_{max} > K_{IC,H}$. On the other hand, based on the fracture toughness in air, K_{IC} , it was expected that the fracture of all pressure vessels occurred by LBB, since $K_{max} < K_{IC}$. The present experimental results show that all pressure vessels failed

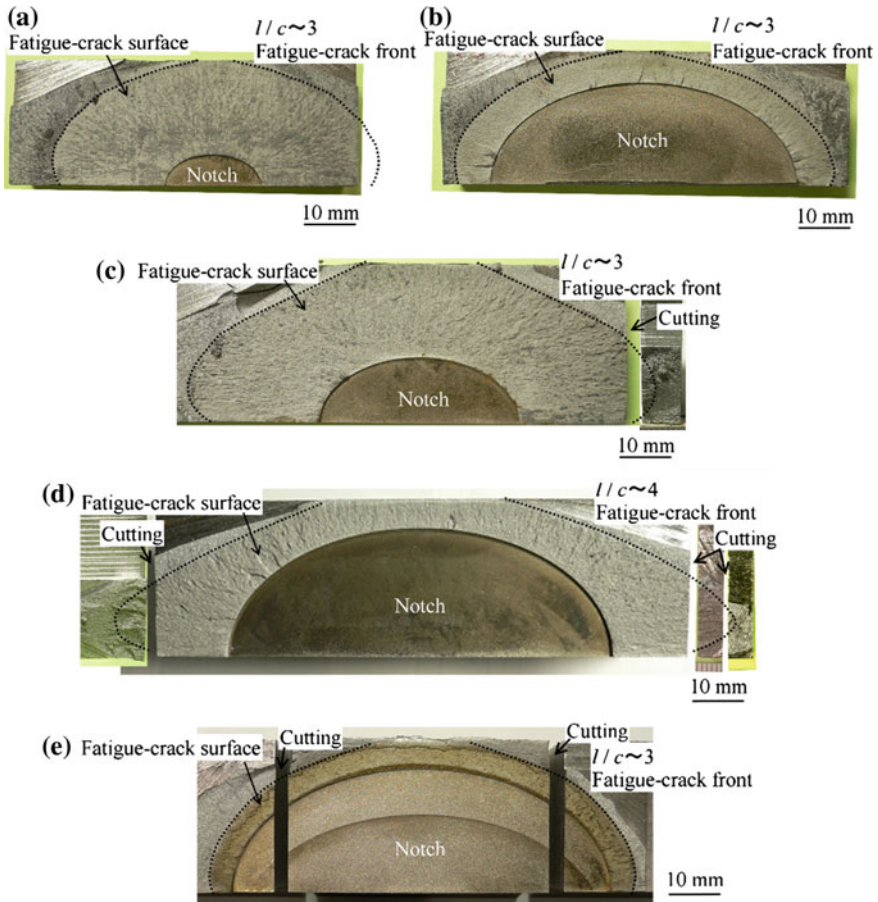


Fig. 32.6 Fatigue crack extensions from notches in pressure vessels during hydrogen-pressure or hydraulic cycling [16]. **a** A-1 pressure vessel (notch depth: 6.0 mm, wall thickness: 25.5 mm). **b** A-2 pressure vessel (notch depth: 18.0 mm, wall thickness: 25.5 mm). **c** B-1 pressure vessel (notch depth: 12.0 mm, wall thickness: 30.0 mm). **d** B-2 pressure vessel (notch depth: 24.0 mm, wall thickness: 30.0 mm). **e** B-3 pressure vessel (notch depth: 24.0 mm, wall thickness: 30.0 mm)

by LBB. Accordingly, the LBB assessment based on $K_{IC,H}$ may be conservative. Hence, the failure behavior of these pressure vessels should be assessed by using K_{IC} rather than $K_{IC,H}$.

Figure 32.6 shows fatigue crack extensions originating from the notches at the inner surface of the A-1, A-2, B-1, B-2, and B-3 pressure vessels during hydrogen-pressure or hydraulic cycling. Compared to the initial length-to-depth ratio of the notches ($l_0/c_0 = 3$), the length-to-depth ratio of the through-wall cracks (l/c) was likewise nearly 3 for the A-1, A-2, B-1, and B-3 pressure vessels.

Therefore, the fatigue cracks of these pressure vessels approximately maintained their aspect ratios during crack growth. In contrast, the length-to-depth ratio of the through-wall crack was approximately 4 for the B-2 pressure vessel, and therefore, the fatigue crack became flatter during crack growth.

32.6.3 Fatigue-Life Assessment

The N_f values of the pressure vessels with hydrogen-pressure cycling were calculated by using the accelerated FCG rates in the presence of hydrogen based on the fracture mechanics approach. The fatigue life of the pressure vessel with hydraulic cycling was also calculated by using the $da/dN-\Delta K$ curve in air as shown in Fig. 30.7. Assuming a semi-elliptical surface crack with $l/c = 3$ for the A-1, A-2, B-1, and B-3 pressure vessels or that with $l/c \approx 4$ for the B-2 pressure vessel during crack growth, the number of cycles for a crack to propagate across the entire wall thickness was calculated by using the ΔK values at the surface and at the deepest point. Then, the lower number of cycles was regarded as N_f .

Table 32.1 shows the experimentally observed and predicted fatigue lives of the A-1, A-2, B-1, B-2, and B-3 pressure vessels subjected to hydrogen-pressure or hydraulic cycling. The experimental fatigue lives of all the pressure vessels were 1.1–2.8 times longer than the predicted ones, although the number of cycles for crack initiation from the machined notches was not considered. The fatigue life prediction based on the fracture mechanics approach was somewhat conservative, but this error is acceptable for the present Cr–Mo steels with inner notches. Thus, the fracture mechanics approach using the accelerated FCG rate in the presence of hydrogen can be used for the fatigue life prediction of real Cr–Mo steel pressure vessels with inner notches under gaseous hydrogen.

Table 32.1 Experimental and predicted fatigue lives of pressure vessels with hydrogen-pressure or hydraulic cycling [16]

Pressure vessel	Test environment	Notch depth (mm)	ΔK_i^a (MPa·m ^{1/2})	N_f (cycles)	
				Experimental	Predicted
A ($t = 25.5$ mm)	$0.6 \Leftrightarrow 45$ MPa H ₂	6.0	39	1760	805
		18.0	80	177	63
B ($t = 30.0$ mm)	$0.6 \Leftrightarrow 45$ MPa H ₂ gas	12.0	35	675	564
		24.0	71	47	41
	$0.5 \Leftrightarrow 45$ MPa compressed water	24.0	67	3621	2844

^aInitial ΔK at the surface or deepest point with N_f

References

1. Murakami Y, Matsuoka S, Kondo Y, Nishimura S (2012) Mechanism of hydrogen embrittlement and guide for fatigue design. Yokendo, Tokyo
2. Gangloff RP, Somerday BP (eds) (2012) Gaseous hydrogen embrittlement of materials in energy technologies. Woodhead Publishing, Cambridge
3. ASME (2010) ASME boiler & pressure vessel code, section VIII. Alternate rules high pressure vessels, division 3. Article KD-10. Special requirements for vessels in high pressure gaseous hydrogen transport and storage service. American Society of Mechanical Engineers, New York
4. ANSI/CSA, CHMC 1-2014 (2014) Test method for evaluating material compatibility in compressed hydrogen applications—Phase I—Metals. Canadian Standards Association, Mississauga, ON
5. San Marchi C, Somerday BP, Nibur KA (2014) Development of methods for evaluating hydrogen compatibility and suitability. *Int J Hydrogen Energy* 39:20434–20439
6. Kobayashi H (2008) Safety factor in mechanical engineering field. *J Jpn Landslide Soc* 44:326–329
7. JSA. JIS B 8265 (2003) Construction of pressure vessel: general principles. Japanese Standards Association, Tokyo
8. JSA. JIS B 8267 (2008) Construction of pressure vessel. Japanese Standards Association, Tokyo
9. ASME (2001) ASME boiler & pressure vessel code, section VIII. Rules for the construction of pressure vessels. Division 1. American Society of Mechanical Engineers, New York
10. JSA (2003) JIS B 8266. Alternative standard for construction of pressure vessels. Japanese Standards Association, Tokyo
11. ASME (2007) ASME boiler & pressure vessel code, section VIII. Construction of pressure vessels, division 2. American Society of Mechanical Engineers, New York
12. UNM. EN 13445 (2004) Unfired Pressure Vessels; Courbevoie: Union de Normalisation de la Mécanique
13. KHK. KHK 0220 (2010) KHK standard for pressure equipment containing ultrahigh pressure gas. High Pressure Gas Safety Institute of Japan, Tokyo
14. Yamabe J, Matsunaga H, Furuya Y, Hamada S, Itoga H, Yoshikawa M, Takeuchi E, Matsuoka S (2014) Qualification of chromium–molybdenum steel based on the safety factor multiplier method in CHMC1-2014. *Int J Hydrogen Energy* 40:719–728
15. Matsunaga H, Yoshikawa M, Itoga H, Yamabe J, Hamada S, Matsuoka S (2014) Tensile- and fatigue-properties of low alloy steel JIS-435 and carbon steel JIS-SM490B in 115 MPa hydrogen gas (PVP2014-28511). In: Proceedings of PVP-2014: ASME pressure vessels and piping division conference. American Society of Mechanical Engineers, Anaheim, California, New York, USA, 20–24 July 2014
16. Yamabe J, Itoga H, Awane T, Matsuo T, Matsunaga H, Matsuoka S (2016) Pressure cycle testing of Cr–Mo steel pressure vessels subjected to gaseous hydrogen. *J Press Vess Technol ASME* 138:011401:1–13
17. Miyamoto T, Matsuo T, Kobayashi N, Mukaie Y, Matsuoka S (2012) Characteristics of fatigue life and fatigue crack growth of SCM435 steel in high-pressure hydrogen gas. *Trans JSME A* 78:531–546
18. Takeuchi E, Furuya Y, Hirakawa H, Matsuo T, Matsuoka S (2013) Effect of hydrogen on fatigue crack growth properties of SCM435 steel used for storage cylinder in hydrogen stations. *Trans JSME A* 79:1030–1040

19. Itoga H, Matsuo T, Orita A, Matsunaga H, Matsuoka S, Hirotsu R (2014) SSRT and fatigue crack growth properties of high-strength austenitic stainless steels in high-pressure hydrogen gas (PVP2014-28640). In: Proceedings of PVP-2014: ASME pressure vessels and piping division conference. American Society of Mechanical Engineers, Anaheim, California, New York, USA, 20–24 July 2014
20. Yamabe J, Matsumoto T, Matsuoka S, Murakami Y (2012) A new mechanism in hydrogen-enhanced fatigue crack growth behavior of a 1900-MPa-class high-strength steel. *Int J Fract* 177:141–162

Chapter 33

Future Perspectives

Junichiro Yamabe

Abstract This chapter describes future perspectives of the hydrogen safety achieved by combination of understanding hydrogen embrittlement (HE), hydrogen gas safety management, and hydrogen in practice. New materials having lower cost and higher resistance to HE and appropriate design methods in consideration for HE are introduced.

Keywords Hydrogen embrittlement · Safety · Strength design · Fatigue · Fretting fatigue · Steel · Hydrogen safety

This part of the book reviewed hydrogen embrittlement (HE), hydrogen gas safety management, and hydrogen safety in practice. Hydrogen safety will be achieved by combination of these three issues (Fig. 33.1).

The chapters relating to HE (Chaps. 26, 29–32) reviewed the fundamental principles and recent progress on the tensile and fatigue properties of various materials in the presence of hydrogen, focusing on the following topics: (1) the mechanism of HE; (2) new materials having lower cost and higher resistance to HE under high-pressure gaseous hydrogen; (3) appropriate design methods in consideration of HE; and (4) fretting fatigue in the presence of hydrogen. The conclusions and future perspectives can be summarized as follows.

Mechanisms of HE: The susceptibility of metallic materials to HE is dependent on their tensile strength. High-strength steel with $\sigma_B > 1000$ MPa in particular is severely degraded by hydrogen [1]. In the fatigue crack growth (FCG) behaviors of low- or medium-strength steels with $\sigma_B < 1000$ MPa, such as carbon, Cr–Mo, and austenitic stainless steels, slip deformations were localized only at the crack tip by hydrogen, and consequently the FCG rate was accelerated [2–8]. For example, the FCG rates of Cr–Mo steels with tensile strengths less than 900 MPa in the presence of hydrogen were 30 times higher than those for noncharged specimens. However,

J. Yamabe (✉)

International Research Center for Hydrogen Energy, Kyushu University,
Fukuoka 819-0395, Japan
e-mail: yamabe.junichiro.575@m.kyushu-u.ac.jp

© Springer Japan 2016

K. Sasaki et al. (eds.), *Hydrogen Energy Engineering*,
Green Energy and Technology, DOI 10.1007/978-4-431-56042-5_33

453

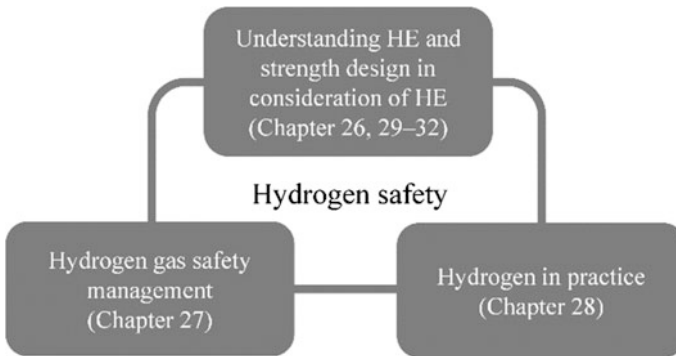


Fig. 33.1 Hydrogen safety achieved by combination of understanding HE, hydrogen gas safety management, and hydrogen in practice

there was an upper bound of FCG acceleration [4, 9, 10]. From detailed observation of fatigue crack and fracture surface morphologies, FCG acceleration in the presence of hydrogen can be explained in terms of the hydrogen-enhanced localized plasticity (HELP) model [11–13] rather than the hydrogen-enhanced decohesion (HEDE) model [14–16].

On the other hand, for high-strength steel in the presence of hydrogen, intergranular (IG) fracture surfaces were often observed, and there was no upper bound of FCG acceleration [17]. Therefore, it is manifest that a mechanism different from that of the HELP model caused the hydrogen-accelerated fatigue crack growth rate. Thus, a new model associated with hydrogen-induced deformation twins was introduced [17]. However, a few fracture processes are presumed to be mutually coupled for IG fracture in the presence of hydrogen; therefore, the mechanism of HE is complicated. The IG fracture causes significant degradation of material properties; thus, further studies are needed.

Furthermore, the relative FCG rate (RFCGR) of various low- and medium-strength steels gradually increased with decreasing test frequency before suddenly decreasing close to 1.0 [7–9]. The mechanism of this peculiar frequency dependence of the FCG rate must be elucidated, although the present explanations are performed in terms of the hydrogen-enhanced successive fatigue crack growth (HESFCG) model [6, 8] or the oxygen effect [18]. For strength design of hydrogen components based on design by rule or design by analysis, it is important to establish the presence of a fatigue limit and an upper bound of FCG acceleration for various steels in high-pressure gaseous hydrogen [2, 9, 19].

New materials having lower cost and higher resistance to HE: In austenitic stainless steels, the susceptibility of the FCG to hydrogen can be correlated with their austenitic stabilities, which are quantifiable with the nickel equivalent [20–26]. Steel with a higher austenitic stability possesses a higher FCG resistance to hydrogen. Therefore, the nickel equivalent can serve as an effective grading criterion in the selection of the austenitic stainless steels to be used in high-pressure

hydrogen gas atmospheres. Types XM-19 and HP160 with high nickel equivalents demonstrated excellent FCG resistance, which was hardly degraded even in high-pressure hydrogen gas of up to 95–100 MPa [20, 26]. We will continue to develop new materials having lower cost and higher strength.

Appropriate design method in consideration of hydrogen effect: In addition to the development of new materials having lower cost and higher strength, appropriate design methods have to be established based on the resulting scientific understanding for the widespread commercialization of hydrogen energy systems. We can use the safety factor multiplier method in the CHMC 1-2014 (Test Method for Evaluating Material Compatibility in Compressed Hydrogen Applications—Phase I—Metals) standard [27, 28]; however, this method provides overly conservative safety factors for various steels [19]. Thus, we should always use generally accepted design methodology based on design by rule or design by analysis for specific component application.

We therefore suggest that hydrogen service components can be designed via conventional design-by-rule methodology, provided the following criteria are satisfied at the maximum design pressure of the hydrogen gas: first, that there is no degradation in the tensile strength in SSRT; and second, that there is no degradation in the fatigue limit [2, 9, 19].

It is also suggested that components for hydrogen service can be designed by conventional design-by-analysis, provided the following criteria are satisfied at the maximum design pressure of the hydrogen gas: first, that there is no degradation in the tensile strength in SSRT; and second, that there is an upper bound on the acceleration of fatigue crack growth in the hydrogen environment. There is an additional requirement that the maximum stress intensity factor of a near-through wall crack is less than the value of the fracture toughness in air for the leak before break (LBB) failure of the components [2, 9, 19].

It is also to be noted that consideration of the operational history is crucial for precise prediction of the FCG life of hydrogen service components [19].

Fretting fatigue in the presence of hydrogen: Fretting causes some special effects associated with hydrogen-assisted fatigue fracture. As a result, the fretting fatigue strength under the effect of hydrogen could be significantly reduced. In other words, fretting provides hydrogen with a place to actively react. Adhesion between the contacting surfaces during fretting fatigue in hydrogen gas is very important. The microstructural changes that occur due to adhesion might also play a key role in the reduced fretting fatigue strength in hydrogen.

Other than solution heat-treated austenitic stainless steels, for which the results of the fretting fatigue test are described here, work-hardened austenitic stainless steels [29], low-alloy steel, heat-resistant steel, and low-alloy steel with nitriding [30] were investigated. Furthermore, the effects of the hydrogen concentration in the material [31] and the addition of oxygen and water vapor to the hydrogen gas [32] were studied. However, the effects of the hydrogen gas pressure, temperature, loading frequency, contact pressure, materials combination, slip range, long life, etc., on the fretting fatigue properties in hydrogen gas have not yet been clarified. Further study is necessary to ensure the safety of hydrogen equipment.

References

1. NASA (1997) Safety standard for hydrogen and hydrogen systems. Washington, D.C: NSS 1740.16
2. Matsunaga H, Yoshikawa M, Kondo R, Yamabe J, Matsuoka S (2015) Slow strain rate tensile and fatigue properties of Cr–Mo and carbon steels in a 115 MPa hydrogen gas atmosphere. *Int J Hydrogen Energy* 40:5739–5748
3. Matsuoka S, Tsutsumi N, Murakami Y (2008) Effects of hydrogen on fatigue crack growth and stretch zone of 0.08 Mass% low carbon steel pipe. *Trans JSME A* 74:1528–1537
4. Tanaka H, Homma N, Matsuoka S, Murakami Y (2007) Effect of hydrogen and frequency on fatigue behavior of SCM435 steel for storage cylinder of hydrogen station. *Trans JSME A* 73:1358–1365
5. Kanezaki T, Narazaki C, Mine Y, Matsuoka S, Murakami Y (2008) Effects of hydrogen on fatigue crack growth behavior of austenitic stainless steels. *Int J Hydrogen Energy* 33:2604–2619
6. Murakami Y, Kanezaki T, Mine Y, Matsuoka S (2008) Hydrogen embrittlement mechanism in fatigue of austenitic stainless steels. *Metall Mater Trans A* 39:1327–1339
7. Yoshikawa M, Matsuo T, Tsutsumi N, Matsunaga H, Matsuoka S (2014) Effects of hydrogen gas pressure and test frequency on fatigue crack growth properties of low carbon steel in 0.1–90 MPa hydrogen gas. *Trans JSME A* 80
8. Matsuo T, Matsuoka S, Murakami Y (2010) Fatigue crack growth properties of quenched and tempered Cr–Mo steel in 0.7 MPa hydrogen gas. In: *Proceedings of the 18th European conference on fracture (ECF18)*
9. Yamabe J, Itoga H, Awane T, Matsuo T, Matsunaga H, Matsuoka S (2016) Pressure cycle testing of Cr–Mo steel pressure vessels subjected to gaseous hydrogen. *J. Press Vess Technol ASME* 183–011401:1–13
10. Miyamoto T, Matsuo T, Kobayashi N, Mukaie Y, Matsuoka S (2012) Characteristics of fatigue life and fatigue crack growth of SCM435 steel in high-pressure hydrogen gas. *Trans Jpn Soc Mech Eng A* 78:531–546
11. Sofronis P, McMeeking RM (1989) Numerical analysis of hydrogen transport near a blunting crack tip. *J Mech Phys Solid* 37:317–350
12. Birnbaum HK, Sofronis P (1994) Hydrogen-enhanced localized plasticity: a mechanism for hydrogen-related fracture. *Mater Sci Eng A* 176:191–202
13. Robertson IM, Birnbaum HK (1986) An HVEM study of hydrogen effects on the deformation and fracture of nickel. *Acta Metall* 34:353–366
14. Morlet JG, Johnson HH, Triano AR (1958) A new concept of hydrogen embrittlement in steel. *J Iron Steel Inst* 189–1:37–41
15. Troiano AR (1960) The role of hydrogen and other interstitials in the mechanical behavior of metals. *Trans ASM* 52:54–80
16. Oriani RA, Josephic H (1974) Equilibrium aspects of hydrogen-induced cracking of steels. *Acta Metall* 22:1065–1074
17. Yamabe J, Matsumoto T, Matsuoka S, Murakami Y (2012) A New mechanism in hydrogen-enhanced fatigue crack growth behavior of a 1900-MPa-class high-strength steel. *Int J Fract* 177:141–162
18. Somerday BP, Sofronis P, Nibur KA, San Marchi C, Kirchheim R (2013) Elucidating the variables affecting accelerated fatigue crack growth of steels in hydrogen gas with low oxygen concentrations. *Acta Mater* 61:6153–6170
19. Yamabe J, Matsunaga H, Furuya Y, Hamada S, Itoga H, Yoshikawa M, Takeuchi E, Matsuoka S (2014) Qualification of chromium–molybdenum steel based on the safety factor multiplier method in CHMC1-2014. *Int J Hydrogen Energy* 40:719–728

20. Itoga H, Matsuo T, Orita A, Matsunaga H, Matsuoka S, Hirotsu R (2014) SSRT and fatigue crack growth properties of high-strength austenitic stainless steels in high-pressure hydrogen gas (PVP2014-28640). In: Proceedings of PVP-2014: ASME pressure vessels and piping division conference. American Society of Mechanical Engineers, Anaheim, California, USA, July 20–24 ASME, New York
21. Hirayama T, Ogirima (1970) Influence of chemical composition on martensitic transformation in Fe–Cr–Ni stainless steel. *J Jpn Inst Met Mater* 34:507–510
22. Sanga M, Yukawa N, Ishikawa T (2000) Influence of chemical composition on deformation-induced martensitic transformation in austenitic stainless steel. *J Jpn Soc Technol Plast* 41:64–68
23. Yamada T, Kobayashi H (2012) *J High Press. Gas Safety Inst Jpn* 49:885–893
24. Hirayama T, Ogirima M (1970) Influence of martensitic transformation and chemical composition on mechanical properties of Fe–Cr–Ni stainless steel. *J Jpn Inst Met Mater* 34:511–516
25. Oshima T, Habara Y, Kuroda K (2007) Effects of alloying elements on mechanical properties and deformation-induced martensite transformation in Cr–Mn–Ni austenitic stainless steels (transformations and microstructures). *Tetsu- to- Hagane* 93:544–551
26. Itoga H, Matsuo T, Orita A, Matsunaga H, Matsuoka S (2013) SSRT and fatigue crack growth properties of two types of high strength austenitic stainless steels in high pressure hydrogen gas. *Trans JSME A* 79:1726–1740
27. ANSI/CSA, CHMC 1-2014 (2014) Test method for evaluating material compatibility in compressed hydrogen applications—Phase I—Metals. Mississauga, In: Canadian Standards Association
28. San Marchi C, Somerday BP, Nibur KA (2014) Development of methods for evaluating hydrogen compatibility and suitability. *Int J Hydrogen Energy* 39:20434–20439
29. Mizobe K, Shiraishi Y, Kubota M, Kondo Y (2011) Effect of hydrogen on fretting fatigue strength of SUS304 and SUS316L austenitic stainless steels. In: Proceedings. ICM&P2011, Corvallis, Oregon, USA: ICMP2011-51138
30. Kubota M, Tanaka Y, Kondo Y (2007) Fretting fatigue properties of SCM435H and SUH660 in hydrogen gas environment. *Trans JSME A* 73:1382–1387
31. Kubota M, Nishimura T, Kondo Y (2010) Effect of hydrogen concentration on fretting fatigue strength. *J Solid Mech Mater Eng* 4:816–829
32. Komoda R, Kubota M, Furtado J (2015) Effect of addition of oxygen and water vapor on fretting fatigue properties of an austenitic stainless steel in hydrogen. *Int J Hydrogen Energy* 40:16868–16877

Part VI

Applications and Perspectives

Kazunari Sasaki¹⁻³ and Stephen M. Lyth⁴⁻⁶

¹International Research Center for Hydrogen Energy, Kyushu University, Fukuoka, Japan

²Next-Generation Fuel Cell Research Center (NEXT-FC), Kyushu University, Fukuoka, Japan

³International Institute for Carbon-Neutral Energy Research, Kyushu University, Fukuoka, Japan

⁴CREST, Japan Science and Technology Corporation, Kawaguchi, Japan

⁵Department of Mechanical Engineering, Sheffield University, Sheffield, UK

⁶School of Chemical and Process Engineering, Leeds University, Leeds, UK

This final part covers a wide range of practical applications including automotive, residential, industrial, and portable applications. Infrastructure, business model, public acceptance, popularization strategies, and educational aspects are further considered. All these considerations are helpful to realize a fuel-cell-powered hydrogen-utilizing society for our future.

Chapter 34

Development of the MIRAI Fuel Cell Vehicle

Yoshikazu Tanaka

Abstract This chapter describes the development of the Toyota MIRAI, Japan's first mass-production fuel cell vehicle. The MIRAI was developed as a pioneering vehicle for moving towards a hydrogen society. Specifications and various technological and design efforts are described in making fuel cell-powered vehicles reality.

Keywords Fuel cell vehicle MIRAI · Background · Concept · Specification · Design · Performance · Safety · External power supply · Life cycle assessment

34.1 Introduction

The motor vehicle has contributed to economic, social, and cultural development by offering the freedom to travel at any time, from anywhere, and to any destination. At the same time, vehicles have adversely affected the Earth's environment, by contributing to global warming through CO₂ emissions and air pollution from environmentally hazardous substances. The Toyota Motor Corporation considers addressing environmental issues to be one of its central tasks, and to that end, it has pursued the principles of energy conservation, fuel diversity, and broad impact of eco-friendly vehicles on the environment through wide distribution. Toyota launched the world's first commercial hybrid vehicle (HV), the Prius, in 1997. Hybrid technology has contributed significantly to improving the environment as it has evolved, adopted in more vehicle models, and grown more popular globally.

On the other hand, vehicles' impact on the environment will become increasingly severe as emerging markets develop economically and the world's population increases. It has become more important than ever to address environmental problems to ensure that vehicles remain useful and continue to enrich people's lives in the next one hundred years [1].

Y. Tanaka (✉)

Toyota Motor Corporation, 1 Toyota-Cho, Toyota City 471-8571, Aichi Prefecture, Japan
e-mail: yoshikazu_tanaka_ab@mail.toyota.co.jp

© Springer Japan 2016

K. Sasaki et al. (eds.), *Hydrogen Energy Engineering*,

Green Energy and Technology, DOI 10.1007/978-4-431-56042-5_34

34.2 Significance of Hydrogen Energy

Fossil fuels such as gasoline are very convenient sources of energy as vehicle fuel because storage and transport are easy and energy density is high. However, fossil fuel deposits are limited, and supplies are often insecure. Furthermore, the use of gasoline produces environmental problems, such as global warming from greenhouse gases like CO₂, and air pollution from environmentally hazardous substances.

Convenient fossil fuels should be used carefully with energy conservation in mind, while production of greenhouse gases and environmentally hazardous substances should be suppressed. Energy conservation will be addressed by the deployment of HVs and in the improvement of the fuel economy of conventional vehicles.

In addition, promoting the use of alternate fuel, the principle of accommodating diversity in fuel, is also important in addressing energy problems. Because each type of alternative fuel has different advantages and disadvantages, narrowing down to a single candidate is difficult (Table 34.1). It will therefore become more important to take advantage of characteristics of each fuel and apply them to different types of vehicles. Electric cars yield zero emissions during use, is quiet when driven, and can be easily charged in households. However, disadvantages include long charge time and low energy density (short cruising range). As a result, pure electric vehicles (EVs) are suitable for small cars driven over short distances, as in the case of personal mobility vehicles.

A plug-in hybrid vehicle (PHV) is considered the electricity-using vehicle that is most suitable for popularization, because PHVs have the merits of both HVs and EVs, and battery depletion is not a concern.

Hydrogen is one of the most abundant elements on Earth, most notably in the form of water; therefore, there is no concern that the resource will be depleted. The energy density of hydrogen is greater than that of electricity, which makes it advantageous in terms of cruising range. Hydrogen is also easier to transport and store. It can be produced by breaking down water using electricity from, e.g., wind and photovoltaic power, and then storing and transporting it. This ease of access

Table 34.1 Characteristics of alternative fuels

	Electricity	Hydrogen	Biofuels	Natural gas
Well-to-wheel CO ₂	Poor to excellent	Poor to excellent	Poor to excellent	Good
Supply volume	Excellent	Excellent	Poor	Good
Energy density (cruising range)	Poor	Excellent	Excellent	Good
Charging/refueling time	Poor	Excellent	Excellent	Excellent
Dedicated infrastructure	Good	Poor	Excellent	Good

offsets the unpredictability of natural energy resources and covers regional energy imbalances. Hydrogen can even be obtained from sewage sludge. It is expected to be a promising energy source of the future for Japan, which is limited in natural resources. In particular, hydrogen can be used as fuel for fuel cell vehicles (FCVs). FCVs are driven by motors that use electricity generated by chemical reactions of hydrogen and oxygen in the air in a fuel cell (FC) stack.

The characteristics of FCVs include high energy efficiency because hydrogen is not combusted as in internal combustion engines, but instead generates electricity through chemical reactions. Furthermore, FCVs require a short refueling time because the vehicle is supplied with fuel instead of recharged with electricity. Finally, FCVs in use emit only water, not environmentally hazardous substance emissions. FCVs have the potential to serve as the “ultimate ecological car” that contributes to a sustainable and mobile society.

34.3 Development of the MIRAI: Japan’s First Mass-Production FCV

The development concept for the MIRAI (see Fig. 34.1) was to create a H₂ pioneer for the next century. The MIRAI was developed as a pioneer vehicle in moving toward a hydrogen society, providing unprecedented value as vehicles advance in the next 100 years.

Designers selected the sedan package as the body styling, based on the development concept and the following goals: (1) to maximize the positive aspects of FCVs, such as its fun to drive quality and fuel economy, (2) to appeal to a wide range of customers, and (3) to use a compact power train that eases adoption of other vehicle models in the future.



Fig. 34.1 The MIRAI FCV

34.3.1 Newly Developed Toyota Fuel Cell System (TFCS)

Toyota has a history of over 20 years of FCV development since the company first recognized the potential of hydrogen and started to develop FCs in 1992. Toyota became the first automaker in the world to launch FCVs on a limited lease basis. New models were launched in 2005 and 2008, and Toyota's FCVs have been driven a total of over two million kilometers in Japan, the US, and Europe. The latest MIRAI is loaded with the Toyota fuel cell system (TFCS) a significant advancement leveraging feedback from the past development. Key specifications of the MIRAI are listed in Table 34.2. The enhancement is characterized by (1) a substantial cost reduction, (2) size reduction and increased performance, and (3) a simplified system.

34.3.2 Vehicle Package

The vehicle package is an important factor that defines every aspect of the vehicle, from comfort and usability to design and performance (see Fig. 34.2). Important characteristics include positioning the FC stack below the front seat, and locating the high-pressure hydrogen tanks below the rear seat and above the rear axle. The components of the hydrogen system, such as the FC stack and high-pressure hydrogen tanks, are located below the floor and outside the vehicle cabin. The lighter than air hydrogen can therefore easily disperse into the atmosphere in the unlikely event of a hydrogen leak. Furthermore, placing heavy components low down in the center of the vehicle lowers the center of gravity and optimizes the front/rear weight balance, thereby enhancing dynamic performance.

Table 34.2 Key specifications of the MIRAI

Issue	Specification
Stack max. power output	114 kW
Driving range (JC08 mode, measured at Toyota)	ca. 650 km (ca. 700 km ^a)
H ₂ gas fueling time	ca. 3 min

^aCruising range extended to about 700 km using the new type of standard hydrogen station expected to start operation after fiscal year 2016

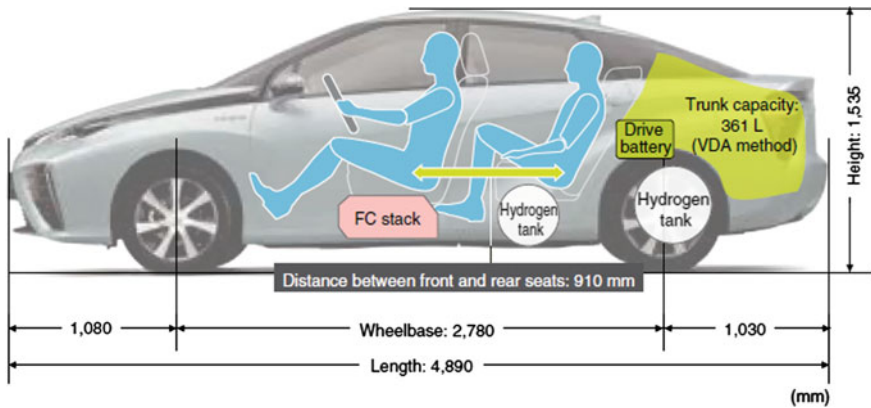


Fig. 34.2 Vehicle package

34.3.3 Advanced Design and Future Mobility

The exterior design is extremely important to the concepts and goals of this vehicle (see Fig. 34.3). An advanced design immediately recognizable as an FCV, considered the future form of mobility, is a key element. However, a design that is too eccentric, that appears so futuristic as to deter drivers, cannot lead the way to a hydrogen-based society and infrastructure. The objective of the design is to appeal to people living in areas without hydrogen infrastructure, thereby stimulating the demand to build infrastructure so as to be able to ride the attractive vehicle.

The development concept of the exterior design was “embodiment of ingenuity.” The critical functions of the FCV were incorporated as design expressions, with the aim of creating a design that immediately identifies the vehicle as an FCV. Our ultimate goal is to make the design of the MIRAI the de facto design of FCVs, just as the triangular shape of the Prius represents HVs. The large side grilles are prominent examples of design features that achieve this aim. FCVs need to intake large amounts of air (oxygen) for power generation and cooling (which can in turn generate water). This is represented in the novel and bold three-dimensional side grille design. The side profile takes the form of a flowing water drop form with a dynamic silhouette.



Fig. 34.3 Exterior design

The design concept of the interior is “remodeling with sophisticated functionality” (see Fig. 34.4). A seamless space is created by refining each functional design using shapes and structures, rather than relying on futuristic equipment. Novelty and innovations are demonstrated; the front pillars merge with the meter hood, connect with the ceiling, and extend continuously to the rear windows. Moreover, in the instrument panel, thin panel elements surround a core element, which extends from the side to the center, from above and below.

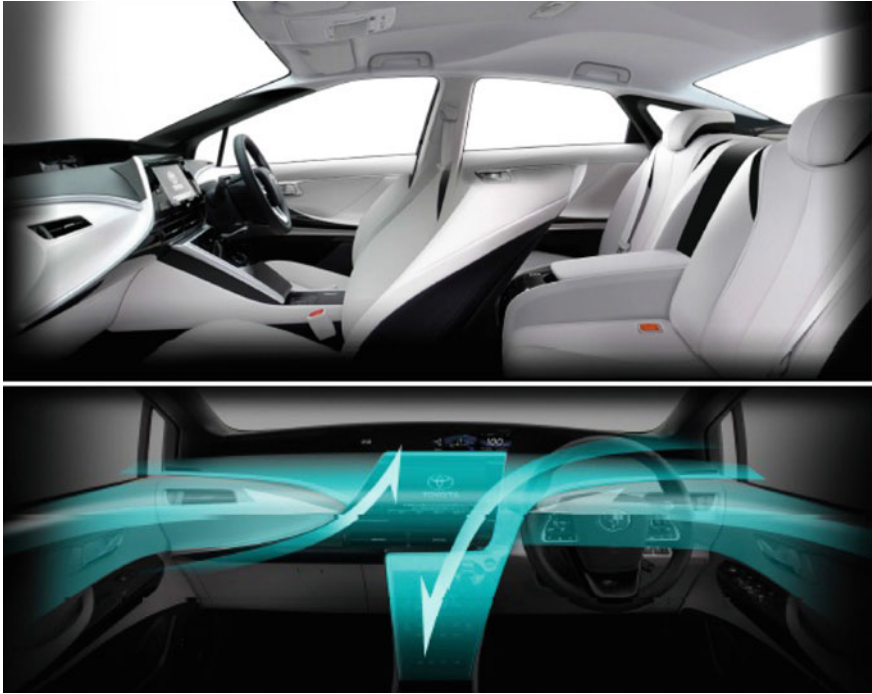


Fig. 34.4 Interior design

34.4 Outstanding Vehicle Performance

The MIRAI is an eco-friendly vehicle and, needless to say, ecological performance took top priority in development. However, to become a widely accepted pioneer of a future hydrogen-energy society, the MIRAI must also be a vehicle that is attractive and fun to drive. The MIRAI was therefore developed as an exciting and comfortable vehicle that appeals to drivers over the long-term, rather than serving only as a standard eco-friendly vehicle.

34.4.1 Aerodynamic Performance

Aerodynamics is a critical aspect of performance that determines fuel economy and driving stability (see Fig. 34.5). In FCVs, the coefficient of drag (C_D) performance is important to enhance fuel economy; however, achieving good C_D performance is difficult because intake of a large amount of air is necessary for power generation and cooling. Taking advantage of the fact that there are no high-temperature emission tubes in an FCV, the positioning of the FC stack and hydrogen tank under

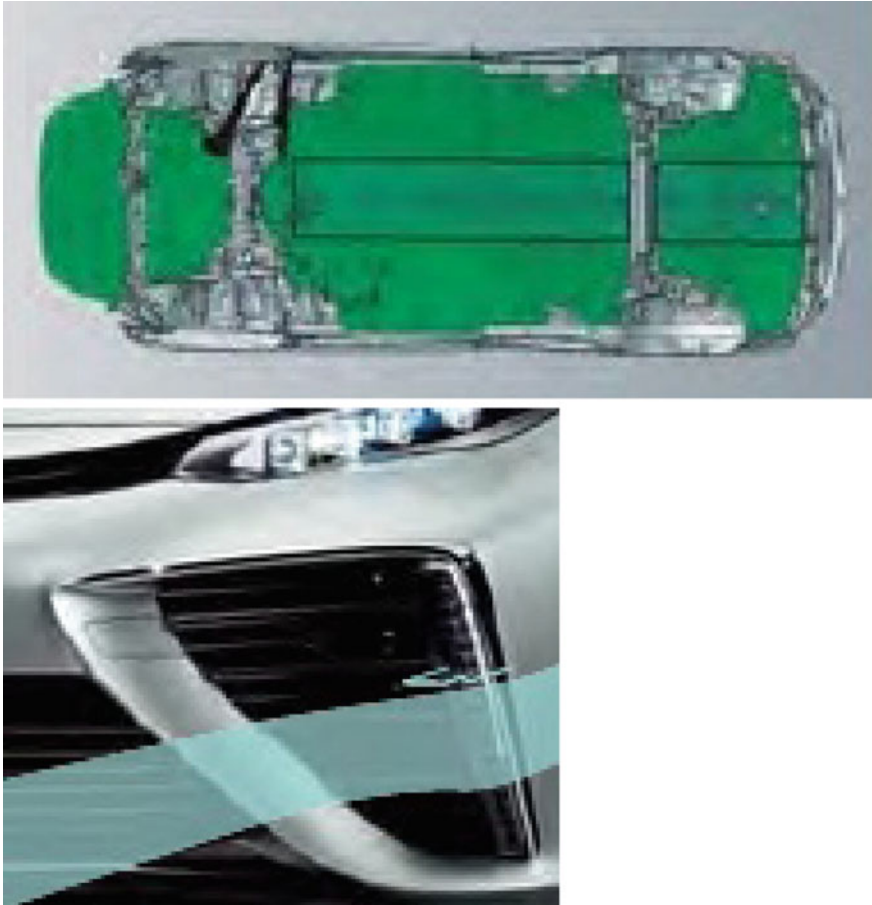


Fig. 34.5 Measures to improve aerodynamic performance

the floor allows for the adoption of a full under-cover. As a result, despite the large openings at the front of the vehicle, the MIRAI achieves one of the best C_D values in its segment. Daytime running lights (DRLs) were placed near the characteristic side grilles to serve aerodynamic and design functions.

34.4.2 *Noise and Vibration Performance*

Noise and vibration (NV) performance was one of the most important factors considered when developing the MIRAI (Fig. 34.6). Customers expect a very quiet

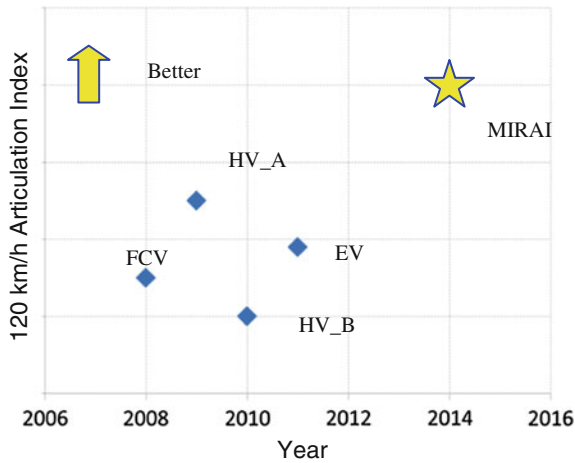


Fig. 34.6 NV performance (conversation intelligibility)

vehicle because there is no engine in MIRAI. However, the lack of engine noise makes other noises prominent that might go unnoticed in vehicles with engines. An even higher NV performance than that of standard vehicles is therefore required for occupants to feel the silent and dynamic performance of the motor. Wind and road noise were decreased, a high NV performance was achieved by maximizing sound insulation through the adoption of acoustic glass in all doors, and thorough countermeasures were taken against wind noise and vibration around the side mirrors. Noise intrinsic to the FC system was decreased as much as possible, given the unique difficulties posed by the new system. NV analysis was carried out to reduce noise generated by individual parts as well as to investigate noise transmitted through the vehicle body and radiated to surrounding air. Measures against vibration and noise were implemented to substantially reduce NV.

34.4.3 Crash Safety

Crashworthiness is the most crucial parameter of a vehicle (see Fig. 34.7). The MIRAI was developed to have the highest crash safety standards. The increased vehicle weight from the FC system posed a challenge; however, high voltage safety comparable to HVs and hydrogen safety unique to FCVs were secured.

Specifically, the MIRAI's results on Toyota's Global Outstanding Assessment (crash safety assessment) were the highest in its class, thanks to its all-around compatibility (which results in co-safety if vehicles with different weights and

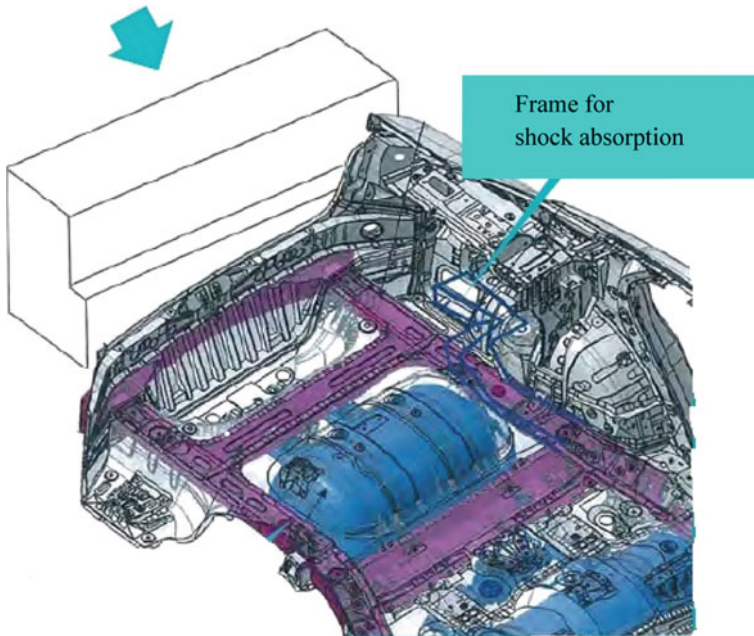


Fig. 34.7 Crash safety analysis results (rear-end collision)

heights crash). Hydrogen safety is secured by locating hydrogen-related components between the front and rear tires, thereby reducing force inputs. High voltage safety reflects proven elements of HV technology, such as the appropriate positioning of high voltage parts in the motor compartment.

34.4.4 Dynamic Performance, Drivability, Driving Stability, and Ride Comfort

The dynamic performance was developed to appeal to drivers by emphasizing the EV's fun to drive qualities.

The smooth feel of an EV comes from low levels of vibration and good response at maximum torque, a characteristic unique to motor-driven vehicles. Development of the MIRAI focused on a comfortable flat feel, emphasizing low vibration of the vehicle and sufficient driving stability to make use of the rapid motor response. As a result, many measures were incorporated, including the use of cross members in the motor room containing FC system parts and underfloor stack frames, additional spot welds, body adhesives, and additional braces near the rear suspension. The result is a torsional stiffness about 1.6 times that of a typical Toyota front-engine, front-drive vehicle.

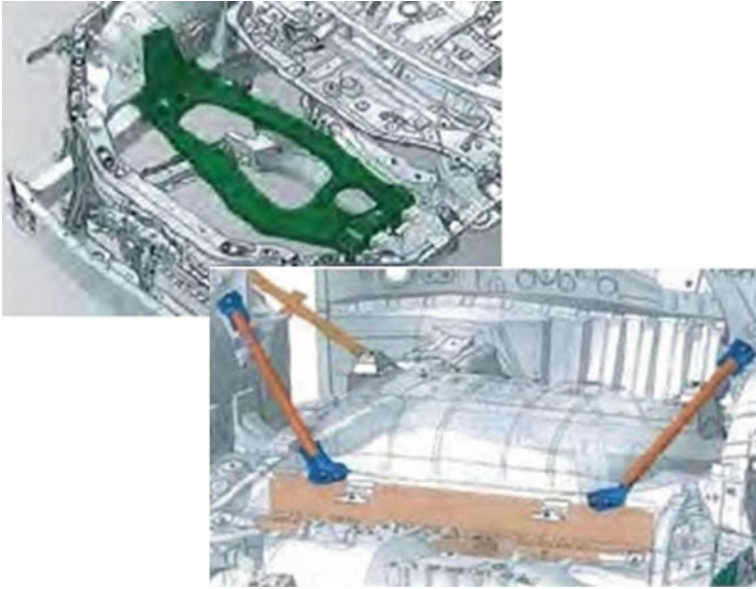


Fig. 34.8 Measures to improve body stiffness

The MIRAI achieved a good feel and driving stability through appropriate positioning of heavy parts, in combination of the highly stiff body, resulting in a vehicle that emphasizes the smooth, dynamic feel of the motor (see Fig. 34.8).

34.4.5 Air Conditioning Performance

Because EVs do not have a heat source, large amounts of energy are used for heating, and the cruising range in winter is affected. In contrast, FCVs benefit from a heat source that uses waste heat from the FC stack. The MIRAI offers a high-eco air conditioning mode that heats primarily using waste heat, in addition to the normal eco air conditioning mode. Furthermore, seat heaters in both the front and rear seats as well as steering wheel heaters are installed as standard equipment on all vehicles. These ensure comfort and suppress decreases in fuel economy in cold regions (see Fig. 34.9).

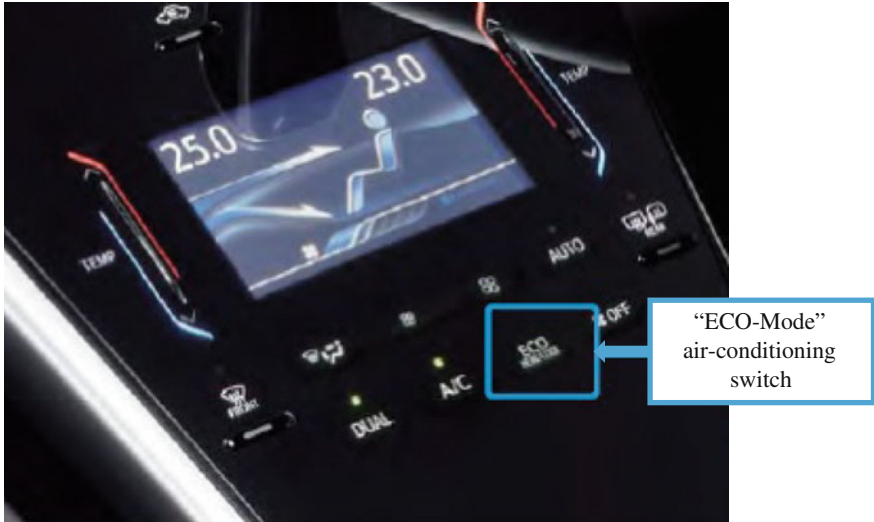


Fig. 34.9 Air conditioning

34.5 Advanced Equipment

FCVs cannot drive without hydrogen infrastructure. In the early stages of FCV introduction, hydrogen stations will not be as ubiquitous as gas stations. Therefore, it is very important that the driver has information such as the location of hydrogen stations. Such information is made available on a navigation system and as a smartphone app. Providing information on existing hydrogen stations (locations, business hours, and distance from current location) as well as information on newly opening hydrogen stations, will alleviate drivers' anxieties about the convenience of hydrogen stations (see Fig. 34.10).

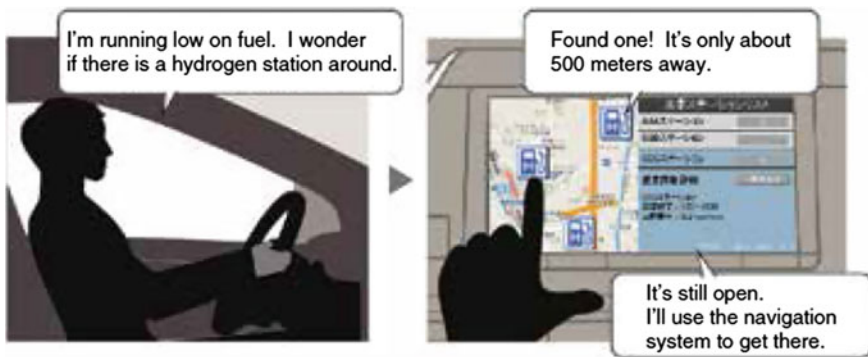


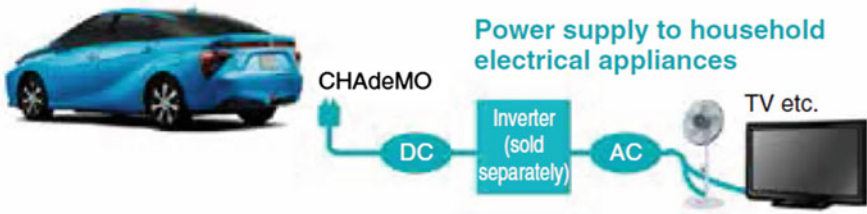
Fig. 34.10 Hydrogen station information service

The navigation system also provides a “MIRAI monitoring service.” In the unlikely event of a malfunction, the information will be sent to a Toyota dealer, allowing for immediate consultation on the best course of action. This measure is meant to alleviate users’ concerns regarding the new technology and allow them to drive with confidence.

34.6 External Power Supply

The cruising range of FCVs is proportional to the amount of supplied electricity. The FC’s generated power can be supplied externally instead of being used for driving via the emergency external power supply functionality, developed and configured exclusively for emergencies. A CHAdeMO terminal in the luggage compartment provides DC output, and a maximum of 9 kW can be supplied in combination with an external inverter. A DC output without a DC/AC inverter was selected, because it is inefficient to carry a large inverter onboard as an emergency external power supply. The CHAdeMO terminal (the standard protocol for DC power supply and discharge in Japan) was chosen so that the external power supply functionality of the FCV would use the same standard as EVs, making the system more versatile. The maximum power supply capacity of the MIRAI is about

Example of DC power supply usage



Example of AC power supply usage

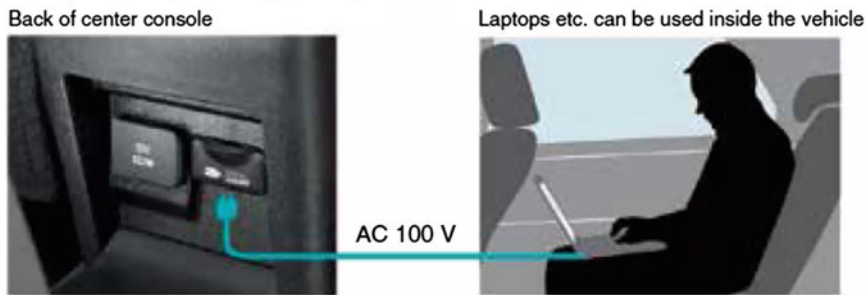


Fig. 34.11 External power supply functionality

60 kWh, which is several times larger than an EV, thereby making long-term supply possible (see Fig. 34.11).

The MIRAI is also installed with a 1500 W AC power supply, already adopted in HVs and PHVs, which can be used as AC power in the vehicle and as an external power supply in an emergency.

34.7 Environmental Performance

34.7.1 Life Cycle Assessment (LCA)

The LCA of an FCV is significantly affected by CO₂ emitted during hydrogen generation. Figure 34.12 shows a comparison of LCAs calculated for gasoline vehicles, HVs, and current and future FCVs, based on the assumptions in the figure. The environmental burden is expected to substantially decrease when hydrogen can be efficiently generated using renewable energy, and FCVs have the potential to be close to CO₂-free according to the LCA.

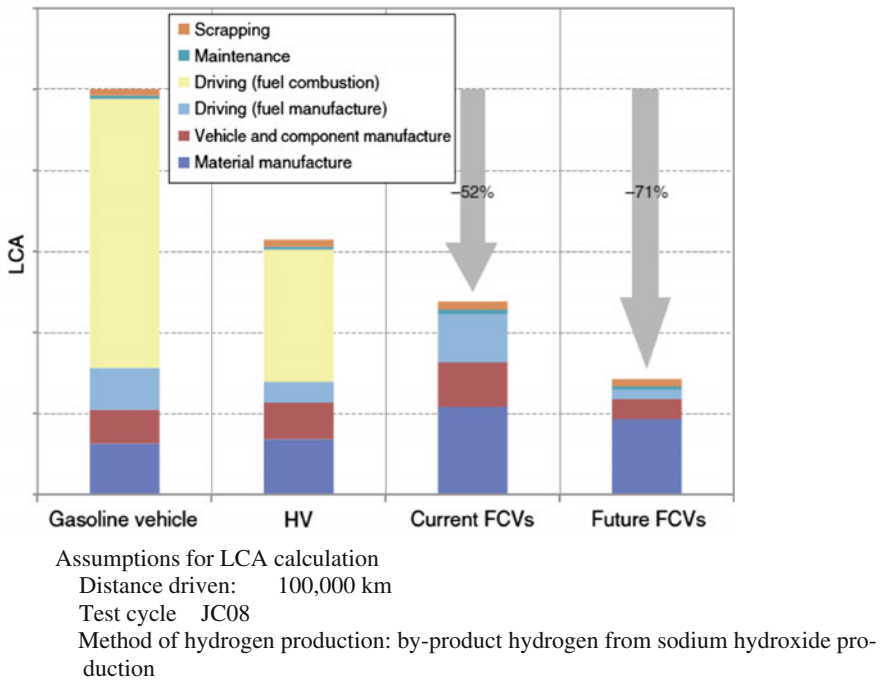


Fig. 34.12 Life cycle assessment (LCA)

34.8 Conclusions

The globally adopted name of the vehicle, “MIRAI,” means “future” in Japanese, and reflects Toyota’s investment in the future of vehicles, the Earth, and future production. The teams who developed and manufactured MIRAI wanted this vehicle to be a pioneer in achieving a hydrogen-energy society, communicating to people one hundred years from now that vehicles remain convenient and enjoyable.

We at Toyota are proud of having produced MIRAI, an excellent vehicle that is both environmentally high performing and fun to drive.

Popularizing hydrogen-fueled FCVs will likely take many years. It is of course necessary to further reduce costs, enhance performance, and continue to work on developing better vehicles. In the meantime, Toyota hopes that the MIRAI will be accepted as the first definite step toward achieving a hydrogen-energy society.

Reference

1. Tanaka Y, Inui F, Takeo H (2015) The Mirai FCV as the forerunner of the next century of vehicle development. TOYOTA Tech Rev 61

Chapter 35

Residential Applications: ENE-FARM

Yoshio Matsuzaki

Abstract This chapter describes the development and commercialization of residential fuel cell power units, based on polymer electrolyte fuel cells (PEFCs) and solid oxide fuel cells (SOFCs). The merits of cogeneration in residential applications are also described. The cumulative sales of such system in Japan are shown, approaching ca. 150,000 units in 2015.

Keywords Residential fuel cell ENE-FARM · Polymer electrolyte fuel cells · Solid oxide fuel cells · Cogeneration · Efficiency · Cumulative sales

35.1 Introduction

In 2009, the world's first commercialization of residential fuel cell systems using polymer electrolyte fuel cells (PEFCs) was realized in Japan. All the combined heat and power (CHP) systems based on the fuel cells for a residential use in Japan have been named "ENE-FARM." The first residential CHP system using solid oxide fuel cells (SOFCs) was launched in 2011 with the same name, "ENE-FARM," with the additional identifying code of "Type-S." Thus ENE-FARM can be currently classified by the type of fuel cell used: PEFC or SOFC. "ENE-FARM PARTNERS" was established in 2013, as an alliance of ENE-FARM-related industries for promoting ENE-FARM, which has excellent merits in reductions of both energy consumption and CO₂ emission.

Y. Matsuzaki (✉)
Fundamental Technology Department, Tokyo Gas Co., Ltd.,
1-5-20 Kaigan, Minato-ku, Tokyo 105-8527, Japan
e-mail: matuzaki@tokyo-gas.co.jp

Y. Matsuzaki
Kyushu University, Fukuoka, Japan

35.2 Features and Merits of ENE-FARM

Figure 35.1 shows a schematic illustration of a residential CHP system based on a fuel cell (ENE-FARM) connected to home energy systems through the lines of electricity, heat, and hot water. Electricity generated from fuels by electrochemical reactions in ENE-FARM is used for electric appliances such as televisions, lighting, and refrigerators, resulting in power saving by the reduction of the purchase of electricity from a power company. As well as electrical power, exhaust heat from ENE-FARM can be used for the residential needs of hot water supply to bathrooms and kitchens, as well as needs of heating systems.

Figure 35.2 indicates the energy losses and efficiencies in the generation and transmission of energy from primary energy to consumption in individual homes. Figure 35.2 explains the case of (a) a large-scale power generation system, and (b) ENE-FARM.

In the case of a large-scale power generation system, the energy loss caused by unutilized thermal energy generated during power generation at a thermal electric

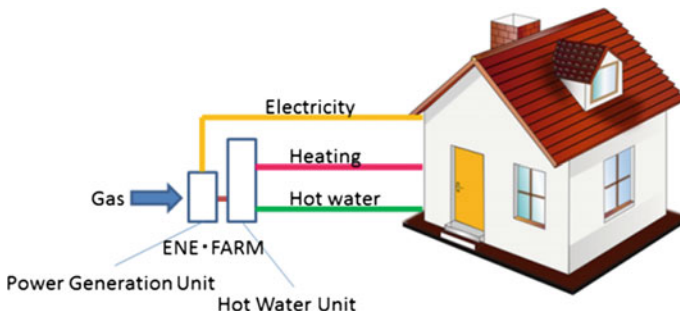


Fig. 35.1 Schematic illustration of an ENE-FARM fuel cell connected to home energy systems

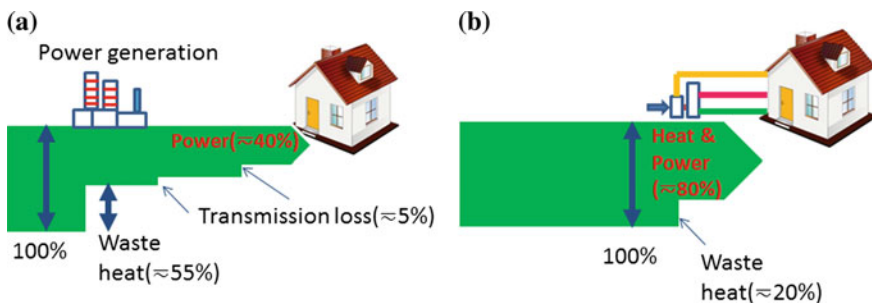


Fig. 35.2 Energy losses and efficiencies in the generation and transmission of energy from primary energy to consumption in individual homes: a large-scale power generation systems, and b ENE-FARM

power plant is approximately 55 %, and the energy loss caused by transmission of electric power for long distance from the plants to individual houses is approximately 5 %. Consequently the total energy loss and efficiency are approximately 60 and 40 %, respectively.

In the case of ENE-FARM, the energy loss can be reduced thanks to the on-site power generation that enables the use of thermal energy generated during power generation and eliminates the transmission loss, resulting in a higher energy efficiency of 80 % and more. Therefore promoting the use of ENE-FARM should lead to energy saving and environmental benefits.

Figure 35.3 shows external views of ENE-FARM. As described above, ENE-FARM can be classified by the type of fuel cell, PEFC or SOFC. Toshiba and Panasonic are manufacturers of the PEFC-based ENE-FARM, and AISIN is a manufacturer of the SOFC-based ENE-FARM. The electrical efficiency of the SOFC-type is approximately 52 %, which is much higher than the approximately 39 % electrical efficiency of the PEFC-type.

For the PEFC-based ENE-FARM, the market price was successfully reduced to less than 2 M yen in 2013, and then further reduced to 1.6 M yen in 2015. This is, however, still much higher than the target price of 0.5–0.6 M yen. As described below, PEFC-based ENE-FARM units for use in condominiums, the first of this type of specification in the world, have also been developed and released in 2014.

For the SOFC-based ENE-FARM, the world's first commercialization was made by JX Nippon Oil & Energy Corporation in 2011. Then, Osaka gas began to sell the same type of ENE-FARM in 2013. The selling price of 1.83 M yen is higher than the 1.6 M yen of the PEFC-type at this time. However, the SOFC-type has flexibility for a variety of fuels to allow simple fuel processing, and is expected to have a relatively large margin for cost reduction because of the higher possibility of simplifying the system configuration.

The marketability of ENE-FARM has been improved by factor such as enabling operation by smartphone, and/or visualizing the energy generation and consumption. In the case of operation by smartphone, floor heating and hot water supply to a



Adapted from “Hydrogen white paper [1]

Fig. 35.3 Exterior views of three types of ENE-FARM

bathtub can be controlled. The quantity of electric power generation and consumption illustrated on the smartphone display also results in higher awareness of energy conservation.

35.3 Sales of Residential Fuel Cell CHP Systems

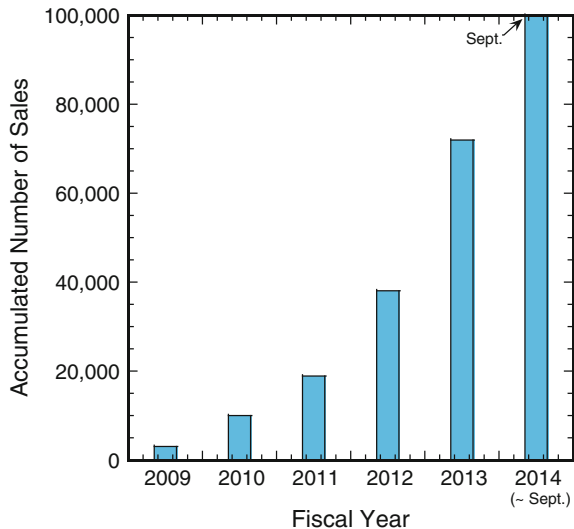
Figure 35.4 indicates the cumulative sales of ENE-FARM. The sales of ENFAM began in 2009 with approximately 3000 units sold. This increased to approximately 10,000 cumulative units in 2010. After that, cumulative sales increased year by year up to 100,000 units in September 2014. The targets of cumulative sales are 1,400,000 and 5,300,000 units in 2020 and 2030, respectively.

35.4 Improving the Specifications

35.4.1 Off-Grid Operation in the Event of Grid Power Outage

ENE-FARM did not originally operate without grid power, because electric power was necessary for start-up. This would be inconvenient especially in a disaster situation, or emergency. Therefore, an optional unit has been developed and released, which enables ENE-FARM to operate without grid power by using a secondary battery. Additionally, another type of optional unit, which is a switching

Fig. 35.4 Cumulative sales of ENE-FARM



unit for successive power generation, has been developed and released, by which an electric power of 500 W can be utilized for a maximum of four days (96 h) even in the event of grid power outage.

35.4.2 Modifications for Condominium Installation

In April 2014, sales of ENE-FARM specifically for condominiums began. This type of ENE-FARM enables all the units, including the fuel cell, a hot water storage, and backup boiler, to be installed in the pipe shaft of the apartment building. This specification was without precedent in the world at that time. Although installation is highly limited for a condominium when compared to a single-family house, installation in pipe shafts in corridors has been realized by enhancing the gas tightness of the system. According to installation standards in condominiums, resistance to earthquakes and wind has been increased, resulting in systems able to be operated even on upper floors of high-rise apartment blocks. Saving of energy bills and CO₂ emissions per year for a condominium-based ENE-FARM unit has been estimated to be 30,000–40,000 yen and 1 ton, respectively, by a model calculation.

35.5 Summary

In April 2014, the “New Strategic Energy Plan” was formulated by the government of Japan [1–3]. In this plan, ENE-FARM was described by the following sentences: “The hydrogen-related technology that has been most accepted in society is ENE-FARM. In Japan, commercial stationary fuel cells were introduced into households for the first time in the world based on the background of the country’s superiority in fuel cell technology. More than 60,000 units have already been installed in houses, and other locations, and the possibility of developing overseas markets is now within sight. Now is the time to develop domestic and overseas markets.”

For the further spread and expansion of ENE-FARM in order to achieve cumulative sales target numbers by 2020 and 2030, innovative improvements such as considerable cost reduction, increase in electrical efficiency, and the enhancement of product values, are required. Fundamental technologies and academic industrial alliance should be advanced to support innovative improvements.

References

1. Hydrogen White Paper 2014, Website by NEDO (2014) <http://www.nedo.go.jp/content/100567362.pdf>. Accessed 15 Dec 2015 (in Japanese)
2. Strategic Road Map for Hydrogen and Fuel Cells, Website by METI (2014) <http://www.meti.go.jp/press/2014/06/20140624004/20140624004-2.pdf> (in Japanese). http://www.meti.go.jp/english/press/2014/0624_04.html (English summary). Accessed 15 Dec 2015
3. New Strategic Energy Plan, Website by METI (2014) http://www.enecho.meti.go.jp/en/category/others/basic_plan/pdf/4th_strategic_energy_plan.pdf. Accessed 15 Dec 2015

Chapter 36

Distributed Power Generation

Yoshinori Kobayashi

Abstract This chapter describes stationary fuel cell applications for distributed power generation. After briefly describing the history of stationary fuel cell power systems development, experiences are given in developing industrial fuel cell systems with their demonstration results. Future perspectives are also described including the power generation with digestion gas and the trigeneration to supply electricity, heat, and hydrogen gas.

Keywords Industrial fuel cells · Cell development · System specification · Durability · Solid oxide fuel cell · Hybrid system · Digestion gas · Tri-generation

36.1 Introduction

As discussed repeatedly from the beginning of this book, it is necessary to create a low-carbon society and enhance energy consumption efficiency in order to simultaneously solve global warming, the energy crisis, and economic problems. Along with this background, focus has been given to the development of technologies for stationary power plants, with the aim of achieving high efficiency. Natural gas-fired gas turbine combined cycle (GTCC) plants, coal-fired ultra-supercritical (USC) plants, and integrated coal gasification combined cycle (IGCC) plants are being put to practical use, especially in large-scale power generation systems that are used as central power supplies. On the other hand, the ENE-FARM scheme has a higher efficiency than normal power generation systems and is a prospective

Y. Kobayashi (✉)

Mitsubishi Hitachi Power Systems Ltd., Minatomirai 3-chome,
Nishi-ku, Yokohama 220-8401, Japan
e-mail: yoshinori_kobayashi@mhps.com; yosikoba@iis.u-tokyo.ac.jp

Present Address:

Y. Kobayashi
The Institute of Industrial Science (IIS), The University of Tokyo,
4-6-1 Komaba, Meguro-ku, Tokyo 153-8505, Japan

© Springer Japan 2016

K. Sasaki et al. (eds.), *Hydrogen Energy Engineering*,
Green Energy and Technology, DOI 10.1007/978-4-431-56042-5_36

483

household fuel cell system. This contributes to the improvement of energy consumption efficiency by increasing the total power generation efficiency for city gas through cogeneration using waste heat from power generation for heating water. It is considered that there is still room for further improvements in the efficiency of large-scale distributed power sources for business and industrial use, partly because of the difficulty in cogeneration.

In pursuit of the best energy mix, the so-called “3E+S” policy is currently advocated to realize energy security, economic growth, and environmental conservation on the major premise of safety assurance. On the premise of safety assurance of nuclear power plants, there are three objectives of improving energy self-sufficiency, reducing the cost of electric power, and improving world-leading environmental compatibility. In order to reduce CO₂ emissions, distributed power sources will be combined depending on the location and capacity, based on existing fundamental power infrastructure built with high-efficiency central power supplies, and new forms of energy such as renewable sources of energy will be introduced as much as possible in the most economical and rational manner.

In addition to the requirement that distributed power sources should be independent, economical, stable, and have high flexibility, they are now also required to have a powerful business continuity planning (BCP) function. In this sense, the disaster-prevention function of distributed power sources has attracted attention after the Fukushima disaster in Japan. However, conventional emergency power sources generally have low power generation efficiency in order to reduce the installation costs. Moreover, their everyday use may cause environmentally unfavorable results. Therefore, the key to expanding the use of distributed power sources is to use high-efficiency power generation systems, with the main focus being on using fuel cells for business and industrial applications. In particular, in recent years, the accelerated introduction of solid oxide fuel cells (SOFCs), which offer the highest power generation efficiency in stationary power plants, has become a key national policy (Fig. 36.1).

36.2 Fuel Cells for Distributed Generation

Fuel cells have been introduced as distributed generation systems under atmospheric pressure. Typical examples of SOFCs include the 200 kW system commercialized by Bloom Energy (US) with total sales of more than 150 MW, taking advantage of the subsidy system of the US federal and state governments [1]; and the 1.2 MW system for Osaka prefecture in Japan, sold as a disaster-resistant power source in the power trading scheme emphasizing power source security [2]. Fuel Cell Energy (US) is building a large-scale 60 MW plant in Korea utilizing molten carbonate fuel cell (MCFC) technology developed by POSCO (Korea) [3]. Similarly, Doosan (Korea) took over former Clear Edge Corporation (US) and entered into the market of distributed power generation with phosphate acid fuel cells (PAFCs) [4]. With strong support from the Korean government, these two

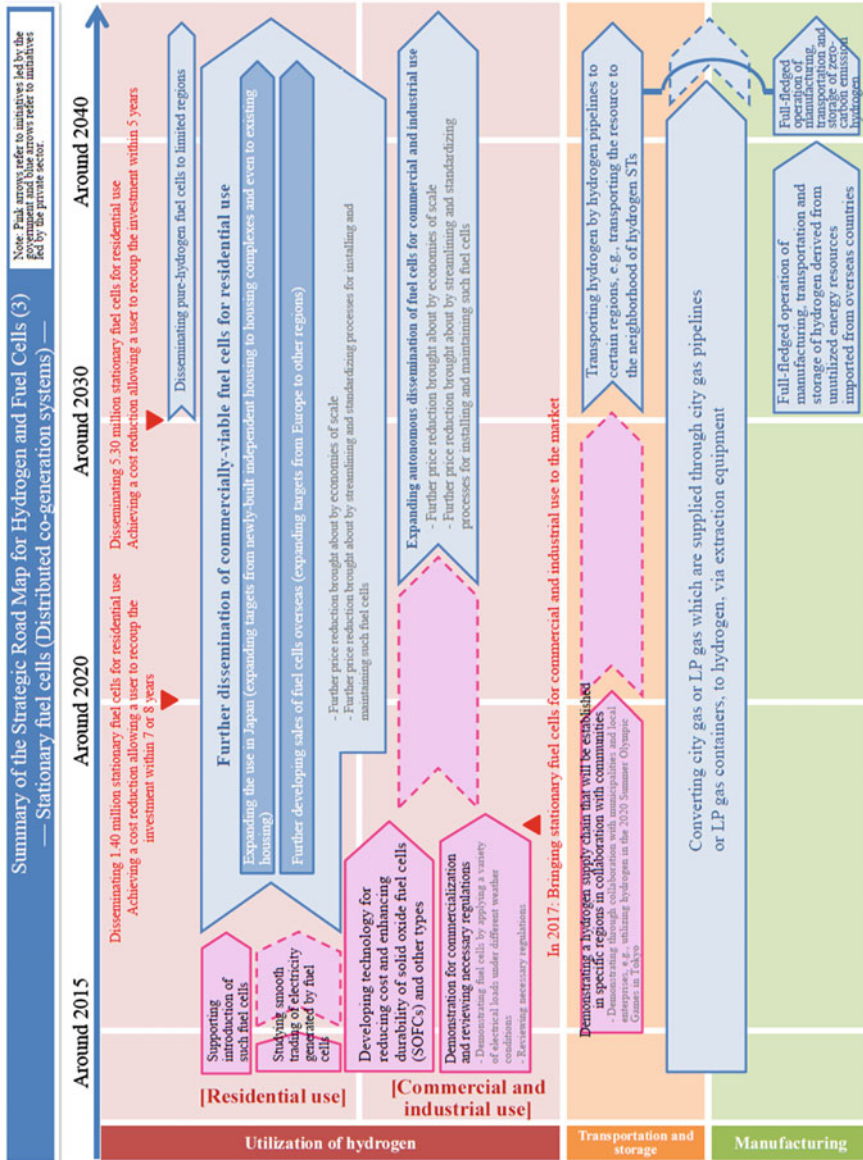


Fig. 36.1 Summary of the strategic road map for hydrogen and fuel cells. *Source* Summary of the strategic road map for hydrogen and fuel cells, Agency for Natural Resources and Energy, METI (June, 2014)

companies are rapidly increasing the number of products sold and have jointly announced the construction of the world's largest fuel cell plant, at 360 MW [5]. In Japan, Fuji Electric was among the first companies to introduce and sell PAFC systems domestically, and is actively developing markets in other countries, including Germany. They are also focusing on fire safety by using nitrogen-rich effluent gas [6], as well as power generation using digestion gas.

In large-scale industrial distributed power generation systems, considerable effort has been invested for decades to develop SOFC systems for large-scale, high-pressure power generation plants [7–10]. After the pioneering work of Westinghouse (US), who demonstrated a several hundred kW-class SOFC system [7], Rolls-Royce [11, 12] and Mitsubishi Heavy Industries [13–15] have continuously been developing SOFC systems that could surpass the efficiency of the latest GTCC plant. In particular, the triple combined cycle system, in which the SOFC is connected to the upstream portion of the GTCC, has attracted attention as a higher efficiency technology, which could achieve power generation efficiency of over 70 % LHV, reflecting the fact that natural gas is attracting attention owing to the occurrence of the shale gas revolution. Bloom Energy started full-scale production and sales of several hundred kW-class SOFC systems working at atmospheric pressure; the distributed power sources operable during an emergency indicate that the distributed power supply using SOFC is already entering the stage of practical use.

36.3 Examples of SOFC High-Efficiency Power Generation Systems

Here, we discuss in detail a hybrid, high-efficiency distributed power supply, combining an SOFC system, and a micro gas turbine (MGT) which is being developed and tested by Mitsubishi Hitachi Power Systems (MHPS). To realize the most efficient fuel cell power generation system, the hybrid system generates a greater amount of electrical energy by the cascade (two-stage) extraction of input chemical energy, which is realized by operating fuel cells in the early part of an existing heat cycle. In this system, an all-ceramic solid structure is required because the fuel cells are operated at high temperatures in the high-pressure section of the upstream portion of the MGT combustor; therefore, tubular SOFC cells were specially developed by MHPS.

36.3.1 Cell Stack

Figure 36.2 shows the tubular SOFC cell stack structure manufactured by MHPS. The power generation cells are made up of a sandwich structure of fuel electrode (anode), electrolyte, and air electrode (cathode). These are formed on the outer surface of the substrate tube (which acts as a structural element) and are mutually tandem connected with electrically conductive ceramics called interconnectors. The

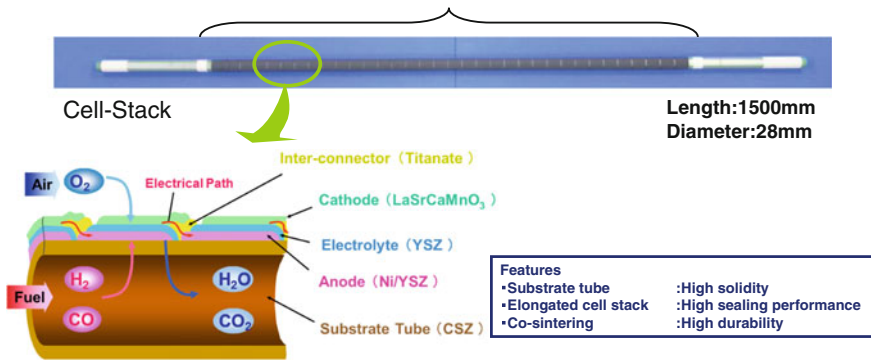


Fig. 36.2 Structure of cell stack

various constituent elements of a cell have different thermal expansion properties, which makes the manufacture of durable devices more challenging. The performance and durability can be improved using constitutive materials having similar coefficients of thermal expansion; reducing the production costs by the use of integral sintering through improved production technology; and improving the compatibility between neighboring materials.

MHPS has developed an original high-performance cell stack. The cell performance was improved by optimizing the, e.g., the electrolyte, electrodes, and interconnectors, as well as by adjusting the particle size in the active layers. However, in the segmented-in-series tubular type cell stack, belt-shaped cells (so-called power generation cells) are connected in series by interconnects in the longitudinal direction. These are formed on the outer surface of the long tubular cell stack. The output is increased simply by reducing the width of each cell, and placing as many cells as possible in each stack. In a cell stack using “Model 10” cells, the output per stack is improved by 30 % by increasing the number of cells up to 85. In addition, in the cell stack using “Model 15” cells that is designed to achieve further technological advances, the output density is increased by 50 % with respect to the cell stack using the Model 10 cells, by improving the interface between the electrode and electrolyte (Fig. 36.3).

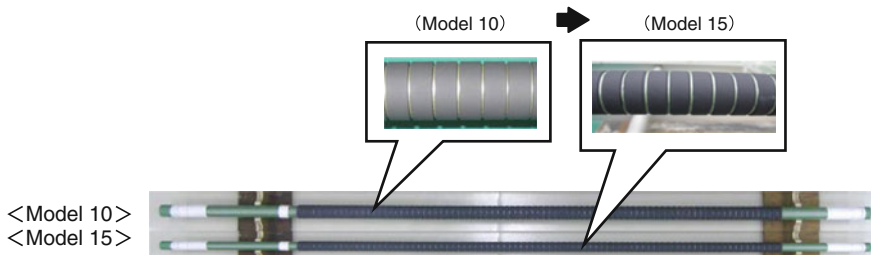


Fig. 36.3 Tubular SOFC cell stack

36.3.2 Cartridge

Cell stacks are bundled to form a cartridge to generate several tens of kW of electricity, and a batch of cartridges is accommodated in a pressure vessel to constitute a module having a desired capacity (Fig. 36.4). This type of layer structure aims at systematization, considering the installation and maintenance. In addition, we can cope with the required range of electrical output by adjusting the number of cartridges and modules.

The cartridges are designed with the aim of improving the output density per unit volume and the compactness. While the heat generation density increases with the packing density, heat transfer equivalent to the conventional level is ensured at the power generation section and the heat exchange sections, which are placed above and below the power generation section, by optimizing the heat transfer and cooling design of the cartridge and controlling the heat transfer. In the cell stack using Model 15 cells, it is possible to increase the output density per volume and reduce the installation area by reducing the diameter and increasing the length of the cell stack (Fig. 36.5).

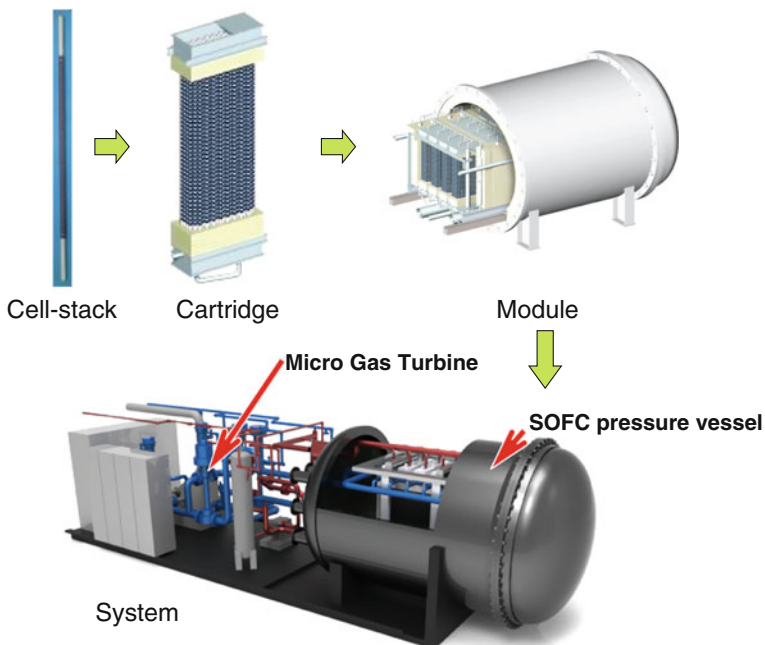


Fig. 36.4 Composition of SOFC–MGT hybrid system

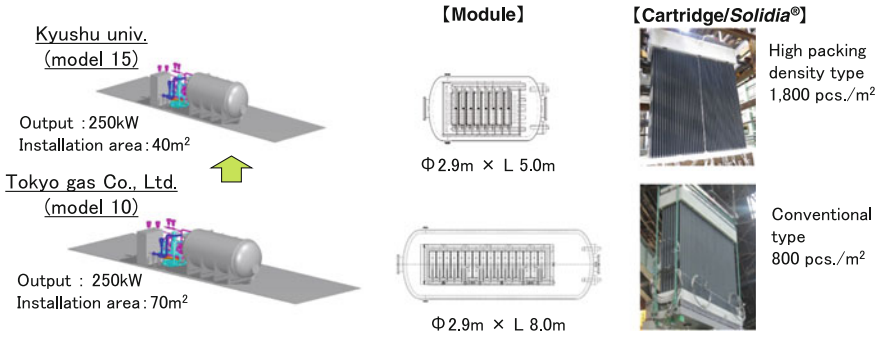


Fig. 36.5 Development of cell stack/cartridge for low-cost mass production

36.3.3 Hybrid System

Figure 36.6 shows a flow diagram of the hybrid power generation system. This system generates electricity from both the SOFC and the gas turbine (GT). The SOFC generates electricity from natural gas (city gas) and the ambient air compressed by the GT. As the SOFC exhaust fuel gas contains a certain amount of unused fuel and still remains at a high temperature, the SOFC exhaust fuel gas can be utilized to additionally generate electricity by the coupled GT. This effective two-stage use of the fuel leads to a higher power generation efficiency, compared to the power generation by SOFC only. In addition, exhaust heat from GT can be used to supply steam or hot water.

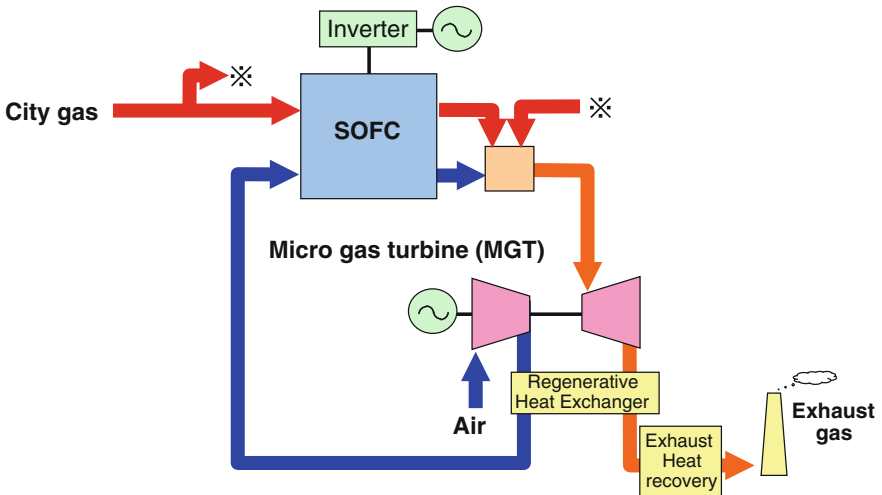


Fig. 36.6 SOFC–MGT hybrid system

This system uses compressed air from the GT. The pressurized operation of the SOFC system leads to a higher power output of SOFCs, as shown in Fig. 36.7 [16, 17].

36.4 System Verification

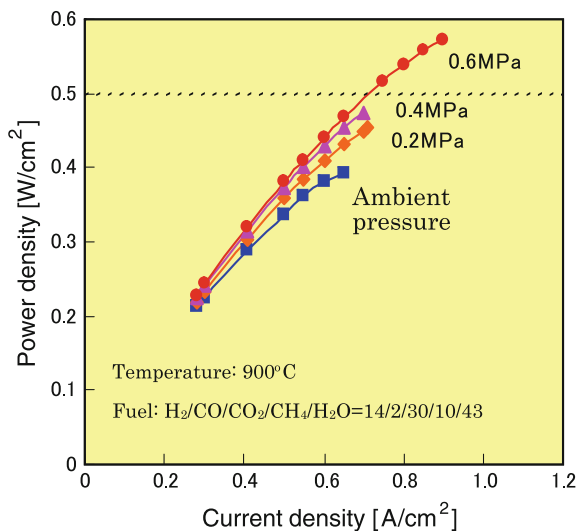
36.4.1 Verification of Long-Term Durability

Based on earlier results, we developed and evaluated a 250 kW grade SOFC–MGT hybrid power generation demonstration system using the Model 10 cells, at the Tokyo Gas Senju Techno Station in a NEDO project during a 3-year period (2011–2014). Note that the MGT was the product of Toyota Turbine and Systems (Fig. 36.8).

In order to analyze technological issues and promote the introduction of SOFC–MGT hybrid systems, we acquired long-term durability test data and the emergency response data from this demonstration system, concerning start–stop operation, load change, and abnormality of the system. As a result, the reliability and safety of the system have been demonstrated.

Stable operation was confirmed through long-term durability evaluation, including heavy loads in the summer season. The system was continuously operated for more than 4100 h until the test plan was completed; no time-dependent degradation was observed under the constant rated load, and a voltage reduction rate of 0 %/1000 h was achieved (Fig. 36.9).

Fig. 36.7 Pressurized characteristic of the cell. Operating pressure dependence of power density [16]



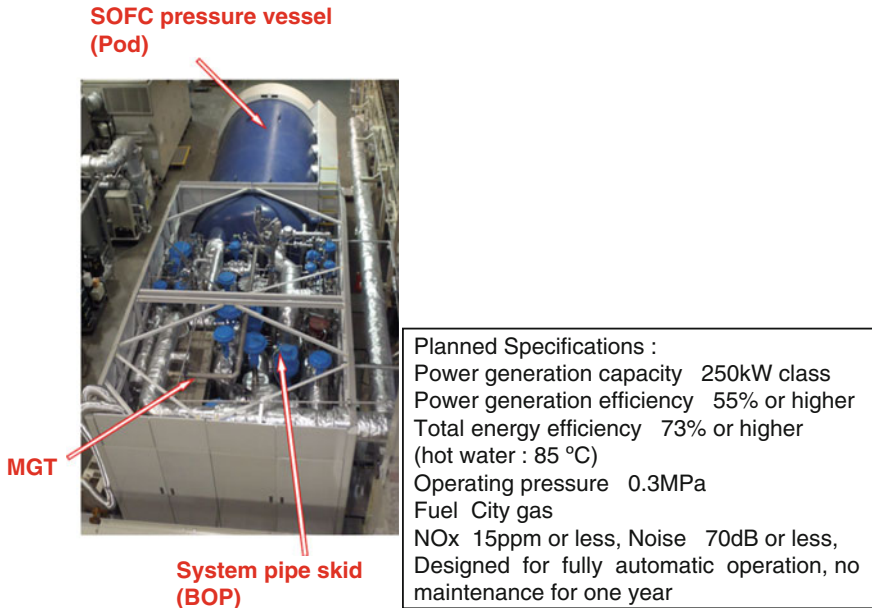


Fig. 36.8 SOFC–MGT hybrid system for demonstration using the Model 10 cells

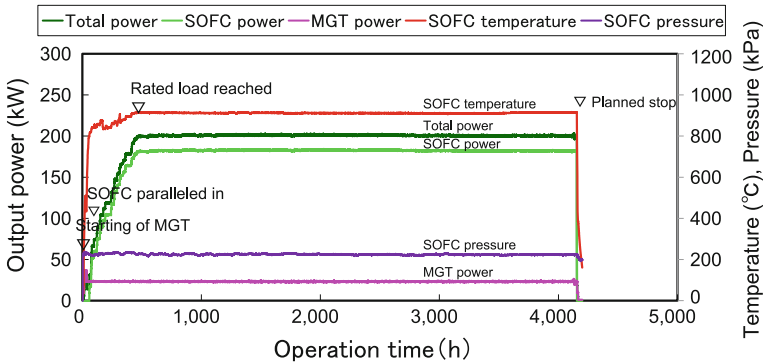


Fig. 36.9 Result of durability test for a SOFC–MGT hybrid system

36.4.2 Start-up Characteristics of the System

Today, improvement and performance evaluation of the system are conducted using start-up characteristics, an important determinant of the distributed power generation supplies. Efforts are being made to overcome the disadvantages of the very large heat storage capacity of ceramics. Figure 36.10 shows the process of cold start-up from room temperature. In the start-up of an SOFC, first the pressure of the

pressure container is increased. Then hot air is passed through the regenerative heat exchanger connected to the MGT compressor exit, and distributed into the SOFC air system to heat the pipes and the SOFC module within the pressure container. The hot air from the MGT is used for heating the generator space up to approximately 400 °C; after that, fuel is burned in the SOFC air system for heating the generator space up to 800 °C. Finally, the fuel for power generation is injected into the SOFC so that the start-up process is completed.

The result of the verification test confirms that the cold start-up takes approximately 24 h while the start-up time could be reduced to approximately 12 h if the MGT air is heated to more than 600 °C using an apparatus such as a duct burner at the initial stage of heating. This level of performance is equivalent to that of the cold start-up of the coal-fired power generation system widely used in large-scale power stations. Furthermore, a restart time of 8 h was confirmed in a hot restart from 600 °C; a further reduction in start-up time is considered possible depending on the holding temperature during the stoppage time of the unit. In other words, there is a prospect of complying with the Daily Start & Stop (DSS) mode of the SOFC, which is considered a key base load power source.

36.4.3 System Verification

Based on the successful results for the demonstration system using the Model 10 cells, an advanced demonstration system was designed using the Model 15 cells and installed in the Ito campus of Kyushu University in March 2015. This demonstration system will further be used in studies for verifying the Smart Fuel Cell Demonstration Project of the Green Asia Fukuoka International Strategic Zone, at the Next-Generation Fuel Cell Research Center (NEXT-FC), Kyushu University. It is in the basic research program for

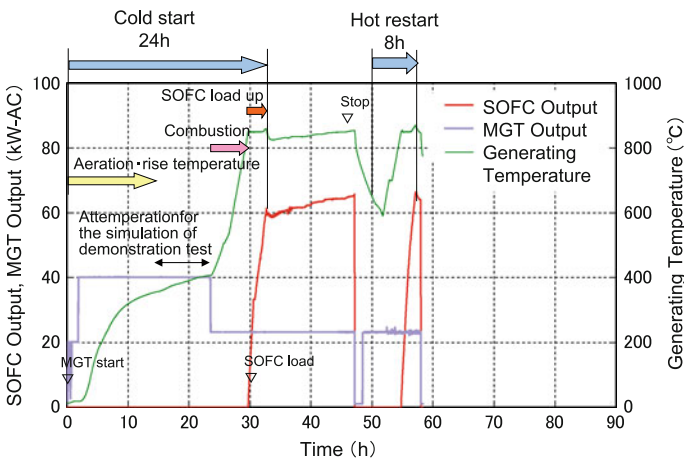


Fig. 36.10 Start-up characteristics of a SOFC hybrid system

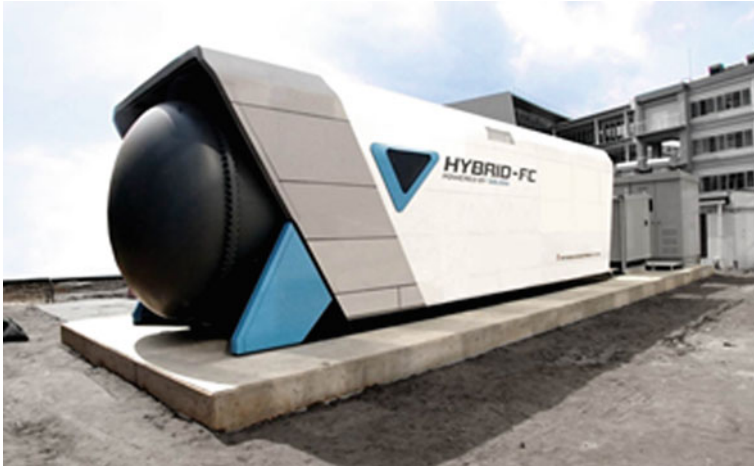


Fig. 36.11 SOFC–MGT hybrid system for advanced demonstration using the Model 15 cells

improving the performance, durability, and reliability of SOFCs (Fig. 36.11). The NEXT-FC center was established at Kyushu University for close industry-academia collaborations to realize a fuel cell-powered society.

36.5 Future Introduction and Development


It is expected that, in the foreseeable future, city gas—fired distributed power sources will be introduced in business and industrial sectors such as hospitals, hotels, banks, and data centers of various types, owing to advantages such as high-efficiency cogeneration, low noise, and good environmental characteristics. Table 36.1 lists the system specifications for the product that MHPS plans to sell. It is scheduled to bring the prototype to market in 2015 for evaluation; full-scale sales will start in 2017. It is expected that the durability and portability will be continuously improved, making use of the features and evaluation provided by the prototype design. In the future, we will develop systems with more competitive specifications and lower costs.

36.6 Road to a Hydrogen Society

36.6.1 Multi-energy Station

While a SOFC as a high-efficiency distributed power supply is expected to contribute to a low-carbon society through its use in the business and industrial sectors,

Table 36.1 Specification of the system

		250 kW SOFC–MGT hybrid system
Appearance		
Rated output	kW	250
Net efficiency	%-LHV	55
Total heat efficiency	%-LHV	73 (hot water) 65 (steam)
Dimensions of the unit	m	12.0 × 3.2 × 3.2
Operation		For cogeneration
		These specifications indicate planned values

it is also expected that the SOFC be introduced to hydrogen filling stations so that we can move a step toward a hydrogen society, making use of the internal reforming function, which is another beneficial feature of the SOFC. As shown in Fig. 36.12a, an SOFC generates electricity and heat using hydrogen and carbon monoxide produced by the internal steam reforming of city gas. Note that we can directly take out a part of hydrogen produced by internal steam reforming, as shown in Fig. 36.12b, instead of using it for power generation; thus, it is possible that electricity, heat, and hydrogen are simultaneously supplied. Moreover, the Quatrogen[®], which supplies city gas (fuel), can also be realized. By using the system in a hydrogen station, we can simultaneously supply fuel not only to fuel cell-powered vehicles (FCV) but also to low-carbon vehicles such as electric vehicles (EVs) and compressed natural gas vehicles (CNGVs); a considerable improvement in profitability is expected in stations where profitability is the greatest problem during the early stage of FCV introduction (Fig. 36.12c).

36.6.2 Local Production of Energy for Local Consumption (Use of Renewable Energy)

It is conceivable that we generate electricity using digestion gas generally available at sewage treatment plants in urban areas. Furthermore, since digestion gas consists of approximately 60 % methane, high-efficiency power generation fueled by digestion gas could be established using high-purity methane as fuel and techniques of CO₂ separation. By using the earlier-mentioned Quatrogen, “urban-produced hydrogen” is produced from digestion gas, and the concept of “local production of energy for local consumption in urban areas” is realized (Fig. 36.13).

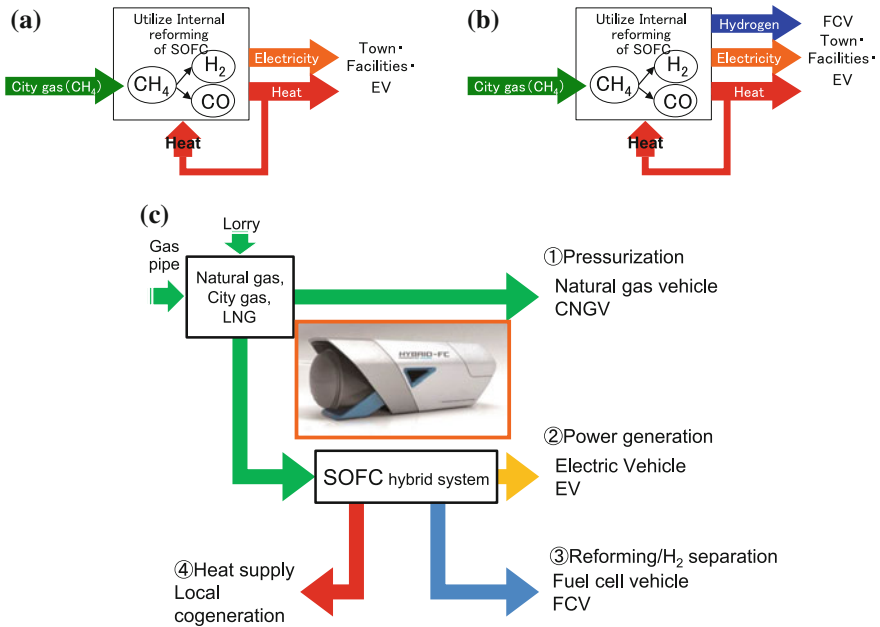


Fig. 36.12 Image of quaternogen. **a** Electricity and heat conventionally supplied by SOFC. **b** Supply of hydrogen formed by internal reforming. **c** Application to hydrogen station

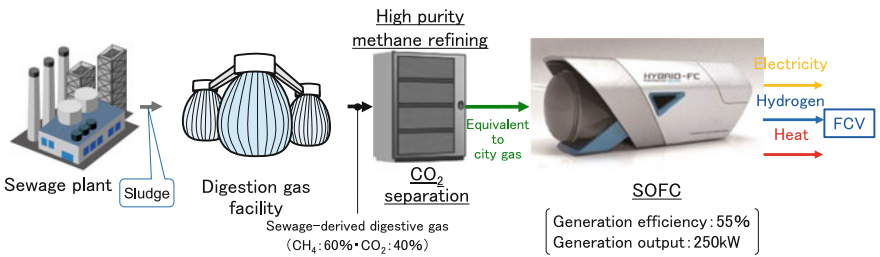


Fig. 36.13 SOFC power generation using digestion gas

The introduction of SOFC-based distributed power supply systems is going to be accelerated through the creation of an additional value by focusing on a hybrid system utilizing digestion gas.

36.7 Summary

The Ministry of Economy, Trade and Industry (METI) formulated the Strategic Road Map for Hydrogen and Fuel Cells in June 2014, in which fuel cells for the business and industrial sectors are predicted to appear in the market in 2017.

High-efficiency power generation systems using SOFC will be put to practical use as distributed power at an early date, greatly contributing to the construction of a safe and sustainable low-carbon society in the future.

References

1. Bloom Energy Homepage (2015) Press releases. April 21
2. Bloom Energy Japan Homepage (2015) News press releases, March 9
3. Fuel Cell Energy Homepage (2013) Press releases, October 24
4. Doosan Corporation Homepage (2014) Press Releases, July 21
5. Doosan Corporation Homepage (2014) IR Materials, 2014 Doosan's management performance in Q2
6. FUJI ELECTRIC CO., LTD. (2011) Fuel cell system demonstration plant with low-oxygen-concentration air supply. *Fuji Electric J* 84(1):46 (in Japanese)
7. Singhal SC, Kendall K (2003) *High-temperature solid oxide fuel cells: fundamentals, design and applications*. Elsevier LTD, UK
8. Minh NQ, Takahashi T (1995) *Science and technology of ceramic fuel cells*. Elsevier Science, Amsterdam
9. Minh NQ (1993) Ceramic fuel cells. *J Am Ceram Soc* 76(3):563–588
10. Stolten D (2010) *Hydrogen and fuel cells*. Wiley-VCH, Weinheim
11. Gardner FJ, Day MJ, Brandon NP, Pashley MN, Cassidy M (2000) SOFC technology development at Rolls-Royce. *J Power Sources* 86:122–129
12. Haberman B, Baca CM, Ohm T (2011) IP-SOFC performance measurement and prediction. *ECS Trans* 35(1):451–464
13. Hisatome N, Ikeda K, Takatsuka H, Mori Y, Iwamoto K (2000) Development of tubular type solid oxide fuel cells. *Mitsubishi Heavy Ind Tech Rev* 37(1):30–33
14. Nishiura M, Koga S, Kabata T, Hisatome N, Kosaka K, Ando Y, Kobayashi Y (2007) Development of SOFC-Micro gas turbine combined cycle system. *ECS Trans* 7(1):155–160
15. Kobayashi Y, Ando Y, Kabata T, Nishimura M, Tomida K, Matake N (2011) Extremely high-efficiency thermal power system-solid oxide fuel cell (SOFC) triple combined-cycle system. *Mitsubishi Heavy Ind Tech Rev* 48(3):9–15
16. Kobayashi Y, Ando Y, Kishizawa H, Tomida K, Matake N (2013) Recent progress of SOFC-GT combined system with tubular type cell stack at MHI. *ECS Trans* 51(1):79–86
17. Kobayashi Y, Nishimura M, Kishizawa H, Tomida K, Hiwatashi K, Takenobu H (2015) Development of next-generation large-scale SOFC toward realization of a hydrogen society. *Mitsubishi Heavy Ind Tech Rev* 52(2):111–116

Chapter 37

Triple Combined Cycle Power Generation

Yoshinori Kobayashi

Abstract This chapter describes highly efficient power generation with larger-scale stationary fuel cell system. After describing the history of thermal power plant development with increasing thermal efficiency, concepts of gas turbine–fuel cell (GTFC), and coal-fired triple combined cycle power generation (IGFCs), and elementary technology for triple combined cycle systems are explained.

Keywords Power plant · Power generation efficiency · Solid oxide fuel cell · Gas turbine · Steam turbine · Combined cycles · Triple combined cycle

37.1 Introduction

A hybrid system in which a solid oxide fuel cell (SOFC) is combined with a micro gas turbine (MGT) was discussed in detail in the previous chapter (Chap. 36). However, from the viewpoint of global warming and the energy security for a country like Japan, the most urgent and requisite need is the efficient use of fossil fuels by introducing and promoting super-high-efficiency thermal power generation in large-scale centralized power plants.

Historically, the use of thermal energy began with the wood-burning stove. Wood was subsequently replaced by coal, which has a greater caloric force, after which early stage steam engines were invented to facilitate mechanized water pumping. Following improvements to practical steam engines that led to the Industrial Revolution, the first Rankine-cycle thermal power station was built with a boiler and

Y. Kobayashi (✉)
Mitsubishi Hitachi Power Systems Ltd., 3-1, Minatomirai 3-chome, Nishi-ku,
Yokohama 220-8401, Japan
e-mail: yoshinori_kobayashi@mhps.com; yosikoba@iis.u-tokyo.ac.jp

Present Address:

Y. Kobayashi
Institute of Industrial Science (IIS), The University of Tokyo, 4-6-1 Komaba,
Meguro-ku, Tokyo 153-8505, Japan

a steam turbine (ST). Concomitant with the march to modernization, the power generation efficiency of the first-generation simple cycle systems was increased through improvements to the conditions under which steam was generated and used (increase in steam temperature and pressure), and finally the first ultra super critical (USC) thermal power station was built with an efficiency greater than 40 % by the end of the twentieth century. The conditions used were 25 MPa and 600 °C at the high-pressure ST inlet and 600 °C at the low-pressure ST inlet. An advanced ultra-supercritical pressure (A-USC) thermal power station is currently aggressively being developed, and early implementation is expected following the development of excellent heat-resistant metal materials and evaluation of their reliability. The expected conditions will be: 35 MPa and 700 °C at the high-pressure and intermediate-pressure ST inlets; 720 °C at the primary low-pressure ST inlet; and 720 °C at the secondary low-pressure ST inlet.

The efficiency of thermal power generation plants has been significantly improved by using a Brayton-cycle double hybrid power system, wherein a gas turbine was placed in the upstream of a boiler as a steam generator. Consequently, today there are power stations with power generation efficiency over 60 % (gas turbine inlet gas temperature: 1600 °C) realized as a result of improvements to the gas turbine inlet gas conditions (i.e., increases in the combustion gas temperature and pressure). Improvements toward realizing a gas turbine inlet gas temperature of 1700 °C are also being carried out to produce a second-generation double hybrid power system. Invariably, excellent heat-resistant metal materials, ceramic heat shield materials, and cooling technology need to be developed and implemented for further efficiency improvements [1].

As indicated by Carnot's theorem (Nicolas Leonard Sadi Carnot, France, 1796–1832), the limit of the efficiency in heat engines depends on the temperature difference between the two heat sources. Conventional combustion heat engines have a maximum efficiency limit because the maximum temperature of the heat source on the high-temperature side is limited by heat-resistance of materials.

Note that, in conventional heat engines, the chemical energy of the fuel is first converted via combustion to thermal energy, which is then converted to the kinetic energy of the turbine using steam as the working medium, and the kinetic energy is finally converted to electrical energy using a generator or other devices. The total efficiency achieved in a practical system is smaller than in theory because additional energy loss occurs at every energy conversion step.

In order to surpass the power generation efficiency limit of conventional heat engines and achieve further efficiency improvements, combinatorial use of fuel cells that can convert the chemical energy of the fuel directly to electrical energy, instead of combustion engines, may be required. "Third generation" triple combined cycle systems including gas turbine fuel cell combined cycle (GTFC) power plants—in which the SOFC, which can use a variety of fuel sources at high temperatures, is combined with a natural gas-fired gas turbine combined cycle (GTCC) plant—and integrated coal gasification fuel cell combined cycle (IGFC) power plants—in which the SOFC is combined with an integrated coal gasification combined cycle (IGCC) power plant (Fig. 37.1)—are particularly needed.

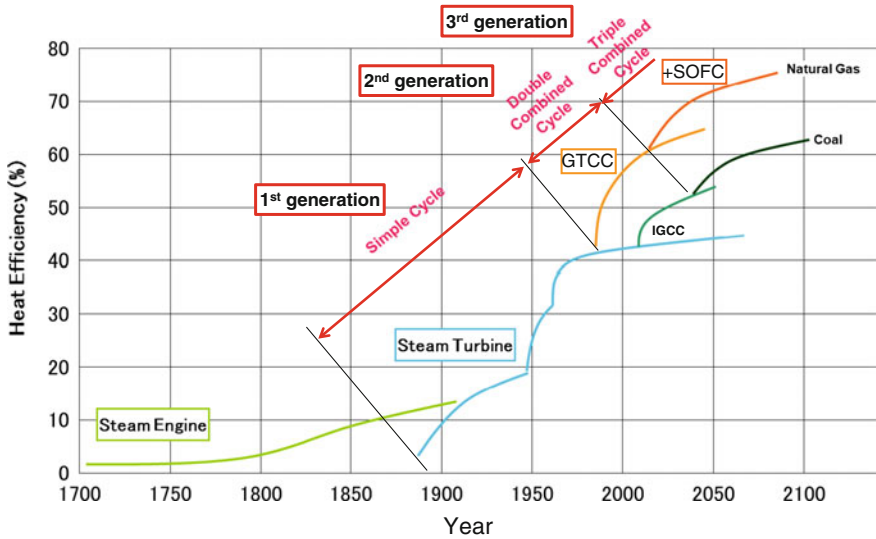


Fig. 37.1 History of power generation efficiency improvements (power generation efficiency in lower heating value (LHV) is shown in the figure)

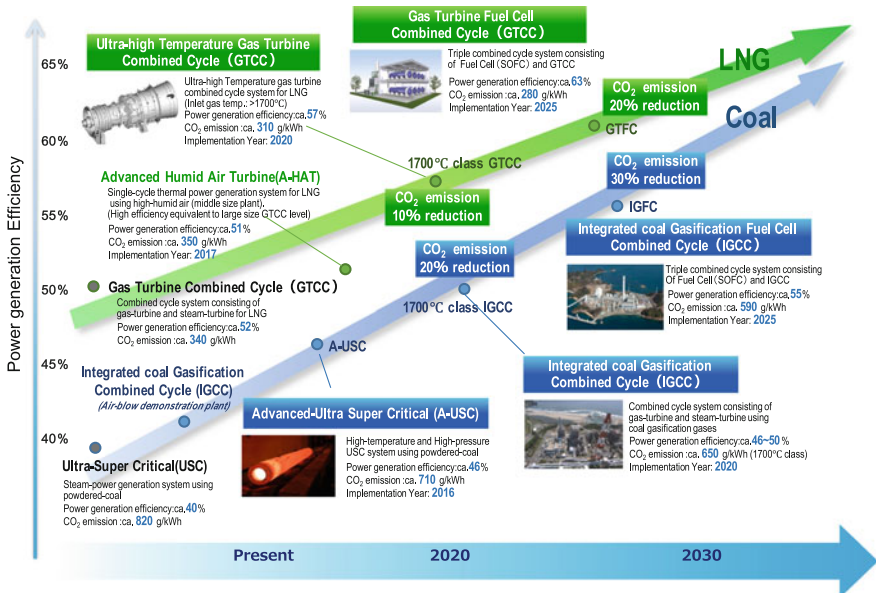


Fig. 37.2 Roadmap for the thermal power generation technology of the next generation (Chart from the third METI meeting for the early realization of next generation thermal power systems, July 6, 2015. Power generation efficiency in higher heating value (HHV) is shown in the figure)

The Agency for Natural Resources and Energy, Ministry of Economy, Trade and Industry, is currently preparing a technology roadmap for next generation power generation technology and is also presently discussing the implementation of next generation power generation systems combined with SOFC technology (Fig. 37.2).

37.2 Gas Turbine Fuel Cells (GTFCs)

Very high power generation efficiency can be realized by using the high-temperature exhaust heat of an SOFC combined with a GTCC and operated at high temperature. The approach taken by Mitsubishi Hitachi Power Systems in their development of a triple combined cycle system, GTFC, is discussed in detail below.

A triple combined cycle system is a unified system in which the SOFC is placed in the upstream section of the GTCC so that the energy of the fossil fuel is converted to electricity via a three-stage cascade, comprising SOFC, GT, and ST (Fig. 37.3). Extremely high power generation efficiency can be realized: up to 70 %-LHV in 100 MW class systems and over 60 %-LHV in 10 MW class systems, by using natural gas as the fuel [2].

The best choice is for the SOFC to be cylindrical with a solid ceramic when it is installed in the high-pressure section in the upstream portion of the gas turbine burner. Figure 37.4 shows the typical energy balance of a triple combined cycle system. When the energy of the fossil fuel, including coal, is utilized by the cascade system comprising the three stages—SOFC, GT, and ST—an extremely high overall power generation efficiency of 63 % can be achieved without the restriction of the Carnot efficiency for thermal systems. This is accomplished using the principle of the triple combined cycle system. The GTCC with a power generation efficiency of 53 %, and a gas turbine inlet gas temperature as low as 1200 °C, and

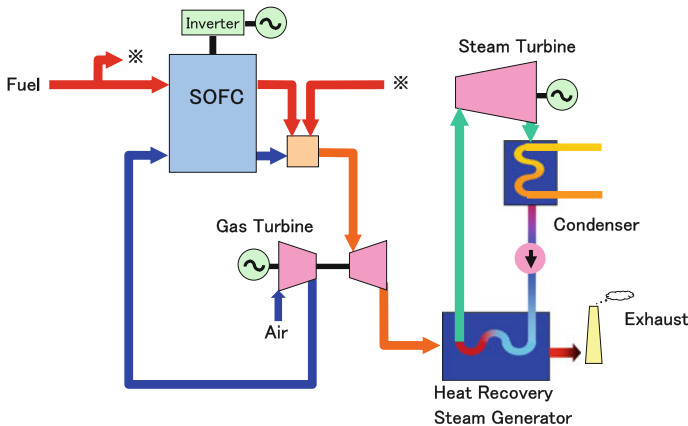
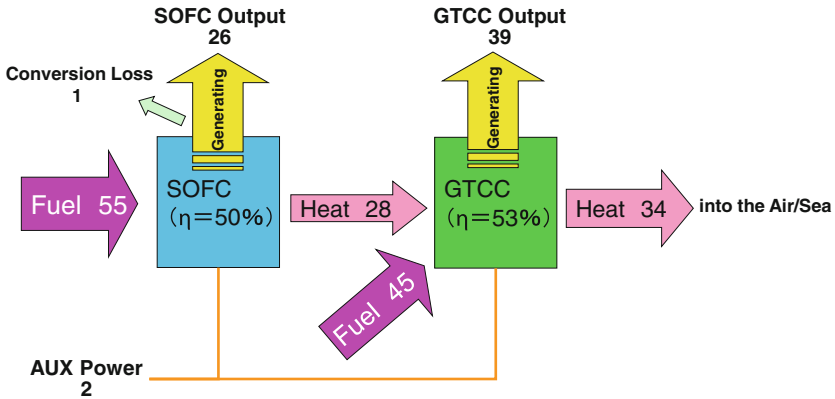


Fig. 37.3 SOFC-GT-ST triple combined cycle system



$$\text{Efficiency (Net} \cdot \text{LHV)} = \frac{\text{SOFC Output 26} + \text{GTCC Output 39} - \text{AUX Power 2}}{\text{SOFC Fuel 55} + \text{GTCC Fuel 45}} \times 100 = 63\%$$

Fig. 37.4 Energy balance of triple combined cycle system

the SOFC with a power generation efficiency of 50 %. A considerable efficiency improvement is expected, compared with existing heat engines.

Besides the future implementation of an extra-large triple combined power generation plant, a small-scale unit is currently being planned with consideration for installment of either a small- or medium-scale centralized power supply system in the inland area (Fig. 37.5). The plant is being designed for an output of approximately 100,000 kW (100 MW) and sending-end efficiency (net thermal efficiency)

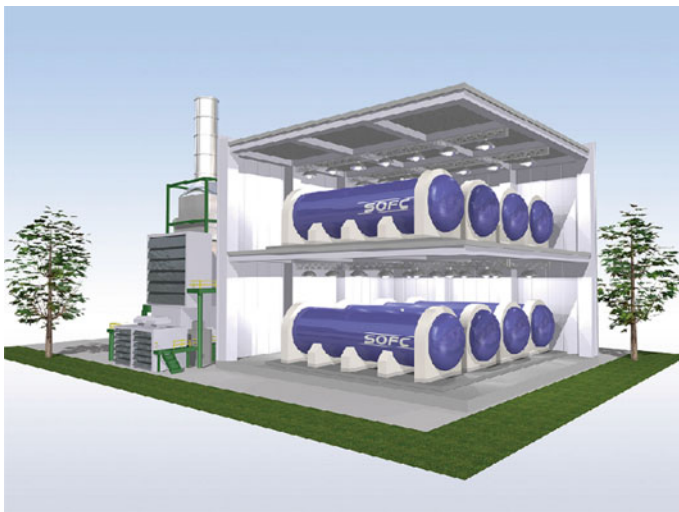


Fig. 37.5 Small-scale triple combined cycle system

of at least 60 % (LHV base). Because the working pressure is as high as 1.5 MPa, development and validation are scheduled to be carried out in order to fully verify the power generation characteristics and long-term durability of the cell stack under a corresponding high pressure. In addition, field evaluation tests of the actual small-scale triple combined system will be conducted.

37.3 Coal-Fired Triple Combined Cycle Power Generation (IGFCs)

Among the various triple combined cycle systems, natural gas-fired systems, which are both clean and easy to deal with, will probably be developed and implemented first, as discussed above. However, because an SOFC can use coal gasification gas as a fuel, development of a triple combined cycle system, IGFC, consisting of an IGCC system and an SOFC system, is possible as illustrated in Fig. 37.6. The IGFC system is being considered as especially advantageous because it can overcome the environmental problems currently associated with coal-fired power plants without harming the economic viability of coal. High efficiency of 60 % is expected from such a coal-fired power generation system (sending-end efficiency; LHV base), excluding the power used for CO₂ collection from the exhaust, in a 700 MW class coal-fired IGFC triple combined cycle plant. IGFC will be easily realized in the future by optimizing the system used to clean up the syngas generated in the gasifier furnace and advancing the system product technologies both for the natural gas-fired SOFC triple combined cycle and the IGCC.

37.4 Elemental Technology for Triple Combined Cycle Systems

As regards development of elemental technology for triple combined systems, new studies are being conducted to validate the power generation characteristics and durability of GT for the SOFC at working pressures in the range of 1–2 MPa, to develop interconnect technology for SOFC and GT, to examine suitable design of GT, and to develop low calorie burners for GT. In addition, studies are being conducted on low-cost materials and mass production technologies for SOFC with the goal of determining the cost target of SOFC production. More specifically, efforts are underway to make prototype cell stacks using inexpensive raw materials, and to study and validate the manufacturing processes and facilities needed for mass production.

The basic power generation characteristics under pressure were tested for the cell stack, i.e., the most important component used in the power generation process. Current–voltage characteristics under pressure, pressure dependence, and reliability

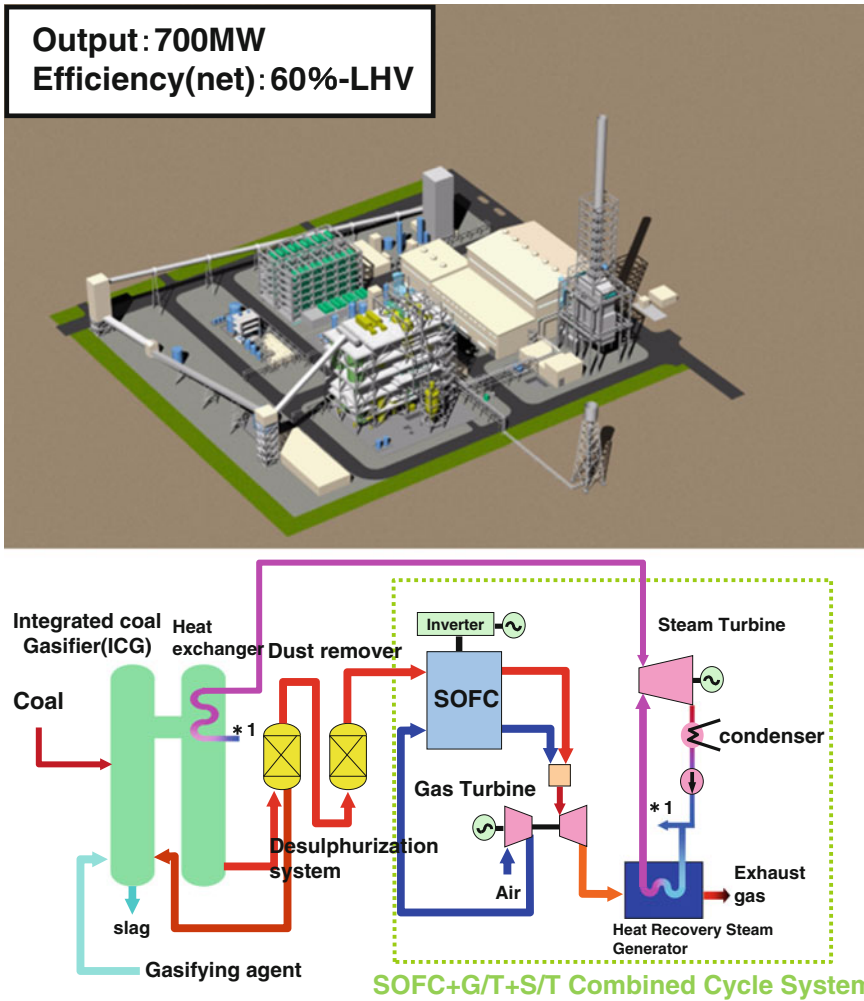


Fig. 37.6 Integrated coal gasifier gas combined cycle plant system

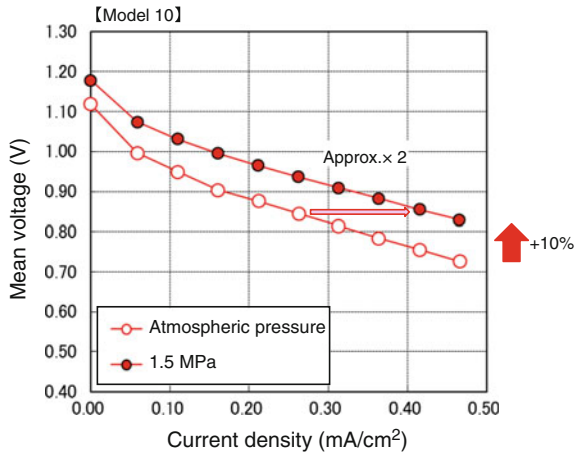
issues including start–stop operation and durability characteristics were tested. For power generation in the elevated pressure range of 1.0–2.0 MPa, the high-pressure cell stack test equipment shown in Fig. 37.7 was designed, fabricated, and used for the evaluation.

When electricity was generated at 1.5 MPa, the voltage at 0.45 A/cm² was 0.82 V, which is about 10 % higher than the voltage at the atmospheric pressure. In addition, the current density was 0.48 A/cm², approximately twice the current density of power generation at the atmospheric pressure, at 0.85 V. This result proves that power generation at high pressures effectively improves the performance of fuel cells, facilitates downsizing of the system, and reduces costs (Fig. 37.8).



Fig. 37.7 Test apparatus of segmented-in-series tubular type cell stacks under high pressure

Fig. 37.8 Comparison of *I-V* characteristics of a cell stack at atmospheric pressure and at 1.5 MPa



37.5 Summary

A roadmap for next generation thermal power generation technology has been formulated by the Agency for Natural Resource and Energy, Ministry of Economy, Trade and Industry in which the importance of SOFC triple combined cycle and coal-fired power generation systems is outlined. Furthermore, there is increasing demand for early implementation of super-high-efficiency power generation systems using fossil fuels as it is imperative that viable technologies that can both reduce CO₂ emission and ensure a steady supply of electricity be developed. Along with this background, there is growing expectation that the SOFC triple combined

cycle power generation system will be the key technology for reducing CO₂ emission in the future, to facilitate the construction of an ecologically and energy sustainable society in this century.

References

1. Mori M, Liu Y, Hashimoto S (2009) Influence of pressurization on the properties of $(La_{1-x}Sr_x)_{1-z}(Co_{1-y}Fe_y)O_{3-\delta}$ ($x = 0.4$; $y = 0.8$; $z = 0-0.04$) as cathode materials for IT-SOFCs. *Electrochemistry* 77(2):140–142
2. Kobayashi Y, Ando Y, Kishizawa H, Tomida K, Matake N (2013) Recent progress of SOFC-GT combined system with tubular type cell stack at MHI. *ECS Trans* 51(1):79–86

Chapter 38

Fuel Cells with Biofuels

Yusuke Shiratori and Quang-Tuyen Tran

Abstract This describes fuel cell-based power generation using biofuels. After giving an overview of biofuels which are available, such as biogas, bioethanol, and biodiesel oil, hydrogen production and power generation with solid oxide fuel cells are explained based on cell performance data. Technological issues such as carbon deposition and impurity poisoning are discussed.

Keywords Biofuel · Biogas · Solid oxide fuel cell · Hydrogen production · Reforming reaction · Durability · Carbon deposition

38.1 Biofuels

38.1.1 Biogas

As described in Chap. 8, biogas is produced from organic waste materials such as agricultural residue, livestock manure, and municipal waste such as garbage and sewage, by anaerobic fermentation with bacteria in a closed reactor. The main components of biogas are methane (CH_4) and carbon dioxide (CO_2), with trace impurities such as H_2S (Table 38.1). The production rate of biogas depends strongly on the kind of feedstock (e.g., with different C/N ratios) and the temperature of the reactor [1].

Y. Shiratori (✉)

Department of Mechanical Engineering, Faculty of Engineering, Kyushu University,
Fukuoka 819-0395, Japan

e-mail: y-shira@mech.kyushu-u.ac.jp

Q.-T. Tran

International Research Center for Hydrogen Energy, Kyushu University,
Fukuoka 819-0395, Japan

e-mail: tran.tuyen.quang.314@m.kyushu-u.ac.jp

© Springer Japan 2016

K. Sasaki et al. (eds.), *Hydrogen Energy Engineering*,

Green Energy and Technology, DOI 10.1007/978-4-431-56042-5_38

Table 38.1 Composition of biogas produced by anaerobic fermentation of organic wastes

Components	Concentration	References
CH ₄	55–70 vol%	[2]
CO ₂	30–45 vol%	[2]
H ₂ S	500–4000 ppm (raw) <1.0 ppm (desulfurized)	[2, 3]
H ₂ O	<1.0 vol%	[2]

38.1.2 Bioethanol

Bioethanol can be produced by converting biomass resources with different processes, as shown in Fig. 38.1. The simple, cheap, and fast way to produce bioethanol is fermentation of glucose, which is contained in sugar cane molasses. Glucose can also be obtained by processing starch crops by using saccharifying enzymes. For lignocellulosic biomass (woody biomass), pretreatment of the raw materials to remove lignin is needed to increase the digestibility of cellulose. Subsequently, the glucose fermented and turned into bioethanol by adding yeast. Bioethanol is now used for ethanol-blended petrol and used as an alternative fuel in the transportation sector. By blending bioethanol into gasoline, fuel combustion is improved due to the increasing octane number and oxygen content in order to reduce tailpipe emissions such as CO and unburned hydrocarbons [4]. Bioethanol is currently blended at 22 vol% (E22) and 10 vol% (E10) with gasoline for transportation vehicles in Brazil and the U.S., respectively.

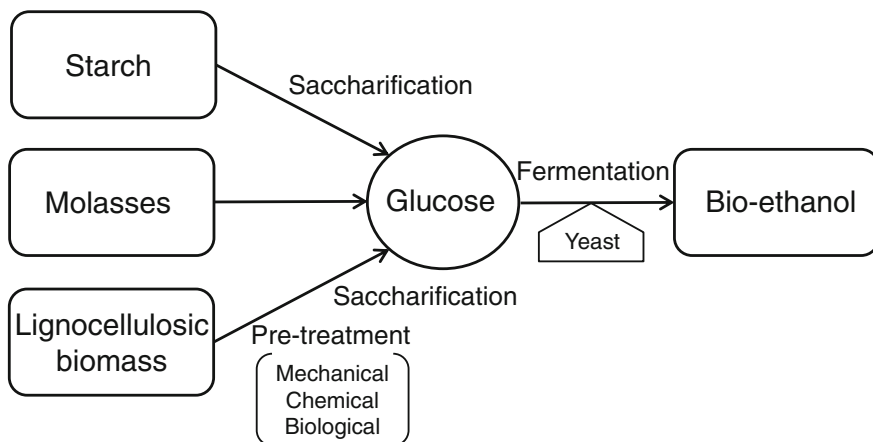


Fig. 38.1 Bioethanol production processes for different raw materials

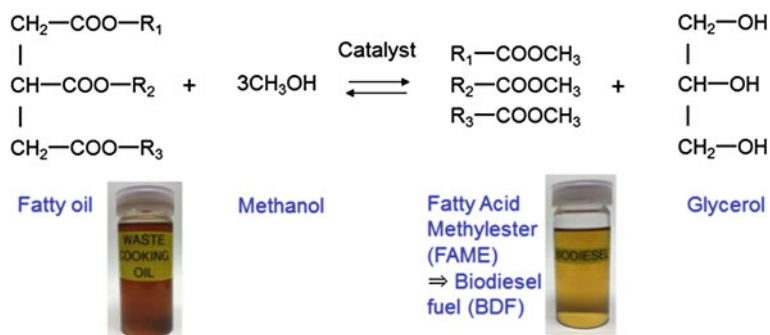


Fig. 38.2 Transesterification reaction for BDF production

38.1.3 Biodiesel

Biodiesel fuel (BDF) is nontoxic, biodegradable, and renewable fuel, which is produced from animal fats, vegetable and waste cooking oils. BDF is prepared by reacting long-chain fatty oils (triglycerides) and an alcohol, in the presence of acid, alkali or enzyme. Using a homogeneous alkaline catalyst (i.e., sodium or potassium methoxide or hydroxide) is most common technique for large-scale BDF production, through the transesterification reaction shown in Fig. 38.2. Acids and enzymes are not industrially applied due to the slow reaction rate and high cost [5, 6]. Recently, a new technology known as the supercritical alcoholysis process has been developed [7]. This is promising non-catalytic alternative to traditional processes. However, this process is performed under the extreme reaction conditions (350–400 °C and >80 atm), and the very high molar ratio of alcohol to oil (42:1).

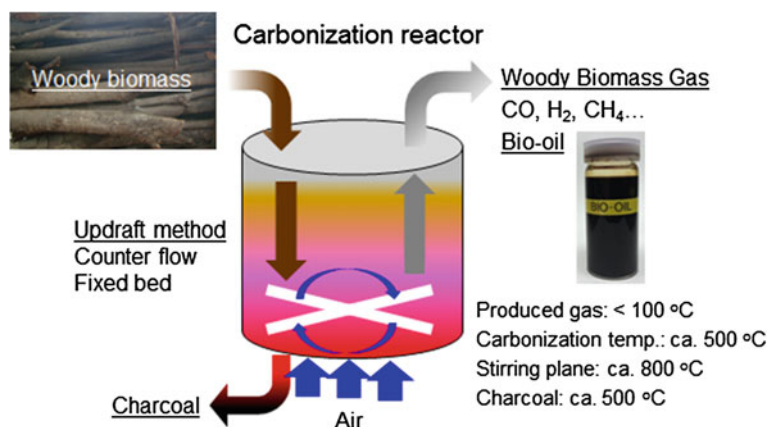
BDF is a mixture of fatty acid methyl esters (FAMES), and the main chemical components are lauric-, myristic-, palmitic-, stearic-, oleic-, linoleic- and lolenic-FAMES, as listed in Table 38.2. BDF mainly consists of shorter carbon chains in comparison to original oils, but components with long carbon chains (with carbon numbers between 14 and 20) still exist. The physical and chemical properties of BDFs are similar to those of petro-diesel fuel. BDFs, oxygenated fuel with low sulfur levels and large H₂ content, are promising as an alternative fuel for H₂ production [5, 8].

38.1.4 Bio-Oil

Bio-oil is a liquid fuel collected from biomass gasification gas via rapid cooling and separation processes, and helps us achieve carbon-neutral energy utilization. Figure 38.3 illustrates the updraft method, one of the techniques to produce bio-oil

Table 38.2 Main components of common biodiesel fuels [9]

Main components	Concentration/wt%						
	Raw feedstock						
	Canola	Coconut	Jatropha	Palm	Rapeseed	Soybean	Sunflower
Lauric-FAME (12:0)		47.7	0.1	0.3	0.1	0.1	0.1
Myristic-FAME (14:0)		18.5	0.3	1.1		0.1	0.1
Palmitic-FAME (16:0)	4.2	9.1	14.9	42.5	4.2	11.6	6.4
Stearic-FAME (18:0)	2.0	2.7	6.1	4.2	1.6	3.9	3.6
Oleic-FAME (18:1)	60.4	6.8	40.4	41.3	59.5	23.7	21.7
Linoleic-FAME (18:2)	21.2	2.1	36.2	9.5	21.5	53.8	66.3
Linolenic-FAME (18:3)	9.6	0.1	0.3	0.3	8.4	5.9	1.5

**Fig. 38.3** Updraft method for the production of charcoal, biomass gasification gas, and bio-oil from woody biomass

from woody biomass developed by Maywa Co, Ltd. (Kanazawa, Japan). Composition and physical properties of bio-oil produced from wood chip (cedar chips in this case) are summarized in Table 38.3. It is tar-like substance obtained by freezing the intermediate products of thermal decomposition of cellulose, hemicellulose, and lignin (the main components of woody structures). According to GC-MS analysis, bio-oil derived from cedar chip is composed of more than 100 organic compounds with average carbon number of 8–10, including saturated, unsaturated linear chain, unsaturated cyclic, and aromatic compounds [10], and is

Table 38.3 Composition and physical properties of bio-oil produced from cedar chip provided by Maywa Co, Ltd. (Kanazawa, Japan)

C/wt%	33.3
H/wt%	6.4
N/wt%	0.2
O/wt%	60.1
H ₂ O/wt%	34.0
S/ppm	83
pH	2.45
Specific gravity/g ml ⁻¹	1.19
Heat value/MJ kg ⁻¹	20

considered to form an emulsion in which lignin fragments are dispersed in the aqueous solution resulting from carbohydrate decomposition.

38.2 H₂ Production from Biofuels

To move away from the present situation in which more than 95 % of hydrogen is produced by steam reforming of fossil fuels, utilization of alternative fuels such as biofuels must be promoted to increase the percentage of renewable hydrogen. Catalyst materials for the reforming of biofuels, such as biogas [11, 12], bioethanol [13, 14], bio-oil [15, 16], and biodiesel fuels (BDFs) [17, 18] have been widely investigated by many research groups focusing on the enhancement of tolerance to sulfur poisoning and coking resistance.

Oxide-supported Ni is the most popular catalyst material for biofuel reforming in terms of cost and performance. Pt, Ru, Pd, Rh, Ir, and Co are also sometimes selected [12–18], whilst the choice of oxide support considering surface acidity, strong metal-support interaction (SMSI), oxygen mobility, and oxygen storage capacity (OSC) is crucial to obtain the desired catalytic activity.

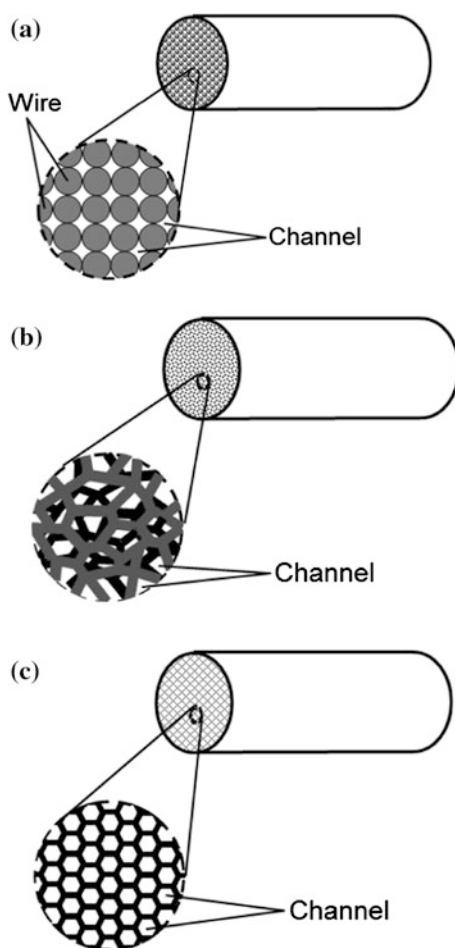
It is well known that oxides, such as γ -Al₂O₃, having large number of acid sites on the surface promote coke formation in the feed of hydrocarbons [19]. To suppress coking, the use of basic oxide supports such as MgO, CaO, La₂O₃, and BaTiO₃ are effective [16–18, 20–24]. Moreover, doped CeO₂ with high oxygen mobility and large OSC can contribute to removal of carbonaceous species on the catalyst surface [25–28]. To enhance metal catalyst dispersion, formation of metal particles from an oxide solid solution containing metal catalyst in its crystal structure is highly effective. For example, fine Ni particles are formed by a reduction treatment of (Ni, Mg)O solid solution [20–22] and hydrotalcite-derived (Mg, Ni, Al)O solid solution [29–31].

38.2.1 Structured-Catalysts for Practical Applications

From a practical standpoint, above-mentioned catalyst materials are applied onto a structured-framework such as strings [32], foams [33] and honeycombs [34] to form a structured-catalyst (see Fig. 38.4). For example, a honeycomb structure with parallel-arranged channels is widely used for three-way catalytic converters to clean up exhaust gas from gasoline engines. However, these structures have some drawbacks such as high weight density of foam and the restriction of radial mixing of reactant gases for the honeycomb [35].

Architectonics of a structured-framework is important to maximize the catalytic effect. Paper-structured catalysts (PSCs) based on inorganic fiber networks have been developed, and advantages of PSCs arising from the enhancement of 3-D

Fig. 38.4 Types of structured-catalyst; **a** string, **b** foam and **c** honeycomb types



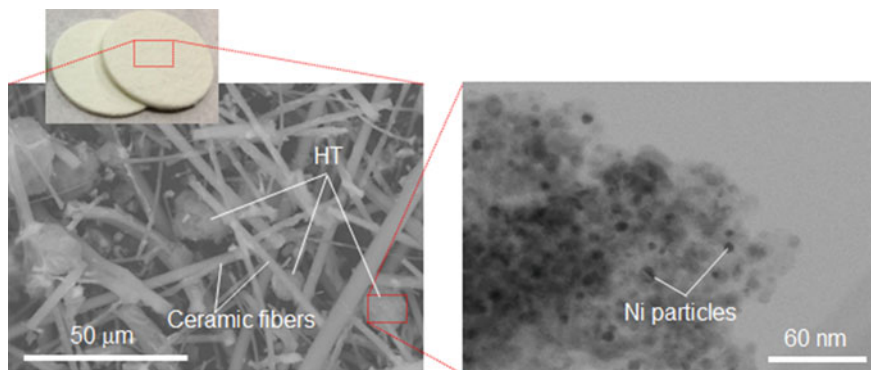


Fig. 38.5 Structure of a typical paper-structured catalyst (PSC) for biofuel reforming [31]

diffusion of reactants and products have been demonstrated for alcohol reforming [36, 37] and catalytic reduction of nitrogen oxides [38, 39].

Recently, PSCs for biofuel reforming (steam reforming of BDF or dry reforming of methane which simulates biogas reforming) have been investigated aiming at application in solid oxide fuel cells (SOFCs) [18, 31, 40]. The structure of a PSC developed for biofuel reforming is shown in Fig. 38.5 [31]. This fiber network can be prepared by a simple paper making process during which hydrotalcite (HT) particles are dispersed, followed by Ni loading by an impregnation process to

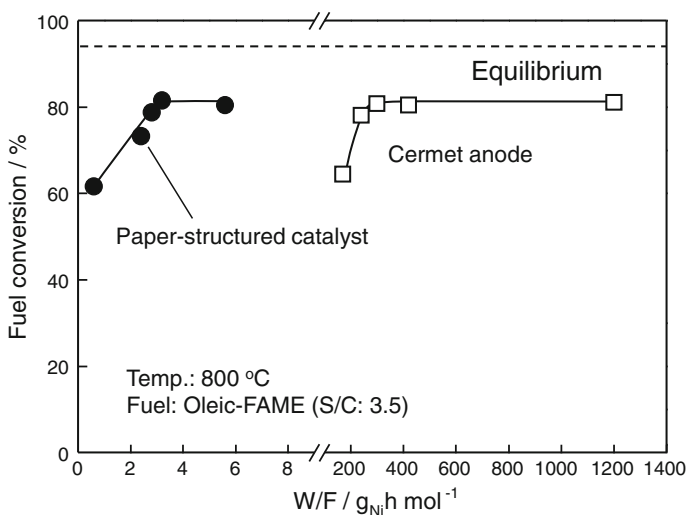


Fig. 38.6 BDF conversion as a function of contact time W/F (ratio of weight of Ni metal to molecular flow rate of fuel), showing the comparison of catalytic activity between Ni-loaded PSC and porous Ni-ScSZ cermet anode for steam reforming of oleic-FAME ($C_{19}H_{38}O_2$), one of the main components of practical BDFs, at 800 °C and $S/C = 3.5$ [31]

form fine Ni particles on the HT-derived oxide support. This PSC exhibits excellent catalytic activity for steam reforming of BDF at 800 °C, which is close to the operating temperature of an SOFC. Fuel conversion of model BDF (oleic fatty acid methyl ester (FAME)) was comparable to that for typical anode material used for SOFCs (porous Ni-ScSZ cermet) with less than 1 % of the Ni weight, as shown in Fig. 38.6.

38.3 Application of Biofuels to Solid Oxide Fuel Cells

Among the different types of fuel cells, high temperature SOFCs can accept a direct feed of hydrocarbon fuels such as fossil fuels and biofuels without a pre-reforming process, contributing to increase in the system efficiency [41]. Operation of a direct internal reforming SOFC (DIR-SOFC) is shown schematically in Fig. 38.7. Hydrocarbons supplied to the SOFC are reformed in a porous anode material containing Ni, the most common reforming catalyst, to produce H_2 and CO. This is followed by electrochemical oxidation to generate electricity and heat.

DIR-SOFC operation, results in several advantages. These include downsizing and cost reduction of fuel cell systems; and the reduction in energy consumption to mitigate stack cooling caused by endothermic reforming reactions due to the supply of excess air [42]. DIR-SOFC running on natural gas, petroleum fuels, and crude oil have been systematically investigated [43–49]. As for the direct conversion of

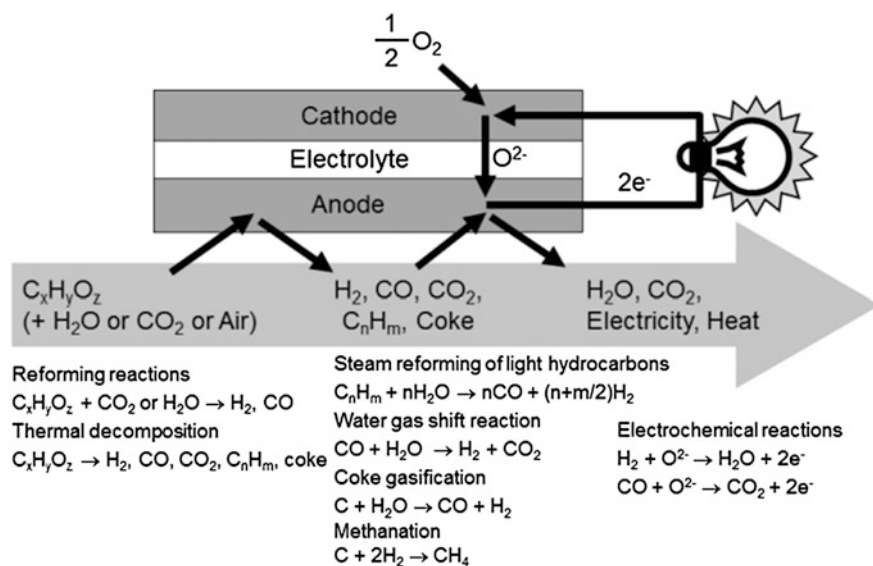


Fig. 38.7 Schematic illustration of the direct internal reforming SOFC operated by a biofuel ($C_xH_yO_z$)

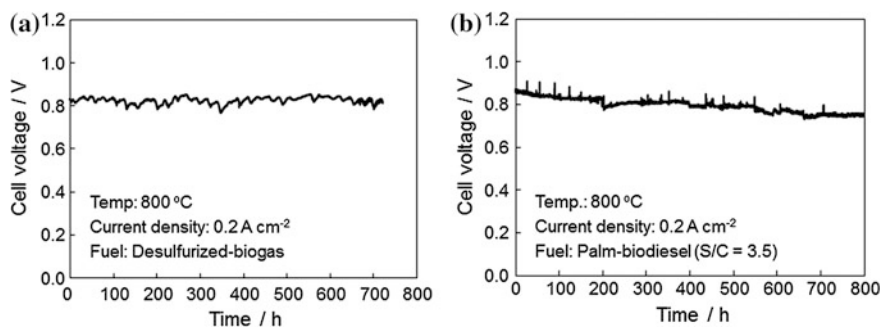


Fig. 38.8 Cell voltage of NiO-ScSZ/ScSZ/ScSZ-LSM anode-supported button cells fuelled by **a** desulfurized-biogas [51] and **b** palm-biodiesel (S/C = 3.5) measured at 800 °C under 0.2 A cm⁻² for 1 month [52]

biofuels using an SOFC, a limited number of groups in Japan [50–52], the U.K. [53–56], Italy [57, 58], Greece [59, 60], and the U.S. [61, 62] are actively engaged on R&D. A group of Kyushu University had succeeded to achieve stable operation of DIR-SOFCs with a direct feed of practical biofuels, biogas, and palm-BDF for 1 month, as shown in Fig. 38.8.

38.3.1 Biogas

It has been demonstrated that DIR-SOFCs can work with simulated and practical biogases to have sufficient power density at a high temperature range between 600 and 1000 °C [50, 51, 53–55, 57–61, 63–69, 72]. The performance of biogas-fuelled DIR-SOFCs is affected by biogas composition, operating temperature, SOFC configuration (electrolyte- or anode-supported) and the type of anode material (cf. Table 38.4).

Staniforth et al. reported that direct electrochemical oxidation of methane in biogas does not proceed to generate electricity, but the methane contributes to the formation of hydrogen and carbon monoxide via the dry reforming reaction ($\text{CH}_4 + \text{CO}_2 \rightarrow 2\text{H}_2 + 2\text{CO}$), which are electrochemically oxidized at the triple phase boundary (TPB) to generate electricity and heat [55]. At the operating temperature of 850 °C, rate of methane dry reforming on the anode is maximized at the CH₄ molar ratio of 45 %, close to the equimolar ratio of CH₄/CO₂, to exhibit maximum output power in a tubular cell [55]. However, methane rich biogas (cf. Table 38.1) causes coke formation on the anode surface to block electrochemical active sites, resulting in a large increase in anodic overvoltage.

Steam, air, or pure oxygen is added to biogas to suppress degradation attributed to coking [67, 68]. However, it should be taken into consideration that the addition of oxygen or air to biogas would bring about a loss of the chemical energy of CH₄ by direct combustion, lowering the electrical efficiency of the SOFC. At low

Table 38.4 Electrochemical performance of SOFCs in the direct feed of simulated biogas

Anode/electrolyte/cathode	Fuel composition (CH ₄ :CO ₂ :N ₂)	Peak power density/mW cm ⁻² (Temperature (°C))	References
<i>Electrolyte-supported tubular type</i>			
Ni(Au)-GDC/GDC/LSM	50:50:0	60 (640)	[59]
<i>Electrolyte-supported planar type</i>			
Ni-YSZ/YSZ/LSM	50:50:0	Approx. 80 (875)	[60]
<i>Anode-supported planar type</i>			
Ni-YSZ/YSZ/LSM-YSZ	52.2:46.3:1.5	424 (800)	[63]
Ni-SnO ₂ -YSZ/YSZ/LSM-YSZ	52.2:46.3:1.5	272 (800)	[63]
Ni-Al ₂ O ₃ -YSZ/YSZ/LSM-YSZ	52.2:46.3:1.5	478 (800)	[63]
<i>Anode-supported planar type with additional catalyst layer</i>			
Ni-CeO ₂ -YSZ/YSZ/LSM-YSZ	50:50	547 (850) 411 (800) 313 (750)	[61]
Ni-YSZ (LiLaNi-Al ₂ O ₃ /Cu layer)/YSZ/LSM-YSZ	66.7:33.3:0	988 (850)	[64]
Ni-YSZ (LiLaNi-Al ₂ O ₃ layer)/YSZ/LSM-YSZ	66.7:33.3:0	1013 (850)	[64]
Ni-YSZ (Ru-Al ₂ O ₃ layer)/YSZ/LSM-YSZ	66.7:33.3:0	929 (850) 705 (800) 478 (750) 282 (700) 134 (650)	[65]
Ni-YSZ (CuO-CeO ₂ layer)/YSZ/LSM-YSZ	60:40:0	Approx. 270 (750)	[66]
Ni-YSZ (Cu _{1.3} Mn _{1.7} O ₄ layer)/YSZ/LSM-YSZ	60:40:0	Approx. 260 (750)	[66]
Ni-YSZ (Y _{0.08} Sr _{0.92} Ti _{0.8} Fe _{0.2} O _{3-δ} layer)/YSZ/LSM-YSZ	60:40:0	Approx. 250 (750)	[66]

operating temperature, water is more effective than CO₂ to prevent carbon deposition, but at high temperature their effects are comparable [67]. In the view of material development, doped Ni-based catalysts have been reported to suppress carbon formation in a porous cermet anode [63]. Furthermore, the application of catalyst layers on the surface of a cermet anode has been tested to enhance the catalytic activity of the anode [61, 64–66]. However, sometimes a catalyst layer can cause an increase in ohmic loss and can reduce the rate of gas diffusion [71].

One of the most difficult issues of DIR-SOFC is the generation of thermal stress caused by the strong endothermic reforming reaction. Figure 38.9 shows the steady-state 2-D temperature distribution appearing in a porous Ni-ScSZ anode-support (5 × 5 cm²) with a dense ScSZ electrolyte film during the feed of a mixture of CH₄ and CO₂ (CH₄/CO₂ = 1.5, 100 ml min⁻¹) to the porous anode [68]. During this test, destruction of the electrolyte thin film sintered on the porous

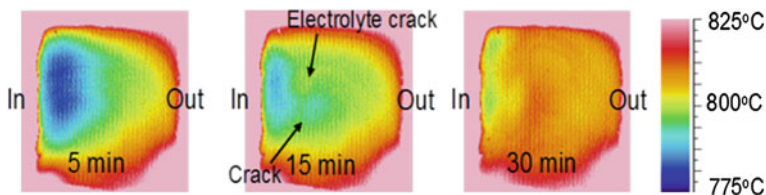


Fig. 38.9 Steady-state 2-D temperature distribution in porous Ni-ScSZ anode-support during the feed of simulated biogas ($\text{CH}_4/\text{CO}_2 = 1.5$), showing strong endothermicity of the reforming reaction and resulting electrolyte cracking [68]

anode-support occurs due to the generation of large thermal stresses. Addition of air is quite effective to suppress thermal stresses. For a typical biogas composition ($\text{CH}_4/\text{CO}_2 = 1.5$), an air/biogas ratio of 0.7 was optimal in view of reforming efficiency. However, an air/biogas ratio of >1.0 is recommended to ensure mechanical reliability and to avoid carbon formation.

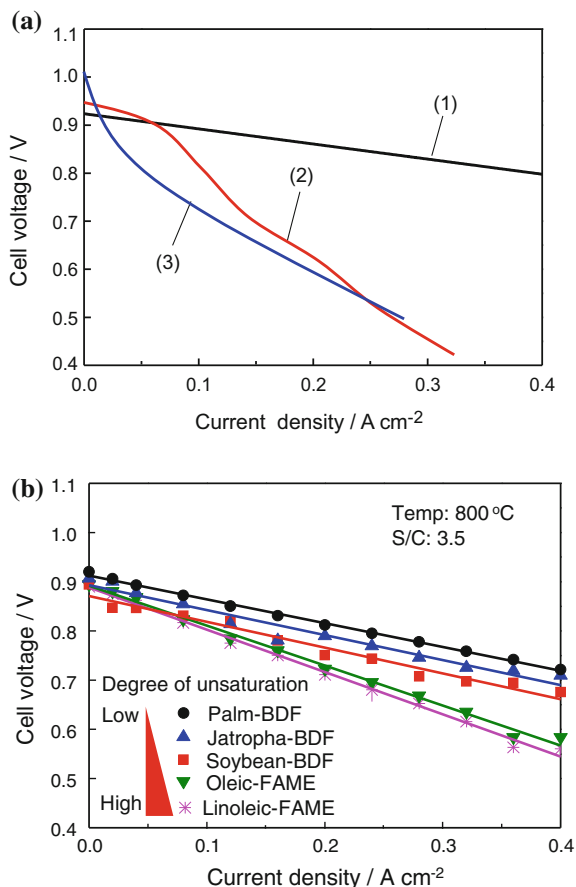
Raw biogas generally contains high levels of H_2S in a concentration range between several hundred and several thousand ppm [2, 3]. Even for high temperature SOFCs, a desulfurization process prior to fuel feeding to the anode is necessary. The influence of trace H_2S in biogas on the performance of DIR-SOFC has been investigated. For an electrolyte-supported cell operated at 1000°C with a direct feed of simulated biogas, the addition of 1 ppm H_2S caused about a 9 % voltage drop and a 40 % decrease in the reaction rate of internal reforming [72]. For an anode-supported cell operated at a lower temperature of 800°C , the influence of H_2S was more pronounced, with a 20 % voltage drop and an 80 % decrease in reforming rate [72]. This is due to chemisorption of H_2S -derived sulfur species on the active sites for electrochemical and reforming reactions. It is reported that anodes modified with basic oxide [70] or perovskite [73] can reduce sulfur chemisorption on Ni by lowering the chemical potential.

38.3.2 Biodiesel

It has been demonstrated that the chemical energy of BDFs can be directly converted to electricity through DIR-SOFC operation [52, 56, 62]. Reported I-V curves of SOFCs fuelled by BDFs are compared in Fig. 38.10a. To overcome the coking problem, high operating temperature and high S/C ratio are required. McPhee et al. reported a novel liquid-tin anode SOFC, which can perform direct oxidation of BDF at 1000°C [62]. For conventional Ni-ScSZ anode-supported button cells operated by various practical- and chemical-BDFs at 800°C , the cell performance is strongly affected by the degree of saturation in BDFs, as shown in Fig. 38.10b. BDFs with lower degree of saturation tend to produce larger amount of C_2H_4 in the reformat, which causes coking to degrade power density. In long-term tests, a direct feed of practical BDFs to Ni-based porous anodes causes carbon

Fig. 38.10 a Current-voltage (I-V) curves of SOFCs in a direct feed of: (1) palm-BDF to a NiO-ScSZ/ScSZ/ScSZ-LSM anode-supported button cell with S/C = 3.5, at 800 °C [52]; (2) emulsified rapeseed-BDF (20 % BDF) to a NiO-YSZ/YSZ/YSZ-LSM anode-supported tubular cell at 800 °C [56]; and (3) BDF to a liquid-Sn/YSZ/LSM tubular cell under S/C = 0 and 1000 °C [62].

b Dependence of electrochemical performance of a Ni-ScSZ anode-supported button cell on the degree of saturation of BDFs [77]



deposition in the anode material accompanied by the formation of C₂H₄. This is more significant for fuels with lower degree of saturation and at lower operating temperature. The surface of the anode is most susceptible to coking because of the position with lowest S/C ratio during SOFC operation. Severe coking on the anode surface causes rapid degradation because gas diffusion of the reactants and products is prevented, and sometimes the anode can be destroyed by accumulated carbon [74–76]. Therefore, suppressing coking on the surface of the anode is the most crucial issue in DIR-SOFCs running on BDF.

The long-term stability of DIR-SOFC operated with palm-BDF (S/C = 3.5) was evaluated under 0.2 A cm⁻² at 800 °C. A degradation rate of 15 %/1000 h was recorded, as shown in Fig. 38.8b [52]. This is significantly high compared to that of simulated biogas (0.4 %/1000 h) [51]. Severe coking occurs on the surface of the anode-support after long-term operation with palm-BDF, causing delamination of the current collector mesh from the anode surface, as shown in Fig. 38.11.

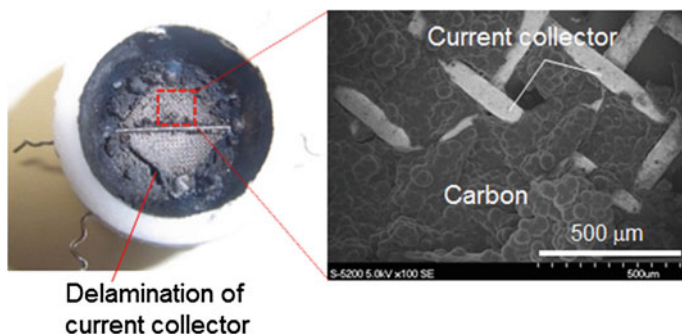


Fig. 38.11 A FESEM image of surface of a Ni-ScSZ anode-support after 800 h DIR-SOFC durability test on palm-BDF (S/C = 3.5) at 0.2 A cm^{-2} and $800 \text{ }^\circ\text{C}$ [52]

References

1. Divya D, Gopinath LR, Christy PM (2015) A review on current aspects and diverse prospects for enhancing biogas production in sustainable means. *Renew Sustain Energy Rev* 42:690–699
2. Alves HJ (2013) Overview of hydrogen production technologies from biogas and the applications in fuel cells. *Int J Hydrogen Energy* 38:5215–5225
3. Magomnang AASM, Villanueva EP (2014) Removal of hydrogen sulfide from biogas using dry desulfurization systems. In: *Proceedings of international conference on agricultural, environmental and biological sciences*, Phuket, Thailand, pp 65–68
4. Wyman CE (1996) *Handbook of bioethanol*. Taylor & Francis, London, pp 4–5
5. Nahar G, Dupont V (2012) Hydrogen via steam reforming of liquid biofeedstock. *Biofuels* 3:167–191
6. Leung DY, Wu X, Leung MKH (2010) A review recent advancement in catalytic materials for biodiesel production. *Appl Energy* 87:1083–1095
7. Karmakar A, Karmakar S, Mukherjee S (2010) Properties of various plants and animals feedstocks for biodiesel production. *Bioresour Technol* 101:7201–7210
8. Nahar GA (2010) Hydrogen rich gas production by the autothermal reforming of biodiesel (FAME) for utilization in the solid-oxide fuel cells: a thermodynamic analysis. *Int J Hydrogen Energy* 35:8891–8911
9. Hoekman SK, Broch A, Robbins C, Cenicerros E, Natarajan M (2012) Review of biodiesel composition, properties, and specifications. *Renew Sustain Energy Rev* 16:143–169
10. Miyachi K, Miyagawa M, Katagiri M, Kanda N, Norinaga K (2010) Identification of tar chemical species obtained from pyrolysis of grass biomass. *Mitsui Zosen Tech Rev* 199:47–53
11. Effendi A, Hellgardt K, Zhang Z-G, Yoshida T (2005) Optimising H_2 production from model biogas via combined steam reforming and CO shift reactions. *Fuel* 84:869–874
12. Muradov N, Smith F (2008) Thermocatalytic conversion of landfill gas and biogas to fuels. *Energy Fuels* 22:2053–2060
13. Zhang B, Tang X, Li Y, Cai Y, Xu Y, Shen W (2006) Steam reforming of bio-ethanol for the production of hydrogen over ceria-supported Co, Ir and Ni catalysts. *Catal Commun* 7:367–372
14. Mondal T, Pant KK, Dalai AK (2015) Catalytic oxidative steam reforming of bio-ethanol for hydrogen production over Rh promoted Ni/CeO₂-ZrO₂ catalyst. *Int J Hydrogen Energy* 40:2529–2544
15. Basagiannis AC, Verykios XE (2007) Steam reforming of the aqueous fraction of bio-oil over structured Ru/MgO/Al₂O₃ catalysts. *Catal Today* 127:256–264

16. Vagia EC, Lemonidou AA (2008) Hydrogen production via steam reforming of bio-oil components over calcium aluminate supported nickel and noble metal catalysts. *Appl Catal A Gen* 351:111–121
17. Laosiripojana N, Kiattikittipong W, Charojrochkul S, Assabumrungrat S (2010) Effects of support and co-fed elements on steam reforming of palm fatty acid distillate (PFAD) over Rh-based catalysts. *Appl Catal A Gen* 383:50–57
18. Shiratori Y, Tran TQ, Umemura Y, Kitaoka T, Sasaki K (2013) Paper-structured catalyst for the steam reforming of biodiesel fuel. *Int J Hydrogen Energy* 38:11278–11287
19. Lercher JA, Bitter JH, Hally W, Niessen W, Seshan K (1996) Design of stable catalysts for methane-carbon dioxide reforming. *Stud Surf Sci Catal* 101:463–472
20. Nakayama T, Ichikuni N, Sato S, Nozaki F (1997) Ni/MgO catalyst prepared using citric acid for hydrogenation of carbon dioxide. *Appl Catal A Gen* 158:185–199
21. Tomishige K, Chen Y, Fujimoto K (1999) Studies on carbon deposition in CO₂ reforming of CH₄ over nickel-magnesia solid solution catalysts. *J Catal* 181:91–103
22. Hou Z, Yashima T (2004) Meso-porous Ni/Mg/Al catalysts for methane reforming with CO₂. *Appl Catal A Gen* 261:205–209
23. Sun J, Qiu XP, Wu F, Zhu WT (2005) H₂ from steam reforming of ethanol at low temperature over Ni/Y₂O₃, Ni/La₂O₃ and Ni/Al₂O₃ catalysts for fuel-cell application. *Int J Hydrogen Energy* 30:437–445
24. Urasaki K, Sekine Y, Kawabe S, Kikuchi E, Matsukata M (2005) Catalytic activities and coking resistance of Ni/perovskites in steam reforming of methane. *Appl Catal A Gen* 286:23–29
25. Narula CK, Haack LP, Chun W, Jen HW, Graham GW (1999) Single-phase PrO_y-ZrO₂ materials and their oxygen storage capacity: a comparison with single-phase CeO₂-ZrO₂, PrO_y-CeO₂, and PrO_y-CeO₂-ZrO₂ materials. *J Phys Chem B* 103:3634–3639
26. Takeguchi T, Furukawa SN, Inoue M (2001) Hydrogen spillover from NiO to the large surface area CeO₂-ZrO₂ solid solutions and activity of the NiO/CeO₂-ZrO₂ catalysts for partial oxidation of methane. *J Catal* 202:14–24
27. Srinivas D, Satyanarayana CVV, Potdar HS, Ratnasamy P (2003) Structural studies on NiO-CeO₂-ZrO₂ catalysts for steam reforming of ethanol. *Appl Catal A Gen* 246:323–334
28. Shotipruk A, Assabumrungrat S, Pavasant P, Laosiripojana N (2009) Reactivity of CeO₂ and Ce-ZrO₂ toward steam reforming of palm fatty acid distilled (PFAD) with co-fed oxygen and hydrogen. *Chem Eng Sci* 64:459–466
29. Shishido T, Sukenobu M, Morioka H, Furukawa R, Shirahase H, Takehira K (2001) CO₂ reforming of CH₄ over Ni/Mg-Al oxide catalysts prepared by solid phase crystallization method from Mg-Al hydrotalcite-like precursors. *Catal Lett* 73:21–26
30. Li D, Wang L, Koike M, Nakagawa Y, Nakagawa Y, Tomishige K (2011) Steam reforming of tar from pyrolysis of biomass over Ni/Mg/Al catalysts prepared from hydrotalcite-like precursors. *Appl Catal B Environ* 102:528–538
31. Tran TQ, Kaida T, Sakamoto M, Sasaki K, Shiratori Y (2015) Effectiveness of paper-structured catalyst for the operation of biodiesel-fueled solid oxide fuel cell. *J Power Sources* 283:320–327
32. Horny C, Renken A, Kiwi-Minsker L (2007) Compact string reactor for autothermal hydrogen production. *Catal Today* 120:45–53
33. Twigg MV, Richardson JT (2007) Fundamentals and applications of structured ceramic foam catalysts. *Ind Eng Chem Res* 46:4166–4177
34. Nishihara H, Mukai SR, Yamashita D, Tamon H (2005) Ordered macroporous silica by ice templating. *Chem Mater* 17:683–689
35. Patcas FC, Garrido GI, Kraushaar-Czarnetzki B (2007) CO oxidation over structured carriers: a comparison of ceramic foams, honeycombs and beads. *Chem Eng Sci* 62:3984–3990
36. Fukahori S, Kitaoka T, Tomoda A, Suzuki R, Wariishi H (2006) Methanol steam reforming over paper-like composites of Cu/ZnO catalyst and ceramic fiber. *Appl Catal A* 300:155–161

37. Fukahori S, Koga H, Kitaoka T, Nakamura M, Wariishi H (2008) Steam reforming behavior of methanol using paper-structured catalysts: experimental and computational fluid dynamic analysis. *Int J Hydrogen Energy* 33:1661–1670
38. Koga H, Umemura Y, Ishihara H, Kitaoka T, Tomoda A, Suzuki R, Wariishi H (2009) Paper-structured fiber composites impregnated with platinum nanoparticles synthesized on a carbon fiber matrix for catalytic reduction of nitrogen oxides. *Appl Catal B Environ* 90:699–704
39. Ishihara H, Koga H, Kitaoka T, Wariishi H, Tomoda A, Suzuki R (2010) Paper-structured catalyst for catalytic NO_x removal from combustion exhaust gas. *Chem Eng Sci* 65:208–213
40. Shiratori Y, Ogura T, Nakajima H, Sakamoto M, Takahashi Y, Wakita Y, Kitaoka T, Sasaki K (2013) Study on paper-structured catalyst for direct internal reforming SOFC fueled by the mixture of CH₄ and CO₂. *J Hydrogen Energy* 38:10542–10551
41. Wachsman ED, Marlowe CA, Lee KT (2012) Role of solid oxide fuel cells in a balanced energy strategy. *Energy Environ Sci* 5:5498–5509
42. Ge XM, Chan SH, Liu QL, Sun Q (2012) Solid oxide fuel cell anode materials for direct hydrogen carbon utilization. *Adv Energy Mater* 2:1156–1181
43. Liu J, Barnett SA (2003) Operation of anode-supported solid oxide fuel cells on methane and natural gas. *Solid State Ionics* 158(1–2):11–16
44. Liu J, Madsen BD, Ji Z, Barnett SA (2002) A fuel-flexible ceramic-based anode for solid oxide fuel cells. *Electrochem Solid-State Lett* 5:A122–A124
45. Iida T, Kawano M, Matsui T, Kikuchi R, Eguchi K (2007) Internal reforming of SOFCs: carbon deposition on fuel electrode and subsequent deterioration of cell. *J Electrochem Soc* 154(2):B234–B241
46. Kishimoto H, Yamaji K, Horita T, Xiong Y, Sakai N, Brito M, Yokokawa H (2007) Feasibility of liquid hydrocarbon fuels for SOFC with Ni-ScSZ anode. *J Power Sources* 172:67–71
47. Kim H, Park S, Vohs JM, Gorte RJ (2001) Direct oxidation of liquid fuels in a solid oxide fuel cell. *J Electrochem Soc* 148(7):A693–A695
48. Hou X, Marin-Flores O, Kwon BW, Kim J, Norton MG, Ha S (2014) Gasoline-fueled solid oxide fuel cell with high power density. *J Power Sources* 268:546–549
49. Zhou ZF, Gallo C, Pargue MB, Schobert H, Lvov SN (2004) Direct oxidation of jet fuels and Pennsylvania crude oil in a solid oxide fuel cell. *J Power Sources* 133:181–187
50. Shiratori Y, Oshima T, Sasaki K (2008) Feasibility of direct-biogas SOFC. *Int J Hydrogen Energy* 33:6316–6321
51. Shiratori Y, Ijichi T, Oshima T, Sasaki K (2010) Internal reforming SOFC running on biogas. *Int J Hydrogen Energy* 35:7905–7912
52. Tran TQ, Shiratori Y, Sasaki K (2013) Feasibility of palm-biodiesel fuel for a direct internal reforming solid oxide fuel cell. *Int J Energy Res* 37:609–616
53. Staniforth J, Kendall K (1998) Biogas powering a small tubular solid oxide fuel cell. *J Power Sources* 71:275–277
54. Staniforth J, Kendall K (2000) Cannock landfill gas powering a small tubular solid oxide fuel cell—a case study. *J Power Sources* 86:401–403
55. Staniforth J, Ormerod RM (2003) Running solid oxide fuel cells on biogas. *Ionics* 9:336–341
56. Nahar G, Kendall K (2011) Biodiesel formulations as fuel for internally reforming solid oxide fuel cell. *Fuel Process Technol* 92:1345–1354
57. Lanzini A, Leone P (2010) Experimental investigation of direct internal reforming of biogas in solid oxide fuel cells. *J Power Sources* 35:2463–2476
58. Guerra C, Lanzini A, Leone P, Santarelli M, Beretta D (2013) Experimental study of dry reforming of biogas in a tubular anode-supported solid oxide fuel cell. *Int J Hydrogen Energy* 38:10559–10566
59. Yentekakis IV (2006) Open- and closed-circuit study of an intermediate temperature SOFC directly fueled with simulated biogas mixtures. *J Power Sources* 160:422–425

60. Papadam T, Goula G, Yentekakis IV (2012) Long-term operation stability tests of intermediate and high temperature Ni-based anodes' SOFCs directly fueled with simulated biogas mixtures. *Int J Hydrogen Energy* 37:16680–16685
61. Xu C, Zondlo JW, Gong M, Elizalde-Blancas F, Liu X, Celik IB (2010) Tolerance tests of H₂S-laden biogas fuel on solid oxide fuel cells. *J Power Sources* 195:4583–4592
62. McPhee WAG, Boucher M, Stuart J, Parnas RS, Koslowski M, Tao T, Wilhite BA (2009) Demonstration of a liquid-tin anode solid-oxide fuel cell (LTA-SOFC) operating from biodiesel fuel. *Energy Fuels* 23:5036–5041
63. Wang F, Wang W, Ran R, Tade MO, Shao Z (2014) Alumina oxide as a dual-functional modifier of Ni-based anodes of solid oxide fuel cells for operating on simulated biogas. *J Power Sources* 268:787–793
64. Wang W, Su C, Ran R, Park HJ, Kwak C, Shao Z (2011) Physically mixed LiLaNi-Al₂O₃ and copper as conductive anode catalysts in a solid oxide fuel cell for methane internal reforming and partial oxidation. *Int J Hydrogen Energy* 36:5632–5643
65. Wang W, Ran R, Shao Z (2011) Combustion-synthesized Ru-Al₂O₃ composites as anode catalyst layer of a solid oxide fuel cell operating on methane. *Int J Hydrogen Energy* 36:755–764
66. Szymcewska D, Karcrewski J, Bochentyn B, Chrzan A, Gazda M, Jasinski P (2015) Investigation of catalytic layer on anode solid oxide fuel cells operating with synthetic biogas. *Solid State Ionics* 271:109–115
67. Assabumrungrat S, Laosiripojana N, Piroonlerkgul P (2006) Determination of the boundary of carbon formation for dry reforming of methane in a solid oxide fuel cell. *J Power Sources* 159:1274–1284
68. Takahashi Y, Shiratori Y, Furuta S, Sasaki K (2012) Thermo-mechanical reliability and catalytic activity of Ni-zirconia anode supports in internal reforming SOFC running on biogas. *Solid State Ionics* 225:113–117
69. Smith TR, Wood A, Birss VI (2009) Effect of hydrogen sulfide on the direct internal reforming of methane in solid oxide fuel cells. *Appl Catal A* 354:1–7
70. Silva ALD, Heck NC (2015) Oxide incorporation into Ni-based solid oxide fuel cell anodes for enhanced sulfur tolerance during operation on hydrogen or biogas fuels: a comprehensive thermodynamic study. *Int J Hydrogen Energy* 40:2334–2353
71. Zhan Z, Barnett SA (2005) An octane-fueled solid oxide fuel cell. *Science* 308:844–847
72. Shiratori Y, Ijichi T, Oshima T, Sasaki K (2009) Generation of electricity from organic bio-wastes using solid oxide fuel cell. *ECS Trans* 25:1051–1060
73. Liu JH, Fu XZ, Luo JL, Chuang KT, Sanger AR (2012) Application of BaTiO₃ as anode materials for H₂S-containing CH₄ fueled solid oxide fuel cells. *J Power Sources* 213:69–77
74. Kim H, Lu C, Worrell WL, Vohs JM, Gorte RJ (2002) Cu-Ni cermet anodes for direct oxidation of methane in solid-oxide fuel cells. *J Electrochem Soc* 149:A247–A250
75. Singh A, Hill JM (2012) Carbon tolerance, electrochemical performance and stability of solid oxide fuel cells with Ni/yttria stabilized zirconia anodes impregnated with Sn and operated with methane. *J Power Sources* 214:185–194
76. Shiratori Y, Tran TQ, Sasaki K (2013) Performance enhancement of biodiesel fueled SOFC using paper-structured catalyst. *Int J Hydrogen Energy* 38:9856–9866
77. Shiratori Y, Tran TQ, Takahashi Y, Sasaki K (2011) Application of biofuels to solid oxide fuel cell. *ECS Trans* 35:2641–2651

Chapter 39

Portable Applications

Masaru Tsuchiya

Abstract This chapter describes portable application of fuel cells. After a brief discussion on the advantages of fuel cells over batteries, recent efforts to develop portable fuel cells are summarized by the kind of fuels they use. Direct liquid fuel cells, polymer electrolyte membrane fuel cells, and solid oxide fuel cells are discussed in this chapter.

Keywords Portable devices · Battery · Power density · Direct methanol fuel cells · Direct borohydride fuel cells · Polymer electrolyte fuel cells · Solid oxide fuel cells · Thin film technology · Micro-tubular cells

39.1 Introduction

Portable fuel cells have emerged as one of the key application areas of fuel cells in recent years, due to a surge in energy consumption of portable electronic devices such as cellular phones and laptop computers. Fuel cells have higher energy density than batteries because they can take advantage of high energy density stored in fossil fuels. Fuel cells can power an electronic device as long as fuel is supplied. The energy densities of typical fuels used in portable fuel cell applications are shown in Fig. 39.1.

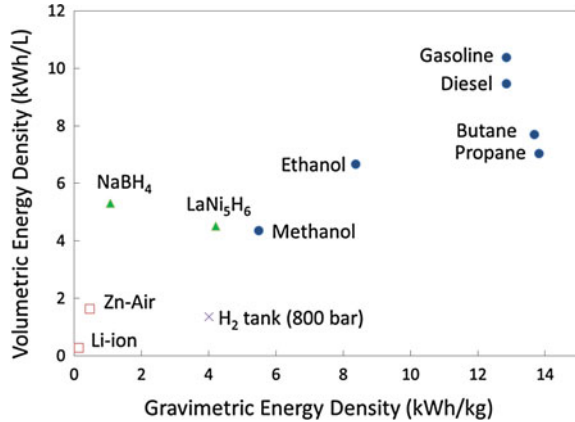
While commonly used fuels possess substantially higher energy density than batteries as shown in Fig 39.1, the effective energy density of a fuel cell system (E_{Net}) is different from the energy density of the fuel. This can be expressed by the following equation:

$$E_{\text{Net}} = e_{\text{F}} \times U_{\text{F}} \times \eta_{\text{cell}} \times \eta_{\text{sys}} \times V(\text{or } W)$$

M. Tsuchiya (✉)
SiEnergy Systems, LLC, 85 Bolton Street, Cambridge, MA 02140, USA
e-mail: tsuchiya@post.harvard.edu

M. Tsuchiya
Kyushu University, Fukuoka, Japan

Fig. 39.1 Energy density of various fuels and batteries. Liquid fuels (circles), hydrides (triangles), compressed hydrogen tank (cross mark), and batteries (open squares)

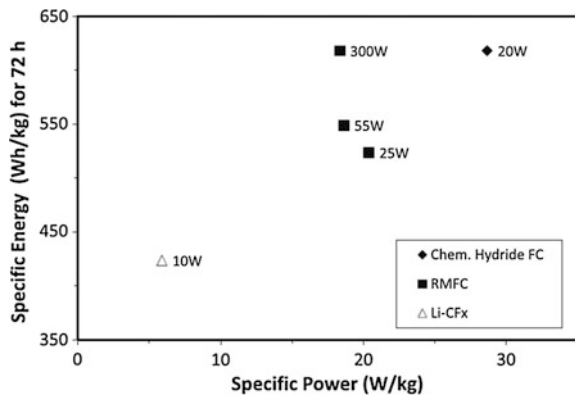


where e_F is the energy density of the fuel (as shown in Fig. 39.1), U_F is the fuel utilization, η_{cell} is the cell efficiency, η_{sys} is the system efficiency (i.e., parasitic losses), V is the volumetric fraction of fuel, and W is the gravimetric fraction of fuel. The net energy density of portable fuel cell system is approximately 300–600 Wh/L for most systems. The actual energy and power of fuel cell systems tested by the US Army are shown in Fig. 39.2 [1].

The advantage of portable fuel cells over primary and secondary battery technology becomes substantial when users are off-grid for many hours. The longer the mission length, the larger the difference in weight becomes. Figure 39.3 shows fuel cell is the lightest power source for military missions over 8 h.

There are three major types of fuel cell chemistries used in portable applications as shown in Table 39.1. While other fuel cell chemistries such as reformed borohydride fuel cells, reformed ammonia fuel cells, and direct ethanol fuel cells have been proposed and demonstrated before, these fuel cell chemistries are not included in this chapter because of low commercialization activities.

Fig. 39.2 Specific power and energy of fuel cell systems [1]. The energy density of a lithium fluoride battery (LiCF_x), reformed methanol fuel cell systems (RMFC), and a aluminum hydride-based fuel cell system (Chem. Hydride FC) are shown. (Reprinted from Ref [1] with permission from Elsevier.)



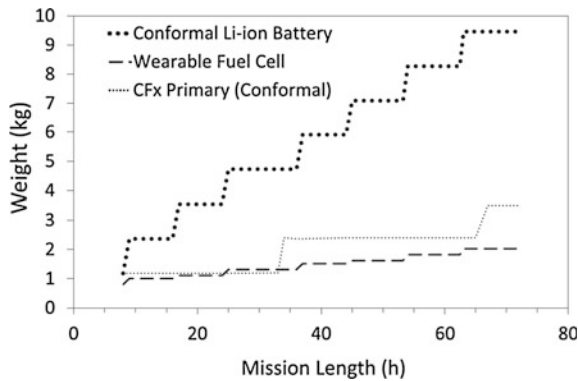


Fig. 39.3 Weight of a fuel cell (20 W, AlH_3 system) and a rechargeable battery (Li-ion) required for various mission lengths [1]. (Reprinted from Ref [1] with permission from Elsevier.)

Table 39.1 Major fuel cell chemistries for portable applications

Type	Fuel
Direct liquid fuel cell	Methanol (DMFC) Borohydride (DBFC)
Polymer electrolyte membrane fuel cells	Hydrogen (metal hydride) Reformed methanol (RMFC) Powder + water (NaSi , CaH_2 , or AlH_3)
Solid oxide fuel cells	Liquefied petroleum gas (propane and/or butane)

39.2 Application Areas

The application areas for fuel cell based portable energy sources can be categorized into three areas: handheld mobile chargers ($\sim 1\text{--}10$ W); wearable battery chargers ($\sim 10\text{--}50$ W); and portable or small stationary fuel cells ($\sim 50\text{--}500$ W). A handheld mobile charger is an off-grid charger for cell phones. A wearable fuel cell is a backpack size device that can provide power for multiple electronic devices such as laptops, radios, or a Global Positioning System (GPS). A portable or small stationary fuel cell ($50\text{--}500$ W) can be used as off-grid power sources for remote locations, as well as power sources for unmanned aerial vehicles (UAVs), and unmanned undersea vehicles (UUVs). Small stationary fuel cells have been deployed in oil and gas pipeline monitoring, border protection, wind tower management, and auxiliary power units for sailboats and recreational vehicles. Examples of application areas for portable fuel cells are shown in Fig. 39.4.

Fig. 39.4 Application areas for portable fuel cells

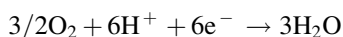


39.3 Direct Liquid Fuel Cells

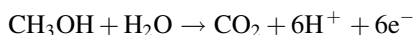
39.3.1 Direct Methanol Fuel Cells (DMFCs)

Direct methanol fuel cell (DMFC) is one of the most actively studied fuel cell chemistry for portable applications. Direct oxidation of methanol enables fuel cells to operate at near room temperature without reforming. Additionally, the technology works in both passive and active modes. Passive mode uses no power consuming balance-of-plant components, and relies on pressure/concentration gradient and capillary forces to supply fuel to the membrane electrode assembly (MEA). On the other hand, active mode uses blowers and pumps to move fuels to the MEAs [2]. For DMFCs, the half-cell and overall cell reactions are as follows.

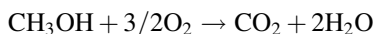
Cathode Reaction



Anode Reaction



Overall Reaction



The thermodynamic open circuit voltage (OCV) of DMFCs is ~ 1.2 V. However, the practical OCV of DMFCs is in the range of 0.6–0.8 V due to methanol crossover. The large overpotential required to oxidize methanol is another major issue for this technology. Additionally, the relatively high precious metal loading (>5 mg/cm²) is required to achieve reasonable power density (>50 mW/cm²) [3].

Fig. 39.5 Toshiba's Dynario fuel cell system [5]



There have been tremendous amounts of research and development activities performed on DMFCs since the early 2000s. Companies attempted to commercialize the DMFC include Toshiba, Sony, MTI Micro Fuel Cells, LG Chem, Samsung, Hitachi, NEC, Panasonic, and Fujitsu [4]. Most of these companies started R&D by envisioning internal integration of fuel cells into cell phones. However, most of them shifted their R&D from internal battery replacement to external battery charger due to various technical issues. Development of DMFC for portable applications faced numerous technical challenges such as low power density, fluid management, and high cost. For the mobile fuel cell market (1–10 W), Toshiba is the only company successfully launched a product (Dynario™). Even Toshiba's Dynario was not a commercially successful product (sold around 3,000 units only), due to very limited operating temperature and humidity range (10–35 °C, and from 30 to 90 % relative humidity) and high price (29,800 JPY for the system, and 3150 JPY for 5 fuel cartridges) [5]. A picture of the Dynario system is shown in Fig. 39.5.

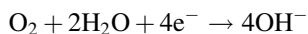
The most successful DMFC manufacturer today is SFC Energy in Germany. They offer 45–110 W DMFC products for leisure applications such as marine activities and camping (EFOY Comfort); industrial application such as off-grid power for oil and gas, the wind industry, and surveillance (EFOY Pro); and military applications (EFOY defense). The company reported sales of 1029 units for security and industry, and 1450 units to the consumer market in 2014, according to their 2014 annual report [6].

39.3.2 Direct Borohydride Fuel Cell (DBFC)

Direct borohydride fuel cell (DBFC) is another direct liquid fuel cell actively studied for portable applications. DBFC has been an attractive choice for portable fuel cells because it does not require precious metal catalysts for fuel oxidation, and it does not generate toxic byproducts. The power density of DBFCs is also relatively high; over

150 mW/cm² is commonly demonstrated at 70–80 °C. The DBFC uses OH⁻ to transport ions with the following half-cell and overall reactions.

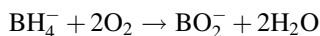
Cathode Reaction



Anode Reaction

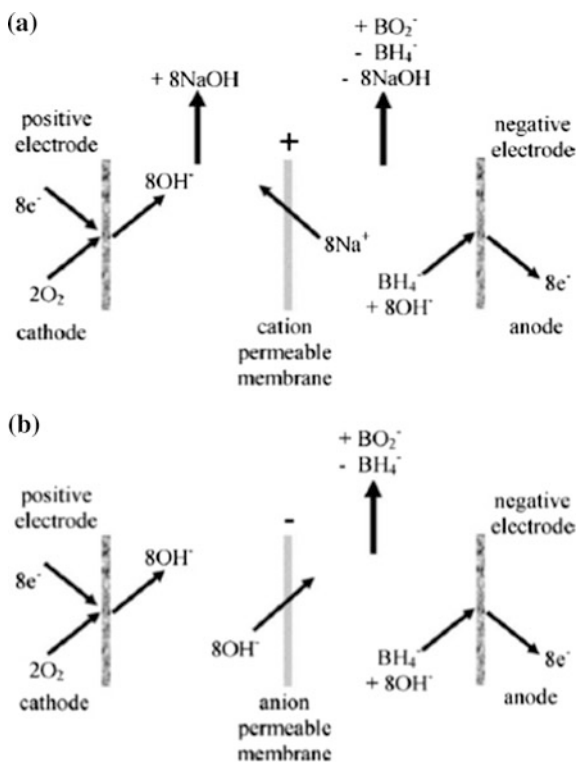


Overall Reaction



The overall reaction provides an OCV of 1.64 V, which is favorable for portable fuel cell applications requiring high energy density, while practical cells generally produce an OCV of around 1.2 V. NaBH₄ is the most commonly used borohydride in portable fuel cells. This type of fuel cell works with either cation or anion ionomer membranes, as shown in Fig. 39.6.

Fig. 39.6 Borohydride fuel cells utilizing: **a** cation permeable membrane, and **b** an anion permeable membrane [7]. (Reprinted from Ref [7] with permission from Elsevier.)

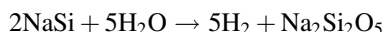


Medis Technology, an Israeli start-up that used to be listed in NASDAQ, invested substantial resources to develop and sell this technology. They received an UL certification (Underwriters Laboratories) and launched the “Medis 24/7 Power Pack” in late 2006. A year later, they expanded their manufacturing facility to support a production volume of 1.5 million units per month [6]. However, their sales projection was too optimistic. By the end of 2008, the company had accumulated a deficit of \$371 million [8]. The company was delisted from NASDAQ and terminated its operation in late 2009. While Medis’ DBFC technology was simple and well suited for portable applications, they had several drawbacks such as the corrosive and irritant nature of sodium borohydride, and difficulties in recharging the borohydride after use. The Medis 24/7 Power Pack was a one-time use only (i.e., disposable) product that was not an economical solution for the bulk of consumers.

39.4 Polymer Electrolyte Membrane Fuel Cells

The polymer electrolyte membrane fuel cell (PEMFC) is the most actively studied fuel cell chemistry in recent decades, particularly due to strong R&D investments made by automotive manufactures. PEMFCs can operate at near room temperature and can respond quickly to dynamic power loads. Compared to other fuel cell chemistries, PEMFCs have relatively mature supply chains for the electrolyte membranes, catalysts, and system components. As of now (year 2016), the PEMFC is the most widely deployed fuel cell chemistry for portable fuel cells.

While PEMFCs have numerous advantages over other fuel cell chemistries, the biggest obstacle for the PEMFC is the lack of hydrogen supply infrastructure. Thus, companies have explored various methods to produce hydrogen. For example, SiGNa Chemistry, a company in California, invented a process to create hydrogen from sodium silicide (NaSi) and water. Sodium silicide reacts readily with water, and produce gaseous hydrogen and sodium silicate. The chemical reaction for the hydrogen production using NaSi is as follows:



The reaction is an exothermic reaction with a Gibbs free energy of ~ 175 kJ/mol. The hydrogen storage density of this reaction is 9.8 wt% on a powder basis (NaSi), or 4.0 wt% including both the H_2O and NaSi. This chemistry to create hydrogen is used in the fuel cell system by Powertrekk, sold by a Swedish Company, myFC.

Another interesting approach to generate hydrogen with water is the technology commercialized by a Japanese start-up company, Aquafairy. They used calcium hydride to generate water through the following reactions:

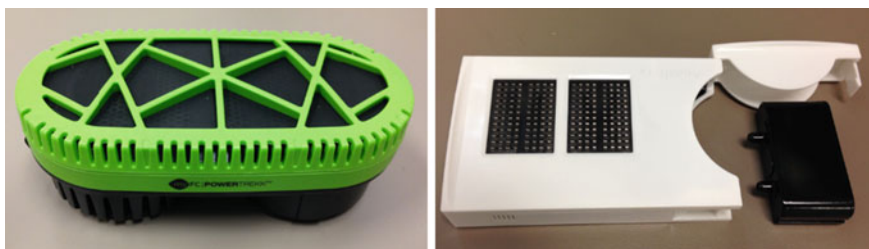
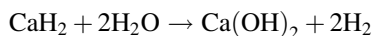


Fig. 39.7 The myFC PowerTrek (*left*), and the Aquafairy AF-M3000 (*right*) fuel cell chargers

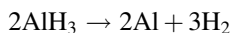


The hydrogen storage density of this reaction is 9.5 wt% on a powder basis (CaH_2) or 5.1 wt% including both the H_2O and CaH_2 . Pictures of the portable fuel cell systems released by myFC and Aquafairy are shown in Fig. 39.7.

Horizon Fuel Cells and Intelligent Energy chose to use metal hydride to store hydrogen. Lanthanum Nickel Hydride (LaNi_5H_6) is the most common metal hydride that can store hydrogen reversibly at room temperature. The advantage of a hydride is simple system and good start–stop capability. On the other hand, the hydrogen storage density of LaNi_5H_6 is only 1 wt%, which is impractical for applications requiring large amount of fuel to operate. For example, Horizon’s MiniPak requires a canister of 105 g to generate 14 Wh of energy [9]. Intelligent Energy’s Upp system requires a 385 g cartridge to generate 25 Wh of energy [10]. Another issue is the lack of hydrogen infrastructure. A user needs to buy an electrolyzer or special hydrogen canister from the manufacturers. The cost to refill hydrogen is still relatively high. Horizon’s fuel cell requires purchase of a hydrogen recharge station that is priced at around 160–250 USD (sold by Brunton, as of June 2016) and the Upp system requires a replacement cartridge priced at 49.95 GBP. The system cost for Horizon’s MiniPak is 109.99 USD [11] and Intelligent Energy’s Upp is 149.00 GBP [12].

For wearable and small stationary fuel cells (10 W and above), reformed methanol is often employed because steam reforming of methanol takes place at relatively low temperatures (200–300 °C) [13]. Examples of PEMFC based systems using methanol reformation (also known as RMFC) include the XX55, and Blade systems from Ultracell and the M300-CX from Protonex. These products are mainly sold for military applications.

Most recently, a fuel cell system using aluminum hydride (Alane) was explored by US Army CERDEC [14]. This is an interesting approach, since Alane can store up to 10 wt% hydrogen. Alane produces hydrogen through an endothermic reaction as follows:



Based on CERDEC's evaluation, the Alane system had specific energy of 582 Wh/kg and an energy density of 667 Wh/L that are higher than existing wearable fuel cell systems based on commercial DMFCs and RMFCs. While technical issues still remain in several areas including proper thermal control of the dehydrogenation, fuel utilization, and safety measures, the technology seems a very attractive option for wearable power [15].

39.5 Solid Oxide Fuel Cells

Solid oxide fuel cell (SOFC) has also been investigated as a portable power source in recent years. SOFCs operate at temperature range above 650 °C. The key advantage of SOFCs for portable applications is the ability to utilize high energy density fuels, such as butane and propane. Due to the potential to demonstrate high energy density, particularly when integrated into a silicon platform, micro-SOFCs have been actively studied since the 2000s at various institutions around the world. Institutions studied micro-SOFC technology include Lawrence Livermore National Laboratories [16], Massachusetts Institute of Technology [17], ETH Zurich [18], Stanford University [19], Harvard University [20, 21], and Catalonia Institute for Energy Research [22]. More than 10 years of cumulative research at these intuitions resulted in demonstration of high power density ($>1 \text{ W/cm}^2$) at below 500 °C using ultra-thin film electrolytes [21, 23]. An example of a thin film membrane-based SOFC integrated on silicon platform is shown in Fig. 39.8.

The most notable development for micro-SOFCs performed so far is by Lilliputian Systems in the United States, as shown in Fig. 39.9. The company raised over \$150 million dollars to develop a SOFC-based cell phone charger [24]. The company developed a small fuel cell chip-based SOFC that generates 2–3 W of

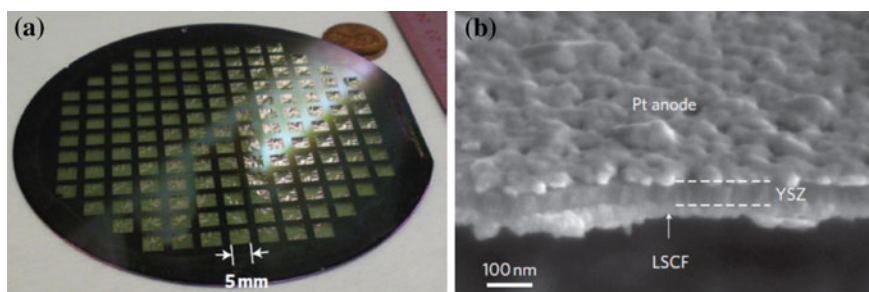


Fig. 39.8 a Ultra-thin film SOFC integrated in a silicon platform. b Cross-sectional electron micrograph of the membrane [20]

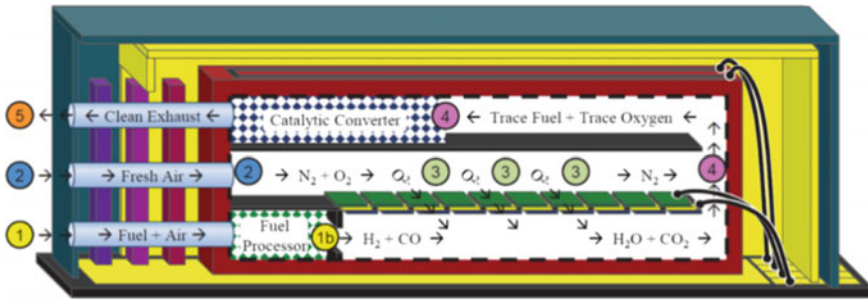


Fig. 39.9 The structure of Lilliputian's fuel cell chip. The *bottom layer* is the anode chamber with catalytic partial oxidation chamber. The *middle layer* is the cathode chamber, and the *top layer* is the exhaust gas chamber containing catalytic converter to clean up the exhaust gas. Fuel cell chips were bonded with glass seals and they were vacuum packaged. [25]

power. The fuel cell chip was integrated into a handheld fuel cell system. A prototype of Nectar™ fuel cell charger demonstrated by Lilliputian in 2013 had a compact system (~ 150 cc, ~ 200 g) with a small, replaceable butane fuel canister (~ 50 cc, ~ 35 g). One butane canister was designed to provide 55 Wh of electrical energy, corresponding to ~ 1 kWh/L or 15–20 % net energy efficiency. The company developed not only a compact fuel cell chip, but also compact system components, such as mass flow sensors, oxygen sensors, air pumps, fuel valves, and thermal management systems.

Their fuel cell chip contained many first-of-a-kind features, such as vacuum packaging for compact heat insulation, silicon-based heat exchangers, vacuum-tight sealing glass, and in-plane electrical stacking via Pt rivets, as shown in Fig. 39.10. The fuel cell chip generated over 1 W/cm² at 800 °C [25]. Despite very impressive technical development, the technology was unable to reach the market likely due to its high cost compared to lithium batteries. It was a very unfortunate ending, since the Lilliputian team demonstrated working prototypes after very intense technology development spanning more than 10 years.

Fraunhofer IKTS is another institution that has actively investigated planar SOFC-based portable power sources. Fraunhofer developed a compact 100 W Eneramic® system using an electrolyte-supported cell with glass seals. They used catalytic partial oxidation to crack propane and developed a compact system as shown in Fig. 39.11. The net efficiency of their system is approximately 20–25 %.

In addition to these developments using planar SOFCs, substantial developments were also made in micro-tubular SOFCs for portable applications. Micro-tubular SOFCs use millimeter-scale tubes that have high power densities compared to centimeter-scale tubes used in the early generation tubular SOFC technology [27, 28]. The advantages of tubular SOFC designs are rapid start-up and robustness against thermal cycling. Also, tubular technology does not require seals that often cause numerous poisoning issues in planar SOFCs. Companies which have developed tubular SOFC-based portable fuel cell systems include Ultraelectronics AMI

Fig. 39.10 Lilliputian's platinum rivets for in-plane electrical stacking [25]

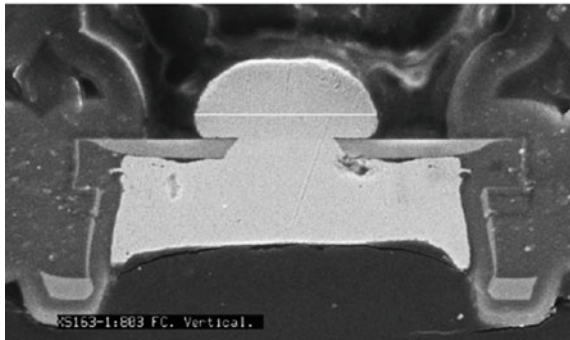
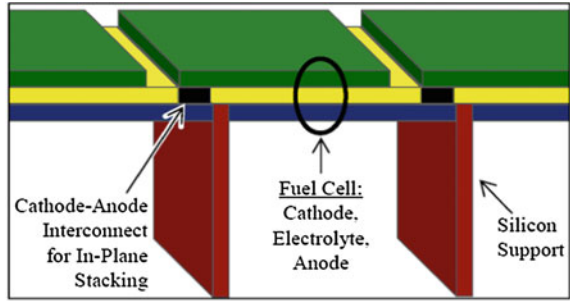
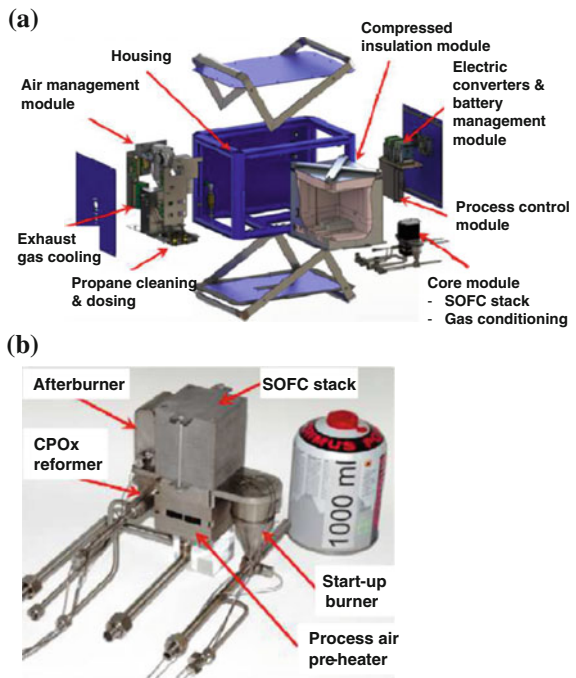


Fig. 39.11 Eneramic® fuel cell developed by Fraunhofer IKTS [26]



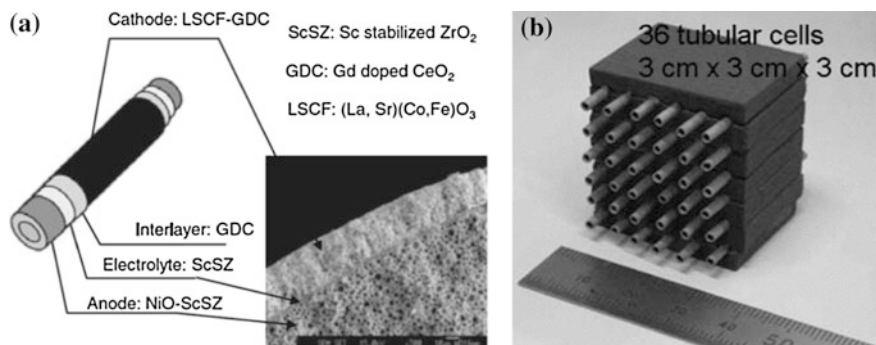


Fig. 39.12 **a** Cross-sectional SEM of micro-tubular SOFC developed at AIST, and **b** an example of tubular cell stack [29, 31]. (Reprinted From Ref [29] and [31] with permission from AAAS and Elsevier.)

(formally known as Adaptive Materials), Protonex (who acquired Mesoscopic Devices), and Watt Fuel Cells (licensed fuel cell intellectual property developed by NanoDynamics Energy). The main customers of these companies are the US Department of Defense (DoD). The technology has been used in portable and wearable fuel cells, UAVs, and UUVs by the US DoD [1].

All of these commercial systems utilize catalytic partial oxidation of propane fuel, and operate at relatively high temperature (>700 °C). While high temperature operation is favorable for fuel reforming, it accelerates degradation of fuel cells. To overcome temperature-related challenges such as metal agglomeration and corrosion, there are active ongoing research projects to reduce the operating temperature of tubular SOFCs. For example, the National Institute of Advanced Industrial Science and Technology (AIST) in Japan demonstrated a micro-tubular SOFC with a power density of over 1 W/cm^2 at 600 °C by optimizing anode microstructure [29]. They also reported tubular stacks with various designs [30, 31]. An example is shown in Fig. 39.12. By using similar tubular design, the group recently demonstrated fuel cell operation with direct hydrocarbon fuel at <600 °C using ceria functional layer [32, 33].

39.6 Summary

Portable fuel cells have emerged as an important application area for fuel cells due to a surge in energy consumption by portable electronic devices with increased functionality. Fuel cells have successfully been commercialized as external cell phone chargers, wearable power for soldiers, off-grid power generators for remote locations, and prime power for unmanned vehicles. Following the successful commercialization of direct liquid fuel cells such as DMFCs and DBFCs, PEMFCs and SOFCs entered the market to further enhance fuel cell's capability as a portable

power source in recent years. Further development of PEMFCs and SOFCs, in particular hydrogen storage materials development for PEMFCs and low operating temperature stack development for SOFCs, is expected to play an important role in broadening the application areas of portable fuel cells in the future.

References

1. Thampan T, Shah D, Cook C, Novoa J, Shah S (2014) Development and evaluation of portable and wearable fuel cells for soldier use. *J Power Sources* 259:276–281. doi:[10.1016/j.jpowsour.2014.02.099](https://doi.org/10.1016/j.jpowsour.2014.02.099)
2. Aricò AS, Baglio V, Antonucci V (2009) Direct methanol fuel cells: history, status and perspectives. In: *Electrocatalysis of direct methanol fuel cells*. Wiley-VCH Verlag GmbH & Co. KGaA, Weinheims, pp 1–78
3. Baglio V, Di Blasi A, Modica E, Creti P, Antonucci V, Arico A (2006) Electrochemical analysis of direct methanol fuel cells for low temperature operation. *Int J Electrochem Sci* 1:71–79
4. Li X, Faghri A (2013) Review and advances of direct methanol fuel cells (DMFCs) part I: design, fabrication, and testing with high concentration methanol solutions. *J Power Sources* 226:223–240. doi:[10.1016/j.jpowsour.2012.10.061](https://doi.org/10.1016/j.jpowsour.2012.10.061)
5. https://www.toshiba.co.jp/about/press/2009_10/pr2201.htm (2009). Accessed 1 Aug 2015
6. http://www.sfc.com/investors/en/downloads/SFC_GB2014_E_24.03.2015_safe.pdf. Accessed 1 Aug 2015
7. de Leon CP, Walsh FC, Pletcher D, Browning DJ, Lakeman JB (2006) Direct borohydride fuel cells. *J Power Sources* 155(2):172–181. doi:[10.1016/j.jpowsour.2006.01.011](https://doi.org/10.1016/j.jpowsour.2006.01.011)
8. [http://www.wikinvest.com/stock/Medis_Technologies_\(MDTL\)/Filing/10-K/2009/F5277113](http://www.wikinvest.com/stock/Medis_Technologies_(MDTL)/Filing/10-K/2009/F5277113) (2008)
9. <http://www.horizonfuelcell.com/#!minipak/c156u>. Accessed 1 Aug 2015
10. <http://www.zdnet.com/article/upp-fuel-cell-review-off-grid-gadget-power-at-a-price/>
11. <http://www.amazon.com/Horizon-Fuel-Cell-Technologies-Handheld/dp/B009R13Y38>. Accessed 9 Aug 2015
12. <http://www.beupp.com/store/cart>. Accessed 9 Aug 2015
13. Sá S, Silva H, Brandão L, Sousa JM, Mendes A (2010) Catalysts for methanol steam reforming—a review. *Appl Catal B* 99(1–2):43–57. doi:[10.1016/j.apcatb.2010.06.015](https://doi.org/10.1016/j.apcatb.2010.06.015)
14. Grew KN, Brownlee ZB, Shukla KC, Chu D (2012) Assessment of Alane as a hydrogen storage media for portable fuel cell power sources. *J Power Sources* 217:417–430. doi:[10.1016/j.jpowsour.2012.06.007](https://doi.org/10.1016/j.jpowsour.2012.06.007)
15. Thampan T, Shah D, Cook C, Shah S, Atwater T (2015) Development and user evaluation of an AlH₃ wearable power system (WPS). *ECS Trans* 65(1):205–217
16. Jankowski AF, Hayes JP, Graff RT, Morse JD (2002) Micro-fabricated thin-film fuel cells for portable power requirements. *Mat Res Soc Symp Proc* 730, V4.2.1
17. Baertsch CD, Jensen KF, Hertz JL, Tuller HL, Vengallatore ST, Spearing SM, Schmidt MA (2004) Fabrication and structural characterization of self-supporting electrolyte membranes for a micro solid-oxide fuel cell. *J Mater Res* 19(9):2604–2615
18. Evans A, Bieberle-Hutter A, Rupp JLM, Gauckler LJ (2009) Review on microfabricated micro-solid oxide fuel cell membranes. *J Power Sources* 194(1):119–129. doi:[10.1016/j.jpowsour.2009.03.048](https://doi.org/10.1016/j.jpowsour.2009.03.048)
19. Huang H, Nakamura M, Su P, Fasching R, Saito Y, Prinz FB (2007) High-performance ultrathin solid oxide fuel cells for low-temperature operation. *J Electrochem Soc* 154(1):B20–B24

20. Tsuchiya M, Lai B-K, Ramanathan S (2011) Scalable nanostructured membranes for solid-oxide fuel cells. *Nat Nano* 6(5):282–286. <http://www.nature.com/nnano/journal/v6/n5/abs/nnano.2011.43.html#supplementary-information>
21. Kerman K, Ramanathan S (2014) Complex oxide nanomembranes for energy conversion and storage: a review. *J Mater Res* 29(03):320–337
22. Garbayo I, Pla D, Morata A, Fonseca L, Sabate N, Tarancon A (2014) Full ceramic micro solid oxide fuel cells: towards more reliable MEMS power generators operating at high temperatures. *Energy Environ Sci* 7(11):3617–3629. doi:10.1039/c4ee00748d
23. An J, Kim Y-B, Park J, Gür TM, Prinz FB (2013) Three-dimensional nanostructured bilayer solid oxide fuel cell with 1.3 W/cm² at 450 °C. *Nano Lett* 13(9):4551–4555
24. <http://www.betaboston.com/news/2014/07/31/lilliputian-systems-mit-spin-out-that-raised-150-million-runs-out-of-fuel/> (2014). Accessed 1 Aug 2015
25. Schaevitz SB (2012) Powering the wireless world with MEMS. In: Proceedings of SPIE 8248, micromachining and microfabrication process technology XVII, p 824802
26. Reuber S, Pönicke A, Wunderlich C, Michaelis A (2013) Eneramic power generator—a reliable and cycleable 100 W SOFC-system. *ECS Trans* 57(1):161–169
27. Howe KS, Thompso GJ, Kendall K (2011) Micro-tubular solid oxide fuel cells and stacks. *J Power Sources* 196(4):1677–1686
28. Kendall K (2010) Progress in microtubular solid oxide fuel cells. *Int J Appl Ceram Technol* 7(1):1–9
29. Suzuki T, Hasan Z, Funahashi Y, Yamaguchi T, Fujishiro Y, Awano M (2009) Impact of anode microstructure on solid oxide fuel cells. *Science* 325(5942):852–855. doi:10.1126/science.1176404
30. Suzuki T, Funahashi Y, Yamaguchi T, Fujishiro Y, Awano M (2008) New stack design of micro-tubular SOFCs for portable power sources. *Fuel Cells* 8(6):381–384. doi:10.1002/fuce.200800047
31. Funahashi Y, Shimamori T, Suzuki T, Fujishiro Y, Awano M (2007) Fabrication and characterization of components for cube shaped micro tubular SOFC bundle. *J Power Sources* 163(2):731–736
32. Sumi H, Yamaguchi T, Hamamoto K, Suzuki T, Fujishiro Y (2013) Development of microtubular SOFCs for portable power sources. *ECS Trans* 57(1):133–140. doi:10.1149/05701.0133ecst
33. Suzuki T, Yamaguchi T, Hamamoto K, Fujishiro Y, Awano M, Sammes N (2011) A functional layer for direct use of hydrocarbon fuel in low temperature solid-oxide fuel cells. *Energy Environ Sci* 4(3):940–943

Chapter 40

Hydrogen Infrastructure

Hideyuki Dohi, Masahiro Kasai and Kiyooki Onoue

Abstract This chapter describes hydrogen infrastructure for hydrogen energy society. After considering the energy supply chain using electricity, city gas, and gasoline, storage forms of hydrogen as an energy carrier are compared, followed by technological and economic analysis of hydrogen infrastructure.

Keywords Electricity · City gas · Gasoline · Compressed hydrogen · Liquid hydrogen · Methylcyclohexane · Hydrogen transportation · Hydrogen filling station · Economic evaluation

40.1 Energy Infrastructure

In the field of energy, we define the facilities used for the production (i.e., conversion), storage, transportation, and distribution of energy as infrastructure. This covers the whole supply chain from production to consumption, as well as the systems used to control and manage them. For example, Table 40.1 shows the supply chain of electricity, city gas, and gasoline, which are the basic energy sources in Japan. In Japan, facilities for import and stockpiling are important components, as the country depends on imports for most of its primary energy supply. The reserves of primary energy resources are 30 days consumption for coal,

H. Dohi (✉) · M. Kasai
International Research Center for Hydrogen Energy, Kyushu University,
Fukuoka 819-0395, Japan
e-mail: dohi.hideyuki.722@m.kyushu-u.ac.jp

M. Kasai
e-mail: kasai.masahiro.987@m.kyushu-u.ac.jp

K. Onoue
Office for the Promotion of Safety and Health, Kyushu University,
Fukuoka 819-0395, Japan
e-mail: onoue.kiyooki.852@m.kyushu-u.ac.jp

Table 40.1 Energy supply chain in Japan

	Stockpile	Production conversion	Storage	Transportation	Distribution
Electricity	Stocked as primary energy	Power plant	Pumped hydro	Grid	Power distribution
City gas	LNG receiving terminal	Vaporization	Gas holder	High pressure pipeline	Low pressure pipeline
Gasoline	Crude oil tank	Refinery	Tank	Costal tanker	Tank truck and service station

14 days for LNG, and 170 days for oil [1]; Japan maintains large stockpiles of oil for energy security, as it is greatly dependent on the Middle East.

For facilities used in producing or converting electricity, city gas, and oil, a typical scale-merit economy is achieved in that the facility cost and operating cost generally decrease and conversion efficiency improves with scaling up. Therefore, the facilities and mechanisms for shipping from a large central production plant to local distribution (consumption) systems are also important components of the energy infrastructure.

In addition, in the production/conversion facilities, continuous operation to maintain the production volume is economically advantageous. However, consumption is not constant because it is dependent on consumers. Therefore, storage plays an important role by acting as a buffer to compensate for the temporal differences in usage patterns between production and consumption; additional storage facilities such as product tanks are constructed for this purpose. In the case of oil, in addition to crude oil inventories, we keep a product inventory of more than 30 days for production and distribution [2]. Therefore, in the existing energy infrastructure, the optimized structure is determined from the viewpoint of security, economy, convenience, and safety.

40.2 Characteristics of Hydrogen Infrastructure

At ambient temperature and pressure, hydrogen has a volume energy density of 0.013 MJ/L. This is around 1/3000th that of gasoline (liquid fuel). Therefore, it is difficult to store and transport hydrogen at ambient temperature and pressure economically. Hence, conversion processes are needed, including compression, liquefaction, and production of organic chemical hydrides, which are different from the existing energy infrastructure. Table 40.2 shows the characteristics of representative storage systems for compressed hydrogen, liquid hydrogen, and organic chemical hydride.

Compressed hydrogen, which has lower energy density than other media, is disadvantageous in terms of cost for long distance transportation and long-term

Table 40.2 Storage forms of hydrogen (A.P.: Ambient Pressure)

	Conversion process	Storage density kg-H ₂ /m ³	Storage conditions (Temp./pressure)	FCV refueling method
Compressed H ₂	Compression	23	R.T./35 MPa	Compression
Liquid H ₂	Cryogenic liquefaction	70	-253 °C/A.P.	Vaporization and compression
Methylcyclohexane	Hydrogenation of toluene	47	R.T./A.P.	Dehydrogenation and compression

storage. However, its energy efficiency is relatively high. Liquid hydrogen is disadvantageous because energy is required for liquefaction and maintaining cryogenic temperatures for storage. However, it is advantageous from the viewpoint of long distance transportation because of its high-energy density. Organic chemical hydrides are advantageous from the viewpoint of long distance transportation and long-term storage because they can be transported and stored at ambient temperature and pressure. However, energy is consumed in the dehydrogenation process.

In addition, some other techniques including ammonia and hydrogen storage materials have also been proposed to store and transport hydrogen.

40.3 Characteristics of the Methods

Compressed hydrogen: The compressed hydrogen method increases the density using high-pressure hydrogen for storage and transportation, and it is widely used in e.g., the electronics and chemical industry. The use of even higher pressures is being tested for enabling the large-scale consumption of hydrogen energy, such as for fuel cell vehicles (FCVs). Figure 40.1 shows a photograph of a trailer used for transporting hydrogen, in which 260 kg of hydrogen is transported through 24 high-pressure cylinders at 45 MPa. The density of hydrogen compressed at 45 MPa is around 340 times that at atmospheric pressure (see Fig. 40.2).

In using high pressure for supplying hydrogen to FCVs, the compressed hydrogen method is advantageous in that energy for compression is well used, and its overall energy efficiency is higher than that of other methods. Table 40.3 shows the supply chain using the compressed hydrogen method and the energy efficiency of the respective processes. The scale factor (refer to Sect. 40.5) for the major constituents of the supply chain, namely, compressors and high-pressure containers, is larger than that for the major constituents used in other methods [3, 4], and the cost competitiveness does not improve appreciably with an increase in scale. In addition, the cost per unit energy for storage containers is larger than that of other methods, and the method becomes more costly and less advantageous as the transportation distance and storage time increase. Improved technology is needed to reduce the cost of compressors and high-pressure containers.



Fig. 40.1 45 MPa trailer (JX Nippon Oil & Energy Corporation)

Fig. 40.2 Density of hydrogen at 298 K

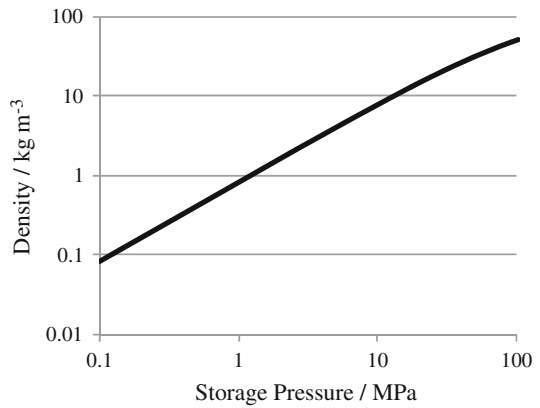


Table 40.3 Supply chain for compressed hydrogen [5]

	Production conversion	Storage	Transportation	Distribution
Main components	Compressor	Curdle	Trailer	Compressor and dispenser
Energy efficiency (%)	96.2	100	97.4	88.7

Liquid hydrogen method: Liquid hydrogen is characterized by a high density of 70 kg/m^3 , three times that of compressed hydrogen (35 MPa) and 1.5 times that of methylcyclohexane. Because of its large density, this method is being used increasingly in various fields of industry.

Table 40.4 shows the supply chain of the liquid hydrogen method considering application to FCVs. At present, the liquefaction process requires $\sim 12 \text{ kWh/kg}$ of energy [6], which corresponds to $\sim 30 \%$ of the energy contained in 1 kg of hydrogen. Owing to the large energy consumption, the overall energy efficiency is inferior to that of the compressed hydrogen method. However, there is enough room for improvement as the energy needed for the liquefaction of hydrogen is theoretically 3.2 kWh/kg . Therefore, efforts are continuing to improve the efficiency. In addition, boil-off during storage and transportation is not negligible when the storage time and transportation distance are large, and therefore, methods for reducing boil-off are being developed.

On the other hand, the equipment cost of the liquid hydrogen method reduces greatly with an increase in scale. The scale factor for the major equipment is estimated to be 0.57–0.65 for liquefiers and 0.7 for the low-temperature containers [3, 4]. Therefore, this method is characterized by improved economies with scale.

Organic chemical hydride method: The organic chemical hydride method is a method for storing and transporting hydrogen using a system with materials such as toluene and methylcyclohexane, in which a hydrogenation reaction and a dehydrogenation reaction advance easily. 3 mol of hydrogen is stored in 1 mol of methylcyclohexane (Fig. 40.3). The energy density corresponds to $47 \text{ kg H}_2/\text{m}^3$, which is between that of compressed hydrogen (35 MPa) and liquid hydrogen.

Once hydrogen is converted to methylcyclohexane by the hydrogenation reaction of toluene, storage and transportation are feasible at ambient temperature and pressure. Therefore, we can use the existing infrastructure such as tank trucks, which are widely used for the supply of gasoline and chemical products, and enjoy

Table 40.4 Supply chain for liquid hydrogen [5]

	Production conversion	Storage	Transportation	Distribution
Main components	Liquefier	Dewar	Trailer	Vaporizer, compressor, and dispenser
Energy efficiency (%)	73	98.2	98 (excluding boil off)	88.7

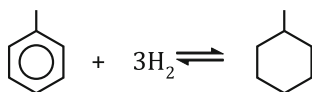


Fig. 40.3 Equilibrium reaction of toluene and methylcyclohexane

Table 40.5 Supply chain for organic hydrides [5]

	Production conversion	Storage	Transportation	Distribution
Main components	Hydrogenation plant	Chemical tank	Tank truck	Dehydrogenation unit, compressor, and dispenser
Energy efficiency (%)	97.9	100	99.5	76.7

the benefit of easy handling. Table 40.5 shows the supply chain for methylcyclohexane. Before hydrogen can be used, methylcyclohexane must be dehydrogenated to take out hydrogen. Because this dehydrogenation reaction is an endothermic reaction requiring 68 kJ of energy per mol of hydrogen, the overall energy efficiency is lower than that of the compressed hydrogen method. In addition, it is also necessary to return the toluene produced in the dehydrogenation process back to the hydrogen production process; this is another disadvantage compared with other methods. However, this method is relatively better suited for storage over a longer period and transportation over a longer distance because the equipment cost for storage is extremely small and the loss during storage is negligible.

40.4 Cost Structure of Hydrogen Supply

The cost of supplying hydrogen to FCVs has been calculated; in this regard, the cost structure shows problems unique to hydrogen supply. In 2006, at the University of California, a detailed analysis was conducted for compressed hydrogen, liquid hydrogen, and pipelines in terms of the sensitivity to transportation distance, supply quantity, and market penetration [4]. Assuming market penetration of 16 % for FCVs and a supply quantity of 500 kg/day/station for the station, the analysis showed that the compressed hydrogen method is the most economical method. In addition, the analysis showed that the liquid hydrogen method and pipeline method are the most economical methods for a market penetration of 100 % for FCVs and supply quantity of 1800 kg/day/station. In all cases, the station cost accounts for the largest part, and the electrical power cost for liquefaction and the equipment cost for trailers and liquefaction facilities account for the second-largest part. It should be noted that in these calculations, the percentage of storage cost is low because storage is assumed to be only 2 days for the liquid hydrogen method and only 0.5 days for the compressed hydrogen and pipeline methods.

In 2005, the Japan Atomic Energy Research Institute performed similar calculations [7]; their calculation of the percentage of the station cost was higher than that of the University of California (Table 40.6).

Table 40.6 Cost breakdown of hydrogen

	Compressed H ₂ JP-Yen/kg	Liquid H ₂ JP-Yen/kg
Station	661 (60 %)	648 (55 %)
Transportation	219 (20 %)	65 (6 %)
Conversion (compression or liquefaction)	55 (5 %)	296 (25 %)
Production	159 (15 %)	159 (14 %)
Total	935 (100 %)	1009 (100 %)

Thus, unlike the energy cost structure of the past where the fuel accounts for the largest proportion of cost, for hydrogen the expense of infrastructure, including the refueling station accounts for the largest proportion. As this increases the ratio of fixed costs, the cost performance rapidly degrades as the operation rate is decreased. Therefore, the economic efficiency is low, especially during the early stages of market launch. An important consideration for market expansion is developing technology for lowering costs, particularly that of the refueling station.

40.5 The Hydrogen Station

In Japan, commercial operation of hydrogen stations was started in 2014, after accumulation of technical and managerial data from field tests, which started in 2002. Figure 40.4 shows the first integrated service station for gasoline and hydrogen established in Japan. Currently, dedicated hydrogen fueling stations and mobile stations are being operated or planned.

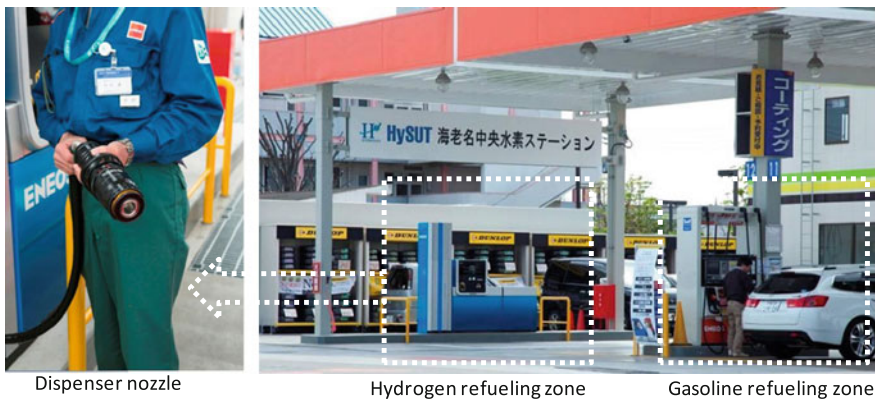


Fig. 40.4 Integrated hydrogen refueling station (JX Nippon Oil & Energy Corporation)

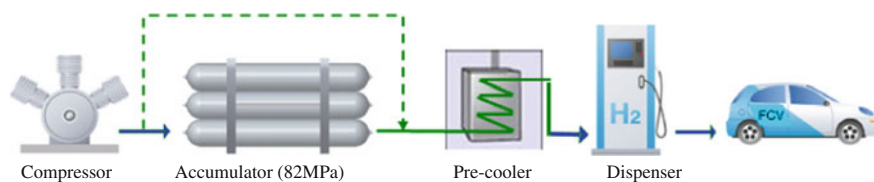


Fig. 40.5 System components in a refueling station

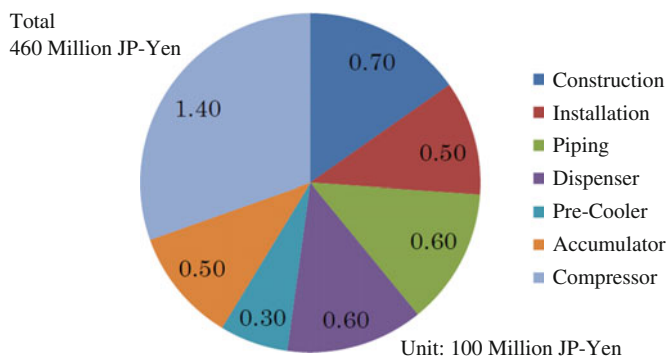


Fig. 40.6 Construction cost of a hydrogen refueling station [8]

The expansion of hydrogen stations is indispensable for realizing the higher prevalence of FCVs. However, for compressed hydrogen, liquid hydrogen, and organic chemical hydride methods, the expense for the hydrogen station accounts for a considerable part of the hydrogen supply costs (Table 40.6). Figure 40.5 shows the equipment configuration common to all methods and Fig. 40.6, the actual construction costs [8]. The compressor, accumulator, pre-cooler, and dispenser account for $\sim 60\%$ of the construction costs. Furthermore, a vaporizer is needed in the liquid hydrogen method, and a dehydrogenation unit is needed in the organic chemical hydride method. On the other hand, pumps are being actively developed to achieve high-pressure gasification directly from liquid hydrogen to simplify the facilities and improve the energy efficiency [9]. Therefore, technology development is an important challenge for reducing the cost of this equipment and improving the efficiency.

40.6 Economic Evaluation of Energy Infrastructure

As discussed, the compressed hydrogen, liquid hydrogen, and organic chemical hydride methods have been examined for the construction of hydrogen energy infrastructure. Economic evaluation is an important aspect when comparing these methods. Each method has different equipment costs, device lifetimes, operational costs, and maintenance costs. In addition, as the role of hydrogen is to store energy,

a comparison with other energy storage methods such as batteries is necessary. In this chapter, some viewpoints are discussed for the economic evaluation of energy infrastructure.

LCOE: For comparing the costs in the field of energy, the LCOE (levelized cost of energy) is generally used, where the typical unit is \$/kWh (currency unit/energy unit). As shown in Eq. (40.1), this is the value obtained by dividing the total expense during the lifetime (i.e. capital investment, operational and maintenance expenses, fuel costs, and other costs), by the total amount of energy produced during the lifetime. In adding them up, both the expense and energy are discounted to the following value:

$$\text{LCOE} = \frac{c_0 + \sum_{i=1}^y \frac{c_i}{(1+d)^i}}{\sum_{i=1}^y \frac{e_i}{(1+d)^i}}, \quad (40.1)$$

where c_0 is the initial investment; c_i is the total cost annually; y is the lifetime; d is the discount rate; and e_i is the quantity of energy produced annually.

Equation (40.2) shows the cost in which both c_i and e_i are constant over the years, is useful in a preliminary examination. Here, $d/(1 - (1+d)^{-y})$ is called the capital recovery factor.

$$\text{LCOE} = \left(\frac{d}{1 - (1+d)^{-y}} c_0 + c_i \right) / e_i \quad (40.2)$$

When, for example, we observe the relationship between the initial investment (c_0) and the equipment lifetime (y) by using the LCOE, the capital recovery factors are 0.142 and 0.094, respectively, for equipment lifetime of 10 and 20 years, respectively, if a discount rate of 7 % is assumed. Therefore, increasing the lifetime of the equipment from 10 to 20 years is equivalent to reducing initial investment by 34 %. Thus, by using the LCOE, it becomes possible to quantitatively evaluate the influence of various factors solely using an index of energy cost. For information on the concrete calculation, refer to [10].

Scaling factor (power-sizing exponent) The scaling factor is α in Eq. (40.3), which approximately indicates the relationship between the scale of the facility and the equipment cost using a power function:

$$c_B = c_A (s_B/s_A)^\alpha \quad (40.3)$$

where c_A and c_B are the costs of equipment A and B, respectively, and s_A and s_B are the sizes or capacities of equipment A and B, respectively.

This relational expression is used to roughly estimate the cost of the target equipment from the cost of equipment of a different scale. α should be previously known or should be estimated by regression analysis using the data of the cost of

several pieces of equipment with different scales; α is typically in the range of 0.5–1.0. The unit cost, which is obtained by dividing the equipment cost by the capacity, is constant regardless of the scale, assuming $\alpha = 1$. The unit cost decreases with a smaller value of α . For example, for $\alpha = 0.6$, the unit cost decreases by 60 % when the equipment size is increased by 10 times.

Storage time: Generally, we can divide the energy storage facility into a part that performs energy conversion and another part that stores the converted energy. In the compressed hydrogen method, the conversion section consists of a compressor whose size p is expressed by a unit of power (energy per unit time) such as kg-H₂/h. On the other hand, the storage section consists of a high-pressure container whose capacity c , which is expressed by a unit of energy such as kg-H₂, is given by $c = pt$ assuming a storage time t . In the case of a battery, similarly, the conversion section consists of an inverter and a charge-discharge controller and the storage section consists of a battery cell; their respective capacities are expressed in units of kW and kWh. Thus, for the storage of energy, the scale of a facility is decided by the power and storage time. Therefore, the cost of an energy storage facility could be considered a function of p and t . An approximate formula like Eq. (40.4), which gives the total cost considering the scale factor as mentioned above, reduces to Eq. (40.5) if the proportionality to capacity ($\alpha = \beta = 1$) is assumed.

$$c_S = c_p p^\alpha + c_e (pt)^\beta \quad (40.4)$$

$$c_S = (c_p + c_e t) p \quad (40.5)$$

where c_S is the system cost; c_p , the unit cost of the converting part; c_e , the unit cost of the storage part; p , the power; and t , the number of hours of storage. α and β are scaling factors.

It should be noted that in the energy storage process, two parameters, power and storage time, are required to express the scale of a facility. In addition, it becomes possible to evaluate the case with a different storage period if the unit prices are evaluated by dividing the system into the conversion section and the storage section. Furthermore, the hydrogen storage facility can be divided into the conversion section and the storage section, as shown in Table 40.7.

The construction of the infrastructure required for realizing a hydrogen society is promoted in such a way that the demand-side components such as FCVs and

Table 40.7 Conversion and storage part in the hydrogen storage process

	Conversion part		Storage part
	Charge	Discharge	
Compressed H ₂	Compressor	–	High pressure tank
Liquid H ₂	Liquefier	Vaporizer	Dewar
Methylcyclohexane	Hydrogenation process	Dehydrogenation process	Chemical tank

stationary fuel cells exert a pull. In the supply-side, today, hydrogen is produced using fossil fuels and by-product hydrogen. However, hydrogen from renewable energy will soon begin to be introduced, and its ratio will gradually increase.

On the other hand, in the electricity infrastructure, first, an energy storage facility with comparatively short storage time is installed for system stabilization as photovoltaic and wind power systems are introduced. A battery is a major candidate for this purpose. However, as renewable energy is introduced more widely, energy storage for longer time periods becomes necessary for adjusting supply and demand, and the needs of energy storage rapidly increase in terms of both scale and storage time. Considering future requirements, the development of various energy storage technologies is being promoted. Hydrogen production from renewable energy is expected to be a promising technology that not only secures CO₂-free hydrogen but also plays a large role in long-term energy storage.

It is necessary to consider the entire landscape of energy generation in pursuing the construction of future hydrogen infrastructure and technology development for that purpose. To achieve this, a comparison of various techniques and conditions is required. The proposed techniques discussed herein (i.e., scaling factor, calculation of equipment costs considering storage time, and evaluation by LCOE using these values) are useful for performing such comparisons.

References

1. Advisory Committee for Natural Resources and Energy (2015) Subcommittee on long-term energy supply-demand outlook, 30 Mar 2015. http://www.enecho.meti.go.jp/committee/council/basic_policy_subcommittee/mitoshi/005/pdf/005_05.pdf. Accessed 11 Dec 2015
2. Ministry of Economy Trade and Industry (METI) (2011) METI committee, 2 Dec 2011. http://www.meti.go.jp/committee/kenkyukai/energy/sekiyu_gas_antei_wg/003_06_00.pdf. Accessed 11 Dec 2015
3. National Renewable Energy Laboratory (NREL) (1999) Costs of storing and transporting hydrogen. NREL/TP-570-25106, <http://www.osti.gov/bridge/servlets/purl/6574-OBMIES/webviewable/>. Accessed 11 Dec 2015
4. Yang C, Ogden J (2007) Determining the lowest-cost hydrogen delivery mode. *Int J Hydrog Energy* 32(2):268–286
5. Japan Automobile Research Institute (JARI) (2010) Analysis of total efficiency and greenhouse gas emission. <http://www.jari.or.jp/Portals/0/jhfc/data/report/2010/pdf/result.pdf>. Accessed 11 Dec 2015
6. New Energy and Industrial Technology Development Organization (NEDO) (2015) Hydrogen energy white paper. <http://www.nedo.go.jp/content/100567362.pdf>. Accessed 11 Dec 2015
7. Japan Atomic Energy Research Institute (2005) JAERI-Tech 2005-038. <http://jolissrch-inter.tokai-sc.jaea.go.jp/search/servlet/search?31773>. Accessed 11 Dec 2015
8. Agency for Natural Resources and Energy (2014) Strategic road map for hydrogen and fuel cells. <http://www.meti.go.jp/press/2014/06/20140624004/20140624004-2.pdf>. Accessed 11 Dec 2015
9. NEDO Interim Report (2005) <http://www.nedo.go.jp/content/100091321.pdf>. Accessed 11 Dec 2015
10. IPCC Working Group III Contribution to AR5 (2014) Metrics and methodology. *Clim Chang* 2014 Mitig Clim Chang 1281–1328

Chapter 41

Business Model Analysis of Hydrogen Energy

Megumi Takata

Abstract This chapter explores business model analysis for the hydrogen energy sector. Hydrogen energy businesses are characterized from an economical viewpoint, as a large-scale capital-intensive business sector dealing with a commodity where long-term perspectives and governmental support are needed. Case studies are then described using a business model for hydrogen infrastructure for FCVs.

Keywords Business model · Business model canvas · Customer segment · Value proposition · Hydrogen infrastructure for FCVs

41.1 Characteristics of Energy-Related Business

Here the characteristics of energy related businesses who work with hydrogen are explained. Every field of business has a characteristic profile. For example, smartphone apps have a very low entry barrier, and products developed by non-experts can make enormous impact in the market. On the other hand, logistics requires significant infrastructure such as cargo trucks, planes, warehouses, IT systems, and human resources, making it difficult to enter into this market. What are the profiles of energy business which aim to monetize hydrogen? Generally, they have the following characteristics:

Characteristic 1: Large-scale and Intensive Capital

Businesses in the energy sector tend to provide services over a wide area, and are not generally able to simply terminate operation after the business is set up. Large-scale infrastructure, a wide-range of equipment, and long-term maintenance investments are required for secure and stable business operation. These

M. Takata (✉)

Department of Business and Technology Management (Business School),
Faculty of Economics, Kyushu University, Fukuoka 812-8581, Japan
e-mail: mtakata@econ.kyushu-u.ac.jp

© Springer Japan 2016

K. Sasaki et al. (eds.), *Hydrogen Energy Engineering*,
Green Energy and Technology, DOI 10.1007/978-4-431-56042-5_41

549

make the business scale and investment size larger, and create a broad range of related industries. In the start-up phase, growth can be slow. However, in the growth phase, expansion accelerates and the number of users increases with *network externality*¹. Hydrogen energy is new in the market, so it necessary to build up new facilities and infrastructure for production and delivery of hydrogen with large scale investment.

Characteristic 2: Commodity Price to all Levels of Society

Energy is commodity, so it must provide a cheap and non-discriminatory price in the service area. The unit price of energy (e.g. electricity or heat) can be easily compared side-by-side by the end user, no matter what source is used. Therefore, the hydrogen energy provider needs to set the price of the commodity, offsetting the higher cost with other profitable businesses, or using government subsidies in the early start-up phase. In addition, in the energy sector, it is not possible to stop operation suddenly once operation begins. This is entirely different from e.g. closing one convenience store in a town, when other stores can easily be found. With electricity it is still usually possible to replace the service with other operators on the grid. However, in the case of fuel cell vehicles (FCVs), once the local hydrogen station closes, finding an alternative is a serious problem.

Characteristic 3: Long-term Perspectives

It is necessary for new hydrogen-related businesses to have long-term perspectives for diffusion and investment recovery, due to reasons of scale of business. Uncertainties surrounding technological development or government deregulation are another reason to develop long-term perspectives. Such perspectives require that attention be paid to differences in the business model in the start-up, growth, and mature phases.

Characteristic 4: Utilizing Existing Supply Chains

It is necessary for energy-related businesses to develop a consistent supply chain system, such as procurement, production, delivery, sales, and maintenance, but these require huge investment. Therefore, utilizing existing supply chains decreases the size of investments, and helps business entities enter new markets. In the case of hydrogen production for fuel cells, utilizing existing city gas infrastructure makes it more advantageous in the start-up and growth phases, decreasing investment costs, as well as gradually raising the amount of available renewable energy for later phases.

¹Network externality is the effect that one user of a good or service has on the value of that product to other people. If benefits increase with the number of other users, this is regarded as positive network externality.

Characteristic 5: The role of Government (Policy, Regulation, and Subsidies)

In terms of the stability and safety of energy supplies, there are large numbers of regulatory issues in the energy sector. The business model must suit government regulations. Especially in hydrogen supply, hydrogen embrittlement of metal parts and the high-pressure hydrogen tank require higher safety levels and have strict regulatory issues. This affects the uncertainty of business models more than in other areas of the energy sector. Although the hydrogen energy sector requires large amounts of investment, it should offer a low commodity price to the end user. For this purpose, the government has to design and offer a variety of political incentives such as subsidies to the business entities and end users. At first, the government must show a clear and long-term vision of a hydrogen society to citizens and industries. The government has a large and extremely important role to play in the energy business sector.

41.2 What Is the Business Model?

The term “business model” has various meanings, but can basically be defined as:

- A conceptual model representing a business, and its money-earning logic.
- A business layer between business strategy and processes.

Thus, a business model is used to explain and share business concepts between stakeholders (e.g. senior management, employees, shareholders, business partners, and customers), and it ties corporate business strategy to execution. However, the business model contains various business elements, which should be carefully considered. These elements in turn affect others elements with a change in external business environment, and complexity/uncertainty of the business. This complex situation makes it more difficult for stakeholders to understand the model, and can cause misunderstandings. To help with this problem, Pigneur and Osterwalder created the “Business Model Canvas” as a standard business tool [1, 2]. This canvas simplifies complex business model concepts, and therefore can be used to reach a wider audience. As a result, this tool helps reduce misunderstandings amongst stakeholders, and ties corporate business strategy to execution in a more appropriate manner.

The Business Model Canvas consists of nine boxes (Fig. 41.1): *Value Proposition*; *Customer Segment*; *Customer Relations*; *Channel*; *Revenue Stream*; *Key Activities*; *Key Resources*; *Key Partners*; and *Cost Structure*. These nine elements represent the whole structure of the business model and increase stakeholder comprehension. Each element is defined as follows:

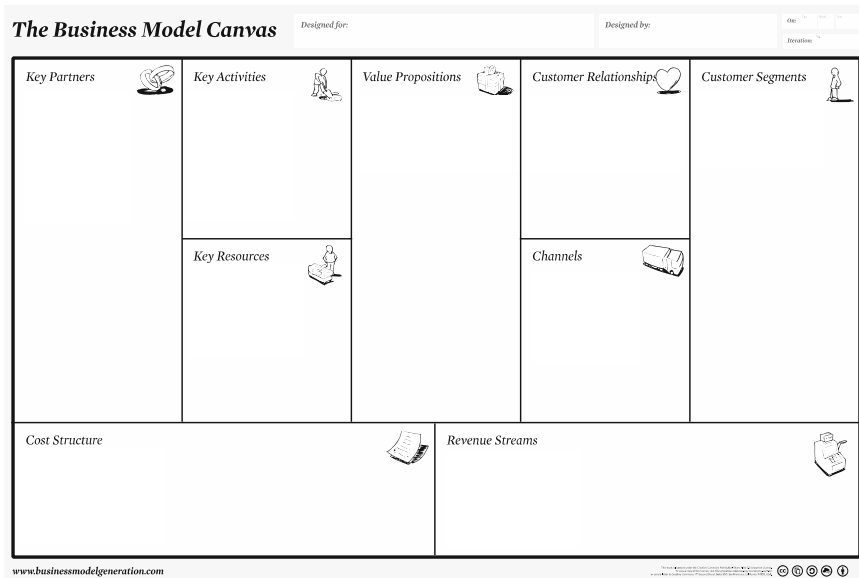


Fig. 41.1 The Business Model Canvas

(1) Customer Segments

- For whom is the business model creating value?
- Who are the most important customers?
- Includes e.g. mass markets, niche markets, and segmented markets.

(2) Value Propositions

- What value does the business model deliver to the customer?
- Which of a customer's problems does the business model solve?
- Which customer needs is the business model satisfying?
- Includes e.g. novelty, performance, customization, practicality, design, price, cost reduction, risk reduction, accessibility, and usability.

(3) Channels

- Through which channels do the Customer Segments want to be reached?
- How are they being reached now? Which channels are cost-efficient?
- Includes e.g. raising awareness, evaluation, purchase, and delivery of value.

(4) Customer Relationship

- What relationship does the Customer Segment expect to establish and maintain?
- How are they integrated with the rest of the business model? How costly are they?

- Include e.g. personal assistance, self-service, automated services, communities, and co-creation.
- (5) Revenue Stream
- What value are the customers really willing to pay?
 - What do the customer currently pay? How are they currently paying? How would they prefer to pay?
- (6) Key Activities
- What key activities do the value propositions require? Distribution channels? Customer relationships? Revenue streams?
 - Includes e.g. production, problem solving, and platform/network.
- (7) Key Resources
- What Key Resources do the Value Propositions require? Distribution Channels? Customer Relationships? Revenue Streams?
 - These include physical resources, intellectual (brand patents, copyright, and data), human, and financial resources.
- (8) Key Partners
- Who are the key partners? Who are the key suppliers? Which key resources is the business model acquiring from partners? Which key activities do partners perform?
 - Key partners are motivated by e.g. optimization and economy, reduction of risk and uncertainty, and acquisition of particular resources/activities.
- (9) Cost Structure
- What are the most important costs inherent in the business model?
 - Which key resources are the most expensive? Which key activities are the most expensive? Cost driven, or value driven?
 - Factors include e.g. fixed costs (salaries, rents, and utilities), variable costs, economies of scale, and economies of scope.

41.3 Business Model in Energy-Related Field

Herein, a business model canvas is analyzed for the energy sector, specifically hydrogen stations for FCVs. The influence of the characteristics of energy-related businesses have on the business model are discussed. Firstly, the most important boxes on the canvas are “Value Proposition” and “Customer Segment”.

(1) Customer Segment

Currently the initial market launch of FCVs is underway. The main users are highly environmentally conscious people, as well as governments/companies for demonstration purposes. An important factor is that the motivation for purchase changes between the introduction phase and the growth phase of the market lifecycle. In the introductory period, purchase of an FCV is mainly for demonstration purchases by government or corporations. The cost performance is not considered to be a major purchasing factor. However, as infrastructure spreads, and mass production contributes to an affordable price, the perception of the user shifts towards convenience, functionality, and price. This has to be taken into account in the growth period.

(2) Value Proposition

The most important value proposition of hydrogen energy is “environmental load reduction”. This effect is increased compared with the case of a gasoline or even a hybrid car. If the well-to-wheel CO₂ emissions from a gasoline car are normalized to 1, the value for a hybrid car is 0.6. For an FCV using natural-gas-derived hydrogen, the value is 0.4. For an FCV using hydrogen derived from renewable energy, the value can be as low as 0.1. Other important points are convenience and price compared with a gasoline car. In the introduction period of the market lifecycle, there are a limited numbers of hydrogen stations with large associated costs. However the price of hydrogen at the pump must be at least comparable with gasoline. To achieve this comparable level, supplementation by government subsidies, or in-house profit-allocation are necessary.

(3) Channel

The channel through which the value is delivered to a customer. In this case, the point of contact between the value and the customer is the hydrogen station.

(4) Customer Relationship

The FCV user visits a hydrogen refueling station repeatedly. Therefore the relationship between the station and the customer is one of familiarity. It is thus necessary to find a suitable location for a station in a place that is convenient for the FCV user. The average travel time to a refueling station will be ideally within 7~8 min. Creating a “safe and secure” image of hydrogen energy will be also be an important point when building and maintaining a relationship with the customer.

(5) Revenue Stream

The revenue stream derives from sales of hydrogen. The fuel for a car is a commodity, so it is necessary to realize a price compatible with an average gasoline car.

(6) Key Activities

The key activity to deliver value to a customer is the establishment and operation of a hydrogen station. Furthermore, technological development for cost reduction is also necessary for widespread distribution and popularization.

(7) Key Resources

The key resources are a refueling station that is low in cost and safe, as well as technology and capitals towards that goal.

(8) Key Partners

The most important partner is the automobile company that sells FCVs. This issue is often compared to the “chicken and egg” situation. The equipment manufacturer related to the hydrogen station, and the gas utility company, which delivers hydrogen are important partners. The government is another important partner who indicate the vision of a hydrogen society, and design political incentives and subsidies for achieving it. Citizens and NGOs are also important partners for raising social acceptance with reasonable understanding of new energy carriers such as hydrogen.

(8) Cost Structure

This is appropriated as the main cost of establishment and operation of a hydrogen station, as well as technological development.

“Government” is also an important partner. It indicates the vision of the hydrogen society, and designs the political incentives and subsidies for reaching it. “Citizens and NGOs” are also important partners to raise social acceptance with reasonable understanding of new energy such as hydrogen.

(9) Cost Structure

It’s appropriated as the main cost of “establishment and operation of a hydrogen station” and “technological development”.

In the business model illustrated in Fig. 41.2, the elements all influence each other. In other words, once the nine elements are adjusted appropriately to make a business model, the revenue stream and the cost structure must balance. However, it is difficult for an energy related business to make the cost structure balance with revenue stream at an early stage, due to the factors mentioned above. Therefore in the hydrogen sector, it is necessary to consider the following points.

Firstly, for the convenience of the FCV user, a certain numbers of hydrogen stations are needed with a certain density in a given city. This makes initial investment size larger. A single station costs around US\$1–2M in the U.S. and around US\$4–5 M in Japan, due to government regulation and the higher price for land acquisition (Characteristic 1: Large business scale and intensive capital). On the other hand, fuel is a commodity, so it is not realistic to sell hydrogen at an expensive price to the customer, even in the early introduction stage. This will be a bottleneck in the hydrogen station business (Characteristics 2: Commodity price to all levels of society). Therefore, an increase of the number of FCVs, the mass production effect in the spread of refueling stations, deregulation by the government, and additional technological developments are necessary to make the revenue stream balance with the cost structure. This will require long-term effort. Meanwhile, low profits must be covered by profits from other aspects of the

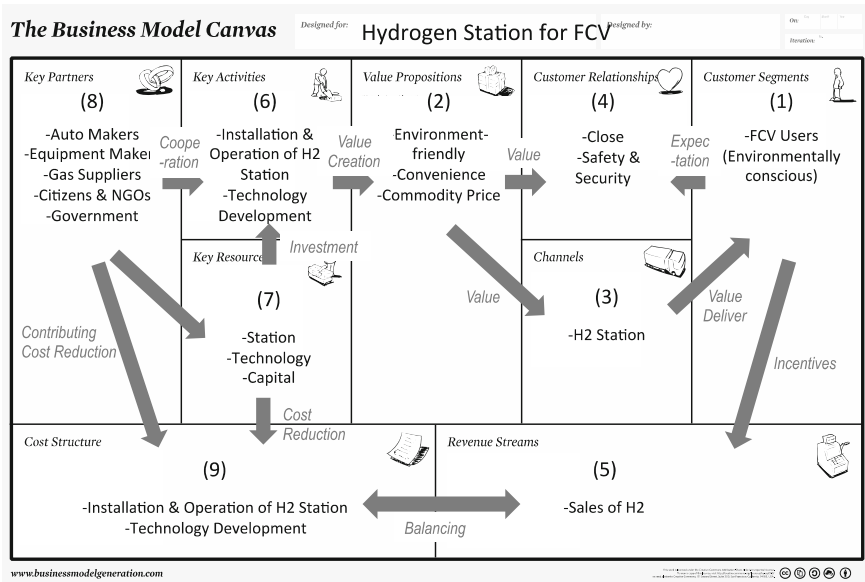


Fig. 41.2 The Business Model Canvas for an FCV hydrogen refueling station

business, and government subsidies (Characteristic 3: Long-term perspectives). Cooperation of the key partners is hugely important in reducing the large-scale and long-term investment required at the introduction stage. It is important to utilize existing city gas infrastructure, and to use the existing gasoline station network for setting up hydrogen refueling stations. To increase the number of FCV users, cooperation with the automobile company is also necessary (Characteristic 4: Utilizing existing supply chains). The most important factor is the role of government to enhance the entry of automobile companies and energy enterprises to the new market, and to expand the number of FCV users. First, the government must indicate a long-term political vision such as the global warming problem and the spread of renewable energy clearly, and design incentives for stakeholders to create the new market. It is also indispensable to develop outreach activities so that a greater understanding may be developed by society about hydrogen energy (Characteristic 5: Role of government).

41.4 Case Study

Features of the hydrogen energy-related business model have been analyzed with emphasis on hydrogen refueling stations for FCVs. Here, a case study is introduced to show a possible route solve the problem outlined above. This study was carried out by

a student team at Kyushu University, and went on to win Grand Prize at the Hydrogen Student Design Contest in 2013, organized by The Hydrogen Education Foundation (HEF) in the U.S. and held every year since 2004 [3, 4]. The contest challenges “multidisciplinary teams of university students to apply their creativity and academic skills in the areas of design, engineering, economics, environmental science, business and marketing to the hydrogen and fuel cell industries”. The 2013 theme was “Development of a Hydrogen Fueling Infrastructure in the Northeastern United States”. Details of the contest and proposal papers can be found on the HEF website: <http://www.hydrogencontest.org>. The Kyushu University team proposal is described below, and can be found in full at <http://www.hydrogencontest.org/2013.asp>:

- (1) A strategy for building refueling stations is considered based on a differentiation of the characteristics of different users, separated into Phase 1 (~2015), Phase 2 (~2020), and Phase 3 (~2025).
- (2) Phase 1 focuses on a large city such as New York, with a small number of on-site-type refueling stations becoming a base for hydrogen production and supply. The proposal also includes parallel establishment of refueling pumps within existing gas stations, and usage of modular-type equipment for decreasing the installation and operation cost of hydrogen stations. Moreover a mobile-type station is proposed for adapting to user demand and lowering the initial investment during the early stage of market introduction.
- (3) In Phase 2, on-site type stations become a base for hydrogen production and supply are added to the model. User demand in sparsely populated suburbs is ascertained by using mobile stations.
- (4) Based on the differences of a customer segment, and the value of each segment places, the marketing strategy should be changed. Phase 1 appeals to celebrities in New York residence for use of FCVs, and takes advantage of media by use in movies or TV programs. Phases 2 and 3 shift from celebrity users to the general public, and have the appeal of convenience of access and almost the same price as gasoline. At the same time, Phases 2 to 3 emphasize education to deepen understanding of hydrogen energy in citizens, with tour of hydrogen stations by children, etc. In the long run, the energy source for hydrogen production should shift from fossil fuel origin (such as natural gas), to renewable energy origin.

Conceptual figures of the proposal by Kyushu University Students are shown in Fig. 41.3 (Phase 1), Fig. 41.4 (Phase 2), and Fig. 41.5 (Phase 3). The business model canvases are shown in Figs. 41.6 (Phase 1) and 41.7 (Phases 2 and 3). The canvas makes it possible to visualize the points and differentiations of the business model in each phase respectively.

Fig. 41.3 Timeline of hydrogen station establishment in Phase 1

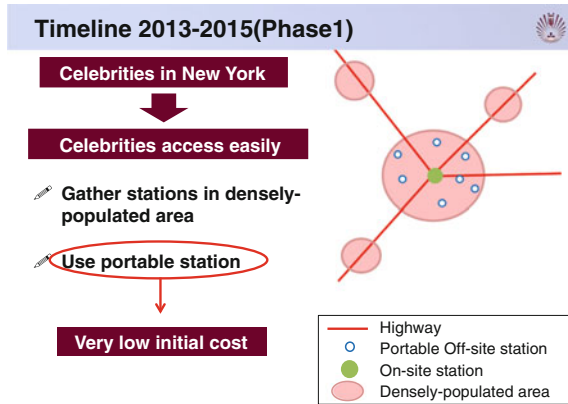


Fig. 41.4 Timeline of hydrogen station establishment in Phase 2

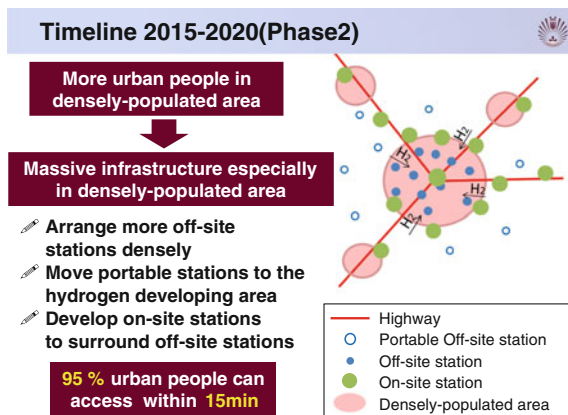
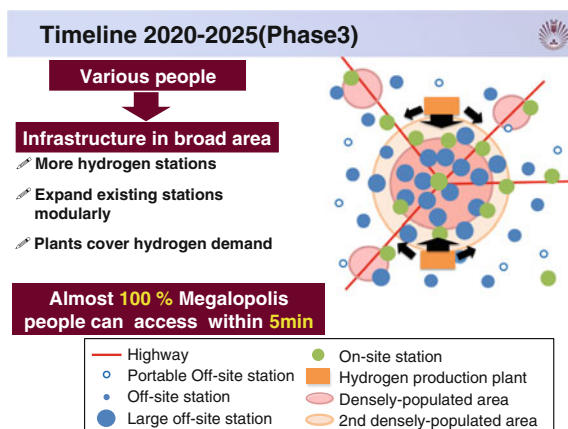


Fig. 41.5 Timeline of hydrogen station establishment in Phase 3



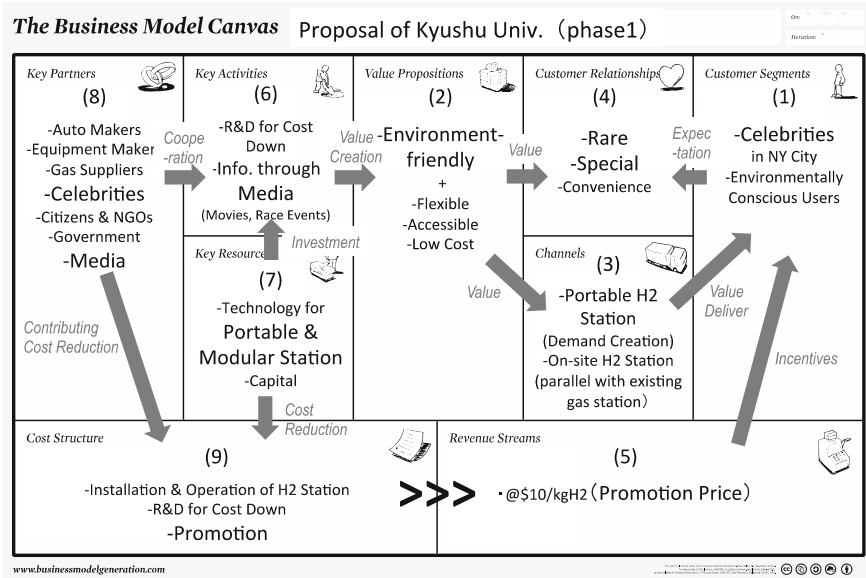


Fig. 41.6 Business model canvas of the proposal by Kyushu University (Phase1)

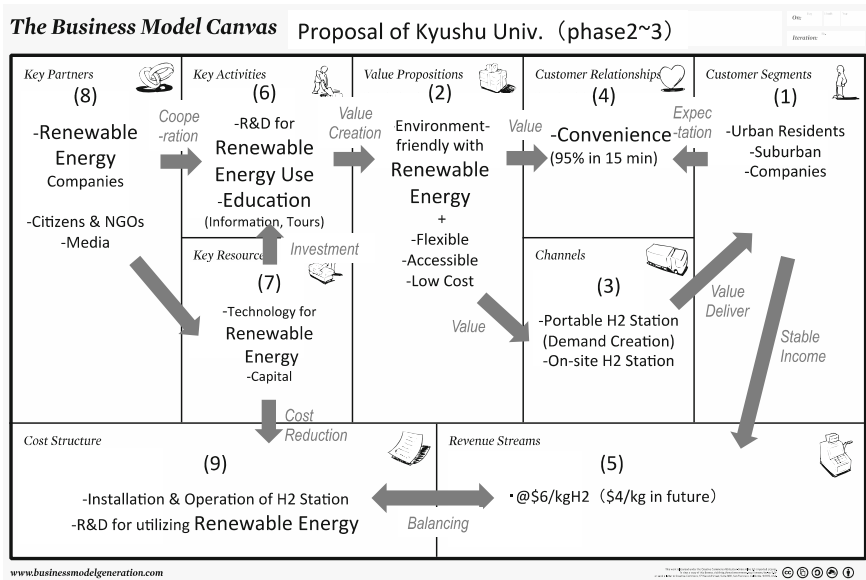


Fig. 41.7 Business canvas of the proposal of Kyushu University (Phases 2 to 3)

41.5 Conclusion

In this section, features of businesses in the energy sector, focusing on hydrogen energy have been explained. A business model canvas used as a standard tool can make even a complicated business model easier to understand by summarizing the points easily and clearly, when considering a business strategy and alignment of business elements. In hydrogen energy-related businesses, the vision of a hydrogen society taking into account price, scale, and public perception (PSP) should be understood and shared between the stakeholders in an appropriate manner. This is being achieved steadily, with long-term perspectives.

References

1. Osterwalder A (2004) The business model ontology—a proposition in a design science approach. Universite de Lausanne
2. Osterwalder A, Pigneur Y (2010) Business model generation: a handbook for visionaries, game changers, and challengers. John Wiley and Sons
3. Tsuda K, Kimura S, Takaki T, Toyofuku Y, Adaniya K, Shinto K, Miyoshi K, Hirata K, Christiani L, Takada M, Kobayashi N, Baba S, Nagamatsu Y, Takata M (2014) Design proposal for hydrogen refueling infrastructure deployment in the Northeastern United States. *Int Associ Hydrog Energy* 39(16):7449–7459
4. Development of Hydrogen Fueling Infrastructure in the Northeastern U.S. (2013) Hydrogen Student Design Contest. <http://www.hydrogencontest.org/2013.asp>. Accessed 10 Dec 2015

Chapter 42

Public Acceptance

Kenshi Itaoka, Aya Saito and Kazunari Sasaki

Abstract This chapter describes public acceptance of hydrogen energy, including sociopolitical acceptance, community acceptance, and market acceptance. Methodologies for quantitative assessment are explained. An overview on public acceptance study in various countries is given for fuel cell systems and hydrogen station.

Keywords Public acceptance · Sociopolitical acceptance · Community acceptance · Market acceptance · Methodology · Questionnaire · Hydrogen safety

42.1 Introduction: The Hydrogen Society and Public Acceptance

Public perception and acceptance of hydrogen and its utilization technologies are considered to be important factors for penetration into society in the future. Since these are emerging technologies, the current status of public acceptance is still unknown. It should be noted that the public perception and acceptance of technologies can be influenced by contemporary trends and incidents. Such examples for hydrogen include the Hindenburg disaster in 1937, and the hydrogen explosion

K. Itaoka (✉)

International Institute for Carbon-Neutral Energy Research (I2CNER),
Kyushu University, Fukuoka, Japan
e-mail: k.itaoka@i2cner.kyushu-u.ac.jp

A. Saito

Mizuho Information and Research Institute Inc., Tokyo, Japan
e-mail: aya.saito@mizuho-ir.co.jp

K. Sasaki

International Research Center for Hydrogen Energy, Kyushu University,
Fukuoka, Japan
e-mail: sasaki@mech.kyushu-u.ac.jp

© Springer Japan 2016

K. Sasaki et al. (eds.), *Hydrogen Energy Engineering*,
Green Energy and Technology, DOI 10.1007/978-4-431-56042-5_42

at Fukushima Daiichi Nuclear Power Plant in 2011. This chapter examines the definition of public acceptance, the theoretical background, and the metrics and methodology used to evaluate public acceptance. It then looks at the current status of awareness, perception, and opinions about hydrogen and utilization technologies. Finally, a basic concept of public outreach on hydrogen and utilization technology is introduced.

42.2 Definitions

Social acceptance is categorized into three dimensions: sociopolitical acceptance; community acceptance; and market acceptance [1], as illustrated in Fig. 42.1.

Sociopolitical Acceptance: Sociopolitical acceptance is at the most general level, over a wide geographical area, and is usually discussed at the national level, as case studies shows later in this chapter. It involves two target groups of people: stakeholders, and the general public. The reasoning behind such categorization is based on the level of interest in the targeted technologies and policies. Stakeholders are subdivided into two groups: direct stakeholders (whose interests are directly related to the target technology/policy), and indirect stakeholders. The former includes businesses related to the development, utilization, and installation of the target technologies, as well as government departments promoting policies related to these

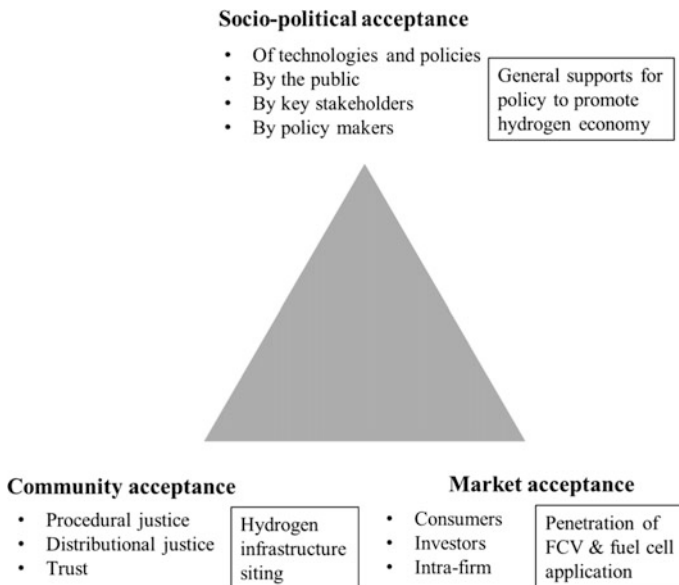


Fig. 42.1 The three dimensions of social acceptance, based on [1]. The text relating to public acceptance of hydrogen energy was added by the authors

technologies. The latter includes nongovernmental organizations (NGOs) and academic experts. In the case that activities of an NGO are directly related to promotion of the target technologies, it can be classed as a direct stakeholder. The most frequently used index related to sociopolitical acceptance is the *degree of acceptance* obtained from social surveys (questionnaires). However, there is as yet no consensus among researchers as to what type of questionnaire is appropriate to use as an index.

Community Acceptance: Community acceptance is at the level of site-specific local projects. The time period is limited from the initial listing of potential project sites to project completion (with installation and running of the facility), or project discontinuation. The level of community acceptance very likely differs from sociopolitical acceptance. Opposition by residents to a proposed project close to them (known pejoratively as NIMBYism, an acronym for *not in my backyard*) is often cited as one of the major factors in the difference between sociopolitical and community acceptance [1]. Another possible factor is regional externality (i.e., a cost/benefit imposed on someone as a result of actions taken by others) in economic thinking. These factors are considered to result from concerns about indirect environmental effects by those residing or working near the target site. If cost–benefit analysis is conducted applied from the framework of economics, regional environmental effects, and risks are considered as a negative aspect (cost) and regional economy profits are considered as a positive influence (benefit). Since perception of risk associated with installation of facilities sometimes depends on the characteristics of community, it is often difficult to obtain a clear-cut result from the cost–benefit approach. Besides, the distribution of cost and benefit within a community are essentially not considered [2]. Moreover, the procedure for implementation of a project and trust of the project implementer are often regarded to be more important than economic issues [2]. In conclusion, factors influencing community acceptance include distributional justice, the distribution itself, and procedural justice.

Market Acceptance: Market acceptance refers to small technologies among those spread through the market. It involves manufacturers, distribution companies, and consumers (users). Market acceptance is measured by the attractiveness of a product that reflects the technology. Attractiveness consists of the balance of user benefits generated from the product and the expense (price). Price is one of the most influential factors. The problem is the potential negative effect of other factors such as risk and negative influence. The risks of a product employing new technologies are not always clear or fully understood, and this can become a factor that interferes in market acceptance.

Various terms associated with public acceptance are used in the academic literature. The term “public acceptance” is often associated with a top-down approach, and therefore there have been efforts to use more terms stemming from a bottom-up approach, such as “public participation”, “public engagement,” and “public outreach.” Table 42.1 shows definitions of some terms related to social acceptance, taken from the literature.

Table 42.1 Terminology relevant to public acceptance

Term	Explanation
Consensus building	“It is not only a voting process but a serious taking of everyone’s input, and trust in each person’s discretion in follow up actions.” [2]
Confidence building	“It is a tool for both conflict reduction and resolution.” [25]
Public acceptance	“To accept corporations, facilities or new technologies in a regional society and/or a country with public understanding and approval.” [26] “Social acceptance is an often used term in the practical policy literature, but clear definitions are rarely given.” [1]
Public engagement	“It is the involvement of specialists listening to, developing their understanding of, and interacting with non-specialists.” [27]
Public relations	“It is the attempt to influence another’s perception of an event, individual or institution by presenting a specific, directed, outward image.” [28]
Public outreach	“It involves both the transfer of information and a mean to gauge the success of the transfer.” [29]
Public perception	“It is simply the type of information obtained from a public opinion survey.” [30]
Public involvement	“It is a process that involves the public in the decision-making of an organization, for example a municipality or a corporation.” [31]
Public participation	“It encompasses a group of procedures designed to consult, involve, and inform the public to allow those affected by a decision to have an input into that decision.” [32]

42.3 Theoretical Background

Research into the social acceptance of hydrogen and utilization technologies has been active outside Japan. The academic approach of such research is categorized to two main types: the economic approach, and the social-psychological approach.

Economic Approach: The economic approach is based on welfare economics and research conducted on social acceptance is from an economic perspective. This is implemented mainly via consumer surveys of products, focusing on “willingness-to-pay” (WTP) for e.g., fuel cell vehicles, in order to give suggestions for policymakers and/or for marketing fields. WTP is used to express the value of a commodity in monetary terms, and is defined as the maximum amount of money an individual is willing to pay for a product, or to avoid something undesirable. WTP can be measured via the stated preference approach (i.e., in a questionnaire survey) or the revealed preference approach (through market data analyses). In the stated preference approach, a respondent expresses their WTP by answering questions in a questionnaire or an interview. The most popular methodology to determine WTP is by contingent valuation and conjoint analyses. In contingent valuation, respondents are directly asked their WTP for a product (which is often hypothetical). The attribute of the products and the conditions associated with the purchase opportunity are provided in the hypothetical question. In conjoint analyses, WTP can be

measured together with attributes of attractiveness of a product. The respondents' choices of a product from hypothetical alternatives to have different level of attributes presented to respondents in order to elicit an estimate of relative the importance of particular attributes. For example in marketing a commercial car, the relative value of important attributes influencing the purchase decision (such as price, power, size, fuel economy etc.) can be measured at the same time.

Social-Psychological Approach: The social-psychological approach is based on social-psychology and analyses perception and attitude. Attitudes are an especially important concept in acceptability research. They are defined as "a psychological tendency that is expressed by evaluating a particular entity [or attitude object] with some degree of favor or disfavor" [3]. The recent dominant trend in social acceptance studies is to analyze the relationship between attitude and intended behavior in the basis of the Theory of Planned Behavior [4]. As a part of social-psychology studies, risk perception studies have been often conducted because the perception of risk relevant to a particular technology is considered a major factor in technology acceptance [5]. Furthermore, the result of a risk perception study is also interpreted in the concept of risk benefit analysis, which is often utilized to explain intentional behavior of people [6]. For risk benefit analysis, perceived risk is often more important to explain people's behavior rather than actual risk. To quantify the tendency of public acceptability in social-psychology studies, public surveys are mainly used to determine the extent that respondents answer yes/no to an asked question (on perception, attitude, behavior etc.) and the proportion of people (i.e., what percentage of the population) to do so. To quantify the extent of yes/no answers, the question needs to include a numerical metric in the answer. A typical metric attached to a given question is the Likert scale. The lowest number (usually 1) is allocated as "no," and the highest number (typically 5) is allocated as "yes." The respondent chooses a number from 1 to 5 depending on how strongly they feel they can answer yes or no. This scale assumes that the respondent perception and attitude can be measured in linear and even intervals, but that assumption does not always hold. Meanwhile, the use of this kind of scale allows researchers to conduct various statistical analyses. Researchers can also use a verbal scale to ask a respondent to what extent their answer is yes or no. For example, "No," "Lean no," "?," "Lean yes," and "Yes" can be used. When the Likert scale is not used in a questionnaire, the statistical analysis of the study is limited. For instance, a mean (i.e., average) answer cannot be determined, and only median or modal answers can be determined. Meanwhile, the results presented as simple descriptive statistics can avoid unnecessary bias and error associated with statistical treatment. Social-psychology studies are conducted to assess social acceptability at a national level, and the attitude and risk perception of facility placement (e.g., hydrogen stations and pipelines) in order to provide suggestions for communication and discussion of such decisions, outside the economic perspective. When using the two above approaches simultaneously in one study, the social-psychological technique is the main approach, whilst the economic approach is partially adopted.

42.4 Methodology

Two methods are used to assess public acceptability in the economic and social-psychological approaches, namely quantitative and qualitative [7]. The former is mainly obtained from questionnaire surveys and the latter from focus groups and interviews. In this section, points of appropriate implementation of the methodologies are introduced.

42.4.1 Quantitative Assessment

Questionnaire Methodology and Implementation: Methods of questionnaire surveys include mail surveys (paper questionnaire), visit-placement method (paper questionnaire), face-to-face interviews (paper questionnaire + interview), telephone surveys (interview), and online surveys. Face-to-face interviews are the most expensive among those, while mail surveys are relatively less costly. Online surveys are the least expensive. However, both mail and online surveys are difficult to achieve a high response rate. Furthermore, online surveys have a problem in randomness (refer to the following chapter for details).

Sampling and Methods: Securing the representativeness of a sample is an important factor in conducting public surveys. With a representative sample, the results of analyses display some attributes of a subjective population. If a representative sample is not used, the results only show some attributes of that particular sample. Obtaining a highly representative sample should be the first priority in sampling. In order to do so, it is necessary to satisfy the following conditions:

- (a) *Random Sampling from a Target Population:* If a survey targets “The Japanese general public living in areas near existing gasoline stations,” it is an absolute condition that samples are extracted at random from the target population. For example, if an online survey conducts sampling from registrants, even if a random extraction is used, the sample is not a random extraction from the target population because the registrants themselves are not extracted at random.
- (b) *Decent Response Rate:* Response rate is an important index in questionnaire surveys in order to determine representativeness. Surveys related to official government statistics require a response rate of more than 80 or 90 % in order to secure very high representativeness. However in general, social surveys cannot achieve this, owing to budget limitations. In surveys whose response rates are under 30 % (recently many online surveys frequently conducted to collect responses in a short period of time have 10–20 % response rates), response bias is a concern.
- (c) *Securing Sample Size:* A certain quantity of samples (i.e., several hundred) secures the representativeness from the perspective of sample quantity. The

- bigger a sample size, the lower the standard error in responses, therefore bigger sample size is an advantage when examining differences in responses.
- (d) *Less Bias in Basic Attributes:* Basic attributes of respondents such as ages and male or female is likely to impact on responses, therefore, it is desirable that the attributes of the respondents reflect those of the target population as much as possible. This effort does not need to be perfect, because the information of the existing attributes can be revised by giving some weights to a certain groups when collecting responses.

42.4.2 Qualitative Assessment

A focus group is defined as “a group of individuals selected and assembled by researchers to discuss and comment on, from personal experience, the topic that is the subject of the research” [8]. Focus groups are a form of group interviewing but it is important to distinguish between the two. Group interviewing involves interviewing a number of people at the same time, the emphasis being on questions and responses between the researcher and participants. Focus groups however utilize more “group dynamics,” i.e., interaction within the group based on topics that are supplied by the researcher [9]. A focus group is less expensive to conduct and easier to prepare compared to a public survey. It is often conducted as an exploration process in social science to elucidate perception and attitude of the public as well as the logic and reasoning behind specific attitudes and opinions. However, it should be noted that there is no representativeness in a focus group due to the small sample size and dynamic process of data collection.

42.5 Current Status: Awareness, Perception, and Opinion

Public perception and acceptability have been repeatedly studied in Europe, the United States, and Japan over the past two decades. There are some common findings in studies using the social-psychological approach. Acceptability of commodities using hydrogen and fuel cell technologies (such as FCVs) was generally positive, whereas such positive results are not apparent in questions about the location of hydrogen stations. For example, in a quantitative survey conducted in the UK, a positive attitude to hydrogen stations was seen in 25 % of respondents. However, 59 % requested more information, and a negative attitude was found in 9 % [2]. Qualitative research has also shown both negative and positive attitudes and no strong objections [2, 10]. People are found to be more prudent about hydrogen station placement at least partially due to the perception of risk in hydrogen transfer and storage [2]. Therefore, the risk perception of hydrogen use and acceptance of infrastructure including hydrogen station siting is becoming a

major focus of public acceptance studies. Meanwhile, studies using an economic approach have been conducted less frequently compared with the social-psychological approach. This is probably due to the low availability of commercial FCVs. In the following paragraphs, a recent study for each of three regions is discussed. These were chosen because of their understandable presentation, and the results are introduced focusing on awareness, perception and acceptance of hydrogen technologies.

42.5.1 Japan

There are several existing surveys on the social acceptance of hydrogen and fuel cells in Japan, including those by the Mizuho Information and Research Institute (MHIR) commissioned by NEDO in 2008 [11] and 2009 [12], and by Kyushu University in 2015. Here, we present parts of the survey data from MHIR (2008) and Kyushu University (2015) to show the variation in awareness and perception about hydrogen and fuel cells in Japan over time. Table 42.2 shows a brief overview of these two surveys.

Awareness: Compared to other types of energy, awareness of hydrogen energy is not high (Fig. 42.2). About 32 % of respondents have heard of hydrogen as an energy carrier in 2015. This is a much lower value than for nuclear energy, solar energy, or wind energy, at over 80 %. However, since 2008 the percentage of respondents who know about hydrogen energy has increased by 12 points from 20 %.

The awareness of fuel cell technology has increased significantly from 2008 to 2015, especially in terms of FCVs. More than one-third of respondents know about FCVs, and 89 % have heard of FCVs (Fig. 42.3). The awareness of hydrogen stations is at about the same level as the residential fuel cell system (i.e., EneFarm) despite the fact that most respondents have probably never seen a real hydrogen station, whilst residential fuel cell systems have been on the market since 2009.

Table 42.2 Overview of social surveys conducted by NEDO and Kyushu University

	2008 survey	2015 survey
Survey period	February 2008	March 2015
Survey area	Across Japan	
Survey method	Random walk	Internet
Sampling method	Two stage stratified sampling	Stratified sampling
<i>N</i>	1188	3133
Response rate	50.9 %	17.5 %
Average age	49.0	45.4
Ratio of female respondents	51.0 %	50.1 %
Average years of education	13.1	14.1

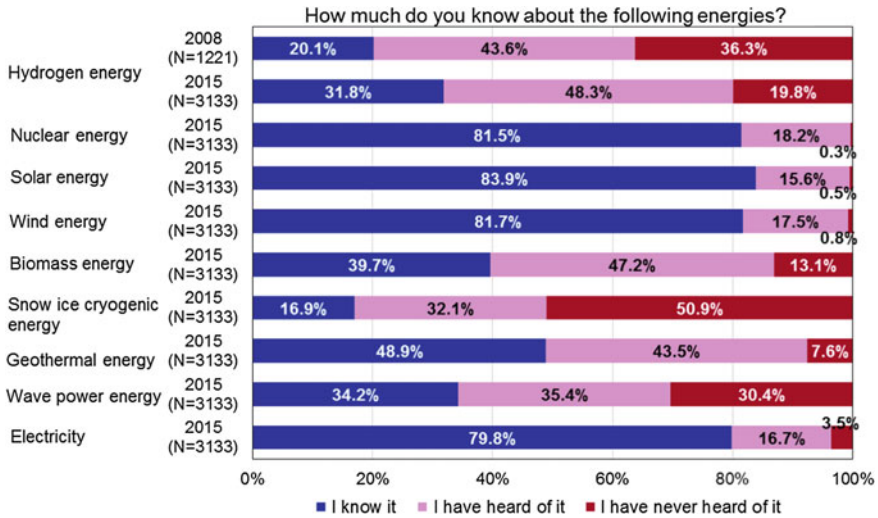


Fig. 42.2 Awareness of renewable energy and secondary energy

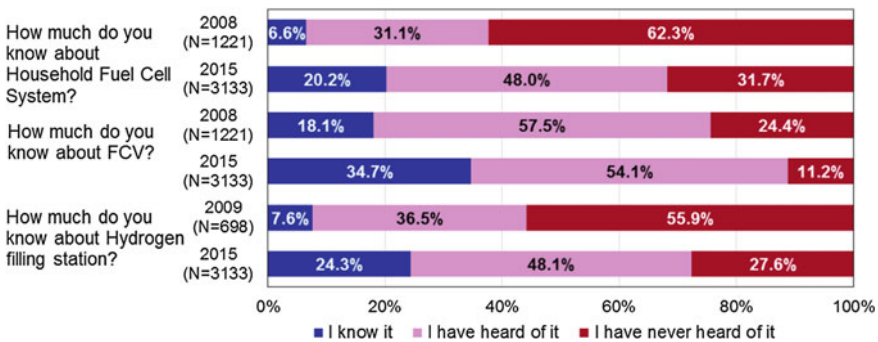


Fig. 42.3 Awareness of household fuel cell system, FCV and hydrogen station

Perception: We gave respondents questions related to hydrogen stations. The questions were created based on opinions collected in focus groups conducted before designing the questionnaire in 2009. For the statements “Hydrogen itself at hydrogen station makes us worried” and “Technical reliability at hydrogen filling station is low,” the tendency of the answers is not much changed from 2009 to 2015 (Fig. 42.4). About 40–50 % of respondents took a neutral position for these questions. As for the statement “We do not know what kind of accidents would happen,” strong agreement decreased, but more than half of respondents supported the statement in 2015. For the statement “Hydrogen stations are needed for society from now on,” agreement decreased significantly but more than half of respondents supported the statement.

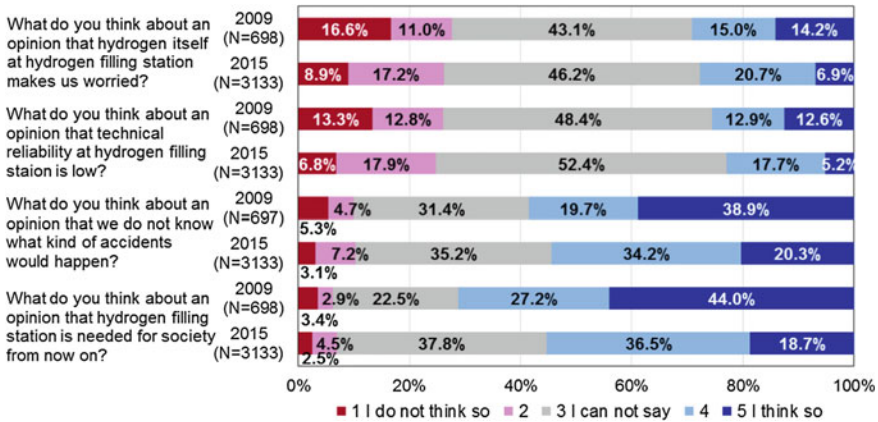


Fig. 42.4 Perception relevant to hydrogen stations

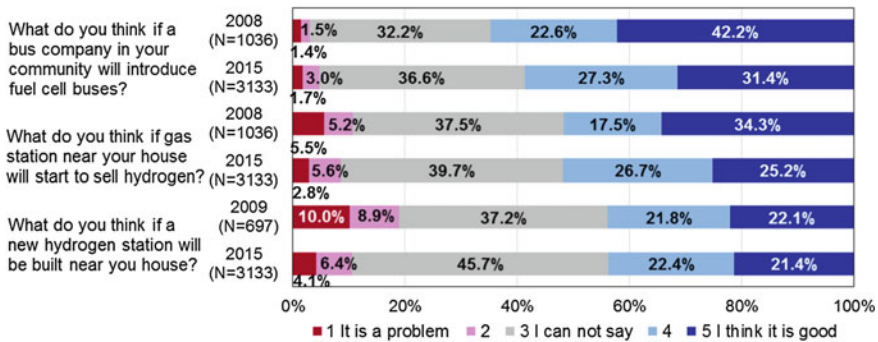


Fig. 42.5 Potential acceptance of hydrogen station and fuel cell bus operated near the respondents' house

Acceptance: To assess acceptability of hydrogen infrastructure in the future, we asked opinions about three hypothetical cases: “if a bus company in your community will introduce fuel cell buses”; “if a gasoline station near your house will start to sell hydrogen,” and “if new hydrogen station will be built near your house.” As for the introduction of fuel cell buses, the positive opinion decreased slightly from 2008 (Fig. 42.5). 52 % of respondents displayed a positive opinion for selling hydrogen at the nearest gasoline station, and 44 % of respondents displayed a positive opinion about locating a new hydrogen station near the respondents' house in 2015, but the percentages have not increased since 2009.

42.5.2 Europe/Germany

In Europe, social acceptance studies on hydrogen technologies have been conducted in Germany [13], the Netherlands [14], Norway [15], Sweden and the United Kingdom [16]. The recent trend is to find determinants using sophisticated statistical methodologies such as structural equation modeling (SEM) [17]. However, as a result of this, the explicit situation of public acceptance of hydrogen technologies has tended to be obfuscated. In the HyTrust project in Germany, several social surveys were conducted with a focus on acceptance of hydrogen technologies and the trust the public puts in technology-driving players, providing relatively clear results [13]. The project was funded by the Federal Ministry of Transport/Nationale Organisation Wasserstoff- und Brennstoffzellentechnologie (NOW), and conducted from September 2009 to August 2013. The results of Computer-Assisted Telephone Interviews (CATI) conducted in the HyTrust project are described below. The total number of respondents, who lived in Germany and were over 18 years old, was 1011.

Awareness: For the statement “Have you ever heard of hydrogen-powered cars?,” 70.6 % of the respondents answered “I have heard or read about them,” and another 15.4 % respondents answered “I have heard about them and have used a hydrogen-powered car/bus” as shown in Fig. 42.6. On the other hand, 13.9 % of the respondents answered “No, never.” These results are similar to awareness of FCVs in Japan.

Perception/Acceptance: Fig. 42.7 shows the results of whether respondents would purchase a hydrogen-powered automobile or a conventional one if they had the choice the next time they bought a car. The automobile respondents chose in this question were designed to have the same conditions (such as price, features, design, brand, etc.) as other types of cars. 63.3 % of respondents chose a hydrogen-powered car, and 23.7 % of respondents chose a conventional car, while

Fig. 42.6 Awareness of hydrogen-powered cars in Germany [13]

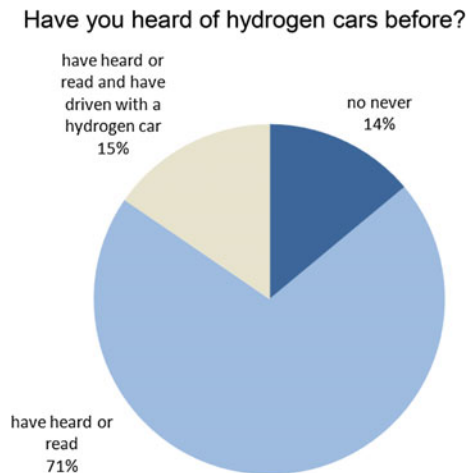


Fig. 42.7 Purchasing preference if price, features, design, and brand, etc. are identical for hydrogen-powered and conventional cars ($n = 1011$) [33]

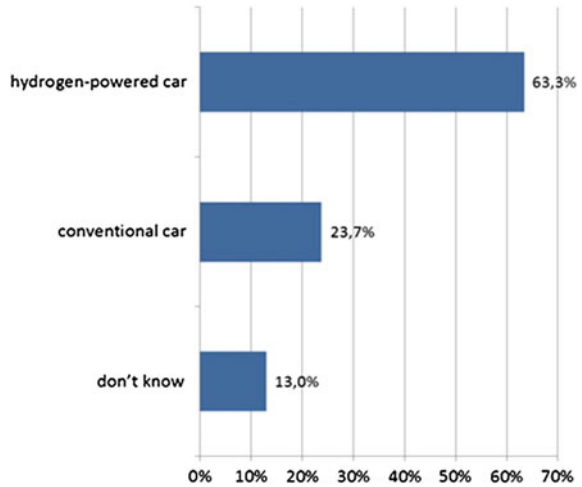
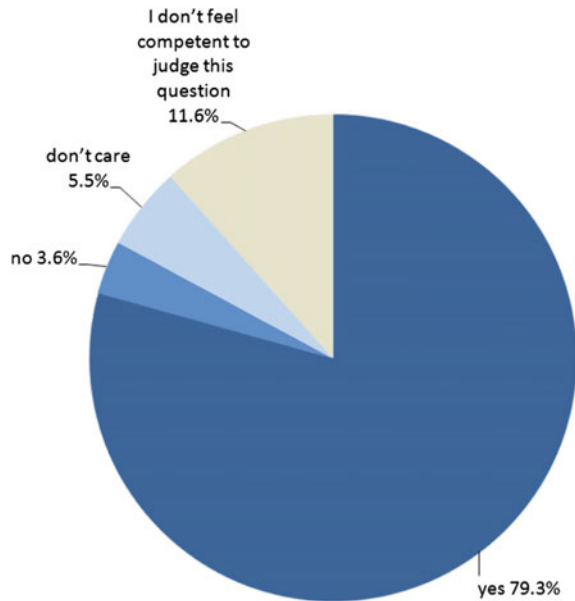


Fig. 42.8 Relevance of the method of producing hydrogen ($n = 1011$) [33]



13.0 % of respondents did not have an opinion. The question “Considering everything you know about hydrogen-powered cars or have just heard about them: Are you for or against the introduction of hydrogen-powered cars?” was asked, and 79 % of respondents answered that they were for the introduction of hydrogen-powered cars (Fig. 42.8).

42.5.3 The United States

In the United States, existing studies conducted in the early or mid 2000s generally focused on hydrogen as alternative automobile fuel, and FCVs. The number of studies conducted has decreased in the 2010s, probably due to the large cut of government funding for research and development of hydrogen technologies at that time. No recent studies are available. The study conducted by the U.S. Department of Energy (DoE) is relatively old but still comprehensive as a public acceptance study, asking the public for knowledge and opinions on hydrogen technologies. The U.S. DoE conducted social surveys targeted to four types of stakeholders: the general public; students; state/local government officials; and potential large-scale users in industries, businesses needing uninterrupted power supply, and transportation.

Awareness: Eleven technical questions related to hydrogen and fuel cells were used to estimate technical knowledge. The results in Fig. 42.9 shows that the percentage of correct answers from the general public and students were low (around 30 %). For every population, the percentage of correct answers for fuel cell questions were lower than those for the other technical questions.

Perception: Fig. 42.10 shows the ratio of agreement on the statements of hydrogen safety in the four survey populations. More respondents in the general public and students would feel hydrogen was dangerous or not safe than those in state/local government officials and potential large-scale user populations.

Acceptance: In terms of acceptance of hydrogen stations (Fig. 42.11), “Pleased or at ease” dominates in each population. The share in “general public and students” is smaller than in the other populations, showing similar results in perception of

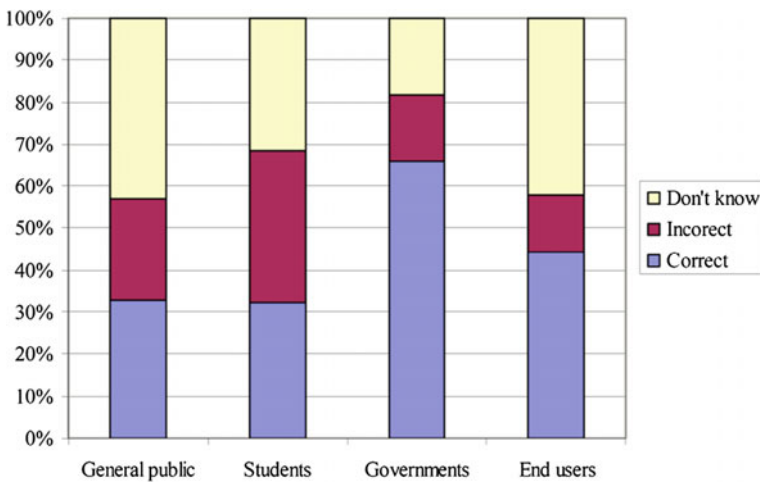


Fig. 42.9 Percentage of correct, incorrect, and “Don’t know” responses to the eleven technical knowledge questions for each of the four populations [23]

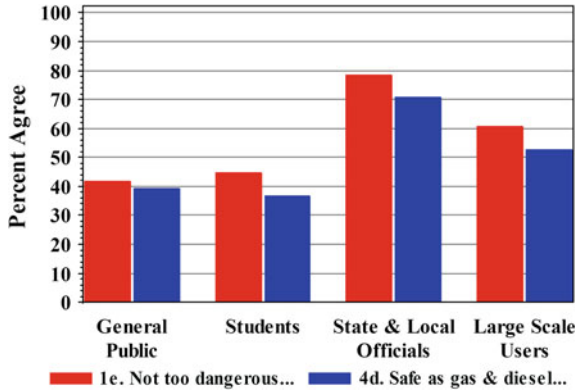


Fig. 42.10 The distribution of responses to safety questions about the everyday use of hydrogen from all four survey populations [24]

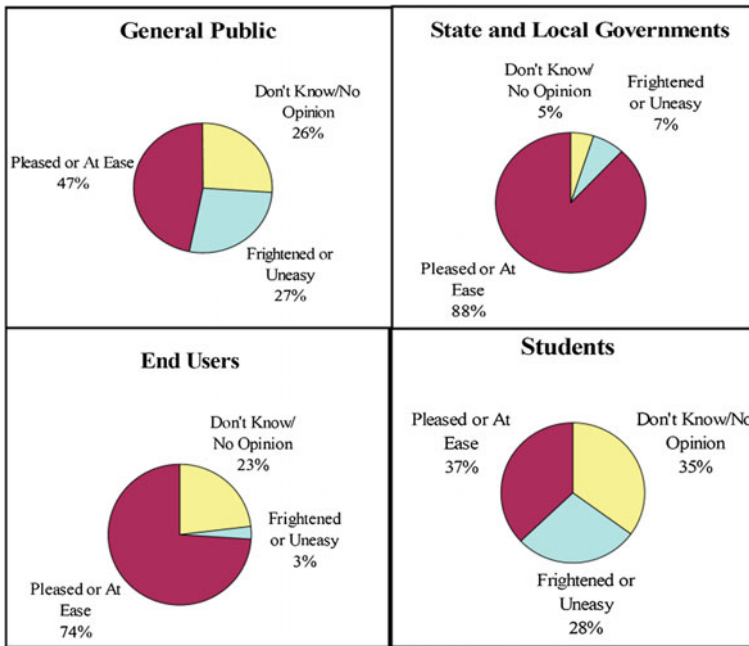


Fig. 42.11 Percentage of responses for each of the four populations to the question, “How would you feel if your local gas station also sold hydrogen?” [23]

hydrogen safety. As shown in Fig. 42.12, technical understanding appeared to influence opinions about safety. For the General Public, Student, and Large-Scale End User Surveys, respondents with above-average scores on the eleven technical

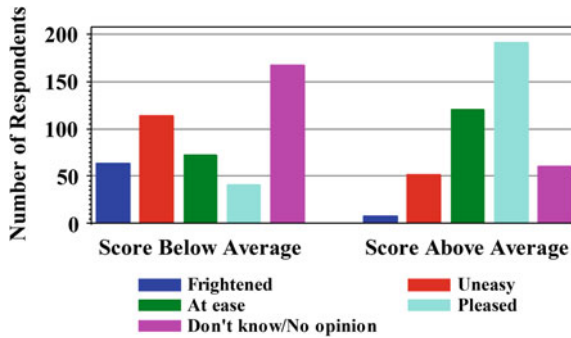


Fig. 42.12 Percentage of responses for each of the four populations to the question, “How would you feel if your local gas station also sold hydrogen?” [24]

questions were more likely to have a positive opinion (i.e., “Pleased” or “At ease”) on selling hydrogen at their local gasoline station.


Based on the results described above, the DOE published the “H2 EDUCATE Teacher Guide” in 2005 to provide information for students and schoolteachers. The DoE has also used another tool “INCREASE YOUR H2IQ,” which consists of factsheets and videos, for the general public from 2006. The factsheets contain technological and political information and market status of hydrogen and FCVs.

42.6 Practice

In order to enhance public acceptance of FCVs, promotion of public experience of real FCVs and hydrogen infrastructure has often been conducted in various countries. In particular in Japan such activities have been heavily promoted, such as tours of hydrogen stations and FCV test-rides for mass media and the public, as well as educational campaigns for schools, etc. The effectiveness was generally qualitatively assessed [18]. In California, FCV test-drive events were held and the influence on perception of hydrogen energy as alternative fuel and hydrogen stations were analyzed quantitatively [19]. In Germany and Italy, driving FCVs and use of hydrogen stations have also been experienced as demonstration projects providing socioeconomic implication [20].

By contrast, for installation of hydrogen stations, no actual practice to improve public acceptance is reported so far, whilst the number of installations of commercial hydrogen stations is still limited. Going back to the principle of public acceptance of citing facilities entailing some risk and benefits, key of appropriate procedures of locating facilities are the concepts of “public participation” [21]. Therefore, we introduce the basic rule and practice of public participation recommended by the International Association for Public Participation (IAP2) [22]. Table 42.3 shows IAP2’s Public Participation Spectrum, which includes goals and

Table 42.3 IAP2 spectrum of public participation [22]

					
	<i>Inform</i>	<i>Consult</i>	<i>Involve</i>	<i>Collaborate</i>	<i>Empower</i>
Public participation goal	To provide the public with balanced and objective information to assist them in understanding the problem, alternatives, opportunities and/or solutions.	To obtain public feedback on analysis, alternatives and/or decisions.	To work directly with the public throughout the process to ensure that public concerns and aspirations are consistently understood and considered.	To partner with the public in each aspect of the decision including the development of alternatives and the identification of the preferred solution.	To place final decision-making in the hands of the public.
Promise to the public	We will keep you informed.	We will keep you informed, listen to and acknowledge concerns and aspirations, and provide feedback on how public input influenced the decision.	We will work with you to ensure that your concerns and aspirations are directly reflected in the alternatives developed and provide feedback on how public input influenced the decision.	We will look to you for advice and innovation in formulating solutions and incorporate your advice and recommendations into the decisions to the maximum extent possible.	We will implement what you decide.
Example techniques	<ul style="list-style-type: none"> • Fact sheets • Web sites • Open houses 	<ul style="list-style-type: none"> • Public comment • Focus groups • Surveys • Public meetings 	<ul style="list-style-type: none"> • Workshops • Deliberative polling 	<ul style="list-style-type: none"> • Citizen advisory committees • Consensus-building • Participatory decision-making 	<ul style="list-style-type: none"> • Citizen juries • Ballots • Delegated decision

promise at each level of public participation. Basic concepts of communication to the public extracted from Table 42.3 and other surveys are listed below:

Maintaining Openness and Transparency of Projects: Laypersons tend to distrust the government and/or project developers if accurate information of projects is not provided. It is therefore important for developers to be open and transparent at all stages of the project and to show their willingness to provide information to the public.

Providing Accurate Information of Projects: Project developers must provide accurate information of projects, as well as contexts and/or circumstances of projects to the public in order to prevent misunderstanding. Information with uncertainty would be provided if necessary. Residents living near hydrogen stations would need information on safety of such stations (i.e., measures for safety during normal operations, types and measures of possible accidents, measures for disasters, etc.) [12].

Providing Information from Reliable Sources: Information should be provided not only from project developers, but also other independent and reliable sources.

Attitude to Work with the Public: Project developers must develop the project with the best technologies, and also work with the public on implementation of hydrogen energy, on behalf of the public and all the stakeholders in the project.

Sharing Awareness and Perception on the Significance of Hydrogen in the Context of National Energy Policy: Japanese national surveys show that the perception “hydrogen is needed for the future society” has positive impact on public acceptance of hydrogen and its utilization technologies [12]. It is important that project developers and governments provide information on the significance of hydrogen in the context of national energy policy, and that they share the perception of needs and their reasons of hydrogen energy for future society with the public.

42.7 Conclusions

Public perception and acceptance of hydrogen and utilization technologies are considered to be important factors for the penetration of hydrogen energy technology into future society. Hydrogen utilization is an emerging technology to the public, and the current status of public acceptance is still unknown in terms of risk and benefits, and especially with the siting of hydrogen infrastructure.

Social acceptance is categorized into three dimensions: sociopolitical acceptance; community acceptance; and market acceptance. Sociopolitical acceptance is relevant to general perception and attitude on hydrogen energy and utilization technology of stakeholders and the general public. Community acceptance is mainly relevant to siting of hydrogen infrastructure including hydrogen stations. Market acceptance is mainly relevant to FCV and hydrogen as a fuel.

There are economic approaches and social-psychological approaches to evaluate social acceptance. The social-psychological approach is mainly used to evaluate sociopolitical acceptance and community acceptance, whilst the economic approach is mainly used to evaluate market acceptance.

In terms of the current status of social acceptance, a significant increase in awareness was found (about 80 % have heard of hydrogen energy and 89 % have heard of FCVs in 2015), as well as a relatively a small improvement in knowledge of hydrogen energy, hydrogen infrastructure and FCVs compared to the status several years ago in Japan. In contrast little change in perception of the risks and benefits of a hydrogen society or public acceptance of hydrogen infrastructure in Japan was found. In Germany, the awareness of hydrogen energy is high (about 80 % had heard or read about hydrogen-powered cars in 2013). Furthermore, at the next opportunity of purchasing a car, the majority expressed a desire to buy a hydrogen-powered car if other conditions including price were equal. In the United States, the latest evidence on public acceptance is not available although public and students used to show rather less safety perception and less pleased opinion on hydrogen technologies compared to local governments and hydrogen users.

In summary, in order to evaluate public acceptance of hydrogen energy and utilization technologies, awareness, perception and attitude of the public to the technologies have been repeatedly assessed by questionnaire surveys across the world. As the Japanese public indicated, awareness of hydrogen energy and FCVs are much improved, probably due to publicity from the media related to FCVs. Meanwhile, knowledge and attitude to hydrogen station siting near the homes of respondents are not changed, but the attitude is still generally positive or neutral. It is important to promote better understanding of social acceptance of hydrogen and utilization technologies.

References

1. Wüstenhagen R, Wolsinkb M, Bürera MJ (2007) Social acceptance of renewable energy innovation: an introduction to the concept 35(5):2683–2691
2. Ricci M, Bellaby P, Flynn R (2008) What do we know about public perceptions and acceptance of hydrogen? A critical review and new case study evidence. *Int J Hydrog Energy* 33(21):5868–5880
3. Eagly AH, Chaiken S (1993) *The psychology of attitudes*. Harcourt Brace Jovanovich College Publishers
4. Ajzen I (1991) The theory of planned behavior. *Organ Behav Hum Decis Process* 50:179–211
5. Gupta N, Fischer AR, Frewer LJ (2011) Socio-psychological determinants of public acceptance of technologies: a review. *Public Underst Sci*, 0963662510392485
6. O'Garra T, Mourato S, Pearson P (2007) Public acceptability of hydrogen fuel cell transport and associated refuelling infrastructures. In: Flynn R, Bellaby P (eds) *Risk and the public acceptance of new technologies*. Palgrave Macmillan, Basingstoke, pp 126–153
7. Roche MY, Mourato S, Fishedick M, Pietzner K, Viebahn P (2010) Public attitudes towards and demand for hydrogen and fuel cell vehicles: a review of the evidence and methodological implications. *Energy Policy* 38:5301–5310
8. Powell RA, Single HM (1996) Focus groups. *Int J Qual Health Care* 8(5):499–504
9. Morgan DL (1997) *Focus groups as qualitative research*, 2nd edn. Sage Publications, London
10. Xiong C, Li D, Jin L (2008) Draft consensus building in hall for workshop of meta-synthetic engineering. *Wuhan Univ J Nat Sci* 13(1):45–49
11. Mizuho Information and Research Institute (2008) *Suiso shakaijuyousei ni kansuru chousa (Hydrogen's social acceptance research)* (in Japanese)
12. Mizuho Information and Research Institute (2009) *Nenryoudenchi, suiso ni kansuru shakaijuyouseichousa (PEFC, Hydrogen's social acceptance research)* (in Japanese)
13. Zimmer R (2011) *Full steam ahead? Hydrogen Technology between Technological Vision and Public Acceptance*
14. Huijts NMA, Van Wee B (2015) The evaluation of hydrogen fuel stations by citizens: the interrelated effects of socio-demographic, spatial and psychological variables. *Int J Hydrog Energy* 40(33):10367–10381
15. Tarigan AKM, Bayer SB, Langhelle O, Thesen G (2012) Estimating determinants of public acceptance of hydrogen vehicles and refuelling stations in greater Stavanger. *Int J Hydrog Energy* 37(7):6063–6673
16. O'Garra T, Mourato S, Pearson P (2008) Investigating attitudes to hydrogen refueling facilities and the social cost to local residents. *Energy Policy* 36(6):2074–2085
17. Huijts NMA, Molin EJE, Van Wee B (2014) Hydrogen fuel station acceptance: a structural equation model based on the technology acceptance framework. *J Environ Psychol* 38: 153–166

18. Horii H, Okumura N, Kawakami A, Maeda S, Tezuka T (2014) Efforts on the public acceptance improvement of FCV and hydrogen stations (in Japanese). *J Hydrog Energy Syst Soc Jpn* 39(3):177–180
19. Martina E, Shaheena SA, Lipmanc TE, Lidicker JR (2009) Behavioral response to hydrogen fuel cell vehicles and refueling: results of California drive clinics. *Int J Hydrog Energy* 34 (20):8670–8680
20. Lienkamp H, Rasatogi A (2012) Achievements and lessons learnt in the EU Project Zero Regio, Procedia-Social and Behavioral Sciences, 48, PP2201–2210, Transport Research Arena, Europe
21. Rowe G, Frewer LJ (2000) Public participation methods: a framework for evaluation. *Sci Technol Hum Values* 25(1):3–29
22. IAP2 (International Association for Public Participation) (2014) IAP2's Public Participation Spectrum
23. Cooper C, Truett T, Schmoyer RL (2006) The U.S. department of energy hydrogen baseline survey: assessing knowledge and opinions about hydrogen technology. In: Abstracts of WHEC 16, Lyon, France, 13–16 June 2006
24. Schmoyer RL, Truett T, Cooper C (2006) Results of the 2004 knowledge and opinions surveys for the baseline knowledge assessment of the U.S. department of energy hydrogen program. In: Report prepared for the U.S. Department of Energy
25. Bzostek R, Rogers A (2014) Oslo +20: reassessing the role of confidence building measures. *Soc Sci J* 51(2):250–259
26. Shogakukan (2015) Degital daigisen. <https://kotobank.jp/word/%E7%A4%BE%E4%BC%9A%E7%9A%84%E5%8F%97%E5%AE%B9%E6%80%A7-681590>. Date of access: 28 Dec 2015
27. Higher Education Funding Council for England: Beacons for Public Engagement (2006)
28. Goodfellow EM (1980) Public relations and promotion: a few ideas for group practices. *Gr Pract J* 29(9):5–7, 26
29. U.S. Department of Energy (2013) Best practice for: public outreach and education for carbon storage projects
30. Dowler E, Bauer MW, Green J, Gasperoni G (2006) Assessing public perceptions: issues and methods. In: Dora Carlos (ed) Health, hazard and public debate: lessons for risk communication from the BSE/CJD Saga. WHO, Geneva, pp 40–60
31. Vääntänen A, Marttunen M (2005) Public involvement in multi-objective water level regulation development projects—evaluating the applicability of public involvement methods. *Environ Impact Assess Rev* 25(3):281–304
32. Rowe G, Frewer LJ (2000) Public participation methods: a framework for evaluation. *Sci Technol Human Values* 25(1):3–29
33. Zimmer R, Welke J (2012) Let's go green with hydrogen! The general public's perspective. *Int J Hydrog Energy* 37:17502–17508

Chapter 43

Numerical Analysis of the Optimal Distribution of Hydrogen Filling Stations

Yuya Tachikawa, Teppei Sugiura, Motoaki Shiga, Ryusuke Chiyo
and Kazunari Sasaki

Abstract This chapter describes possible numerical analysis for optimizing the distribution of hydrogen filling station. An algorithm is described to simulate the optimal geographical distribution of new hydrogen stations. A case study to specify possible locations of additional hydrogen filling stations in Japan is described, using statistical data on traffic flow, local employee numbers, and population in each region.

Keywords Hydrogen filling station · Fuel cell vehicles · Simulation algorithm · Statistical data · Population · Traffic flow · Optimal locations

43.1 Introduction

The Japanese Ministry of Economy, Trade and Industry (METI) has recently published their strategic road map for hydrogen and fuel cells [1], and a strategic energy plan [2]. They highlight that the MIRAI FCV launched in December 2014 by Toyota Corporation is a key technology toward realization of a hydrogen society. In order to accelerate the commercialization and acceptance of FCVs, a network of hydrogen filling stations should be established. However, the initial cost to set up a hydrogen filling station is extremely high. Therefore, the distribution of

Y. Tachikawa (✉)

Center for Co-Evolutional Social Systems (CESS), Kyushu University, 744, Motoooka,
Nishi-ku, Fukuoka 819-0395, Japan
e-mail: tachikawa.yuya.657@m.kyushu-u.ac.jp

T. Sugiura · M. Shiga · R. Chiyo

Kozo Keikaku Engineering Inc., 4-38-13 Honcho, Nakano-Ku, Tokyo 164-0012, Japan
e-mail: teppei-sugiura@kke.co.jp

K. Sasaki

International Research Center for Hydrogen Energy, Kyushu University, 744, Motoooka,
Nishi-ku, Fukuoka 819-0395, Japan
e-mail: sasaki@mech.kyushu-u.ac.jp

hydrogen stations should be optimized to fulfill the FCV fuel demand with the lowest initial investment. Such optimization has already been performed for hydrogen infrastructure deployment in California [3] and Spain [4]. In order to evaluate the optimal distribution of hydrogen stations in Japan, a numerical simulation tool has been developed to model the potential hydrogen supply and demand based on published station location data. Such models can help to theoretically determine the optimal locations for new station deployment. In this chapter, the numerical analysis of results obtained from this model is presented.

43.2 Simulation Algorithm

A framework of the station location simulation is presented in Fig. 43.1. The hydrogen demand for refueling FCVs is calculated using a geographic information system (GIS) database, which includes statistical data about, e.g., traffic flow, local employee numbers, population, etc. in each region. It is assumed that the statistical data for FCVs and their users is linearly distributed. Based on the refueling capacities of already-established or planned commercial hydrogen stations in Japan [5], the distribution of potential hydrogen supply can be calculated. Based on the GIS database, the distribution of hydrogen demand for refueling FCVs can also be calculated. Using these two distributions, the simulation can automatically calculate the optimum site to establish a new station. Furthermore, the effect of an additional station with a manually selected location can be investigated.

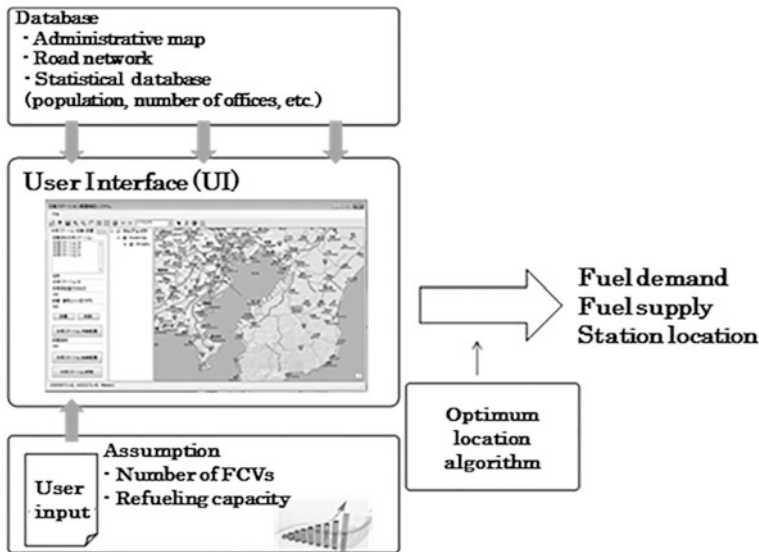


Fig. 43.1 Schematic diagram simulating the optimal geographical distribution of new hydrogen stations

The optimum location for deployment of new hydrogen stations is selected by looking for the site where the highest fuel demand is observed. The fuel demand (D_{ST}) is calculated using the FCV hydrogen demand, and the station hydrogen supply using Eq. 43.1.

$$D_{ST} = N_{Car} \times F_{FCV} \times \frac{B_{ST}}{B_{Total}} \times D_{FCV} - S_{ST} \quad (43.1)$$

where N_{Car} is the total number of FCVs, F_{FCV} is the ratio of FCV ownership to the total number of vehicles in Japan, B_{ST} is the total number of employees in the vicinity of the hydrogen station as determined from the GIS database, B_{Total} is the total number of employees in Japan, D_{FCV} is the amount of hydrogen needed by the FCV, and S_{ST} is the total amount of hydrogen supplied by the station.

43.3 Optimal Locations for Hydrogen Stations

The whole of the Japanese region was considered in simulating the optimal locations of hydrogen stations. Figure 43.2 shows the distribution of the 81 established or planned commercial hydrogen stations in Japan, as of autumn 2015. Exact addresses of the hydrogen stations were obtained from [5], and the location was assumed to be the prefectural capital when an exact address was not available. Simulations were performed using the hydrogen station distribution as an initial

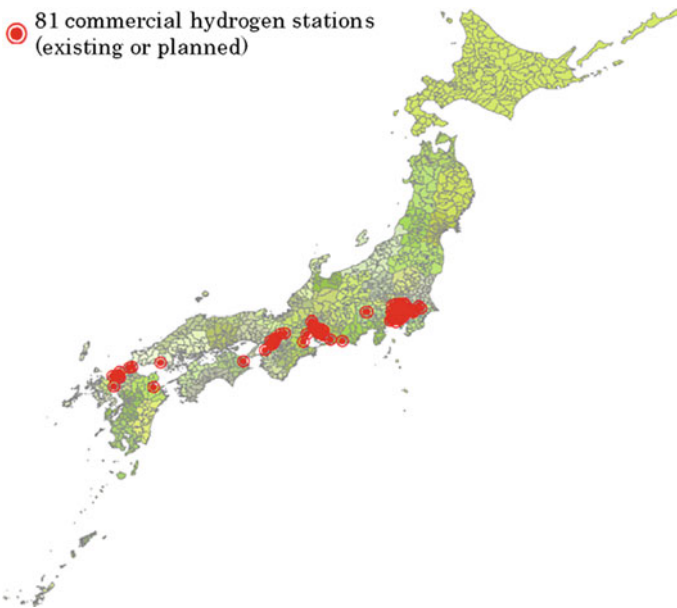


Fig. 43.2 Distribution of 81 existing and planned commercial hydrogen stations in Japan [5]

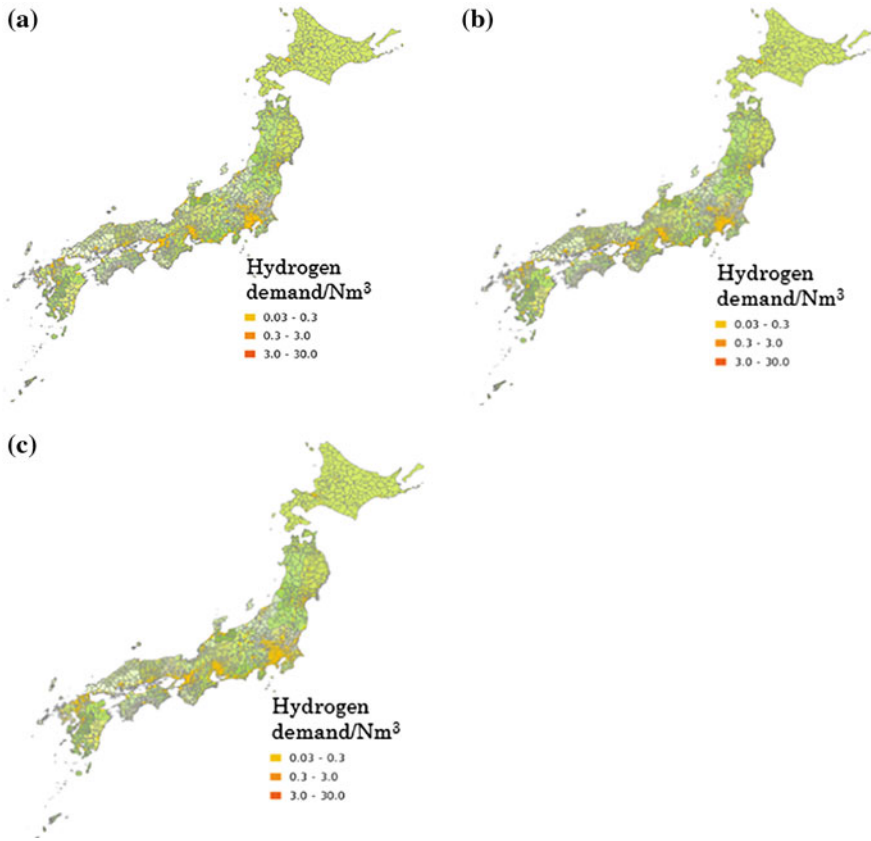


Fig. 43.3 Simulated distributions of hydrogen demand from 1000 FCVs in Japan, based on **a** local employee numbers, **b** population, and **c** traffic flow

condition, as well as the fact that approximately 1000 FCVs are currently being used in Japan. Simulated hydrogen demand distribution for all of Japan is presented in Fig. 43.3. Three cases are explored, in which (a) number of employees, (b) local population, and (c) traffic flow are taken into account. The hydrogen demand in all three cases is concentrated in urban metropolitan areas, and the three cases have roughly the same distribution. The distribution of hydrogen demand specifically in the South Kanto area is shown in Fig. 43.4, using (a) population and (b) traffic flow as inputs. In this case, hydrogen demand is more widely distributed toward the suburbs when traffic flow is used as an input rather than local population.

In the Kyushu and Yamaguchi prefectures (i.e., the Kyushu–Yamaguchi region) there are 11 existing and planned commercial hydrogen stations as of September 2015. As a test case, the deployment of 9 new hydrogen stations in this region was simulated. The results based on (a) number of local employees and (b) traffic flow are presented in Fig. 43.5. These results show that the optimal locations of new stations when the number of employees in the area is taken into account are near the

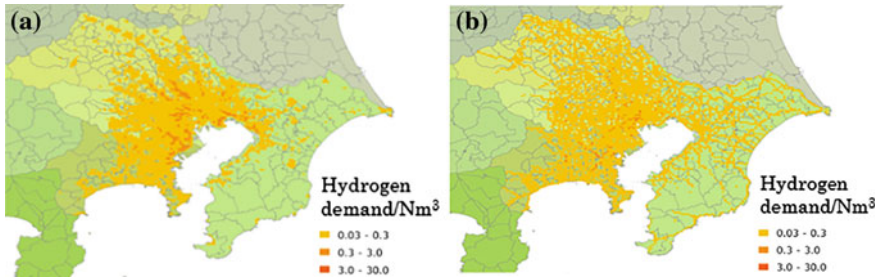


Fig. 43.4 Simulated hydrogen demand in the South Kanto area, based on **a** population, and **b** traffic flow

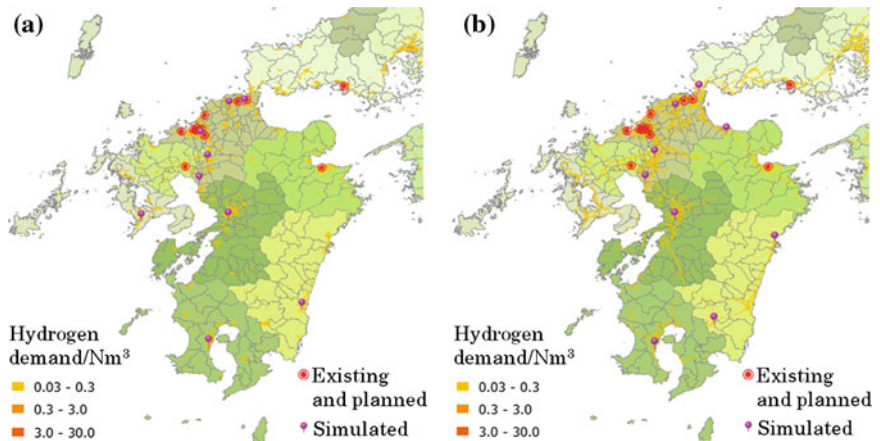


Fig. 43.5 The location of 11 existing and planned hydrogen stations in the Kyushu–Yamaguchi region, overlaid with the optimal simulated locations of 9 new hydrogen stations, based on **a** local employee distribution, and **b** traffic flow

prefectural capitals, and are concentrated in northern Kyushu. However, when traffic flow is taken into account, the distribution is more evenly distributed across the whole Kyushu–Yamaguchi area.

43.4 Conclusions and Perspectives

An algorithm for the simulation of the optimum location for hydrogen stations was developed, using input parameters such as FCV distribution, local populations, and traffic conditions. The model was applied to Japan as a whole, the South Kanto region, and the Kyushu–Yamaguchi region. From the simulation results based on population, the distribution of new hydrogen stations should be concentrated near

metropolitan urban areas. When the simulation results are based on traffic flow, a more even optimal distribution of hydrogen stations is obtained. This suggests that in the early adoption period when FCV users are few, and most FCVs are used as official vehicles, the optimum locations should be simulated using the number of employees/local population. Once the FCV is popularized, the optimal location of new hydrogen stations should be determined using traffic flow.

References

1. Agency for Natural Resources and Energy (2014) Ministry of economy, Trade and Industry, Strategic Road Map for Hydrogen and Fuel Cells, Japan. http://www.meti.go.jp/english/press/2014/0624_04.html. Accessed 27 Sep 2015
2. Agency for Natural Resources and Energy (2014) Ministry of economy, Trade and Industry, Strategic Energy Plan, Japan. http://www.enecho.meti.go.jp/en/category/others/basic_plan/pdf/4th_strategic_energy_plan.pdf. Accessed 27 Sept 2015
3. Stepheno-Romero SD, Brown TM, Kang JE, Recker WW, Samuelsen GS (2010) Systematic planning to optimize investments in hydrogen infrastructure deployment. *Intl J Hydrog Energy* 35:4652–4667
4. Brey JJ, Carazo AF, Brey R (2010) Using AHP and binary integer programming to optimize the initial distribution of hydrogen infrastructures in Andalusia. *Intl J Hydrog Energy* 37:5372–5384
5. Toyota Motor Corporation (2015) MIRAI homepage. <https://ssl.toyota.com/mirai/fcv.html>. Accessed 27 Sep 2015

Chapter 44

Hydrogen Energy Education

Kazunari Sasaki and Kohei Ito

Abstract This final chapter considers educational activity for hydrogen energy engineering, including hydrogen production, hydrogen storage, hydrogen utilization with fuel cells, hydrogen safety, while social and industrial aspects such as energy policy and public acceptance should be taken into account. The concept, experiences, and educational activities are described in Department of Hydrogen Energy Systems in Graduate School of Engineering, Kyushu University, where graduate students can have a clear overview on hydrogen energy and can learn related scientific aspects.

Keywords Scientific discipline · Hydrogen production · Hydrogen storage · Hydrogen utilization · Fuel cells · Hydrogen safety · Carrier development pathways

44.1 Introduction

Hydrogen energy technology is expected to become a key technology in realizing a low-carbon society. Before we can realize the widespread use of hydrogen energy, it will be necessary to solve several technological issues and to develop new/alternative technologies. Hydrogen energy is a challenging field of research, because a research result could be a technical breakthrough to drastically change energy society. It is also an area where students and young researchers can make revolutionary contributions to the future world.

K. Sasaki (✉)
International Research Center for Hydrogen Energy,
Kyushu University, Fukuoka 819-0395, Japan
e-mail: sasaki@mech.kyushu-u.ac.jp

K. Ito
Department of Mechanical Engineering, Faculty of Engineering,
Kyushu University, Fukuoka 819-0395, Japan
e-mail: kohei@mech.kyushu-u.ac.jp

44.2 Education at a Graduate School Level

Graduate school level education is essential to educate future leaders for this technological field. As an example, we describe our decade-long experience in educational programs. The Hydrogen Energy Systems Course is now being offered in the Graduate School of Engineering at Kyushu University, since April 2010. This course is the first of its kind in the world, and offers a consistent education in science and technology related to hydrogen energy. For the realization of a low-carbon society, this new course aims to develop researchers and engineers who will master the basic scientific principles of environmentally friendly energy technologies, including hydrogen energy technology.

Scientific disciplines related to hydrogen energy are schematically summarized in Fig. 44.1. Mechanical engineering can be a basis for energy system design. Since hydrogen is produced and used by conversion of energy resources, it is also essential to understand the processes of chemical reactions. It is also necessary to understand the design of materials such as various metals, polymers, and ceramics to be used in such energy systems. In addition, knowledge regarding safety is required to promote public acceptance of hydrogen technologies as safe and secure. Since these scientific fields of study are common in the energy technologies, the Hydrogen Energy Systems Course takes an interdisciplinary approach to provide an education in energy technology focusing on hydrogen energy. Related industrial fields are schematically illustrated in Fig. 44.2.

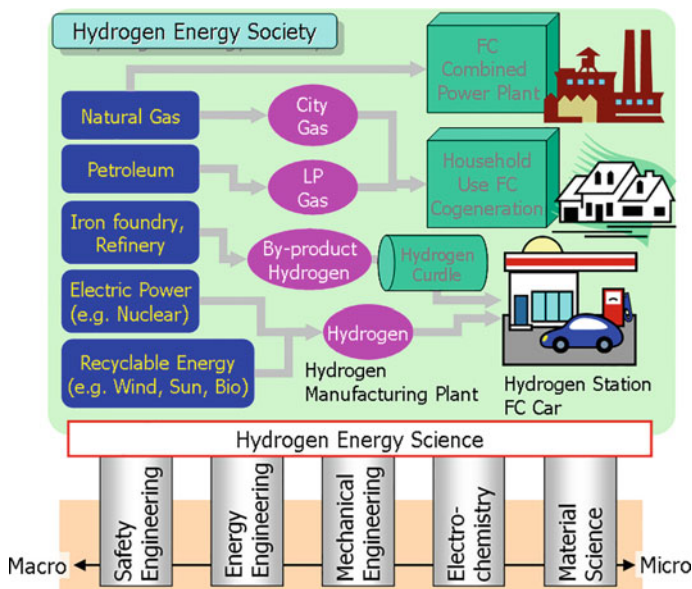


Fig. 44.1 Scientific disciplines for hydrogen energy

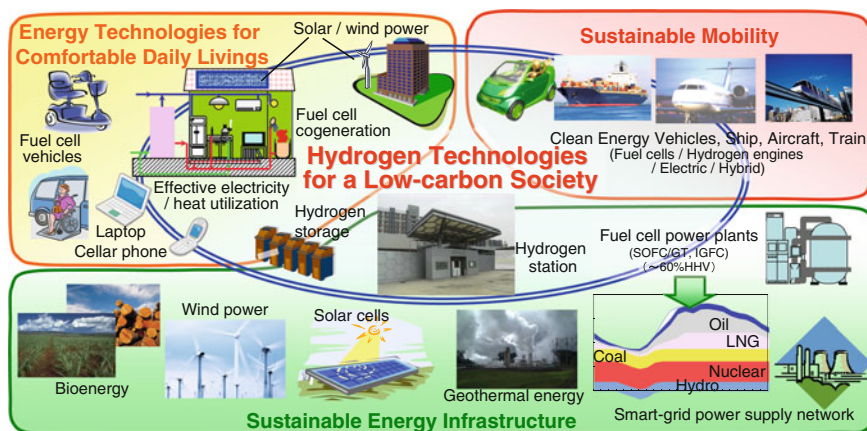


Fig. 44.2 Related technologies and industrial fields

General and Global courses are available in the master's program, and the Advanced Global Course is available in the doctoral program. Japanese language skills are NOT essential to complete these graduate studies at both the master and

Table 44.1 Major lectures available in the hydrogen energy systems course

Lectures	Year-semester	Lectures	Year-semester
Hydrogen Production	1-Winter	Structural Materials	1-Summer
Hydrogen Storage	1-Winter	Functional Materials	1-Winter
Hydrogen Utilization Processes	1-Summer	Electrochemistry	1-Winter
Hydrogen Utilization Systems	1-Winter	Fuel Cell Systems	1-Winter
Hydrogen Energy Society	1-Summer	Energy Policy	1 or 2-Summer
Safety Management	1-Summer	Technology Management	1 or 2-Summer
Hydrogen Energy Engineering	1-Summer	Advanced Energy Engineering I	1 or 2-Summer
Clean Energy Technologies	1-Winter	Advanced Energy Engineering II	1 or 2-Summer
Fatigue Strength	1-Summer	Fundamental Mechanical Eng. I	
Tribology	1-Summer	Fundamental Mechanical Eng. II	
Heat and Mass Transfer	1-Summer	Fundamental Mechanical Eng. III	
Reactive Gas Dynamics	1-Summer	Engineering Analysis I	
Mechanical Vibration and Acoustics	1-Summer	Engineering Analysis II	
Computational Mechanics	1-Summer	Japanese Industry	

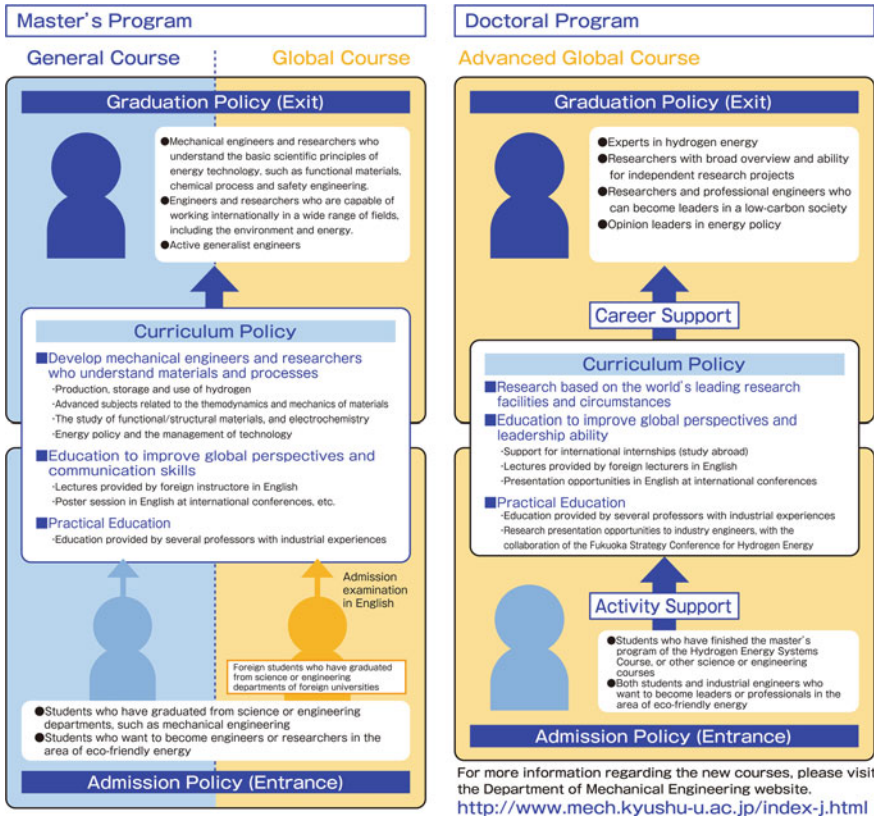


Fig. 44.3 Admission, curriculum and graduation policies

Ph.D degree levels. Lectures available in the Hydrogen Energy Systems Course are listed in Table 44.1. Under the admission, curriculum and graduation policies shown in Fig. 44.3, this course will present a clear path to develop the talents needed to lead a hydrogen energy society. An overview of carrier development pathways is schematically described in Fig. 44.4.

Students of the Hydrogen Energy Systems Course in the doctoral program can request financial assistance to allow them to concentrate on their studies. Moreover, we can help them build their careers together with the Fukuoka Strategy Conference for Hydrogen Energy and other collaborative institutions such as International Research Center for Hydrogen Energy and Next-Generation Fuel Cell Research Center (NEXT-FC). Students can join the university either from April 1 (from Spring Semester) or from October 1 (from Autumn Semester), after the entrance examinations. For more detailed information including the entrance examinations, please see the official homepage of Faculty of Engineering, Kyushu University [1].

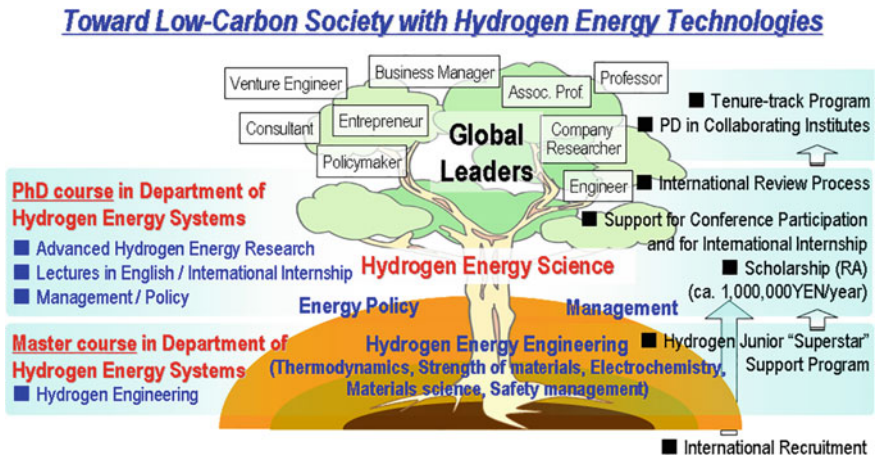


Fig. 44.4 Carrier development pathways

44.3 Educational Courses for Different Levels

For the popularization of hydrogen energy technologies, an increasing number of people should be involved in such activities. Whilst university graduates with higher educational degrees may contribute to the research and development of advanced technologies, corporate managers should have a good overview on this technology and technicians are needed for daily operation of hydrogen-related facilities, e.g., hydrogen filling stations. In the long term, we should stimulate younger generations including high school students to have a certain interest in such future energy technologies.

Responding to demand from industries, as an example, the Fukuoka Strategy Conference for Hydrogen Energy and the International Research Center for Hydrogen Energy jointly offer courses at the Fukuoka Personnel Training Center for Hydrogen Energy throughout the year for business managers and engineers. Table 44.2 summarizes the comprehensive educational program over the past decade, covering the educational needs and social interest for different levels. These courses provide industrial engineers with a wide basis of education relating to hydrogen and fuel cell technologies. In 2011, fuel cell vehicle course aimed at business managers and corporate executives, who are engaged in automotive and related industries started. Lectures are given on development trends and market forecasting for fuel cell vehicles, which were launched into the domestic market in 2014. Since the center opened in 2005, a total of >1,000 students and company employees have attended the courses to deepen their knowledge of hydrogen and fuel cells. Such programs, open to the public, will surely improve the industrial basis for these new technologies as well as the public acceptance of hydrogen

Table 44.2 Educational program on different levels, an example, by Kyushu University and the Fukuoka strategy conference for hydrogen energy

For businesses	Managers	<ul style="list-style-type: none"> • Fukuoka Personnel Training Center for Hydrogen Energy (Business managers' general course) This course is intended for corporate executives who are interested in hydrogen energy. In addition to basic knowledge about the characteristics of hydrogen and fuel cells, the market trends and technologies/requirements needed for new entrants into the market are explained in a simplified manner.
		<ul style="list-style-type: none"> • Fukuoka Personnel Training Center for Hydrogen Energy (Business managers' fuel cell vehicle course) This course is intended for corporate executives who are in automobile or related industries. The course provides the development trend of fuel cell vehicles and explanations for market forecasting after 2015.
	Engineers	<ul style="list-style-type: none"> • Fukuoka Personnel Training Center for Hydrogen Energy (Engineers' course) This course is intended for engineers at hydrogen related companies that wish to enter the market. Professors from Kyushu University and engineers from leading hydrogen—related companies deliver lectures on a broad range of issues and provide hands—on training.
For students	Ph.D. course	<ul style="list-style-type: none"> • Doctoral course, Department of Hydrogen Energy Systems An international doctoral course is open since April 2010. Ph.D. students can perform various fuel cell and hydrogen related research using advanced research facilities. International and industrial collaborations and financial support for Ph.D. students are also important futures of this course.
	Master course	<ul style="list-style-type: none"> • Master's course, Department of Hydrogen Energy Systems A master course is also open since April 2010. This international masters' degree course is suitable for foreign students for which many lectures are given in English. Lectures cover wide scopes of fundamentals of energy technologies, including thermodynamics, strength of materials, electrochemistry, functional materials, safety management, as well as hydrogen production, storage, and utilization technologies.
For children/members of the public		<ul style="list-style-type: none"> • Public programs, environmental education classes, etc. To raise awareness of fuel cells and energy/environmental issues, open lectures are held for the public and for local elementary/junior high school students on the use of the hydrogen energy utilizing technology and the research facilities of Kyushu University. Assistance is provided to local municipalities when they host an environmental education class or other activities.

energy. Figure 44.5 shows the members of professors, students, researchers, technicians, and support stuffs of this activity.

We really hope that an increasing number of younger students, engineers, and researchers will have more interest in this promising energy technology for the future.

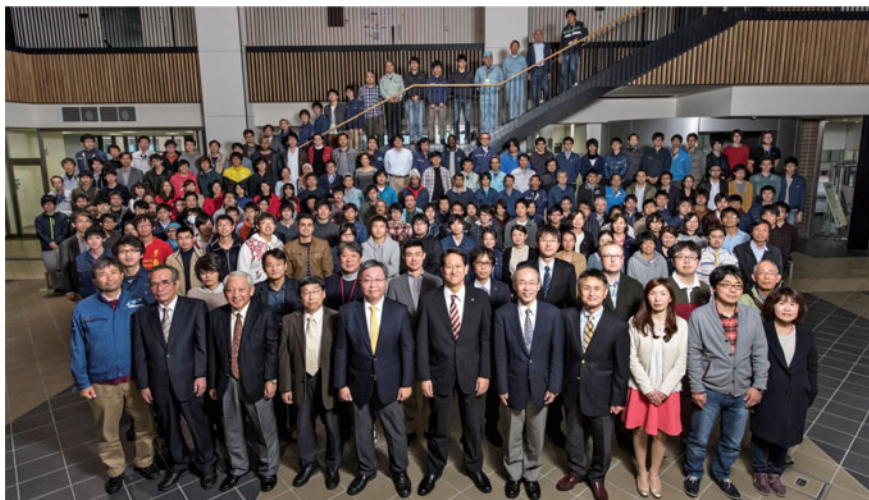


Fig. 44.5 Hydrogen energy research and education team members, including professors, students, researchers, technicians, and support staffs in Kyushu University

Reference

1. Home page of Department of Hydrogen Energy Systems (2015) Graduate School of Engineering, Kyushu University. <http://www.eng.kyushu-u.ac.jp/e/index.html>. Accessed 10 Dec 2015